

Using a Supramolecular Approach for the Design and Synthesis of Molecules Displaying Exotic Spin Topologies

Zur Erlangung des akademischen Grades eines

DOKTORS DER NATURWISSENSCHAFTEN

(Dr. rer. nat.)

von der KIT-Fakultät für Chemie- und Biowissenschaften

des Karlsruher Instituts für Technologie (KIT)

genehmigte

DISSERTATION

von

Yannik Schneider

1. Referentin: Prof. Dr. Annie K. Powell

2. Referent: Prof. Dr. Horst Geckeis

Tag der mündlichen Prüfung: 07.02.2025



This document is licensed under a Creative Commons Attribution-NonCommercial-ShareAlike 4.0 International License (CC BY-NC-SA 4.0):
<https://creativecommons.org/licenses/by-nc-sa/4.0/deed.en>

I. Eidesstattliche Erklärung

Bei der eingereichten Dissertation zu dem Thema

Using a Supramolecular Approach for the Design and Synthesis of Molecules Displaying Exotic Spin Topologies

handelt es sich um meine eigenständig erbrachte Leistung.

Ich habe nur die angegebenen Quellen und Hilfsmittel benutzt und mich keiner unzulässigen Hilfe Dritter bedient. Insbesondere habe ich wörtlich oder sinngemäß aus anderen Werken übernommene Inhalte als solche kenntlich gemacht.

Die, Arbeit oder Teile, davon habe ich bislang nicht an einer Hochschule des In- oder Auslands als Bestandteil einer Prüfungs- oder Qualifikationsleistung vorgelegt.

Die Richtigkeit der vorstehenden Erklärungen bestätige ich.

Die Bedeutung der eidesstattlichen Versicherung und die strafrechtlichen Folgen einer unrichtigen oder unvollständigen eidesstattlichen Versicherung sind mir bekannt.

Ich versichere an Eides statt, dass ich nach bestem Wissen die reine Wahrheit erklärt und nichts verschwiegen habe.

.....

Ort und Datum

.....

Unterschrift

II. Note

Ions shown in illustrations are not to scale. Organic hydrogen atoms have usually been omitted for clarity. Atoms and ions are shown in the following colours in all illustrations:

Element	Colour
Br	Orange
C	Grey
Cl	Pale green
Cu	Cyan
Dy	Lilac
Eu	Pale red
F	Yellow
Fe	Green
H	White
Ho	Rose
I	Purple
N	Blue
O	Red
Sm	Pale yellow
Tb	Light orange
Y	Pale grey
Yb	Dark blue

Numerical quantities such as bond lengths and angles are given with their standard uncertainties in round brackets after the respective values and refer to last digits.

This thesis was prepared from 1st of January 2023 to 27th of December 2024 at the Institute of Inorganic Chemistry (AOC), Faculty of Chemistry and Biosciences of the Karlsruhe Institute of Technology (KIT) under the supervision of Prof. Dr. Annie K. Powell.

III. List of Abbreviations

μ	magnetic moment
μ_0	permeability in vacuum
μ_B	Bohr magneton
A	absorbance
abc	crystallographic reference frame
ab'c*	orthogonal reference frame
AC	alternating current
acac	acetylacetonate
ampdH ₂	2-amino-2-methyl-1,3-propanediol
azo triangle	Dy ₃ triangle with pdavan type ligand
B	magnetic flux density
Br-van	5-Br-2-hydroxy-3-methoxy-benzaldehyde
B _{sw}	switching field
c	concentration
C	Curie constant
CASOCI	complete active space spin-orbit configuration interaction
CASSCF	complete active space self-consistent field
CCC	cyclic coordination cluster
CCD	charge coupled device
CCDC	Cambridge crystallographic data centre
χ	magnetic susceptibility
χ_M	molar magnetic susceptibility
χ_{para}	paramagnetic contribution to χ
Cl-van	5-Cl-2-hydroxy-3-methoxy-benzaldehyde
CN-van	5-CN-2-hydroxy-3-methoxy-benzaldehyde
(Cp) ⁻	cyclopentadienyl
(Cp*) ⁻	pentamethyl cyclopentadienyl
(Cp ^{iPr5}) ⁻	penta-isopropyl cyclopentadienyl
d	optical pathlength
D	axial crystal field splitting parameter
D	Donor
DC	direct current
deaH ₂	dithanol amine
ΔmOD	change in milli optical density
ΔOD	change in optical density
DFT	density functional theory
DMF	dimethylformamide
E	electric field
EA	elemental analysis
EDA	energy decomposition analysis
E _e	excitation energy
ELF	electron localisation function
ϵ	compression factor
ESA	excited state absorption
Et ₃ N	triethylamine
Et-deaH ₂	ethyldiethanolamine

ξ	Euler angle
EtOH	ethanol
Et-teaH ₃	ethyltriethanolamine
FM	ferromagnetic state
fs	femtosecond
FTO	ferrotoroidic order
GSB	ground state bleaching
H	magnetic field strength
H ₂ bovh	(E)-N'-benzylidene-2-hydroxy-3-methoxybenzohydrazide
H ₂ mfbovh	(E)-N'-3-fluorobenzylidene-2-hydroxy-3-methoxybenzohydrazide
H ₂ mhbovh	(E)-N'-3-hydroxybenzylidene-2-hydroxy-3-methoxybenzohydrazide
H ₂ ofbovh	(E)-N'-2-fluorobenzylidene-2-hydroxy-3-methoxybenzohydrazide
H ₂ pcbovh	(E)-N'-4-chlorobenzylidene-2-hydroxy-3-methoxybenzohydrazide
H ₂ pmbbovh	(E)-N'-4-methylbenzylidene-2-hydroxy-3-methoxybenzohydrazide
H ₂ pfbovh	(E)-N'-4-fluorobenzylidene-2-hydroxy-3-methoxybenzohydrazide
H ₂ phbovh	(E)-N'-4-hydroxybenzylidene-2-hydroxy-3-methoxybenzohydrazide
H ₂ pmbovh	(E)-N'-4-methylbenzylidene-2-hydroxy-3-methoxybenzohydrazide
H _c	coercive field
HGSA	hot ground state absorption
HOMO	highest occupied molecular orbital
H _s	saturation field
I	intensity
IR	infra-red
IUPAC	international union of pure and applied chemistry
I-van	5-I-2-hydroxy-3-methoxy-benzaldehyde
j	total angular momentum
J _{nn}	Nearest-neighbour coupling
J _{nnn}	Next-nearest-neighbour coupling
k _B	Boltzmann constant
l	orbital angular momentum
λ	wavelength
Ln ^{III}	lanthanide ions including Y ^{III}
LUMO	lowest unoccupied molecular orbital
M	magnetisation
MCE	magnetocaloric effect
Me ₂ CO	acetone
MeCN	acetonitrile
MeOH	methanol
Me-teaH ₃	methyltriethanolamine
Mn ₁₂	[Mn ₁₂ (OAc) ₁₆ (H ₂ O) ₄ O ₁₂]
M _R	Magnetic remanence
M _S	saturation magnetisation
N _A	Avogadro constant
NMR	nuclear magnetic resonance
NO ₂ -van	5NO ₂ -2-hydroxy-3-methoxy-benzaldehyde
NO ₂ -van'	2-(hydroxymethyl)-6-methoxy-4-nitrophenol
NO ₂ -van''	(2-hydroxy-3-methoxy-5-nitrophenyl)methanediol
NOPA	noncolinear optical parametric amplifier
OAc ⁻	acetate

o-van	2-hydroxy-3-methoxy-benzaldehyde
o-vanillyl hydrazide	2-hydroxy-3-methoxybenzohydrazide
P	polarisation
<i>p</i> -Br-pdavan	4-((4-bromophenyl)diazenyl)-2-hydroxy-3-methoxybenzaldehyde
<i>p</i> -Cl-pdavan	4-((4-chlorophenyl)diazenyl)-2-hydroxy-3-methoxybenzaldehyde
ψ	wavefunction
ψ	Euler angle
PXRD	powder X-ray diffraction
QTM	quantum tunnelling of magnetisation
r	radius
<i>R</i> -H ₂ myrovh	((E)-((1R,5S)-6,6-dimethylbicyclo[3.1.1]hept-2-en-2-yl)methylene)-2-hydroxy-3-methoxybenzohydrazide
ρ	Euler angle
s	Spin
S	total spin
SCXRD	single crystal X-ray diffraction
SE	stimulated emission
S-H ₂ perilovh	S-2-hydroxy-3-methoxy-((4-(prop-1-en-2-yl)cyclohex-1-en-1-yl)methylene)benzohydrazide
δ	chemical shift
SMM	Single molecule magnet
SMT	single molecule toroic
SQUID	superconducting quantum interference device
T	temperature
T	toroidal moment
TA-QTM	thermally assisted QTM
τ	relaxation time
τ	time constant
τ	magnetic torque
T _B	blocking temperature
T _C	Curie temperature
teaH ₃	triethanolamine
θ	Weiss constant
THF	tetrahydrofuran
T _N	Néel temperature
U _{eff}	Energy barrier
UV-Vis	ultraviolet visible light
vanillinol	2-(hydroxymethyl)-6-methoxyphenol
vanoxo	2-(hydroxymethyl)-6-methoxyphenol
XYZ	laboratory reference frame
ZFQTM	Zero field QTM

Table of Contents

1. Kurzzusammenfassung/Abstract.....	1
2. Introduction and Motivation.....	5
3. General Theoretical Background	7
3.1 Light induced processes	7
3.2 Intermolecular interactions.....	9
3.3 Magnetism	15
3.4 Single molecule magnets	19
3.5 Toroidal moments	27
3.6 Single molecule toroics (SMTs).....	31
4. Coordination compounds containing Fe ^{III} and Ln ^{III} ions.....	39
4.1 Introduction to Fe ^{III} -Ln ^{III} coordination clusters	39
4.2 Fe ₂ Ln ₂ Butterflies.....	46
4.2.1 Extending the Fe ₂ Dy ₂ butterfly platform	48
4.2.2 Femtosecond transient absorption spectroscopy on Fe ₂ Dy ₂ butterflies	62
4.3 2D Nuclearity CCCs.....	68
4.3.1 The Fe ₁₀ Ln ₁₀ system	68
4.3.1.1 Extending the Fe ₁₀ Ln ₁₀ platform.....	72
4.3.1.2 Magnetic Studies on Fe ₁₀ Ln ₁₀ clusters.....	77
4.3.1.3 Femtosecond transient absorption spectroscopy studies on Fe ₁₀ Ln ₁₀ rings	82
4.3.2 The Fe ₈ Dy ₁₂ system.....	88
4.3.3 Fe ₁₆ Tb ₄ system	91
4.4 Fe-Ln Systems conclusion and outlook.....	94
5. Dysprosium Triangles	97
5.1 Introduction to Dy ₃ triangles.....	97
5.2 Halogen substituted o-vanillin triangles.....	100
5.2.1 Synthesis optimisation and Lanthanide variation	105
5.2.2 Variation of the ligand to 5-Chloro-2-hydroxy-3-methoxybenzaldehyde	107
5.2.3 Magnetic properties of halogen substituted Dy ₃ triangles	110
5.2.4 Calculations and outlook.....	119
5.3 Dy ₃ triangles based on azo-coupled ligands: Azo-triangles.....	124
5.3.1 Dy ₃ triangles using <i>p</i> -Cl-pdavan (Dy ₃ -39) and <i>p</i> -Br-pdavan (Dy ₃ -40)	127
5.3.2 Magnetic properties of Dy ₃ with <i>p</i> -Cl-pdavan ligands (Dy ₃ -39).....	135
5.4 Schiff base triangles.....	140
5.4.1 (Dy ₃ -49) - Achieving Higher Symmetry.....	141
5.4.1.1 (Dy ₃ -49) – Magnetic properties.....	149

5.4.1.2 (Dy ₃ -49) – Quantum chemical calculations	160
5.4.1.3 Dy ₃ -Hbovh – Torque magnetometry	164
5.4.2 Variations on the Schiff base ligand	171
5.4.2.1 Dy ₃ Triangles with fluoro-substituted benzaldehydes	172
5.4.2.2 Dy ₃ Triangles with hydroxy substituted benzaldehydes.....	181
5.4.2.3 Magnetic Characterisation	186
5.4.2.4 Influencing the crystal packing – Ligand approach.....	193
5.4.2.5 Challenges in data evaluation and side products.....	206
5.4.2.6 Side products	208
5.5 Dy ₃ triangle systems conclusion and outlook.....	213
6. Linked triangles.....	221
6.1 Introduction	221
6.2 Linking <i>via</i> o-vanillin type ligands.....	223
6.2.1 Adding o-vanillinol	224
6.2.2 Using 5-CN-3-methoxy-2-hydroxybenzaldehyde	228
6.2.3 Magnetic characterisation of (Dy ₆ -93) and (Dy ₆ -94)	233
6.3 Linked triangle conclusion and outlook	237
7. General conclusion and outlook.....	240
8. Experimental	245
9. References	290
10. Curriculum Vitae.....	304
11. List of Publications.....	306
12. Acknowledgments.....	307
13. Appendices.....	309
13.1 Table of Figures	309
13.2 Table of Tables	321
13.3 Crystallographic Tables	322

1. Kurzzusammenfassung/Abstract

Kurzzusammenfassung

Während der Arbeit an dieser Dissertation wurden 94 Verbindungen synthetisiert, um die Auswirkungen supramolekularer Ansätze auf die magnetischen und insbesondere die toroidalen Eigenschaften zu untersuchen. Diese Verbindungen wurden mittels Einkristall-Röntgendiffraktometrie, Pulver-Röntgendiffraktometrie, UV-Vis-Spektroskopie, IR-Spektroskopie, Elementaranalyse, SQUID-Magnetometrie, micro-SQUID-Magnetometrie, Cantilever-Torque-Magnetometrie und Femtosekunden-Absorptionsspektroskopie untersucht. Einige dieser Experimente wurden in Zusammenarbeit mit Gruppen innerhalb des Netzwerks des SFB 1573 „4f for Future“ und verschiedenen europäischen Arbeitsgruppen durchgeführt.

Ein Ausgangspunkt für die Studien in dieser Arbeit war die Nutzung und Erweiterung einer Testbed-Philosophie, die auf 3d-4f 1:1 Systemen basiert. Zu diesem Zweck wurden Fe_2Ln_2 -„Butterflies“ reproduziert sowie fünf neue derartige Komplexe synthetisiert und mittels transienter Absorptionsspektroskopie auf einer Femtosekunden-Zeitskala untersucht. Die transiente Absorptionsspektroskopie wurde auch an einer Reihe von bisher unveröffentlichten $\text{Fe}_{10}\text{Ln}_{10}$ -Verbindungen durchgeführt, die reproduziert wurden, um nicht nur Einblicke in die Dynamik, sondern auch in die Auswirkungen der Elliptizität der Ringe zu gewinnen. Für ausgewählte Beispiele wurde auch die magnetische Charakterisierung durchgeführt. Das den zyklischen Fe-Ln-Koordinationsverbindungen mit einer Nuklearität von 20 zugrunde liegende Konzept wurde durch die erfolgreiche Isolierung einer $\text{Fe}_8\text{Dy}_{12}$ -Verbindung mit einer sattelförmigen Struktur und einer $\text{Fe}_{16}\text{Tb}_4$ -„Unendlichkeitsschleife“ ausgeweitet.

Seit der Entdeckung des ersten Moleküls mit einem permanenten toroidalen Moment im Grundzustand im Jahr 2006, hat die Idee der Nutzung eines toroidalen Moments, z. B. für die Datenspeicherung und -verarbeitung, zunehmend an Aufmerksamkeit gewonnen. Allerdings gab es bislang keine systematische Untersuchung des Potenzials eines solchen Systems speziell unter Verwendung supramolekularer chemischer Konzepte.

In dieser Arbeit wurden drei molekülbasierte Ansätze verwendet. Die allgemeine Idee war, den *o*-Vanillin-basierten Liganden zu modifizieren, um intermolekulare und/oder intramolekulare Wechselwirkungen zu fördern. Ein völlig neuer Ansatz konnte durch die Verwendung von Halogenbindungen, durch Einführung von Substituenten an freien Stellen der *o*-Vanillin-basierten Bausteine, realisiert werden. Die Einführung von Halogenwechselwirkungen kann zu Änderungen im magnetischen Verhalten führen. Das Maß der Auswirkungen auf die magnetischen Eigenschaften steht in Korrelation zur Stärke der Halogenbindungen, was durch CASOCI-Berechnungen untermauert werden konnte. Ein wichtiges Merkmal der untersuchten Verbindungen ist das Vorhandensein eines kleinen, aber definierten Sprunges bei einem angelegten Magnetfeld von 0 in der Magnetisierung in Abhängigkeit vom angelegten Feld in den microSQUID-Daten. Dies ist wahrscheinlich das Ergebnis einer Restpopulation ferromagnetischer angeregter Zustände, die bei der Reduktion des Feldes nicht in den toroidalen Zustand übergehen.

Ein zugrundeliegendes Ziel in der Forschung an Dy₃ SMTs ist es eine Kristallpackung der Dreiecke zu erreichen bei der die Ausrichtung aller Dreiecke gleich ist. Dies kann es ermöglichen, das toroidale Moment entlang einer bestimmten Raumrichtung zu maximieren und durch angelegte Felder zu manipulieren. Dieses Ziel könnte durch Ligandenmodifikationen erreicht werden, die in dieser Arbeit im Detail erforscht wurden. Hierfür wurde ein Schiff-Base-Ansatz verwendet, der zu Kristallisation eines neuartigen Dreiecks in einer hochsymmetrischen Raumgruppe, $R\bar{3}$, führte. In diesem Molekül war es möglich, durch Anlegen eines externen Magnetfeldes eine bevorzugte Ausrichtung der toroidalen Momente zu erzwingen. Das Vorhandensein des Inversionszentrums in dieser Raumgruppe führt dazu, dass sich die toroidalen Nettomomente gegenseitig aufheben.

Mit diesem grundlegenden Ansatz wurde eine Bibliothek ähnlicher funktionalisierter Dy₃-Dreiecke erstellt, mit deren Hilfe die Auswirkungen kleiner struktureller Veränderungen auf die Toroidizität und die dynamischen magnetischen Eigenschaften erforscht werden konnten.

Als letzter Ansatz wurde die Verwendung intramolekularer Verbindungen zwischen Dreiecken erforscht, indem der verbrückende Ligand verändert wurde, um eine ferrotoroidische Ordnung in Dy₆-Systemen hervorzubringen. Der Erfolg dieses

molekularen Konzepts wurde durch die Synthese dreier modifizierter Dy₆ Doppel-Dreiecke gezeigt. Allerdings haben die magnetischen Messungen einen toroidalen Charakter des Grundzustandes nicht ausreichend belegen können.

Abstract

During the work on this thesis 94 compounds were synthesised in order to explore the effect of supramolecular approaches on magnetic and in particular toroidal properties. These compounds were investigated using single crystal X-ray diffraction, powder X-ray diffraction, steady-state UV-Vis spectroscopy, IR spectroscopy, elemental analysis SQUID magnetometry, microSQUID magnetometry, cantilever torque magnetometry and femtosecond transient absorption spectroscopy. Some of these were performed in collaboration with groups within the network of the CRC 1573 “4f for Future” and various European partners.

A starting point for the work in this thesis was to use and extend a testbed philosophy based on 3d-4f 1:1 systems. To this end, Fe₂Ln₂ butterfly compounds were reproduced and five further new butterfly complexes synthesised and subjected to transient absorption spectroscopy on a femtosecond timescale. The transient absorption spectroscopy was also performed on a series of as yet unpublished Fe₁₀Ln₁₀ compounds which were reproduced in order to gain insights not only into the dynamics but also the effect of the ellipticity of the rings. For selected examples magnetic characterisation was also performed. The underlying concept behind the 20 nuclearity Fe-Ln cyclic coordination compounds was further adapted through the successful isolation of an Fe₈Dy₁₂ compound with a saddle-shaped structure and an Fe₁₆Tb₄ “infinity loop”.

Since the discovery of toroidal moments, established first for the molecule published in 2006 highlighting its SMM behaviour which resulted from excited states, rather than the ground state, the idea of utilising a toroidal moment, for example for data storage and processing, has gained increasing attention. To date there has been no systematic investigation of the potential of such a system in terms of supramolecular chemical concepts.

In this thesis, three molecule-based approaches were used. The general idea was to employ modifications to the *o*-vanillin-based ligand in order to promote intermolecular and/or intramolecular interactions. A completely new approach using halogen bonding could be realised by introducing substituents on free sites on the *o*-vanillin-based building blocks. In particular, the introduction of halogens can lead to halogen interactions which were shown to have a correlation in terms of the strength of the halogen bonds which could be further substantiated using CASOCI calculations and the resulting magnetic behaviour. An important feature of the investigated compounds is the presence of a small but defined step around zero applied field in the magnetisation as seen in the microSQUID data, likely the result of residual population of ferromagnetic excited states.

The ultimate goal of achieving a crystal packing of the triangles to allow for all triangles to show the same toroidal moment along a specific direction could be achieved through ligand modifications and resulted in a compound which was explored in much detail. For this, a Schiff base approach was used and resulted in crystallisation in the high symmetry space group, $R\bar{3}$. In this molecule it was possible to impose a preferred orientation of toroidal moments by the application of an external magnetic field. The presence of the inversion centre in this space group meant that the net toroidal moments perfectly cancel each other.

This fundamental approach was used to create a library of similar functionalised Dy₃ triangles which were used to gauge the effect of small structural changes on the toroidicity and dynamic magnetic properties.

As a final approach, the use of intramolecular connections between triangles was explored using the idea of modifying the bridging ligand in order to promote ferrotoroidic order within Dy₆ systems. The success of this molecular concept is shown by the synthesis of three modified fused triangle Dy₆ compounds. However, the performed magnetic measurements are not sufficient to assess the toroidal nature conclusively.

2. Introduction and Motivation

In 1993 magnetic bistability was discovered in the Mn_{12} cluster $[\text{Mn}^{\text{III}}_8\text{Mn}^{\text{IV}}_4(\text{OAc})_{16}(\text{H}_2\text{O})_4\text{O}_{12}]$, where magnetic bistability means that when this cluster is magnetised and the magnetic field is switched off it retains its magnetisation below a certain (blocking) temperature, T_B for a given relaxation time.^[1] This behaviour, reminiscent to that of permanent magnets, resulted in the nomenclature “Single Molecule Magnets” (SMMs) since this was identified as a completely molecular-based phenomenon.^[2-3]

This laid the foundation for a new research area within molecular-based magnetism. For such molecules showing SMM behaviour this new class of materials could have quantum-based applications such as high-density data storage,^[4-5] qubits used for quantum computing^[6-12] and spintronics.^[13-16]

In order to design molecules with suitable magnetic and electronic properties for these applications, systematic studies investigating the impact of small structural changes on the resulting properties provide deeper insights. A well-established testbed system to explore such magnetostructural correlations is provided by the tetranuclear 3d-4f M_2Ln_2 butterfly complexes.^[17-25] The versatility of the system arises from the multiple tuning handles such as the transition metal and lanthanide ions as well as ligands and co-ligands which can all be easily modified.

This testbed is therefore ideal for the exploration of the interplay of the electronically excited state landscape and the magnetic response through using time resolved measurements. This enables us to gain the necessary knowledge and insights in order to identify clusters which could be important for the next generation of quantum-based technologies.^[26]

Investigations on these well-defined butterfly systems are required in order to understand the interactions leading to the physical properties. As a result of their infinite electronic structures, larger systems, and in particular cyclic coordination clusters (CCCs),^[27-33] have been identified to exhibit unusual quantum effects. These include proximity to a quantum critical point for an $\text{Fe}_{10}\text{Gd}_{10}$ system^[29] as well as exciton formation in a series of $\text{Fe}_{10}\text{Ln}_{10}$ CCCs.^[34] Since the cyclic structure facilitates this exotic behaviour, investigations in terms of the influence of the topology of the ring

structure through chemical modifications can give or already have given insights into the origin of these effects.^[35-36]

Since the discovery of a triangular Dy₃ compound [Dy₃(μ₃-OH)₂(*o*-van)₃Cl(H₂O)₅]Cl₃·4H₂O·2MeOH·0.7MeCN with a permanent toroidal moment in 2006,^[37] a new research area of molecular magnetism emerged, namely Single Molecule Toroids (SMTs). A toroidal moment results from the vortex-like in-plane arrangement of spins leading to a non-magnetic ground state. This triangular Dy₃ compound is the first example of an SMT.^[38-40] SMTs are promising candidates for high density data storage as a result of the ground state being topologically protected against decoherence effects through fluctuating external magnetic fields.^[41-43]

Dy₃ triangles have been identified as excellent candidates to establish a testbed system based on modifications to the *o*-vanillin ligand and in analogy to the famous butterfly system. This will assist in understanding how to tune toroidicity to for example use SMTs in novel quantum devices. The toroidal spin structure resulting in a non-magnetic ground state means that an ideal SMT can be regarded as magnetically dark. In the static regime they can be regarded as non-radiating anapoles, which are considered as a key ingredient in dark matter.^[44-47] Thus, the study of toroidal molecules could provide fundamental knowledge concerning the composition of the universe.

In this thesis three projects are described. The first makes use of the butterfly testbed and CCCs in order to probe the influence of structural changes in terms of the optical and magnetic properties systematically. The second focuses on the expansion of the family of Dy₃ triangle complexes with the aim to explore the introduction of supramolecular interactions to control toroidicity. The third and final project develops the idea of enhancing toroidicity through coupling Dy₃ units.

3. General Theoretical Background

3.1 Light induced processes

Light-induced processes can be divided into the categories of photophysics and photochemistry.^[48] Photophysics examines processes such as the absorption and emission of light as well as non-radiative transitions during which no chemical bonds are broken. In photochemistry, chemical reactions are initiated by the irradiation of light, an example of this is the light induced [2+2] cycloaddition of 1,2-bis(4-pyridyl)ethene.^[49] Electromagnetic radiation of different wavelengths and therefore energies can interact with matter in different ways. High energy radiation *i.e.* γ -rays can ionise molecules or break bonds whereas low energy radiation for example in the microwave regime only excites rotational modes. IR and UV-Vis spectroscopy are based on the principle of excitation of characteristic vibrational modes and electronic states *via* photon absorption. UV-Vis measurements can be used to determine the absorbance of a sample by measuring the intensity of light of a certain wavelength before and after interacting with the sample. A standard UV-Vis spectrum shows the absorbance for wavelengths in the range 200-800 nm. Mathematically absorbance or optical density can be described using equation 1, the Beer-Lambert law.^[48]

$$A = \log_{10} \frac{I_0}{I} = \varepsilon \cdot c \cdot d \quad \text{equation 1}$$

A is the absorbance, I_0 and I the intensities before and after going through the sample respectively, c the concentration, d the optical pathlength of the cuvette and ε the extinction coefficient.

After excitation there are a variety of processes through which the system can relax to the electronic ground state. This includes photon emitting processes (fluorescence or phosphorescence) and non-radiating processes such as internal conversion followed by vibrational relaxation. Figure 1 shows a Jablonski diagram.^[50]

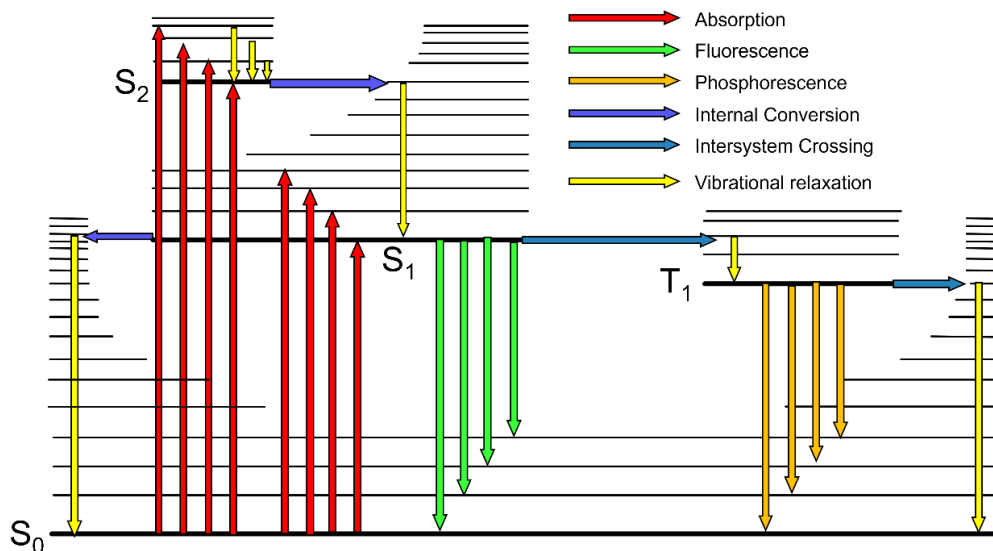


Figure 1. Jablonski diagram with coloured arrows showing possible radiation induced processes.

A sample can be excited from the electronic ground state (S_0) by absorption of a photon. The system is usually excited into different vibrational states of an excited electronic state (S_1) which is described by the Franck-Condon principle. It states that excitations happen on a faster timescale than nuclear vibrations leading to vertical transitions *i.e.* excitation to excited vibrational states of the excited electronic state. The intensity of the different transitions is proportional to the Franck-Condon factor $|S(v_E, v_A)|^2$ which can be derived from equation 2 and describes the integral over the wavefunctions of the ground and excited states. The larger the overlap, the larger the Franck-Condon factor. Identical wavefunctions would give $S = 1$.^[51]

$$S(v_E, v_A) = \int \psi_{v_E}^* \psi_{v_A} d\tau_v \quad \text{equation 2}$$

With ψ_{v_A} and ψ_{v_E} being the wave function of the vibrational state in the electronic ground and excited states respectively. After excitation the system relaxes *via* vibrational relaxation to the vibrational ground state of the electronic excited state. Vibrational relaxation can happen intermolecularly by energy transfer to surrounding solvent molecules for example or intramolecularly *via* interactions with vibrational states of similar energy. From the vibrational ground state of the electronic excited state, it can relax to the electronic ground state either *via* emission of a photon which is called fluorescence or *via* internal conversion which is the interaction with a vibrational excited state of another electronic state followed by vibrational relaxation. Additionally, from the S_1 state the system can undergo the spin forbidden transition

called intersystem crossing which describes the transition from the excited singlet to an excited triplet state changing the spin multiplicity of the system. After vibrational relaxation to the vibrational ground state of the excited triplet state T_1 the system can relax to the electronic S_0 state *via* emission of a photon which is again a spin forbidden transition and called phosphorescence. The process is forbidden and therefore happens over longer timescales (10^{-6} s-10 s) compared with fluorescence (10^{-10} s- 10^{-7} s). Kasha's rule states that fluorescence and phosphorescence always occur starting from the lowest energy state of the given electronic excited state. The observed energy shift between absorption and emission spectra is described by Stokes law. The lower energy of the emission is due to the vibrational relaxation after excitation to higher vibrational modes of the excited electronic state.^[51]

Lanthanide ions in coordination chemistry can generally be regarded as single ions surrounded by ligands with little to no covalent character to the bonding between the 4f and the ligand orbitals. As a result of this, optical properties of lanthanide complexes (in contrast to 3d ion-containing complexes) are hardly sensitive to the ligand field environment but mostly depend on the specific Ln^{III} ion for each of which characteristic f-f transitions can be observed in spectroscopic analysis. These f-f transitions are generally more readily observable than d-d transitions as a result of much stronger spin orbit coupling.^[52-53]

In order to gain further insights into the timescales at which the processes of absorption and emission happen, time-resolved techniques are useful. Whereas the absorption spectroscopy presented above can be regarded as steady-state, one technique employed in this work is femtosecond transient absorption spectroscopy. Using a time delay between a laser pump pulse and a white light probing pulse enables the time-resolved measurement of ultrafast absorption and emission dynamics within excited states.^[26, 54]

3.2 Intermolecular interactions

Intermolecular interactions are a valuable tuning handle to influence the crystal packing and magnetic properties of coordination compounds. Supramolecular chemistry promotes intermolecular interactions for the design of molecules and

architectures with desired chemical, optical or magnetic properties.^[55] Intermolecular interactions can affect any measurement in liquid and solid states whereas in the gas phase they are expected not to be relevant. They cannot be disregarded in the case of magnetic compounds and in particular SMMs which are most commonly investigated in the solid state. Parts of this work focus on the introduction of specific intermolecular interactions in order to steer magnetic properties and crystal packing. To this end, three types of interactions, hydrogen bonds,^[56-57] π - π -stacking^[58-63] and halogen bonds^[64-65] were targeted and will be discussed in the following chapters.^[66]

Hydrogen bonds are the most common intermolecular interaction and are famously known for making water a liquid at room temperature and thus making life on Earth possible as we know it. The importance of hydrogen bonds and their influence on the crystal packing can also be seen for water in the form of ice. A multitude of polymorphs of ice are reported, all of which arrange in a lattice that follows the Bernal-Fowler rules.^[67] One of the Bernal-Fowler rules dictates that in all ice a single hydrogen atom must be between two oxygen atoms to allow for the formation of a space filling hydrogen bonding network. An example of such an ice crystal structure is shown in Figure 2 for ice XIX.^[68]

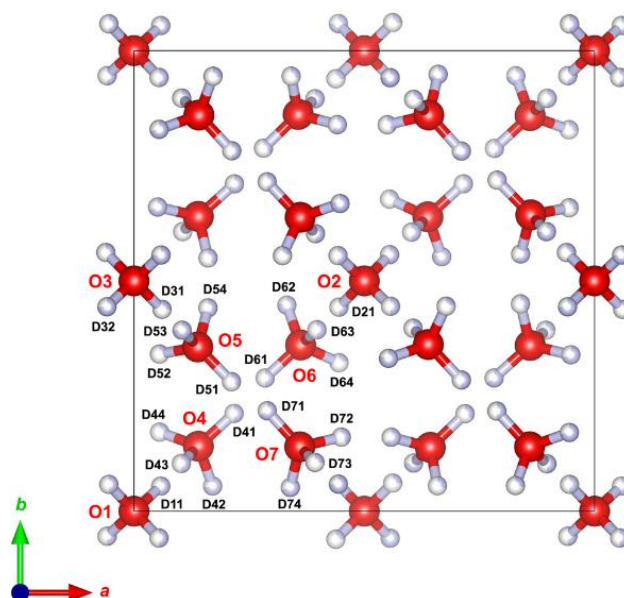


Figure 2. Packing of ice XIX along the crystallographic c axis. Shading of hydrogen atoms corresponds to occupancy. Reprinted with permission from reference^[68] [Springer Nature] copyright [2021].

Together with other interactions such as dipolar- and van-der-Waals interactions,^[69-72] hydrogen bonds are responsible for protein folding and are therefore at the very basis

of life itself.^[73-75] Hydrogen bonds are formed between a hydrogen atom H which is bonded to a strongly electronegative atom X which is most commonly oxygen or nitrogen and the lone pair of another atom Y most commonly N, O or F and in this work also often Cl. An X—H...Y angle as close as possible to 180° is favoured for a hydrogen bonding interaction. Hydrogen bonds can vary in strength between 4 and 50 kJ/mol with any over 15 kJ/mol being considered a strong hydrogen bond.^[76-77] Weak hydrogen bonds are mostly electrostatic interactions whereas stronger ones have additional charge transfer components and are resonance assisted. Resonance assistance here describes the involvement of the hydrogen bond in electron delocalisation.^[56]

π - π stacking/ π - π interactions are a result of the overlap of the electronegative and electropositive regions in aromatic rings. The electron-rich region is located above and below the inside of the aromatic ring whereas the electropositive region is found outside in the plane of the ring (see Figure 3).^[62]

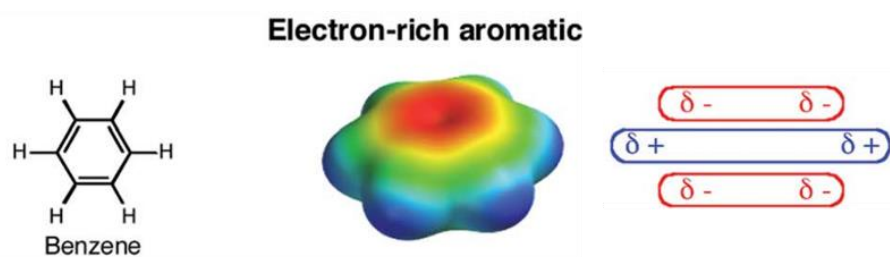


Figure 3. Benzene as an example of an electron-rich aromatic system with electrostatic potential surfaces calculated using DFT and a scheme showing the electronegative and electropositive regions. Adapted from reference with permission from reference^[62] [Royal Society of Chemistry] copyright [2012].

Two possible geometries that are favourable for π - π interactions are an edge-to-face and a parallelly stacked orientation with an offset to avoid electronic repulsion (see Figure 4). The attractive interactions mainly originate from the π - σ interactions outweighing the repulsion between the electronegative π orbitals. A parallelly stacked arrangement without an offset would lead to a repulsive interaction due to the close proximity of the electronegative areas.^[58, 61-62, 78]

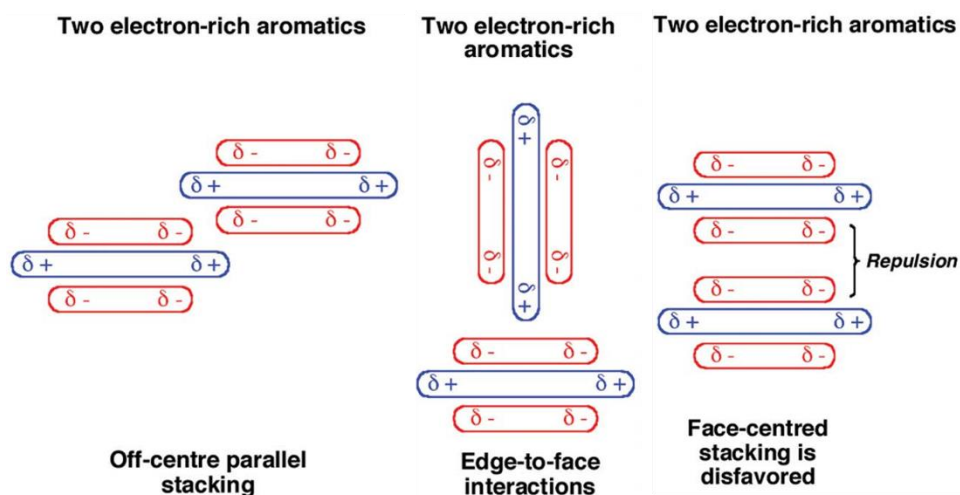


Figure 4. Off-centre parallel stacking and edge-to-face interactions as favoured and face-centred stacking as disfavoured orientations between π - π stacked moieties. Adapted from reference with permission from reference^[62] [Royal Society of Chemistry] copyright [2012].

The third intermolecular interactions used in this work are halogen bonds or halogen interactions in general.^[64, 79-80] As in chalcogen, tetrel or pnictogen bonds, halogen bonds are interactions which characterise the attractive noncovalent interaction between an electron-rich electron density donor and the electropositive σ -hole on a covalently bound tetrel, (group 14 element), pnictogen (group 15 element), chalcogen (group 16 elements) or halogen atom (group 17 elements).^[81] IUPAC defines a halogen bond as any net attractive interaction between an electrophilic region associated with a covalently bound halogen atom and a nucleophilic region in the same or another molecule. Halogen interactions are less common in inorganic coordination clusters but can prove to be an important tool for supramolecular design.^[82]

Halogen bonds are formally denoted as $R-X\cdots Y$ where the three dots represent the halogen bond, $R-X$ is the halogen bond donor, X being the halogen with the electrophilic region and Y being the halogen bond acceptor with a nucleophilic region (lone electron pairs).^[82]

A halogen atom or halide with a spherical distribution of its electrons is usually seen as an electronegative nucleophile. However, once it is covalently bonded, the electron density distribution changes and a σ -hole forms which an electropositive region opposite to the covalent bond (see Figure 5).^[64, 83] This is where the antibonding σ^* orbital is located *i.e.* if it were occupied the $R-X$ bond would be significantly

weakened.^[82] Furthermore, the charge density at the sigma hole depends on the polarisability of the halogen atom as well as the electron withdrawing power of the other substituents on the molecular moiety R. Thus, the strength of the halogen bond is influenced by these features.^[84-85]

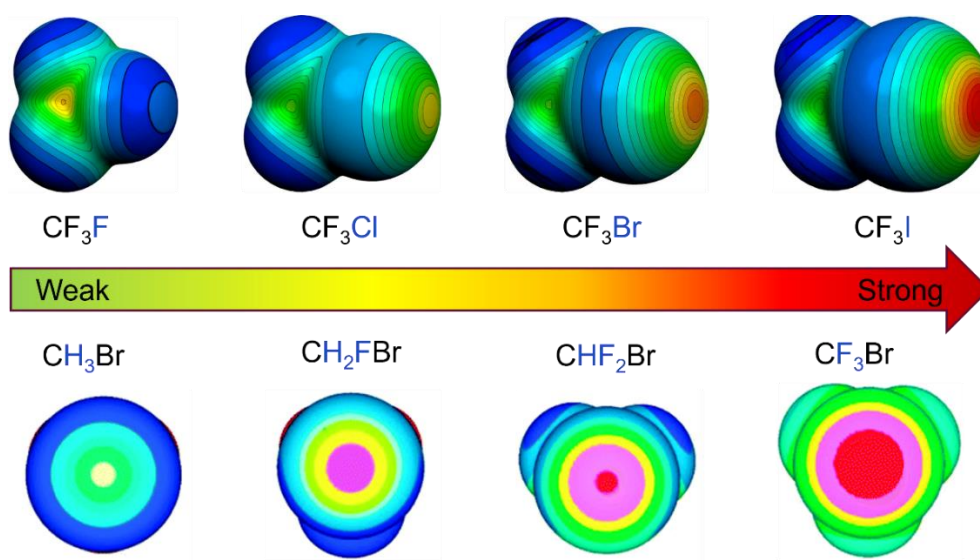


Figure 5. Electrostatic potentials of $\text{CH}_y\text{F}_n\text{Br}$ (bottom) and CF_3X with $\text{X} = \text{F}, \text{Br}, \text{Cl}, \text{I}$ (top) and their influence on the strength of associated halogen bonds. Adapted with permission from reference^[84] [Springer] copyright [2007] and from reference^[85] [Royal Society of Chemistry] copyright [2013].

The distance between the nucleophile Y and the electrophile X is most commonly smaller than their combined van der Waals radii.^[86] The components of these attractive halogen interactions include polarisation, charge transfer and dispersion effects but are mostly electrostatic in nature and lead to the strong directionality of this type of intermolecular interaction.^[82]

For halogen-halogen interactions this directionality is expressed in the form of two commonly observed geometries which can be categorised as Type I and Type II halogen interactions (see Figure 6). The directionality is dictated by the location of the σ hole and the electron density on the nucleophile, which in case of another covalently bound halogen is located in a belt orthogonal to the σ hole. Type I halogen-halogen interactions between two covalently bound halogens $\text{R}-\text{X}$ assume a geometry where the angles θ_1 and θ_2 are close to equal. For Type II halogen-halogen bonds one of the angles is close to 180° . Here the σ -hole of X is oriented exactly towards the nucleophilic counterpart on the other halogen (see Figure 6).^[87]

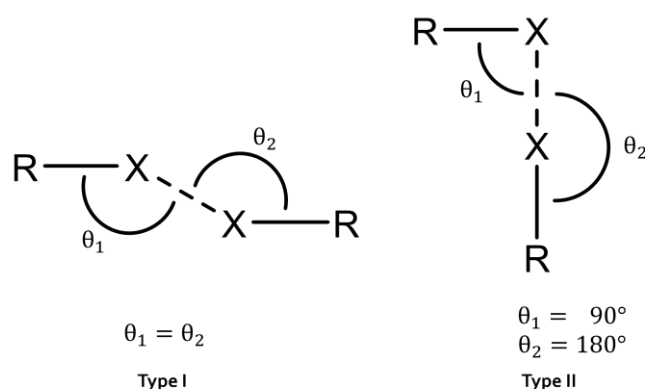


Figure 6. Geometries in Type I halogen-halogen interactions and Type II halogen-halogen bonds.

In 2022 Scheiner showed that contrary to belief at that time the Type I geometry does in fact have an attractive component and is not just a geometric arrangement which minimises repulsive forces. This attractive component is almost as strong as for a Type II halogen bond. For Type I the attractive interactions consist of what can be referred to as two bent weaker halogen bonds in both directions (see Figure 7).^[88]

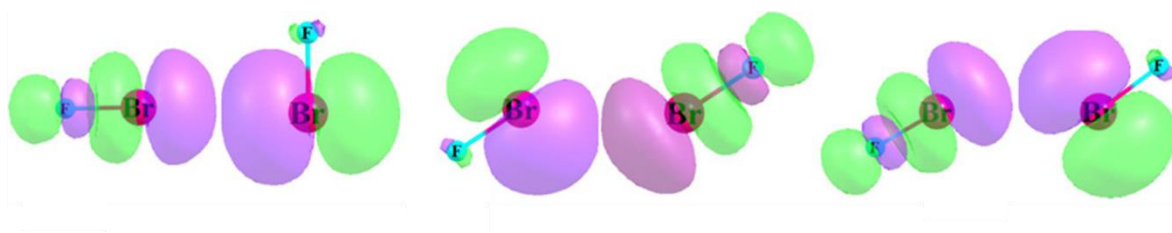


Figure 7. Orbital overlap in strict Type II geometry (left) and the two contributions from weaker overlap in the Type I geometry (middle and right) in FBr. Purple and green indicate opposite signs of the wavefunction. Adapted with permission from reference^[88] [American Chemical Society] copyright [2022]

In this work an Electron Localization Function (ELF) was used to calculate halogen bond-containing systems and for the visualisation of any donor acceptor interactions.^[89] The ELF is a tool which quantifies the local kinetic energy excess caused by Pauli repulsion. It is normalised where zero (blue) corresponds to the absence of electrons, 1 (red) corresponds to perfectly localised electrons and 0.5 to the situation in between of a free electron gas. The ELF method is used to map electron localisation in planes through the molecules and an example of this is shown in Figure 8.

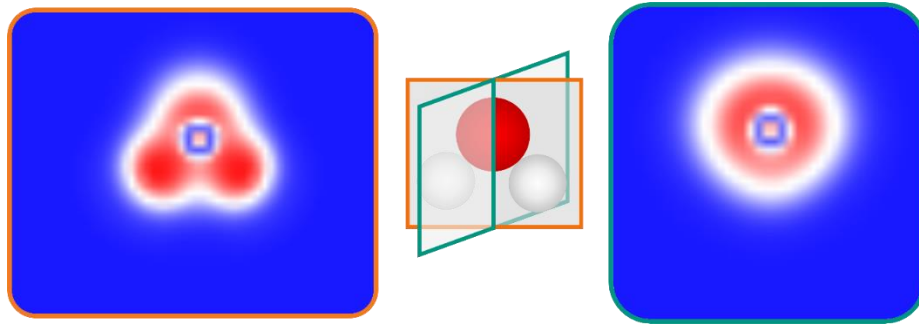


Figure 8. ELF along two planes through a water molecule.

3.3 Magnetism

Magnetic materials can be classified as paramagnetic or diamagnetic depending on whether they have unpaired or paired electrons. In paramagnetic materials the unpaired electrons align with an external applied magnetic field leading to the magnetic flux density B being larger inside the material than outside since the magnetic force lines are pulled into the material. For diamagnetic materials the opposite effect is observed where the material produces a counteracting magnetic field resulting in a weaker field inside the material than outside. This behaviour is schematically shown in Figure 9.^[90-91]

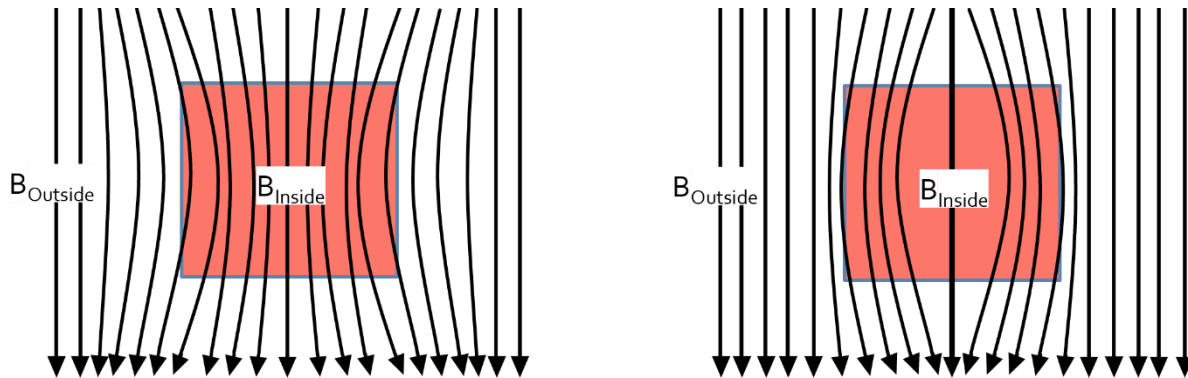


Figure 9. Paramagnetic (left) and diamagnetic (right) material in a magnetic field. Field lines as black arrows. Adapted from reference^[90].

The resulting magnetic flux density is given by the sum of the applied field H and the magnetisation M in the material multiplied with the vacuum magnetic permeability μ_0 . The magnetic susceptibility χ is often used to describe the magnetic character of a sample. It is defined as the first derivative of the magnetisation M in respect to the applied field strength H and is shown in equation 3.

$$\chi = \frac{\partial M}{\partial H} \quad \text{equation 3}$$

χ increases exponentially with decreasing temperature for paramagnetic materials whereas diamagnetic contributions are temperature independent. For paramagnets χ takes positive and for diamagnets negative values. A perfect diamagnet (superconductor) has a value of $\chi = -1$. Figure 10 shows the temperature dependence of χ for paramagnets and diamagnets.^[90-91]

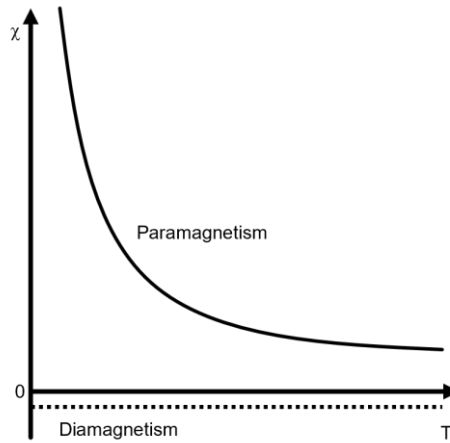


Figure 10. Temperature dependence of χ for diamagnetic and paramagnetic materials. Adapted from reference^[90].

The magnetic susceptibility of a pure paramagnets follows the Curie-law

$$\chi_{\text{para}} = \frac{C}{T} \quad \text{equation 4}$$

which was further expanded in the Curie-Weiss law by the addition of the Weiss constant θ to account for cooperative effects such as ferromagnetism, ferrimagnetism or antiferromagnetism. The Curie-Weiss law is only valid for high temperatures and low magnetic fields.

$$\chi_{\text{para}} = \frac{C}{T - \theta} \quad \text{equation 5}$$

C in theses equations is the Curie constant which is defined as

$$C = \mu_0 \cdot N_A \cdot \frac{\mu^2}{3k_B} \quad \text{equation 6}$$

with N_A being the Avogadro constant, μ being the magnetic moment, μ_0 the permeability of the vacuum and k_B the Boltzmann constant.^[90-92] Weiss-domains^[93]

(which are areas with one orientation of magnetic moment) are formed as a result of long-range ordering effects in magnetic materials and are separated by Bloch walls^[94] to neighbouring domains. The orientation of the magnetic moments in ferro-, ferri-, and antiferromagnetically coupled materials is illustrated in Figure 11. In ferromagnetic materials spins align parallel whereas in antiferromagnetic materials spins align antiparallel to each other. In ferrimagnets spins are aligned antiparallely between spins of different overall magnitude, resulting in a net magnetic moment.^[91] A well-known example of a ferrimagnet is magnetite (Fe_3O_4) where the octahedrally coordinated $\text{Fe}^{2+/3+}$ ions and the tetrahedrally coordinated Fe^{3+} ions are coupled antiferromagnetically but do not cancel each other out completely resulting in an overall magnetic moment.^[95]

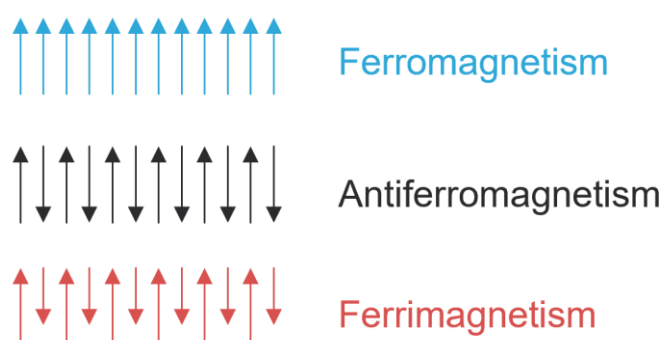


Figure 11. Types of collective magnetism and the orientation of spins associated with them.

Figure 12 shows the behaviour of para-, ferro-, ferri-, and antiferromagnetic material in three types of plots which are commonly used to show the temperature dependence of susceptibility data. The graph plotting $1/\chi$ against T can be referred to as a Curie-Weiss plot. A linear fitting routine (Curie-Weiss fit) which is usually limited to the higher temperature values, where the curve follows the Curie-Weiss law, can be used to determine θ and C .^[96] A parallel arrangement of spins leads to an intercept with the positive part of the x axis (positive θ) whereas a negative θ indicates an antiparallel arrangement. Long-range order effects can be observed below a certain temperature characteristic for any given material. For ferromagnets this is called Curie-temperature T_C and for antiferromagnets Néel temperature T_N . Above these temperatures the spins are randomly oriented and the material behaves like a Curie paramagnet.^[90]

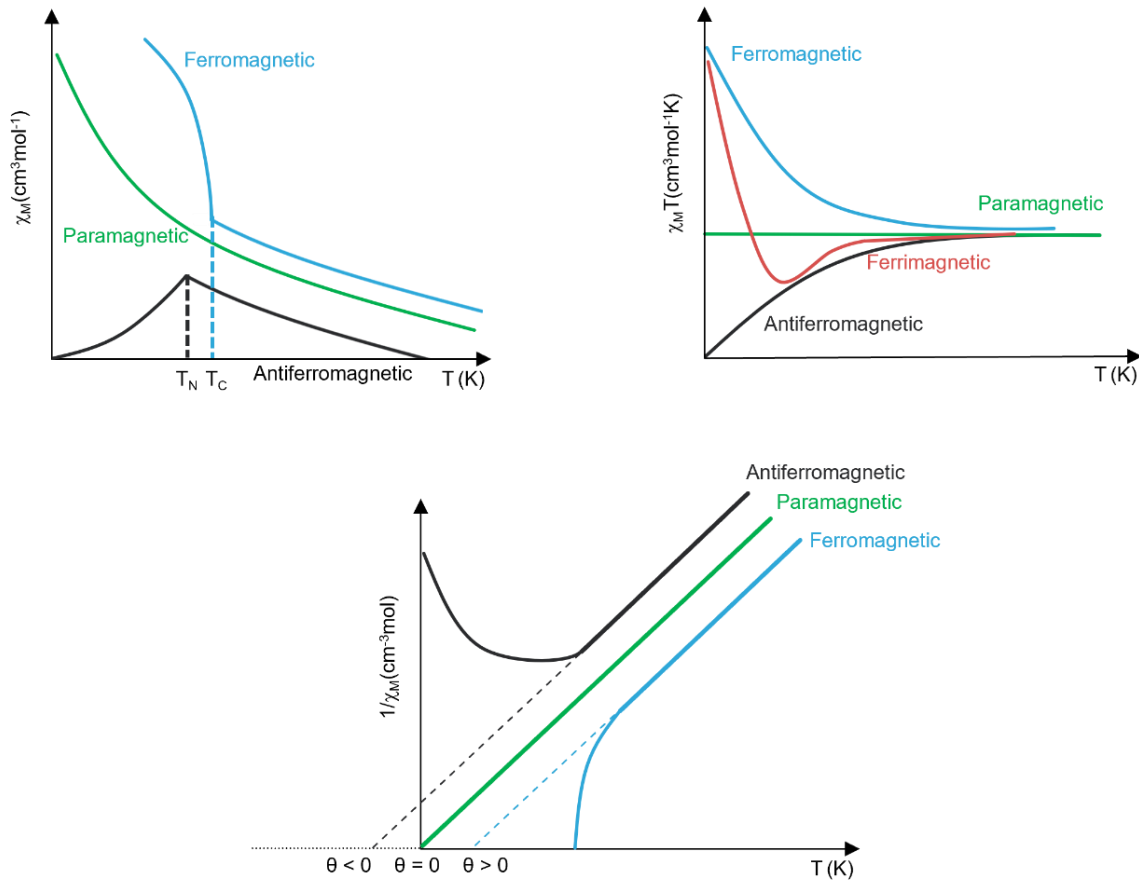


Figure 12. χ against T (top left), χT against T (top right), and $1/\chi$ against T (Curie-Weiss plot) (bottom) for para-, ferro-, ferri-, and antiferromagnetic materials. Adapted from reference^[90].

Ferro- and ferrimagnetic materials can show magnetic hysteresis when a magnetic field is swept. Once a magnetic field H is applied the magnetisation of a material increases following the initial curve (red curve in Figure 13). Once all spins are aligned with an applied magnetic field (H_s) saturation is reached (M_s). Then on reversing the field the point at which it crosses the y axis is known as the magnetic remanence M_R and on further decreasing the field the point at which it crosses the x axis defines one limit of the coercive field H_C .^[90-91]

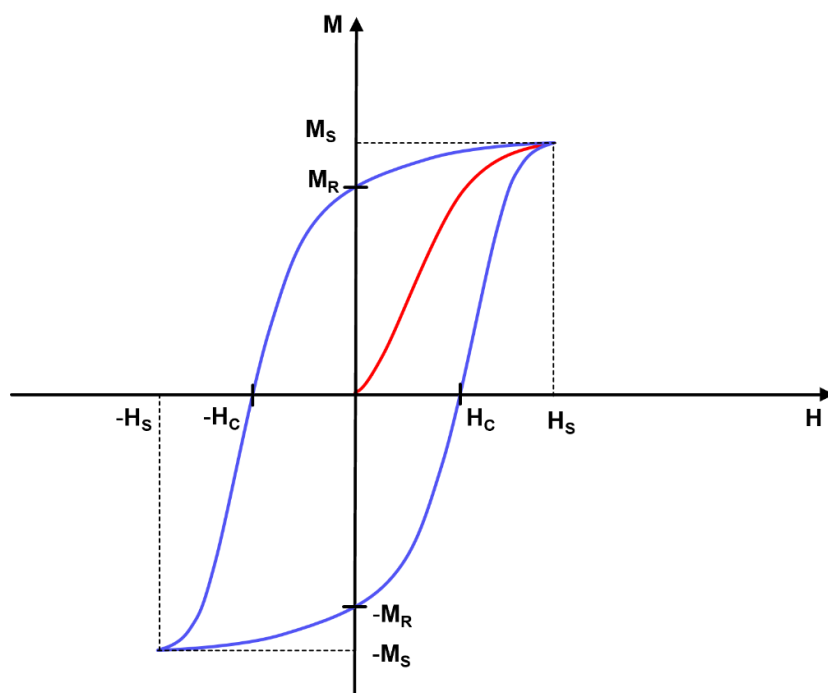


Figure 13. Magnetic hysteresis in blue with new curve in red. M_R is the magnetic remanence, M_S the saturation magnetisation, H_C the coercive field and H_S the saturation field.^[90]

3.4 Single molecule magnets

Single molecule magnets (SMMs) are bistable coordination compounds that, below a characteristic blocking temperature T_B , show slow relaxation of magnetisation. This means SMMs retain a magnetisation M for a time period τ in the absence of an external magnetic field H . This means that magnetic hysteresis can be observed for SMMs. The first SMM discovered is a Mn_{12} cluster with the molecular formula $[Mn_{12}(OAc)_{16}(H_2O)_4O_{12}]$. The crystal structure was first reported in 1980 by Lis^[97] who noted that this molecule should be magnetically interesting. It was magnetically characterised in 1993 by Sessoli and Gatteschi *et al.*^[1] where it was identified to be the first example of a molecule exhibiting magnetic bistability, an SMM. SMMs quickly became a hot research topic since they are candidates for high-density storage devices^[4-5] and quantum computing^[6-12].

Slow relaxation of magnetisation in SMMs is possible due to an energy barrier U_{eff} separating the M_S sub-levels. This energy barrier can be shown schematically in terms of a double well potential (Figure 14).^[3] In equilibrium with no magnetic field applied the degenerate states of the ground state on either side of the energy barrier are

equally populated leading to a total magnetic moment of zero. Once a magnetic field is applied to the system one side of the double well becomes energetically favoured (the side on which the spins are aligned parallel to the external magnetic field) while the other shifts to higher energies. This leads to a preferred population of the energetically favoured state. After removal of the applied magnetic field both states return to degeneracy but, as a result of the energy barrier, relaxation back to the original equilibrium is hindered. This leads to magnetic remanence and slow relaxation of magnetisation. The nature of the Mn_{12} system means that it can be easily analysed in terms of relaxation process which follows the Arrhenius law.^[1]

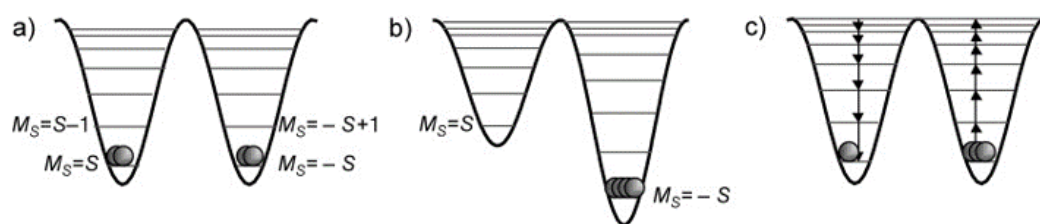


Figure 14. Double well potential and population of states for the example of a 3d ion-containing SMM in zero field (a), with an applied field (b) and after the external field is switched off (c). Adapted with permission from reference^[98] [John Wiley & Sons] copyright 2003].

The energy barrier for this particular system can be defined by the anisotropy given by the absolute value of the axial crystal field splitting parameter D and the square of the total ground state spin of the system. The energy barrier for systems with non-integer ground state spin can be calculated as^[3]

$$U_{eff} = (S^2 - \frac{1}{4})|D| \quad \text{equation 7}$$

and for systems integer ground state spins as

$$U_{eff} = S^2|D| \quad \text{equation 8}$$

The equation for U_{eff} suggests that maximising S should be the easiest way to achieve high energy barriers. However, the example of a Mn_{19} cluster published by Powell *et al.*^[99] with a spin ground state of $S = 83/2$ shows this not to be the case since Mn_{19} does not show any SMM behaviour. Although the compound contains 12 Mn^{III} ions they are arranged in the form of two large octahedra the Jahn Teller axes of the Mn^{III} ions perfectly cancel each other's effects. Thus, the lack of SMM behaviour in Mn_{19} could be explained by the lack of anisotropy which was experimentally shown by the near perfect overlap of the magnetisation curve at 2K with the Brillouin function for

$S = 83/2$. Waldmann later showed that since D is inversely proportional to S^2 a large spin is not the deciding factor in targeting good SMM properties but rather D is the parameter to optimise.^[100]

The magnetic anisotropy is a result of the non-spherical distribution of electron density and leads to a preferred direction along which magnetising the system is easiest. If a system has a negative D value this direction is referred to as the easy axis whereas for systems with positive D it corresponds to an easy plane.^[3, 92]

As a result of their significant intrinsic anisotropy based on large spin-orbit coupling, along with their high-spin ground state, makes lanthanides particularly valuable for research in SMMs. The shape of the anisotropy in the lanthanide series changes with the number of electrons and their distribution as shown in Figure 15.^[101]

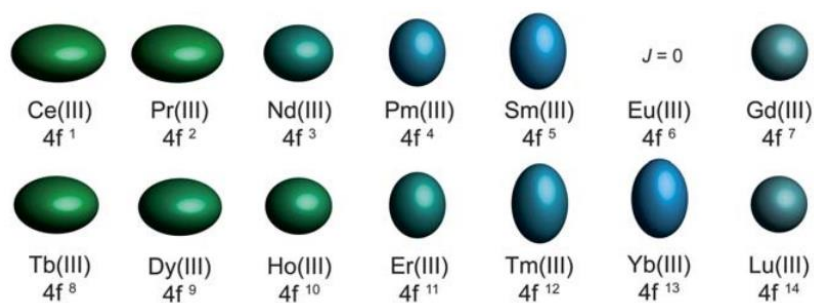


Figure 15. 4 f electron densities approximation for Ln^{III} ions. Adapted with permission from reference^[101] [Royal Society of Chemistry] copyright [2011].

Ions with integer spin such as the lanthanides Tb^{III} , Ho^{III} , Tm^{III} are non-Kramers ions while ions with non-integer spin such as Dy^{III} , Er^{III} , Gd^{III} are Kramers ions. The Kramers theorem states that Kramers ions always have a doubly degenerate ground state.^[102] Dy^{III} is of particular interest in SMM research^[103] since it is a Kramers ion with a high spin ground state and large magnetic anisotropy. Although non-Kramers ions can also lead to SMM behaviour these need a specific ligand field in order to exhibit ground state degeneracy.^[104-106]

The shape of the lanthanide single ion anisotropy has a significant impact on how SMMs should be designed since the effect can either be enhanced or weakened by the ligand field as shown in Figure 16. An axial ligand field should be applied to a lanthanide ion with an oblate anisotropy ellipsoid such as Dy^{III} ^[101, 106-109] whereas an equatorial ligand field should be used for lanthanide ions with prolate anisotropy

ellipsoids such as like Er^{III} .^[110-112] This maximises the respective anisotropy by reducing the electronic repulsion between the electron density of the lanthanide ion and the electron density on the ligands leading to low energy $m_J = J$ states.^[101, 113]

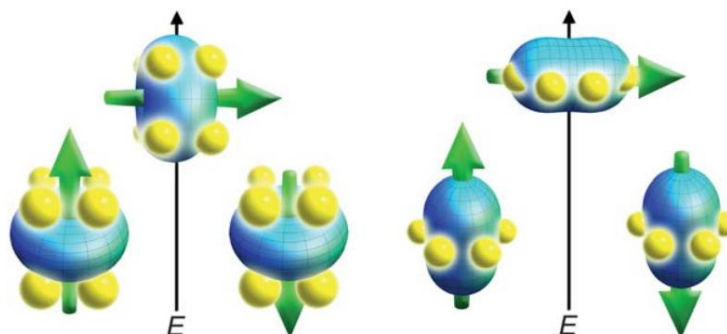


Figure 16. Illustrations of the low- and high-energy arrangements of 4f-orbital electron density in relation to the crystal field environment for a 4f ion with oblate (left) and prolate (right) electron density distributions. Adapted with permission from reference^[101] [Royal Society of Chemistry] copyright [2011].

High energy barriers U_{eff} alone are not sufficient to create SMMs with high blocking temperatures since not all systems follow the desired Orbach relaxation (Arrhenius law) over the energy barrier. Other relaxation processes which provide pathways for magnetic relaxation through the energy barrier and are particularly prevalent in lanthanide SMMs include quantum tunnelling of magnetisation (QTM), thermally assisted quantum tunnelling of magnetisation (TA-QTM), the Raman process and the direct process.^[104, 114]

QTM and TA-QTM describe the tunnelling through the energy barrier to states of the same energy either between ground states (QTM) or excited states (TA-QTM). QTM can completely quench SMM behaviour but can be counteracted by splitting the involved Kramers' doublets using an applied magnetic field thus lifting the degeneracy of states. Compounds which can only show SMM behaviour in this way are often referred to as field-induced SMMs. The direct process involves the relaxation from an excited state to a lower state on the other side of the energy barrier. It is a one phonon process for which the energy difference when transitioning between two states of a Kramers' doublet split by Zeeman interactions is compensated by an acoustic phonon. The Raman process is a two-phonon process which involves a virtual state. The phonon mediated relaxation mechanism for the direct and Raman process are illustrated in Figure 17.^[104, 114-116]

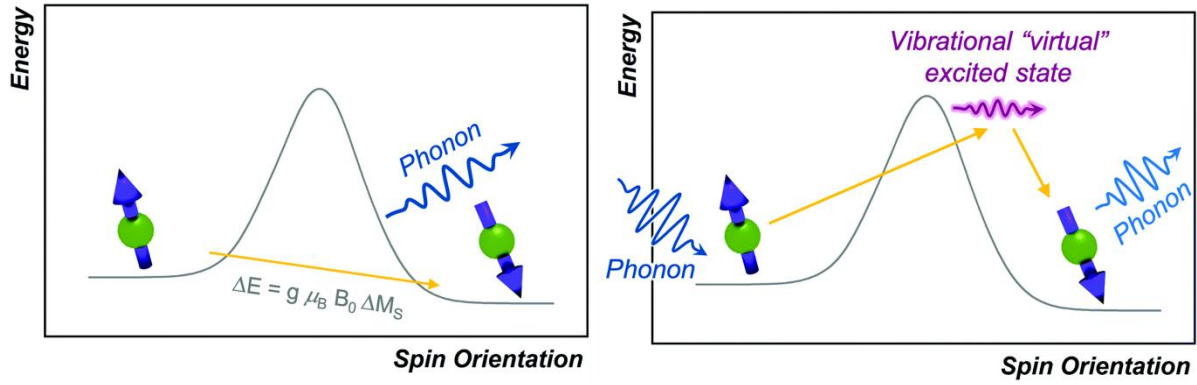


Figure 17. Illustration of direct process (left) and Raman process (right). Adapted with permission from reference^[115] [Royal Society of Chemistry] copyright [2021].

Equation 9 is a popular way to determine the contribution of each process to the overall relaxation dynamics in the system.

$$\tau(T)^{-1} = AT + B + CT^n + \tau_0^{-1}e^{-\frac{U}{k_B T}} \quad \text{equation 9}$$

Direct QTM Raman Orbach

A, B and C are parameters describe the rates of the direct process, QTM and Raman process, respectively, n is the Raman exponent, τ_0 denotes the pre-exponential factor of the Orbach process, U is the thermal energy barrier and k_B is the Boltzmann constant. Recently two working groups^[117-119] have individually proposed alternative equations which mainly address the use of the power law for the Raman process in equation 9. Equation 10 shows the work of Lunghi *et al.* describing the Raman process with an exponential function.^[117]

$$\tau(T)^{-1} = AT + B + V \frac{\exp\left(-\frac{w}{k_B T}\right)}{\left(\exp\left(-\frac{w}{k_B T}\right) - 1\right)^2} + \tau_0^{-1} \exp\left(-\frac{U}{k_B T}\right) \quad \text{equation 10}$$

Here A and B also describe the direct process and zero field QTM while the Raman process is defined by the preexponential factor V and an energy barrier w for the Raman relaxation. The Orbach term consists of the preexponential factor τ_0 and the corresponding energy barrier U.

The relaxation time τ depends on the height of the system's energy barrier as well as the efficiency of relaxation processes which can go through the energy barrier. An energy barrier determined by fitting of AC data with the aforementioned formulae often equates to the energy of the systems first excited Kramers' doublet due to high

efficiency of TA-QTM. The increased efficiency of TA-QTM in excited states is a result of larger contributions from transverse components of the anisotropy.^[98, 120-121]

The blocking temperature can be defined as the temperature at which an open hysteresis loop can still be observed. Other definitions are the temperature at which maxima are observed in the AC out-of-phase susceptibility at the benchmark frequency of 1000 Hz or the maximum observed in a zero-field-cool measurement of the susceptibility. Furthermore, it can be defined as the temperature at which the relaxation time is equal to 100 s or for some high-performing SMMs 1000 s (T_B^{100} or T_B^{1000}) which some consider more sensible since there is no defined coercive field at which a hysteresis is considered to be closed. Recently the use of T_{switch} has been proposed by Chilton *et al.* (see Figure 18) to compare SMM behaviour. T_{switch} is the relaxation time at which the Raman process becomes more efficient than the Orbach process.^[122]

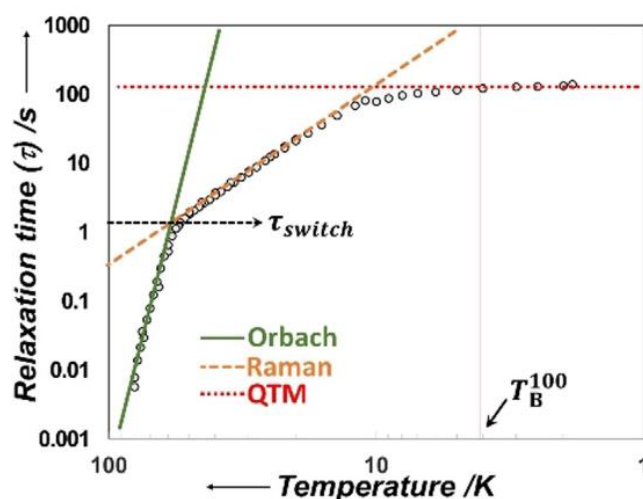


Figure 18. Relaxation time τ against temperature, showing T_{switch} and T_B^{100} . Adapted with permission from reference ^[123] [Elsevier] copyright [2020].

Strategies to quench QTM^[116] and thus improve SMM behaviour include the use of radical ligands. These benefit from additional paramagnetic interactions leading to stronger magnetic coupling. The first example where this was shown to be an effective strategy is the N_2^{3-} radical bridged Dy^{III} dimer by Long *et al.*^[124] Since then many more examples of radical bridged complexes have been published.^[125] Other strategies include using Dy^{III} in axial coordination environments and thus taking advantage of the shape of the single ion anisotropy^[109, 123, 126-127] as well as designing mixed 3d/4f

coordination compounds in which the advantages of 3d ions and 4f ions can be utilised in full.^[20, 128-130]

The involvement of phonons in the different relaxation processes is the basis for some possible strategies of quenching relaxation pathways such as the Raman process by eliminating the possibility of having vibrations in the molecule or lattice available at these specific energies.^[114, 122, 131]

The main difference between 3d and 4f compounds is the electronic structure and in particular the radial distribution of the electrons in 3d or 4f orbitals. For 4f ions the valence electrons usually do not participate in any bonding which means the influence of spin orbit coupling is much larger than the crystal field splitting induced by the ligands. The typical magnitudes of the influences on the splitting of states for lanthanide ions are shown in Figure 19.^[91, 123]

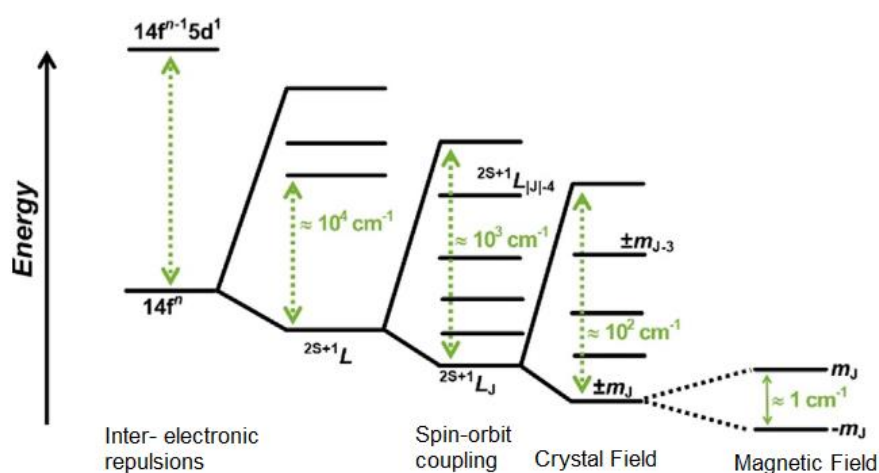


Figure 19. Influence of different effects on the splitting of electronic states in lanthanide ions and their respective energies. Adapted from reference^[123].

The interest in the field of 3d/4f SMMs increased rapidly after the discovery of the first 3d/4f SMM in 2003 by Osa *et al.*^[132] It was shown that using 3d and 4f ions in combination will have the positive effects of the anisotropy and a large spin ground state of the lanthanide while also benefitting from stronger magnetic exchange interactions due to the radial extension and more localised nature of the 3d orbitals. This means that 3d-4f interactions are usually magnitudes larger than similar Ln-Ln interactions and are sufficient to quench QTM.^[20, 25, 133-134] Research in this field into controlling the interactions within the metal core made it possible to construct compounds with exotic quantum-physical and -chemical properties. This includes the

formation of excitons in $\text{Fe}_{10}\text{Ln}_{10}$ clusters^[34] or approaching a quantum critical point with an infinite number of ground states^[29] by variation of the nuclearity and thus the size of the Fe_nGd_n ring analogues.^[135] The interactions between 3d and 4f ions has also been used to mediate coupling between toroidal moments by linking triangular Dy_3 units such as in the one-dimensional CuDy_3 polymers,^[136] the CrDy_6 triangle pairs^[137] or the large $\text{Fe}_{18}\text{Dy}_6$ cluster^[138] (more details on toroidal clusters in section 3.6).

The approach of optimising the axial ligand field to increase the anisotropy of the Dy^{III} ion in a low nuclearity purely 4f compound yielded the most promising results in terms of blocking temperatures observed for SMMs to date.^[139-142] The record value is currently held by two Dy^{III} based complexes with an open hysteresis observed at 80 K which is a remarkable achievement since blocking temperatures above 77 K allow for liquid nitrogen cooling rather than using liquid helium. One of these compounds is a dysprosocenium complex with the formula $[\text{Dy}(\text{Cp}^*)(\text{Cp}^{\text{iPr5}})][\text{B}(\text{C}_6\text{F}_5)_4]$.^[143] The second record holding molecule was published in 2022 by Long *et al.*^[144] and combines the axial ligand field in another dysprosocenium-type complex with the addition of single electron bridging between Ln^{III} ions. It has the formula $[\text{Dy}_2(\text{Cp}^{\text{iPr5}})_2\text{I}_3]$ and contains a Dy-Dy bond with a bond order of 0.5. This bond increases the interaction strength between the Ln^{III} centres and leads to an energy barrier of 1621 cm^{-1} . The strong interactions lead to collinear spins of all magnetic centres including the bonding electron, resulting in an open hysteresis up to 80 K and a T_B^{1000} of over 60 K. It thus matches the mononuclear dysprosocenium in terms of blocking temperature but has a much longer relaxation time (T_B^{1000} at ca. 30 K for the mononuclear dysprosocenium). The molecular structures of both compounds are shown in Figure 20.^[143-144]

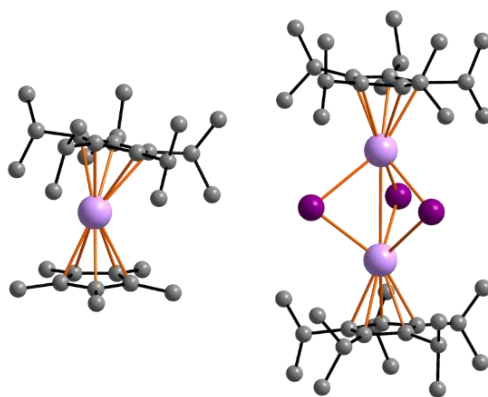


Figure 20. Molecular structure of dysprosocenium-type high temperature SMMs.^[143-144]

3.5 Toroidal moments

Interactions between metal centres either through exchange interactions along bonds or dipolar interactions between magnetic dipoles through space can lead to ferro- or antiferromagnetic coupling of Ising spins (only two possible orientations, up or down) in complexes. In the example of a triangular metal core and ferromagnetic interactions all spins can align parallel, whereas for antiferromagnetic interactions the antiparallel arrangement of all three Ising spins is not possible. In such a case transition metal complexes such as Fe_3 triangles show spin frustration.^[145-153] Since this magnetic frustration is the result of the triangular geometry of the system it is also referred to as geometric frustration.^[154] This may also be observed in other geometries and topologies such as squares and tetrahedra provided the J_{nn} (nearest-neighbour) and J_{nnn} (next-nearest-neighbour) are of equal strength as shown in Figure 21.

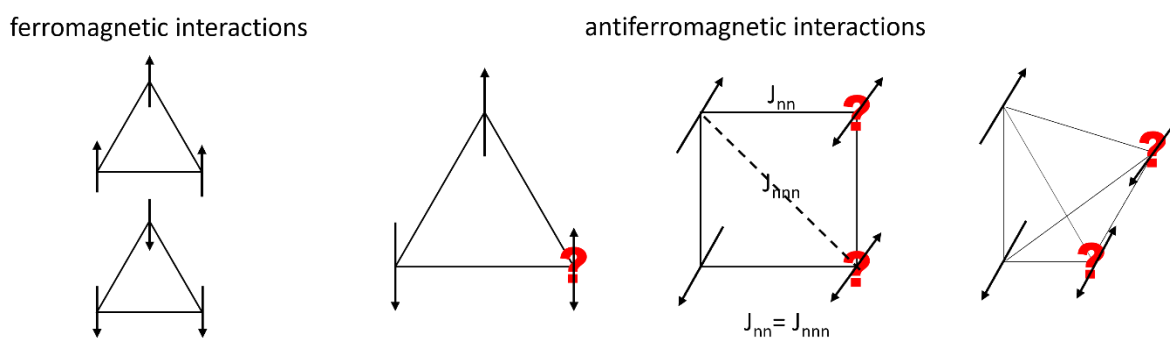


Figure 21. Ferromagnetic arrangement of Ising spins in a triangular metal core (left). Spin frustration in different geometries for antiferromagnetic coupling (right). Adapted with permission from reference^[154] [Royal Society of Chemistry] copyright [2000]

Lanthanide ions, if arranged in a similar fashion, can avoid magnetic frustration by assuming an in-plane vortex-like arrangement of spins. A result of this vortex arrangement of spins is a toroidal moment. There are two possible degenerate orientations, either clockwise or anticlockwise. This in-plane arrangement can also be assumed in geometries other than triangles such as squares (see Figure 22).^[137, 155-156]

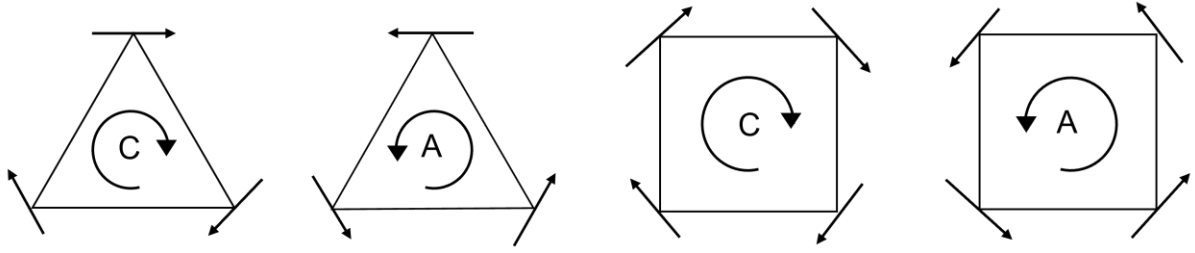


Figure 22. Toroidal clockwise (C) and anticlockwise (A) arrangement of spins in a triangular and a square core.

A toroidal dipole moment T is generated by poloidal currents on a torus *i.e.* currents wrapping around the surface of a torus, generating a magnetic field B only inside the toroid (see Figure 23).^[47] The charge current distribution given by a toroidal dipole was first described in the context of non-radiating states and hypothesised to be an example of an anapole in the **static** regime by Zel'dovich *et al.* in 1957.^[157] The anapole moment was first experimentally observed in 1997 by Wood *et al.*^[46] who investigated caesium nuclei with an inhomogeneous applied magnetic field.^[47]

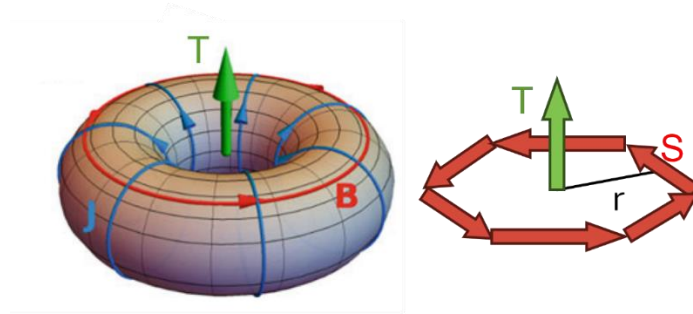


Figure 23. Formation of a toroidal moment T (green arrow) as a consequence of a poloidal electric current J (blue arrows) which induces a toroidal magnetic field B (left) or resulting from head to tail arrangement of spins S (red arrows) in a vortex in-plane formation around a centre with the radius r (right). Adapted from reference^[158].

In general, an anapole moment equates to a toroidal dipole moment arising from the multipole decomposition of a charge-current configuration. In other words the electric and magnetic dipole moments describe the field, whereas the anapole moment describes the charge current distribution. Its existence can be explained by the more general theorem regarding non-radiating (*i.e.* dark) excitations.^[44-45, 47, 159]

For the **dynamic** regime the anapole is a superposition of electric/magnetic and toroidal dipoles (see Figure 24). The radiation from each interferes destructively, rendering anapoles entirely non-radiating and thus undetectable. This property makes anapoles a promising candidate for insights into dark matter.^[45, 47]

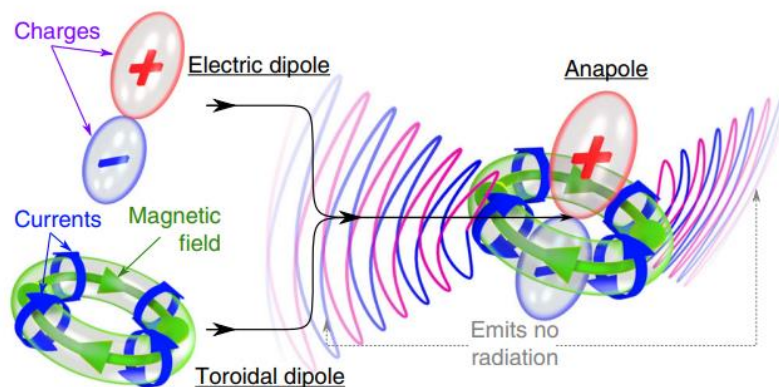


Figure 24. Combination of toroidal dipole and electric dipole forming an anapole. Adapted with permission from reference^[45] [Springer] copyright [2019].

Toroidal dipoles are part of a group of four multipoles which form a complete set to define the Hilbert space under the space-time inversion group. These are the magnetic, electric, magnetic toroidal and electric toroidal multipoles. Toroidal magnetic moments reverse the sign of both parity and time-reversal operations meaning the direction of the toroidal moment is inverted under both inversion (parity and time reversal) of current direction and spatial coordinates. The toroidal electric moment is invariant to both operations, the magnetic multipole reverses sign under time reversal symmetry and the electric dipole and space inversion symmetry (see table 1). Multipole theory can be used to describe system in terms of their multipole components.^[159]

Table 1. Multipoles and their respective symmetry towards parity (space inversion) and time reversal with (-) indicating odd (change of sign) and (+) even symmetry (no change of sign).^[159]

	Parity (P)	Time reversal (T)
electric (E)	-	+
magnetic (M)	+	-
electric toroidal (ET)	+	+
magnetic toroidal (MT)	-	-

A toroidal moment can be calculated as the cross product of the spins s_n and their respective distance r_n from the centre of the molecule.^[160]

$$\sum_{n=0}^n r_n \times s_n \quad \text{equation 11}$$

Unlike magnetic dipole moments, which interact linearly with an applied magnetic field, the toroidal moment interacts with field inhomogeneities described by the curl of the magnetic field which can be expressed as the cross product of the nabla operator and the field \mathbf{B} ($\nabla \times \mathbf{B}$). This has significant implications for molecular systems with toroidal moments both for investigation purposes and application. The field of what are now known as Single Molecule Toroids (SMTs) focuses mainly on developing quantum computing and high-density data storage devices. These systems are resilient to stray dipolar fields meaning they can be packed closer in novel data storage devices, but also means that they are more difficult to manipulate due to the challenges of creating the required field inhomogeneities at a molecular level.^[158]

Ferrotoroidic order (FTO) is an effect that describes a spontaneous long-range ordering of toroidal moments and is necessary to create multiferroic materials. Multiferroics are a class of material which combine the properties of two or more ferroic phases (ferromagnetic, ferroelectric, ferroelastic and ferrotoroidic).^[161] This allows for the manipulation of magnetic or toroidal properties using, for example, the magnetoelectric effect *i.e.* the phenomenon where a magnetisation \mathbf{M} is induced by an applied electric field \mathbf{E} or a polarisation \mathbf{P} is induced by applying a magnetic field \mathbf{H} . The prerequisite for this effect is a magnetic and electric order in the multiferroic material. Figure 25 shows the four fundamental ferroic orders as well as their time-reversal and space inversion symmetry. Ferroic materials can show hysteresis and memory effects due to the formation of domains for differently ordered states.^[158] FTO was first observed in the solid state material LiCoPO_4 in 2007.^[162] Coupling between toroidal moments in molecular systems was also shown to be possible, for example by introducing transition metals and taking advantage of the stronger 3d/4f coupling. This can lead to the desired ferrotoroidic order and in turn an enhancement of the collective toroidal moment of the system.^[163] Examples where this was achieved are the Dy_6Cr triangle pair by Murray *et al.*^[137] or the $\text{Fe}_{18}\text{Dy}_6$ cluster by Powell *et al.*^[138]

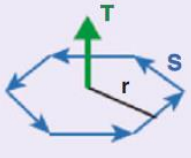
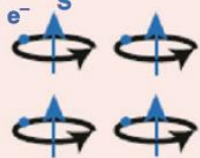
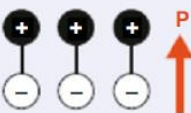

<div>SPACE</div> <div>TIME</div>	CHANGE	INVARIANT
	CHANGE	INVARIANT
CHANGE	a.) Ferrotoroidic 	b.) Ferromagnetic 
	c.) Ferroelectric 	d.) Ferroelastic 
INVARIANT		

Figure 25. The four primary ferroic orders and their symmetry regarding space-inversion or time-reversal. Reprinted with permission from reference^[161] [Science Direct] copyright [2019].

3.6 Single molecule toroics (SMTs)

A single molecule toroic (SMT) is a coordination compound with a bistable non-magnetic toroidal ground state. The field of SMTs began with the discovery of a trinuclear Dy^{III} complex with three *o*-vanillin ligands surrounding the triangular metal core exhibiting a non-magnetic ground state by Powell *et al.* in 2006 (see Figure 26).^[37]

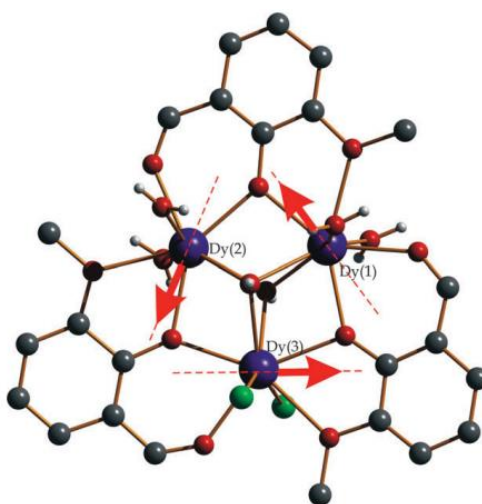


Figure 26. Molecular structure of the original toroidal Dy_3 with tangential in-plane arrangements of anisotropy axes (red arrows). Reprinted with permission from reference^[38] [John Wiley & Sons] copyright [2008].

The compound was initially published to highlight its SMM behaviour observed in the thermally excited spin states. In this paper the unusual S-shape of the magnetisation as well as the rather unusual dynamics of the ac susceptibility measurements were commented on. Subsequently the availability of a suitable single crystal for further physical measurements and the collaboration with theoreticians Ungur, Chibotaru and Soncini led to the publication of two papers in 2008 both explaining the non-magnetic ground state and toroidal nature of the system.^[38-39] This was substantiated by microSQUID data and the calculation of the toroidal arrangement of the anisotropy axes. The observed in-plane non-collinear vortex spin structure gave an example of the first molecule showing a permanent toroidal moment in the ground state.

Subsequently more triangular Dy₃ compounds^[164-166] showing toroidal behaviour were discovered along with Dy₄ compounds,^[155, 167-168] hexagonal Dy₆ wheels,^[28, 169] Dy₆ double triangles^[170-172] and a snub-square Dy₈.^[173] Toroidal moments were also observed for complexes using Tb^{III} or Ho^{III} ions which form hexanuclear wheels^[174] and single^[175] or double triangles^[176] or squares.^[177-178]

The field of SMTs further extended by the implementation of transition metal ions such as in a series of heptanuclear triangle pairs linked by a transition metal ion by Murray *et al.*^[137, 179] or 1D-Dy₃Cu polymers by Powell *et al.*^[136] The addition of transition metals was shown to allow for ferrotoroidic coupling between toroidal units in these compounds.

The first example of a toroidal ground state in a compound with a Dy₄ core was published in 2012.^[155] The four Dy^{III} ions are coplanar with their anisotropy axes almost in-plane and in a vortex arrangement (see Figure 27 a). In 2018 a Dy^{III} Cubane structure was published by Sessoli *et al.*,^[167] adding to the family of SMTs with a nuclearity of four and being the first example for a non-magnetic ground state in a non-planar arrangement of magnetic centres (see Figure 27 b). Subsequently, in 2022 another such example, now with a tetrahedral core of Dy^{III} ions, was published by Tang *et al.* (see Figure 27 c).^[168]

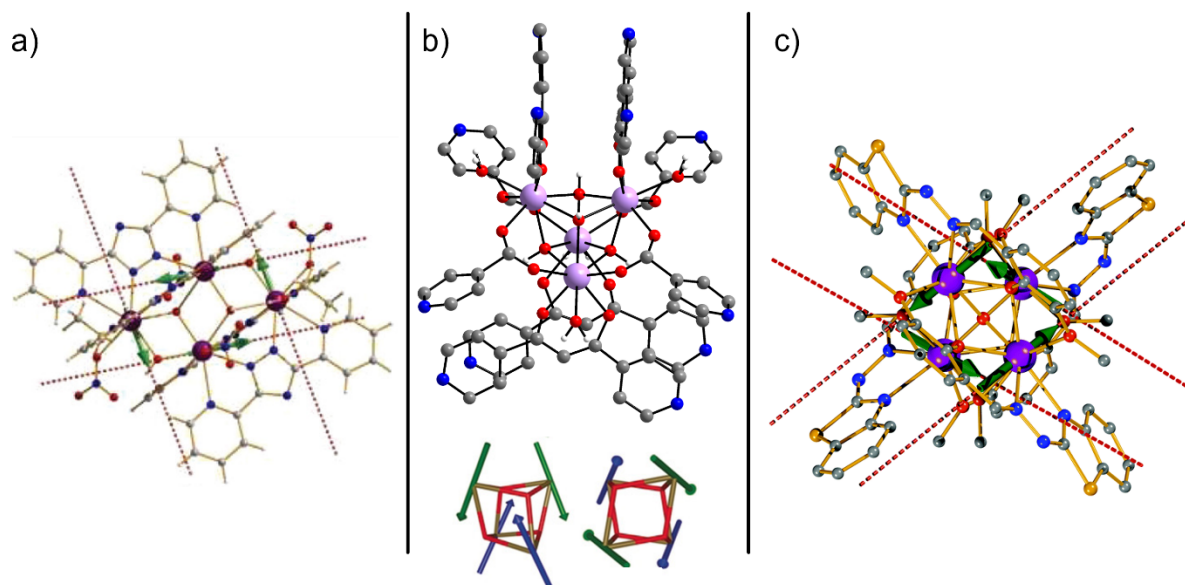


Figure 27. Planar Dy_4 with anisotropy axes as green arrows in a), reprinted with permission from reference^[155] [American Chemical Society] copyright [2012], cubane Dy_4 with anisotropy axes in core below in b), reprinted with permission from reference^[167] [John Wiley & Sons] copyright [2018], and tetrahedral Dy_4 with anisotropy axes as green arrows in c), reprinted with permission from reference^[168] [Royal Society of Chemistry] copyright [2022].

The influence of the ligand field and particularly the charge of the terminal ligands on the orientation of anisotropy axes in compounds with a $[\text{Dy}_3-(\mu_3\text{-OH})_2]$ core was shown in 2016 in the work of Tang *et al.*^[172] In this study two previously published Dy_3+Dy_3 double triangle complexes^[180] with NO_3^- and SCN^- terminal ligands were compared to a similar compound with terminal water ligands. Magnetic measurements and *ab initio* calculations revealed that the use of charged terminal ligands leads to the orientation of the anisotropy axes out of plane. By exchanging the terminal ligands by water the axes become oriented in-plane leading to a toroidal ground state (see Figure 28).

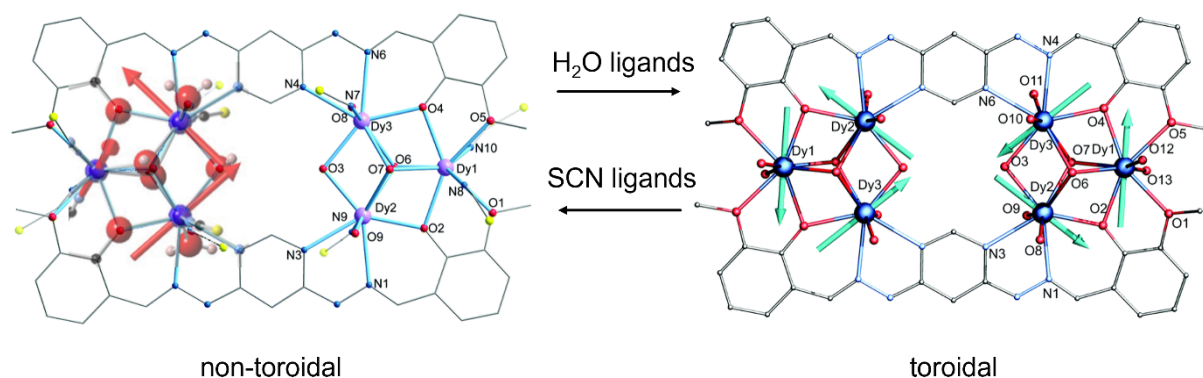


Figure 28. Dy_3+Dy_3 with SCN^- ligands (left) with one anisotropy axis out of plane and in-plane arrangement of spins for Dy_3+Dy_3 with water ligands (right). Adapted with permission from reference^[180] [Royal Society of Chemistry] copyright [2015] (left) and from reference^[172] [Royal Society of Chemistry] copyright [2016] (right).

The bridging mode of the ligands in the centre of the triangular core was also investigated as it is possible to keep the triangular metal core geometry intact while exchanging the $(\mu_3\text{-OH})_2$ moiety for a bridging carbonate,^[181] peroxide,^[182-183] or fluoride^[184] ligand. This can also lead to a toroidal ground state as shown for the case of a carbonate-bridged Zn_3Dy_3 compound by Chandrasekhar *et al.*^[181] However, it can also lead to a situation in which the anisotropy axes are flipped towards the middle as was observed for the hard F^- bridging ligand in the centre of a Dy_3Cr_3 cluster published by Zheng *et al.*^[184] Whereas the Zn_3Dy_3 shows the expected non-magnetic ground state in the microSQUID, the Dy_3Cr_3 shows a hard, wide and open hysteresis due to an avoided level crossing.

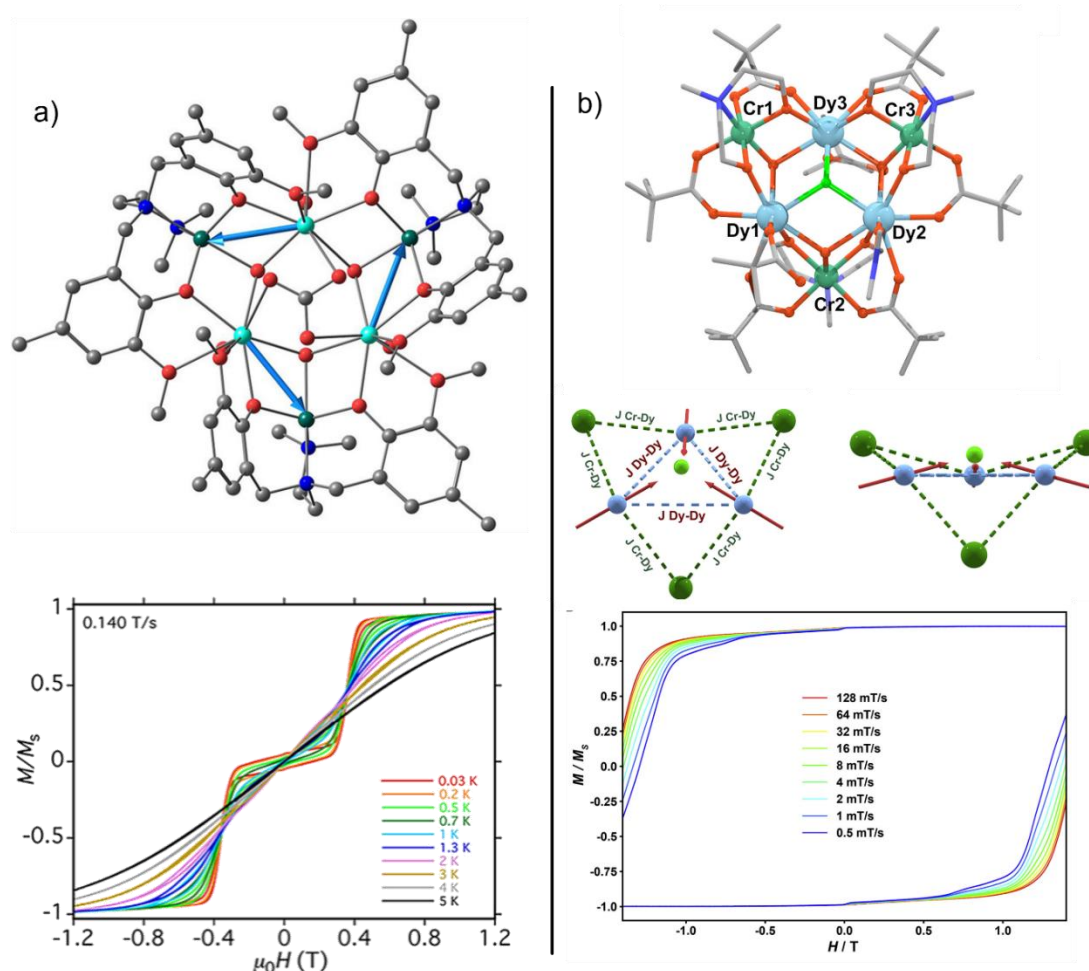


Figure 29. Molecular structure and orientation of anisotropy axes with microSQUID for Zn_3Dy_3 in a), adapted with permission from reference^[181] [American Chemical Society] copyright [2016], and for Dy_3Cr_3 in b), adapted with permission from reference^[184] [Elsevier B.V.] copyright [2022].

An example of a larger cyclic compound with a net toroidal magnetic moment in the ground state was published by Murray *et al.*^[169] in the form of a Dy_6 -triethanolamine

ring and also a similar Dy₆ ring using a different ligand by Powell *et al.*^[28] (see Figure 30).

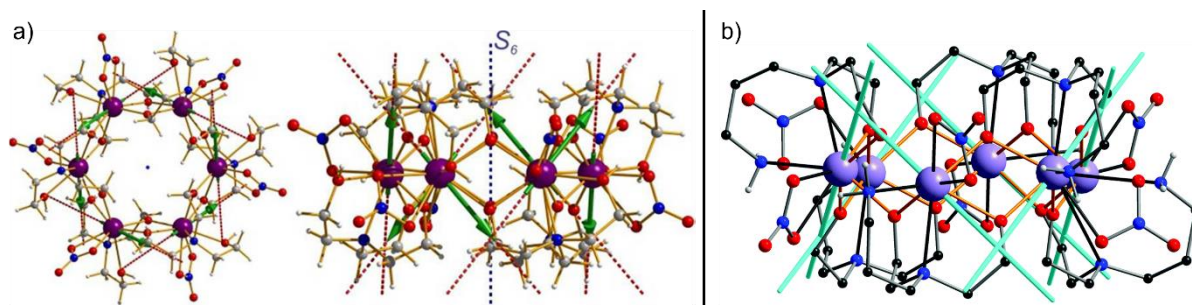


Figure 30. Dy₆ by Murray *et al.* in a) by Powell *et al.* in b). Adapted with permission from reference^[169] [American Chemical Society] copyright 2012 in a) and adapted with permission from reference^[28] [Royal Society of Chemistry] copyright [2015] in b).

Although research on SMTs was primarily focused on Dy^{III} as the paramagnetic centre owing to its high anisotropy it was later shown to be possible to achieve the non-magnetic toroidal ground state in Tb₃ and Ho₃ rings^[175] as well as Tb₄ squares^[178] (see Figure 31). This opened new pathways for the design and synthesis of novel SMTs.

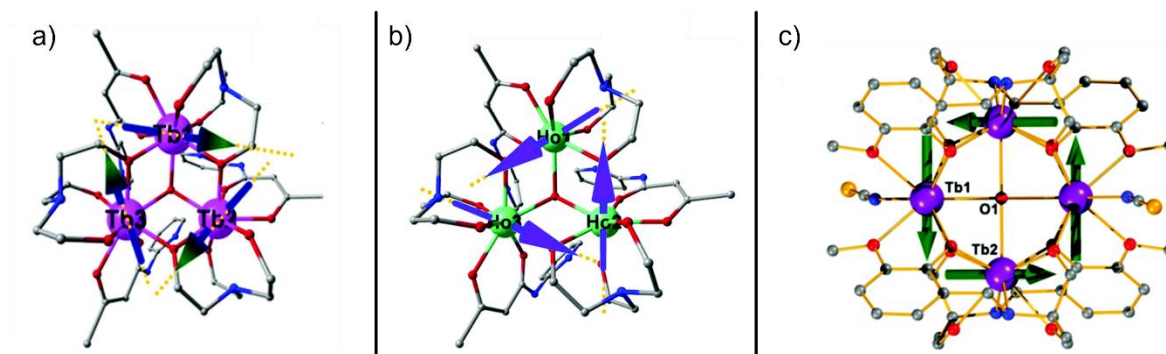


Figure 31. Toroidal Tb₃ in a), Ho₃ in b) and Tb₄ in c). Adapted with permission from reference^[175] [Royal Society of Chemistry] copyright [2019] a) and b). Adapted with permission from reference^[178] [Royal Society of Chemistry] copyright [2022] in c).

The introduction of 3d ions into compounds with a Dy₃ toroidal moiety was shown to promote coupling between toroidal moments leading to ferroic order. This effect was observed in the Cu^{II}/Dy^{III}1D chiral polymers published by Powell *et al.* in 2012,^[136] a Cr^{III}Dy^{III}₆ triangle pair published by Murray *et al.* in 2017,^[137] as well as the large Fe₁₈Dy₆ by Powell *et al.* in 2020^[138] (see Figure 32). In these compounds the ferroic order is introduced through the Cu^{II}/Cr^{III} ions or the strongly antiferromagnetically coupled Fe^{III}₁₈ ring between Dy₃ moieties.

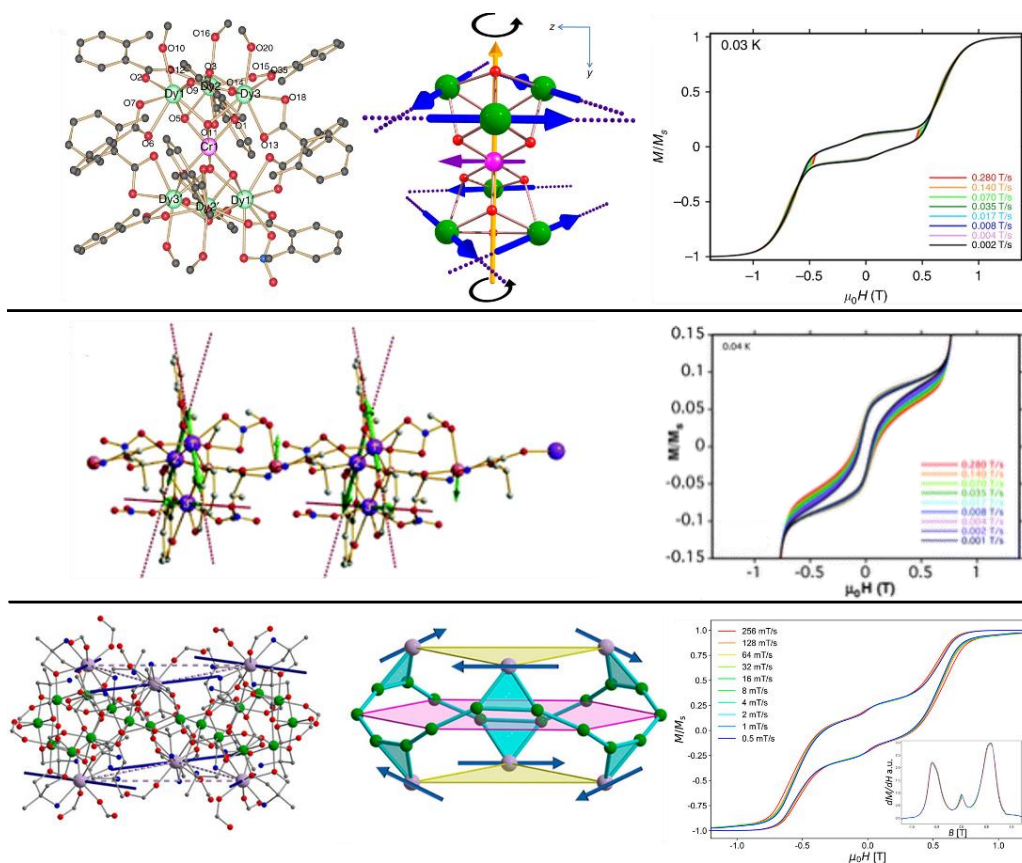


Figure 32. Structure and orientation of anisotropy axes with microSQUID for CrDy_6 (top), adapted with permission from reference^[137] [Springer] copyright [2017], CuDy_3 polymer (middle), adapted with permission from reference^[136] [Royal Society of Chemistry] copyright [2012], and $\text{Fe}_{18}\text{Dy}_6$ (bottom), adapted with permission from reference^[138] [American Chemical Society] copyright [2020].

Other ways of implementing 3d metals include the alternation of 3d and 4f ions in a ring. Examples for this are the Dy_6Cu_6 and Tb_6Cu_6 by Tang *et al.*^[156] or the Fe_8Dy_8 by Zheng *et al.*^[185] (see Figure 33) which were shown to have SMT properties. Here the 3d ions also act as bridges by coupling to 4f ions.

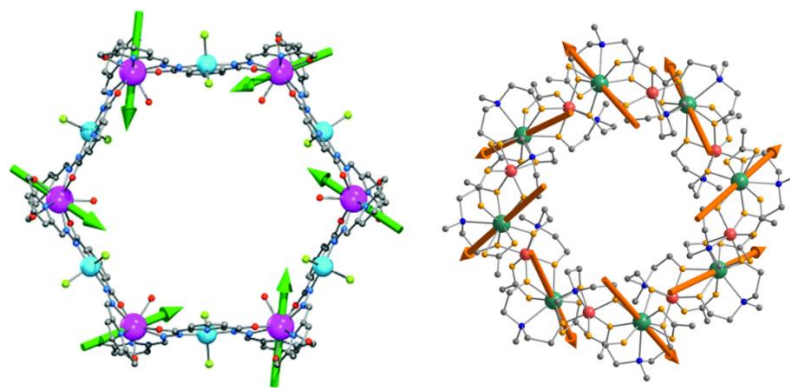


Figure 33. Molecular structures and anisotropy axes of Ln ions in top-down view of Tb_6Cu_6 (left) and Fe_8Dy_8 (right). Adapted with permission from reference^[156] [Royal Society of Chemistry] copyright [2018] left and with permission from reference^[185] [Elsevier Inc.] copyright [2020] right.

The toroidal properties of SMTs can be characterised using different magnetic measurement techniques. A standard field dependent magnetisation measurement on randomly oriented powder sample shows for compounds with a toroidal ground state that there is an inflection point leading to an S-shape which indicates a level crossing at the switching field. This corresponds to the point where the applied field is strong enough to flip spins and thus the toroidal state ceases to be the ground state. This behaviour is best evaluated from the corresponding Zeeman diagrams. Two single crystal measurement techniques which allow for the determination of the orientation of the anisotropy axes, and therefore the presence of a toroidal ground state, are angle dependent microSQUID measurements^[186] and cantilever torque magnetometry.^[187] Torque measurements in combination with theoretical calculations can determine exactly the two angles at which the anisotropy axes deviate from the perfect in-plane arrangement as well as the tangential orientation, respectively. Furthermore, microSQUID measurements can, in combination with the Zeeman diagrams, also give an idea of the transitions between toroidal and ferromagnetic states at the switching field.

The switching field is an important characteristic for toroidal compounds since it identifies the field at which the toroidal state is no longer the ground state. This can be determined by using the first derivative of the magnetisation plot or of the microSQUID data and can also be seen in the Zeeman plot. The main differences between the two measurement techniques are the temperature range they are performed at and the sample preparation. For microSQUID a single crystal is used whereas for SQUID magnetisation measurements an immobilised randomly oriented powder is used. The switching fields determined by means of these techniques will be different and in the case of single crystal measurements will also show angle dependence. Zeeman diagrams calculated for different angles of the applied field with respect to the compound can rationalise this behaviour (see Figure 34).

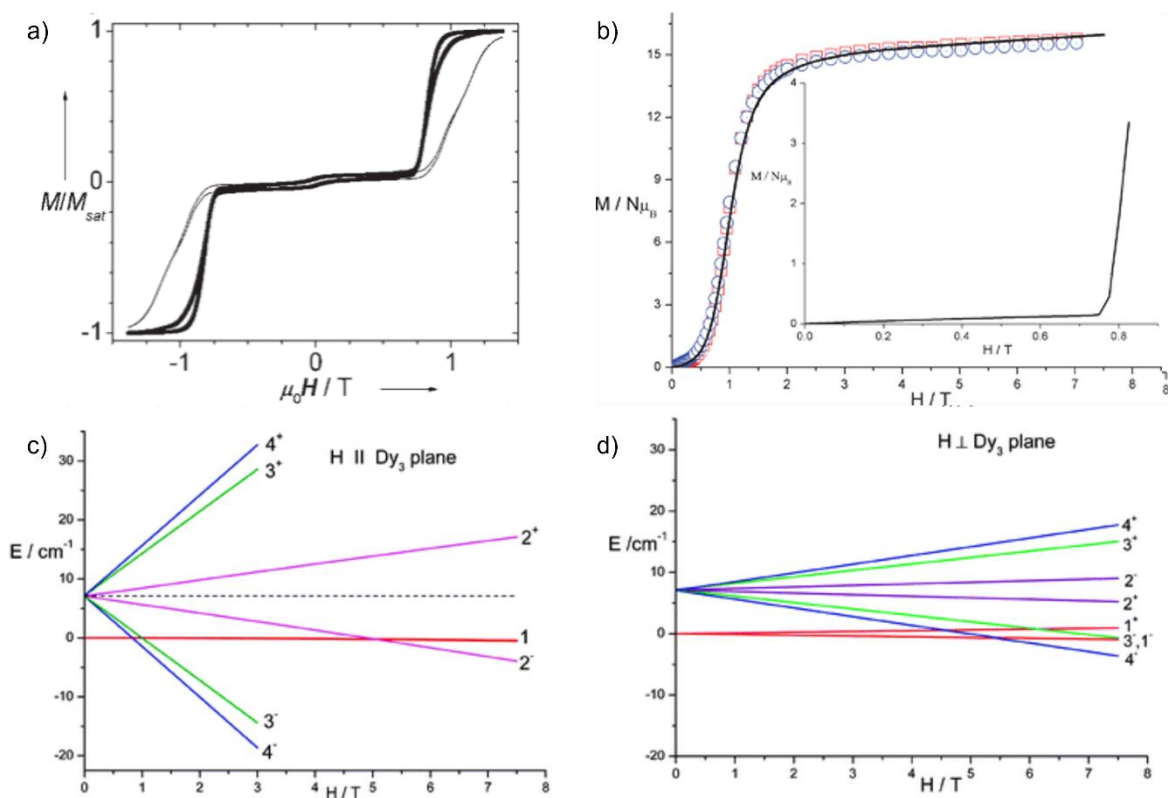


Figure 34. MicroSQUID in-plane and perpendicular to the triangle plane a) reprinted with permission from reference^[37] [John Wiley & Sons] copyright [2006], magnetisation with inset of low field range b), Zeeman diagrams for an applied field in and out of the plane of the triangle in c) and d) for the Dy_3 with *o*-vanillin ligands by Powell *et al.*, reprinted with permission from reference^[40] [Royal Society of Chemistry] copyright [2009].

MicroSQUID measurements are generally performed along the easy axis of a system but in some cases it can be sensible to measure along intermediate axes as well. From temperature dependent microSQUID measurements the stability of the toroidal state in regard to thermal effects can also be investigated.

4. Coordination compounds containing Fe^{III} and Ln^{III} ions

4.1 Introduction to Fe^{III}-Ln^{III} coordination clusters

Here the focus is on the study of 3d-4f compounds corresponding to the highly adaptable Fe₂Ln₂ butterfly systems as well as cyclic coordination clusters (CCCs) with a nuclearity of 20. Amongst these, the M₂Ln₂ butterfly motif has gained recognition as a valuable testbed system as a result of its synthetic versatility and wide range of tuning handles.^[17-20, 22-25, 188-197] These attributes enable detailed investigations into how structural and chemical modifications influence magnetic properties.

The core structure of M₂Ln₂ butterflies consists of two Ln^{III} ions and two 3d ions. These ions occupy specific positions to form two structural types: Type I or Type II. In Type I structures, the transition metal ions occupy the body positions, whereas the lanthanides occupy the wingtips. This arrangement is reversed in Type II butterflies, where the lanthanides form the body and the transition metals take the wingtip positions (see Figure 35).^[22]

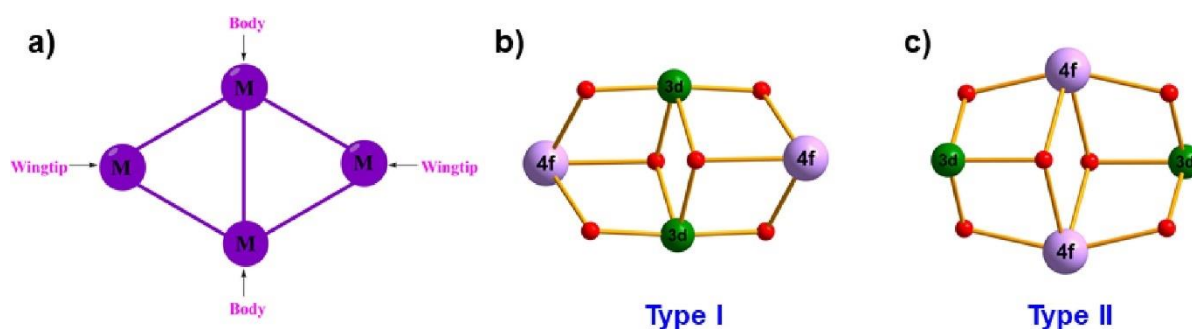


Figure 35. Scheme showing the body and wingtip positions of a butterfly type structure in a), core of a Type I in b) and core of a Type II butterfly in c). Reprinted with permission from reference^[22] [John Wiley & Sons] copyright [2021].

Butterfly systems commonly use substituted diethanolamine-type ligands *e.g.* triethanolamine (teaH₃) or methyl-diethanolamine (Me-deaH₂) and carboxylates such as benzoates as co-ligands which can be both bridging and terminal. Both types of ligands, as well as the transition metals and lanthanides, can be exchanged or functionalised (see Figure 36).

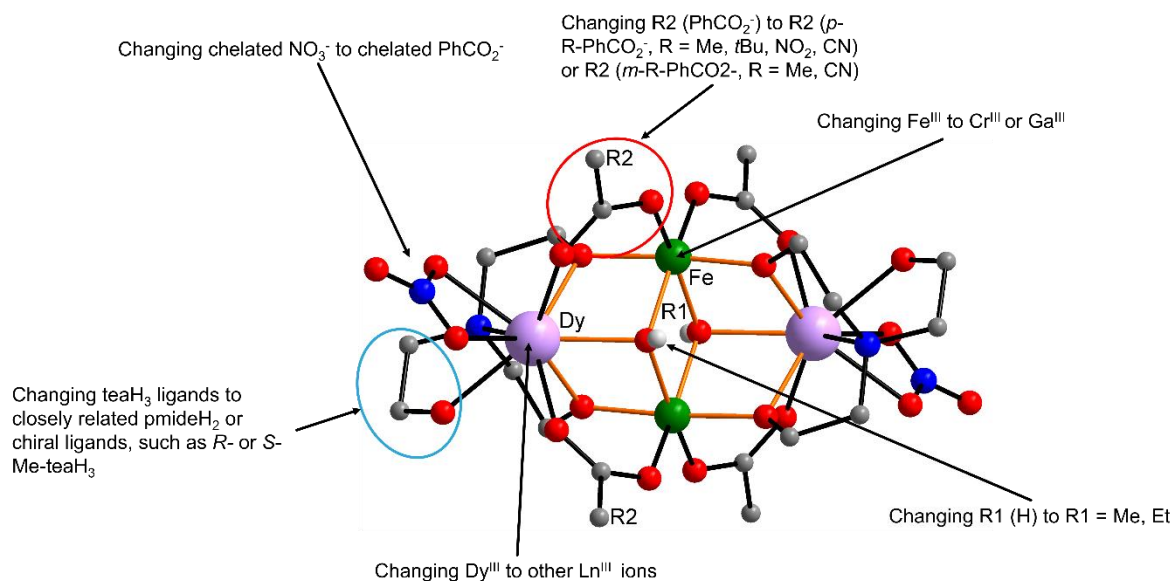


Figure 36. Possible modifications on the Fe_2Ln_2 testbed system on the example of $[\text{Fe}_2\text{Dy}_2(\mu_3\text{-OH})_2(\text{teaH})_2(\text{O}_2\text{CPh})_4(\text{NO}_3)_2]\cdot 6\text{MeCN}$. Adapted from reference with permission^[22] [John Wiley & Sons] copyright [2021].

These modifications allow for magnetostructural correlations revealing the effects of ligand substitution and electronic changes on magnetic behaviour. In particular the carboxylate co-ligands play a significant role in determining magnetic properties, as substitution with electron-withdrawing groups have been shown to reduce ZFQTM and thus enhance SMM properties.^[24, 133, 196, 198]

One of the key advantages of the butterfly system is its ability to provide insights into the magnetic interactions between 3d and 4f ions. These interactions are central to the system's overall magnetic behaviour and can be explored in detail by using diamagnetic ions to substitute the paramagnetic ones to effectively suppress their contributions. Despite the relatively low nuclearity of butterfly systems, understanding their magnetic properties remains a significant challenge due to the complexity of 3d-4f interactions. Butterfly-type structures with a variety of 3d metals, including Cr^{III} , Mn^{III} , Fe^{III} , Al^{III} , Co^{III} , Ni^{III} , Zn^{II} , and Mg^{II} , have been reported in the literature.^[23-25, 194, 196]

This work focuses on Type I Fe_2Ln_2 butterfly compounds. The first example of such an Fe_2Ln_2 butterfly was reported by Christou *et al.* in 2006,^[21] with the formula $[\text{Fe}_2\text{Ho}_2(\mu_3\text{-OH})_2(\text{teaH})_2(\text{O}_2\text{CPh})_4(\text{NO}_3)_2]\cdot 6\text{MeCN}$. This compound featured a Type I structure and was synthesised using an oxo-centred Fe^{III} triangle precursor (see Figure 37). Since then, numerous Fe_2Ln_2 butterflies have been developed with various ligand combinations as also highlighted in a recent review.^[22]

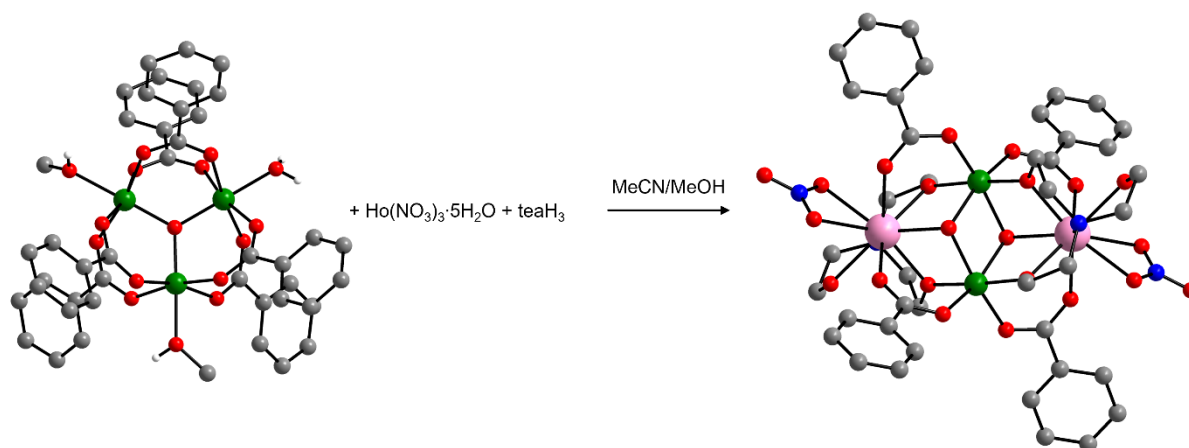


Figure 37. Synthesis and molecular structures of the Fe_2Ho_2 by Christou *et al.* and the Fe^{III} triangle precursor.^[21]

A study on the M_2Dy_2 Type I butterflies with $\text{M} = \text{Al}^{\text{III}}$, Mn^{III} , Fe^{III} and Cr^{III} showed that the SMM behaviour originates from the Dy^{III} since no Y^{III} analogues showed SMM behaviour. Using diamagnetic Al^{III} revealed that the dipolar interactions between Dy^{III} centres suppresses ZFQTM.^[25]

A notable example of Type II butterfly systems is a series of Cr^{III} -based structures studied by Murray *et al.*^[20] These butterflies were synthesised using functionalised diethanolamine ligands (R-deaH_2 , where $\text{R} = \text{Me}$, Et , or n-Bu) combined with acetylacetonate (acac) co-ligands or benzoates (see Figure 38). All members of this series adopted a Type II structure. Magnetic characterisation of the Cr_2Ln_2 butterfly with the formula $[\text{Cr}_2\text{Dy}_2(\text{OMe})_2(\text{O}_2\text{CPh})_4(\text{mdea})_2(\text{NO}_3)_2]$ revealed a large thermal energy barrier of 77 K. A comparison to the Co^{III} version in which the Co^{III} is low spin and therefore diamagnetic revealed that both compounds have a similar energy barrier but the use of paramagnetic Cr^{III} led to the compound also showing hysteresis behaviour. The reason for this was found to be the strong exchange interactions between Dy^{III} and Cr^{III} which reduce QTM and led to increased relaxation times. The Cr_2Dy_2 butterfly did in fact show SMM behaviour equal to the best 3d-4f SMMs at the time.^[20, 24]

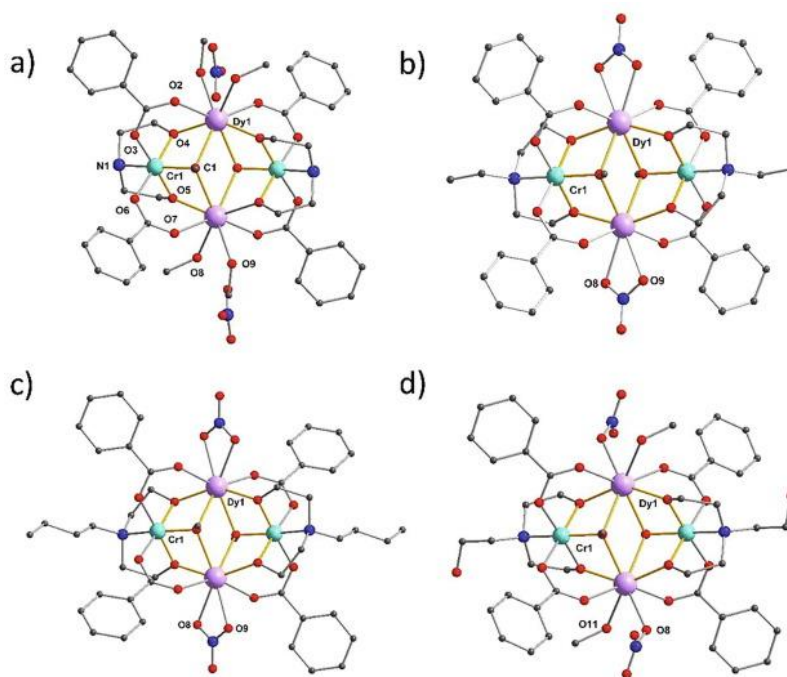


Figure 38. Molecular structures of Cr_2Dy_2 butterflies with benzoate as co-ligand and dea^{2-} in a), Et-dea^{2-} in b), $n\text{Bu-dea}^{2-}$ in c), teaH^{2-} in d) as ligand. Reprinted with permission from reference^[24] [Elsevier Inc.] copyright [2021].

Beyond standard butterfly structures, variations with other metal distributions have also been reported. Powell *et al.* presented a structure with three Fe^{III} ions and one Ln^{III} ion, with the formula $[\text{Fe}_3\text{Ln}(\mu_3\text{-O})_2(\text{CCl}_3\text{COO})_8(\text{H}_2\text{O})(\text{THF})_3] \cdot \text{THF} \cdot \text{C}_7\text{H}_{16}$ ^[19] as well as a Dy_4 complex in which both the body and wingtip positions are occupied by Dy^{III} ions.^[199] Furthermore, homochiral butterfly compounds were synthesised by Powell *et al.* using enantiopure Me-teaH₂ ligands.^[18] Remarkably, the compounds showed enhanced slow relaxation of magnetisation, further highlighting the impact of ligand design and chirality on magnetic properties.

Aim of this work was to expand on the synthetic studies of modifications on the Fe_2Ln_2 system by variation of both ligands with the intention of synthesising magnetically interesting variations. To achieve this Dy^{III} was used as the Ln^{III} ion and benzoates with electron-withdrawing groups were employed. Additionally, 2-amino-2-methyl-1,3-propanediol (ampdH₂) was used instead of the diethanolamine-type ligand which so far has not been reported in any Fe_2Dy_2 butterfly structures.

The second part of the research on $\text{Fe}^{\text{III}}\text{-Ln}^{\text{III}}$ containing coordination compounds has focused on CCCs with a nuclearity of 20. Three systems were investigated including studies on the well-established $\text{Fe}_{10}\text{Ln}_{10}$ rings,^[27, 29, 34, 200] alongside the recently published and structurally related $\text{Fe}_8\text{Dy}_{12}$ ^[36] and the $\text{Fe}_{16}\text{Ln}_4$ ^[35] clusters.

The term CCC describes a cyclic system usually containing open shell metal ions. Such cyclic systems can show interesting physical properties due to their closed finite chain nature. By cyclisation of a chain into a ring the previously finite electronic structure is turned into what is in effect an infinite loop.^[27-33]

First synthesised by Dr. Amer Baniodeh, the $\text{Fe}_{10}\text{Ln}_{10}$ system is a promising candidate for investigating these physical properties.^[201] The compounds with the formula $[\text{Fe}^{\text{III}}_{10}\text{Ln}^{\text{III}}_{10}(\text{Me-tea})_{10}(\text{Me-teaH})_{10}(\text{NO}_3)_{10}]$ (see Figure 39) are synthesised using Me-teaH_3 as a ligand and yield isostructural compounds for $\text{Ln}^{\text{III}} = \text{Nd}^{\text{III}}, \text{Eu}^{\text{III}}, \text{Gd}^{\text{III}}, \text{Tb}^{\text{III}}, \text{Dy}^{\text{III}}, \text{Ho}^{\text{III}}, \text{Er}^{\text{III}}, \text{Tm}^{\text{III}}, \text{Yb}^{\text{III}}, \text{Lu}^{\text{III}}$ and Y^{III} . In this synthesis racemic Me-teaH_3 is used and the formation of the cluster leads to chiral separation where all of the *S*- Me-teaH_3 is coordinating from above and the *R*- Me-teaH_3 from below the ring.

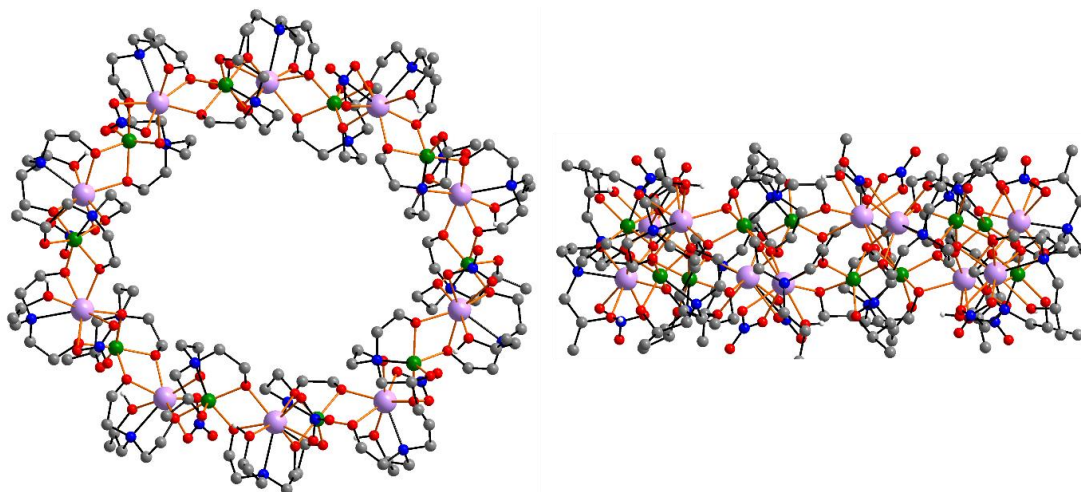


Figure 39. Molecular structure of $\text{Fe}_{10}\text{Dy}_{10}$ with Me-tea^{3-} and Me-teaH^{2-} ligands with a top- (left) and sideview (right).^[201]

To study the electronic properties of this system, femtosecond absorption spectroscopy was performed by Dr. Yu Liang in 2014 where both exciton formation and electron hopping between molecules was found.^[34] Additionally, the system was under investigation regarding the high spin ground state of $S = 60$ of the Gd^{III} analogue.^[29] In this study it was shown that the magnetic interactions in the cluster place it in proximity to a quantum critical point at which the system has an infinite number of energetically degenerate ground states. The Fe-Fe coupling in the ring is frustrated since the coupling between neighbouring Gd^{III} and Fe^{III} ions is ferromagnetic with $J_1 = 1.0 \text{ K}$ and the nearest neighbour Fe-Fe coupling is antiferromagnetic with $J_2 = -0.65 \text{ K}$. This leads to the overall observed ferromagnetic interaction and thus the

massive spin ground state but also to proximity to a quantum critical point which is located at $\alpha = |J_2|/J_1 = 0.7$.^[29]

As a result of its promising physical properties, it was chosen to expand the range of $\text{Fe}_{10}\text{Ln}_{10}$ compounds by modifying the ligand and to investigate the magnetic properties of the resulting compounds. Furthermore, any similarities in structural characteristics such as the chiral separation and ellipticity of the ring structure were analysed.

The second 20 nuclearity system described here is the recently published $\text{Fe}_8\text{Dy}_{12}$ showing its intricate nested spin structure. It is structurally similar to the $\text{Fe}_{10}\text{Ln}_{10}$ system with modified building blocks making up the ring shown in Figure 40. Whereas the $\text{Fe}_{10}\text{Ln}_{10}$ system has a 1:1 ratio of Fe^{III} to Ln^{III} , for the $\text{Fe}_8\text{Dy}_{12}$ it is 2:3. This explained by the fact that the fundamental wave like repeating unit is the same for both but the sequence of metals is Dy-Fe-Dy-Fe-Dy-Dy for the $\text{Fe}_8\text{Dy}_{12}$ where as for the $\text{Fe}_{10}\text{Dy}_{10}$ the sequence is Dy-Fe-Dy-Fe-Dy-Fe.^[36]

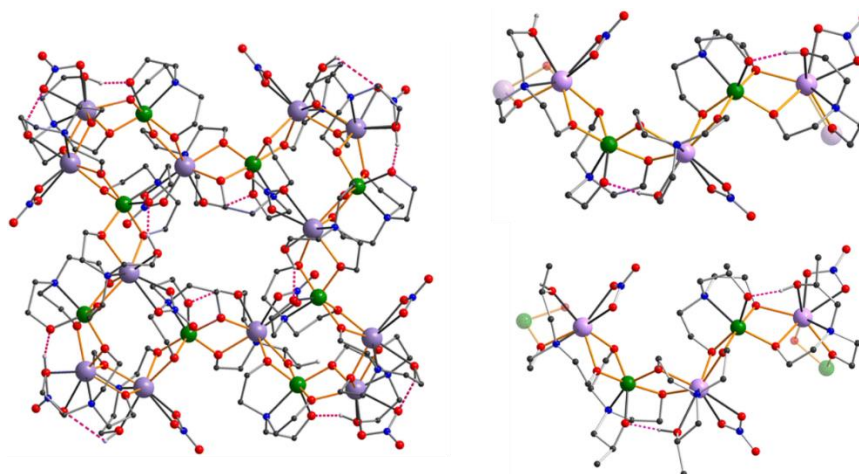


Figure 40. Molecular structure of $\text{Fe}_8\text{Dy}_{12}$ (left) and building blocks making up the $\text{Fe}_8\text{Dy}_{12}$ (top right) and $\text{Fe}_{10}\text{Dy}_{10}$ (bottom right) with differences marked as pale Fe^{III} or Dy^{III} ions. Reproduced from reference^[36].

A MAGELLAN^[202] analysis on the compound revealed three distinct sets of anisotropy axes (see Figure 41): an inner set, forming a distorted tetrahedron with a spin ice-like arrangement of spins (pink), a middle set (burgundy) assuming a toroidal arrangement of spins and an outer set (cyan). The outer set consists of two axes perpendicular to the toroidal distorted square of the middle set and two axes which are angled at 30.1° to them.

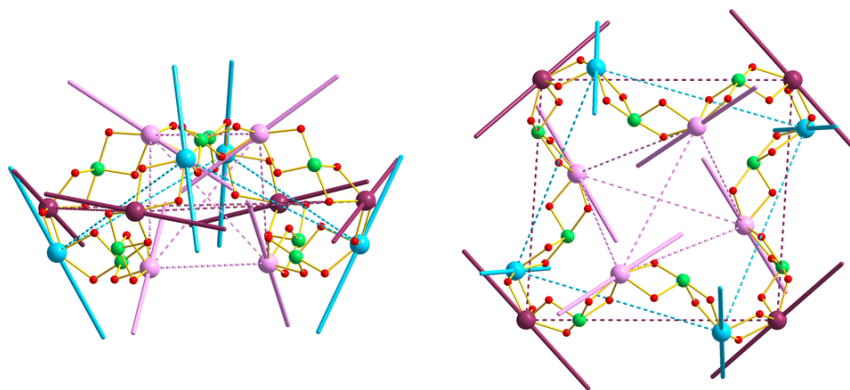


Figure 41. Three sets of anisotropy axes from the MAGELLAN^[202] analysis of Fe₈Dy₁₂ marked in different colours. Reprinted from reference^[36].

The effect of the structural change from the Fe₁₀Ln₁₀ to the Fe₈Dy₁₂ on the magnetic characteristics is not fully understood and requires further investigation. A target of this work was to reproduce and optimise the synthetic procedure of the Fe₈Dy₁₂ compound. Since the compound was an unexpected result of an attempted synthesis of an Fe₁₀Dy₁₀ ring by a previous member of the Powell group, Dr. Yan Peng. Additionally, an optimised procedure is used to investigate the accessibility of other Ln variations similar to the series of Fe₁₀Ln₁₀ compounds.

The last CCC to be discussed in this section is the Fe₁₆Ln₄ system which has the general formula [Fe₁₆Ln₄(tea)₈(teaH)₁₂(μ-O₂CCH₃)₈](NO₃)₄·16H₂O·XMeCN Ln = Sm^{III}, Eu^{III}, Gd^{III}, Tb^{III}, Dy^{III} and Ho^{III} (X = 10/11) (see Figure 42).^[35]

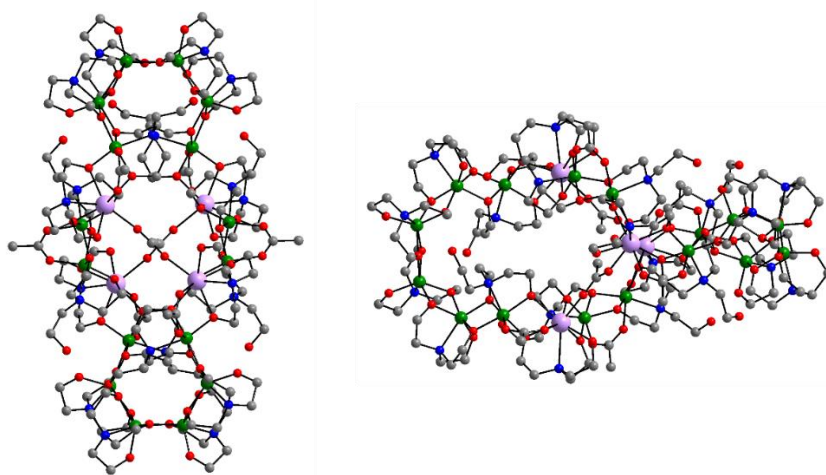


Figure 42. Molecular structure of Fe₁₆Dy₄ with view from the top and side of the molecule.^[35]

It was first published in 2011 by Powell *et al.*^[35] highlighting the strong antiferromagnetic coupling interactions within the Fe₆ and Fe₂ sub chains. Furthermore, there is a pinning effect that these chains have on the central lanthanide

spins as revealed in the Gd^{III} analogue as a result of 3d-4f coupling interactions. The magnetic properties for the series of systems were investigated using magnetisation measurements, applied AC and DC field experiments and ^{57}Fe Mössbauer spectroscopy.

The complexity of the system and in particular the intricacy of the Fe-Ln coupling demands further investigation. This includes microSQUID measurements for the single crystal magnetic characterisation of the $\text{Fe}_{16}\text{Tb}_4$ which shows an inflection point in the magnetisation data. Given that the other analogues do not show any similar behaviour it is difficult to rationalise this feature without more exotic measurements.

4.2 Fe_2Ln_2 Butterflies

Fe_2Ln_2 butterfly complexes are part of a well-known system used as a testbed to determine the influence of tuning handles such as the exchange of the lanthanide ions or ligands on the magnetic properties of the resulting compound.^[17-18, 22-24] This system is composed of two lanthanide ions, two transition metal ions, carboxylate ligands, substituted diethanolamine-based ligands as well as a $\mu_3\text{-OR}$ group holding the core together. This butterfly motif is ideal as a testbed as a result of its adaptable structure.

The $\text{Fe}^{\text{III}}_2\text{Ln}^{\text{III}}_2$ compounds are synthesised using an Fe^{III} triangle precursor $[\text{Fe}_3\text{O}(\text{O}_2\text{CR})_6\text{L}_3]\text{X}$ (X = anion, L = solvent)^[149, 203-205] which contains a carboxylate ligand with different substituents (see Figure 43).

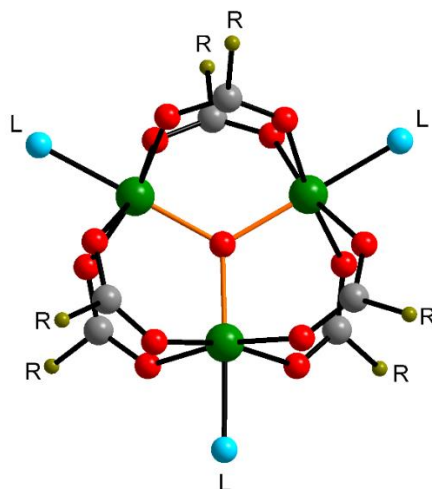


Figure 43. Molecular structure of an Fe_3 precursor. Adapted with permission from reference^[22] [John Wiley & Sons] copyright [2021].

This approach utilises the principle of cluster-assisted self-assembly which involves using a preformed cluster to facilitate the formation of 3d/4f complexes.^[206-207] Initial synthetic attempts with iron nitrate instead of the $\{\text{Fe}^{\text{III}}_3\text{O}\}^+$ cluster mostly resulted in purely 3d ion containing complexes. By using the $\{\text{Fe}^{\text{III}}_3\text{O}\}^+$ precursor the reaction kinetics are likely slowed down since the $\{\text{Fe}^{\text{III}}_3\text{O}\}^+$ complex must first be broken down, limiting the amount of Fe^{III} ions available in the reaction solution. This enables the formation of 3d/4f complexes with higher nuclearities.

This $\{\text{Fe}^{\text{III}}_3\text{O}\}^+$ precursor is added to a MeOH/MeCN mixture containing the lanthanide nitrate and a diethanolamine ligand. As highlighted in a recent review, at least 33 compounds with the general formula $[\text{Fe}^{\text{III}}_2\text{Ln}^{\text{III}}_2(\mu_3\text{-OH})_2(\text{L}')_2(\text{O}_2\text{CR})_6]$ (L' = ethanolamine type ligand) were reported until 2020.^[22]

In most cases a benzoic acid was used as the source of the carboxylate ligand. This allows for variation through substitution in the *meta* or *para* position. Another commonly used tuning handle is changing the R-group on the diethanolamine ligand (see Figure 44).^[24]

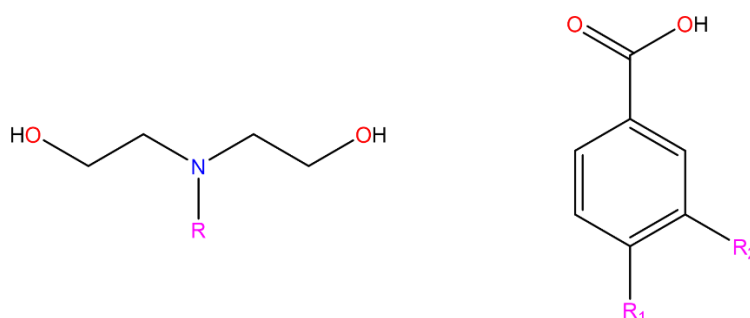


Figure 44. Diethanolamine based ligand and benzoic acid which can be varied by substitution at the highlighted positions.

In the present work five new Fe_2Dy_2 butterflies were synthesised for which both the benzoic acid and the diethanolamine ligand were varied simultaneously rather than systematically.^[24] These complexes were investigated using femtosecond transient absorption spectroscopy in the context of the Master project of Julia Weyandt working in the group of Prof. Dr. Andreas-Neil Unterreiner.^[208]

The Fe_2Dy_2 butterfly system was specifically chosen for this type of systematic spectroscopic study due to its testbed nature described above. This was similarly proposed in a recent concept article published by our group.^[26] The combination of iron and lanthanide ions was shown to behave similarly to purely iron containing

Fe₂O₃ nanoparticles. This was reported in a study investigating Fe₁₀Ln₁₀ CCCs which exhibit the same number of time constants but with some minor changes in the lifetimes of the excited states compared to the Fe₂O₃ nanoparticles.^[34, 209-210]

Having established that exchanging the iron for lanthanides does not change the nature of the fundamental ultrafast relaxation processes the butterfly system was chosen to study the effect of ligand substitution. For this, benzoic acid, *p*-NO₂-benzoic acid, *p*-^tBu-benzoic acid, and *p*-CN-benzoic acid as well as teaH₃, Me-teaH₃, Et-teaH₃ and ampdH₂ ligands (see table 2) were used and their influence on the lifetimes of the photoexcited states were investigated.

4.2.1 Extending the Fe₂Dy₂ butterfly platform

The starting point of this work was the reproduction of the Fe₂Dy₂ butterflies using [Fe₃O(O₂CPh)₆(H₂O)₃](O₂CPh) and [Fe₃O(O₂CC₆H₄-^tBu)₆(H₂O)₃](NO₃) as precursors in addition to teaH₃ and Me-teaH₃ respectively leading to (**Fe₂Dy₂-1**) [Fe₂Dy₂(μ₃-OH)₂(Htea)₂(O₂CPh)₆]·3MeCN and (**Fe₂Dy₂-2**) [Fe₂Dy₂(μ₃-OH)₂(Me-teaH)₂(O₂CC₆H₄-*p*-^tBu)₆]·4MeCN·2(HO₂CC₆H₄-*p*-^tBu). The phase purity of the obtained compounds was confirmed from PXRD measurements. Additionally, SCXRD was performed on a single crystal of (**Fe₂Dy₂-2**) to improve the data set obtained previously in the group and the molecular structure is shown in Figure 46.

Using an optimised synthetic procedure and by variation of the iron triangle and diethanolamine ligand five new compounds [Fe₂Dy₂(μ₃-OH)₂(Et-teaH)₂(O₂CC₆H₄-*p*-^tBu)₆]·4MeCN·2(HO₂CC₆H₄-*p*-^tBu) (**Fe₂Dy₂-3**), [Fe₂Dy₂(μ₃-OH)₂(Me-teaH)₂(O₂CC₆H₄-*p*-NO₂)₆]·6MeCN (**Fe₂Dy₂-4**), [Fe₂Dy₂(μ₃-OH)₂(Et-teaH)₂(O₂CC₆H₄-*p*-NO₂)₆]·6MeCN·H₂O (**Fe₂Dy₂-5**), [Fe₂Dy₂(ampd)₂(ampdH)₂(O₂CC₆H₄-*p*-NO₂)₆]·8MeCN (**Fe₂Dy₂-6**) and [Fe₂Dy₂(ampd)₂(ampdH)₂(O₂CC₆H₄-*p*-CN)₆]·2MeCN (**Fe₂Dy₂-7**), were synthesised (see Figures 46, 50 and 54). For the optimised procedure the composition of the MeOH/MeCN solvent mixture and the reaction time were changed.

All of these compounds are of the Type 1 butterfly meaning the lanthanides occupy the wingtips and the transition metals the body positions. The substituted diethanolamine ligands and ampdH₂ which were used in compounds (**Fe₂Dy₂-1**)-(**Fe₂Dy₂-7**) are shown in Figure 45.

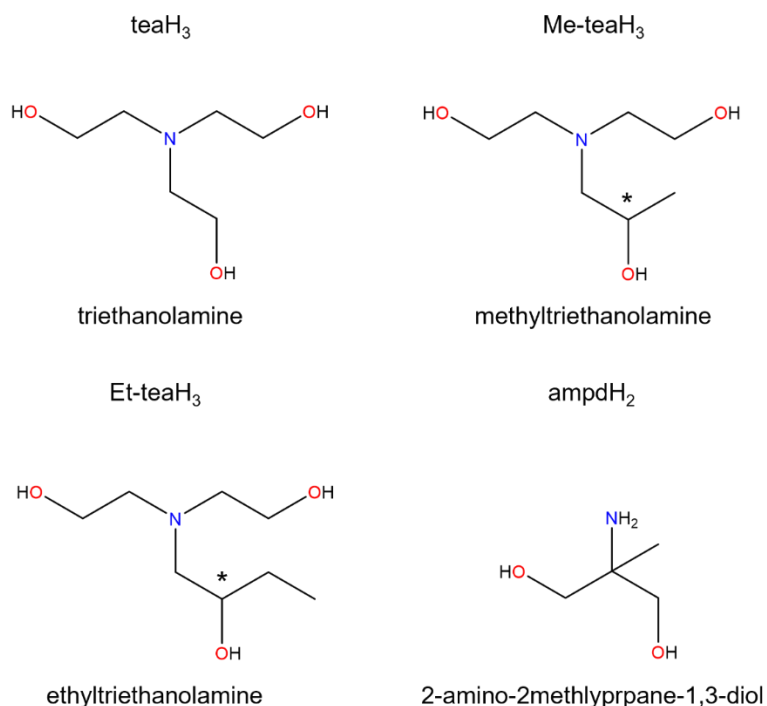
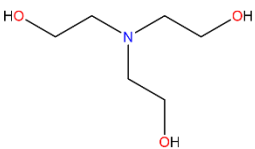
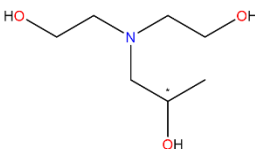
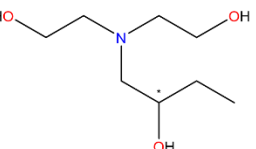
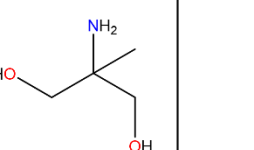
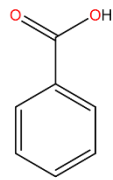
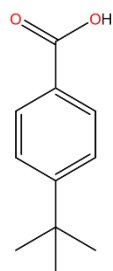
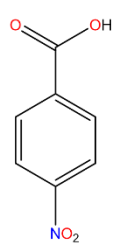
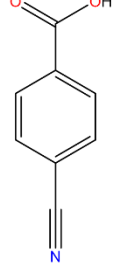


Figure 45. Molecular structure of ethanolamine type ligands used for Fe₂Dy₂ butterflies.

The difference between (**Fe₂Dy₂-2**) and (**Fe₂Dy₂-3**) is the nature of the substituted diethanolamine ligand using Me-teaH₃ and Et-teaH₃ respectively. This is in combination with *p*-^tBu-benzoic acid. For compounds (**Fe₂Dy₂-4**) and (**Fe₂Dy₂-5**) the same Me-teaH₃/Et-teaH₃ variation was performed but with *p*-NO₂-benzoic acid to observe changes in optical behaviour caused by the sterically more challenging Et-teaH₃. These changes can then be investigated in combination with the two differently substituted benzoic acids. (**Fe₂Dy₂-6**) and (**Fe₂Dy₂-7**) are made using ampdH₂ as ligand in combination with *p*-NO₂-benzoic acid and *p*-CN-benzoic acid. Using this ampdH₂ ligand changes the μ₃-bridging situation in the molecule from μ₃-OH to μ₃-OR with O being the alkoxy oxygen of the ampd²⁻ ligand. This leads to different angles and distances within the core. Table 2 shows the ligand combinations in compounds (**Fe₂Dy₂-1**) to (**Fe₂Dy₂-7**).

Table 2. Ligand combinations in compounds (**Fe₂Dy₂-1**)-(**Fe₂Dy₂-7**).

				
	(Fe₂Dy₂-1)			
		(Fe₂Dy₂-2)	(Fe₂Dy₂-3)	
		(Fe₂Dy₂-4)	(Fe₂Dy₂-5)	(Fe₂Dy₂-6)
				(Fe₂Dy₂-7)

Compounds (**Fe₂Dy₂-2**) and (**Fe₂Dy₂-3**) for which the molecular structure is shown in Figure 46 crystallise in the triclinic space group $P\bar{1}$ with half a molecule in the asymmetric unit. The additional CH₂ group on the Et-teaH₃ ligand occupies a space which in the compound using the smaller Me-teaH₃ ligand remained unoccupied. This leads to almost identical cell parameters. The coordination spheres of the Dy^{III} and the Fe^{III} in the two structures are identical, thus only the structure of (**Fe₂Dy₂-2**) is described here.

The core structure contains two μ_3 -OH⁻ groups (O(1)) which both bridge the two central Fe^{III} ions and are further linked to the wingtip Dy^{III} ions. Furthermore, four μ_2 -alkoxy

oxygen atoms from two different Me- or Et-teaH²⁻ ligands (O(2) and O(3)) bridge between the Fe^{III} and Dy^{III} ions. The coordination sphere of Fe^{III} is completed by two benzoate oxygen atoms from the coordinated *p*-^tBu-benzoates (O(7) and O(5)). Dy^{III} is additionally coordinated by an ethanolamine nitrogen N(1), the remaining alcohol oxygen O(4) of the Me- or Et-teaH²⁻ ligand and four benzoate oxygen atoms from three different *p*-^tBu-benzoate ligands.

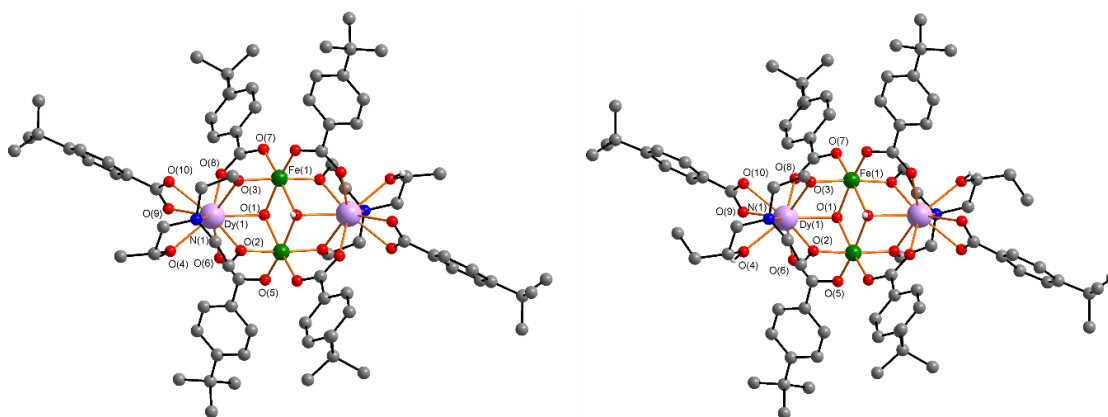


Figure 46. Molecular structures of (**Fe₂Dy₂-2**) (left) and (**Fe₂Dy₂-3**) (right).

PXRD and IR measurements were performed to confirm phase purity of the samples and the composition of the bulk material. The results are shown in Figure 47. The powder patterns of both compounds are in good agreement with the simulation. The IR spectra of both compounds are essentially identical due to the similarity of the structures.

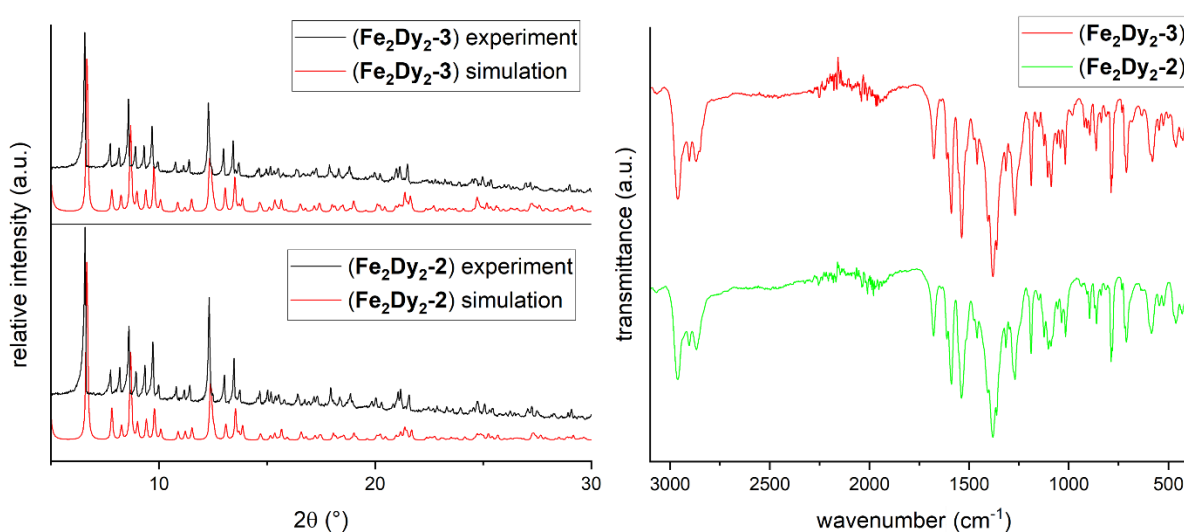


Figure 47. Experimental and simulated powder patterns (left) and IR spectra (right) for compounds (**Fe₂Dy₂-2**) and (**Fe₂Dy₂-3**).

The packing of the cores which is identical for both compounds (**Fe₂Dy₂-2**) and (**Fe₂Dy₂-3**) is shown schematically in Figure 48 along the three crystallographic axes.

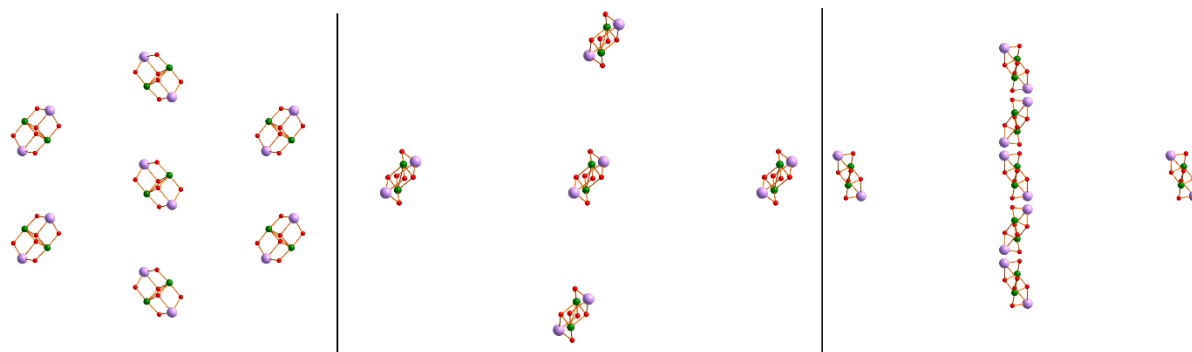


Figure 48. Scheme showing the packing of the core structures of (**Fe₂Dy₂-2**) and (**Fe₂Dy₂-3**) along the crystallographic a (left), b (middle) and c (right) axes.

The lattice acetonitrile and *p*-^tBu-benzoic acid solvent molecules around the complex engage in hydrogen bonding. Due to the absence of other intermolecular interactions towards neighbouring molecules no network is formed and units of Fe₂Dy₂ are left mainly isolated in the lattice reducing magnetically relevant interactions in the crystal. Because of this, emphasis is put on the “single molecule” characteristic in any magnetic characterisation which therefore can be proof of SMM behaviour *i.e.* single molecules behaving like tiny magnets. Since both complexes (**Fe₂Dy₂-2**) and (**Fe₂Dy₂-3**) exhibit the same behaviour, Figure 49 exemplarily only illustrates the intermolecular interactions in (**Fe₂Dy₂-2**). Each of the two MeCN lattice solvents form hydrogen bonds with their nitrogen (N(2)) to the hydrogen atom on the μ₃-OH[−] (O(1)). Furthermore, each of the two non-coordinating *p*-^tBu-benzoic acid molecules hydrogen bond *via* their carboxyl oxygen (O(12)) and OH hydrogen (O(12)) to the hydrogen on the remaining protonated alcohol arm (O(4)) of the Me-/Et-teaH^{2−} ligand and to the oxygen of the carboxylate group (O(9)) on a *p*-^tBu-benzoate.

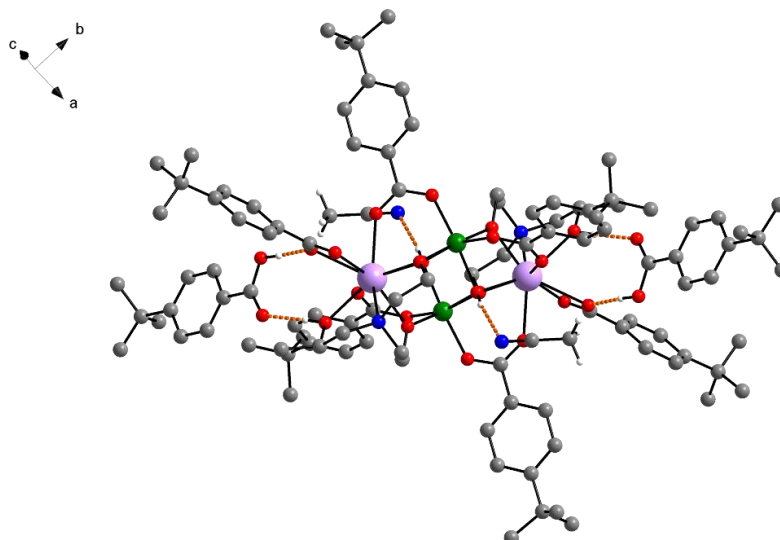


Figure 49. Intermolecular interactions in (**Fe₂Dy₂-2**) showing hydrogen bonds as dotted orange lines.

(**Fe₂Dy₂-4**) and (**Fe₂Dy₂-5**) crystallise in the triclinic space group $P\bar{1}$. Similar to the situation in (**Fe₂Dy₂-3**) the additional CH₂ group of the Et-teaH²⁻ ligands do not require additional space in the packing but fill holes in the crystal packing of (**Fe₂Dy₂-4**). Thus, these two structures are essentially isostructural. The molecular structures for (**Fe₂Dy₂-4**) and (**Fe₂Dy₂-5**) are shown in Figure 50. Comparing the structures of (**Fe₂Dy₂-4**) and (**Fe₂Dy₂-5**) to the ones of (**Fe₂Dy₂-2**) and (**Fe₂Dy₂-3**) reveals that the coordination environment of both Fe^{III} and Dy^{III} centres are the same as previously described for (**Fe₂Dy₂-2**) and (**Fe₂Dy₂-3**).

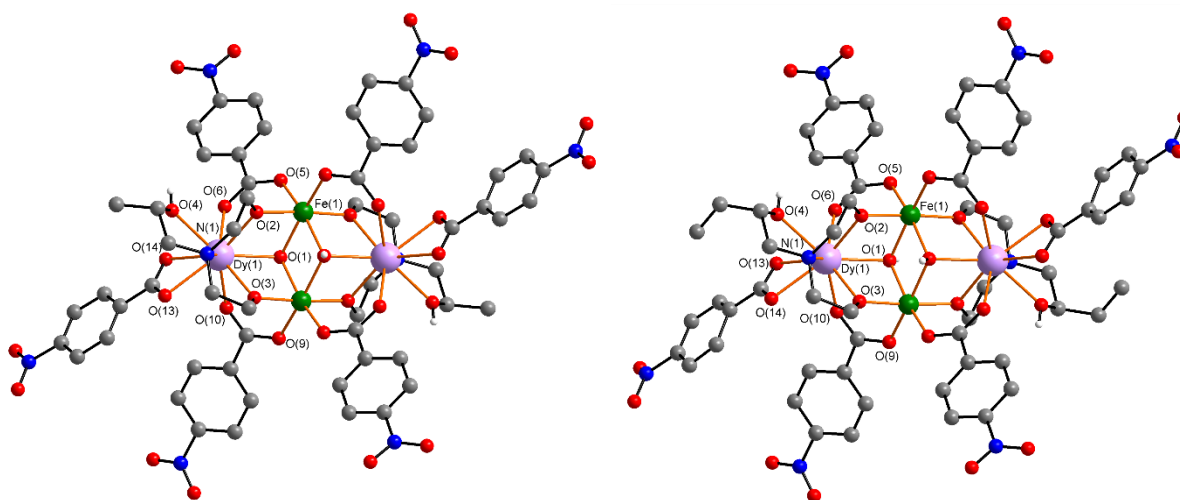


Figure 50. Molecular structures of (**Fe₂Dy₂-4**) (left) and (**Fe₂Dy₂-5**) (right).

To check phase purity PXRD and IR measurements were performed with the results shown in Figure 51. For both samples the powder diffractograms of the experiment

match the simulation confirming phase purity. The IR shows the similarity of the samples and the peaks corresponding to the asymmetric and the symmetric stretching of the NO₂ groups at 1516 cm⁻¹ and 1340 cm⁻¹ are highlighted.

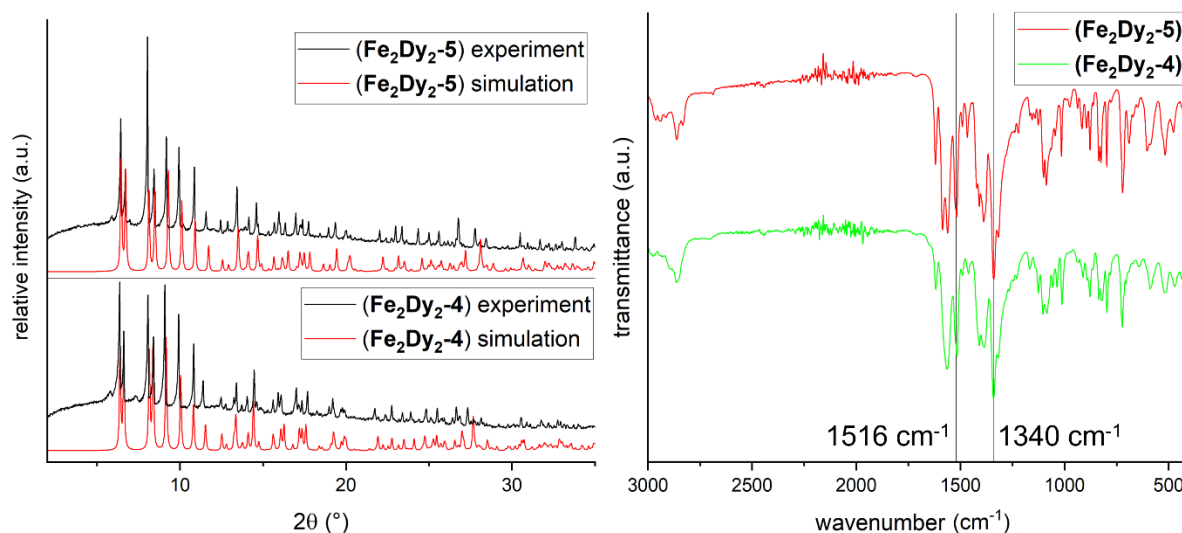


Figure 51. Experimental and simulated powder patterns (left) and IR spectra (right) for compounds (**Fe₂Dy₂-4**) and (**Fe₂Dy₂-5**).

The packing for both compounds is schematically shown by the orientation of the core structures in the lattice in Figure 52.

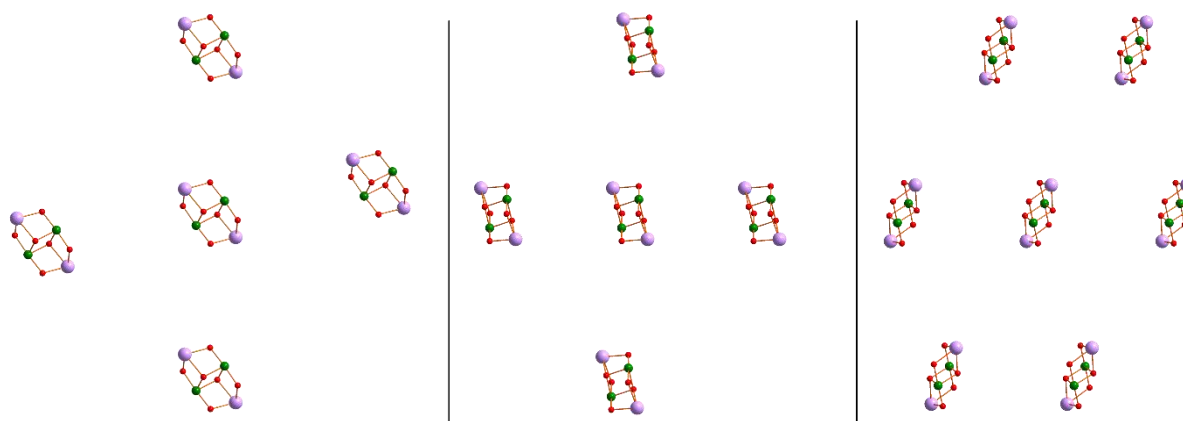


Figure 52. Packing represented by the arrangement of the core structures along the crystallographic a (left), b (middle) and c (right) axis for (**Fe₂Dy₂-4**) and (**Fe₂Dy₂-5**).

Intermolecular interactions in the form of hydrogen bonding between either the R-OH hydrogen of the Me/Et-teaH²⁻ ligand or the μ₃-OH⁻ hydrogen and the nitrogen on the MeCN solvent molecules are shown for (**Fe₂Dy₂-4**) as an example in Figure 53 since both molecules show the same intermolecular interactions. In addition to the hydrogen bonds described above, some non-classical hydrogen bonding^[211] between

carboxylate oxygens and hydrogens on the methyl group of the MeCN molecules was observed.

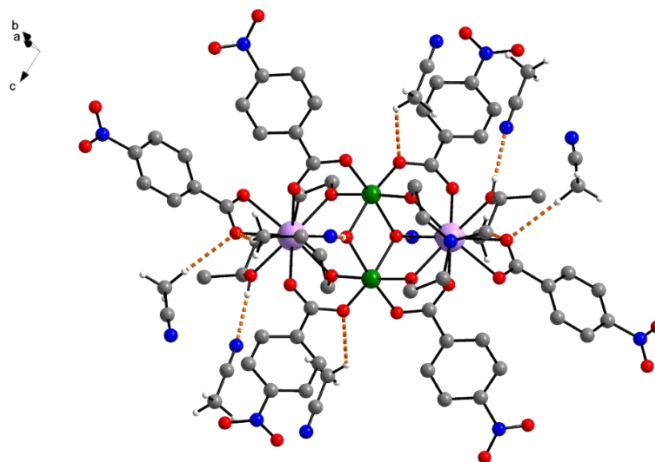


Figure 53. Intermolecular interactions for (**Fe₂Dy₂-4**) and (**Fe₂Dy₂-5**) on the example of (**Fe₂Dy₂-4**). Classical and non-classical hydrogen bonds indicated by orange dotted lines.

Compounds (**Fe₂Dy₂-6**) and (**Fe₂Dy₂-7**) (molecular structures shown in Figure 54) crystallise in the space groups $P\bar{1}$ and $P2_1/c$, respectively, with an inversion centre located in the middle of the molecule in both cases. Here the ampdH₂ ligand was used instead of a triethanolamine-type ligand which leads to a different coordination environment of the Fe^{III} and Dy^{III} ions compared to the compounds described above. The additional change in co-ligand from *p*-NO₂-benzoic acid to *p*-CN-benzoic acid for (**Fe₂Dy₂-6**) and (**Fe₂Dy₂-7**) has no influence on the coordination environment of the metal centres. The substitution on the benzoate significantly affects the compound's structure, altering its packing and influencing magnetic properties, as noted in previous research.^[22, 24, 197] The ampdH₂ ligand has an even greater effect on the magnetic properties. This is because it creates a new coordination environment that changes the distances between metal atoms, directly influencing their magnetic interactions. Although butterfly type complexes with Gd^{III} or Y^{III} ions and ampdH₂ ligands have been made using iron triangle precursors and benzoates,^[201, 207] as well as similar complexes using Cr^{III} triangles,^[207] the two compounds (**Fe₂Dy₂-6**) and (**Fe₂Dy₂-7**) are the first examples using ampdH₂ ligands with both Dy^{III} (as the lanthanide) and Fe^{III} (as the transition metal).

In contrast to the previously described butterflies with substituted diethanolamine ligands the two μ_3 -OH⁻ are replaced by the alkoxy oxygens (O(1)) of two ampd²⁻

ligands which adopt the same μ_3 -bridging mode linking the four metal ions to form the butterfly core structure. The other deprotonated oxygen of the ampd^{2-} ligand (O(2)) forms μ_2 -bridges between Fe^{III} and Dy^{III} while the nitrogen N(1) coordinates to the Fe^{III} . The remaining two ampdH^+ ligands have a bridging μ_2 -alkoxy group between Fe^{III} and Dy^{III} while the oxygen of the protonated OH group and N(2) coordinate to only Dy^{III} . Two of the six *p*-NO₂-benzoates bridge between an Fe^{III} and a Dy^{III} ion whereas the other four are each singly coordinating to a Dy^{III} .

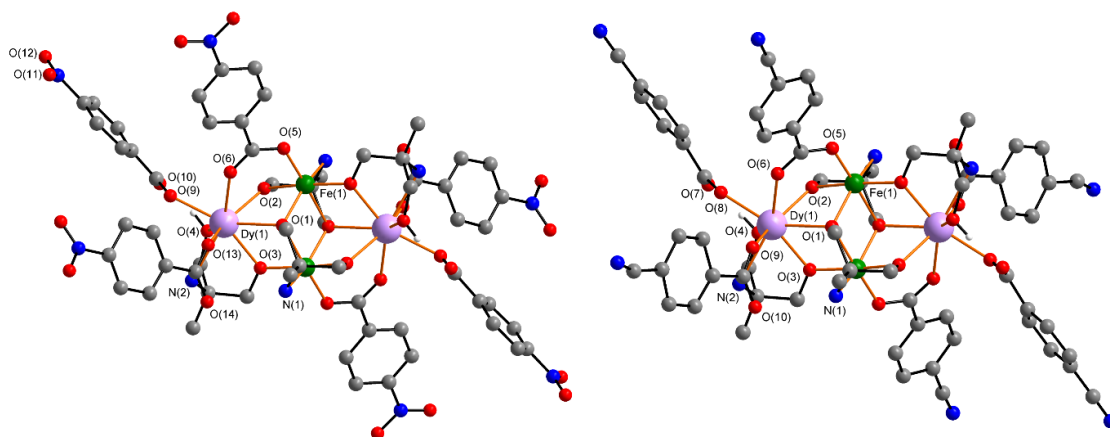


Figure 54. Molecular structures of (**Fe₂Dy₂-6**) (left) and (**Fe₂Dy₂-7**) (right).

PXRD and IR measurements were performed for both compounds. The simulated and experimental powder patterns as well as the characteristic vibrational peaks corresponding to the NO₂ and CN groups are shown in Figure 55. Similarly, as for the other compounds described above which use *p*-NO₂-benzoic acid the asymmetric and symmetric stretching vibrations of the NO₂ groups are visible at 1518 cm⁻¹ and 1341 cm⁻¹, respectively. For (**Fe₂Dy₂-7**) with the *p*-CN-benzoate ligands the peak at 2232 cm⁻¹ can be assigned to the CN stretching vibration. Elemental analysis has confirmed the purity of the bulk sample. The PXRD of compound (**Fe₂Dy₂-6**) does not match the simulated pattern at all which could be a result of decomposition of the compound, problems with the measurement technique possibly due to exposure to moisture in the air or loss of lattice solvent and a subsequent change in crystal parameters. The crystals of the sample are visually homogeneous and the unit cell of multiple single crystals were measured to minimise the possibility of the structure being just a side product in this reaction. Elemental analysis also shows that the bulk sample has the correct composition. However, it was not possible to produce a clean

PXRD or at least one suggesting the presence of the product it was regarded as impure and not used for the femtosecond transient absorption studies.

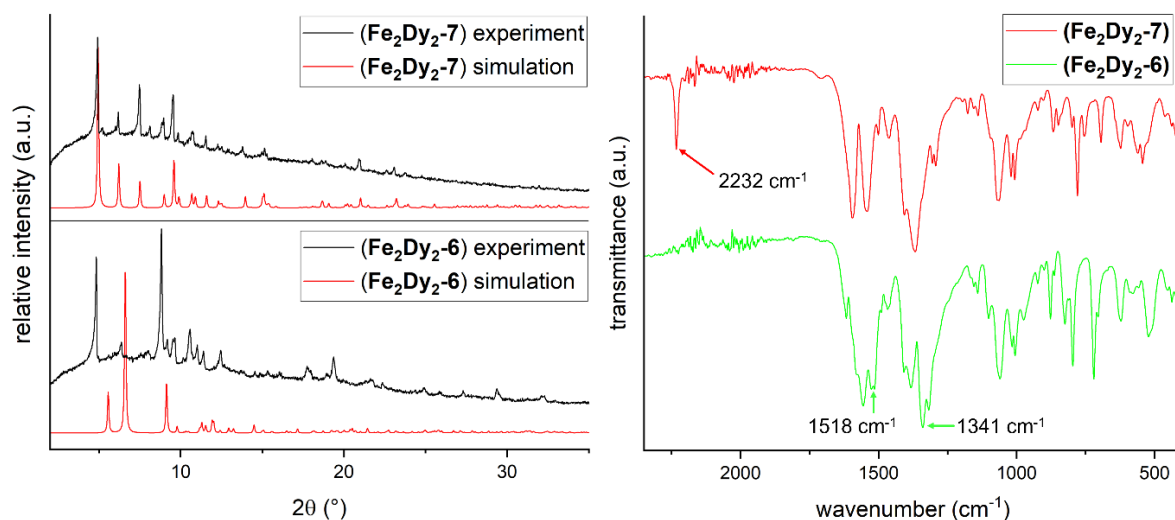


Figure 55. Simulated and experimental powder pattern (left) and IR spectra (right) of (**Fe₂Dy₂-6**) and (**Fe₂Dy₂-7**).

The packing of (**Fe₂Dy₂-6**) is dominated by hydrogen bonds which are shown as orange dotted lines in Figure 56. These intermolecular interactions form a two-dimensional network in the crystallographic **ac** plane.

Hydrogen bonds are formed between oxygens from the nitro groups or the non-coordinating oxygen of the carboxylate groups of the *p*-NO₂-benzoate ligands and hydrogens on the amine moiety of the ampd²⁻ and ampdH⁻ ligands. Each complex molecule forms a total of twelve hydrogen bonds towards four surrounding Fe₂Dy₂ molecules. Eight hydrogen bonds connect both nitro group oxygens (O(11), O(12)) to ampdH⁻ amine (N(2)) hydrogens. For these bonds the molecule in the centre involves two of the six *p*-NO₂-benzoate ligands as well as the two ampdH⁻ ligands. The other four hydrogen bonds connect the non-coordinating carboxylate oxygen (O(14)) of the *p*-NO₂-benzoate ligands and the ampd²⁻ amine (N(1)) hydrogen for which the molecule involves two more *p*-NO₂-benzoate ligands and both ampd²⁻ ligands. The remaining two *p*-NO₂-benzoate ligands which are not participating in any hydrogen bonding are the ones bridging between Fe^{III} and Dy^{III} centres. Additionally, there is intramolecular hydrogen bonding between the alcohol oxygen of the ampdH⁻ ligand (O(4)) and the non-coordinating oxygen (O(10)) of the single coordinated *p*-NO₂-benzoate. Distances of these hydrogen bonds are summarised in Table 3.

Table 3. Intra- and Intermolecular hydrogen bonding in (**Fe₂Dy₂-6**) with donor, acceptor and H atoms as well as corresponding angles and distances.

D	H	A	D...A (Å)	D-H-A (°)
O(4)	H(4)	O(10)	2.562(11)	154(8)
N(1)	H(1A)	O(14)	3.071(9)	155(8)
N(2)	H(2A)	O(14)	3.150(10)	161(9)
N(2)	H(2B)	O(11)	3.259(12)	155(9)
N(2)	H(2B)	O(12)	3.318(16)	154(9)

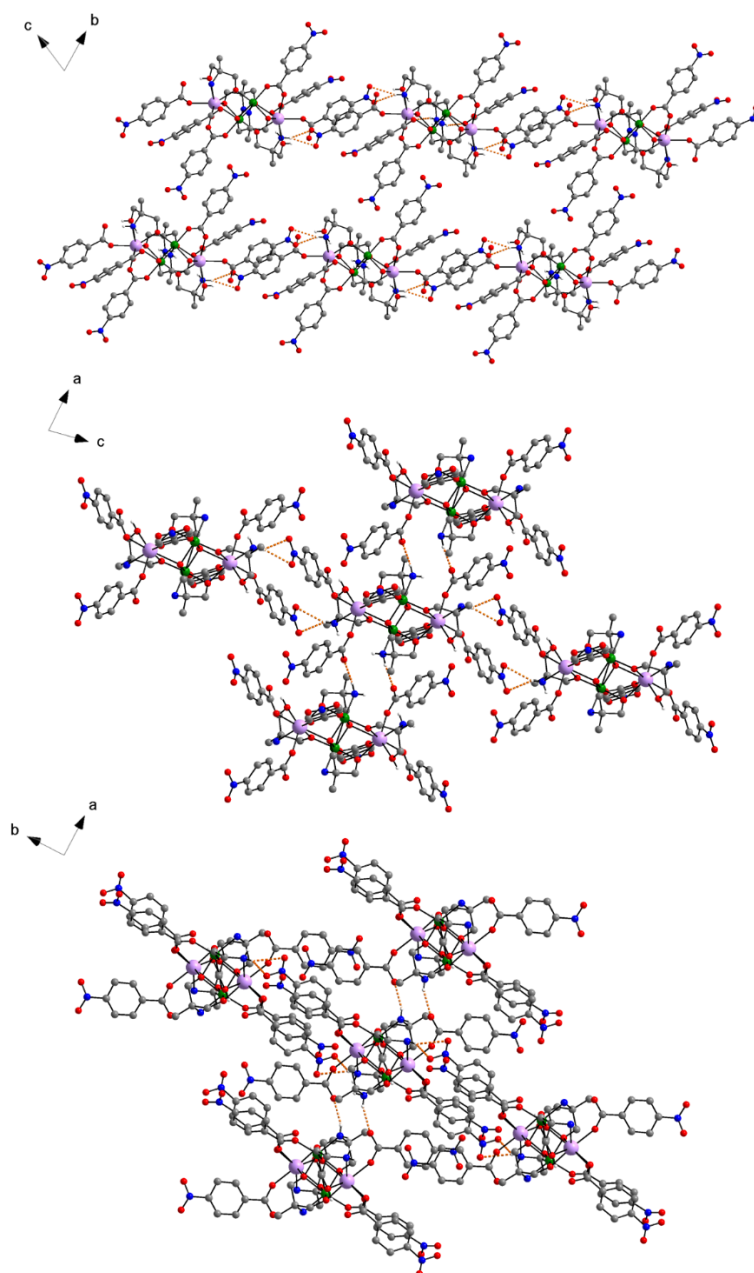


Figure 56. Packing of (**Fe₂Dy₂-6**) along the crystallographic a (top), b (middle) and c (bottom) axis. Hydrogen bonding in the **ac** plane indicated as orange dotted lines (middle).

The packing of (**Fe₂Dy₂-7**) is shown in Figure 57. As for (**Fe₂Dy₂-6**) a network of hydrogen bonds forms sheets in the crystallographic **bc** plane. These intermolecular interactions are shown as orange dotted lines in Figure 57. Eight hydrogen bonds towards six neighbouring molecules are formed. The hydrogen bonds connect an amine hydrogen of the ampdH⁺ or ampd²⁺ ligands (N(2)/N(1)) to a non-coordinating carboxylate oxygen (O(8)/O(10)). The distances of these hydrogen bonds are listed in Table 4.

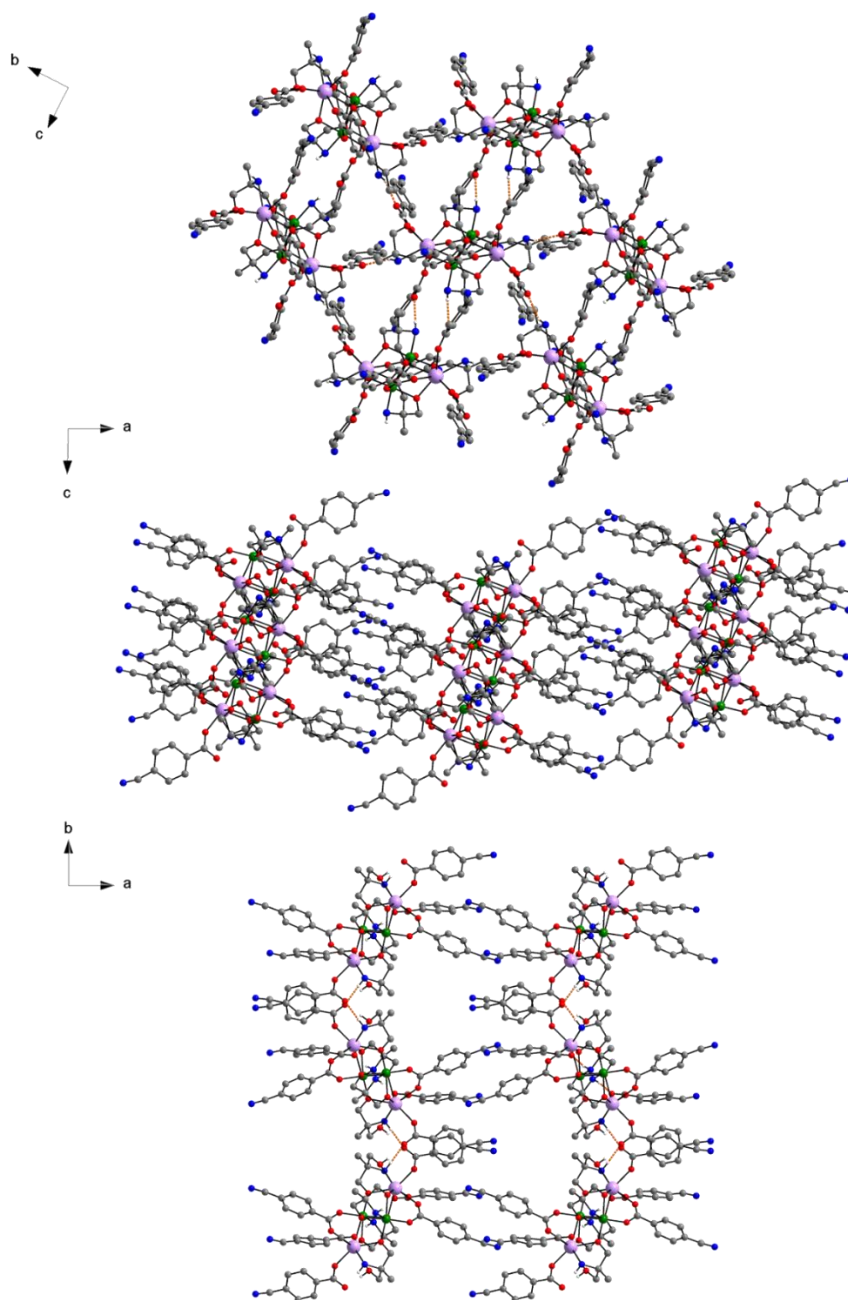


Figure 57. Packing of (**Fe₂Dy₂-7**) along the crystallographic *a* (top), *b* (middle) and *c* (bottom) axis with hydrogen bonds shown as orange dotted lines. Hydrogen bonds in picture showing the view along the *b* axis omitted for clarity.

Table 4. Acceptor, Donor and H atoms involved in hydrogen bonding as well as the respective distances and angles of the formed H-bonds for (**Fe₂Dy₂-7**).

D	H	A	D...A (Å)	D-H-A (°)
O(4)	H(4)	O(8)	2.569(4)	173(5)
N(1)	H(1A)	O(10)	2.941(4)	168(5)
N(2)	H(2A)	O(10)	3.050(5)	149(5)
N(2)	H(2B)	O(8)	3.108(4)	157(5)

The different coordination environment resulting from the use of the ampdH₂ ligand also has an influence on the intramolecular M^{III}...M^{III} distances as well as M^{III}-O-M^{III} angles. Table 5 shows all distances and angles related to the core structure for compounds (**Fe₂Dy₂-2**) to (**Fe₂Dy₂-7**).

Firstly, the similarities seen for compounds (**Fe₂Dy₂-2**), (**Fe₂Dy₂-3**), (**Fe₂Dy₂-4**) and (**Fe₂Dy₂-5**) in terms of structural packing and core structure are noteworthy. When comparing the (**Fe₂Dy₂-2**) and (**Fe₂Dy₂-3**) with the (**Fe₂Dy₂-4**) and (**Fe₂Dy₂-5**) pair it is clear that the core is essentially the same. The values most relevant for magnetostructural correlations are the M^{III}...M^{III} distances for the dipolar interactions and the distances and angles related to bridging oxygens for the exchange coupling. It can be concluded from the literature that a key tuning handle for the magnetic properties is the exchange coupling between metal centres.^[20, 24] Here it is observed that the Dy(1)-O(1)-Fe(1') and the Fe(1)-O(1)-Fe(1') angles are the biggest difference between compounds (**Fe₂Dy₂-2**)-(**Fe₂Dy₂-5**) and (**Fe₂Dy₂-6**)-(**Fe₂Dy₂-7**) with the angles for (**Fe₂Dy₂-6**) and (**Fe₂Dy₂-7**) being ca. 3.5° smaller. This should have an impact on the exchange coupling for these compounds considering the changed orbital overlap.

Table 5. Relevant distances and angles for compounds (**Fe₂Dy₂-1**) to (**Fe₂Dy₂-7**).

	(Fe₂Dy₂-2)	(Fe₂Dy₂-3)	(Fe₂Dy₂-4)	(Fe₂Dy₂-5)	(Fe₂Dy₂-6)	(Fe₂Dy₂-7)
Dy(1)···Fe(1) (Å)	3.435(4)	3.433(5)	3.4474(4)	3.4376(6)	3.537(5)	3.524(5)
Dy(1)···Fe(1') (Å)	3.423(4)	3.4442(5)	3.4366(4)	3.4480(6)	3.437(5)	3.430(4)
Fe(1)···Fe(1') (Å)	3.236(2)	3.244(5)	3.223(2)	3.231(5)	3.155(2)	3.159(5)

Fe(1)···O(1) (Å)	2.061(4)	2.067(2)	2.0536(17)	2.051(6)	2.089(4)	2.079(2)
Fe(1')···O(1) (Å)	2.056(2)	2.051(2)	2.0402(17)	2.052(3)	2.041(4)	2.049(2)
Dy(1)···O(1) (Å)	2.384(4)	2.393(2)	2.4021(18)	2.404(3)	2.503(5)	2.501(2)
Dy(1)···O(2) (Å)	2.3236(19)	2.327(2)	2.3254(18)	2.322(3)	2.350(5)	2.319(2)
Fe(1)···O(2) (Å)	1.992(2)	1.993(4)	1.9546(19)	1.962(3)	1.950(5)	1.943(3)
Dy(1)···O(3) (Å)	2.298(2)	2.303(2)	2.3227(18)	2.323(3)	2.289(5)	2.278(2)
Fe(1')···O(3) (Å)	1.954(2)	1.954(2)	1.9594(19)	1.959(3)	2.002(5)	1.995(2)
Dy(1)-O(1)-Fe(1) (°)	100.473(5)	100.383(5)	101.085(5)	100.719(5)	100.38(7)	100.203(2)
Dy(1)-O(1)-Fe(1') (°)	101.31(4)	101.32(8)	100.897(5)	101.11(11)	97.826(5)	97.346(2)
Fe(1)-O(1)-Fe(1') (°)	103.791(5)	103.965(4)	103.669(5)	103.898(2)	99.604(2)	99.871(5)
Dy(1)-O(2)-Fe(1) (°)	107.558(5)	105.006(4)	106.998(2)	106.230(5)	110.383(5)	111.256(5)
Dy(1)-O(3)-Fe(1') (°)	104.716(5)	107.73(2)	106.400(5)	106.97(12)	106.269(5)	106.607(5)

For the two compounds (**Fe₂Dy₂-6**) and (**Fe₂Dy₂-7**) these parameters are especially interesting in terms of future magnetic characterisation and theoretical calculations since they show small changes in structure that makes systematic correlations and fine tuning interpretations possible.^[22, 24] Two additional advantages of these two compounds are that they use anisotropic Dy^{III} ions which were shown in previous studies in the butterfly testbed to provide the best SMM behaviour. Furthermore the benzoates are substituted with electron-withdrawing groups that enhance the magnetic properties.^[197]

4.2.2 Femtosecond transient absorption spectroscopy on Fe₂Dy₂ butterflies

As a result of the influence of the electron-withdrawing substituents on the benzoate ligands on ultrafast relaxation dynamics,^[212] another literature-known Fe₂Dy₂ butterfly using *p*-CN-benzoic acid and teaH₃ ligands and with the formula [Fe₂Dy₂(μ₃-OH)₂(Htea)₂(*p*-CN-O₂CPh)₆]·4MeOH (**Fe₂Dy₂-8**) was reproduced by the Master student Julia Weyandt and could be verified by SCXRD, albeit as a MeOH solvate rather than the literature-known MeCN/water solvate.^[201]

Femtosecond transient absorption spectroscopy is a pump-probe experiment where a pump pulse is used to excite the sample while the probe pulse detects the evolution of excited states. The setup used for the measurements in this work is described in the following: A femtosecond laser pulse is split using a beam splitter (partially transparent mirror) generating a pump and a probe pulse which are then guided to a Noncollinear Optical Parametric Amplifier (NOPA) and a white light generator, respectively. Going through the NOPA generates the 300 nm – 330 nm wavelength necessary for the excitation of the Fe₂Dy₂ butterflies. A chopper is positioned behind the NOPA blocking every second pump pulse before the beam is guided through the sample. The probe pulse goes through a transition delay stage which controls the time delay of the probe pulse before entering the white light generator where a CaF₂ crystal generates the white light continuum. This technique enables simultaneously probing all wavelengths from 350 – 750 nm. Subsequently, the probe pulse is passed through the sample, overlapping with the pump pulse, while the intensity of the beam is measured before (*I*_{0,S}) and after the sample (*I*_S) using CCD cameras.^[212] As a reference the sample is measured without excitation (*I*_{0,R} / *I*_R). This results in a measurement of the absorbance as a function of the probing wavelength and the chosen time delay and can be evaluated using equation 12.

$$\Delta OD = \log \frac{I_{0,S}(\lambda, \tau)}{I_S(\lambda, \tau)} - \log \frac{I_{0,R}(\lambda, \tau)}{I_R(\lambda, \tau)} \quad \text{equation 12}$$

Here ΔOD is the difference in optical density. The experimental setup for the femtosecond transient absorption spectroscopy is shown in Figure 58.

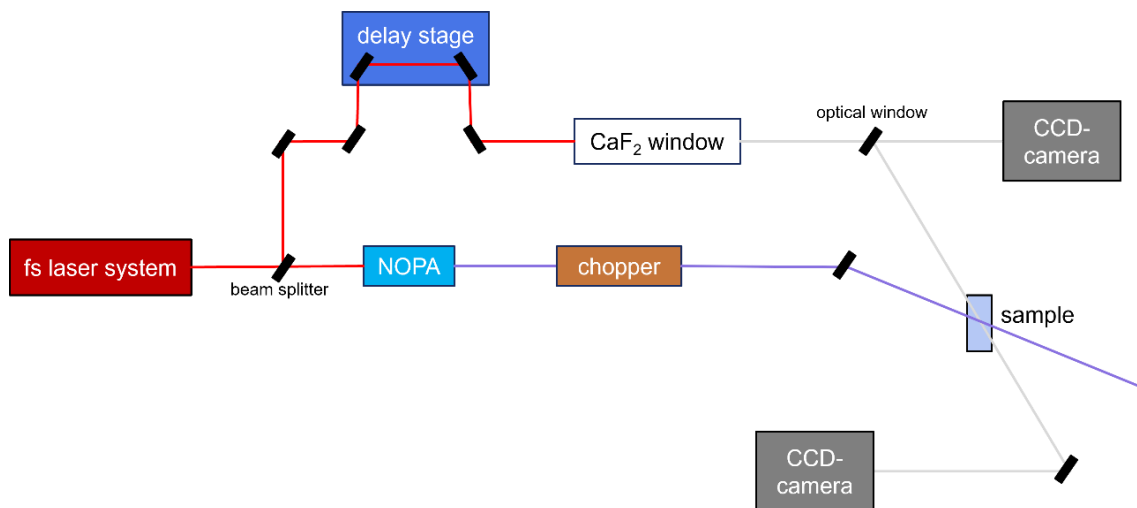


Figure 58. Scheme showing the experimental set-up for the femtosecond transient absorption spectroscopy measurements performed on the Fe-Ln complexes.

Equation 13 was used for the fitting of the single transient absorption spectra.^[34]

$$y = \frac{1}{2} \cdot \left(1 + \operatorname{erf} \left(\sqrt{4 \cdot \ln(2)} \cdot \frac{x - x_0}{\tau_0} \right) \right) \quad \text{equation 13}$$

$$\cdot \left(\left(A_1 \cdot \exp \left(-\frac{x - x_0}{\tau_1} \right) \right) \right.$$

$$+ \left(A_2 \cdot \exp \left(-\frac{x - x_0}{\tau_2} \right) \right)$$

$$+ \left(A_3 \cdot \exp \left(-\frac{x - x_0}{\tau_3} \right) \right)$$

$$+ \left(A_4 \cdot \exp \left(-\frac{x - x_0}{\tau_4} \right) \right)$$

$$\left. + \left(A_5 \cdot \exp \left(-\frac{x - x_0}{\tau_5} \right) \right) \right)$$

Probing the excited state dynamics, processes are observable which have an influence on the absorption spectra. These processes include ground state bleaching (GSB) which leads to negative contributions to the transient spectra since the ground state when probed after excitation is less populated than without pumping. Additionally, stimulated emission (SE) which is emission from excited states induced by the probing pulse have negative contributions to the spectra. Excited state absorption (ESA) where the system is excited to a higher state from an already excited state and hot ground state absorption (HGSA) where the excitation happens from a higher vibrational mode

of the ground state to an excited electronic state both have positive contributions to the transient spectra. These processes are shown schematically in Figure 59.^[212-214]

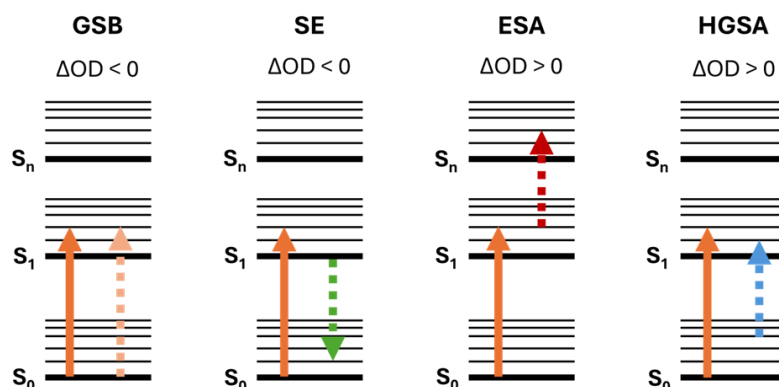


Figure 59. Possible transitions stimulated by the probing pulls (dotted arrows) after excitation of the sample (orange arrow). Adapted from reference^[212].

In the following section, the data obtained from the experiments are firstly presented using the example of (**Fe₂Dy₂-1**). Subsequently, the data for the other measured compounds are presented and compared with each other.

Before and after the transient absorption experiments steady-state UV-Vis spectra were collected to detect any possible decomposition of the compound during the measurement. No decomposition was observed for any of the studied compounds as proven by the identical UV-Vis spectra. This is exemplarily shown for (**Fe₂Dy₂-1**) in Figure 60.

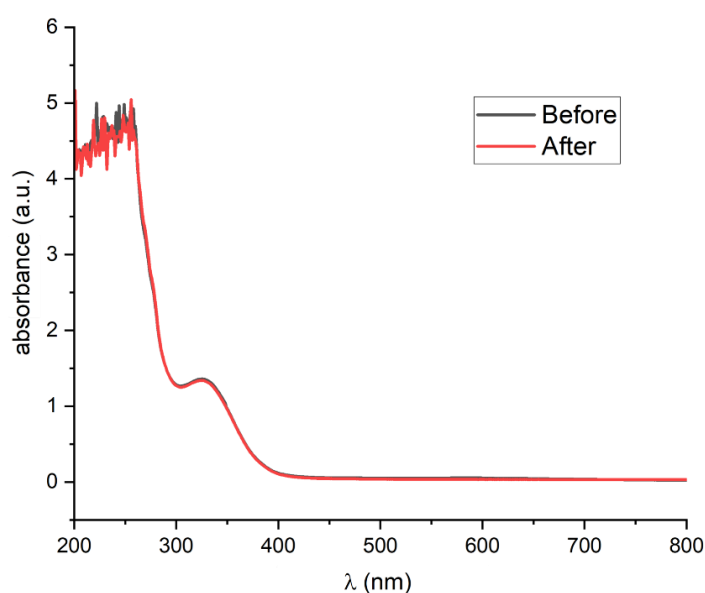


Figure 60. UV-Vis spectra for (**Fe₂Dy₂-1**) before and after the transient absorption spectroscopy measurements.

Transient absorption spectroscopy was performed on (**Fe₂Dy₂-1**) dissolved in DMF in a 1 mm quartz glass cuvette. Figure 61 shows the transient absorption spectrum at different times after excitation at 330 nm, probing using a white light continuum.

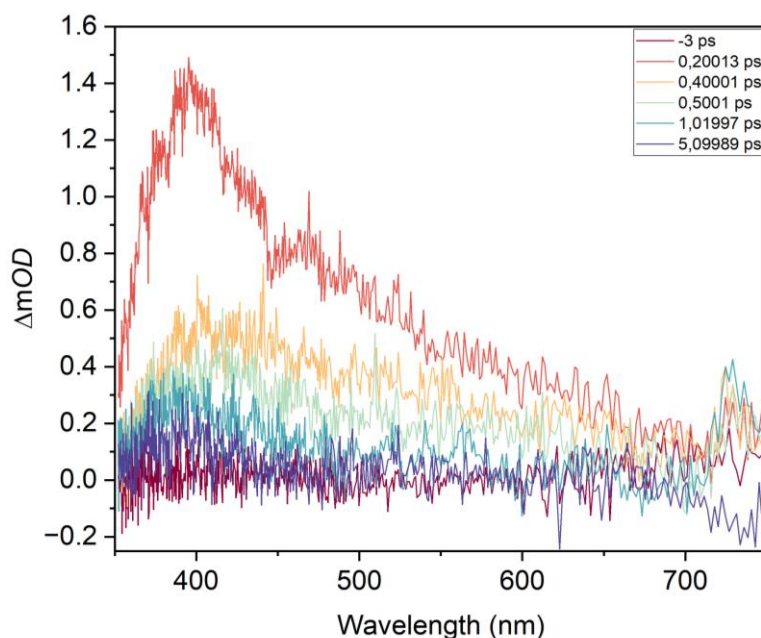


Figure 61. Transient absorption spectra for (**Fe₂Dy₂-1**) in DMF for delay times from 200 fs to 5 ps.

In Figure 62 the fitting of the single transient absorption spectrum for (**Fe₂Dy₂-1**) at a probing wavelength of 554.21 nm is shown. The fit uses equation 13 which has five exponential components, only three of which were needed for the fit yielding three time constants as well as three amplitudes which are shown in Table 6.

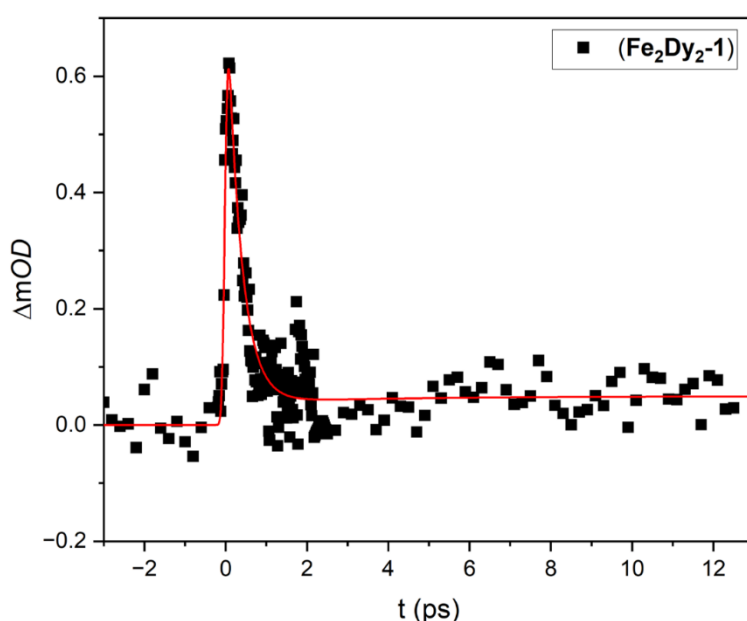


Figure 62. Single transient absorption spectrum for (**Fe₂Dy₂-1**) with fit.

The same experiment was repeated for the compounds (**Fe₂Dy₂-1**) to (**Fe₂Dy₂-8**) apart from the impure compound (**6**). The single transients for all compounds measured between 550 and 560 nm are shown in Figure 63. All samples were measured in DMF in 1 mm glass cuvettes and measured with a 330 nm / 0.5-0.75 μ J pump pulse probed with a 350nm-750 nm white light continuum. For the evaluation of time constants single transients at 550-560 nm were chosen. From these spectra it is clear that the signal-to-noise ratio for all experiments here is an issue leading to high error values for the determined fitting parameters. Qualitative trends between the compounds can nevertheless be observed. The absolute Δ mOD values of the single transients in Figure 63 can only be compared if the same pump energy is used for the measurements. This is because higher pump energies automatically lead to higher Δ mOD values. The difference in Δ mOD values is apparent comparing (**Fe₂Dy₂-3**) and (**Fe₂Dy₂-5**) where the only difference in structure is the change from *p*-^tBu to *p*-NO₂ substituted benzoates.

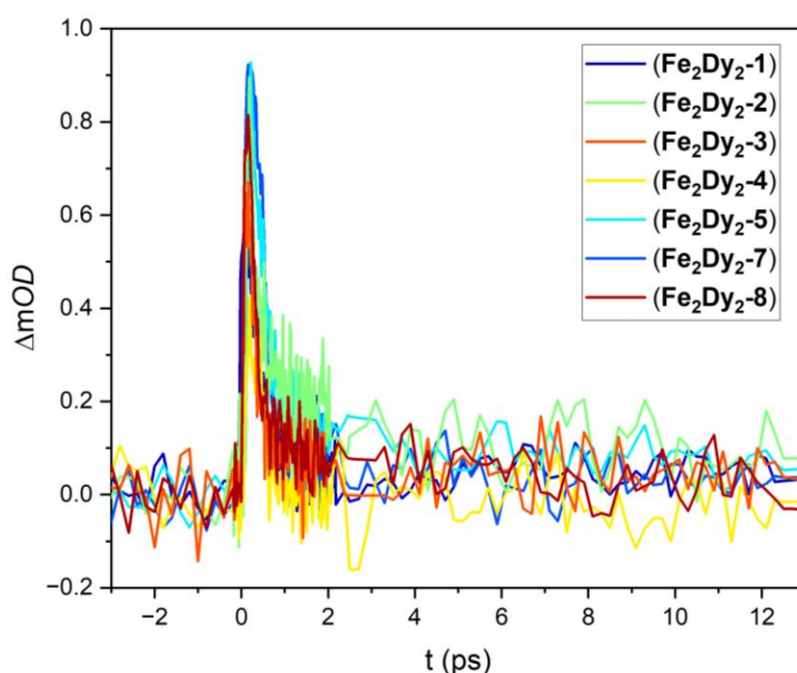


Figure 63. Single transient of the measured Fe₂Dy₂ samples in DMF. 1 mm quartz glass cuvette, 330 nm/0.5-0.75 μ J pump pulse, 550-560 nm probe pulse.

Table 6 shows the results of the fitting of the single transients. For these seven compounds the time constants are all in the regime of 100 fs for the first time constant τ_1 , a few ps for τ_2 and 100 ps for τ_3 . These values are comparable to the Fe₁₀Ln₁₀ complexes which were previously reported^[34] and again measured (see Section

4.3.1.3) and can be related to similar processes. These include vibrational cooling and crossing to shallow states before recombination.^[34] Additionally trap states are formed. In this context, larger values of the time constants can be correlated with greater efficiency of these processes. Comparing the seven samples, ligand effects can be seen although the errors should be considered carefully. Complexes with the same substitution on the benzoate ligands show very similar time constants with *p*-NO₂ substitution leading to the highest τ_1 time constant and the highest relative amplitudes A_1 . This observation is likely linked to a phenomenon already seen in the literature where NO₂ groups in hydrocarbons are responsible for an efficient intersystem crossing process due to low lying $n \rightarrow \pi^*$ levels.^[215] The electron-withdrawing character of the NO₂ groups as well as the CN groups might also have an effect on the time constants due to the large charge transfer character of the excited states.^[216] However, it is difficult to find a clear trend due to the low signal-to-noise ratio in the presented experiments.

Table 6. Fitting parameters, ΔmOD , excitation wavelength and energy as well as probing wavelength for all measured Fe₂Dy₂ samples.

	(1)	(2)	(3)	(4)	(5)	(7)	(8)
τ_1 (fs)	344 ± 30	124 ± 35	151 ± 36	298 ± 44	305 ± 24	163 ± 160	106 ± 161
τ_2 (ps)	6 ± 21	1.2 ± 0.3	0.95 ± 0.6	8.4 ± 17	3.4 ± 1.4	0.19 ± 0.16	0.12 ± 0.16
τ_3 (ps)	122 ± 82	441 ± 211	281 ± 202	273 ± 460	617 ± 284	8 ± 2.7	5.2 ± 1.2
Rel. A_1	0.91	0.72	0.85	0.9	0.83	0.49	0.48
Rel. A_2	0.02	0.2	0.11	0.05	0.1	0.5	0.48
Rel. A_3	0.07	0.08	0.04	0.05	0.07	0.01	0.04
ΔmOD	0.62	0.9	0.67	0.43	0.93	0.92	0.81
λ_e (nm)	330	330	330	330	330	330	330
E_e (μJ)	0.74	0.64	0.64	0.5	0.64	0.7	0.7
λ_p (nm)	554.21	550.5	559.11	551.55	560.22	549.45	550.5

In contrast to the NOPA-NOPA experiment used a decade ago, a primary goal of this work was to probe using the full visible spectrum, which, when implemented effectively, can open up a range of new measurement possibilities. However, this proved challenging, as the systems tested here exhibited very low intensities. The resulting poor signal-to-noise ratio and the large error values became the first challenge. During

the Master thesis of Julia Weyandt two possible ways to reduce the error were implemented and tested.

The first approach was a statistical error consideration for which a variation of the number of averaged values at each delay step was performed. This showed that using multiple measurements could improve the overall quality of the data by reducing variance.

The second approach involved testing the influence of the optical pathlength by using a cuvette with a smaller diameter (0.5 mm). Reducing the pathlength led to a clear improvement in signal-to-noise ratio in the single transients of (**Fe₂Dy₂-2**) and fitting resulted in similar τ_1 and τ_2 time constants as before with smaller error values. τ_3 showed both the most significant improvement and the largest change (441 ± 211 ps to 114 ± 24 ps). This is likely the result of the minimisation of absorption effects of the probe beam which could also be achievable by reducing the concentration of the sample. Overall, more measurements on the butterfly system testing the influence of optical pathlength are necessary to prove the viability of this approach.

4.3 20 Nuclearity CCCs

4.3.1 The Fe₁₀Ln₁₀ system

The compounds of the composition Fe₁₀Ln₁₀ are CCCs which due to their closed finite chain nature and their open shell 3d and 4f metal ions make them attractive subjects for studies of magnetic and electronic properties.^[27] The system consists of ten {FeLn(Me-tea)(Me-teaH)(NO₃)} repeating units forming the cyclic compound which is not planar but instead forms a “standing wave” structure (see Figure 64).^[29] The lanthanide ions can be exchanged resulting in ten isostructural compounds with Ln = Nd^{III}, Eu^{III}, Gd^{III}, Tb^{III}, Dy^{III}, Ho^{III}, Er^{III}, Tm^{III}, Yb^{III}, Lu^{III} and Y^{III} which make up a series of high nuclearity, high spin CCCs of the type [Fe^{III}Ln^{III}(Me-tea)₁₀(Me-teaH)₁₀(NO₃)₁₀] \cdot XMeCN.^[201]

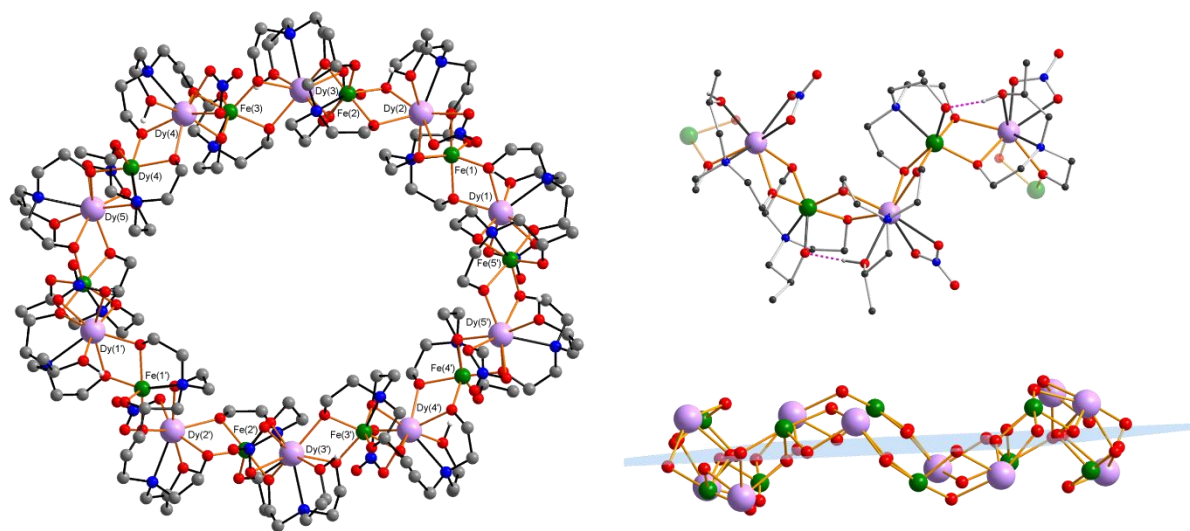


Figure 64. Ring structure of $\text{Fe}_{10}\text{Ln}_{10}$ (left) with repeating unit (top right) and "standing wave" structure alternating above and below the mean plane of the metal ions (bottom right).^[36]

Compounds using the chiral Me-teaH₃ ligand as a racemate results in chiral separation where the *R*-enantiomer of the ligand will always be on one side of the cycle whereas the *S*-enantiomer coordinates on the other side. Exchanging the chiral Me-teaH₃ ligand for achiral teaH₃ is also possible, making this an ideal system for systematic comparisons. Using different solvents during the synthesis results in crystallisation of the $\text{Fe}_{10}\text{Ln}_{10}$ compounds as different solvates of the same cyclic structure. This has an effect on the ellipticity of the ring structure which can be quantified using a compression factor ϵ . The compression factor ϵ was defined by Dr. Christopher E. Anson as shown in equation 14 to quantify the ellipticity of the ring without the need of fitting an ellipse to the uneven metal core.

$$\epsilon = \frac{d_1 - d_2}{d_1} \quad \text{equation 14}$$

The formula uses d_1 which is the longest Dy⋯Dy distance while d_2 is the shortest (see Figure 65).

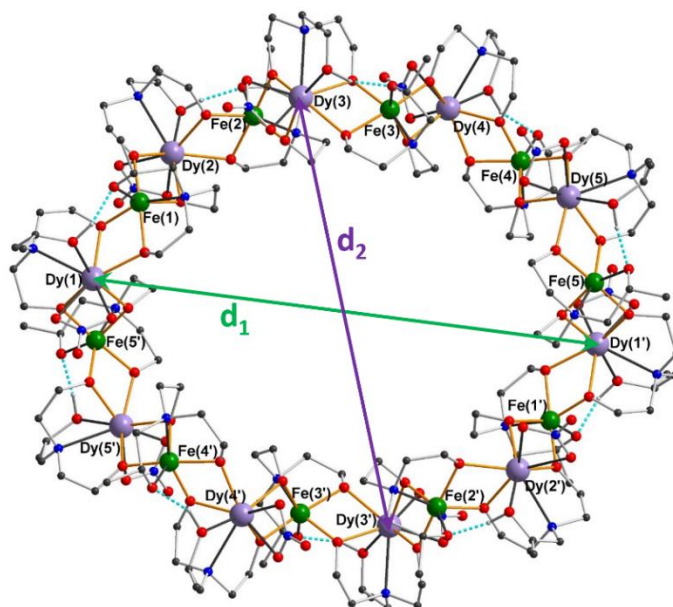


Figure 65. Distances d_1 and d_2 used for calculation of compression factor ϵ on the example of $\text{Fe}_{10}\text{Dy}_{10}$ using teaH_3 ligands.

Three examples for the variation in ellipticity depending on the ethanolamine-type ligand used and the solvent it was crystallised from are shown in Figure 66.

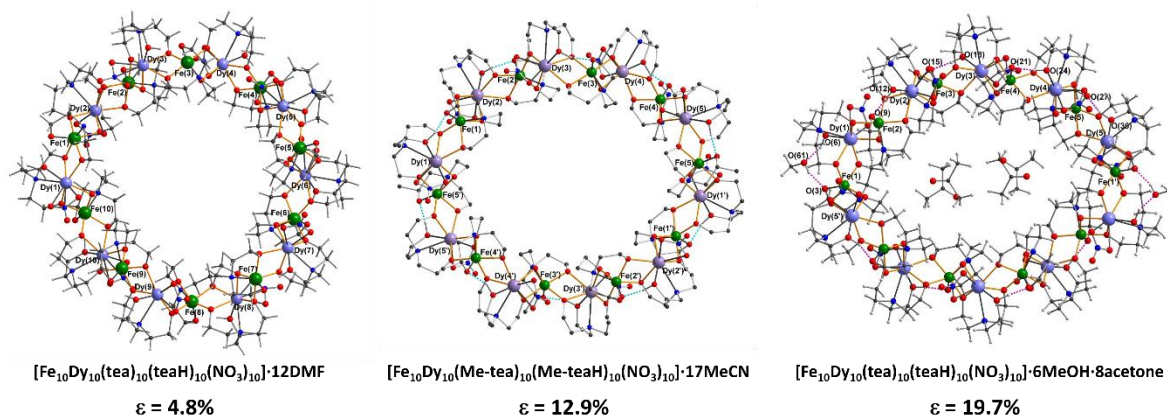


Figure 66. Differences in ellipticity of the three different solvates of $\text{Fe}_{10}\text{Dy}_{10}$ with teaH_3 ligands crystallised from DMF (left), MeCN (middle) and MeOH/acetone (right). Ellipticity quantified with compression factor.

The synthesis of all $\text{Fe}_{10}\text{Ln}_{10}$ compounds starts from the lanthanide nitrate, the corresponding triethanolamine ligand as well as $\text{Fe}(\text{NO}_3)_3 \cdot 9\text{H}_2\text{O}$. Thus in contrast to the Fe_2Ln_2 butterflies, for which it was necessary to use an $\{\text{Fe}_3\text{O}\}^+$ precursor, this is not the case here. It is possible to synthesise these 3d/4f coordination compounds as there seem to be no easily accessible pure 3d metal containing side products available under these reaction conditions. Throughout all testing of reaction conditions in this

work, including the accidental synthesis of $\text{Fe}_{10}\text{Ln}_{10}$ clusters during studies on the similar $\text{Fe}_8\text{Ln}_{12}$ system, no other side products were produced. Each reaction either resulted in $\text{Fe}_8\text{Ln}_{12}$, $\text{Fe}_{10}\text{Ln}_{10}$, or no product at all.

In this work the existing range of $\text{Fe}_{10}\text{Ln}_{10}$ compounds was extended by employing the chiral Et-teaH₃ ligand. In addition to PXRD, IR and elemental analysis the obtained Dy^{III} version was magnetically characterised using SQUID measurements to gauge the effect of this ligand adaptation.

Furthermore, the literature-known compound $[\text{Fe}^{\text{III}}_{10}\text{Tb}^{\text{III}}_{10}(\text{Me-tea})_{10}(\text{Me-teaH})_{10}(\text{NO}_3)_{10}]\cdot\text{XMeCN}^{[201]}$ which had not been magnetically characterised was reproduced for the purpose of investigating the magnetic behaviour using microSQUID measurements in collaboration with the working group of Prof. Dr. Wolfgang Wernsdorfer.

Lastly this system was also chosen as well as the Fe_2Dy_2 butterflies to be investigated using femtosecond transient absorption spectroscopy in the context of the Master project of Julia Weyandt in the working group of Prof. Dr. Andreas-Neil Unterreiner. The $\text{Fe}_{10}\text{Ln}_{10}$ complexes have previously been subjected to femtosecond transient absorption spectroscopy where it could be shown that the intramolecular electronic channels follow a three-step process. This process involves vibrational cooling and crossing to shallow states which is followed by recombination. It was also shown that the lanthanide ions create trap states to form excitons after photoexcitation.^[34] The set-up used for the reported study was a NOPA-NOPA pump-probe experiment which only uses one probing wavelength. Improving on this, the experiment conducted during this work uses a broadband white light continuum for probing, enabling a readout across the range of 350 nm to 750 nm. To test this new setup, measurements were conducted on the $\text{Fe}_{10}\text{Ln}_{10}$ system to reproduce the previously obtained results. In addition, measurements on the $\text{Fe}_{10}\text{Dy}_{10}$ rings crystallised from different solvents varying in ellipticity were also conducted to investigate any possible effects on the ultrafast relaxation dynamics.

4.3.1.1 Extending the Fe₁₀Ln₁₀ platform

The goal of this work was to synthesise a new Fe₁₀Ln₁₀ CCC that shows the same overall structure but uses a different chiral ligand compared to the original compounds. This was successfully achieved by reacting Et-teaH₃ with Dy(NO₃)₃ and Fe(NO₃)₃ in a MeOH/MeCN solution resulting in crystallisation of [Fe₁₀Dy₁₀(Et-tea)₁₀(Et-teaH)₁₀(NO₃)₁₀·18MeCN (**Fe₁₀Dy₁₀-9**). The most challenging part of the synthesis of (**Fe₁₀Dy₁₀-9**) was the crystallisation since exchanging the ligand simply using the literature procedure which was used for the synthesis of the original Me-teaH₃ version only results in microcrystalline powders. However, by changing the order of addition of the reactants as well as the amount of solvent and base it was possible to produce crystals large enough for single crystal XRD measurements. This procedure is not yet fully optimised and is basically an adapted version of the newly found Fe₈Dy₁₂ synthesis discussed in Section 4.3.2.

The molecular structure of (**Fe₁₀Dy₁₀-9**) is essentially identical to the literature-known Me-teaH₃ analogue^[201] and is shown in Figure 67 together with the Et-teaH₃ ligand.

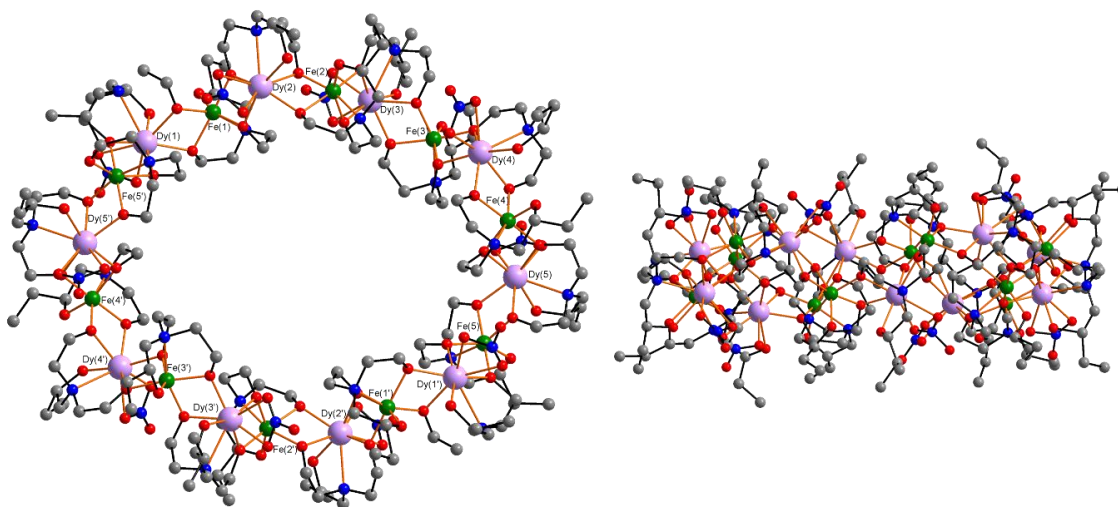


Figure 67. Molecular structure of (**Fe₁₀Dy₁₀-9**) (left) with sideview (bottom right). Hydrogen atoms were omitted for clarity.

(**Fe₁₀Dy₁₀-9**) crystallises in the triclinic space group $P\bar{1}$ with $Z = 2$ with one molecule in the centre of the unit cell and two half molecules on each side (see Figure 68).

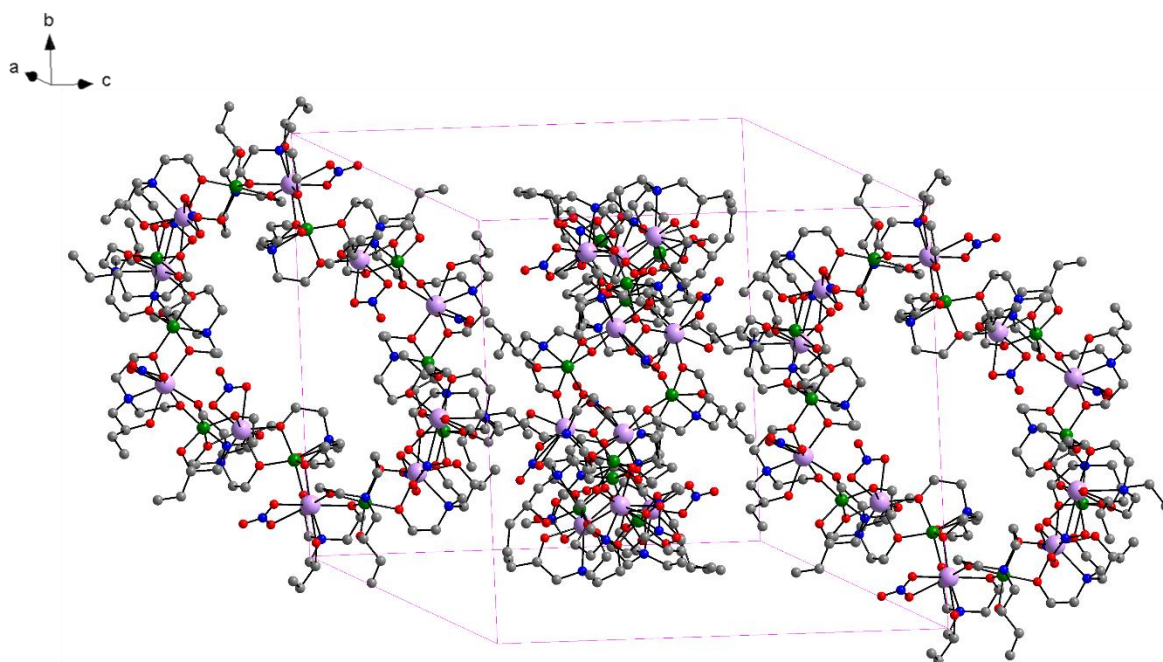


Figure 68. Arrangement of the molecular units making up the unit cell with a Z of two.

The two independent molecules in the unit cell are not co-parallel such as in the analogous compounds with teaH_3 and Me-teaH_3 , but instead almost perpendicular with the mean planes of their $\text{Fe}_{10}\text{Dy}_{10}$ cores making an angle of $83.77(1)^\circ$ to each other (see Figure 69).

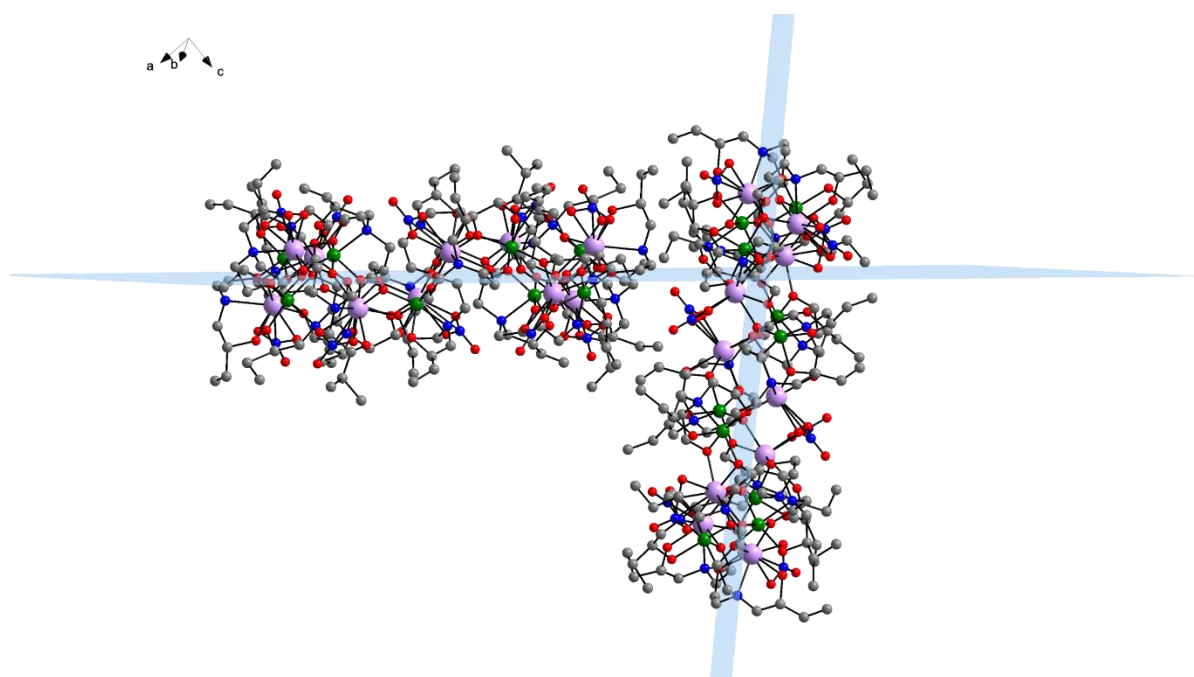


Figure 69. The two molecules of $(\text{Fe}_{10}\text{Dy}_{10}\text{-9})$ in the unit cell with mean planes through the metal atoms of each ring shown in blue.

The top views of both molecules in the unit cell shown in Figure 70 have the same molecular structure but different ellipticities. For ring a) the compression factor ε is 16.66% whereas ring b) is even more elliptical with $\varepsilon = 18.7\%$ just 1% smaller than the largest ellipticity found in the MeOH/acetone solvate making the two rings in (**Fe₁₀Dy₁₀-9**) the second and third most elliptical Fe₁₀Ln₁₀ rings so far. All other compounds of this type were found to have an ε of between 4.8% to 14%.

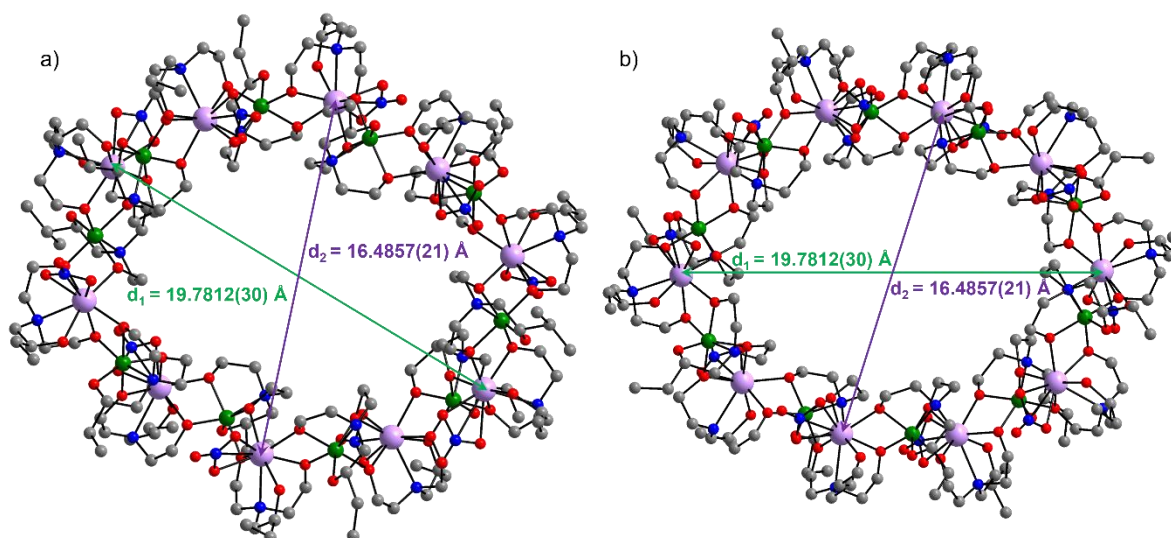


Figure 70. Distances used to calculate the compression factor for both triangles in the unit cell of (**Fe₁₀Dy₁₀-9**).

The packing of (**Fe₁₀Dy₁₀-9**) with alternating rows of parallelly oriented rings almost in the **ac** plane and rings perpendicular to this plane is shown in Figure 71. The perspective along the **a**-axis shows how the rings are stacked, oriented at an angle to the **bc** plane rather than parallel to it, with each ring type displaying a different angle relative to this plane.

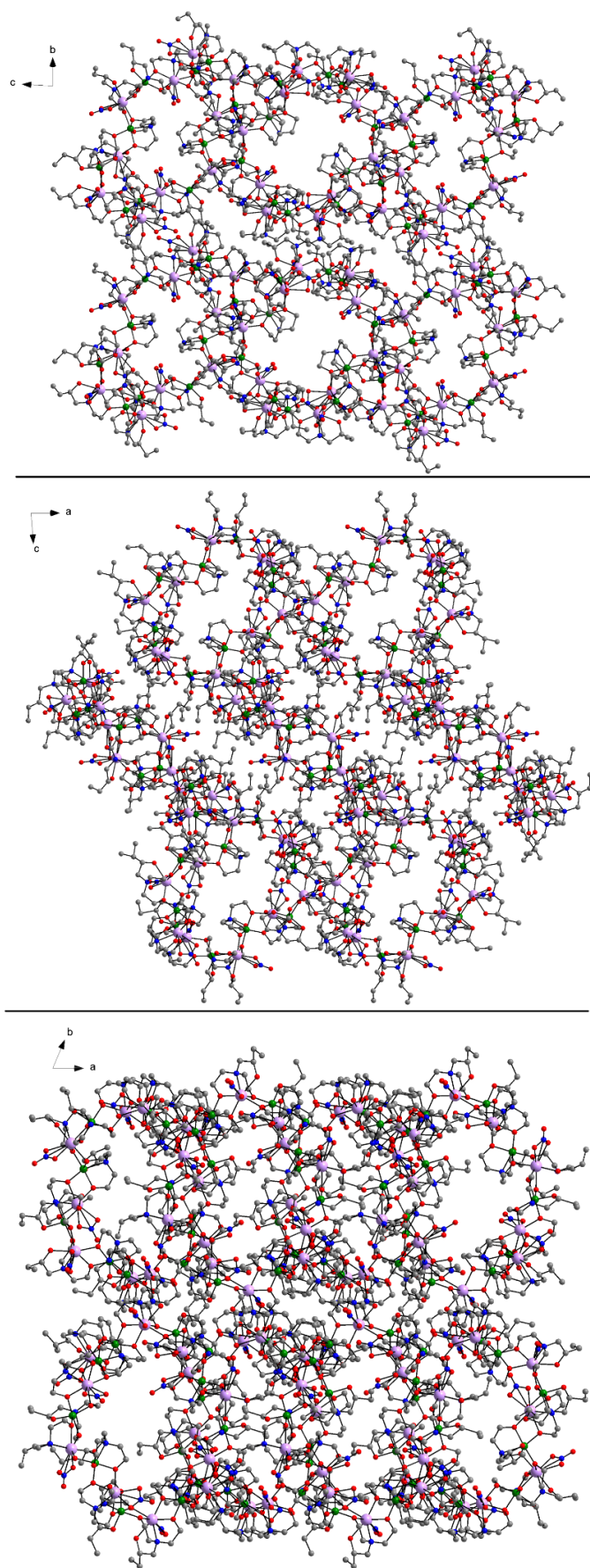


Figure 71. Packing of $(\text{Fe}_{10}\text{Dy}_{10}-9)$ along the crystallographic *a* (top), *b* (middle) and *c* (bottom) axis.

To analyse the purity of the compound first PXRD measurements were performed which are shown in Figure 72. The experimental powder pattern does not match the simulation which could be due the loss of lattice solvent during sample preparation leading to a change of crystal. Subsequent measurements of unit cells of multiple single crystals from the in total homogeneous looking sample gave the same unit cell of the described (**Fe₁₀Dy₁₀-9**) every time. These results together with the elemental analysis which fit for the expected compound showed that some changes in the crystal parameters due to evaporation of lattice solvent led to the non-matching PXRD of this actually pure sample.

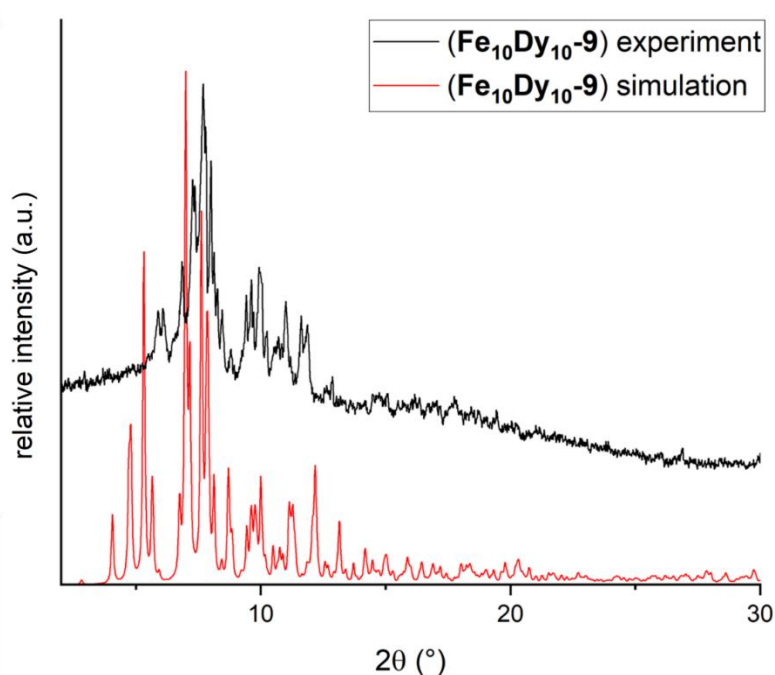


Figure 72. Experimental and simulated powder pattern for (**Fe₁₀Dy₁₀-9**).

Using the same synthetic procedure as for (**Fe₁₀Dy₁₀-9**) but using Ln(NO₃)₃·n(H₂O) (Ln = Y^{III}, Tb^{III} and Ho^{III}) instead of Dy(NO₃)₃·6(H₂O) led to three analogues (**Fe₁₀Y₁₀-10**), (**Fe₁₀Tb₁₀-11**) and (**Fe₁₀Ho₁₀-12**). These show the same experimental powder pattern as (**Fe₁₀Dy₁₀-9**). The similarity in PXRD and also in the IR spectra shown in Figure 73 indicates that these three compounds are likely the isostructural analogues but due to the poor crystal quality no additional single crystal XRD measurements could be performed to confirm this. An elemental analysis done on these compounds also suggests this.

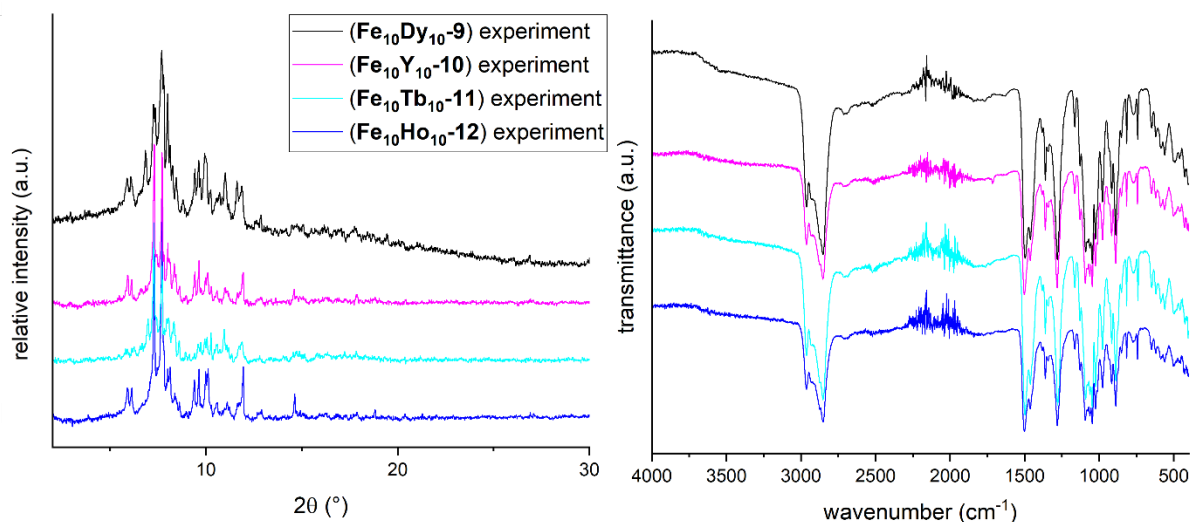


Figure 73. Experimental powder diffractograms for compounds (**Fe₁₀Dy₁₀-9**) to (**Fe₁₀Ho₁₀-12**).

4.3.1.2 Magnetic Studies on Fe₁₀Ln₁₀ clusters

SQUID magnetic measurements were performed on (**Fe₁₀Dy₁₀-9**) to gauge the effect of the Et-teaH₃ ligand on the magnetic properties. Furthermore, magnetic measurements were performed on (**Fe₁₀Tb₁₀-15**) which uses the Me-teaH₃ ligand in order to compare the results to the magnetic characterisation previously done by Baniodeh on the series of isostructural Fe₁₀Ln₁₀ complexes.^[201] To add to the structural characterisation performed by Baniodeh a crystal structure of the compound was recorded during the work on this thesis (see Figure 74).

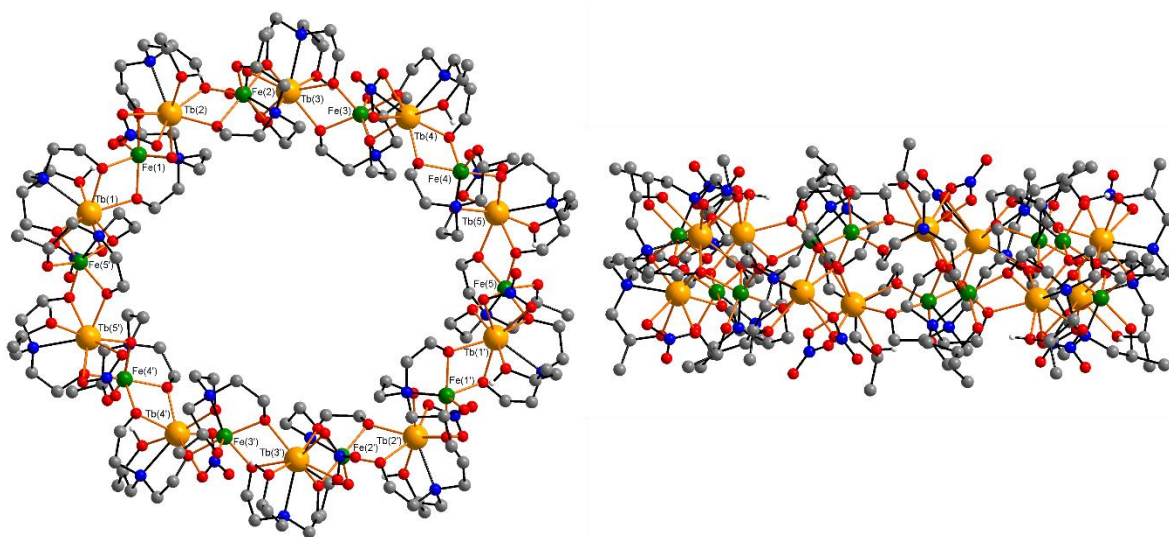


Figure 74. Molecular structure of (**Fe₁₀Tb₁₀-15**) (right), sideview (left).

For (**Fe₁₀Dy₁₀-9**) the magnetic characterisation included AC, DC and magnetisation measurements on an immobilised powder sample whereas (**Fe₁₀Tb₁₀-15**) was subjected to single crystal microSQUID measurements in collaboration with Appu Sunil from the group of Prof. Dr. Wolfgang Wernsdorfer.

The DC susceptibility measurements were carried out under an applied magnetic field of 0.1 T (see Figure 75). At room temperature, the experimental $\chi_M T$ value is 182.3 cm³Kmol⁻¹, close to the theoretical value of 185.2 cm³Kmol⁻¹ expected for ten non-interacting Dy^{III} and high-spin Fe^{III} ions. The $\chi_M T$ value remains constant between 300 K and 50 K below which it sharply increases to reach a maximum value of 308.37 cm³Kmol⁻¹ at 2.8 K before decreasing to a value of 298.48 cm³Kmol⁻¹ at 2 K. This behaviour can be attributed to the dominant ferromagnetic Fe-Dy interactions as similarly shown for related Fe₄Gd₄, Fe₄Y₄ and Fe₁₀Gd₁₀ cyclic systems.^[27, 29]

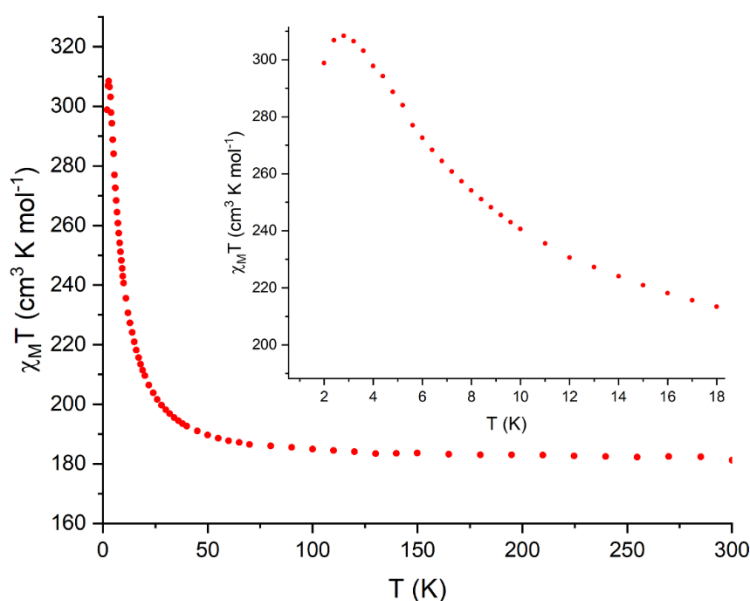


Figure 75. $\chi_M T$ vs T plot for (**Fe₁₀Dy₁₀-9**) measured at 0.1 T with an inset showing the low temperature range.

The presence of ferromagnetic coupling is further confirmed by the Curie-Weiss plot (see Figure 76), a linear fit in the range of 300 – 15 K reveals a Curie constant (C) of 180.18 cm³Kmol⁻¹ and a Weiss constant (θ) of 2.62 K.

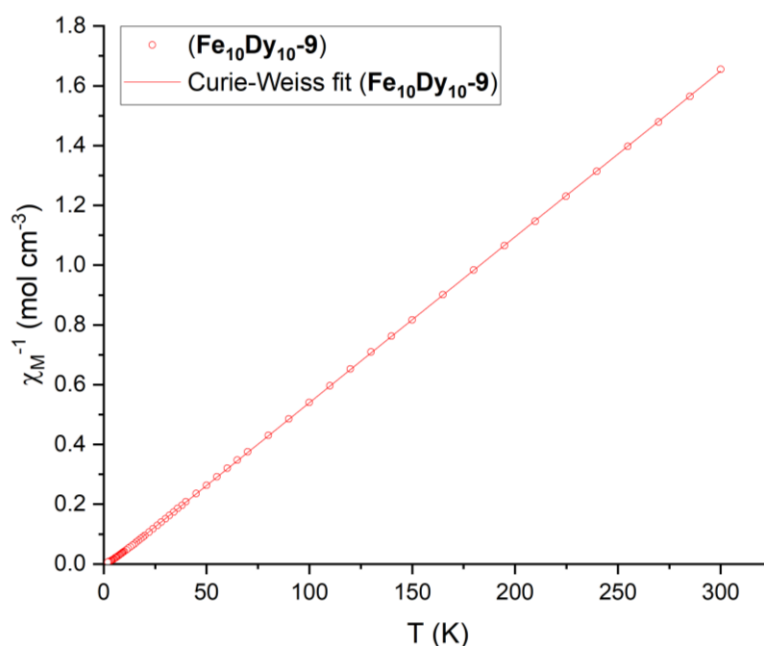


Figure 76. Curie-Weiss plot of (**Fe₁₀Dy₁₀₋₉**) and Curie-Weiss fit (red line).

AC susceptibility measurements were conducted with zero applied DC field in the temperature range 2 K to 3.2 K and frequencies between 100 to 1500 Hz as shown in Figure 77. The reason for the frequency range shown is that no signal was observed at lower frequencies. The out-of-phase (χ'') component increases at higher frequencies with the maximum being outside the available frequency range. As the temperature increases, the extremely weak AC signal decreases significantly before reaching 3 K. Measurements with applied fields did not improve the signal. This is in line with the other literature-known $\text{Fe}_{10}\text{Dy}_{10}$ compounds which also exhibit poor SMM behaviour.^[201] Given that the peak in the zero-field measurement lies beyond the measured frequency range, fitting of the curve was not possible.

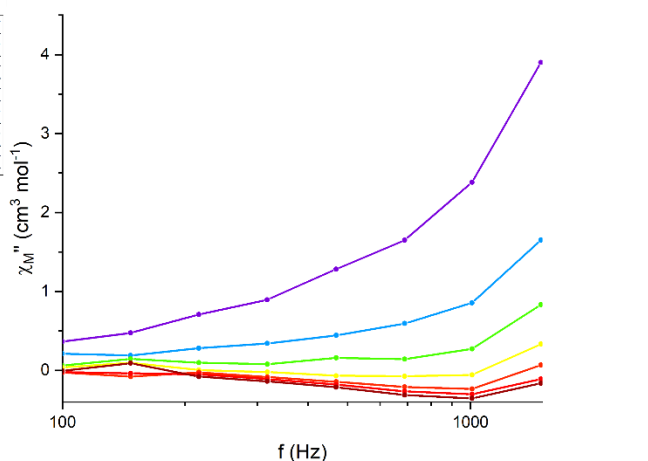
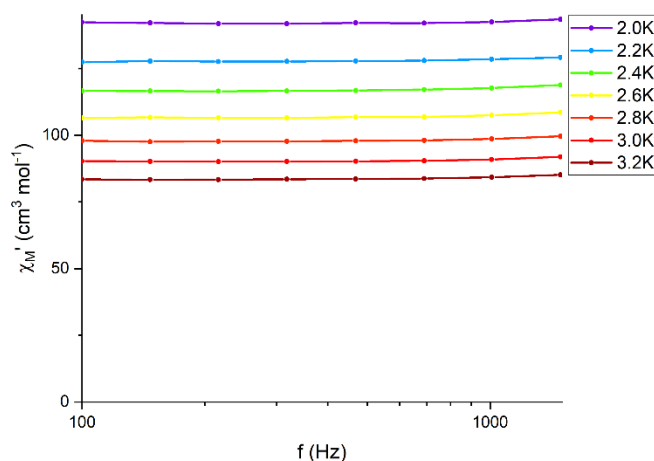


Figure 77. χ_M' against f (left) and χ_M'' against f (right) for (**Fe₁₀Dy₁₀₋₉**), lines are a guide to the eyes.

Magnetisation measurements were carried out between 2 K and 5 K and 0 T to 7 T (see Figure 78). The overall shape of the curve resembles that observed for other $\text{Fe}_{10}\text{Dy}_{10}$ compounds with a steep increase in magnetisation up to approximately 1 T, above which it increases essentially linearly reaching a value of $105.8 \mu_B$ at 7 T. This value is slightly lower than the expected $109.2 \mu_B$ for ten Dy^{III} and Fe^{III} ions.^[217] The reduced magnetisation curves (inset in Figure 78) at different temperatures are non-superposed at larger fields which could be the result of low-lying excited states becoming populated.

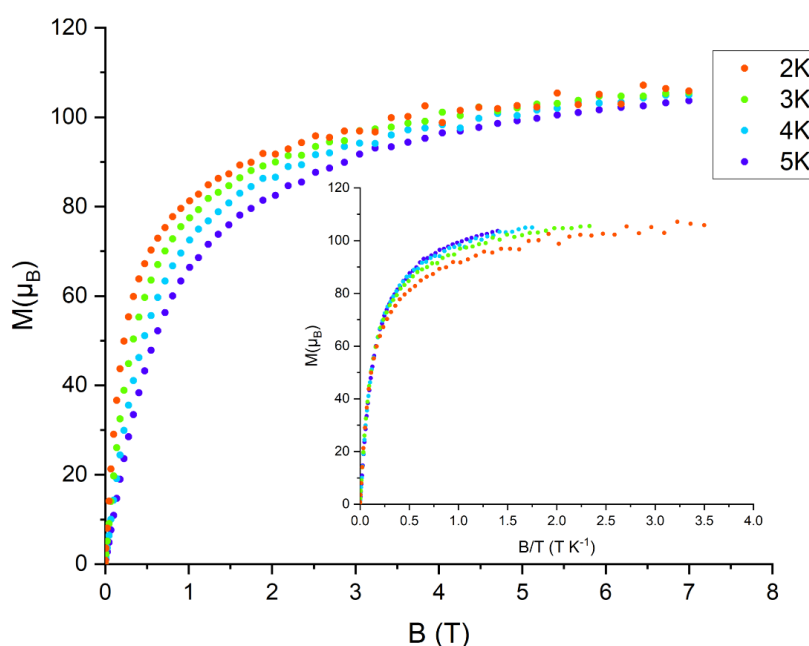


Figure 78. M vs B plot for ($\text{Fe}_{10}\text{Dy}_{10}\text{-9}$) with an inset of the reduced magnetisation plot.

In conclusion the magnetic data measured for ($\text{Fe}_{10}\text{Dy}_{10}\text{-9}$) is in line with the behaviour observed for previously investigated $\text{Fe}_{10}\text{Dy}_{10}$ compounds. Thus, it was not possible to observe any changes related to the modification of the ligand. Additional measurements on single crystals could potentially show how the impact of the ligand on the packing influences the magnetic properties, as the crystal packing *i.e.* the arrangement of the rings in the crystal in relation to each other changes quite drastically in comparison to other $\text{Fe}_{10}\text{Ln}_{10}$ rings.

MicroSQUID data were collected on single crystals of ($\text{Fe}_{10}\text{Tb}_{10}\text{-15}$) measuring at a constant sweep rate of 16 mT/s and in the temperature range 0.03 K to 5 K. The sweep rate dependence was also collected at 0.03 K (see Figure 79). The compound shows non-sweep rate dependent hysteresis up to 0.5 K similar to that of the Dy^{III} version.

The main difference between the Tb^{III} and the Dy^{III} version is the coercive field. The coercive field is important for SMMs as it represents the stability of the bistable magnetic state to field fluctuations. For (**Fe₁₀Tb₁₀-15**) this coercive field is significantly larger than that observed for the Dy^{III} version (see Figure 80).^[201] For the Dy^{III} version the coercive field H_c at 0.03 K was 0.054 T compared to (**Fe₁₀Tb₁₀-15**) which has H_c of 0.13 T at 0.03 K. Therefore, exchanging Dy^{III} for Tb^{III} seems to enhance the coercive field and therefore the SMM properties. However, it does not seem to have a significant effect on the energy barrier since the temperature to which hysteresis is observed does not increase.

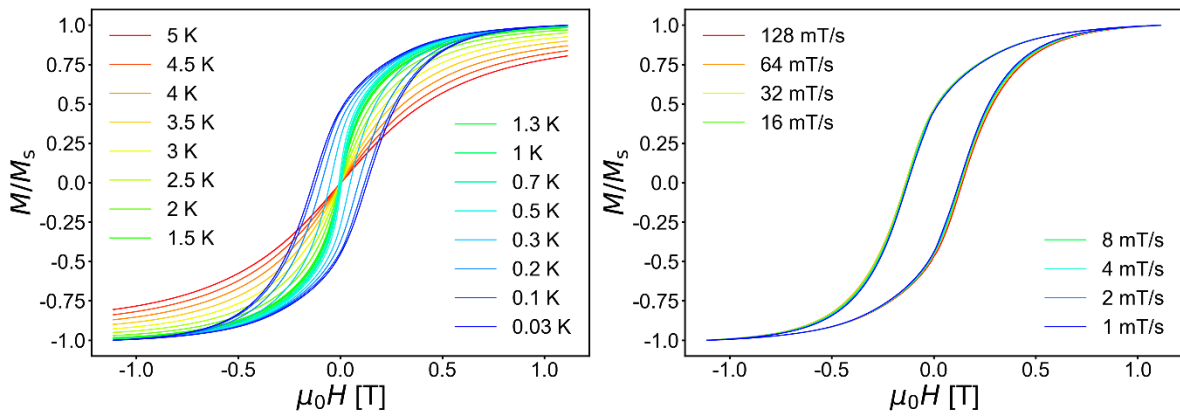


Figure 79. MicroSQUID data for (**Fe₁₀Tb₁₀-15**) at a sweep rate of 16 mT/s at different temperatures (left) and at 30 mK with varying sweep rates (right).

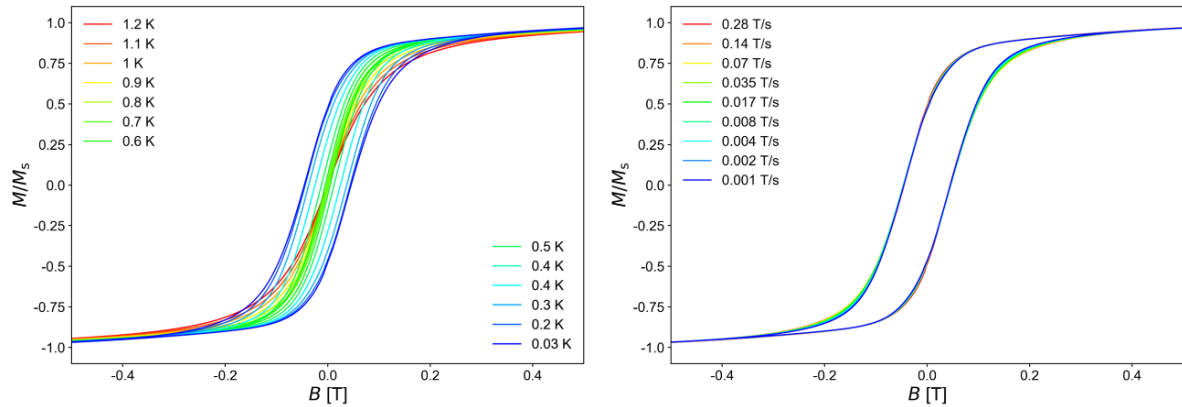


Figure 80. MicroSQUID data for Fe₁₀Dy₁₀ at a sweep rate of 16 mT/s at different temperatures (left) and at 30 mK with varying sweep rates (right).^[201]

4.3.1.3 Femtosecond transient absorption spectroscopy studies on $\text{Fe}_{10}\text{Ln}_{10}$ rings

For the femtosecond transient absorption spectroscopy, a series of $\text{Fe}_{10}\text{Ln}_{10}$ compounds were reproduced from the literature.^[201] These include (**Fe₁₀Dy₁₀-13**) with the formula $[\text{Fe}^{\text{III}}_{10}\text{Dy}^{\text{III}}_{10}(\text{Me-tea})_{10}(\text{Me-teaH})_{10}(\text{NO}_3)_{10}]\cdot\text{XMeCN}$ which contains Me-teaH₃ as well as the isostructural lanthanide variations (**Fe₁₀Tm₁₀-14**) and (**Fe₁₀Tb₁₀-15**). As described above these compounds have been characterised by femtosecond absorption spectroscopy using a different experimental setup before so they serve as a reference point for subsequent measurements. Additionally, (**Fe₁₀Dy₁₀-16**) and (**Fe₁₀Dy₁₀-17**) with the respective formulae $[\text{Fe}_{10}\text{Dy}_{10}(\text{tea})_{10}(\text{teaH})_{10}(\text{NO}_3)_{10}]\cdot 13\text{DMF}$ and $[\text{Fe}_{10}\text{Dy}_{10}(\text{tea})_{10}(\text{teaH})_{10}(\text{NO}_3)_{10}]\cdot 8\text{Me}_2\text{CO}\cdot 6\text{MeOH}$ were synthesised to check for any influence of the ellipticity of the rings on the excited state energy landscape. These compounds were crystallised from different solvents namely DMF and acetone changing the ellipticity of the rings as described above.

To rule out decomposition of the compound during the spectroscopic studies a UV-Vis spectrum was collected before and after transient absorption experiments. Figure 81 shows an example of such proving that the sample remains stable during the measurements. The spectrum shows saturation effects of the detector as the concentration had to be kept high to allow for the use of the same sample for the femtosecond absorption experiments.

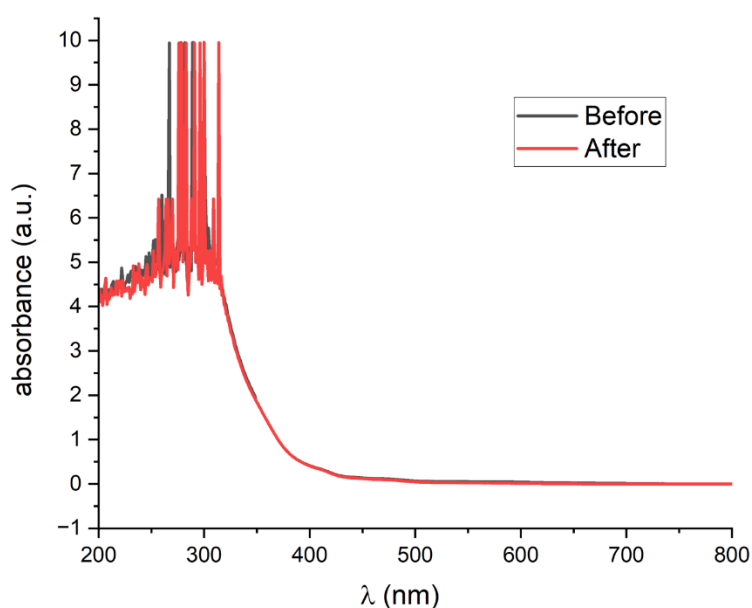


Figure 81. UV-Vis spectra before and after transient absorption experiment for compound (**Fe₁₀Dy₁₀-13**) in water.

Steady-state UV-Vis absorption spectra of all mentioned compounds reveal their similar behaviour (see Figure 82). A pump wavelength of about 310 nm was chosen due to the absorption starting at below 420 nm. The white light continuum probes at 350 nm to 750 nm covering the region below 420 nm where ground state bleaching can occur and the region above which should only record excited state dynamics.

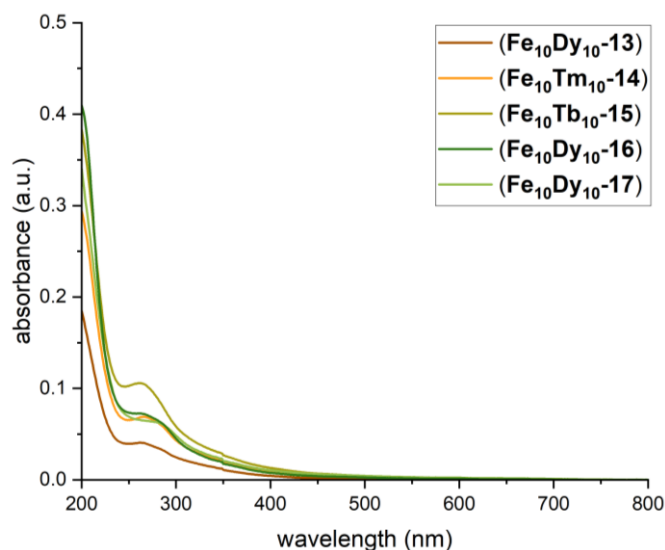


Figure 82. UV-Vis spectra of compounds (**(Fe₁₀Dy₁₀-13)** – (**(Fe₁₀Dy₁₀-17)**) in aqueous solution.

The transient absorption spectra across the whole visible range for (**(Fe₁₀Dy₁₀-13)**) at different delay times are shown in Figure 83. Due to the nature of the previously performed NOPA-NOPA experiments which only probed at one specific wavelength (for which 550 nm was chosen),^[34] it was not possible to see the maximum at 420 nm which can be attributed to an excited state absorption (ESA).^[212-214]

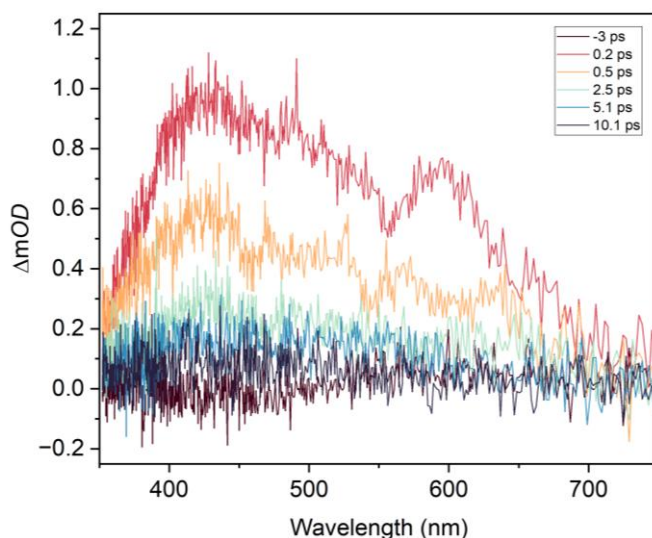


Figure 83. Transient absorption spectrum for (**(Fe₁₀Dy₁₀-13)**).

In order to test whether the new setup reproduces the previous results the fitting routine was applied at a wavelength of ca. 550 nm as shown in Figure 84 for (**Fe₁₀Tb₁₀-15**). This reveals one of the main challenges to overcome as it excels at recording a spectrum at a range of wavelengths but analysing a single one becomes problematic as a result of the poor signal-to-noise ratio. The reason for this is that the use of the white light source prevents the optimisation of the setup in regard to one specific wavelength. This is most clearly seen in the resulting error values of the fitting parameters for all measured compounds which are summarised in table 7.

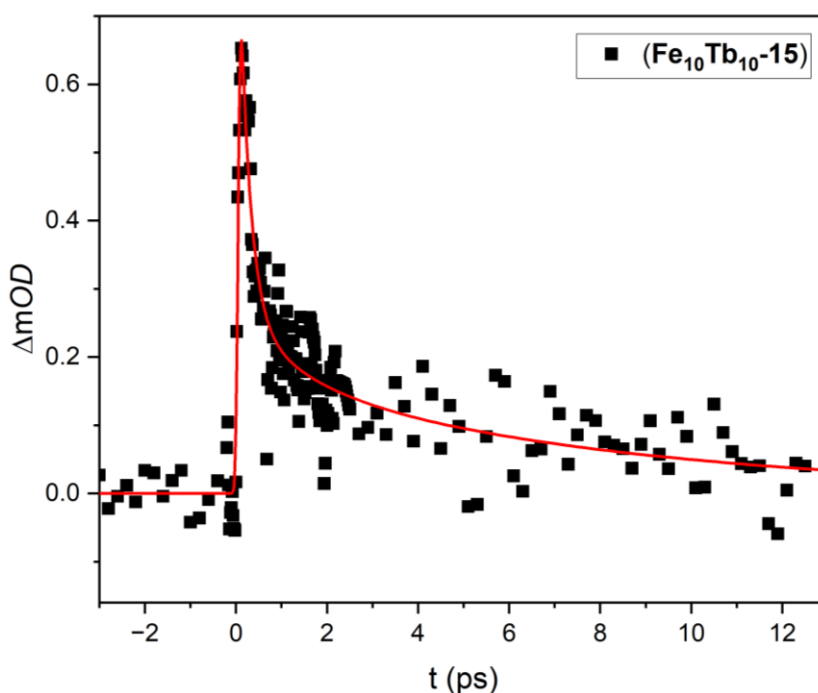


Figure 84. Single transient absorption spectrum at 550 nm for (**Fe₁₀Tb₁₀-15**) with fit.

The single transients are of (**Fe₁₀Tm₁₀-14**) and (**Fe₁₀Tb₁₀-15**) are consistent with those for (**Fe₁₀Dy₁₀-13**) but show slightly different relative optical densities (see Figure 85). However, comparison of the optical density needs to take into account that the value is dependent on the pump pulse energy. For a direct comparison with the previous experiment by Dr. Yu Liang^[34] the same solvent needs to be used in both experiments.

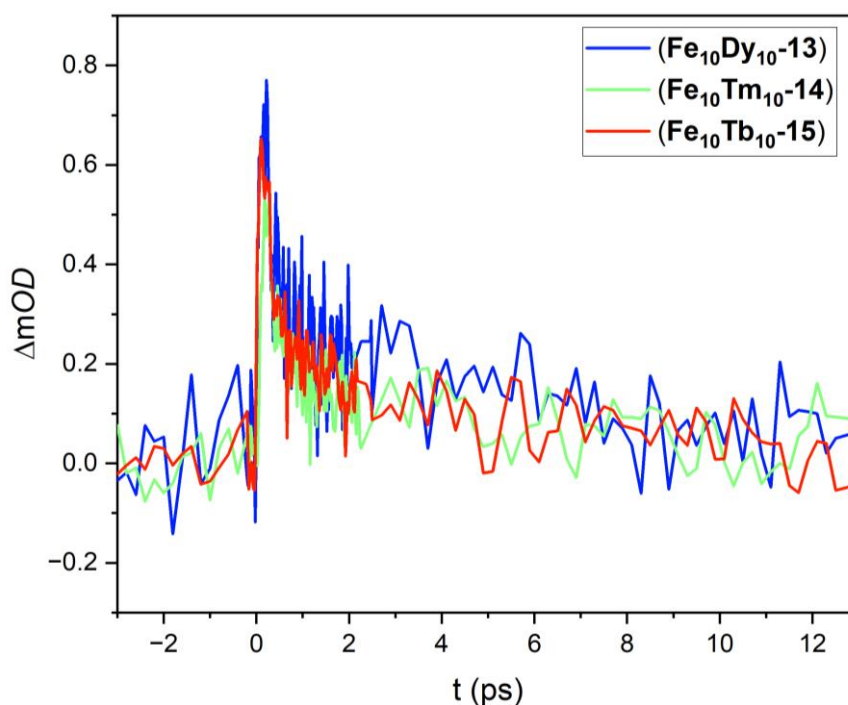


Figure 85. Single transient absorption spectra for compounds (**Fe₁₀Dy₁₀-13**), (**Fe₁₀Tm₁₀-14**) and (**Fe₁₀Tb₁₀-15**). 321 nm/ 0.6 μ J pump pulse, probed at 553.11 nm for (**Fe₁₀Dy₁₀-13**), 330 nm/ 0.74 μ J pump pulse, probed at 552.02 nm for (**Fe₁₀Tm₁₀-14**), 321 nm/ 0.44 μ J pump pulse, probed at 549.87 nm for (**Fe₁₀Tb₁₀-15**). Measured in H₂O solution in a 1 mm quartz glass cuvette.

Table 7 shows the results of the fitting for the three samples (**Fe₁₀Dy₁₀-13**), (**Fe₁₀Tm₁₀-14**) and (**Fe₁₀Tb₁₀-15**). For all samples the first time constant represents the dominant process as the relative amplitude A_1 is the largest which is consistent with previous studies.^[34] Even though (**Fe₁₀Dy₁₀-13**) has a lower pump energy than (**Fe₁₀Tm₁₀-14**) it exhibits the highest ΔmOD values. The ΔmOD values between the compounds are difficult to compare due to the variation in pumping energy. Keeping this in mind, it can be observed that (**Fe₁₀Dy₁₀-13**) has a lower pump energy than (**Fe₁₀Tm₁₀-14**) and exhibits the highest ΔmOD values whereas (**Fe₁₀Tm₁₀-14**) has the highest pump energy but the lowest ΔmOD . The small signal-to-noise ratio poses a significant challenge demanding an optimisation of the experimental setup to make a full analysis and interpretation of the data obtained here possible. Nonetheless it can be concluded that the new experimental setup also gave the three expected time constants with comparable values to the ones obtained 10 years ago.^[34]

Table 7. Fitting parameters, ΔmOD , excitation wavelength/energy and probing wavelength for compounds (**Fe₁₀Dy₁₀-13**), (**Fe₁₀Tm₁₀-14**) and (**Fe₁₀Tb₁₀-15**).

Sample	(Fe₁₀Dy₁₀-13)	(Fe₁₀Tm₁₀-14)	(Fe₁₀Tb₁₀-15)
τ_1 [fs]	196 ± 42	132 ± 52	226 ± 85
τ_2 [ps]	4.1 ± 1.6	1.7 ± 0.4	1.3 ± 3.1
τ_3 [ps]	352 ± 403	202 ± 113	7.9 ± 5
Rel. A_1	0.73	0.69	0.68
Rel. A_2	0.21	0.25	0.11
Rel. A_3	0.06	0.06	0.21
ΔmOD	0.81	0.54	0.65
λ_e [nm]	321	330	321
E_e [μJ]	0.6	0.74	0.44
λ_p [nm]	553.11	552.02	549.87

Figure 86 shows that the single transients of (**Fe₁₀Dy₁₀-16**) and (**Fe₁₀Dy₁₀-17**) exhibit very similar ΔmOD values which can be compared since both measurements use the same pumping energy.

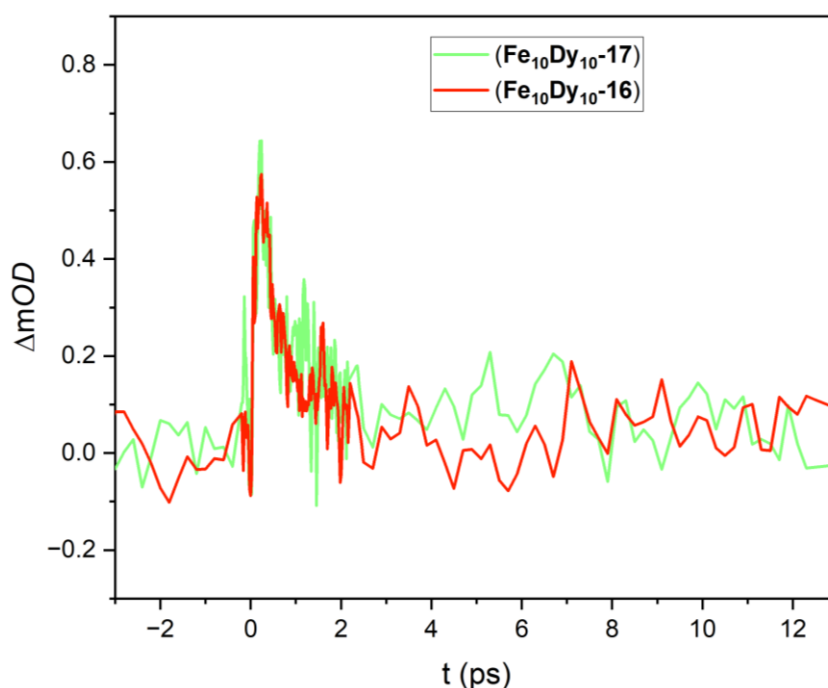


Figure 86. Single transient absorption spectra for compounds (**Fe₁₀Dy₁₀-16**) and (**Fe₁₀Dy₁₀-17**). 321 nm/ 0.5 μJ pump pulse, probed at 554.21 nm for (**16**), 321 nm/ 0.5 μJ pump pulse, probed at 548.8 nm for (**Fe₁₀Dy₁₀-17**). Measured in H₂O solution in a 1 mm quartz glass cuvette.

Table 8 summarises the time constants, relative amplitudes, pump energies, and probe wavelengths for these samples. However, high error values make it difficult to draw quantitative conclusions. The changes in solvate and therefore ellipticity of the ring between the two compounds seems to have an effect on the ultrafast relaxation

dynamics since they have different time constants. This becomes more apparent when comparing the values for τ_1 and τ_3 . The relative amplitudes put further emphasis on these changes but since the focus of this work is on the time constants - which are affected by significant error values - further research with an improved setup is needed to analyse accurately the dynamics.

Table 8. Fitting parameters, ΔmOD , excitation wavelength/energy and probing wavelengths for compounds (**Fe₁₀Dy₁₀-16**) and (**Fe₁₀Dy₁₀-17**).

Sample	(Fe₁₀Dy₁₀-16)	(Fe₁₀Dy₁₀-17)
τ_1 [fs]	69 ± 8	262 ± 144
τ_2 [ps]	1.4 ± 0.4	1.1 ± 0.7
τ_3 [ps]	256 ± 151	47.3 ± 52
Rel. A ₁	0.44	0.64
Rel. A ₂	0.41	0.3
Rel. A ₃	0.15	0.06
ΔmOD	0.64	0.58
λ_e [nm]	321	321
E _e [μ J]	0.5	0.5
λ_p [nm]	554.21	548.8

In the course of this work, strategies to minimise the errors without changing the experimental setup were employed and their impact on the signal-to-noise ratio studied. One such strategy involved consideration of the statistical errors. The previously used experiment consists of one measurement with 1000 averaged data points per time delay and this was changed to ten separate measurements taking 500 averaged data points. A smoothing effect of the measured data when taking the average of the ten measurements was observed, improving signal-to-noise ratio. Unfortunately, this change did not suffice to reduce the error values of the resulting time constants. Furthermore, this resulted in time constants which were much further away from the reference point compared with the previous studies performed in 2014.^[34] Thus, although this approach did reduce the variants in the obtained data it was so far not successful in reducing errors.

4.3.2 The Fe₈Dy₁₂ system

The complex with the formula [Fe₈Dy₁₂(tea)₈(teaH)₁₂(NO₃)₁₂]·8MeCN is a CCC which has the same nuclearity and is comparable to the Fe₁₀Dy₁₀ clusters previously described (see Figure 87). Compound (**Fe₈Dy₁₂-18**) was initially synthesised and magnetically characterised by Dr. Yan Peng, a previous PhD student who was working on the Fe₁₀Dy₁₀ system. Since the compound was the result of a failed synthesis of an Fe₁₀Dy₁₀ ring, reproducing the Fe₈Dy₁₂ compound and optimising the reaction conditions was the first challenge. The optimised procedure could then be used to prepare and investigate further modifications of the compound.

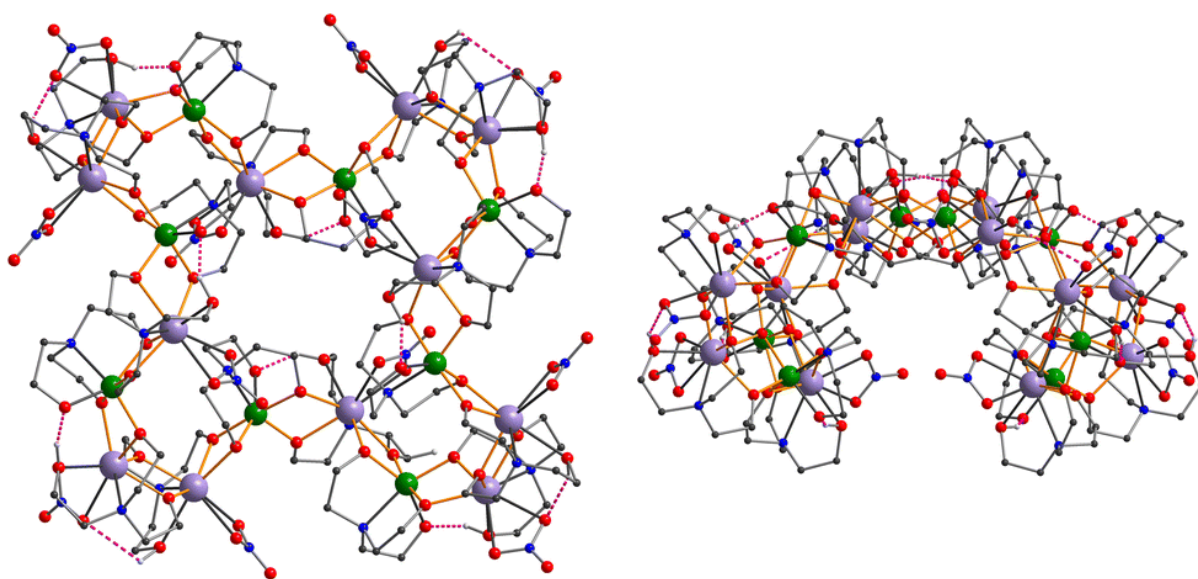


Figure 87. Molecular structure of (**Fe₈Dy₁₂-18**). Reprinted with permission from reference^[36] [Royal Society of Chemistry] copyright 2024.

The original synthetic procedure involved mixing a solution of teaH₃ in MeCN with a solution of Fe(NO₃)₃·9H₂O and Dy(NO₃)₃·6H₂O in MeOH and MeCN. After 5 minutes of stirring, Et₃N was added as a base followed by ten more minutes of stirring.

In the scope of the present work, after extensive testing in order to find the optimal ratio of the reactants, a new, improved and reproducible synthetic procedure was developed which has since been published.^[36] The Fe(NO₃)₃·9H₂O and Dy(NO₃)₃·6H₂O were dissolved in MeOH. The Et₃N was added to a solution of teaH₃ in MeCN. After subsequent addition of the ligand/base solution over the course of 1 minute to the metal-containing solution, the reaction mixture was then stirred for further 10 mins. Subsequently a further 2.4 equivalents of Et₃N were added.

It is important to note that the total amount of base used here is *ca.* 40% less than the amount used in the original procedure. Additionally, the concentrations of the reactants are different since 5 ml less MeCN was used. Adding the same amount of base as in the original procedure was also tested. This resulted in the crystallisation of the right product but in much lower yield. After the successful reproduction of (**Fe₈Dy₁₂-18**) further ligand and metal variations were tested using this procedure. The phase purity of (**Fe₈Dy₁₂-18**) was confirmed by a PXRD measurement which is shown in Figure 88.

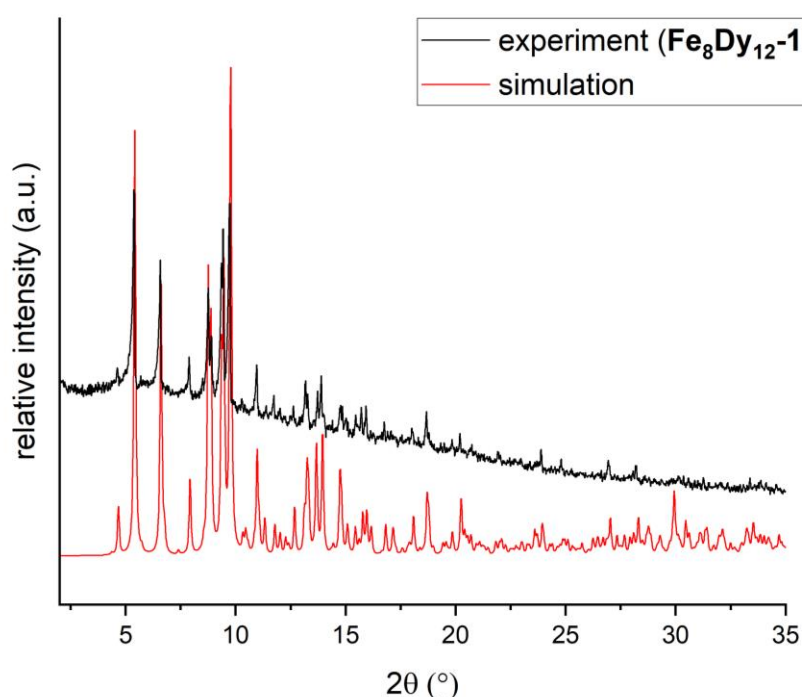


Figure 88. Simulated and experimental powder pattern for (**Fe₈Dy₁₂-18**).

Furthermore, UV-Vis studies were performed on (**Fe₈Dy₁₂-18**) in water and compared to the Fe₁₀Dy₁₀ which bears the same ligand (see Figure 89). It was already known from previous work on these systems that the IR spectra of compounds (**Fe₈Dy₁₂-18**) and (**Fe₁₀Dy₁₀-16**) are essentially identical. The IR spectrum was also collected again to confirm this observation. In the UV-Vis analysis both compounds show strong absorption in the UV region below 250 nm with the maximum located slightly below 200 nm. A second band is observed as a shoulder at 270 nm for both compounds although less pronounced for (**Fe₈Dy₁₂-18**).

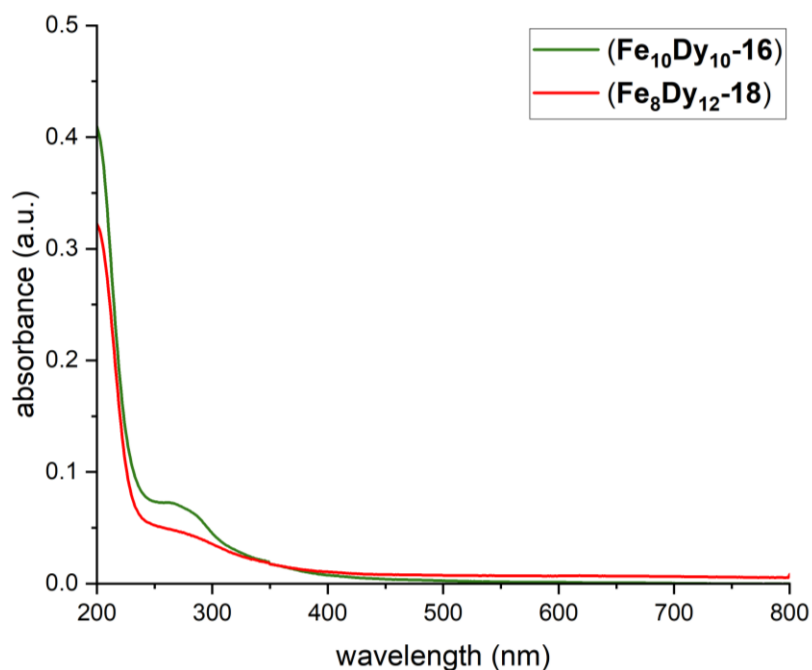


Figure 89. UV-Vis spectra from 200 to 800 nm of compounds (**Fe₈Dy₁₂-18**) and (**Fe₁₀Dy₁₀-16**) measured in aqueous solution.

Consequences of changing the teaH₃ ligand or the lanthanides

Variation of the ethanolamine type ligands such as Me-/Et-teaH₃ yielded the corresponding Fe₁₀Dy₁₀ rings rather than the Fe₈Dy₁₂. The yield and crystal quality found here were in fact better than using any of the previously reported synthetic routes to obtain the Fe₁₀Dy₁₀ rings and therefore became the preferred synthesis for the Me- and Et-teaH₃ containing rings when crystallizing them from an MeCN/MeOH mixture during this work.

Changing the lanthanide ions and keeping the original teaH₃ ligand led to mixed results since for most of the lanthanides a white powder precipitated overnight which was identified to be the Fe₁₀Ln₁₀ using PXRD measurements. An exception of this was the reaction using Ho^{III} where crystals formed in a very low yield after one week. These crystals were characterised using single crystal XRD and found to be the desired Fe₈Ho₁₂. Additionally, a PXRD measurement was performed. As a result of the low yield the signal-to-noise ratio is rather poor and the peaks are significantly broadened, however the peak positions indeed indicate that the Fe₈Ho₁₂ complex was obtained in a pure phase (see Figure 90).

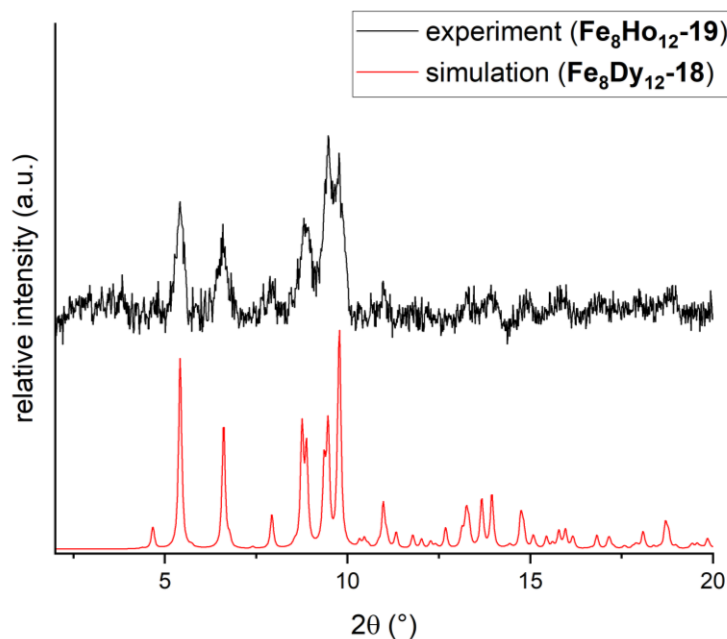


Figure 90. Simulated powder pattern for (**Fe₈Dy₁₂-18**) and experimental powder pattern for (**Fe₈Ho₁₂-19**).

The very low yield precluded further characterisation of (**Fe₈Ho₁₂-19**). Addition of more base to the Ho^{III}-containing reaction appears to make it more reliable as with less base the reaction sometimes yielded the Fe₁₀Ho₁₀ precipitate, this however did not improve the yield of the reaction. A likely explanation for this could be the different amounts of acid left in the used lanthanide salts from their respective synthesis. The Ho(NO₃)₃ salt used here probably contains residual nitric acid which would make the use of more base necessary.

4.3.3 Fe₁₆Tb₄ system

A series of CCCs with the general formula [Fe₁₆Ln₄(tea)₈(teaH)₁₂(μ-O₂CCH₃)₈](NO₃)₄·16H₂O·XMeCN Ln = Sm^{III}, Eu^{III}, Gd^{III}, Tb^{III}, Dy^{III} and Ho^{III} (X = 10/11) were first published by Powell *et al.* in 2011.^[35] It is synthesised using teaH₃ and [Fe^{III}₃O(O₂CCH₃)₆(H₂O)₃]Cl·6H₂O as the iron triangle precursor, with acetate serving as the acid. This results in the formation of a CCC with a nuclearity of 20 but with a different ratio of Fe^{III} to Ln^{III} ions compared to the Fe₁₀Ln₁₀ or Fe₈Ln₁₂ structures. In the context of this thesis the Tb^{III} version (**Fe₁₆Tb₄-20**) was synthesised to enable microSQUID measurements to be performed. The reason for this is the sigmoidal shape of the original field dependent magnetisation observed in SQUID magnetometry

measurements i.e. an inflection point in the magnetisation data.^[35] The molecular structure (**Fe₁₆Tb₄-20**) and magnetic SQUID data are shown in Figure 91. This indicates a level crossing and is not observed in the corresponding data for the Fe₁₆Dy₄ analogue and therefore necessitated further investigation using microSQUID measurements.

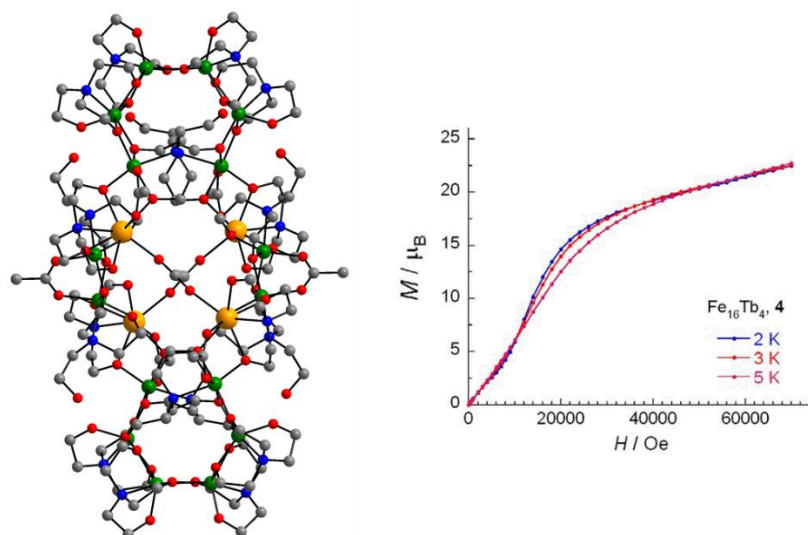


Figure 91. Molecular structure of (**Fe₁₆Tb₄-20**) (left) with magnetisation data (right). Adapted with permission from reference^[35] [Royal Society of Chemistry] copyright [2011].

The reproduction of (**Fe₁₆Tb₄-20**) was successful using an adaptation of the literature procedure^[35, 201] with a much longer crystallisation time. The literature procedure suggested one week while here the vial was kept undisturbed under slow evaporation of the solvent over 3 months. After this time the vial was sealed to prevent complete evaporation of the solvent. With this method large single crystals close to 3x3 mm in size were obtained (see Figure 92). The synthesis of the desired compound was confirmed by a measurement of the unit cell using single crystal XRD.

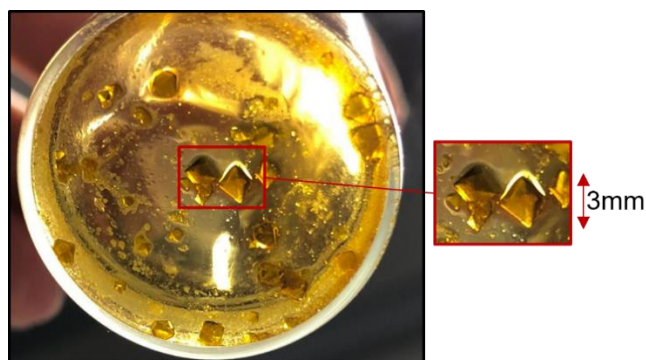


Figure 92. Crystals of compound (**Fe₁₆Tb₄-20**) with approximate dimensions.

The microSQUID measurements for (**Fe₁₆Tb₄-20**) were performed on single crystals (smaller crystals were chosen here) at temperatures between 30 mK and 5 K with a sweep rate of 16 mT/s as well as with varied sweep rates at 30 mK. The results of these experiments are shown in Figure 93. The temperature dependent measurements shows a hysteresis loop between two antiferromagnetic states around zero field which are stable up to *ca.* 1.1 T at which point the curve reaches an inflection point. Afterwards the curve starts to flatten slightly but appears not to saturate at the maximum possible field applicable in this experimental setup. The hysteresis starts to close with increasing temperatures and is essentially closed at 1.3 K. The compound shows negligible sweep rate dependence. Comparing the data obtained here with the magnetisation data showing the S-shape, the level crossing can be related to the transition from the antiferromagnetic state seen at lower fields to the ferromagnetic states occupied above the 1.1 T switching field.

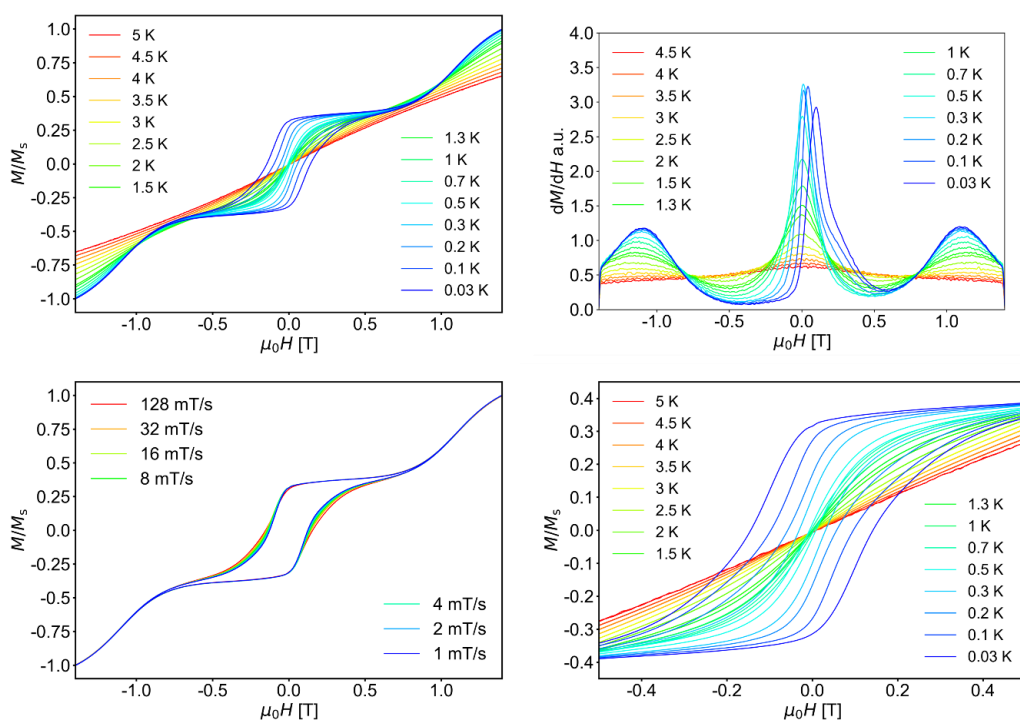


Figure 93. MicroSQUID measurement, temperature dependence at 16 mT/s (top left) with first derivative (top left), sweep rate dependence (bottom left) and temperature dependence zoomed in (bottom right).

As mentioned in the paper previously reporting these compounds an interpretation of the magnetic data is challenging. To further understand this behaviour calculations on the anisotropy axis and further microSQUID data on Ln^{III}-analogues such as the Dy^{III} version and the respective magnetic axis in that compound are necessary.

4.4 Fe-Ln Systems conclusion and outlook

Fe₂Dy₂ butterflies

Five new Fe₂Dy₂ butterflies (**Fe₂Dy₂-3**), (**Fe₂Dy₂-4**), (**Fe₂Dy₂-5**), (**Fe₂Dy₂-6**) and (**Fe₂Dy₂-7**) were synthesised and characterised using single crystal and powder XRD measurements. The compounds use ligand and co-ligand combinations that utilise electron-withdrawing groups on the ligand which were shown to slow down relaxation of magnetisation. Using ampdH₂ as ligand has a small effect on the core geometry. These are the first examples of Fe₂Dy₂ butterfly structures with this ligand.

In addition, three literature-known Fe₂Dy₂ butterflies (**Fe₂Dy₂-1**), (**Fe₂Dy₂-2**) and (**Fe₂Dy₂-7**) were synthesised using an optimised procedure which yielded high quality crystals as is evident from the significantly improved SCXRD structure for (**Fe₂Dy₂-2**). All the successfully synthesised Fe₂Dy₂ butterflies (except for (**Fe₂Dy₂-6**) due to sample impurities) were analysed using femtosecond transient absorption spectroscopy measurements. At the same time this enabled us to test a pump probe experimental setup using a white light continuum.

The results of the femtosecond spectroscopy, which were done in the context of the Master thesis of Julia Weyandt, showed that the Fe₂Ln₂ butterflies behave in a similar way to Fe₁₀Ln₁₀ CCCs as well as Fe nanoparticles.^[34, 208-210] The data could be fitted using three time constants as reported in the literature for Fe₁₀Ln₁₀ as well as for a Ni₂Dy₂ butterfly system.^[34, 218] Furthermore, the time constants and relative amplitudes vary depending on the substituent on the benzoate co-ligand. Additionally, shortcomings of using the white light continuum experimental setup, which are mainly the poor signal-to-noise ratio, could be identified. Approaches to improve the measurement were tested. However, further tests and changes to the experimental setup are required to increase the signal-to-noise ratio in order to provide a conclusive interpretation.

20 nuclearity 3d-4f CCCs

A highlight was the successful synthesis of a new Fe₁₀Dy₁₀ cluster using the chiral Et-teaH₃ ligand in its racemic form (**Fe₁₀Dy₁₀-9**). The structure of the compound was compared to other Fe₁₀Ln₁₀ CCCs with teaH₃ and Me-teaH₃ ligands in terms of packing and ellipticity (*i.e.* deviation from a perfect circle) of the in-plane projection of the

cycles. Here it was found that using Et-teaH₃ changes the relative packing of the rings in terms of orientation changing from an offset parallel arrangement to something closer to face-edge perpendicular.

The use of the Et-teaH₃ ligand has a significant effect on the overall ellipticity. Out of all of the Fe₁₀Ln₁₀ compounds obtained so far this almost perpendicular dual of the two Fe₁₀Dy₁₀ rings individually have the second and third highest factor describing the ellipticity as explained in more detail above. The same chiral separation that was observed for the previously reported Fe₁₀Ln₁₀ clusters, where one enantiomer of the ligand coordinates on the top side of the ring while the other is on the bottom side, could also be observed for (**Fe₁₀Dy₁₀-9**).

Isostructural versions of (**Fe₁₀Dy₁₀-9**) could be obtained by exchanging the lanthanide ions for Y^{III}, Tb^{III}, and Ho^{III}. PXRD, IR and EA were used to characterise these compounds.

Magnetic characterisation of (**Fe₁₀Dy₁₀-9**) revealed similar SMM behaviour to that seen for other Fe₁₀Dy₁₀ rings. The ethyl group on the ligand has a negative influence on the magnetic properties as shown by the very weak AC signals at zero applied DC field.

Additionally, the literature-known Fe₁₀Tb₁₀ with Me-teaH₃ ligands (**Fe₁₀Tb₁₀-15**) was reproduced and structurally characterised using SCXRD. The compound was subsequently investigated using microSQUID measurements. These showed that the use of Tb^{III} rather than Dy^{III} significantly improves the SMM behaviour as shown by the fact that the coercive field is approximately doubled.

Four more literature-known Fe₁₀Ln₁₀ compounds including (**Fe₁₀Tm₁₀-14**), (**Fe₁₀Dy₁₀-13**) and two different solvates of the teaH₃-based Fe₁₀Dy₁₀ were reproduced for femtosecond transient absorption spectroscopy. Whereas (**Fe₁₀Dy₁₀-16**) was crystallised from DMF, (**Fe₁₀Dy₁₀-17**) was crystallised from acetone.

The experiments on the Fe₁₀Ln₁₀ compounds were performed along with measurements on the butterflies within the context of the Master thesis of Julia Weyandt. The aim of this study was to test the new pump probe experiment with white light probing and to investigate the effect of different ellipticities of the Fe₁₀Dy₁₀ solvates. The main reason for using Fe₁₀Ln₁₀ compounds was the possibility to

compare the results to a study performed 10 years ago in which an experiment was performed with a NOPA-NOPA setup. The other $\text{Fe}_{10}\text{Ln}_{10}$ compounds could be compared to. Likewise, as seen for the Fe_2Dy_2 butterflies, the poor signal-to-noise ratio makes interpretation of the data difficult. Nevertheless, it was possible to identify the same three time constants observed 10 years ago.

It was concluded that this experimental setup, although it has the advantage of probing the whole visible light range, is so far not optimised for the characterisation of this type of system.

An $\text{Fe}_8\text{Dy}_{12}$ compound (**$\text{Fe}_8\text{Dy}_{12}$ -18**) which had been previously synthesised within the group but was difficult to reproduce was successfully crystallised in a reasonable yield so that measurements could be carried out on the sample. This system is of interest because it is a variation of the 20 nuclearity theme but with a different Fe^{III} to Ln^{III} ratio compared with the $\text{Fe}_{10}\text{Ln}_{10}$ *i.e.* 2:3 versus 1:1. This improved synthesis was used to extend the range of isostructural $\text{Fe}_8\text{Ln}_{12}$ clusters through variation of the lanthanide ion to Ho^{III} (**$\text{Fe}_8\text{Ho}_{12}$ -19**). The isostructural nature of the compound was verified from the unit cell.

Furthermore, the literature-known compound (**$\text{Fe}_4\text{Tb}_{16}$ -20**) was reproduced and the synthetic procedure adapted to target larger crystals. The compound was characterised using microSQUID measurements in order to verify the position of the inflection point in the magnetisation curve. This was found from the microSQUID measurement to be 1.1 T. The data show a hysteresis loop at temperatures below 1 K and the inflection point could be related to a level crossing between the magnetic ground state and a ferromagnetic excited state. It remains a challenge to adequately describe and understand the reason for this type of magnetic behaviour as well as the nature of the ground state. A reason for this is that theory calculations are currently impossible as a result of the size of the Hilbert space. Therefore, additional magnetic measurements on the Y^{III} version, which effectively deletes the influence of the lanthanide, in addition to using theoretical calculations which reduce the size of the Hilbert space are necessary.

5. Dysprosium Triangles

5.1 Introduction to Dy₃ triangles

The archetypal toroidal Dy₃ published by Powell *et al.* in 2006^[37] [Dy₃(μ₃-OH)₂(*o*-van)₃Cl(H₂O)₅]Cl₃·4H₂O·2MeOH·0.7MeCN uses 2-hydroxy-3-methoxy-benzaldehyde, commonly referred to as *o*-vanillin (in the following abbreviated as *o*-van) as ligand. The Dy^{III} ions form a triangle which is connected by two central (μ₃-OH⁻) groups located above and below the plane of the triangle. Three *o*-van ligands coordinate on each edge of the triangle *via* a bridging phenoxy oxygen and the methoxy and aldehyde oxygens. The coordination sphere of each Dy^{III} is completed by two terminal ligands, one coordinating from below and one from above the triangle plane. There are five neutral terminal water ligands and one charged terminal Cl⁻ ligand. Charge balance is achieved through the presence of three Cl⁻ counterions (see Figure 94).

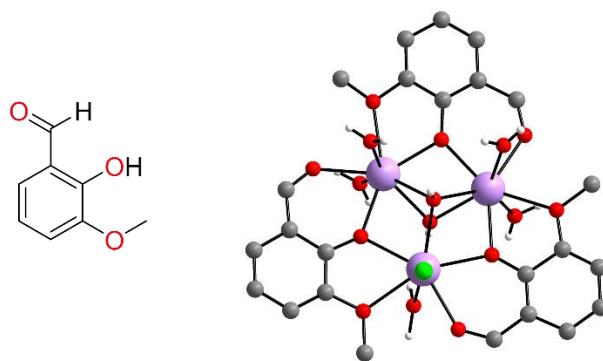


Figure 94. Molecular structure of the *o*-van ligand (left) and the archetypal Dy₃ compound (right).^[37]

Subsequently, research on SMTs has expanded to further triangles^[164] as well as other geometries^[28, 155, 171-172] and compounds incorporating lanthanide ions other than Dy^{III}.^[175, 178] The archetypal Dy₃ motif remains highly relevant for the investigation of the nature of the toroidal ground state. The goal of SMT research is to gain a fundamental understanding of the mechanisms of toroidicity in these molecular motifs. This work aims to modify the Dy₃ motif and find fine-tuning handles which influence the stability of the toroidal ground state in respect to the temperature and the applied magnetic field. A supramolecular approach was chosen to influence the packing of the system to give rise to a desirable symmetry within the Dy₃ system. Ideally to understand a toroidal triangular system it would consist of a single orientation of triangle meaning crystallisation in P1 or P3. This however is chemically challenging.

An initial step in finding a suitable system is targeting crystallisation in space groups based on threefold axes. This can eliminate a fundamental problem of single crystal measurements which are required to characterise toroidal states: different orientations of triangles in the crystal structure complicate the evaluation of the toroidal behaviour of single molecules. Furthermore, imposing threefold symmetry through the centre of the triangle should make measurements along a specific orientation of the triangles possible. This would simplify the model used for theoretical calculations.

To this end, it was necessary to keep the core structure and the $(\mu_3\text{-OH})_2$ bridging mode intact which should allow for the preservation of the toroidal ground state while effects of the ligand could be analysed. To achieve this, a synthetic approach was chosen which preserves the basic *o*-vanillin unit while allowing for the modification of the positions that do not inhibit the formation of the Dy_3 motif. As a proof-of-concept for this approach Tang *et al.* used a Schiff base reaction to modify the *o*-vanillin moiety.^[166] An alternative was described by a former PhD student in the Powell group, Dr. Thomas Ruppert,^[165] who used 2-hydroxy-3-ethoxy-benzaldehyde as the ligand and thus increased the steric hindrance, and more recently, in my Master thesis^[219] where a bromine was added to the 5-position of the *o*-van ligands (see Figure 95). The modifications of the *o*-vanillin type ligand in all of these cases were accompanied by a change in the distribution of charged and neutral terminal ligands as well as the symmetry of the space group in which the compounds crystallised.

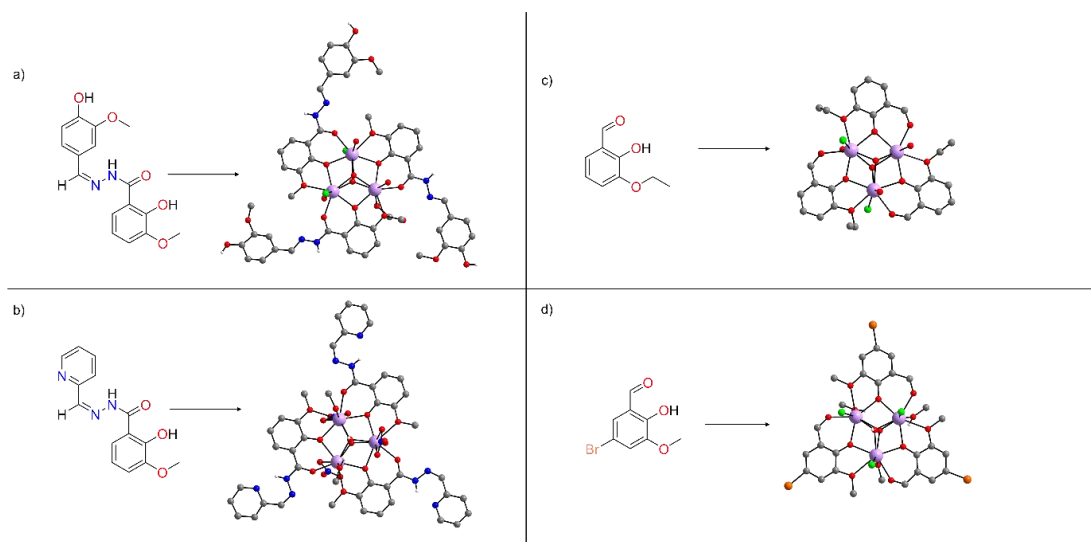


Figure 95. Different ligand modifications and the Dy_3 structure that can be obtained by using them. Dy_3 structures with Schiff base ligands by Tang *et al.* in a)^[166] and b). Dy_3 by Thomas Ruppert in c)^[165] and from my Master thesis in d).^[219]

Figure 96 shows the positions at which the *o*-vanillin ligands can be modified without changing the Dy₃-core structure.

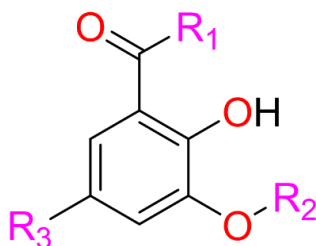


Figure 96. Molecular structure of *o*-vanillin with the modifiable positions highlighted.

Another reason for the design of structures using *o*-vanillin type ligands is the comprehensive magnetic and toroidal characterisation of the archetypal Dy₃ making it ideal for comparative studies. Three types of ligand modifications on two positions on the *o*-vanillin moiety were chosen to be tested.

The first position on the *o*-van unit modified here is the 5-position (R₃) where halogens were introduced to induce the formation of intermolecular halogen interactions. By taking advantage of the directionality of such interactions it should be possible to steer the relative positions of the Dy₃ units in the crystal.

Another possibility is to introduce larger, sterically more demanding residues at the 5-position *via* an azo coupling reaction. These residues could be used to provide aromatic rings which can partake in π - π stacking interactions and influence the packing. Additionally, further oxygen or nitrogen donor groups can be added remote from the Dy₃ core. Since this approach uses aniline derivatives in the azo coupling reaction, a wide range of modifications is possible. By combining both approaches halogens can be introduced on the azo coupled moiety.

The second position modified (R₂) follows the work of Tang *et al.*^[166] using a Schiff base approach in which benzaldehyde derivatives were used to react with the *o*-vanillyl hydrazide. As for the aforementioned approach, where the *o*-vanillin is modified *via* an azo coupling reaction, it is possible to design ligands that include both the *o*-vanillin moiety and groups promoting intermolecular interactions. Such ligands could provide new coordination sites for 3d metal ions or contain functional groups for post-modification or surface attachment. Dy^{III} has been identified the best choice of lanthanide ion for SMTs as a result of its uniaxial magnetic anisotropy and thus the most frequently used lanthanide ion in the synthesis of SMTs. Additionally Dy^{III}

triangles were shown to exhibit ferroelectric bistability.^[164] Nevertheless, it is worthwhile to explore other lanthanide ions for the trinuclear compounds in this work, since they may prove to show different effects. Er^{III} analogues could be investigated for their SMM properties,^[220] Eu^{III} for optical properties,^[221] and Gd^{III} for its magnetocaloric effect (MCE)^[222] while Tb^{III} and Ho^{III} can also potentially show toroidicity.^[175]

5.2 Halogen substituted o-vanillin triangles

By substituting the o-vanillin in the 5-position it is possible to keep the coordinating sites intact which should yield the same coordination geometry and nuclearity as the original Dy₃ with o-vanillin ligands while influencing the balance of intermolecular interactions. For the original Dy₃ those consist mainly of hydrogen bonds. Here the additional halogens on the vanillin ligand promote the formation of additional intermolecular interactions namely halogen bonds. Preliminary results on this topic were obtained during my Master thesis^[219] where [Dy₃(OH)₂(Br-van)₃(Cl)₃(MeOH)₃][Dy₃(OH)₂(Br-van)₃(Cl)₅(MeOH)]·4MeOH (**Dy₃-21**) and [Dy₃(OH)₂(I-van)₃(Cl)₃(MeOH)₂(H₂O)]Cl·3MeOH (**Dy₃-22**) were synthesised. In the same timeframe (**Dy₃-21**) was characterised magnetically whereas for (**Dy₃-22**) no magnetic characterisation was performed since (**Dy₃-22**) could not be obtained as a pure sample. The structures of both compounds are discussed in the following since they were further analysed and compared to other compounds synthesised during the course of this work.

For one of the Dy₃ units in (**Dy₃-21**) the Br-van ligand is twofold disordered (66/33). These two disordered orientations can be interconverted *via* a rotation of 180° effectively swapping positions of the methoxy and aldehyde coordinating arm. The other triangle unit has a 66/33 Cl/MeOH disorder of terminal ligands. The molecular structure of (**Dy₃-21**) and the asymmetric unit which highlights the disorder in the compound are shown in Figure 97, Figure 98 shows the molecular structure of (**Dy₃-22**).

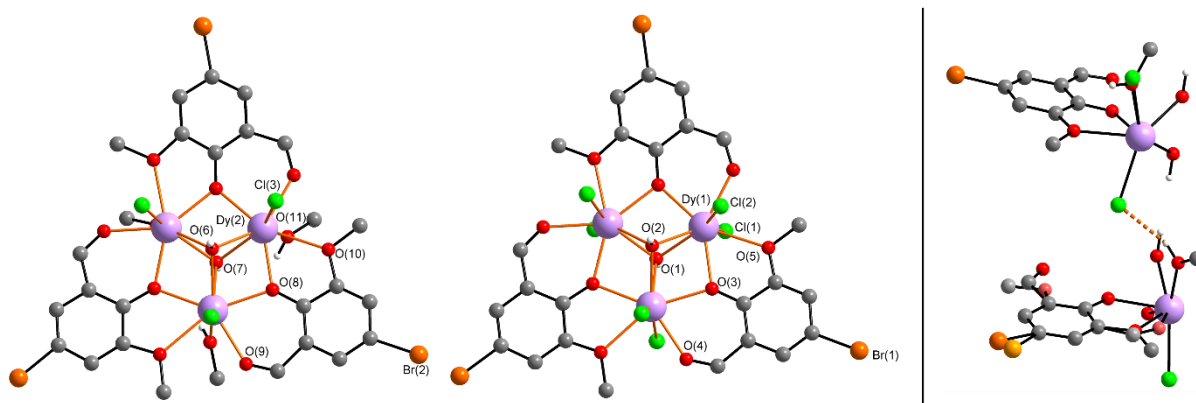


Figure 97. Structure of one formula unit of (**Dy₃-21**) consisting of two triangle moieties (left and middle) where the disorder was omitted for clarity. Asymmetric unit of (**Dy₃-21**) with the disorder indicated by paler coloured atoms and hydrogen bond as orange dotted line.^[219]

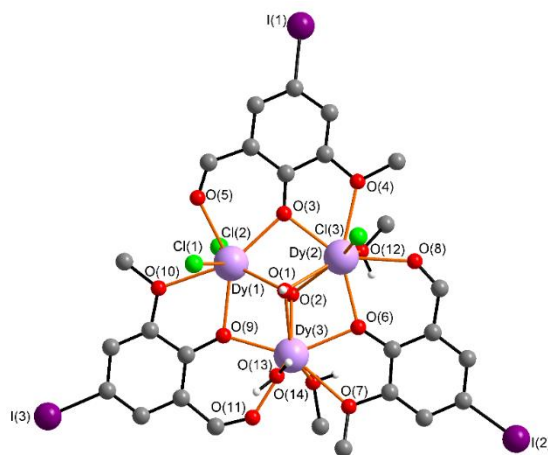


Figure 98. Molecular structure of (**Dy₃-22**).^[219]

These compounds can utilise either the Br- or I-substituted ligand for halogen bonding. There are two disordered R—Br \cdots Cl halogen bonds in (**Dy₃-21**) and three non-disordered R—I \cdots Cl interactions in (**Dy₃-22**). In (**Dy₃-22**) these are, judging by the involved angles and distances, stronger than for (**Dy₃-21**) (see Figure 99). The distance is smaller than the combined van der Waals radii in both cases which indicates the attractive interaction.^[64, 86] The Cl \cdots I bond distance is similar in length compared to the Cl \cdots Br bonds, which, combined with the larger van der Waals radius of iodine, suggests that the halogen bonds in (**Dy₃-22**) are stronger. The bond distances here are 3.398 Å in (**Dy₃-21**) and 3.375 Å in (**Dy₃-22**). The associated bond angles are also closer to the ideal of 180° and 90° for Type II halogen-halogen bonds in (**Dy₃-22**) with 165.944° and 99.510° compared to 154.617° and 110.643° in (**Dy₃-**

21). Theory calculations revealing the different bond strengths are described further in section 5.2.4.

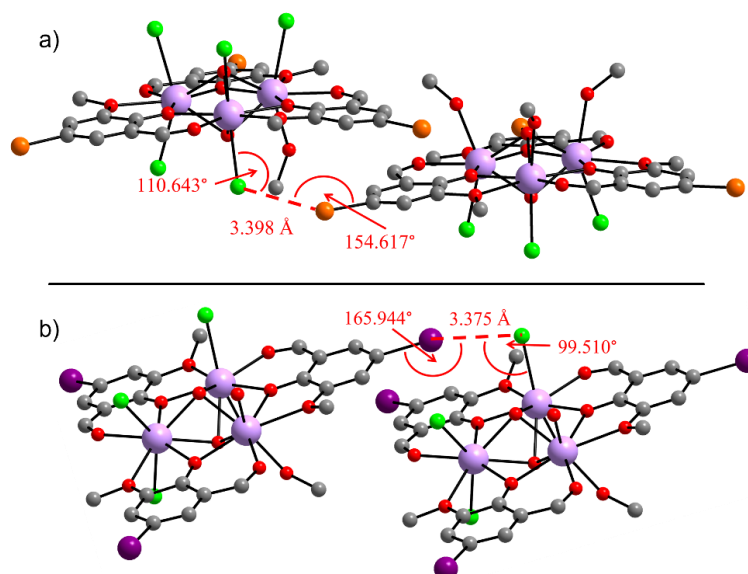


Figure 99. Halogen bonding in (**Dy₃-21**) (a) and in (**Dy₃-22**) (b) with the important angles and distances highlighted (only one example of the halogen bonds is shown here for each molecule).^[219]

This approach of introducing halogen bonds can impose the desired threefold symmetry on the system, since compound (**Dy₃-21**) crystallises in the $R\bar{3}$ space group in contrast to the original triangle which crystallised in the space group $C2/c$.^[37] The packing of (**Dy₃-21**) along the three crystallographic axes is shown in Figure 100. Triangle units are stacked parallelly and turned 60° to each other along the crystallographic c axis which is parallel to the threefold axis. The imposed threefold symmetry does not make this structure easier to analyse because of the two different elements which form the asymmetric unit and alternate in the stacks. Additionally, both triangles have an inversion related counterpart in the structure. This disorder includes the position of the MeOH being threefold disordered across the Dy^{III} ions and the Br⁻ ligands being disordered which makes the whole system rather complex. Nevertheless, the increased symmetry in this compound may serve as a proof-of-concept for the effect halogen bonds can have on the packing.

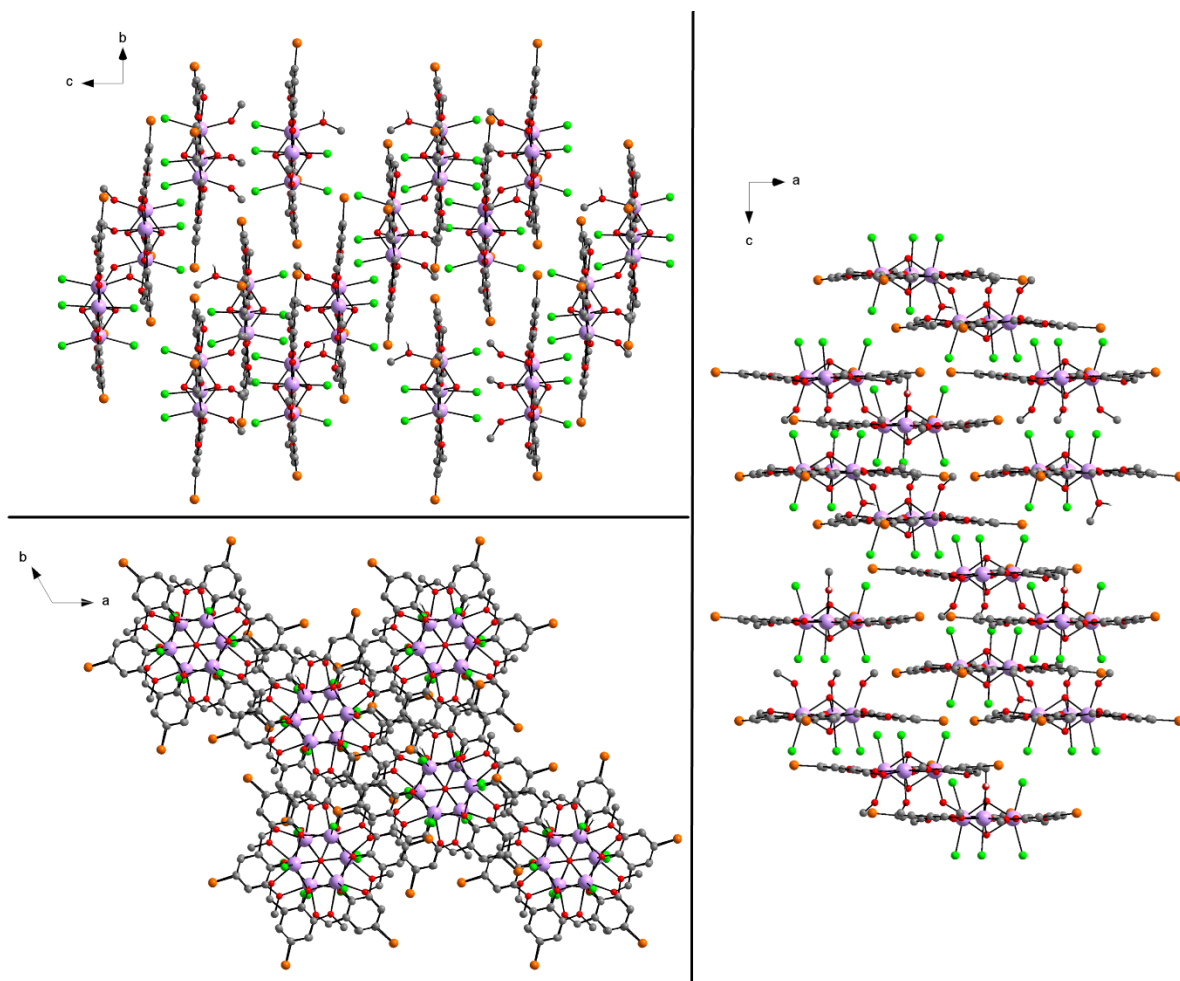


Figure 100. Packing of (**Dy₃-21**) along the crystallographic a (top left), b (right) and c (bottom left) axes.

Compound (**Dy₃-22**) crystallises in the monoclinic space group *Cc* with *Z* = 4. The packing along the three crystallographic axes and one additional orientation highlighting the halogen bond network and the large influence of halogen bonds on the packing is shown in Figure 101.

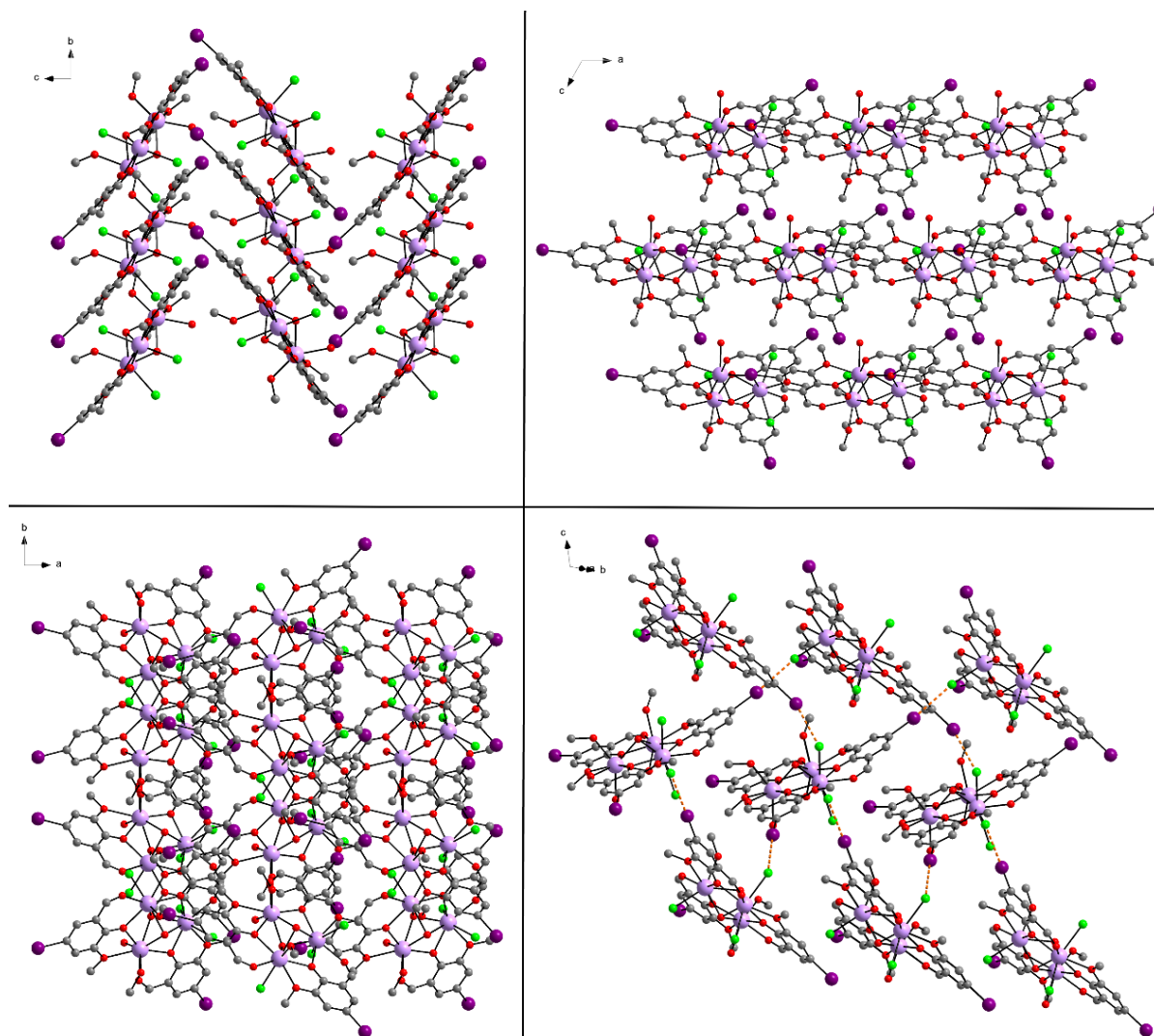


Figure 101. Packing of (**Dy₃-22**) along the crystallographic *a* (top left), *b* (top right) and *c* (bottom left) axes. Additional view of the packing along the crystallographic ***a-b*** vector showing the strong presence of halogen bonds throughout the crystal lattice. Halogen bonds indicated by orange dotted lines.

The objectives at the start of the investigation of this system during the work on this doctoral thesis was the optimisation of the synthetic procedure in order to reliably obtain pure samples. In addition, the goal was to extend the series of compounds by using the Cl-substituted ligand. This would allow for a comparison of the influences of halogen interactions of varying strength on the packing as well as their influence on the targeted toroidal ground state.

5.2.1 Synthesis optimisation and Lanthanide variation

The synthesis optimisation started with the simple synthetic procedure used for (**Dy₃-21**) during the work on my Master thesis^[219] which consists of dissolving the ligand and DyCl₃·6H₂O in a mixture of MeCN and MeOH, adding Et₃N as base and stirring for three hours. This synthesis would either yield aesthetically pleasing brown single crystals or a red-brown amorphous solid which was shown by PXRD measurements to be a side-product. Initially, the method of crystallisation was altered from slow evaporation to ether diffusion to see whether this would favour the crystallisation of the desired product. This resulted in [Dy₃(OH)₂(Brvan)₃(Cl)₄(MeOH)_{0.7}(H₂O)_{1.3}]·3MeOH·0.3H₂O (**Dy₃-23**) a compound which crystallises in the orthorhombic space group Pna2₁ with Z = 4. The molecular structure (Figure 102) shows that the general coordination environment of the Dy^{III} ions is the same as for the other triangles apart from changes in the distribution of the Cl⁻ terminal ligands. The 70:30 disorder between terminal MeOH and H₂O ligands is omitted for clarity in Figure 102.

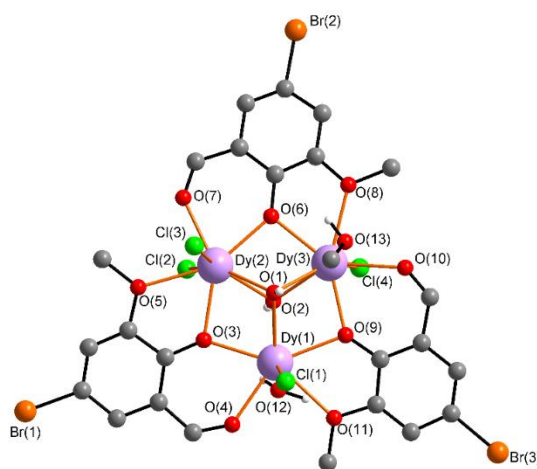


Figure 102. Molecular structure of (**Dy₃-23**).

For compound (**Dy₃-23**) there is no detectable halogen bonding. It was not possible to obtain it in a pure form as revealed by PXRD measurements which showed peaks that must be the result of crystalline impurities. Thus, this type of crystallisation using ether diffusion was pursued further since it did not yield the desired compound (**Dy₃-21**).

Using the same ether diffusion approach with Cl-van and I-van as ligands was however successful in producing the same product as obtained by slow evaporation. This was an additional indication that (**Dy₃-21**) behaves entirely different from a synthetic point

of view. After trying many variations of the ratios between the ligand, solvents and metal salt as well as reaction time and temperature, a solvothermal approach was tested which turned out to be a reliable way of synthesising (**Dy₃-21**) in a high yield with only 24 h of crystallisation time. This new synthetic method is essentially the same as the one described in the beginning of this section, but the reaction solution was put into a glass vial capable of withstanding high temperatures and pressures to allow for crystallisation under solvothermal conditions after stirring. This gave an indication as to why the synthesis of (**Dy₃-21**) stopped working. The determining factor appears to be a change of place where the vials were stored for the crystallisation process and the accompanying change in temperature going from a sunny place near the window in the summer to a dark fume hood in the winter. The new and improved synthetic procedure only worked for Br-van and was subsequently utilised to synthesise a series of isostructural compounds using $\text{LnCl}_3 \cdot 6\text{H}_2\text{O}$ with $\text{Ln}^{\text{III}} = \text{Y}^{\text{III}}, \text{Tb}^{\text{III}}, \text{Ho}^{\text{III}}, \text{Er}^{\text{III}}, \text{Tm}^{\text{III}}$ (**Y₃-24**), (**Tb₃-25**), (**Ho₃-26**), (**Er₃-27**), (**Tm₃-28**)). The compounds were shown to be isostructural from PXRD measurements (see Figure 103). The experimental data agree with the simulation except for (**Tm₃-28**) and (**Tb₃-25**) which show additional peaks.

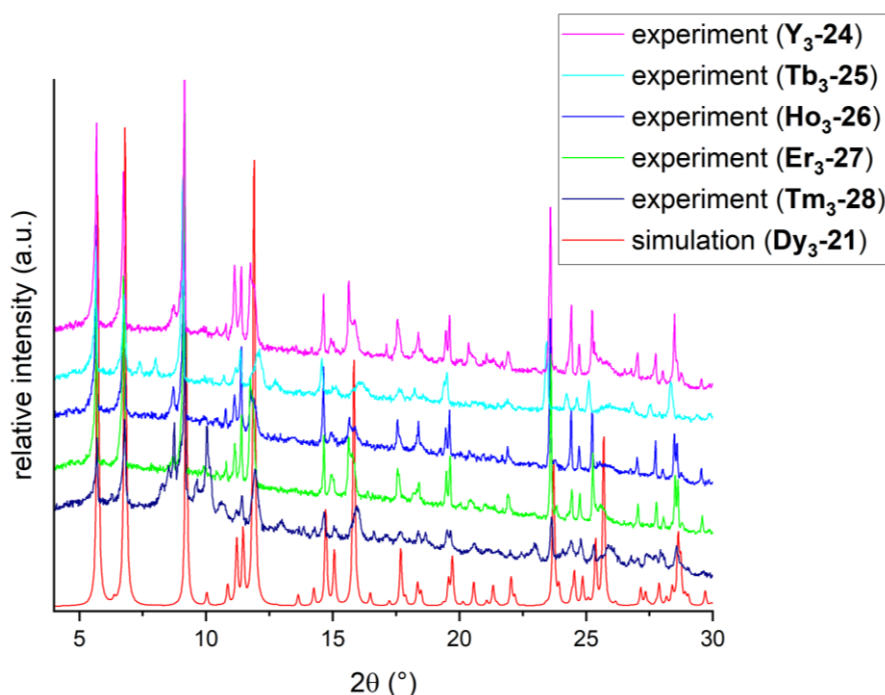


Figure 103. Experimental powder patterns for compounds (**Y₃-24**) to (**Tm₃-28**) compared to simulated pattern for (**Dy₃-21**).

The synthesis for (**Dy₃-22**) using l-van as ligand was optimised by using a higher ratio of lanthanide salt to ligand and yielded a clean product which was analysed using PXRD (see Figure 104) and elemental analysis and was suitable for magnetic characterisation. Additionally, the lanthanide ions were varied using $\text{Ln}^{\text{III}} = \text{Y}^{\text{III}}, \text{Tb}^{\text{III}}, \text{Ho}^{\text{III}}, \text{Er}^{\text{III}}, \text{Tm}^{\text{III}}, \text{Yb}^{\text{III}}, \text{Lu}^{\text{III}}$ which yielded compounds (**Y₃-29**), (**Tb₃-30**), (**Ho₃-31**), (**Er₃-32**), (**Tm₃-33**), (**Yb₃-34**) and (**Lu₃-35**) respectively. The compounds are isostructural to (**Dy₃-22**) and phase pure as shown by the PXRD data in Figure 104.

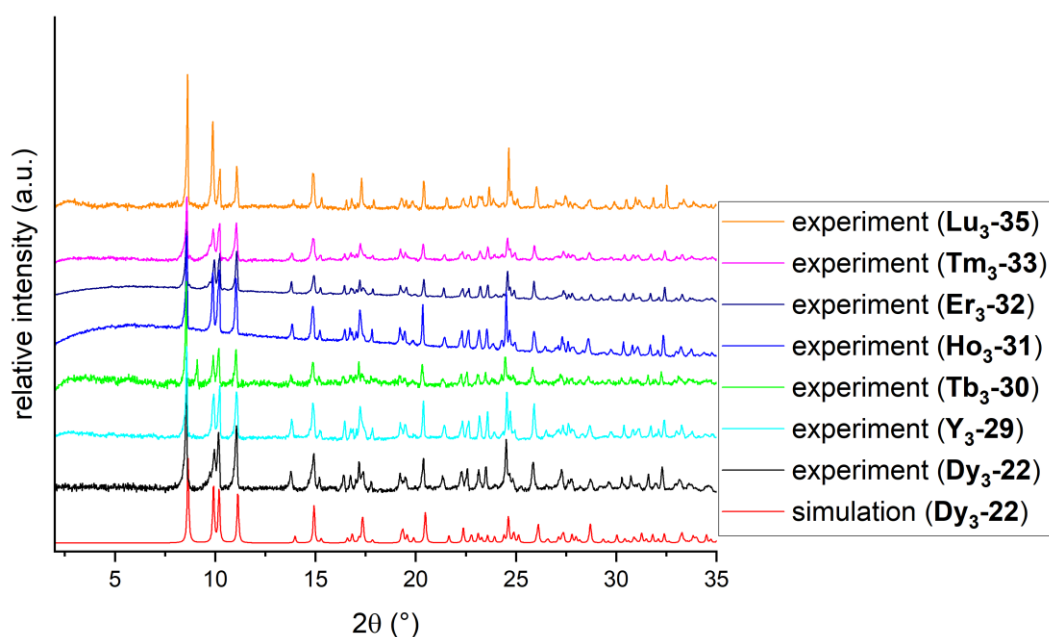


Figure 104. Experimental and simulated powder pattern for (**Dy₃-22**) with experimental powder patterns of compounds (**Y₃-29**) to (**Lu₃-35**).

5.2.2 Variation of the ligand to 5-Chloro-2-hydroxy-3-methoxybenzaldehyde

Using a similar synthetic procedure as for (**Dy₃-22**) but with Cl-van (5-Cl-o-vanillin) and using a different ligand to metal ratio (1:1.5), compound (**Dy₃-36**) with the formula $[\text{Dy}_3(\text{OH})_2(\text{Cl-van})_3(\text{Cl})_3(\text{H}_2\text{O})_{0.5}(\text{MeOH})_{2.5}]\text{Cl} \cdot 2.5\text{MeOH}$ was obtained (Figure 105). (**Dy₃-36**) crystallises in the monoclinic space group $\text{P2}_1/\text{c}$ with $Z = 4$. The coordination environment is preserved since the changes to the ligand do not affect the coordination sites of the vanillin unit. The main differences lie in the terminal chloride and solvent ligands.

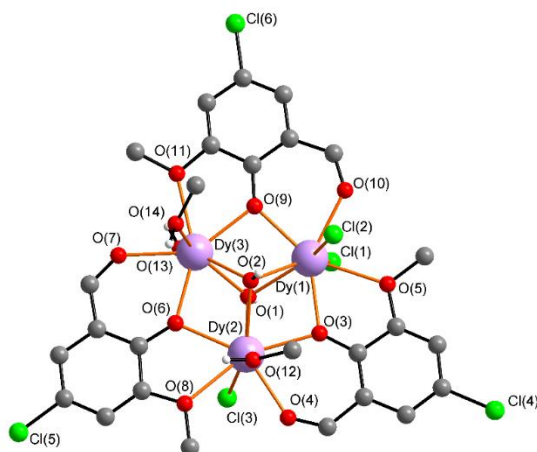


Figure 105. Molecular structure of (**Dy₃-36**), Cl⁻ counterion was omitted.

The packing of (**Dy₃-36**) is comparable to that of (**Dy₃-21**) and (**Dy₃-22**) forming halogen bonds which are shown in Figure 106. As for the other two compounds the halogen bonds are formed between a terminal Cl⁻ (Cl(3)) ligand which serves as the electron density donor and the chlorine atom from a Cl-van ligand (Cl(5)). These are arranged in a geometry favourable to allow for overlap between the σ -hole and the electrondensity of the terminal chloride. The angles are close to the ideal values of 180° and 90° with 172.7(4)° and 89.54(10)°, which is closer to the ideal situation than those for the analogous angles in (**Dy₃-21**). However, the inter-Cl distance of 3.391(4) Å is similar to the Br...Cl distance in (**Dy₃-21**) which, because of to the van der Waals radius of Br being much larger, indicates that this set of halogen bonds in (**Dy₃-36**) is considerably weaker than the ones observed for (**Dy₃-21**). Calculations in section 5.2.4 show that this is actually not the case and the halogen bonds in both compounds are similar in strength.

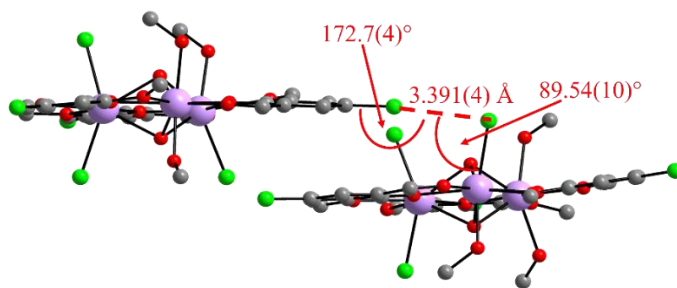


Figure 106. Halogen bonding in (**Dy₃-36**).

The packing is shown along the crystallographic a, b and c axes in Figure 107. The view down the crystallographic c axis shows the effect of the screw axis packing of the triangles.

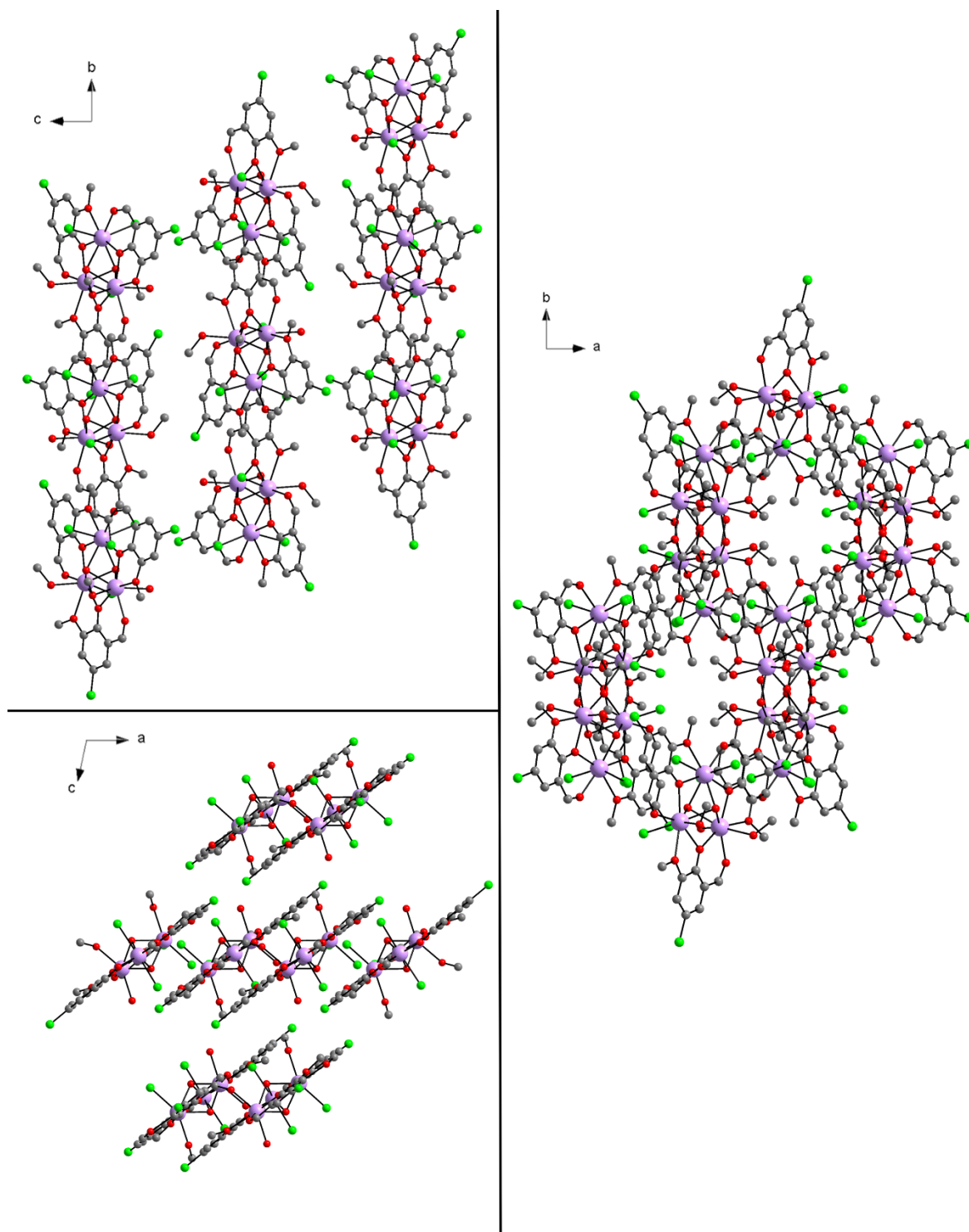


Figure 107. Packing for **(Dy₃-36)** along the crystallographic a (top left), b (bottom left) and c (right) axis.

Using PXRD measurements and elemental analysis the bulk purity of the sample was proven and allowed for the use of additional characterisation techniques such as

magnetic measurements. Varying the lanthanide ions by exchanging $\text{DyCl}_3 \cdot 6\text{H}_2\text{O}$ for $\text{LnCl}_3 \cdot 6\text{H}_2\text{O}$ with $\text{Ln}^{\text{III}} = \text{Ho}^{\text{III}}$ or Er^{III} yielded compounds (**Ho₃-37**) and (**Er₃-38**) which were shown to be isostructural to the Dy^{III} -analogue using PXRD measurements (see Figure 108).

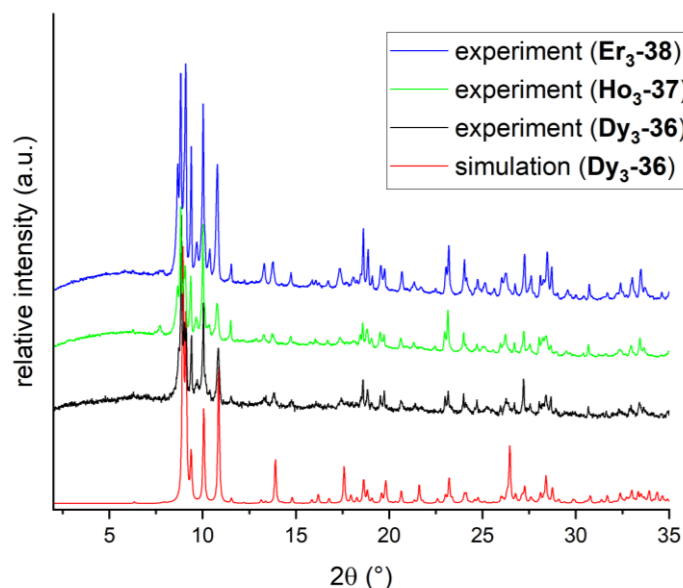


Figure 108. Simulated and experimental powder pattern for (**Dy₃-36**) as well as experimental powder patterns for compounds (**Ho₃-37**) and (**Er₃-38**).

5.2.3 Magnetic properties of halogen substituted Dy_3 triangles

Temperature-dependent DC measurements were conducted on compounds (**Dy₃-36**) and (**Dy₃-22**) which are shown in direct comparison to the data previously obtained for (**Dy₃-21**) (see Figure 109). The theoretical χ_{MT} value for three isolated Dy^{III} ions at room temperature is $42.51 \text{ cm}^3\text{Kmol}^{-1}$ which is slightly higher than the experimentally observed values of $38.9 \text{ cm}^3\text{Kmol}^{-1}$ for (**Dy₃-36**) and $41.0 \text{ cm}^3\text{Kmol}^{-1}$ for (**Dy₃-22**). In the case of (**Dy₃-21**), the molecular structure comprises two independent Dy_3 triangles one positively charged with three terminal Cl^- ligands and one negatively charged with five terminal Cl^- ligands, thus includes six independent Dy^{III} ions. For six Dy^{III} ions, the theoretical χ_{MT} value is $85.02 \text{ cm}^3\text{Kmol}^{-1}$, which is higher than the measured value of $79.2 \text{ cm}^3\text{Kmol}^{-1}$. This discrepancy which amounts to around 7% is consistent with the deviations observed for (**Dy₃-36**) and (**Dy₃-22**) as well as other triangles both

presented here as well as in the literature.^[37, 166] Upon decreasing the temperature, the $\chi_M T$ values for all three compounds remain essentially constant before a rapid decrease below 20 K. This behaviour may be attributed to a combination of m_J sublevel depopulation and antiferromagnetic interactions between the three Dy^{III} ions. A Curie-Weiss fit confirms the presence of antiferromagnetic interactions since it leads to a negative Weiss constant. The parameters determined for all three samples are shown in Table 9. The antiferromagnetic interactions as well as the magnitude and the general trajectory of the DC curve matches what was observed for the original Dy_3 with o-vanillin ligands.

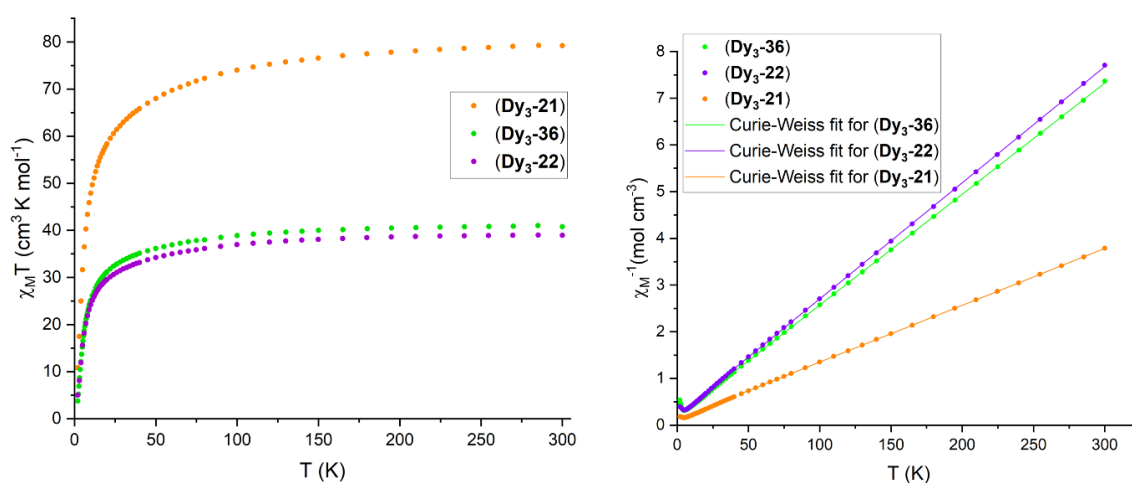


Figure 109. $\chi_M T$ vs T (left) and $1/\chi_M$ vs T with Curie-Weiss fit (right) for (Dy_3-21) , (Dy_3-22) and (Dy_3-36) measured at 0.1 T.

Table 9. C and θ values from the Curie-Weiss fit for compounds (Dy_3-21) , (Dy_3-22) and (Dy_3-36) .

	(Dy_3-21)	(Dy_3-22)	(Dy_3-36)
θ in K	-10.77	-8.67	-8.15
C in $\text{cm}^3 \text{K mol}^{-1}$	82.17	40.20	42.09

AC susceptibility measurements were performed on all compounds under zero applied DC field across in the frequency range 1 to 1500 Hz (see Figure 110). AC signals could be detected between 2 K and 4.8 K for (Dy_3-36) , between 4 K and 8.8 K for (Dy_3-21) and between 4 K and 8.8 K for (Dy_3-22) . The data were fitted using a generalised Debye model. As a result of the weak ac signals with the maxima falling outside the measurement window at higher temperatures, this did not yield sensible values for energy barriers or relaxation times. The overall curve profile varies significantly for all three compounds. None of these are in line with the AC measurements on the archetypal Dy_3 . For the archetypal Dy_3 compound the shape of the out-of-phase data

was described as having a shoulder structure and the intensity increasing with higher temperatures. For the Cl and Br derivatives (**Dy₃-36**) and (**Dy₃-21**) maxima are observed which shift to higher frequencies and lower intensities at higher temperatures. For (**Dy₃-36**), this maximum is barely visible at 2 K, as it is located outside the measurement window. In the case of the I derivative (**Dy₃-22**) the maxima also shift to higher frequencies with increasing temperature, but the fact that the intensity initially increases suggests the population of higher energy states. Overall, the dynamic magnetic behaviour of these compounds appears to be different from what was seen for the archetypal Dy₃ and also differs from the behaviour of the Schiff base triangles described in section 5.4.

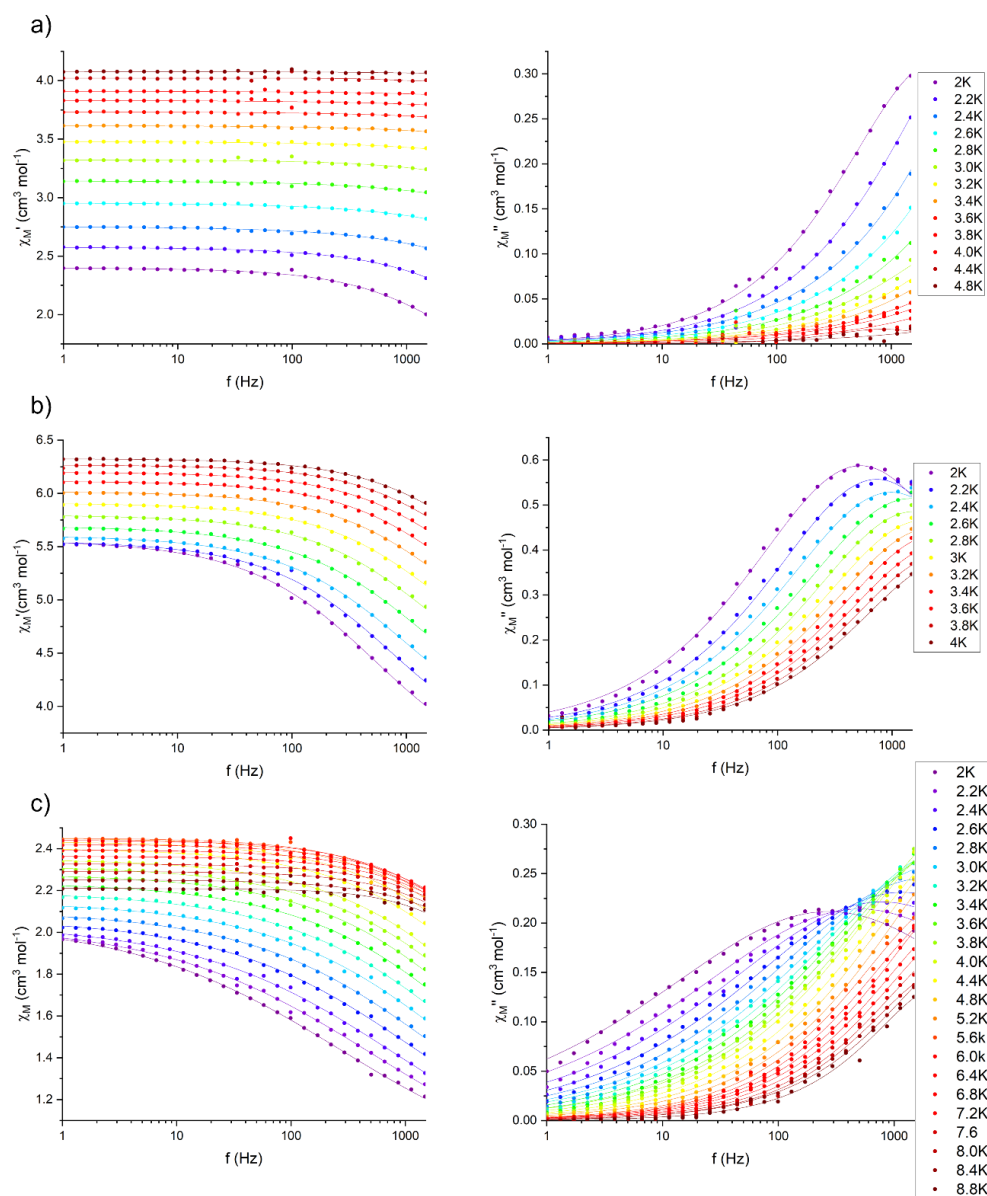


Figure 110. AC in-phase (left) and out-of-phase (right) data for (**Dy₃-36**) in a), (**Dy₃-21**) in b) and (**Dy₃-22**) in c).

Field-dependent DC magnetisation measurements on compounds (**Dy₃-36**), (**Dy₃-22**) and (**Dy₃-21**) (see Figure 111) reveal a steady increase in magnetisation for all three, with inflection points at 0.90 T, 0.93 T, and 0.96 T, respectively. This inflection is characteristic of other toroidal Dy₃ triangles and corresponds to a level crossing where the toroidal non-magnetic ground state crosses with a magnetic excited state. Concerning the switching fields, a trend is observed where the switching field increases from the chlorine to iodine analogues. It should however be noted that the values for the maxima of the first derivatives shown here need to be regarded as estimates since the density of experimental data points does not allow for a more precise determination. The maximum magnetisation values reached at 7 T are 17.00 μ_B for (**Dy₃-36**), 30.8 μ_B for (**Dy₃-21**), and 15.7 μ_B for (**Dy₃-22**), corresponding to 5.67 μ_B , 5.13 μ_B , and 5.23 μ_B per Dy^{III} ion, respectively. These values slightly exceed the expected 5 μ_B per Dy^{III} ion, likely due to the population of low-lying excited magnetic states. This hypothesis is further supported by the observation that magnetic saturation does not occur at 7 T for any of the three compounds.

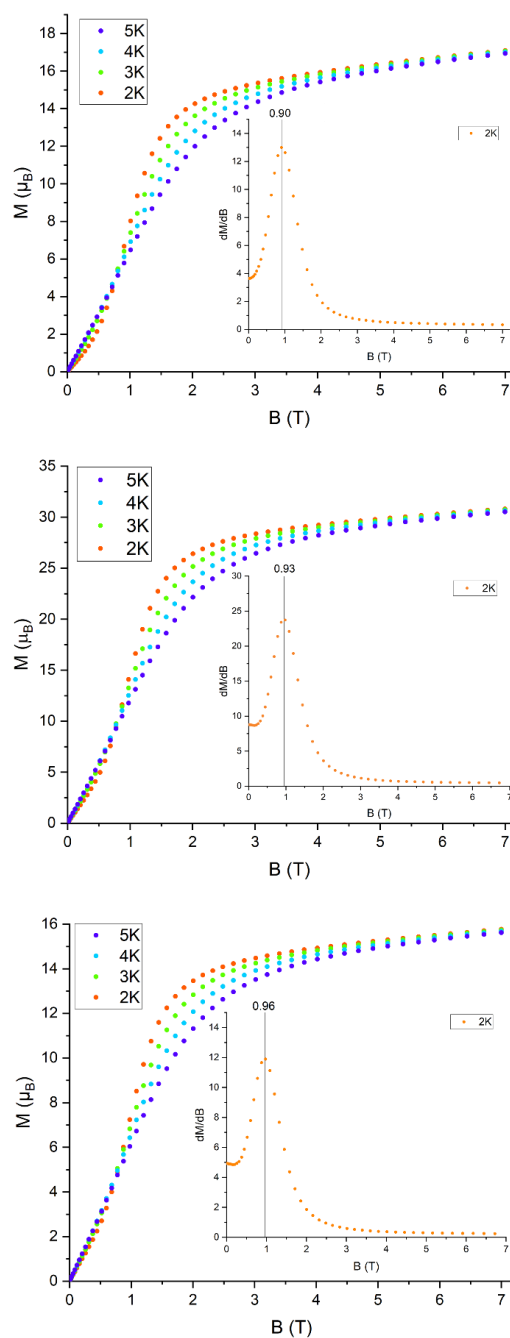


Figure 111. M vs B plots for **(Dy₃-36)** (top), **(Dy₃-21)** (middle) and **(Dy₃-22)** in (bottom) with insets of the first derivative of the magnetisation at 2K with the maxima highlighted.

MicroSQUID measurements were performed on compounds **(Dy₃-36)** and **(Dy₃-22)** and are compared to the data obtained previously for **(Dy₃-21)** (Figure 112). All measurements show a flat region at low fields with a step at zero field to the other flat region which is the largest for **(Dy₃-22)**. A narrow hysteresis with the same general shape can be observed for which the central part increases in size from the Cl- *via*

Br- to I-analogue. The inflection points at which the presumably, non-magnetic (dark) toroidal state stops being energetically favoured, are at 0.78 T for (**Dy₃-36**), 0.84 T for (**Dy₃-21**) and 0.76 T for (**Dy₃-22**). This reflects the angle dependency for single crystal microSQUID measurements compared with the powder magnetisation measurements.

The large step in the middle for all of these compounds suggests that the tunnelling to the toroidal state when sweeping from high fields to lower fields is less efficient than what was observed for the original Dy₃ with *o*-vanillin ligands. In the present case, more triangles appear to remain in a ferromagnetic state resulting in the larger net magnetic moment. It also appears that the increased intermolecular interactions, through halogen bonding, has a significant influence on the relaxation processes and the tunnelling between the antiferromagnetic/toroidal ground state and the ferromagnetic excited states. This has parallels with hydrogen versus halogen bonding for example in spin crossover systems.^[223-224] Furthermore, these are the first examples of halogen bonding connecting the archetypal toroidal Dy₃ triangle leading to a modification of the hysteretic processes.

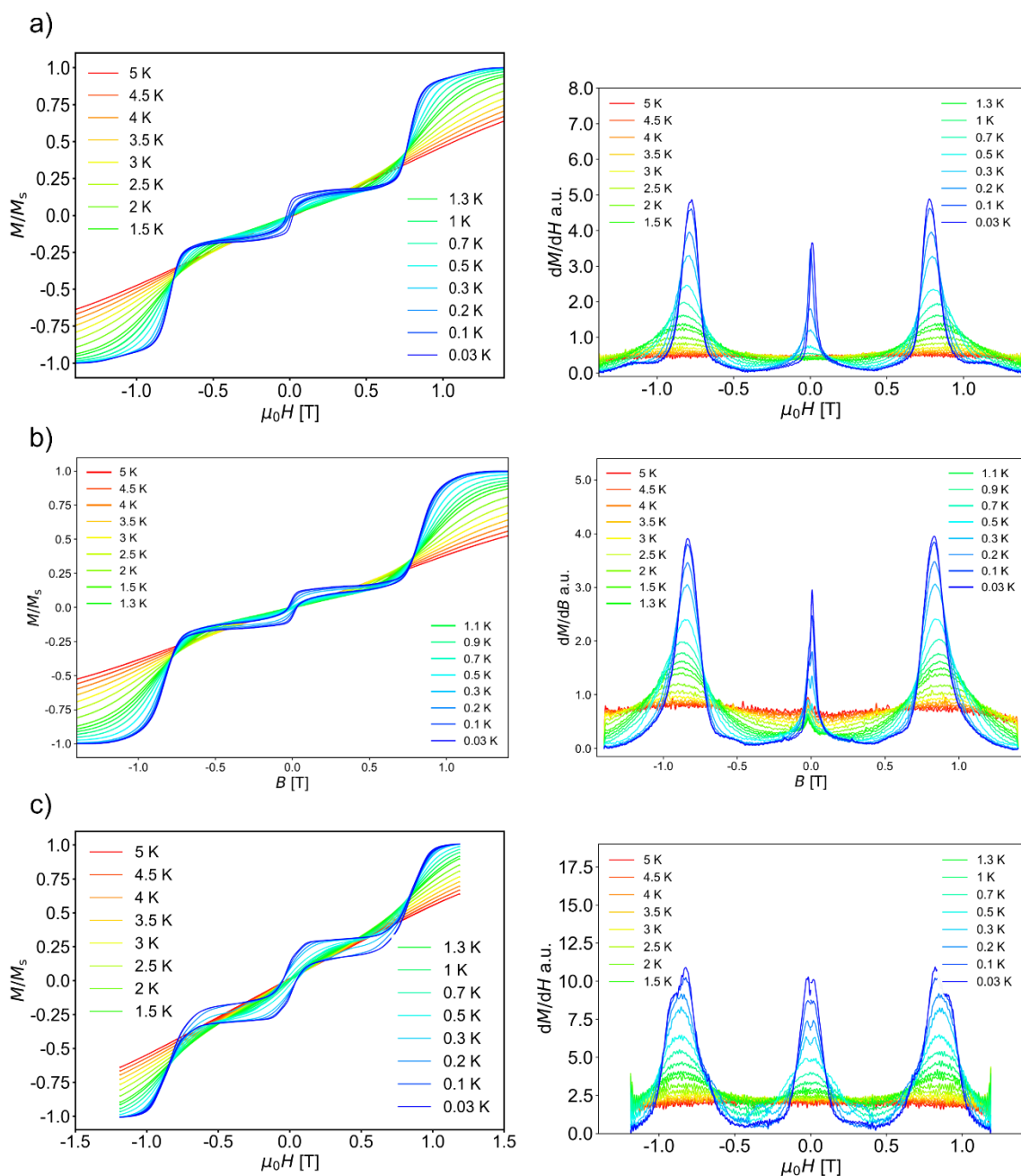


Figure 112. MicroSQUID measurements at varying temperatures at a sweep rate of 8 mT/s (left) and first derivative (right) for (**Dy₃-36**) in a), (**Dy₃-21**) in b) and (**Dy₃-22**) in c).

Another open question concerns the relative orientations of the Dy^{III} magnetic moments and thus the nature of the potentially toroidal ground state. To answer this, calculations or additional experiments are necessary. Figure 113 shows the MAGELLAN^[202] analysis for (**Dy₃-36**), (**Dy₃-22**) and both triangle units of (**Dy₃-21**). In most cases one of the spins is oriented perpendicular to the plane indicating that the terminal ligand distribution, and in particular the negatively charged chloride ligands, play a significant role in providing the orientation of the anisotropy axes. This model

also suggests that in (**Dy₃-21**) the triangle with three Cl⁻ terminal ligands has an in-plane arrangement of spins suggesting a toroidal ground state while the other triangle has one anisotropy axes in the plane of the triangle whereas the other two anisotropy axes are perpendicular to the plane of the triangle.

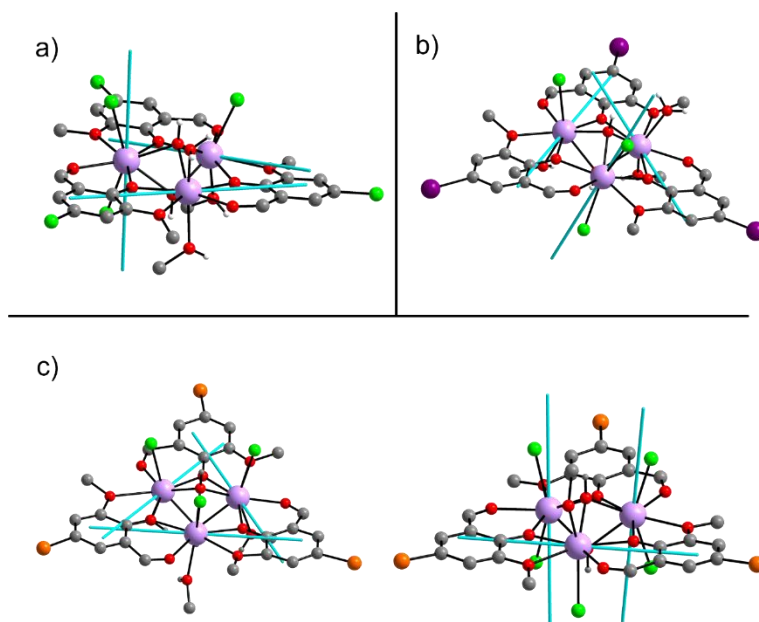


Figure 113. MAGELLAN^[202] analysis of (**Dy₃-36**) in a), (**Dy₃-22**) in b) and (**Dy₃-21**) in c).

Since MAGELLAN^[202] is a purely electrostatic model and only uses charges from the analysed molecule itself and not from additional counterions in the lattice or close by neighbouring molecules, it might not be suitable to adequately describe the situation in the presented molecules. Additional calculations, including producing the Zeeman diagrams for the various states, are necessary in order to gain more insights into the microSQUID data.

Furthermore, sweep rate dependent microSQUID measurements show that measuring at faster sweep rates results in a wider hysteresis loop (see Figure 114). For all three triangles it can be observed that the bottom part of the hysteresis between 0 T and around 0.8 T as well as the top part between 0 T and -0.8 T shift more towards 0 M/Ms when measuring at faster sweep rates which leads to wider open hysteresis.

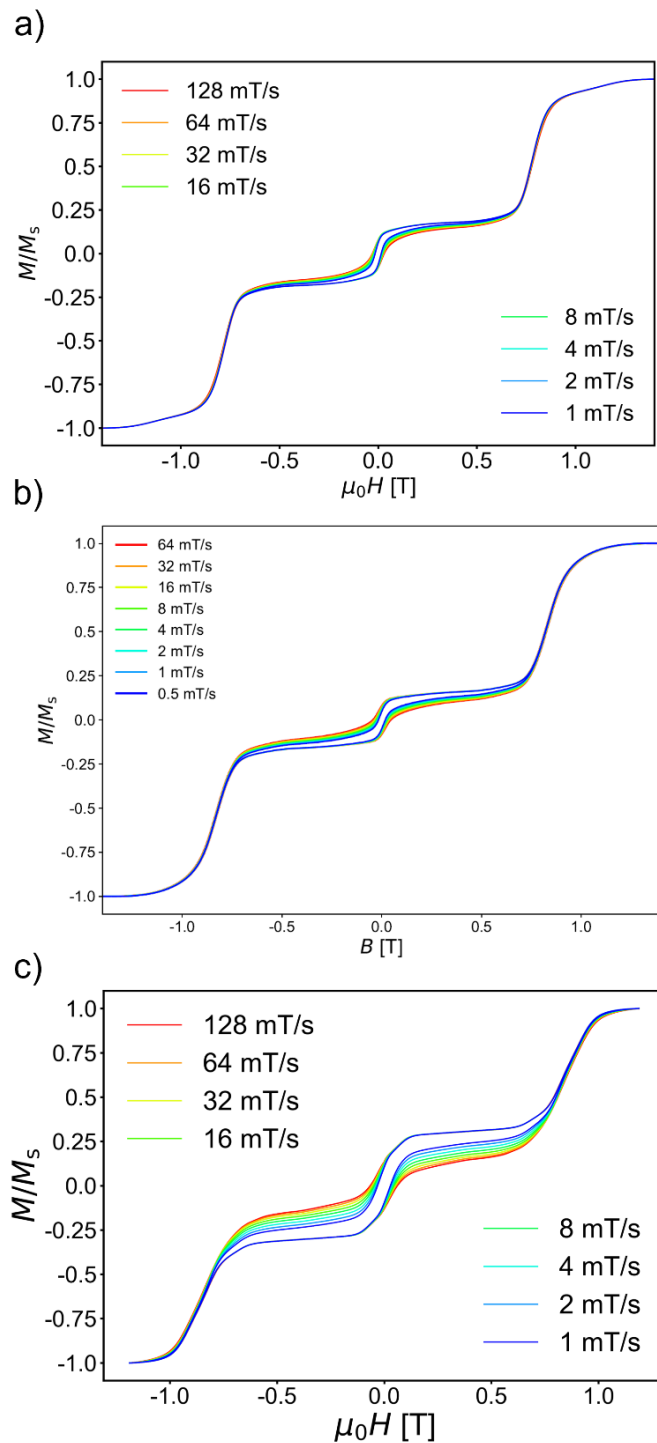


Figure 114. Sweep rate dependent microSQUID measurements at 30 mK for (**Dy₃-36**) in a), (**Dy₃-21**) in b) and (**Dy₃-22**) in c).

As performed for the archetypal Dy_3 and (**Dy₃-49**) in section 5.4.1.1, additional angle-dependent measurements should be conducted to give experimental insights into the orientation of the anisotropy axes for these three compounds. This would be especially interesting for (**Dy₃-21**) since the $R\bar{3}$ packing would allow for an alignment of the

magnetic field with the threefold axis which is the crystallographic *c* axis. Axes tilted out of the molecular plane (perpendicular to the C_3 axis) would result in a larger net magnetic moment in the *c* direction and thus a larger splitting between the two ground states. These can still be considered toroidal (clockwise/counter-clockwise arranged spins) albeit with a canted arrangement.

5.2.4 Calculations and outlook

Calculations on the three Dy_3 complexes (**Dy₃-21**), (**Dy₃-22**) and (**Dy₃-36**) with Br-van, I-van and Cl-van, respectively, were performed in collaboration with Christian Pachl in a joint project between the Powell group and the working group of Prof. Dr. Karin Fink. Firstly, an electron localization function (ELF) was used to map the probability of electron localisation in the three analysed systems (see Figure 115).^[89] Figure 115 shows that for (**Dy₃-21**), (**Dy₃-22**) and (**Dy₃-36**) their one, two and three respective halogen bonds are Lewis-acid-base interactions with free Cl^- electrons donating into the sigma hole on the halogen bound to the *o*-vanillin moiety. This suggests a bonding character of the interaction rather than just being a close contact.

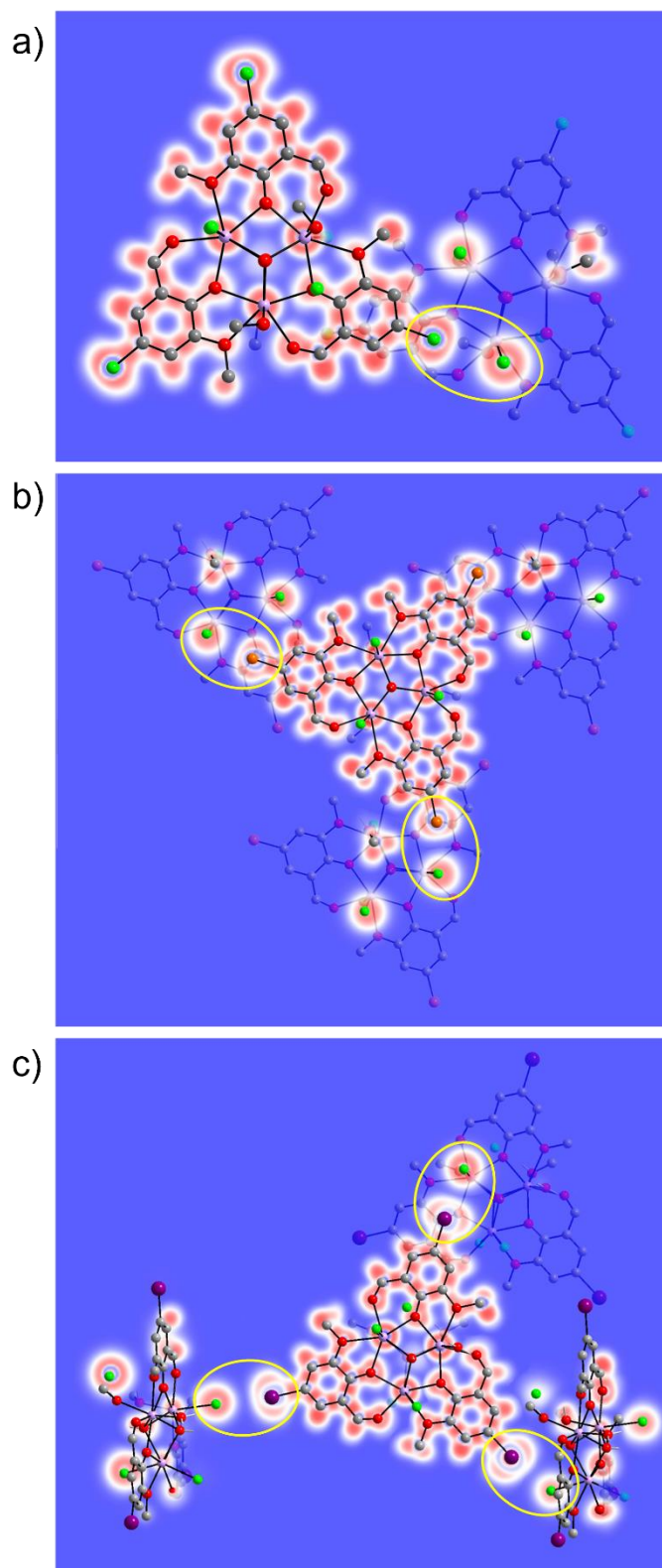


Figure 115. Electron localization function mapped on a molecule of (**Dy₃-36**) (Cl) a), (**Dy₃-21**) (Br) b) and (**Dy₃-22**) (I) c) with their halogen bonding counterparts highlighted by yellow circles. The red areas suggest localized electrons, whereas white is delocalised (free electron gas) and blue an electron localisation probability of zero. The images shown above were modified from the original calculated results for better visual representation focusing on the electron density around the halogen bonds.

In order to perform DFT calculations to investigate the halogen bonds in more detail, a model system was chosen which is shown in Figure 116. Several variations of this model were tested with the one presented here leading to the most convincing results. The model uses the non-hydrogen positions of the halogen substituted *o*-van ligands from the cif file with the Na position fixed and the resulting re-optimised H positions.

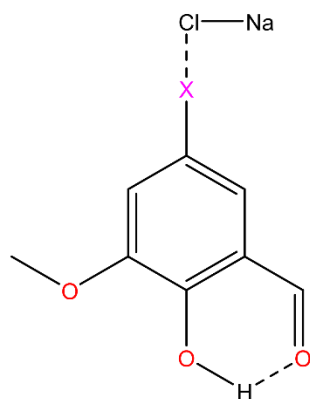


Figure 116. Model for halogen bond calculations. The position of the Na is fixed.

The halogen bond angles, distances and calculated energies are shown in table 10. These were obtained using TURBOMOLE^[225-226] and PBE0-d4/def2-QZVP where PBE0 is a hybrid functional, d4 is a dispersion model proposed by Grimme^[227] and def2-QZVP being the basis set used.^[228]

Table 10. Angles and distances of halogen bonds in (**Dy₃-36**), (**Dy₃-21**) and (**Dy₃-22**) with the respective calculated energies.

	(Dy₃-36)	(Dy₃-21)	(Dy ₃ -22)		
Sum of vdW radii ^[86]	3.50	3.58	3.73		
X...Cl (Å)	3.39	3.40	3.38	3.42	3.49
C-X-Cl (°)	172.7	154.6	165.8	162.8	173.1
Interaction energy (kJ mol ⁻¹)	-9.9	-9.0	-24.4	-19.8	-18.8

As Br has a much larger van der Waals radius the logical assumption would be that this bond should be considerably stronger than the Cl-Cl bond given that the distance is essentially the same. To provide additional insight into the attractive interactions and possibly to explain why the halogen bonds in (**Dy₃-21**) and (**Dy₃-36**) appear to be of similar strength, an energy decomposition analysis (EDA) was performed (see Figure 117). The contributions to the total energy which were considered and calculated are electrostatic interactions, exchange-repulsion, orbital relaxation, correlation interaction

and dispersion. The EDA indicates that, the perhaps unexpected similar strength of the halogen bonds in (**Dy₃-21**) and (**Dy₃-36**), results from exchange repulsion. This is more pronounced for (**Dy₃-21**) since the bond angle which contributes to a larger overlap of electron density compensates the stronger attractive interactions. For (**Dy₃-22**) the three halogen bonds show significant differences in their respective composition which might be a result of the functional used, since when using for example M06-2X the calculations result in closer energies.

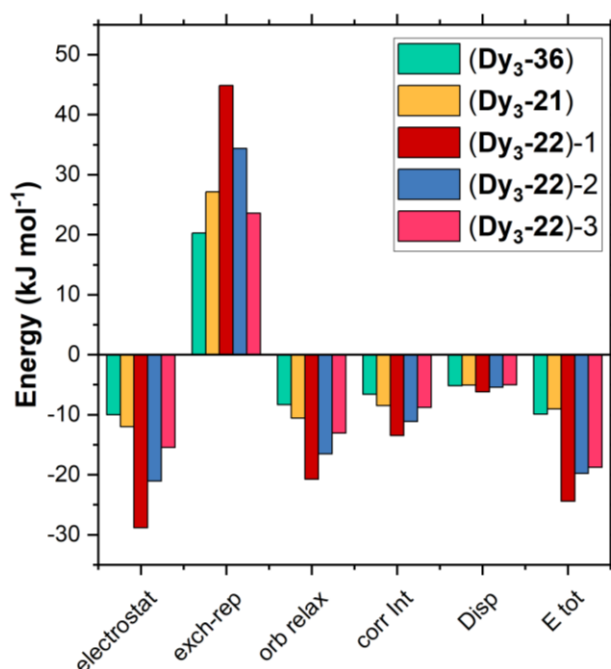


Figure 117. Energy decomposition analysis for (**Dy₃-36**), (**Dy₃-21**) and (**Dy₃-22**). Negative energies correspond to attractive contributions and positive energies refer to repulsion, demonstrating the fine balance between attractive and repulsive forces in the Br-analogue.

In order to investigate the magnetic interactions, CASOCI calculations^[229] were performed on (**Dy₃-21**) to get information on the orientation of the anisotropy axes and the toroidal character of the systems. As mentioned before, MAGELLAN^[202] analysis of the triangle with three Cl⁻ counterions shows an in-plane vortex like arrangement of spins like what would be expected for a toroidal system. Figure 118 shows both the MAGELLAN axes and the axes that resulted from the CASOCI calculations of this triangle unit, which show an in-plane arrangement. To further improve on this approach CASOCI and MAGELLAN^[202] were then performed with additional Cl⁻ ligands of neighbouring Dy₃ clusters included in the model. As can be clearly seen for both the MAGELLAN and CASOCI axes these are now out of the plane of the triangle. Although both MAGELLAN^[202] and CASOCI calculations suggest an out-of-plane orientation,

the relative direction of the axes is different. The reason for this appears to be the purely electrostatic approach MAGELLAN^[202] uses in combination with the available information. In the MAGELLAN case the axis is pointed more towards the chlorides because those were assigned a charge of -1 whereas the MeOH oxygen has a charge of 0. For CASOCI calculations the lone pair on the MeOH oxygen is taken into account which leads to this axis following a different direction that lines up with the MeOH ligand.

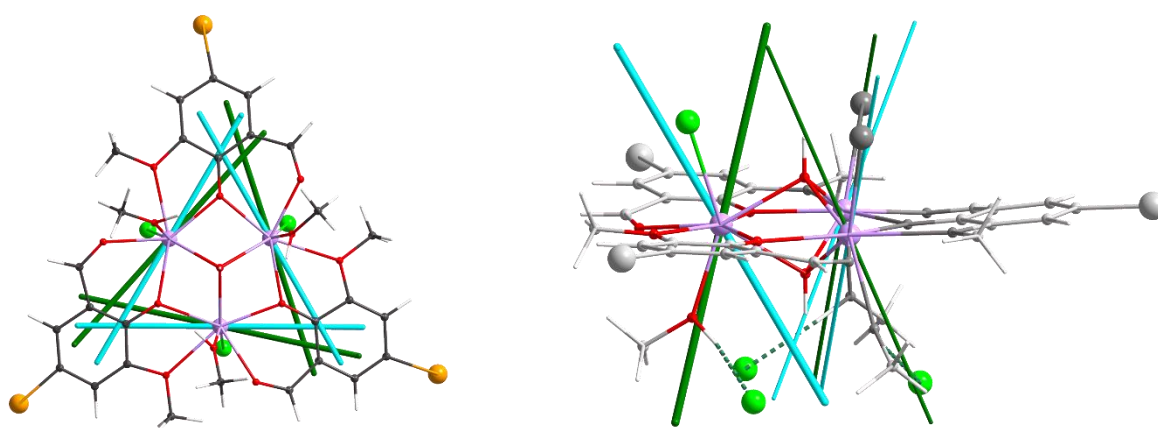


Figure 118. MAGELLAN^[202] (cyan) and CASOCI (green) results for (**Dy₃-21**) of an isolated triangle (left) and with Cl⁻ ions in proximity taken into account (right). Some molecular components discoloured.

The strong influence of the second sphere effect on the orientation of anisotropy axes and as a result the toroidal character of the compound is evidence that the toroidal nature of the Dy₃ compounds is rather sensitive to charge distribution outside the triangle plane. This particularly highlights the importance of including counterions and charged ligands on neighbouring molecules for the analyses. It furthermore emphasises the importance of the charged terminal ligands and their distribution in such triangular Dy₃ clusters.

This can be highlighted from the the Dy₆ linked double triangle system of Tang *et al.* where the exchange of charged SCN⁻ or NO₃⁻ terminal ligands to the neutral H₂O ligand resulted in tipping the anisotropy axes and thus creating a toroidal system from a non-toroidal isomorphous complex.^[172, 180] In other words, exchanging the charged terminal ligands is a potential tool to fine-tune the toroidal character of such systems. Similarly, steering and designing the crystal packing is a way to influence the magnetic behaviour since charges in close proximity apparently an important role as shown from the theory calculations performed here.

The effect of the additional Cl^- ions on the energies of the Kramer's doublets as well as on the g -values has also been investigated and the results are shown in Figure 119. Allowing for the effect of Cl^- in the calculations increases the splitting to the first excited Kramers' doublet considerably from 48 cm^{-1} in the isolated triangle to 90 cm^{-1} thus essentially doubling the energy difference. The g -values also change indicating that the presence of the additional Cl^- suppresses most transversal components through the effects of the additional ligand field.

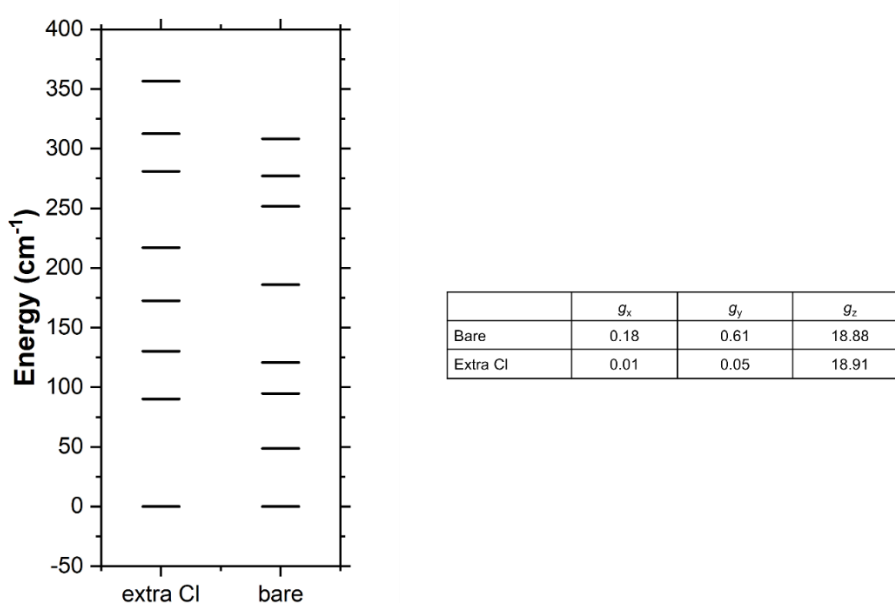
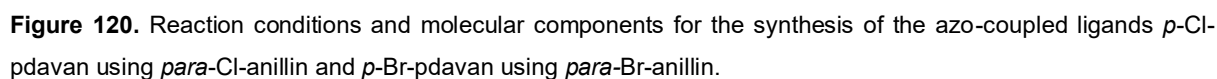


Figure 119. Zero field splitting and g tensors for the ground state of (**Dy₃-21**) with the extra Cl^- ligand from neighbouring molecules considered and without (bare).

5.3 Dy₃ triangles based on azo-coupled ligands: Azo-triangles

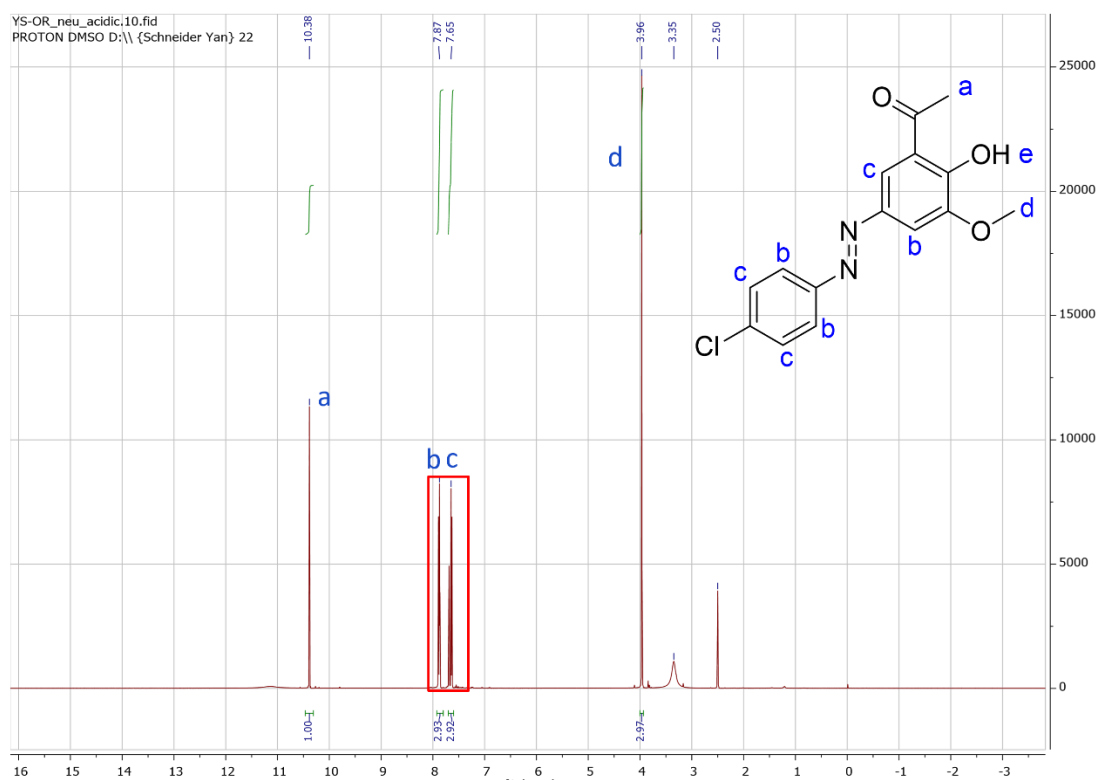
The trinuclear lanthanide complexes here referred to as azo-triangles use a ligand which is synthesised *via* an azo coupling reaction using an anillin derivative and *o*-vanillin. Although the general procedure to access this type of azo-coupled compound is literature-known^[230] their use in coordination chemistry is novel. To date, no structure of any transition metal or f-metal complexes with a ligand of this type has been deposited in the Cambridge Crystallographic Data Centre (CCDC). This ligand modification, or the choice of ligand system in general, is based on the principle of

This approach allows for the exploration of a novel and easily modifiable class of ligands in terms of their suitability to produce new classes of SMTs. The coupling reaction as well as reaction conditions are schematically shown in Figure 120.



The use of base is dictated by the amount necessary to dissolve *o*-vanillin in water which requires deprotonation to a pH level of 9. The reaction is very sensitive and using too much base can lead to it yielding what is presumed to be the sodium salt of the deprotonated ligand. The different amounts of base used are also reflected in the NMR spectra of the compounds as shown in Figure 121. The peaks between 8 ppm and 7 ppm should overlap in a way that leads to two peaks with integrals of 3. For example a different batch where too much base was added has these peaks shifted (see Figure 121 bottom) forming three distinct multiplets.

a)



b)

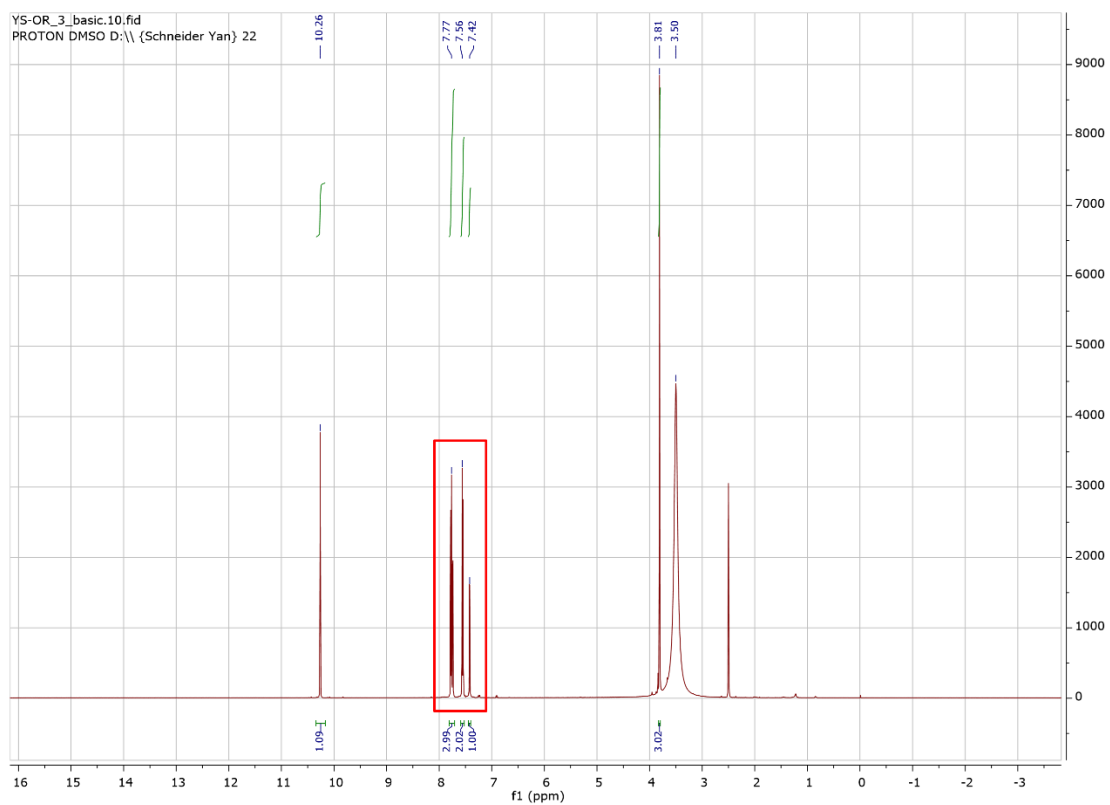


Figure 121. a) ^1H -NMR of *p*-Cl-pdavan with H atoms labelled in the molecular structure; b) ^1H -NMR spectrum of *p*-Cl-pdavan when too much base is added during the synthesis, shifting into three distinct multiplets highlighted.

The amount of base added is a critical point since the deprotonated form of the ligand never yielded any coordination compounds in reactions with Ln^{III} ions and only resulted in high purity NaNO_3 crystals. A procedure which involves dissolving the ligand in MeOH and treating it with concentrated HCl followed by evaporation of the solvent and washing the resulting solid with water converts the deprotonated form of the ligand to the targeted protonated state which can then be used for the reactions with lanthanides.

5.3.1 Dy_3 triangles using *p*-Cl-pdavan (**Dy₃-39**) and *p*-Br-pdavan (**Dy₃-40**)

Using *p*-Cl-pdavan and *p*-Br-pdavan, respectively, the Dy_3 complexes $[\text{Dy}_3(\mu_3\text{-OH})_2(\textit{p}\text{-Cl-pdavan})_3(\text{NO}_3)_3(\text{H}_2\text{O})_3]_3[\text{Dy}_3(\mu_3\text{-OH})_2(\textit{p}\text{-Cl-pdavan})_3(\text{NO}_3)_4(\text{H}_2\text{O})_2](\text{NO}_3)_3 \cdot 2(\text{H}_2\text{O}) \cdot 19(\text{MeCN})$ (**Dy₃-39**) and $[\text{Dy}_3(\mu_3\text{-OH})_2(\textit{p}\text{-Br-pdavan})_3(\text{NO}_3)_3(\text{H}_2\text{O})_3](\text{NO}_3)_3 \cdot (\text{H}_2\text{O}) \cdot 3(\text{MeCN})$ (**Dy₃-40**) were obtained. In both reactions $\text{Dy}(\text{NO}_3)_3 \cdot 6\text{H}_2\text{O}$ is added as the lanthanide salt rather than for example $\text{DyCl}_3 \cdot 6\text{H}_2\text{O}$ which was used to obtain most of the other triangle clusters in this work. For the synthesis of (**Dy₃-39**) and (**Dy₃-40**) the lanthanide salt and ligand are dissolved in a mixture of MeOH/MeCN and stirred for 5 min after which Et_3N is added. The resulting suspension was stirred for further 4 hours after which it was filtered and sealed to allow for crystallisation of the product. Changing the ratio of solvents has a significant impact on the speed of crystallisation as well as the quality of the crystals. In general, it was difficult to obtain crystals suitable for single crystal XRD since the bright orange crystals tend to form agglomerates. However, some very small single crystals could be isolated and used for SCXRD.

It was thus possible to isolate crystals of sufficient quality for SCXRD measurements. Both compounds crystallise in the triclinic space group $P\bar{1}$ with $Z = 1$ for (**Dy₃-39**) and $Z = 4$ for (**Dy₃-40**) and the molecular structures are shown in Figure 122 where for (**Dy₃-39**) all but one triangle were omitted for clarity. The two compounds are isomorphous and crystallise with four Dy_3 moieties in the unit cell which for (**Dy₃-39**) is one molecular unit with the formula $[\text{Dy}_3(\textit{p}\text{-Cl-pdavan})_3(\text{NO}_3)_3(\text{H}_2\text{O})_3]_3[\text{Dy}_3(\textit{p}\text{-Cl-pdavan})_3(\text{NO}_3)_4(\text{H}_2\text{O})_2](\text{NO}_3)_3 \cdot 2(\text{H}_2\text{O}) \cdot 19(\text{MeCN})$.

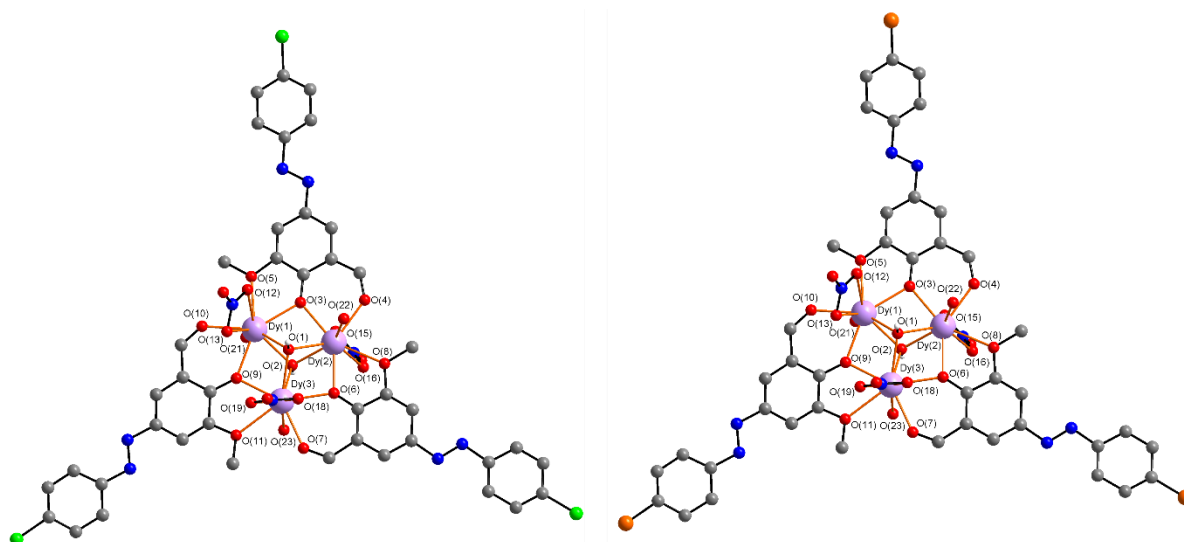


Figure 122. Molecular structure of (**Dy₃-39**) (left) and (**Dy₃-40**) (right). Hydrogen atoms were omitted for clarity.

The pdavan-type ligands coordinate to the Dy^{III} ions *via* the three oxygens from the *o*-vanillin moiety. The overall shape of molecule corresponds to a propeller shape defined by the azo ligands with the difference in the coordination sphere of the Dy^{III} being defined by the number of terminal NO₃⁻/H₂O ligands. Two of the four triangles in the compound have three terminal nitrates, two of which are on one side of the triangles and the other on the opposite side. The terminal coordination site on the opposite side of a nitrate ligand is always occupied by a water ligand. For the other inversion related pair, a unidentate nitrate is very close to the corresponding nitrate on the other molecule. This leads to a disorder where only one of them has a nitrate across this inversion centre whereas the other has a water molecule (see Figure 123).

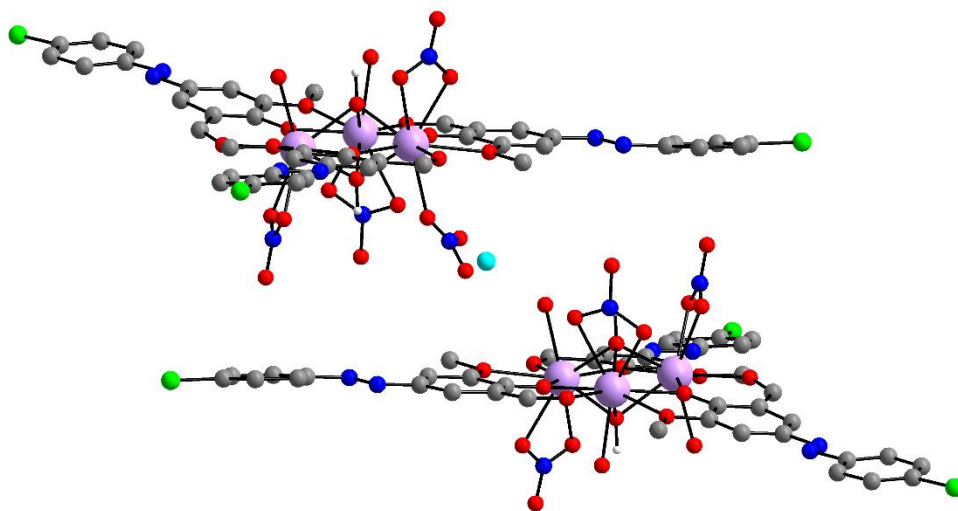


Figure 123. The other two inversion related triangles in (**Dy₃-39**) with unidentate nitrate ligand/water ligand disorder through inversion centre (cyan dot). The disorder was omitted for clarity.

Summarising, there are in total three triangles with three nitrates and one triangle with four nitrates for which one face of the triangle has two bidentate and one unidentate nitrate group. The charge balance is provided by the negative charge of each pdavan-type ligand, the $\mu_3\text{-OH}^-$ groups, the three times three nitrate ligands and one time four nitrate ligands. The further negative charges arise from three nitrates in the lattice which function as counterions. This complicated inversion disorder is not present in (**Dy₃-40**) where just one type of triangle and its inversion related counterpart, which have three bidentate NO_3^- terminal ligands, are found in the structure.

Since the compounds are isomorphous, the packing is only shown for (**Dy₃-39**) in Figure 124 along the three crystallographic axes. A fourth additional view of the packing is shown in Figure 125 which highlights the layered structure throughout the crystal. The distance between the Dy^{III} ions of one triangle and a mean plane through the Dy^{III} ions in the next triangle in the same layer are 2.666(5) Å and 2.8137(5) Å.

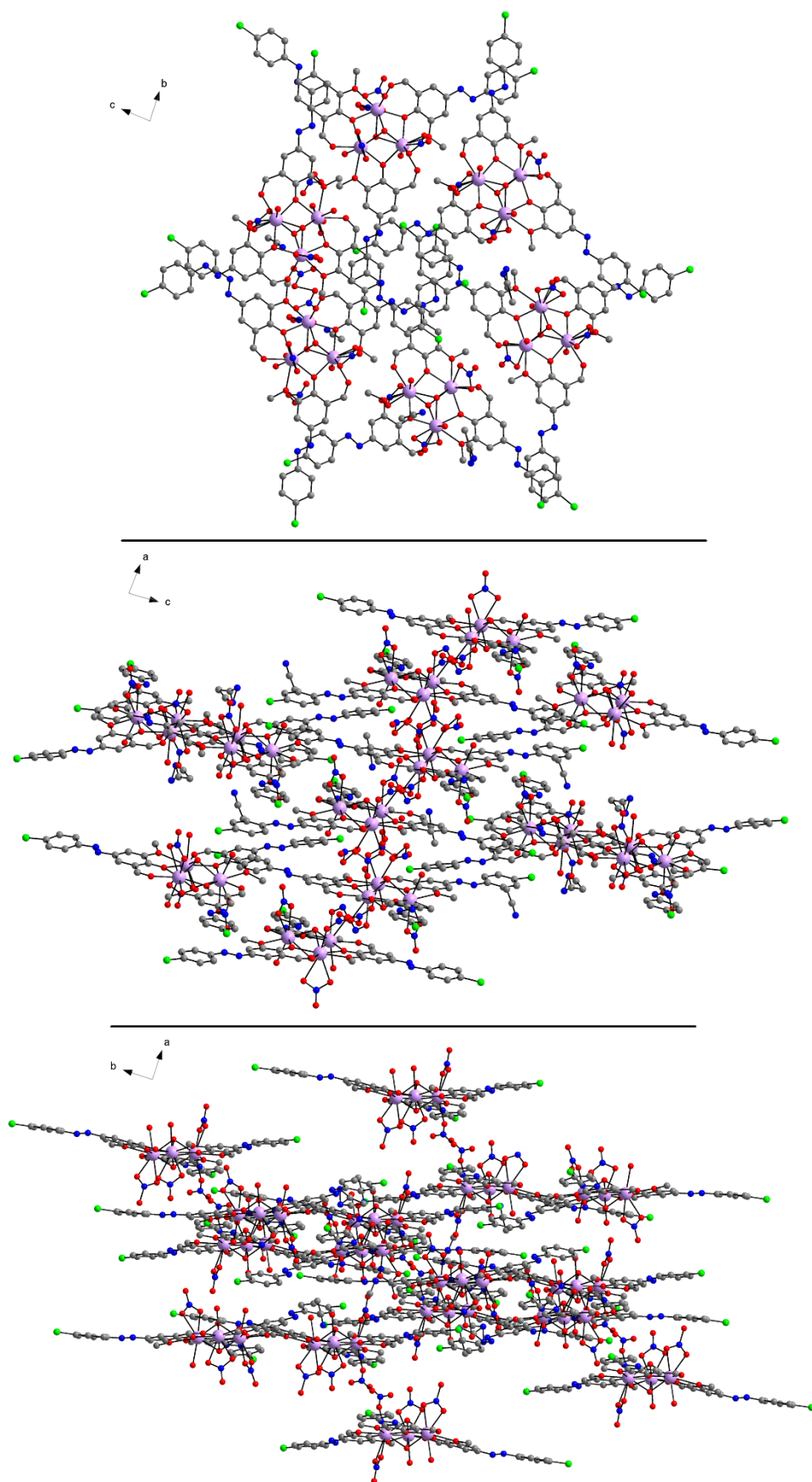


Figure 124. Packing along crystallographic *a* (top), *b* (middle) and *c* (bottom) axis for **(Dy₃-39)**.

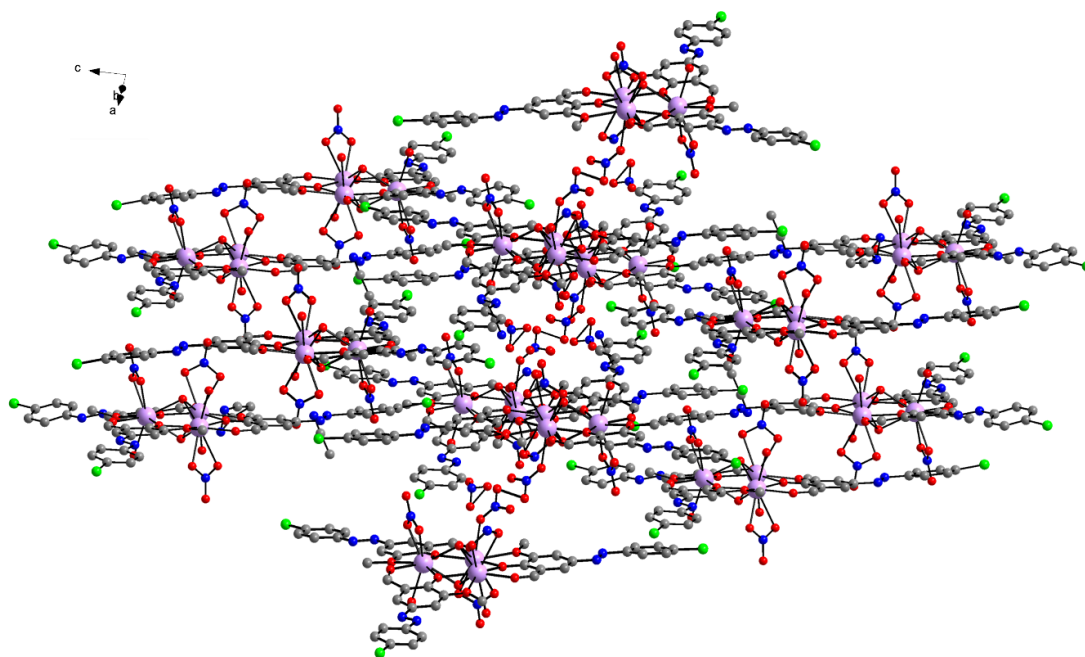


Figure 125. Packing of (**Dy₃-39**) showing the layer structure.

The packing is dominated by intermolecular interactions in the form of π - π stacking between the *p*-Cl-benzyl rings. The approximate distance between rings is 3.45(2) Å (Figure 126). This is defined by taking the distance of the closest C \cdots C (C(23) \cdots (C(56)) contact of π - π stacked rings.

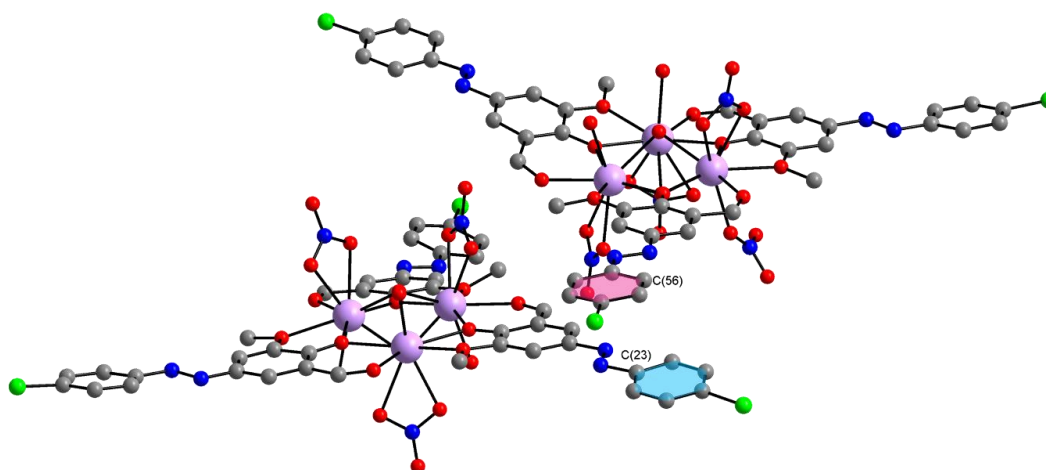


Figure 126. Packing diagram of (**Dy₃-39**) highlighting the benzyl rings involved in the intermolecular π - π stacking.

A second, stronger set of π - π interactions exist and are shown in Figure 127. Here two molecules overlap with two of their ligand's benzyl rings at a distance of 3.25(2) Å, indicative of strong π - π stacking.^[231]

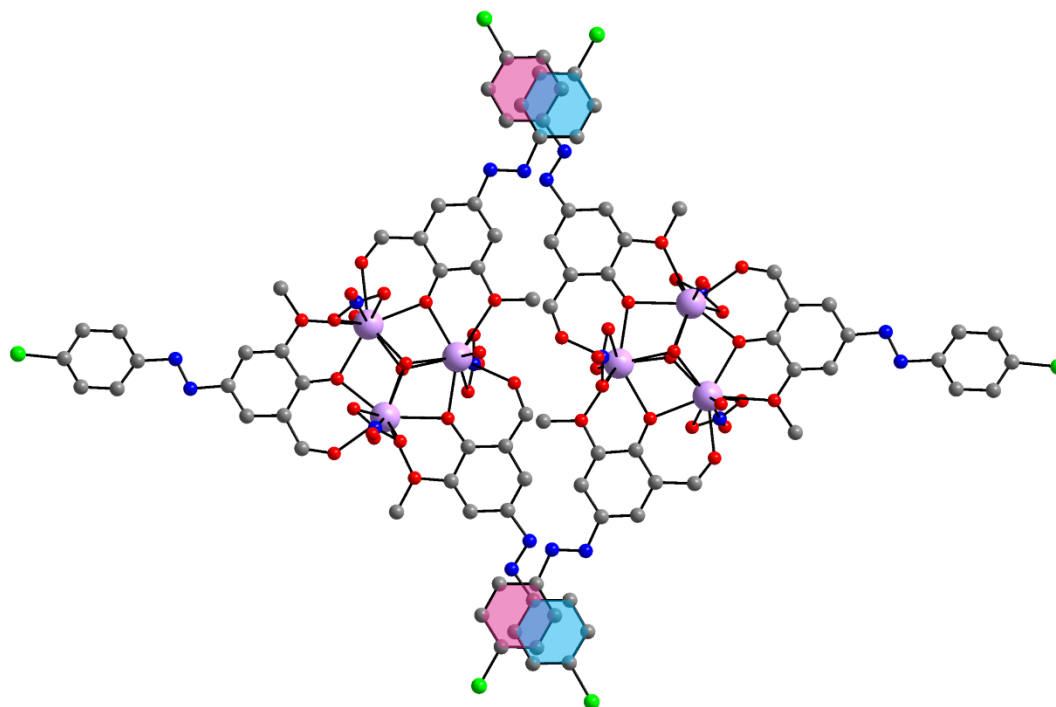


Figure 127. Second set of π - π interactions in (**Dy₃-39**) highlighting the involved benzyl rings.

Furthermore, halogen interactions exist in the structure between the Cl atom on a *p*-Cl-pdavan⁻ ligand and the oxygen of a terminal NO₃⁻ ligand (see Figure 128). The most prominent interactions of this kind are between Cl(3) and O(35) with a distance of 3.054(7) Å.

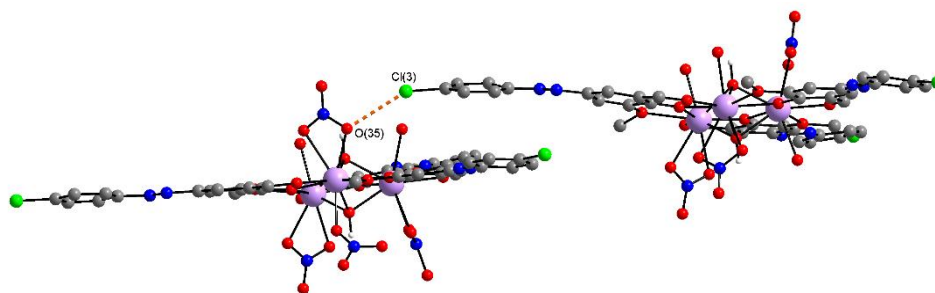


Figure 128. Halogen-nitrate interactions in (**Dy₃-39**).

This type of halogen interaction is also found for (**Dy₃-40**) where the distance between the same atoms Br(3) and O(35) is 3.052(12) Å. The halogen nitrate interactions here are stronger since despite of the larger van-der-Waals radii of Br the distance between halogen bond donor and acceptor is essentially the same when compared to the Cl-analogue (**Dy₃-39**).

Phase purity of (**Dy₃-39**) was investigated using PXRD measurements which are shown in Figure 129. Whereas the measured and simulated diffractograms are in

sufficient agreement at lower angles, at higher angles the simulation does not fit the experimental data. The reason for this could be changes in the crystal packing arising from release or uptake of solvent molecules. To test the purity an elemental analysis was carried out which confirmed the bulk sample to be pure. The compound was found to take up water from air which can lead to changes in cell parameters and may therefore explain the discrepancies in the powder pattern at higher angles.

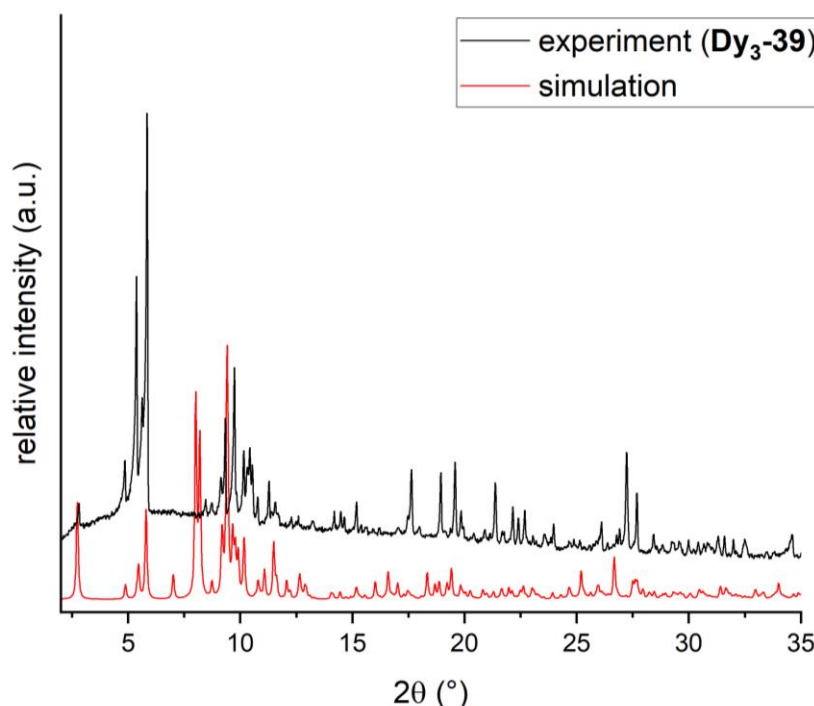


Figure 129. Simulated and experimental powder pattern for (**Dy₃-39**).

The PXRD measurements of (**Dy₃-40**) (Figure 130) indicate that comparable changes in the lattice and of the cell parameters as for (**Dy₃-39**) may also happen for the isomorphous compound (**Dy₃-40**). Again the first four peaks match the simulation followed by similar discrepancies as seen for (**Dy₃-39**) at higher angles. An elemental analysis was carried out which showed that the bulk sample is impure. During this work it was not possible to find reaction conditions or ways of washing the bulk material which would lead to a pure sample of (**Dy₃-40**), thus magnetic measurements were not performed.

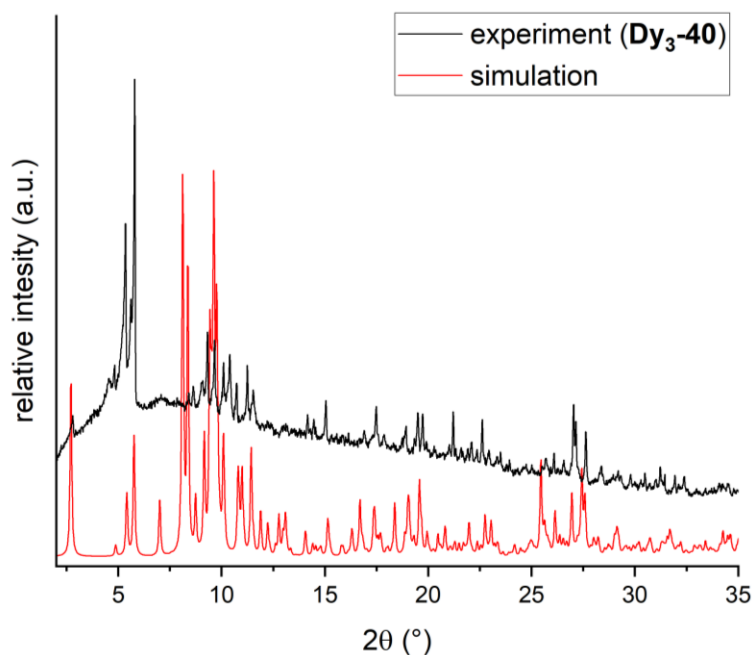


Figure 130. Simulated and experimental powder pattern for (**Dy₃-40**).

Using the same synthetic procedure which proved successful for (**Dy₃-39**) the whole series of lanthanides and yttrium nitrates were used as starting materials. This resulted in eight new compounds (**Y₃-41**), (**Gd₃-42**), (**Tb₃-43**), (**Ho₃-44**), (**Er₃-45**), (**Tm₃-46**), (**Yb₃-47**) and (**Lu₃-48**). PXRD measurements proved these to be isostructural to the Dy^{III}-analogue (see Figure 131).

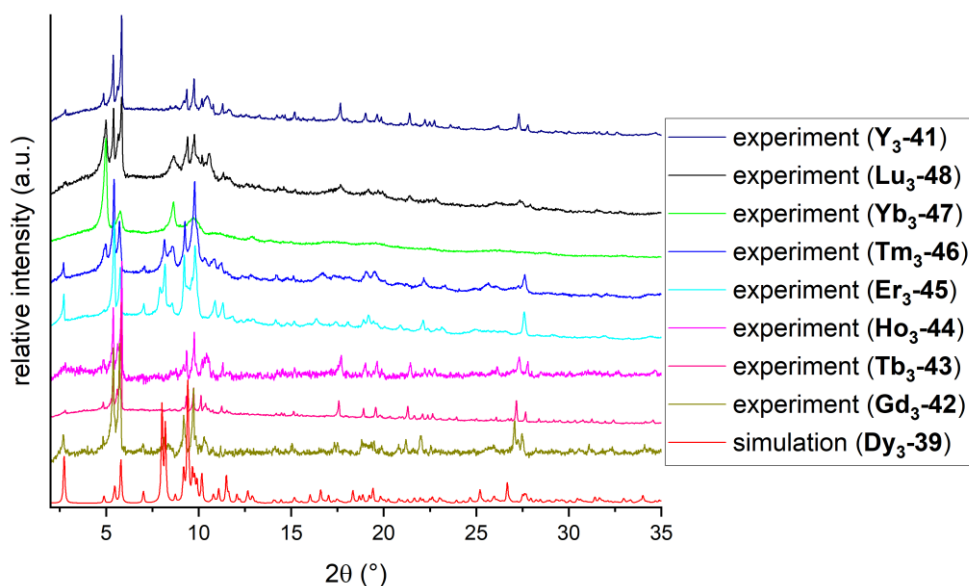


Figure 131. Experimental powder patterns for compounds (**Y₃-41**), (**Gd₃-42**), (**Tb₃-43**), (**Ho₃-44**), (**Er₃-45**), (**Tm₃-46**), (**Yb₃-47**) and (**Lu₃-48**) compared to the simulation of (**Dy₃-39**).

Similarly to the other shown diffractograms of this class of compounds, the signal-to-noise ratio is such that it is difficult to pick out every peak that is predicted by the simulation and only the peaks at lower angles match with the simulation. This behaviour is consistent across all compounds and matches the behaviour of (**Dy₃-39**) which was already proved to be pure. However the comparison of the IR spectra for the compounds which is shown in Figure 132 serves as an additional proof for the presence of the isostructural compounds in the bulk samples.

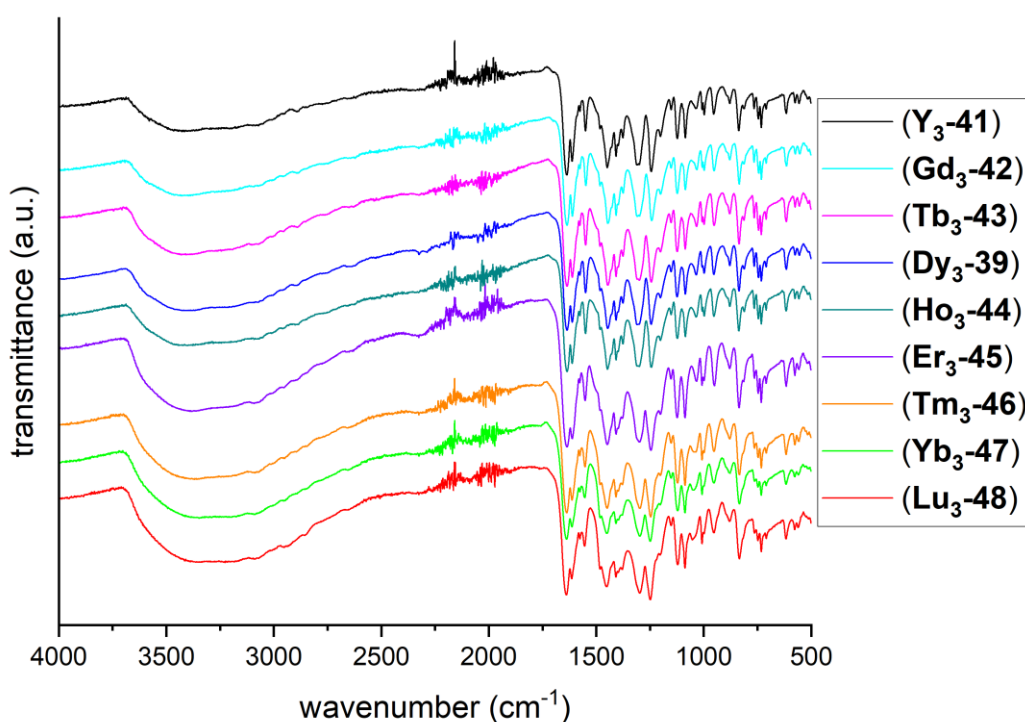


Figure 132. IR spectra of compounds (**Dy₃-39**) to (**Lu₃-48**).

5.3.2 Magnetic properties of Dy₃ with *p*-Cl-pdavan ligands (**Dy₃-39**)

Magnetic characterisation was only performed on bulk samples of (**Dy₃-39**) due to possible impurities in the (**Dy₃-40**) samples as well as the other Ln-variations. DC susceptibility measurements were performed with an applied field of 0.1 T (see Figure 133).

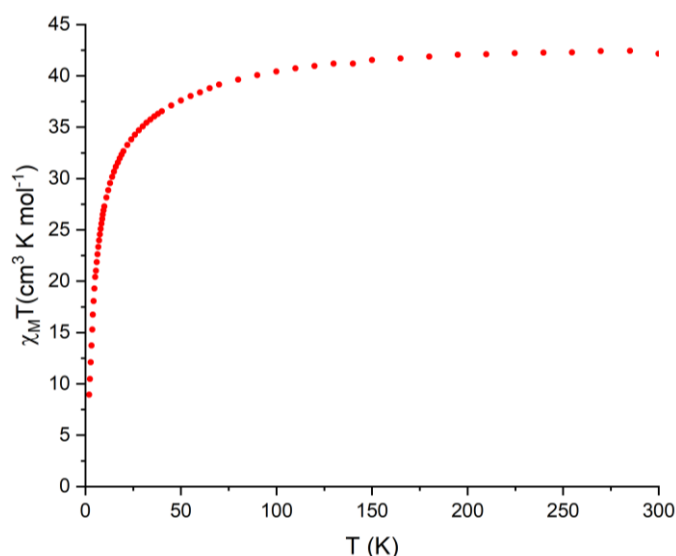


Figure 133. $\chi_M T$ vs T for (**Dy₃-39**) measured at 0.1 T.

The experimental $\chi_M T$ value at RT is $42.4 \text{ cm}^3 \text{Kmol}^{-1}$ which is in excellent agreement with the theoretical value of $42.51 \text{ cm}^3 \text{Kmol}^{-1}$ for three uncoupled Dy^{III} ions. The curve remains flat from 300 K to 50 K below which it begins to decline sharply. This behaviour can be explained by the depopulation of m_J sub-levels and the possible presence of antiferromagnetic coupling. The existence of the antiferromagnetic coupling was confirmed from a Curie-Weiss plot and the corresponding linear fit in the temperature range 50 K to 300 K (see Figure 134). The fit results in a Curie constant $C = 43.5 \text{ cm}^3 \text{Kmol}^{-1}$ and a Weiss constant $\theta = -7.8 \text{ K}$.

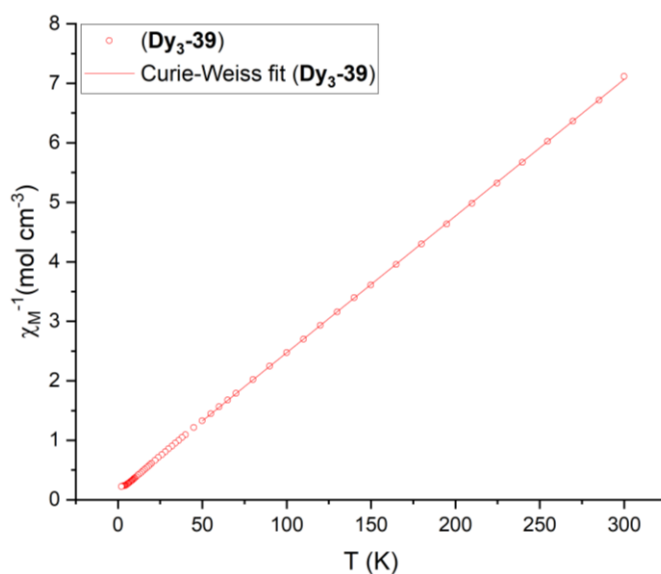


Figure 134. Curie-Weiss plot and fit of (**Dy₃-39**).

AC susceptibility measurements were performed at zero field in the temperature range 2 K to 3.8 K with the results shown in Figure 135. The out-of-phase measurement shows a signal but the maxima lie outside the window of the frequency range measured. At higher temperatures the onset of the maxima is visible but shift to higher frequencies and lower intensities. In an attempt to make the maxima more visible, the 2 K measurement was repeated with applied DC fields of 0.1 T, 0.2 T or 0.3 T all of which showed an increase in intensity of the signals but did not shift the maxima into the measuring window. Given this the in-phase and out-of-phase susceptibility data were fitted simultaneously using a generalised Debye model but no satisfactory fit could be obtained. These observations of the dynamic behaviour may well be the result of both π - π stacking halogen bonding intermolecular interactions.

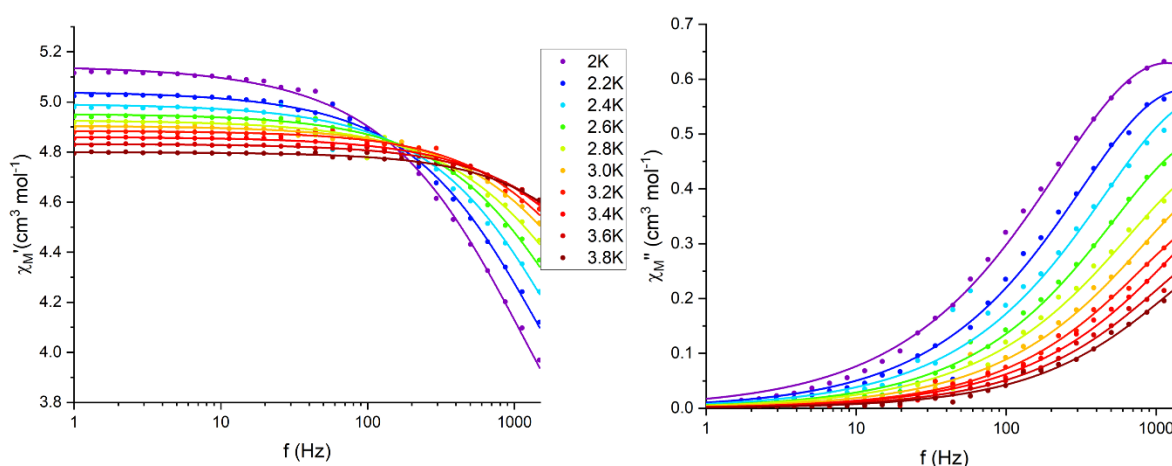


Figure 135. χ_M' against f (left) and χ_M'' against f (right) for (**Dy₃-39**).

Field dependent magnetisation measurements were performed at 2 K to 5 K in the range of 0 T to 7 T (see Figure 136). The general shape of the curve is similar to other Dy₃ triangles in this work with the magnetisation increasing rapidly up to *ca.* 1.5 T above which it starts to flatten. From this point on the magnetisation increases in a linear fashion reaching 17.3 μ_B at 7 T which is slightly higher than the expected value of 15 μ_B for three Dy^{III} ions. This increase could be explained by the contribution of low-lying excited states. The slight fluctuations at higher fields in the 2 K curve are most likely caused by temperature or field instabilities during the measurement. The plot shows an inflection point at 0.87 T, indicating a level crossing where the presumably toroidal state ceases to be the ground state. This S-shape of the magnetisation curve is also observed for other Dy₃ triangles which have been shown

to be toroidal. Therefore, although the inflection point is no proof for toroidicity by itself, it can be assumed that similar magnetic behaviour will be observed for this compound.

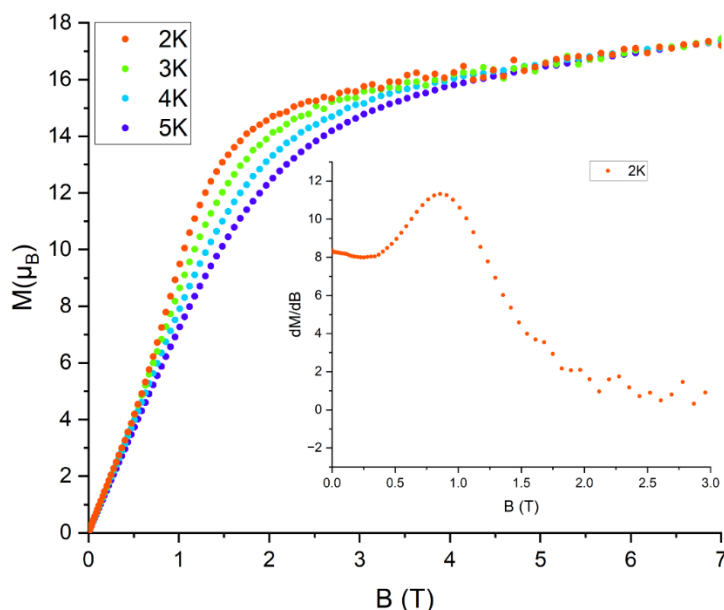


Figure 136. M vs B plot for (**Dy₃-39**) with an inset of the derivative dM/dB for the 2 K curve.

The compound was designed in a way that should preserve the toroidal properties while changing the packing and intermolecular interactions. Additionally, it was possible to completely exchange the Cl^- terminal ligands as well as counterions with nitrates, since the influence of the terminal ligands has been shown above to have a significant impact on the toroidal properties of the Dy_3 core. An inflection point in the magnetisation curve can never simply be assumed to result from the presence of a toroidal moment. Therefore MAGELLAN^[202] was used to get an idea of the orientation of the anisotropy axes. This is influenced solely by the electrostatic properties of the terminal nitrate ligands (see Figure 137). This analysis indicates that the compound might indeed be toroidal, but also that the two triangles differ in the orientation of the anisotropy axes relative to the molecular plane.

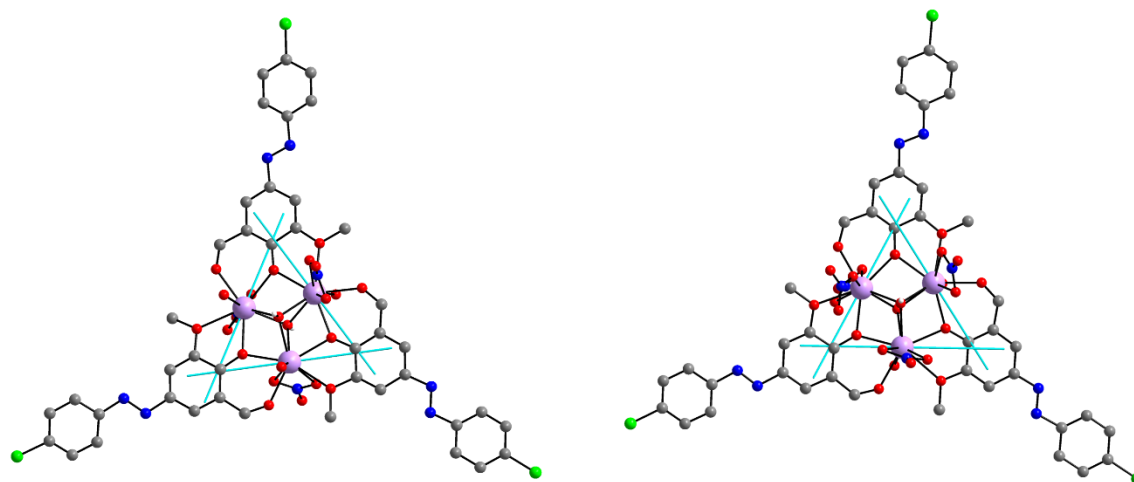


Figure 137. The two independent triangles of (**Dy₃-39**) with the anisotropy axes from MAGELLAN^[202] as cyan lines. MicroSQUID measurements were performed on single crystals of (**Dy₃-39**) and are shown in Figure 138.

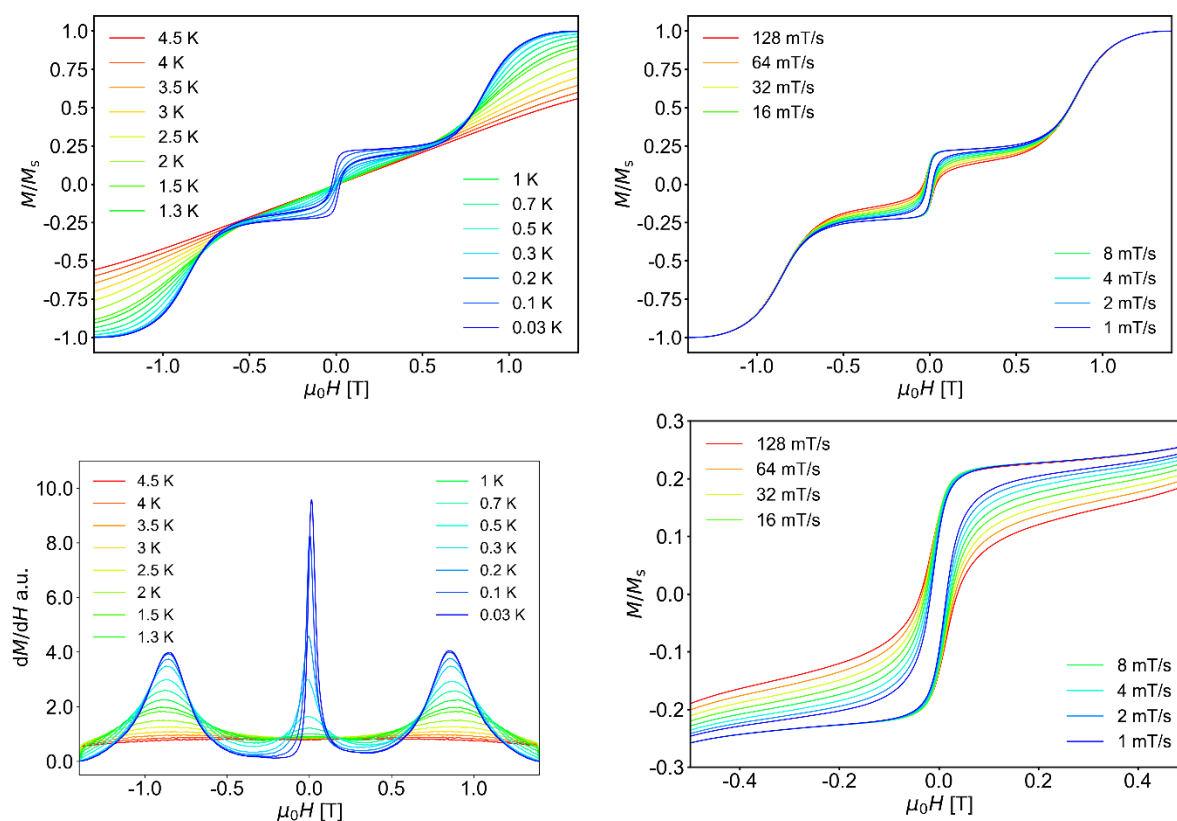


Figure 138. Temperature dependent microSQUID measurements of (**Dy₃-39**) (top left) and derivative (bottom left), sweep rate dependent measurements (top right) with zoomed in excerpt (bottom right).

The data indicate that (**Dy₃-39**) behaves similarly to the halogen substituted *o*-vanillin using triangles discussed above. A non-magnetic state at low fields and a jump in

magnetisation of similar magnitude as seen for the halogen triangles can be observed. Here the sweep rate dependence also clearly shows that a larger hysteresis loop is obtained when measuring at higher sweep rates which is also in line with the behaviour observed for the triangles in section 5.2.3.

5.4 Schiff base triangles

A Schiff base reaction of *o*-vanillyl hydrazide with an aldehyde allows for the synthesis of a wide range of ligands with the *o*-vanillin moiety remaining intact. This means that these Schiff base ligands are suitable for the formation of novel triangular lanthanide complexes. A proof-of-concept for this approach has previously been reported for $[\text{Dy}_3(\mu_3\text{-OH})_2(\text{Hpovh})_3(\text{NO}_3)_3(\text{CH}_3\text{OH})_2(\text{H}_2\text{O})]\text{NO}_3 \cdot 3\text{CH}_3\text{OH} \cdot 2\text{H}_2\text{O}$.^[166]

Here this approach is extended by using various benzaldehyde derivatives along with an *o*-vanillyl hydrazide. The synthetic route for all compounds involves the formation of the Schiff base ligand by refluxing in a mixture of MeOH and MeCN as shown in Figure 139.

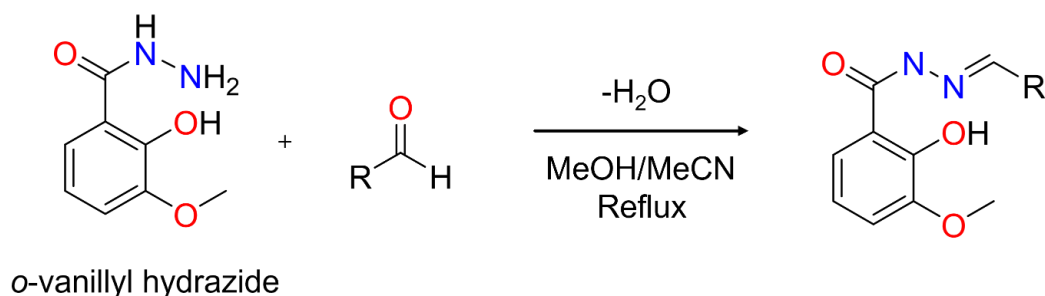


Figure 139. General reaction conditions and molecular components for the synthesis of the Schiff base ligands used in this section. R-CHO here refers to a benzaldehyde derivative.

The solution containing the *in situ* formed Schiff base ligand is then treated with Et_3N as a base and subsequently added to a MeOH/MeCN (4 ml/ 10 ml) solution of a chosen lanthanide chloride. Although in general the Schiff base ligands were not isolated, in some cases these could be obtained through precipitation or else removal of the solvent under reduced pressure. These were obtained pure using column chromatography. However, this method suffers from a loss of yield during column chromatography, which is why the method without isolation of the Schiff base as a solid was the preferred synthetic pathway.

The resulting Dy₃ complexes are inherently chiral since the ligands can assume either a clockwise or anticlockwise orientation with the terminal solvent and Cl⁻ ligands on either side of the triangle. This also leads to a chiral spin structure. Utilising the tuneability of this Schiff base approach it is possible to design ligands to favour crystallisation in higher symmetry space groups or to further impose chirality using chiral aldehydes.

This ligand system proved to be instrumental for the synthesis of a series of triangular Ln^{III} complexes which allowed for the investigation of correlations between ligand design and the crystal structure. Furthermore, a magnetostructural correlation in terms of the toroidicity of the system can be proposed.

5.4.1 (Dy₃-49) - Achieving Higher Symmetry

For the synthesis of compound (**Dy₃-49**), benzaldehyde was used in the Schiff base reaction. This resulted in a yellow solution which intensifies in colour when treated with base. This solution was added to the DyCl₃·6H₂O solution, stirred for 20 minutes, filtered and the vial subsequently sealed to allow for crystallisation of the product. After 3 days colourless block-shaped crystals were obtained, suitable for SCXRD and other advanced single crystal characterisation techniques necessary to assess the toroidicity of the compound. Compound (**Dy₃-49**) with the formula [Dy₃(Hbovh)₃(μ₃-OH)₂(MeOH)₃Cl₃]Cl crystallises in the trigonal space group $R\bar{3}$ with Z = 6. This successfully reduces the magnetic complexity of the system since the number of different non-symmetry related magnetic centres is reduced from three to one with 1/3 of a molecule in the asymmetric unit (Z' = 0.333). The molecular structure is shown in Figure 140.

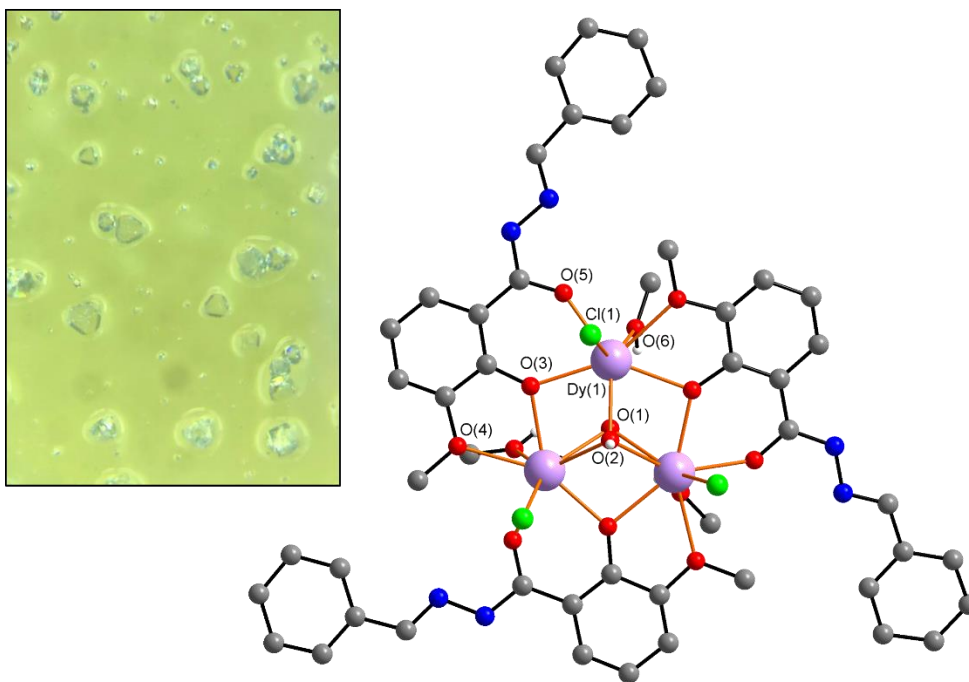


Figure 140. Molecular structure of (**Dy₃-49**) and picture of crystals under a microscope.

The asymmetric unit consist of one third of the central bridging ($\mu_3\text{-OH}^-$)₂ unit, one Dy^{III} ion, the Hbovh⁻ ligand and the terminal ligands which consist of one Cl⁻ and one MeOH above and below the triangle plane respectively. The Hbovh⁻ ligand coordinates in an identical fashion as the o-vanillin in the archetypal Dy₃. Thus the threefold symmetry means the Dy^{III} ions form an equilateral triangle with Dy...Dy distances of 3.5247(5) Å. The H₂bovh ligands are singly deprotonated at the alcohol group when coordinating which together with the bridging hydroxo groups, the three terminal Cl⁻ ligands and the Cl⁻ counterion in the lattice, makes the complex charge neutral. The Hbovh⁻ ligands are significantly angled towards the MeOH side of the terminal ligands forming an angle between the mean plane of the ligand and the Dy₃ triangle of 10.12(8)°. The packing along the crystallographic a axis and along the crystallographic c axis which coincides with the C₃ axis is shown in Figure 141.

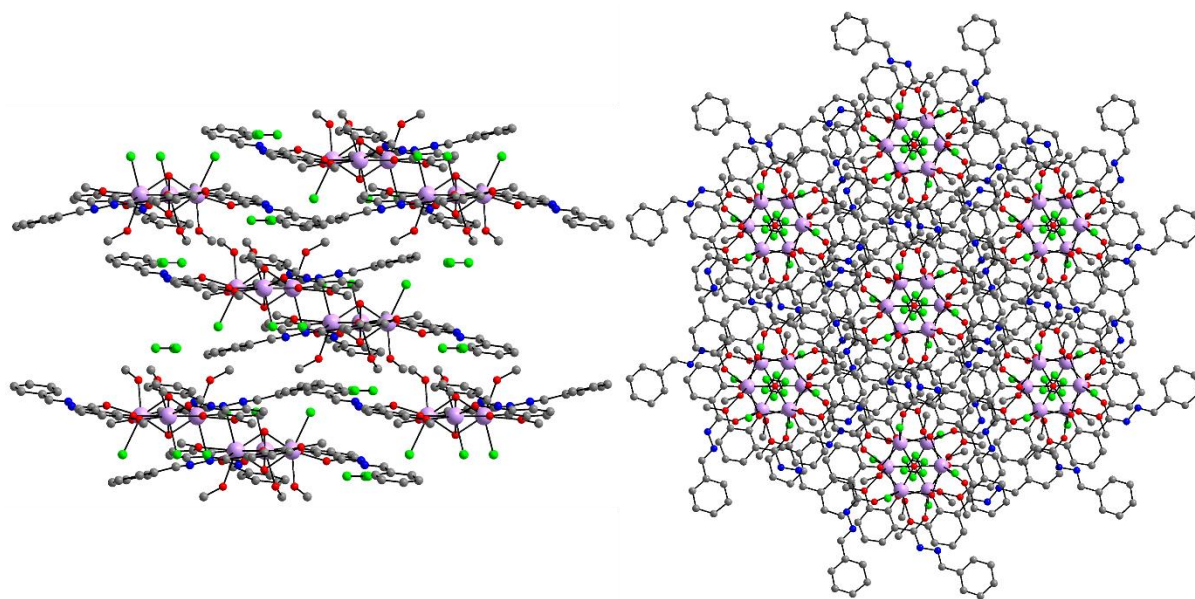


Figure 141. Packing of (**Dy₃-49**) along the crystallographic a (left) and c (right) axes.

The Dy₃ units are stacked along the crystallographic c axis and rotated 60° to each other with the phenyl rests of the ligands bent towards the MeOH side of the triangle plane. The closest intermolecular Dy...Dy distance within a stack is 14.0756(9) Å whereas the closest Dy...Dy distance between ions in neighbouring stacks is 9.0746(7) Å. Depending on the viewing direction along c these are arranged either in a anticlockwise or clockwise fashion (see Figure 141 anticlockwise). The compound forms sheets throughout the crystal lattice in which Dy₃ moieties are connected by hydrogen bonds between the terminal chloride ligands and the hydrogen on the N-H of the Hbovh⁻ ligand. Furthermore, hydrogen bonds between the hydrogen on the terminal MeOH ligands and the chloride counterion form three favourable positions for the chloride, each of which is occupied by 1/3 of the disordered chloride. Both interactions are shown in Figure 142 The distance between the chloride and MeOH oxygen is 3.041(9) Å while the distance between the terminal chloride and the N-H nitrogen is 3.419(7) Å, both of these distances are consistent with values for hydrogen bonds found in the literature.^[76]

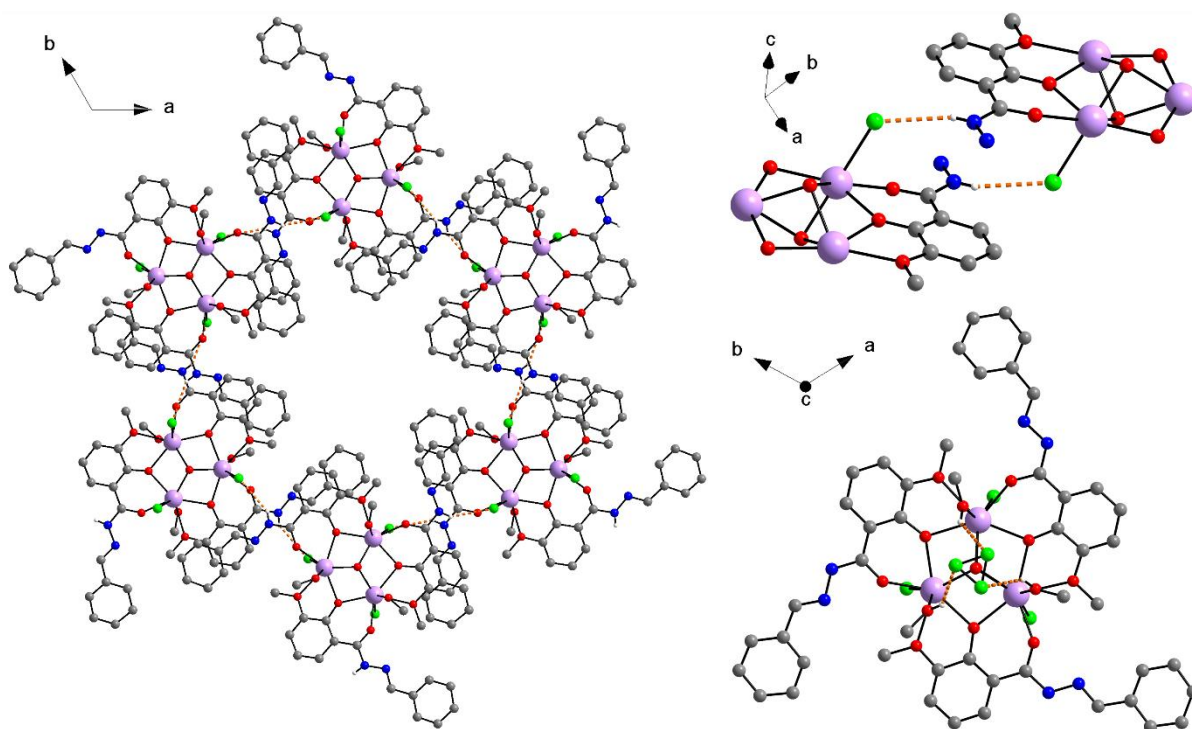


Figure 142. Connection of Dy_3 moieties through hydrogen bonds between Cl and H-N (left), excerpt of two triangles these interactions highlighted (top right), hydrogen bonds between three $1/3$ occupancy chloride counterions and the terminal MeOH ligands (bottom right).

Two inversion related triangles (enantiomers) result from the symmetry of the $R\bar{3}$ space group. This results in a clockwise or anticlockwise orientation of the Hbovh^- ligand. Furthermore this results in there being three MeOH and three Cl^- ligands located above and below the plane of the triangle. The enantiomers are arranged in an alternating fashion within stacks along the C_3 axis. Figures 143 and 144 highlight the formation of the planes through hydrogen bonds and the stacks of alternating enantiomers in the crystal structure. Blue and green as well as yellow and red triangles in Figure 143 have the same orientation in the crystal and are the same enantiomers. Blue and red triangles as well as green and yellow triangles form the aforementioned planes through the crystal.

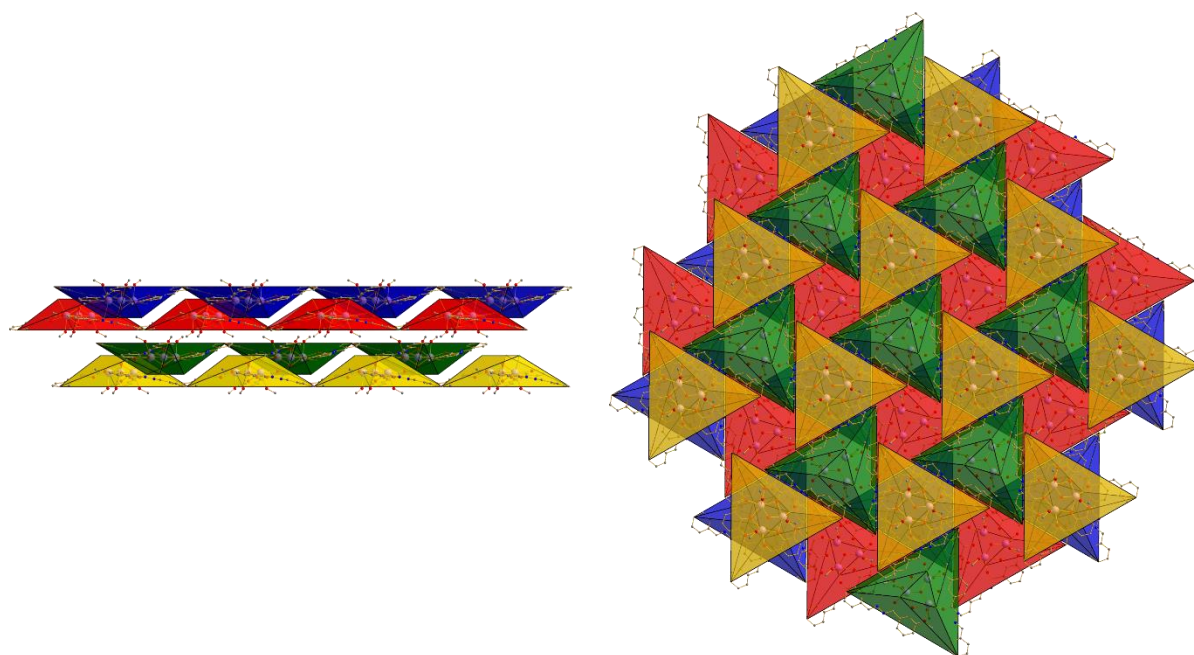


Figure 143. Dy₃ triangles in (**Dy₃-49**) indicated by blue, red, yellow and green polyhedra. Yellow and red as well as blue and green are the same enantiomer. Layers formed by blue and red, as well as green and yellow triangles (left) with the top down view showing how stacks result from overlaying the planes.

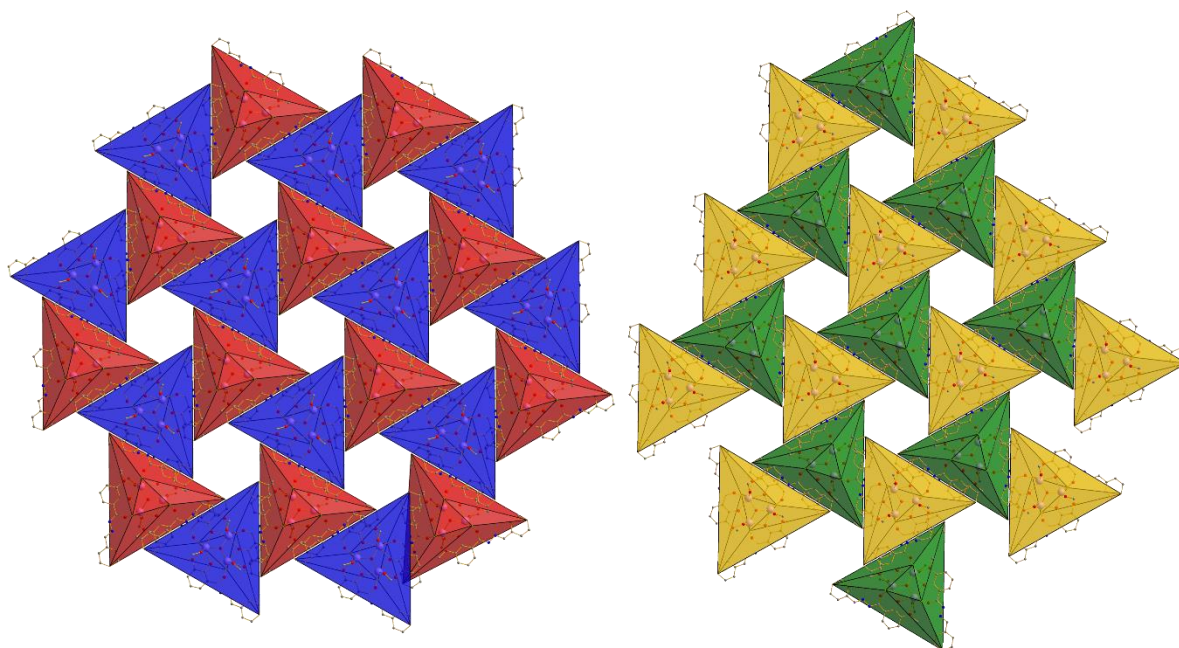


Figure 144. View along the crystallographic c axis showing only the planes made up of red and blue (left) and green and yellow (right) triangles.

This arrangement of the magnetic centres in the crystal assists with the evaluation of the single crystal microSQUID measurements which are described below.

To confirm phase purity of the bulk sample of compound (**Dy₃-49**) PXRD measurements were performed. The comparison of the experimental powder diffractogram with the simulation is shown in Figure 145.

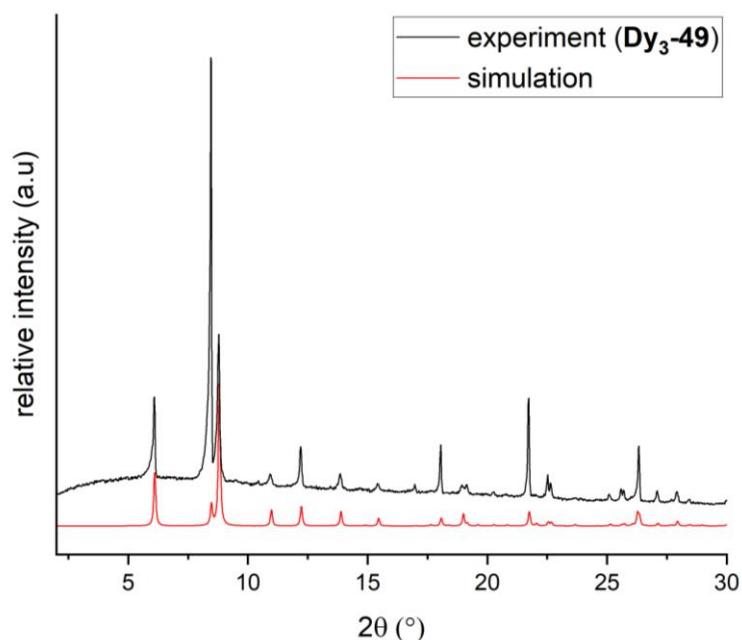


Figure 145. Simulated and experimental powder pattern for (**Dy₃-49**).

Using the same synthetic procedure as for (**Dy₃-49**) but varying the lanthanide ion using $\text{LnCl}_3 \cdot n(\text{H}_2\text{O})$ with $\text{Ln} = \text{Y}^{\text{III}}, \text{Sm}^{\text{III}}, \text{Eu}^{\text{III}}, \text{Gd}^{\text{III}}, \text{Tb}^{\text{III}}, \text{Ho}^{\text{III}}, \text{Er}^{\text{III}}, \text{Tm}^{\text{III}}, \text{Yb}^{\text{III}}$, yielded compounds (**Y₃-50**), (**Sm₃-51**), (**Eu₃-52**), (**Gd₃-53**), (**Tb₃-54**), (**Ho₃-55**), (**Er₃-56**), (**Tm₃-57**) and (**Yb₃-58**). Single crystal XRD measurements were performed on (**Eu₃-52**), the molecular structure of which is shown in Figure 146.

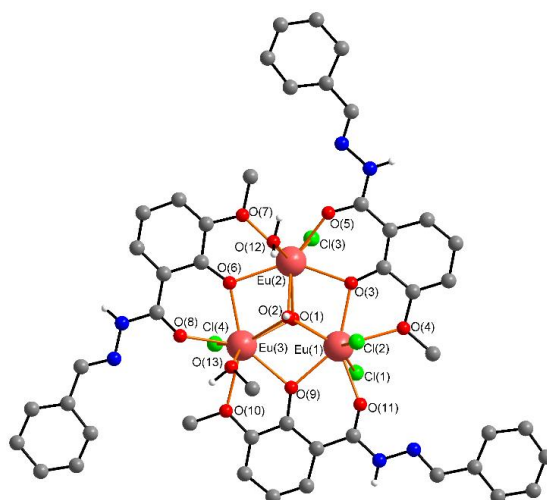


Figure 146. Molecular structure of (**Eu₃-52**).

Compound (**Eu3-52**) has the formula $[\text{Eu}_3(\text{Hbovh})_3(\mu_3\text{-OH})_2(\text{MeOH})(\text{H}_2\text{O})\text{Cl}_4]\cdot 4\text{MeCN}\cdot 2\text{MeOH}\cdot 4\text{H}_2\text{O}$ and crystallises in $P\bar{1}$ with $Z = 2$. The general structure is similar to the Dy_3 triangle analogues described above. The H_2bovh ligands coordinate to the Eu^{III} ions *via* the three oxygens of the *o*-van subunit with the phenoxy oxygen bridging between two of them. In the case of (**Eu3-52**) the terminal ligands are four Cl^- ligands, one water and one MeOH. Three of the Cl^- are on one side of the triangle. The other side of the triangle has the fourth Cl^- , one MeOH and one water ligand. As a result of the additional coordinating Cl^- ligand compared to (**Dy3-49**) no chloride counterion in the lattice is necessary to maintain charge balance.

Compound (**Yb3-58**) could only be characterised using single crystal XRD measurements since the synthesis yielded only very few crystals. (**Yb3-58**) crystallises in $R\bar{3}$ with essentially identical cell parameters to those of (**Dy3-49**). The molecular structures of the compounds are also essentially the same except for the terminal solvent ligands which in the case of (**Yb3-58**) are two MeOH and one water ligand which are disordered over the three sites. Furthermore the disordered water ligand H-bonds to a lattice water molecule with the same inherent disorder. The molecular structure with the formula $[\text{Yb}_3(\text{Hbovh})_3(\mu_3\text{-OH})_2(\text{MeOH})_3(\text{H}_2\text{O})\text{Cl}_3]\text{Cl}\cdot (\text{H}_2\text{O})\cdot 4(\text{MeOH})$ is shown in Figure 147.

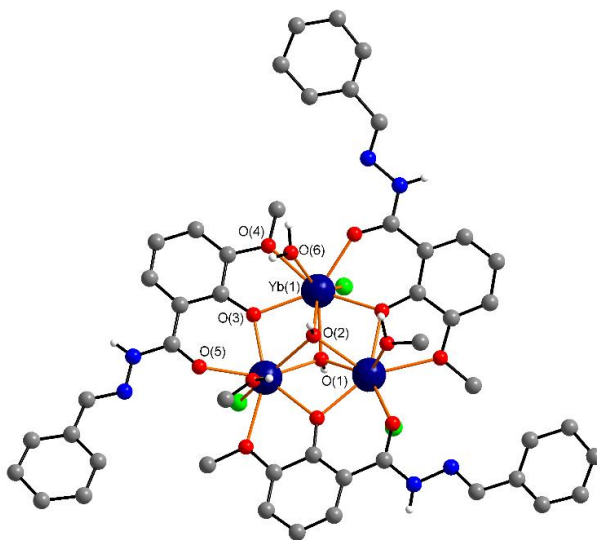


Figure 147. Molecular structure of (**Yb3-58**). The disorder described above is removed for clarity.

PXRD measurements were performed on samples of compounds (**Y3-50**) - (**Tm3-57**) (see Figure 148). Since the samples of (**Sm3-51**), (**Eu3-52**), (**Gd3-53**) and (**Ho3-55**) lose their crystallinity in air, the PXRD measurements were performed on samples

within their mother liquor in a sealed capillary. The compounds appear to draw water from the atmosphere turning the crystals opaque when left in air for a few seconds. This behaviour seems to be more common, but not limited to, the compounds crystallising in $P\bar{1}$. All compounds (**Y₃-50**) - (**Tm₃-57**) are essentially isostructural to either (**Dy₃-49**) or (**Eu₃-52**) as seen from the comparison of the simulated and experimental powder diffractograms (see Figure 148).

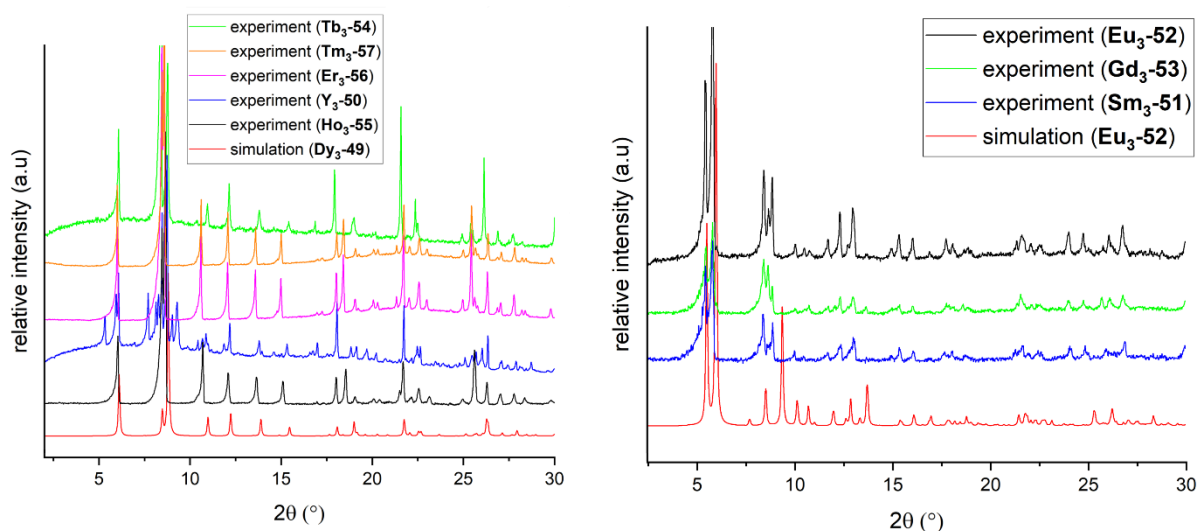


Figure 148. Experimental powder pattern for compounds (**Y₃-50**), (**Tb₃-54**), (**Ho₃-55**), (**Er₃-56**) and (**Tm₃-57**) compared to the simulation of (**Dy₃-49**) and experimental pattern of (**Sm₃-51**), (**Eu₃-52**) and (**Gd₃-53**) compared to the simulation for (**Eu₃-52**) on the left and right respectively.

The powder diffractograms of (**Sm₃-51**), (**Eu₃-52**) and (**Gd₃-53**) are in reasonable agreement with the simulation for (**Eu₃-52**) and all three samples are phase pure. It is important to note that the experimental powder patterns of the (**Eu₃-52**) type structures are shifted to the left with more significant shifts at higher angles in comparison to the simulation. Compounds (**Y₃-50**), (**Tb₃-54**), (**Ho₃-55**), (**Er₃-56**), and (**Tm₃-57**) match the simulation for (**Dy₃-49**) with some additional reflections for (**Y₃-50**) indicating some crystalline impurities.

The reason for the two different structural types could be a result of the lanthanide contraction for which lanthanides with higher atomic numbers have smaller ionic radii. These different ionic radii can lead to different coordination environments within the complex. For this system, lanthanides up to and including Gd^{III} crystallise in the $P\bar{1}$ structure type whereas those with higher atomic numbers crystallise in the $R\bar{3}$ type. Additionally single crystal measurements such as SCXRD for (**Yb₃-58**) show that changing the terminal ligands from MeOH to H₂O or vice versa has very little effect on

the unit cell parameters. This change in terminal solvent ligands might result from different amounts of water in the solvents, different amounts of lattice water in the lanthanide salts or different exposure times in air before the PXRD or single crystal XRD measurements were performed. The elemental analysis of these compounds also indicates the possibility for an exchange of the MeOH ligands for water when the crystals are removed from the mother liquor. To study the effects of exposure to air, IR spectra were recorded and compared to the spectrum of (**Dy₃-49**) which was shown to be pure and stable in air (see Figure 149).

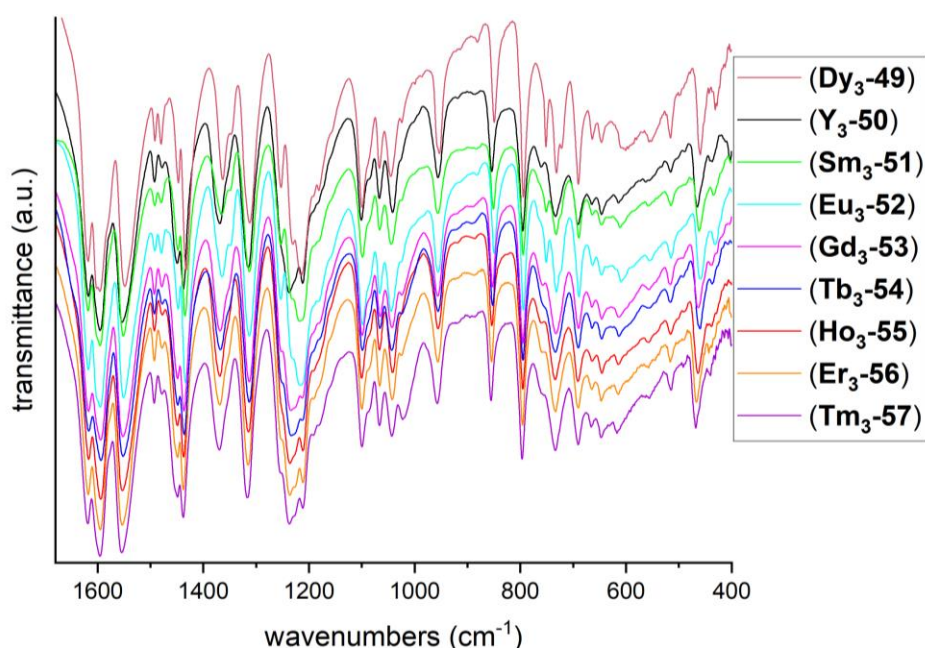


Figure 149. IR spectra of compounds (**Dy₃-49**) to (**Tm₃-57**).

The comparison of the IR spectra results shows that all spectra are consistent, indicating that exposure to air does not alter the molecular structure other than the aforementioned exchange of solvent ligands which leads to a loss of crystallinity in the $P\bar{1}$ structure type.

5.4.1.1 (**Dy₃-49**) – Magnetic properties

The magnetic characterisation for (**Dy₃-49**) was performed in collaboration with Jan Arneth from the group of Prof. Dr. Rüdiger Klingeler at the University of Heidelberg.

In order to get an approximate of the orientation of the anisotropy axes in (**Dy₃-49**) a MAGELLAN^[202] analysis was performed. This uses a purely electrostatic model to

determine directions of anisotropy axes specifically for Dy^{III}-containing compounds. The results of this analysis are shown in Figure 150. The axes are arranged 9° out of the triangular plane in a toroidal arrangement. This gives a first indication that toroidal behaviour could be present.

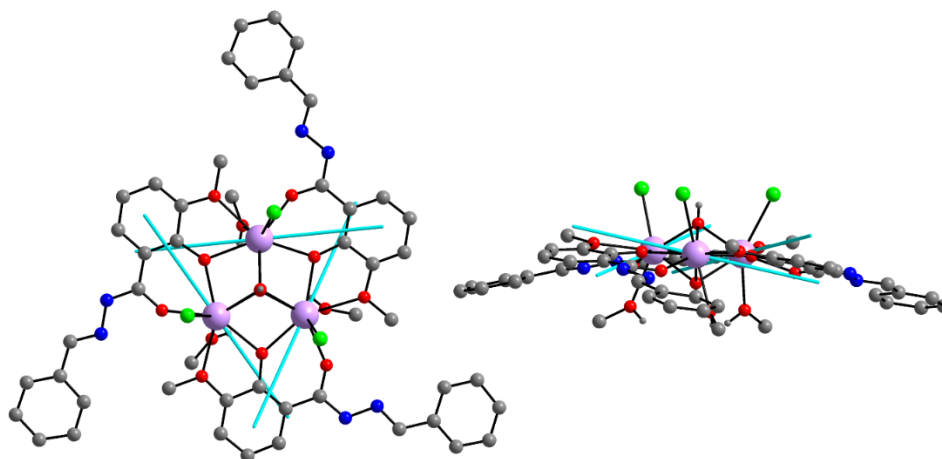


Figure 150. MAGELLAN^[202] analysis of (**Dy₃-49**) with anisotropy axes shown in cyan top (left) and side view (right).

Temperature dependent magnetic susceptibility measurements were performed with an applied DC field of 0.1 T and 1 T (see Figure 151). The experimental $\chi_M T$ value at 300 K is 39.3 cm³Kmol⁻¹ which is below the theoretical value of 42.51 cm³Kmol⁻¹ for three uncoupled Dy^{III} ions. The magnitude of the deviation and the trend towards lower $\chi_M T$ values in the experiment in comparison to the theory fall within the range seen from other measurements and are consistent with other Dy₃ triangles in this work as well as Dy₃ triangles in the literature.^[37, 166]

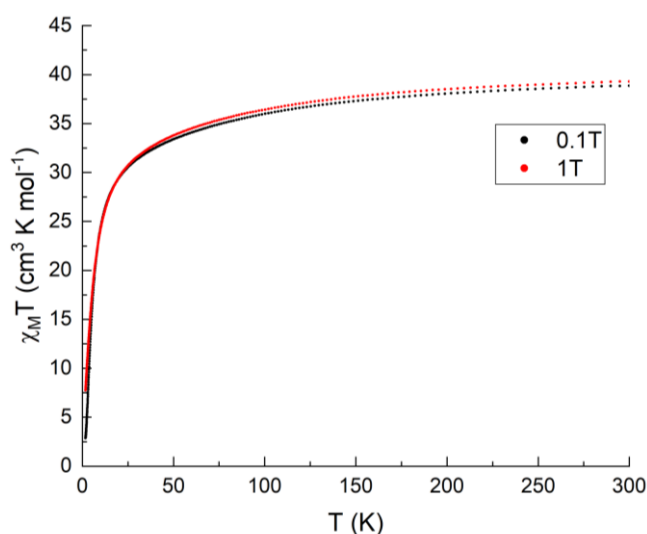


Figure 151. $\chi_M T$ vs T for (**Dy₃-49**) measured at 0.1 T and 1 T.

Upon decreasing the temperature the $\chi_M T$ value first starts to decrease gradually until reaching ca. 11 K below which it decreases rapidly. This behaviour can result from the depopulation of excited m_J sub-levels and/or antiferromagnetic coupling. The possibility of the latter was investigated further using a Curie-Weiss fit (Figure 152). The Curie-Weiss fit was performed in a temperature range of 63 K to 300 K and results in a Curie-constant of $C = 40.03 \text{ cm}^3 \text{Kmol}^{-1}$ and a negative Weiss constant of $\theta = -12.05 \text{ K}$ which suggests the presence of antiferromagnetic interactions in the sample.

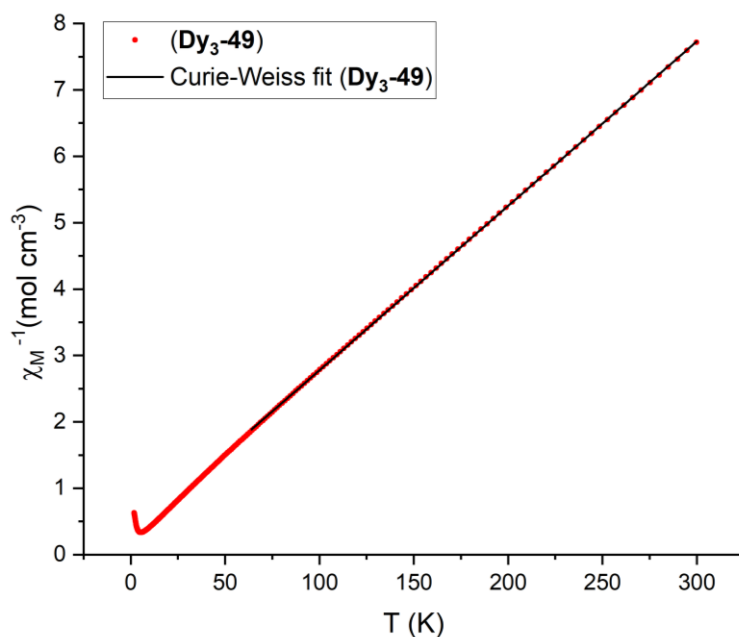


Figure 152. χ_M^{-1} vs T plot with Curie-Weiss fit for (**Dy₃-49**).

AC susceptibility experiments were conducted at zero applied DC field in the temperature range 1.8 K to 13.5 K (see Figure 153). The out-of-phase data show two distinct sets of maxima and show the existence of slow relaxation of magnetisation characteristic for SMMs. A double generalized Debye model (sum of two Debye models) was used to analyse the two sets of relaxation processes. The in-phase and out-of-phase susceptibility data were fitted simultaneously. With increasing temperature, the first maximum in the χ_M'' plot is shifted to higher frequencies and the signal decreases whereas the values of the second set of maxima increase with increasing temperature. The maxima of this second set is only seen up to ca. 5 K after which the relaxation associated with this signal becomes too fast to be observed in the measurement window of this set-up. The increase in intensity with increasing

temperatures could indicate the involvement of excited states in this relaxation behaviour.

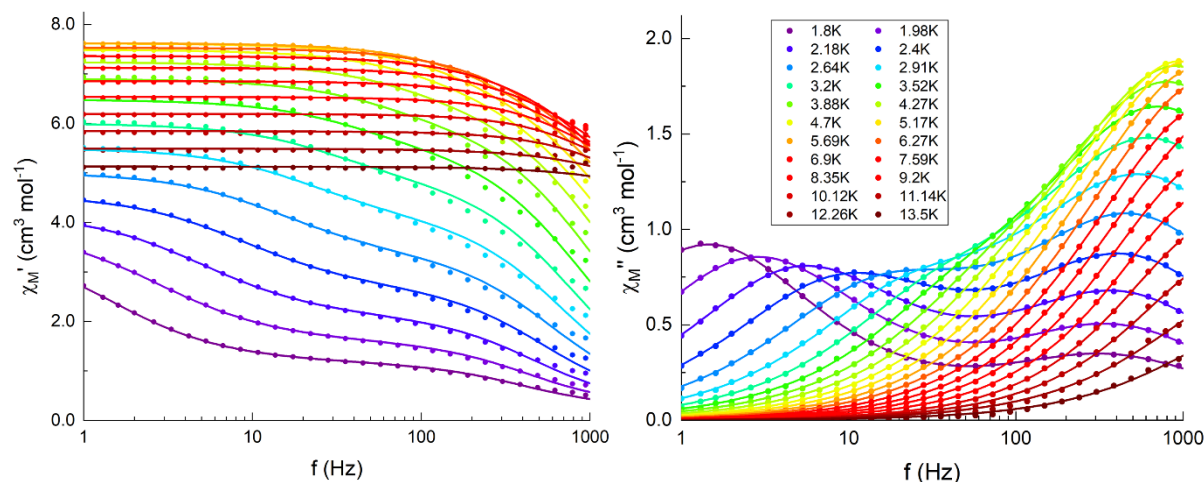


Figure 153. χ_M' against f (left) and χ_M'' against f (right) for (**Dy₃-49**).

To gain further insights into the dynamic processes of this compound, additional AC measurements were performed with applied DC fields. The fields chosen for this were 0.81 T and 1.75 T. The aim here was to investigate at fields where the toroidal state corresponds to the ground state (zero field), where the system is close to the level crossing (0.81 T) and at higher fields (1.75 T) where the system has gone over the level crossing to the magnetic state. The respective data are shown in Figure 154. This represents a preliminary attempt to see if it is possible to correlate applied fields with magnetic behaviour near level crossings. It is clear that this experimental approach needs to be backed up by much more detailed theory calculations.

There are significant differences between the behaviour at zero field and at applied DC fields. The χ_M'' curve at 0.81 T is shifted to lower frequencies with a broad shoulder to the right. The maximum loses intensity at higher temperatures which is opposite to the behaviour observed for the more prominent maximum at zero field. However, it cannot necessarily be assumed that this is the same maximum. At 1.75 T the χ_M'' data show similarities to the signals seen at zero field since two maxima are observed. However, some differences are apparent. The first maximum has the same intensity as the second maximum at low temperatures which at higher temperatures increases more than the second maximum. The first maximum starts to decrease in intensity at ca. 4 K whereas the second continues to increase.

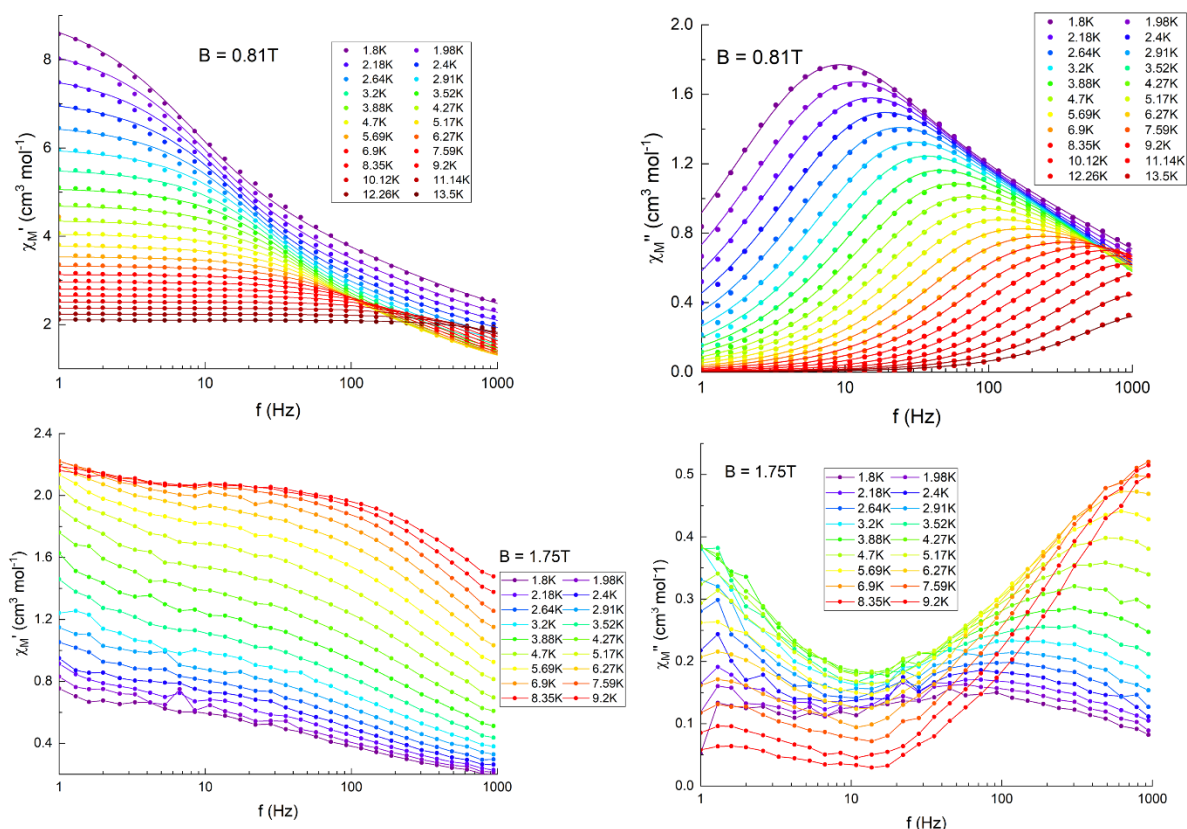


Figure 154. χ_M' against f (left) and χ_M'' against f (right) for (**Dy₃-49**) with an applied field of 0.81 T (top) and 1.75 T (bottom). For 1.75 T the lines are a guide to the eye, for 0.81 T a standard Debye model fit was used.

Field dependent DC measurements from 0 T to 14 T and back to 0 T were performed at 1.8 K, 3 K and 5 K to probe for the possibility of hysteresis (see Figure 155). The resulting M vs B plots show an increase in magnetisation with an inflection point at 0.91 T indicating a level crossing as shown by the derivative dM/dB in the inset of Figure 155. A magnetisation of $15.7 \mu_B$ is reached at 7 T followed by a linear increase up to a maximum value of $16.9 \mu_B$ at 14 T for the 1.8 K measurement. For Dy^{III} -containing compounds the measured saturation magnetisation at these fields is expected to be $5 \mu_B$ per Dy^{III} ion which is half of the theoretically possible value. The reason for the linear increase up to 14 T could be from the contribution of low-lying excited states. The measurement at 1.8 K shows an open hysteresis loop which is essentially closed at 3 K and completely gone at 5 K. For the original Dy_3 archetype by Powell *et al.*,^[37] it was demonstrated that the Dy_3 with *o*-vanillin ligands exhibits SMM behaviour in a thermally excited state. Similar behaviour is observed here, where, after the level crossing at 0.91 T, the new ground state now exhibits hysteresis and thus SMM behaviour. The previously described AC data show a corresponding

relaxation process that was assigned to an excited state given the observed temperature dependence.

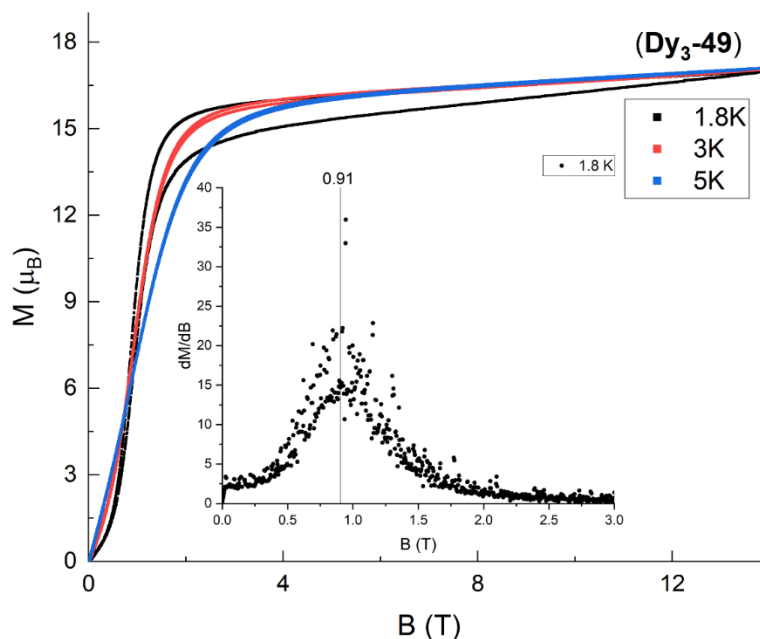


Figure 155. M vs B plot for (**Dy₃-49**) measured using a sweep rate of 40 Oe/s. The inset shows the derivative dM/dB for the 1.8 K curve highlighting the presence of a level crossing below 1 T.

The S-shape of the magnetisation measurement as a result of the level crossing is not definitive proof of a toroidal ground state. To confirm the presence of a toroidal system, other angle dependent measurement techniques such as microSQUID or torque magnetometry must be employed which are described below. However, since the S-shape has also been observed in other Dy₃ triangles that have been shown to be toroidal, it serves as an indication of similar magnetic behaviour. If a compound is in fact toroidal the inflection point can be used as a measure for the stability of the toroidal ground state in terms of field fluctuations.

MicroSQUID measurements were performed on single crystals of (**Dy₃-49**) at temperatures between 30 mK to 4.5 K with a sweep rate of 16 mTs⁻¹ and at 30 mK with sweep rates from 2 mTs⁻¹ to 128 mTs⁻¹ (see Figure 156). These show an open hysteresis loop of the sample including in the ground state for temperatures up to 1 K which again indicates SMM behaviour. This hysteresis in combination with the hysteresis observed in the SQUID measurement may explain the presence of the two sets of maxima in the AC data. The first one would correspond to the slow relaxation from the toroidal ground state and the second one from an excited state. The ground

state is essentially non-magnetic as expected for toroidal moments. Since for (**Dy₃-49**) the anisotropy axes are tilted slightly out of the triangular plane (9° from the MAGELLAN^[202] analysis) a small magnetic moment can be observed. Furthermore, (**Dy₃-49**) exhibits negligible sweep rate dependence in contrast to what was observed for the halogen triangles in section 5.2.2.

The first derivative shows maxima at 0.81 T and -0.81 T which correspond to inflection points in the magnetisation data and provides a measure for the stability of the toroidal ground state. Comparing this switching field to the results of the magnetisation measurement which showed the inflection point at ca. 0.91 T reveals a significant difference. This has previously been addressed in section 5.2.2 where the differences were attributed to the measurements using single crystals compared to powder samples as well as the difference in measurement temperature. Here it is important to emphasise that higher symmetry in the crystal structure has a strong influence on single crystal measurements and no influence when using powder samples with statistically distributed random orientations of crystallites. An additional point to consider is that the inflection point in the microSQUID measurements was found to be angle dependent (see Figure 156).

The derivative field map (Figure 156, bottom left) is constructed using the angle dependent measurements and indicates a large change in magnetisation in the black areas. This shows an antiferromagnetic state at low fields with the anisotropy hexagon around it corresponding to three pairs of antiferromagnetically coupled spins. For a triangle as well as for a Dy₆ hexagon this shape is expected. However the range of accessible fields in the measurement means that the switching field was too large for the missing sides of the hexagon to be reproduced (see Figure 156 bottom left). The angle dependence measurement also indicated that the hysteresis in the middle as well as the hysteresis in the excited state opening at fields of around 0.91 T are angle dependent such that the excited state hysteresis disappears in some orientations.

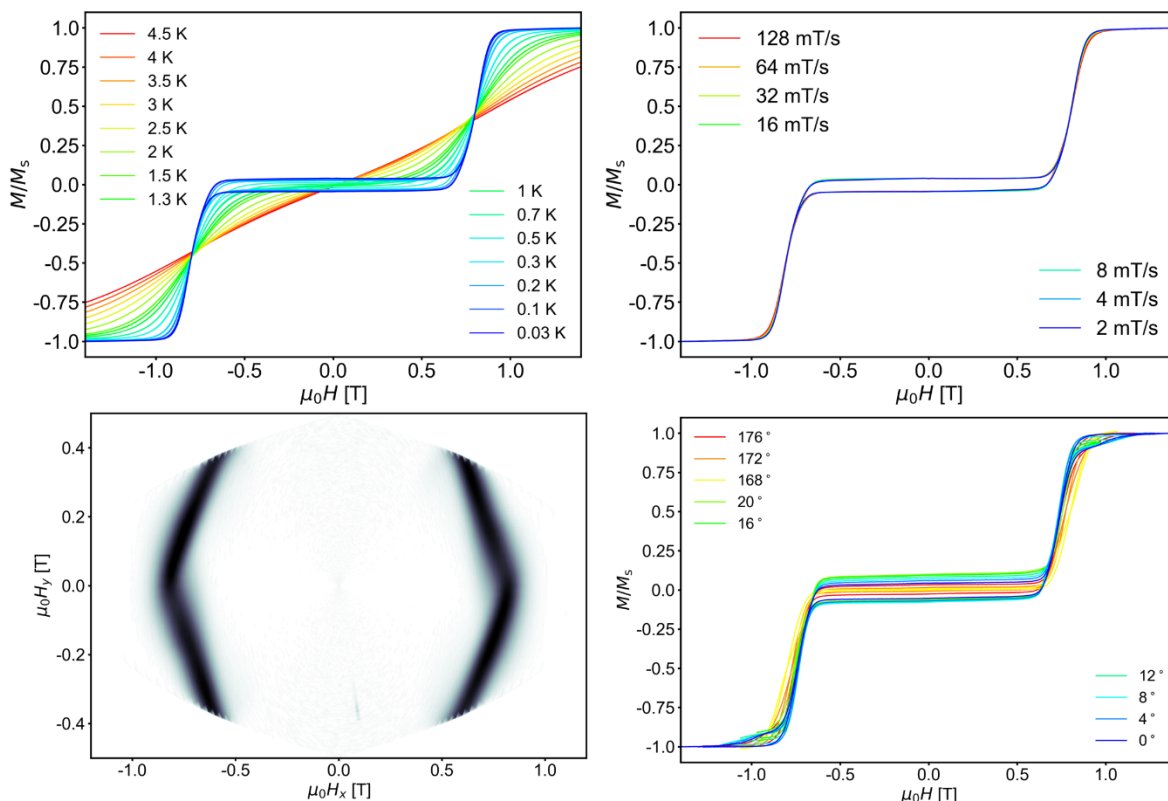


Figure 156. MicroSQUID measurements on (**Dy₃-49**) at different temperatures with a sweep rate of 16 mT/s (top left), at different sweep rates with a temperature of 30 mK (top right), derivative field map (bottom left), angle dependent measurements (bottom right).

The microSQUID data reveal some key differences to the behaviour observed for the archetypal toroidal Dy₃ with *o*-vanillin ligands (see Figure 157). For (**Dy₃-49**) no step is observed at 0.0 T. This step in the archetypal Dy₃ compound is most likely a result of partial occupation of ferromagnetic states that did not fully convert to the toroidal state when sweeping from higher fields to lower fields. This means that (**Dy₃-49**) exhibits a more efficient conversion between excited ferromagnetic states and the toroidal ground state, leading to no observable step in the middle of the hysteresis at 0 T. Another difference is the amount of magnetisation for each system in the flat almost non-magnetic ground state which is also angle dependent.

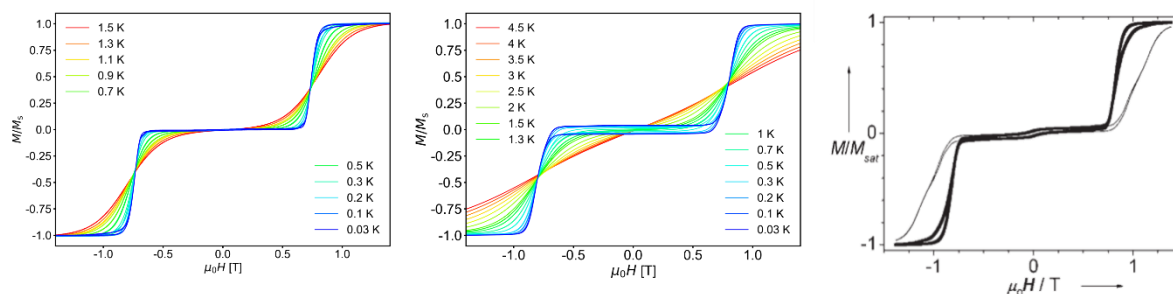


Figure 157. MicroSQUID measurements of (**Dy₃-49**) at different temperatures with a sweep rate of 16 mT/s with the field aligned with the plane of a triangle perpendicular to one anisotropy axis (left) and parallel to one of the axes (middle), in-plane and out of plane of the triangles microSQUID measurement for Dy₃ with *o*-vanillin ligands (right), adapted with permission from reference^[37] [John Wiley & Sons] copyright [2006].

Figure 158 shows three microSQUID measurements along different directions relative to the triangles in the crystal as well as one angle dependent measurement (bottom right). Each Dy₃ molecule in its toroidal ground state has a small net magnetic moment along its *z* direction which corresponds to the crystallographic *c* axes. Whether this is in the positive or the negative *z* direction depends on the orientation of the toroidal moment. In a crystal with a perfect statistical distribution of toroidal moments, as a result of the degeneracy of both states at low magnetic fields and temperatures, a net magnetic moment of 0 would be expected since all moments cancel out. This means that the almost completely closed hysteresis observed here is explained by the toroidal moments being statistically distributed. This behaviour can be seen for one of the measurements shown in Figure 158 top right as well for the archetypal Dy₃ (see Figure 157).

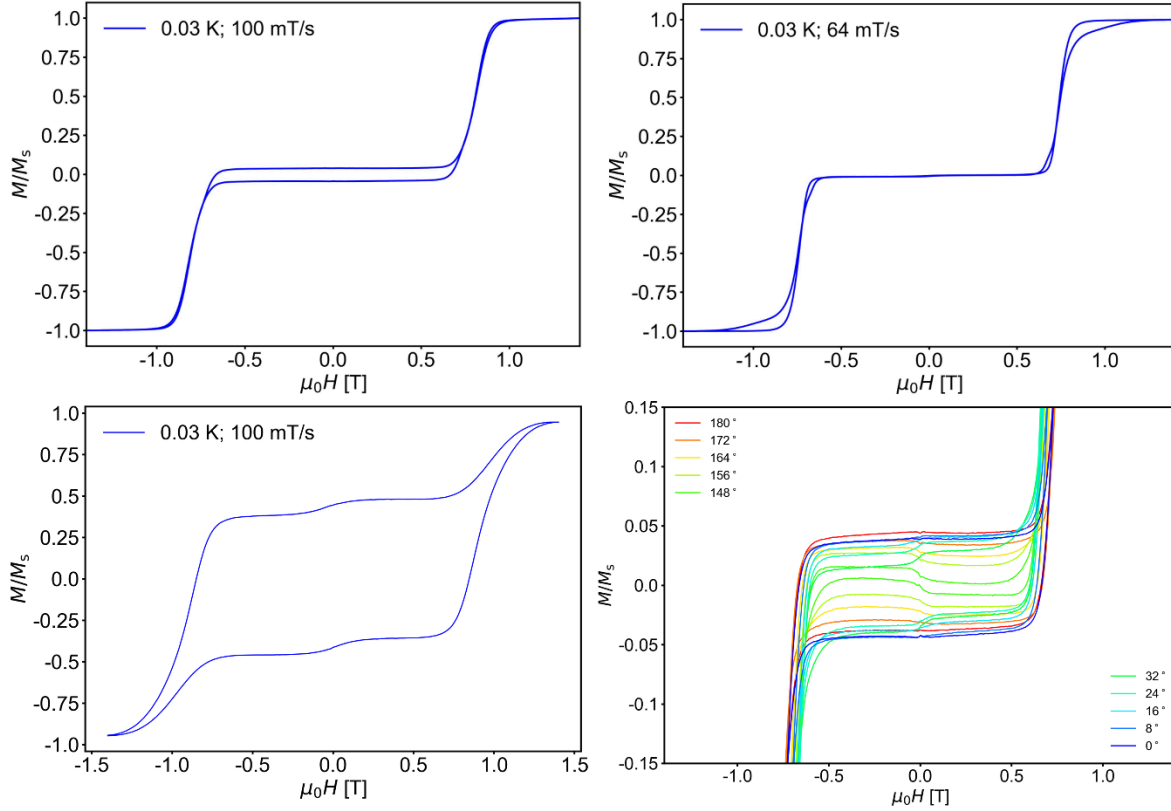


Figure 158. MicroSQUID measurements of (**Dy₃-49**) at 30 mK with a sweep rate of 100 mT/s with the field aligned with the plane of a triangle and parallel to an anisotropy axis (top left), in the plane of the triangle and perpendicular to an anisotropy axis (top right) and perpendicular to the plane of the triangle (bottom left). Excerpt of angle dependent microSQUID measurements showing the angle dependence of the hysteresis width (bottom right) the blue curve (0°) corresponds to the measurement shown in the top left.

By changing the orientation of the crystal (reorienting the crystal by hand before the measurement) or by doing angle dependent measurements (changing the direction in which the magnetic field is applied) it is possible to open up the hysteresis in the case of (**Dy₃-49**). This phenomenon can be explained through ordering of toroidal moments in the crystal using so-called chirality selection (see Figure 159). In other words applying a magnetic field along the easy axis (of the crystal), which is in plane of the triangles and parallel to one of the anisotropy axes of each triangle, forces clockwise and anticlockwise oriented toroidal arrangements to assume the same ferromagnetic state with a large in-plane magnetic moment. Subsequently reducing the field leads to the spin parallel to the applied field being “pinned” (highlighted Figure 159 right). This leads to relaxation of the system to the toroidal state defined by that pinned spin.

This theory is further supported by the Zeeman diagrams which will be discussed in section 5.4.1.2 below.

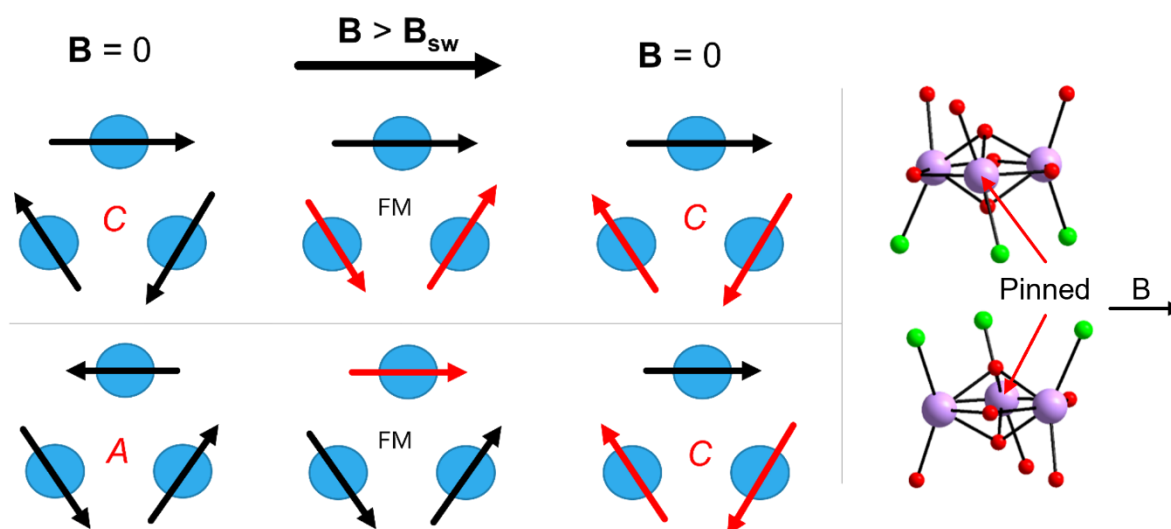


Figure 159. Schematic explanation of chirality selection with the two triangle orientations in the crystal of (**Dy₃-49**). B_{sw} is the switching field A and C are anticlockwise and clockwise, and FM is a ferromagnetic state. Red arrows indicate spins flipping through the change in applied field.

As a result of the crystal packing where the stacks along the c-axis consist of triangles arranged in an alternating fashion with their inversion related “upside down” and 60° turned counterpart, half the triangles assume a clockwise and half an anticlockwise orientation of their spins, since the “pinned” spin is on opposite sides of the triangle through the 60° rotation. This means that the toroidal moments cancel out completely. However simultaneously the net magnetic moment along the z axis is maximised as a result of the inversion symmetry and this leads to an open hysteresis loop. This has the positive effect that the result of this arrangement is observable due to its measurable net magnetic moment. On the other hand, the inversion symmetry means that the net toroidal moment will be zero.

In order to preserve a net toroidal moment and thus to be able to control it, it is necessary to maintain parallel stacks of triangles in the crystal without having inversion symmetry *i.e.* producing a crystal with only one orientation of triangles. This is a major challenge and could only be possible for example with a triangle crystallising in P1 with $Z = 1$ or in P3.

The measurement perpendicular to an anisotropy axis in the plane of the triangle shows how the random distribution of the two degenerate toroidal ground states erases the hysteresis and the magnetic moment measured at low fields becomes zero

(Figure 158 top right). Here the chirality selection cannot operate meaning that no “pinning” will occur and no specific toroidal direction will be preferred when relaxing.

In the case of the measurement in Figure 158, bottom left which shows the largest hysteresis loop the field was applied along the crystallographic c axis. Here the toroidal states (clockwise and anti-clockwise) split due to their magnetic z components and are thus no longer degenerate. The maximum magnetic moment which can be obtained will be the combined z component of all triangles. This situation is almost achieved in the measurement (see Figure 158) where the magnetisation in the hysteresis is now at 0.5 M/Ms. There is a very small step at 0 T which might arise from a minor population of ferromagnetic states. The observed behaviour still indicates flipping of spins and the involvement of ferromagnetic states. This could be, for example, a result of a small amount of twinning within the single crystal or else problems in perfectly aligning the single crystal along the c axis.

In conclusion Figure 158 top left where the crystal is aligned such that the measurement is performed along the easy axis indicates that relaxation to one of the two possible toroidal ground states is preferred leading to the open hysteresis. On the other hand Figure 158 top right shows that aligning perpendicular and in-plane of the triangle annihilates the open hysteresis since there is no preferred toroidal ground state to relax to. Tunnelling from one toroidal state to the other does not occur at low fields since relaxation to the completely non-magnetic random distribution of toroidal states does not occur within the time frame of the measurement.

5.4.1.2 (Dy₃-49) – Quantum chemical calculations

Theory calculations were performed on (Dy₃-49) in collaboration with Prof. Dr. Alessandro Soncini from the University of Padova. Broken-symmetry DFT calculations were used to evaluate the Dy^{III}-Dy^{III} exchange coupling constants and scalar relativistic CASSCF/RASSI-SO/SINGLE_ANISO calculations were used to calculate single ion 4f states and magnetic anisotropy axes. The results of these calculations were used to parameterise the Hamiltonian of the magnetically coupled system in a magnetic field leading to the Zeeman diagrams for three different field directions in relation to the Dy₃ unit.

The calculated Dy-Dy coupling of $J_{\text{Dy-Dy}} = -0.40 \text{ cm}^{-1}$ (using a $-2J$ Hamiltonian) is antiferromagnetic and relatively strong producing a single Kramers' doublet in the ground state described by a toroidal moment with a vanishingly small magnetic moment along the C_3 axis. The first excited state consisting of three Kramers' doublets displays a large almost in-plane magnetic moment parallel to one of the three easy axes which are nearly co-planar to the plane of the triangle.

The g tensors and energy levels of the first eight Kramers' doublets are shown in Table 11.

Table 11. g tensors and energy levels for the eight lowest Kramers' doublets in (**Dy₃-49**).

	Energy (cm^{-1})	g_x	g_y	g_z
KD1	0	0.0335	0.0689	19.64
KD2	102.75	0.4716	0.6509	17.11
KD3	142.98	3.376	4.630	12.25
KD4	184.81	9.116	5.138	0.7050
KD5	238.64	9.402	5.999	0.6418
KD6	288.58	2.174	4.383	13.48
KD7	386.68	0.2407	0.4878	19.02
KD8	452.03	0.0630	0.1505	19.36

The direction of the principle magnetic axis of the g -tensor for KD1 (the ground state) is essentially in the plane of the triangle with a deviation of $\alpha = 8.2^\circ$ from the plane and a deviation $\beta = 14.7^\circ$ of its in-plane projection from the tangential direction (see Figure 160). Figure 160 also shows the easy axes and intermediate axes through the triangle plane and the third axis along the crystallographic c axis. The easy axes are oriented parallel to the anisotropy axes of the Dy^{III} ions while the intermediate axes are oriented orthogonally.

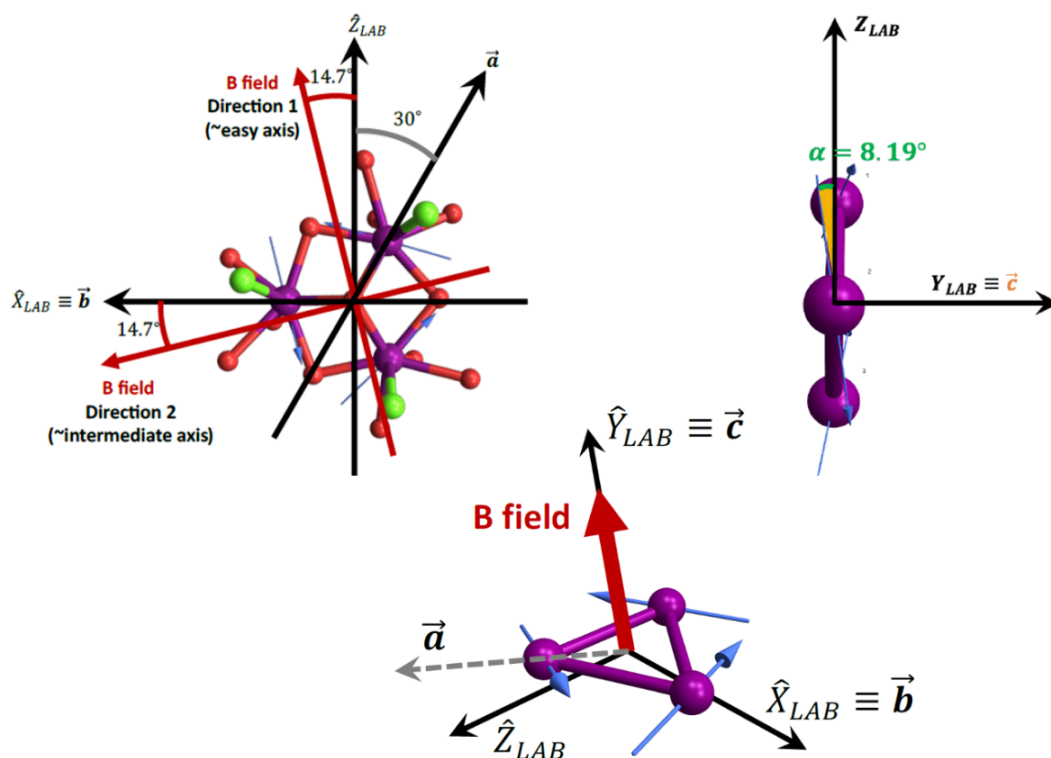


Figure 160. Scheme representing the two in-plane orientations of the magnetic fields intercepting the in-plane projection of the easy axes in the triangle (direction 1) and intermediate axis (direction 2) (top left), angle α and alignment of the Y lab axis with crystallographic c axis (top right), third axis perpendicular to the triangle plane (bottom). For all axes shown here (direction 1, 2 and perpendicular to the triangle plane) a Zeeman diagram is shown in Figure 161.

The Zeeman diagrams in Figure 161 show the effect of the applied field along the three axes (easy axis, orthogonal intermediate axis in-plane, and along crystallographic c axis) explained above.

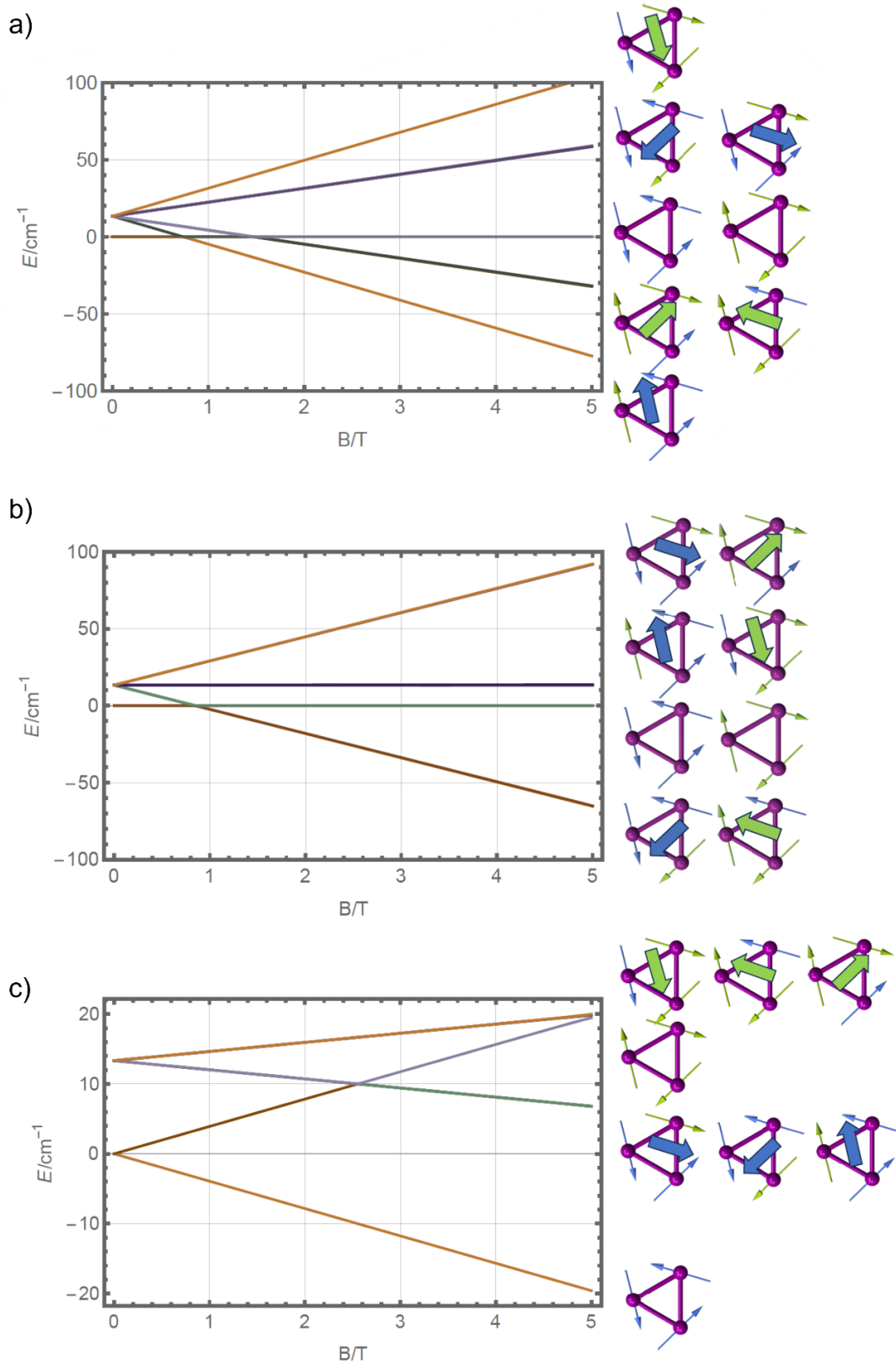


Figure 161. Zeeman levels for a field B parallel to the in-plane projection of one anisotropy axis (easy axis) of Dy_3 in a), for B perpendicular to the in-plane projection of one easy axis of Dy_3 (intermediate axis) in b), for B aligned with the crystallographic c -axis, and thus perpendicular to the Dy_3 plane in c). Related microSQUID is shown in Figure 158 top left for a), top right for b) and bottom left for c).

The microSQUID data shown in section 5.4.1.1 suggest the presence of a pinning effect which was hypothesised to be the result of chiral selection. This hypothesis is further justified given the difference in behaviour shown in the two Zeeman diagrams along in-plane axes in Figure 161. This indicates that the system relaxes from a single excited ferromagnetic state for fields applied parallel to an anisotropy axis (easy axis Figure 161). In contrast when the field is applied perpendicular to an easy axis (intermediate axis Figure 161) it can relax from one of two degenerate ferromagnetic states. The fact that the system relaxes from a single excited ferromagnetic state suggests that the relaxation to one of the two degenerate toroidal ground states is preferred as a result of relative spin orientation (see Figure 158 top). In effect this pins one spin during relaxation. The third Zeeman diagram suggests a theoretically feasible microSQUID measurement which would use a field along the same direction and would show an open hysteresis with a coercive field going beyond the measuring range of -1 T to 1 T *i.e.* two parallel lines.

5.4.1.3 Dy₃-Hbovh – Torque magnetometry

Cantilever torque magnetometry measurements were performed in collaboration with Leonardo Tacconi in the group of Prof. Dr. Mauro Perfetti at the University of Florence. Magnetic torque (τ) is a rotational force of a magnetic dipole moment m to align with a local magnetic field B . This can be mathematically expressed using the vector product of the magnetic moment m_n for atom n and B with the angle ϕ_n between m_n and B .^[187]

$$\tau_n = m_n \times B = m_n B \sin \phi_n \quad \text{equation 15}$$

In a compound with more than one magnetic centre the formula can be adapted to include the sum over all N magnetic moments m_n resulting in:

$$\tau = \sum_{n=1}^N (m_n \times B) = M \times B = M B \sin \phi \quad \text{equation 16}$$

Where τ has the unit Nm and is orthogonal to both vectors M and B . The torque vanishes when M and B are parallel which happens when the field is aligned with the easy axis of the molecule. This will be visible in the data as an x-axis intercept and is often referred to as “easy zero”. Similarly, when the field is applied perpendicular to

the easy axis, since no components of B are oriented along the easy axis, the sample is poorly magnetised in the B direction which results in a τ of zero (“hard zero”).^[187]

During a measurement the magnetic field is static with no changes in direction. The crystal is rotated in a clockwise direction in relation to the axis of rotation. The axis of rotation is orthogonal to the magnetic field as shown in Figure 162.



Figure 162. Rotational axis (red dot, oriented into the paper plane) and direction of B field with θ being the angle the sample was rotated from the origin (aligned with B).

For this measurement an orthogonal reference frame $ab'c^*$ is used where a is the crystallographic a axis, c^* is the vector orthogonal to the ab plane which for (**Dy₃-49**) is exactly the crystallographic c axis and b' is the axis orthogonal to a and c^* . For the measurement great precision and the knowledge of the exact orientation of the crystal in both the laboratory XYZ and the orthogonal reference frame are necessary which requires indexing a suitable crystal before the measurement.

For the characterisation of (**Dy₃-49**) two orientations of the crystal were measured. The resulting molar torque of the sample has the unit Nm/mol , however, as a result of the small size of the crystal it was not possible to determine exactly the mass of the crystal which was thus approximated. This approximation could make the use of a scale factor necessary in any graph shown.

A single crystal of (**Dy₃-49**) was selected and indexed using single crystal XRD to determine the relative position of the lattice planes described by their respective Miller indices. Figure 163 shows a schematic drawing of the first orientation as well as a picture of the actual crystal on the cantilever. The scheme includes the determined hkl indices for the lattice planes and the direction in which the magnetic field B is applied.

From the lattice planes it was possible to determine the relative orientation of the crystallographic c axis (c^*), the angle between c and the B field as well as vectors \vec{V} and \vec{Y} which correspond to the axis of the magnetic field at 0° and the axis of rotation respectively.

$$\vec{V} = [-0.5764, 0.3328, 0.7463]$$

$$\vec{Y} = [0.6108, 0.7819, 0.1230]$$

equation 17

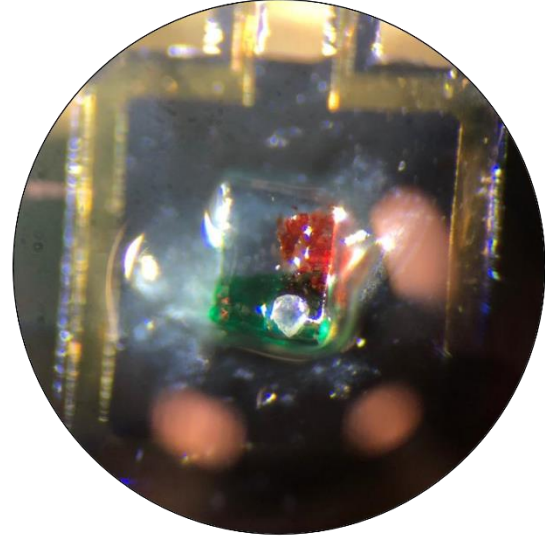
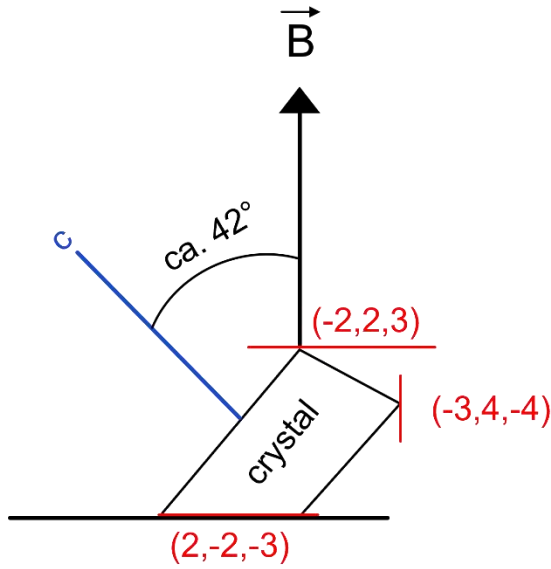


Figure 163. Scheme showing the orientation of the crystal lattice planes in relation to the B field (left). Picture of the chosen and indexed crystal on the cantilever under a microscope (right).

A rotation of \vec{V} by 42° and 132° gives the two vectors \vec{v}_1 and \vec{v}_2 which show that this orientation of the crystal allows for a rotation in a plane that nearly contains the c axis.

$$\vec{V} \cdot R_{\vec{Y}}(42^\circ) = \vec{v}_1 = [-0.065, -0.105, 0.9922]$$

equation 18

$$\vec{V} \cdot R_{\vec{Y}}(132^\circ) = \vec{v}_2 = [0.7889, -0.614, -0.0134]$$

\vec{v}_1 almost matches the c axis and \vec{v}_2 is almost in the **ab** plane (about 38° from the a axis and 128° from the b' axis).

Measurements for this first rotation were performed at 2 K and various magnetic fields between 1 T and 9 T (see Figure 164). The first x-axis intercept of τ is at 45° which is in good agreement with the angle between the projection of the c^* axis and the magnetic field shown before in Figure 164. Furthermore, the c^* axis represents a hard axis for the structure while the plane perpendicular to it represents an easy direction.

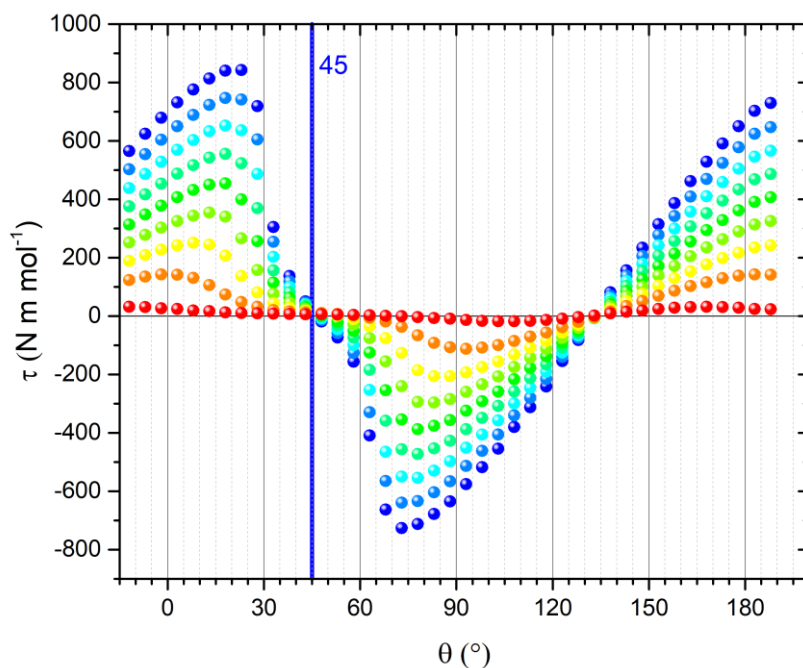


Figure 164. Magnetic torque measurement for (**Dy₃-49**) at 2 K and magnetic field between 1 T (red dots) and 9 T (blue dots). The first 0 for the torque is indicated by a blue line at 45°.

Figure 165 shows further measurements for this crystal rotation at higher temperatures (5 K and 10 K) and fields of 4 T to 6 T and 5 T to 7 T respectively. The feature (flattening at close to 45°) observed in the 2 K measurement which is still visible at 5 K has almost completely vanished at 10 K. This feature is important for the evaluation as it gives additional information on the anisotropy of the system.

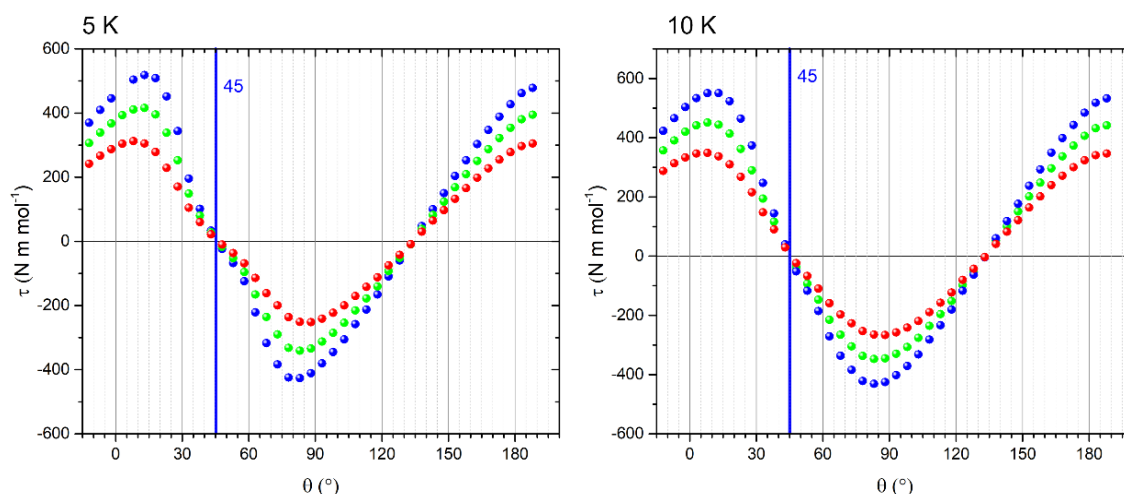


Figure 165. Magnetic torque measured for (**Dy₃-49**) at 5 K and 4 T to 6 T (left) and at 10 K with fields between 5 T to 7 T (right).

A second rotation was performed with the goal of aligning the rotation axis \vec{V} exactly with the c^* axis which corresponds to a rotation in the ab' plane. This was achieved by positioning the crystal as shown in Figure 166. The rotation axis now coincides with the c^* axis resulting in the following vectors \vec{V} and \vec{Y} .

$$\vec{V} = [0.8660, -0.5000, 0.0000]$$

$$\vec{Y} = [0.0000, 0.0000, 1.0000]$$

equation 19

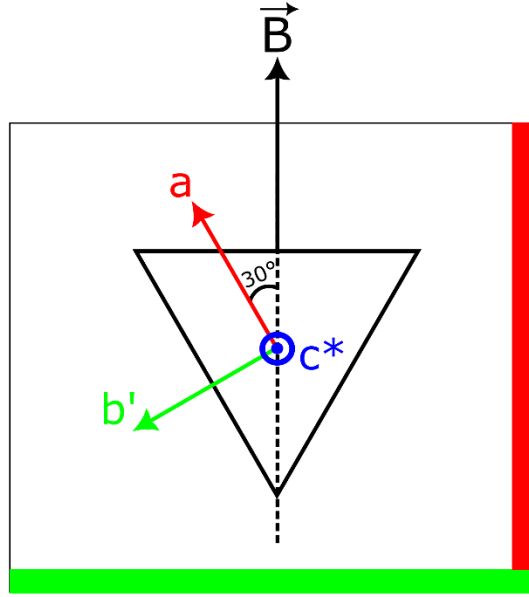


Figure 166. Crystal (triangular face indicating the lattice plane perpendicular to the c^* axis) orientation in relation to the B field. Green and red stripe are visual aids for the experimental alignment of the crystal.

The measurement was performed at 2 K for magnetic fields between 1 T and 9 T (see Figure 167). The first x-axis intercept of τ is at about 15° and represents a hard axis as indicated by the change from positive to negative τ while about 30° from it is the easy axis. The different amplitudes of the oscillations may be due to experimental misalignment. Figure 167 illustrates the positions of the hard and easy axis in relation to the $ab'c^*$ reference frame.

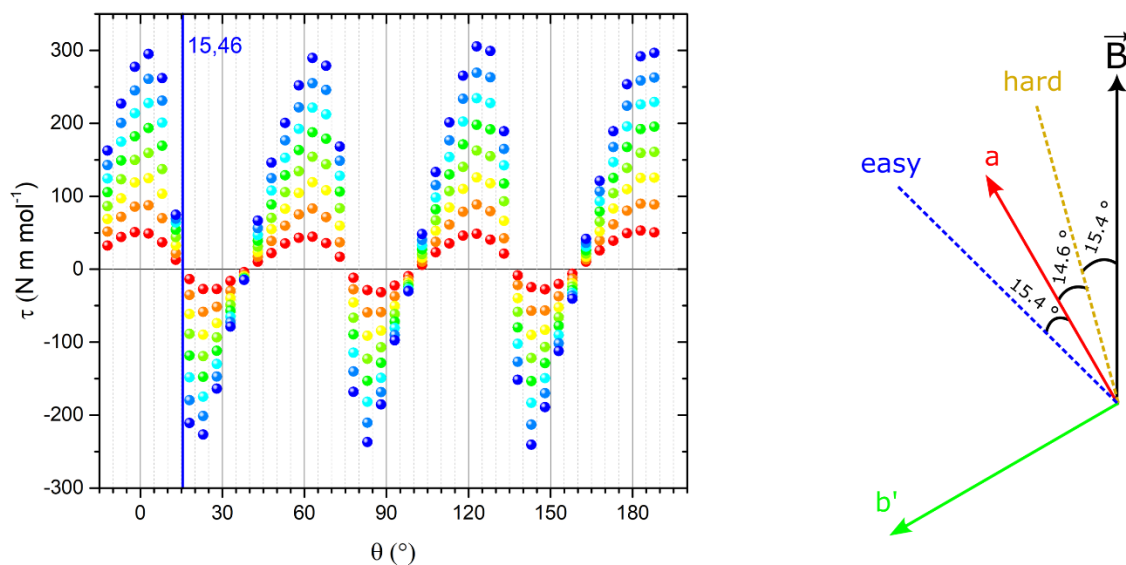


Figure 167. Magnetic torque measurement of (**Dy₃-49**) at 2 K and fields between 1 T and 9 T (left), representation of in-plane experimental axis (right). First zero at ca. 15° indicating a hard axis highlighted (blue line).

The results of the same measurement at higher temperatures and different fields are shown in Figure 168. Here the shape of the curves remains the same over the measured temperature range with a reduction in the torque.

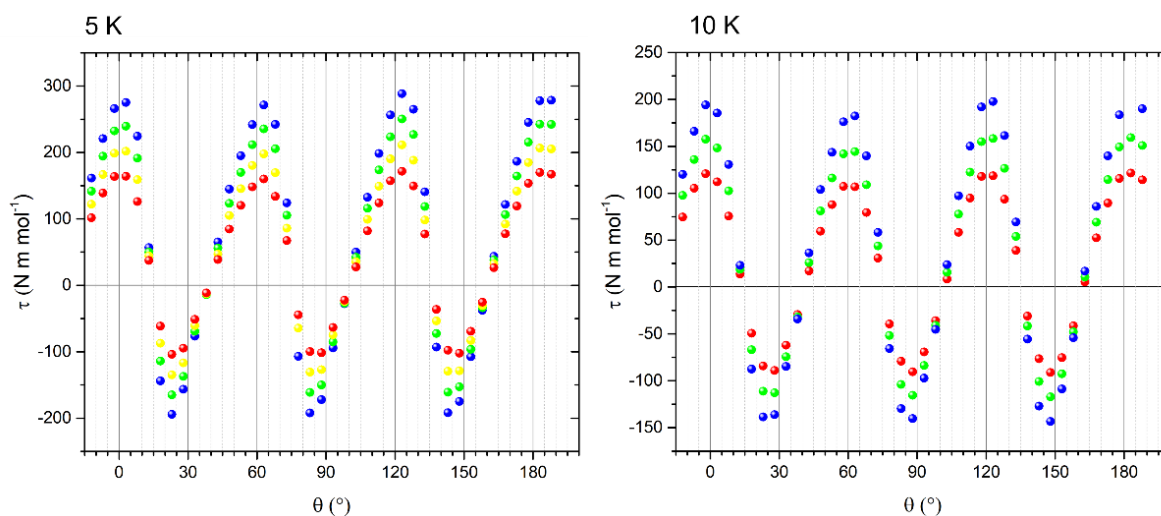


Figure 168. Magnetic torque measurements for (**Dy₃-49**) rotating in the **ab** plane with fields of 6 T to 9 T for the 5 K measurement (left) and 7 T to 9 T for the 10 K measurement (right).

To determine the orientation of the easy axis from these measurements high field modelling with three axial spins $S = \frac{1}{2}$ with g tensor $[0 \ 0 \ 20]$, neglecting magnetic exchange was performed. The resulting fit and the determined Euler angles ψ , ξ and ρ are shown in Figure 169 and table 12.

Table 12. Euler angles extracted from evaluation of high field modelling for the magnetic torque measurements of (**Dy₃-49**).

Spin	1	2	3
ψ	12	132	252
ξ	96	96	96
ρ	0	0	0

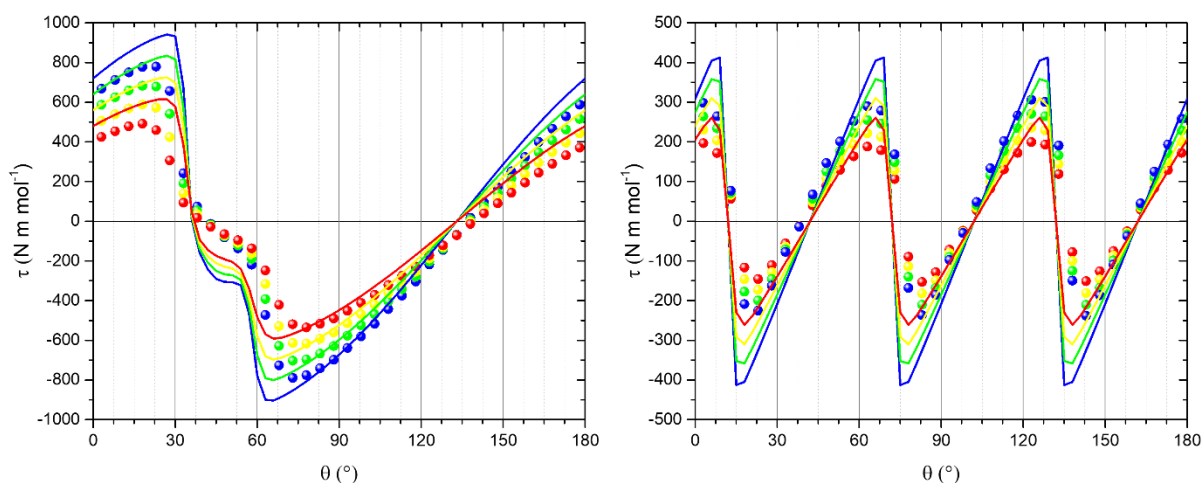


Figure 169. High field modelling fit of magnetic torque measurements of (**Dy₃-49**) for both measured rotations (in a plane nearly containing the c axis (left) and rotation in *ab'* plane (right)).

The Euler angles indicate the rotational transformations of the easy axis from the reference frame to the molecular frame with a starting point of complete alignment with the *c** axis. This results in the direction of the easy axes which are close to the plane with a deviation of 6° (α) and oriented along the tangential direction with an angle of 12° (β) (see Figure 170). These angles are in line with what has been reported in the literature for toroidal systems. The Dy₃ with *o*-vanillin ligands from 2006^[37, 39] has its three anisotropy axis tilted out of the plane at angles of -4.3°, 8.8° and -2.4° for the three individual Dy^{III} centres. The deviation from the tangential is 8.87°, 9.49° and 8.72° in this case.^[38]

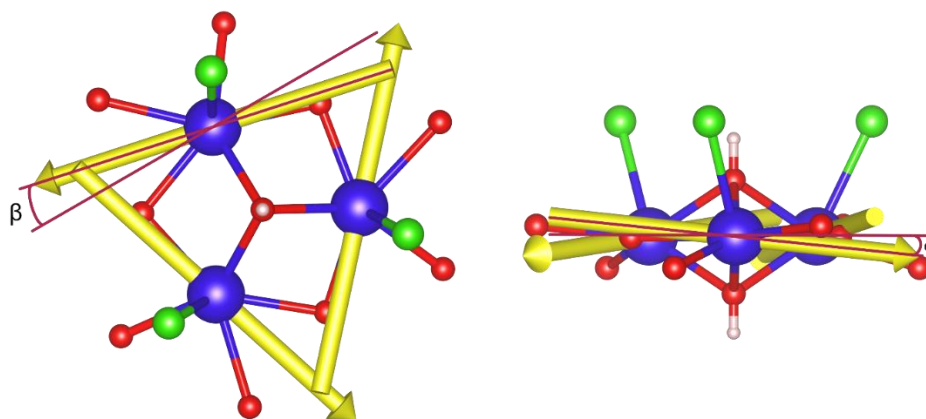


Figure 170. Anisotropy axis (yellow arrows) for (**Dy₃-49**) obtained from magnetic torque measurements. Top-down view on Dy₃ core along c* axis (left) and side view in the ab' plane (right).

An improved fit to the experimental data can be achieved using a Hamiltonian with spins = 15/2, crystal field parameter D and E and magnetic exchange coupling J. The work on these theoretical calculations is conducted in collaboration with Prof. Dr. Alessandro Soncini from the University of Padova but could not be completed during the timeframe of this thesis and are subject to an ongoing investigation

These experimental results prove the system to have an in-plane vortex-like arrangement of spins resulting in a toroidal ground state.

5.4.2 Variations on the Schiff base ligand

During this work it became clear that changing the substituent on the benzaldehyde part of the Schiff base ligand can influence the crystal packing. Furthermore, the changes to the ligand could indirectly influence the distribution of terminal chloride ligands. Both of these influences are important. The simplification of the system by crystallisation in a higher symmetry space group makes it possible to perform measurement that are easier to interpret. Furthermore, the distribution of charged terminal ligands on the triangular Dy₃ motif determines whether or not it has a toroidal ground state.^[172]

In order to explore the effects of the substituents on the aldehyde unit of the Schiff base ligand, three main approaches were tested. The first gauges the effect of substitution in *ortho*-, *meta*- or *para*-position by the use of the respective fluoro-

benzaldehyde. The second utilises hydroxy and methoxy substitution to study the effect of adding additional oxygen donor groups which may also partake in hydrogen bonding. The third and final approach uses chiral aldehydes to force the system to crystallise in an acentric^[232] space group. Thereby removing the inversion centre in the crystal packing in order to get closer to an ideal triangular compound with just one orientation of Dy₃ triangle in the crystal. An ideal example for this would be a compound crystallising in P1 with one single molecule in the unit cell.

5.4.2.1 Dy₃ Triangles with fluoro-substituted benzaldehydes

To gauge the influence of fluoro substitutes in different positions on the benzaldehyde ligand, the same synthetic procedure was employed as for (**Dy₃-49**) but using *para*-fluorobenzaldehyde (**Dy₃-59**), *meta*-fluorobenzaldehyde (**Dy₃-60**) and *ortho*-fluorobenzaldehyde (**Dy₃-61**) instead of plain benzaldehyde.

Compound (**Dy₃-59**) [Dy₃(Hpfbovh)₃(μ₃-OH)₂(MeOH)(H₂O)Cl₄]·4MeCN·4MeOH (Hpfbovh = Hbovh + *p*-F substitution) crystallises in the triclinic space group P $\bar{1}$ with Z = 2. The molecular structure is shown in Figure 171. The coordination environment of the Dy₃ unit is, apart from the terminal ligands, the same as described for (**Dy₃-49**). The terminal ligands in this case consist of four Cl⁻ ligands, three of which coordinate above the plane of the triangle while the fourth and one coordinating water and methanol molecule complete coordinate on the opposite side. Figure 172 shows the packing along the three crystallographic axes.

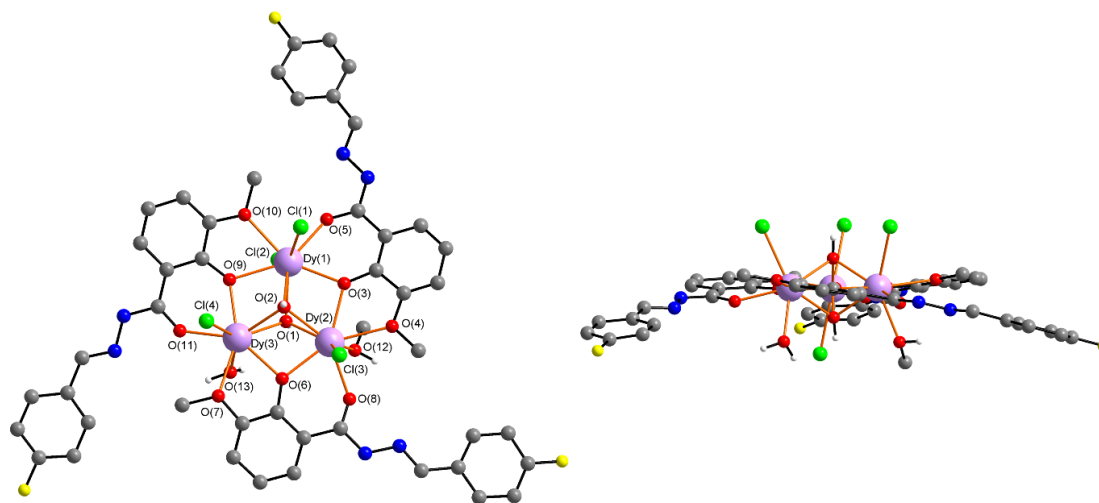


Figure 171. Top (left) and side view (right) of the molecular structure of (**Dy₃-59**).

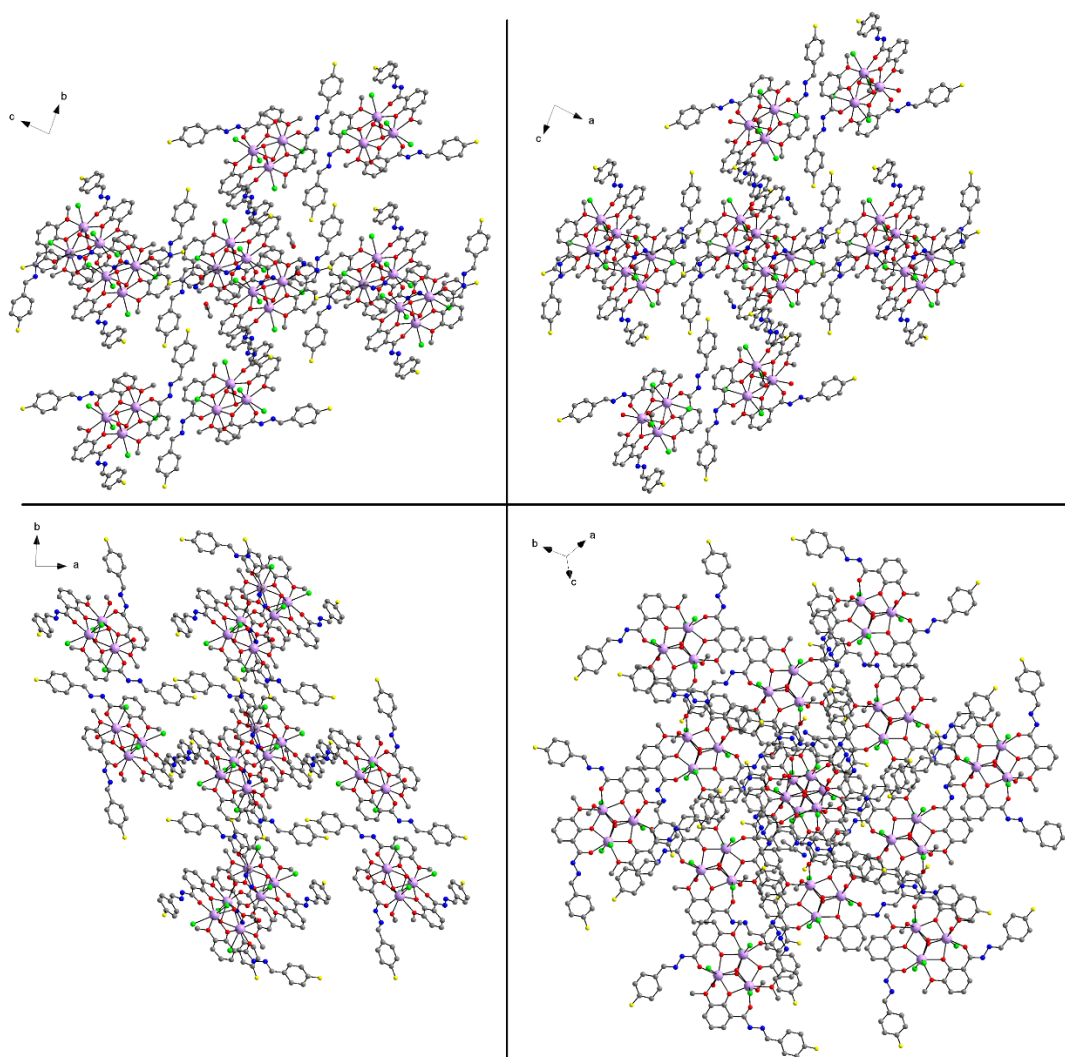


Figure 172. Packing along crystallographic *a* (top left), *b* (top right) and *c* (bottom left) axis as well as an additional view for (**Dy₃-59**) (bottom right).

The packing is dominated by hydrogen bonding which is similar to the situation in (**Dy₃-49**). The similarity is a result of the hydrogen bonds connecting the three terminal chlorides (Cl(1), Cl(3), Cl(4)) on one side of the triangle to N-H hydrogens on the ligand of neighbouring molecules forming what is essentially a plane of hexagons throughout the crystal. The neighbouring molecules are inverted alternating between the triangle face with three terminal Cl⁻ ligands being on top and below the plane which allows for the formation of the same type of hydrogen bond in both directions (see Figure 173 left). The main difference to (**Dy₃-49**) is the formation of a 3D network by linking planes through an additional set of hydrogen bonds involving Cl(2) on the other side of the triangle and the hydrogens on the water ligand O(13) (see Figure 173 bottom right). The MeOH solvent molecules in the lattice form hydrogen bonds with N(4) and OH (O(12)) but are not involved in any further intermolecular interactions.

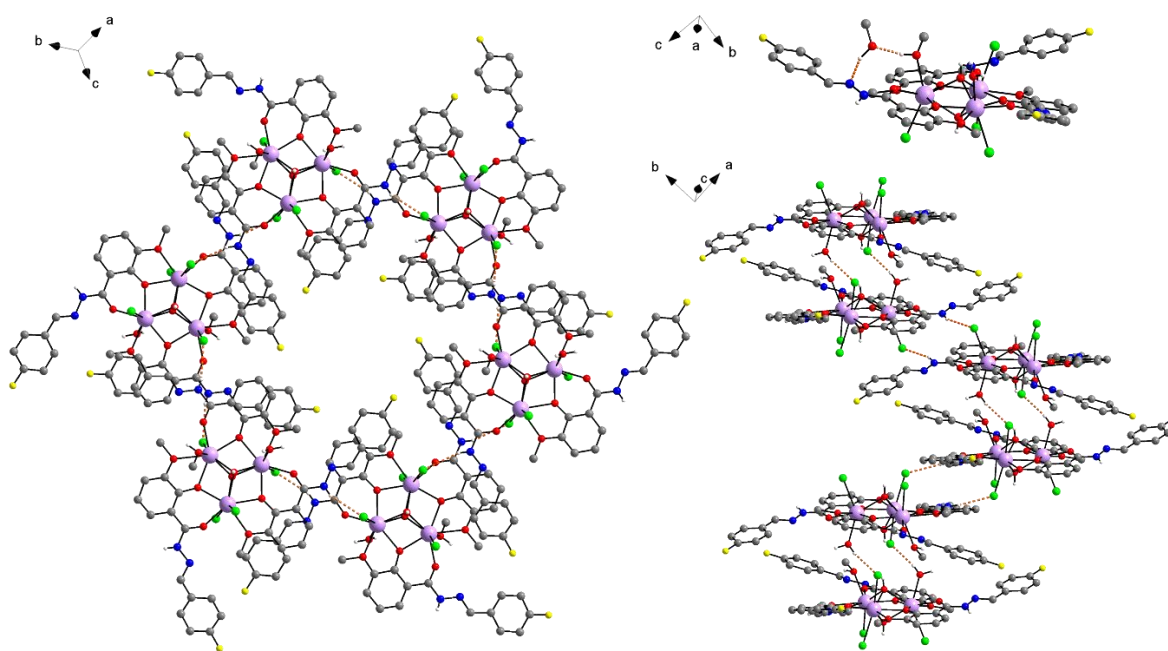


Figure 173. Hydrogen bonds in plane (left), with solvent molecules (top right) and along chain (bottom right) for (**Dy₃-59**).

In air (**Dy₃-59**) rapidly loses its crystallinity, which is likely to be a result of a loss of solvent molecules or exchange of MeOH ligands for water. Because of this, single crystal XRD measurements proved challenging. Putting the crystals into perfluoroether oil together with some mother liquor to keep the exposure to air to a minimum proved to be the most effective strategy to obtain a usable data set. This issue meant that for the PXRD measurements it was necessary to prepare the sample in a capillary tube rather than a disc in order to keep the crystallites in the mother liquor. Overcoming these challenges, allowed the purity of (**Dy₃-59**) to be confirmed *via* PXRD as shown from the results presented in Figure 174. The experimental diffractogram is slightly shifted and the small “hill” towards higher angles is an artefact from the capillary.

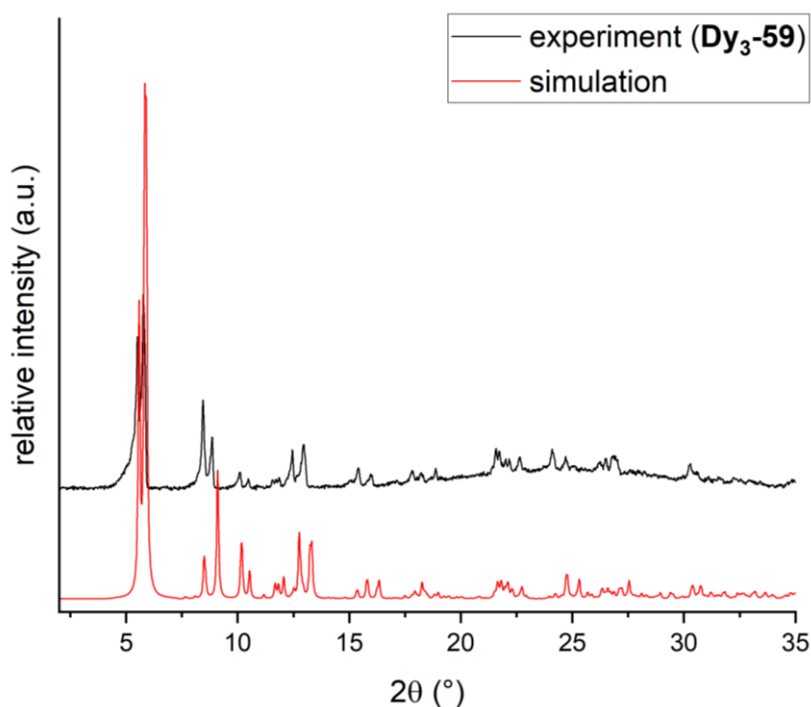


Figure 174. Simulated and experimental powder pattern for (**Dy₃-59**).

In order to investigate whether any further decomposition of the compound occurs (apart from the loss of crystallinity), IR measurements on (**Dy₃-59**) were performed immediately after taking it out of solution and additionally after 1 minute and after 5 minutes in air. The results are shown in Figure 175 and indicate that the compound does not decompose since the vibrations associated with the molecular structure do not change. This behaviour was further investigated using elemental analysis, which showed that similar to other Dy₃ compounds here and also in the literature,^[37] (**Dy₃-59**) takes up water from the air. This does not significantly influence the molecular structure or the magnetic/toroidal properties of the system. This behaviour has to be kept in mind when evaluating magnetic data since the value of the molecular mass is an important parameter.

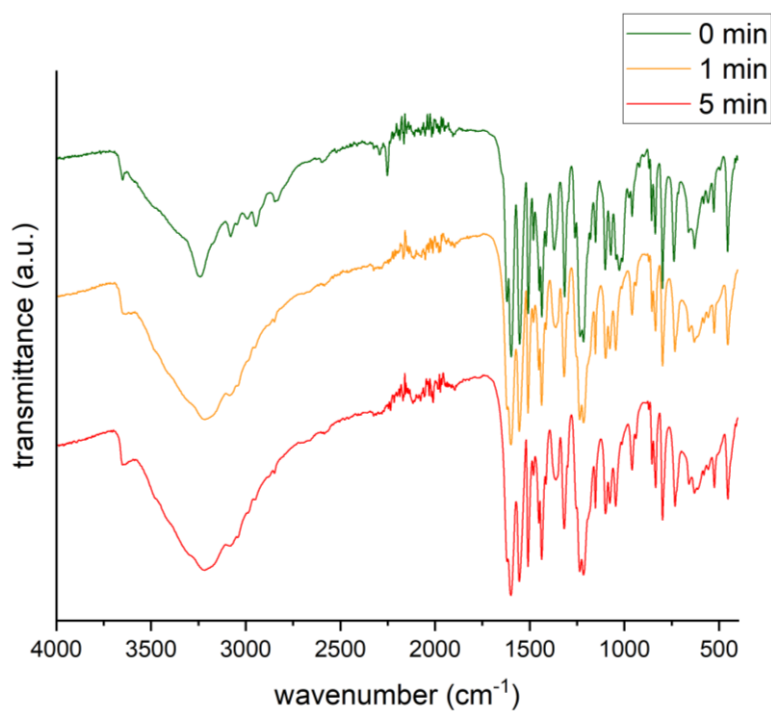


Figure 175. IR measurements immediately, 1 min and 5 minutes after taking the crystals of (**Dy₃-59**) out of the mother liquor.

The synthesis was repeated with the DyCl₃·6H₂O exchanged for LnCl₃·n(H₂O) (Ln^{III} = Y^{III}, Gd^{III}, Tb^{III}, Ho^{III}, Er^{III}, Tm^{III}, Yb^{III}) and yielded compounds (**Y₃-60**), (**Gd₃-61**), (**Tb₃-62**), (**Ho₃-63**), (**Er₃-64**), (**Tm₃-65**) and (**Yb₃-66**). PXRD measurements of these compounds prove them to be isostructural to the Dy^{III} analogue. Furthermore, IR measurements were performed showing essentially identical spectra for these compounds (see Figure 176).

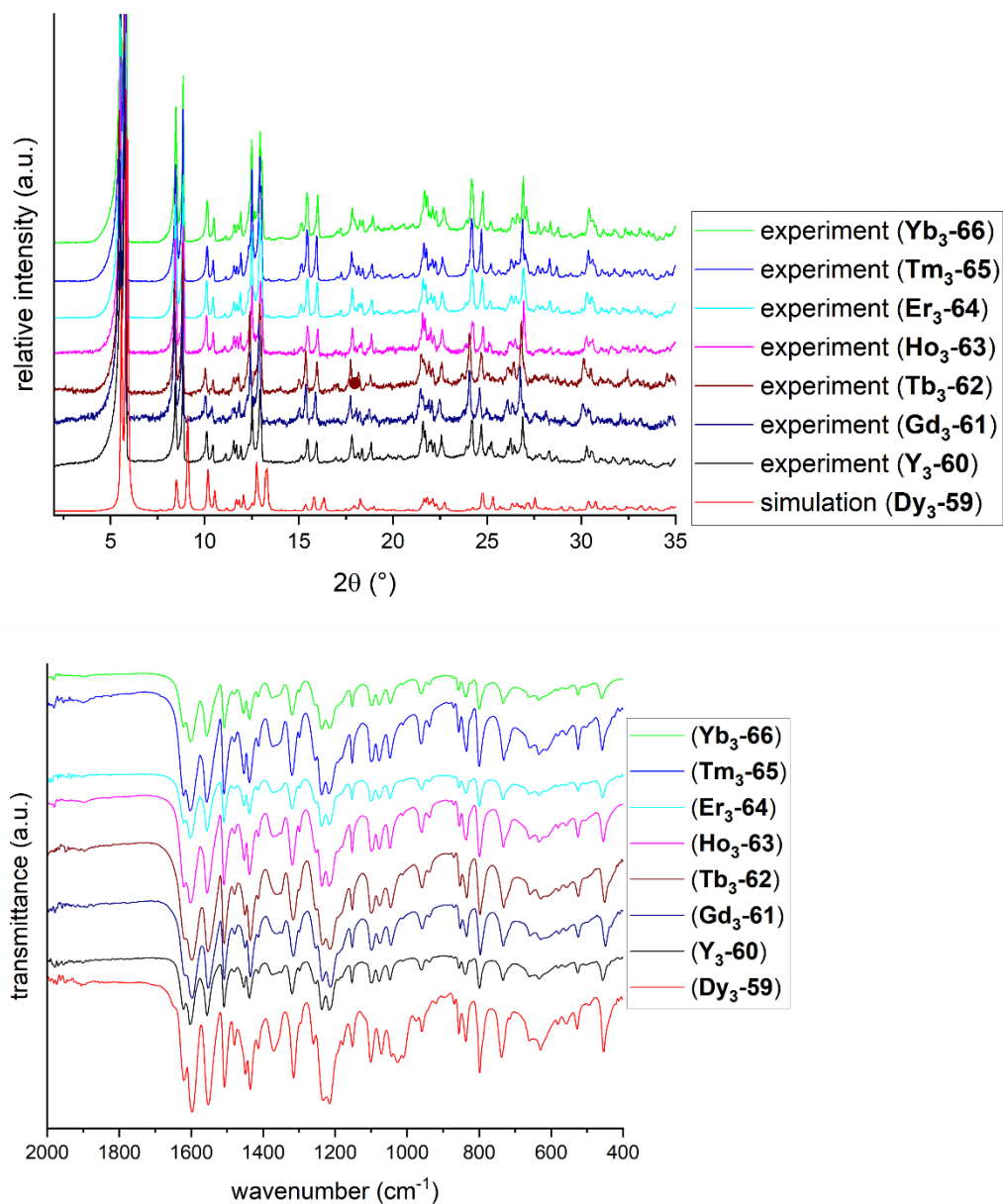


Figure 176. Experimental powder pattern of compounds (**Y₃-60**) to (**Yb₃-66**) with simulation of (**Dy₃-59**) (top). IR spectra of compounds (**Dy₃-59**) to (**Yb₃-66**) (bottom).

The same synthetic procedure but exchanging *p*-fluorobenzaldehyde for *m*- and *o*-fluorobenzaldehyde yielded crystals of (**Dy₃-67**) with the formula [Dy₃(Hmfbovh)₃(μ₃-OH)₂(MeOH)₃Cl₃]Cl·1.5MeCN·0.5MeOH and (**Dy₃-68**) with the formula [Dy₃(Hofbovh)₃(μ₃-OH)₂(MeOH)₃Cl₃]Cl·2MeOH, respectively. Both molecular structures are shown in Figure 177.

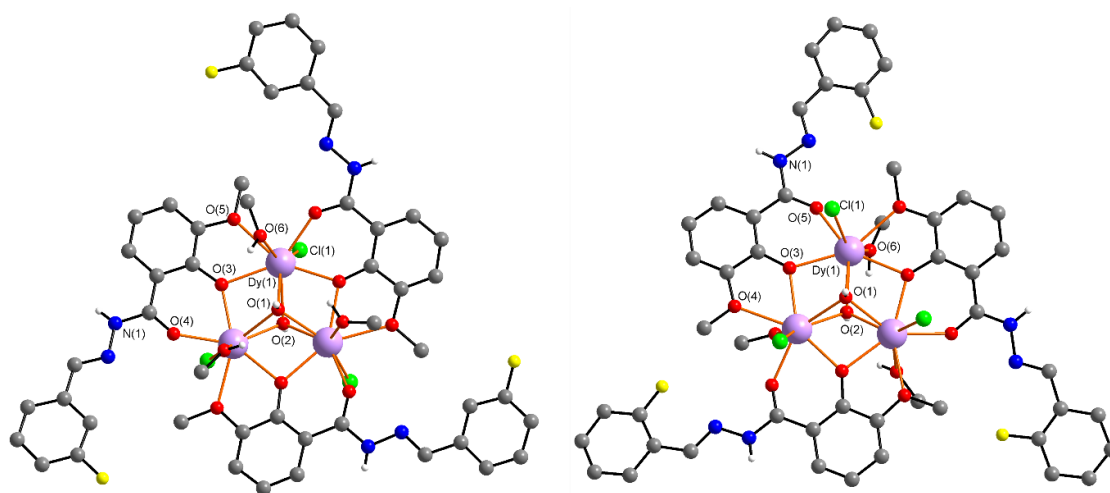


Figure 177. Molecular structure of (**Dy₃-67**) (left) and (**Dy₃-68**) (right).

Both compounds crystallise in the trigonal space group $R\bar{3}$ with $Z = 6$ and are isomorphous to (**Dy₃-49**) described above with the benzaldehyde ligand. The intermolecular interactions are also the same as described for (**Dy₃-49**) *i.e.* forming a two dimensional network through hydrogen bonding between the terminal chlorides and the hydrogen on N(1). For (**Dy₃-67**) the data set was of high enough quality to be able to refine the solvent molecules. These are disordered above the “chloride side” of each triangle and below the chloride counterions on the “MeOH side” (see Figure 178).

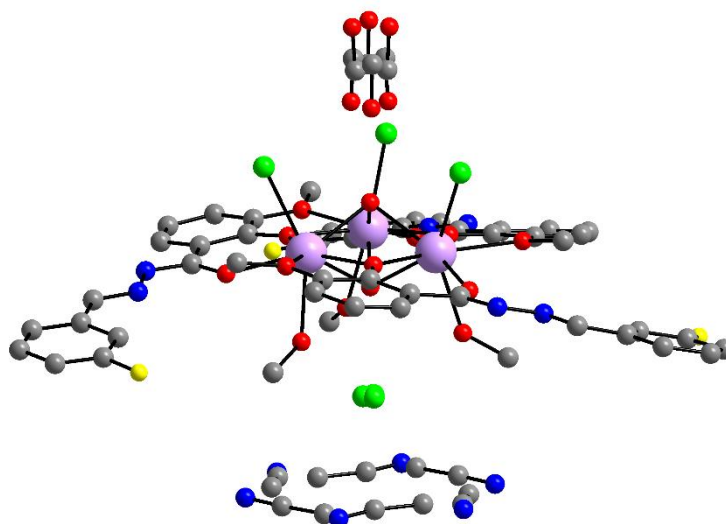


Figure 178. Disorder of solvent molecules (MeOH/MeCN) in (**Dy₃-67**).

This situation leads to an additional set of hydrogen bonds forming between the hydrogen on O(2) and the oxygen of the sixfold disordered MeOH. This leads to a

connection between the 2D planes and between two triangles in a stack (see Figure 179).

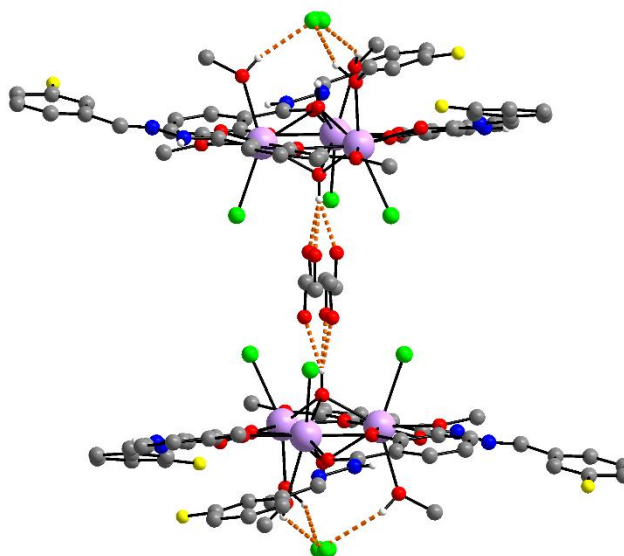


Figure 179. Intermolecular interactions between solvent molecules and counterions forming pairs of two molecules of (**Dy₃-67**) in the stacks in the crystal structure.

The molecules in a stack along the *c* axis are closer to each other than in (**Dy₃-49**) with the closest Dy⋯Dy distance in the stack being 10.2608(8) Å for (**Dy₃-67**) and 14.0756(9) Å for (**Dy₃-49**). The closest Dy⋯Dy distance between stacks stays essentially the same as that for (**Dy₃-49**) as may be expected as a result of the similar hydrogen bonding network.

The synthesis of (**Dy₃-68**) requires further optimisation since the procedure described here only led to a very low yield which made measurements other than single crystal XRD impossible. For the compounds using *m*-fluorobenzaldehyde lanthanide variations were tested. For this purpose, the DyCl₃·6H₂O was exchanged for LnCl₃·H₂O with Ln = Y^{III}, Sm^{III}, Eu^{III}, Tb^{III}, Ho^{III}, Er^{III}, Tm^{III}, Yb^{III}. This yielded compounds (**Y₃-69**), (**Sm₃-70**), (**Eu₃-71**), (**Tb₃-72**), (**Ho₃-73**), (**Er₃-74**), (**Tm₃-75**) and (**Yb₃-76**) the majority of which were analysed using PXRD. In the case of the Sm^{III}, Eu^{III} and Yb^{III} analogues, only single crystal XRD measurements could be performed as a result of the very low yields. The PXRD measurements prove the samples to be phase pure and isostructural to (**Dy₃-67**) (see Figure 180). The unit cells of (**Sm₃-70**), (**Eu₃-71**), and (**Yb₃-76**) indicate that these compounds are isostructural to (**Dy₃-67**).

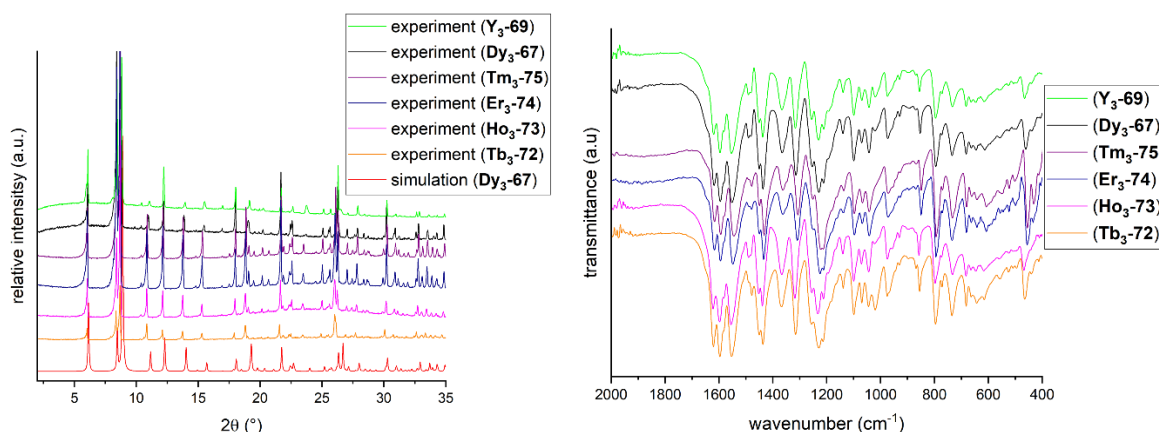


Figure 180. Experimental powder pattern of compounds (**Y₃-69**), (**Dy₃-67**), (**Tb₃-72**) to (**Tm₃-75**) with simulation for (**Dy₃-67**) (left) and IR spectra (right).

For the Eu^{III} and Sm^{III} analogues full single crystal measurements (as opposed to just determining the unit cell) were performed and the molecular structures are shown in Figure 181. The compounds are isostructural to the Dy^{III} version as mentioned above and have the formulae $[\text{Sm}_3(\text{Hmfbovh})_3(\mu_3\text{-OH})_2(\text{MeOH})_3\text{Cl}_3]\text{Cl}\cdot 3\text{MeOH}$ (**Sm₃-70**) and $[\text{Eu}_3(\text{Hmfbovh})_3(\mu_3\text{-OH})_2(\text{MeOH})_3\text{Cl}_3]\text{Cl}\cdot 3\text{MeOH}$ (**Eu₃-71**).

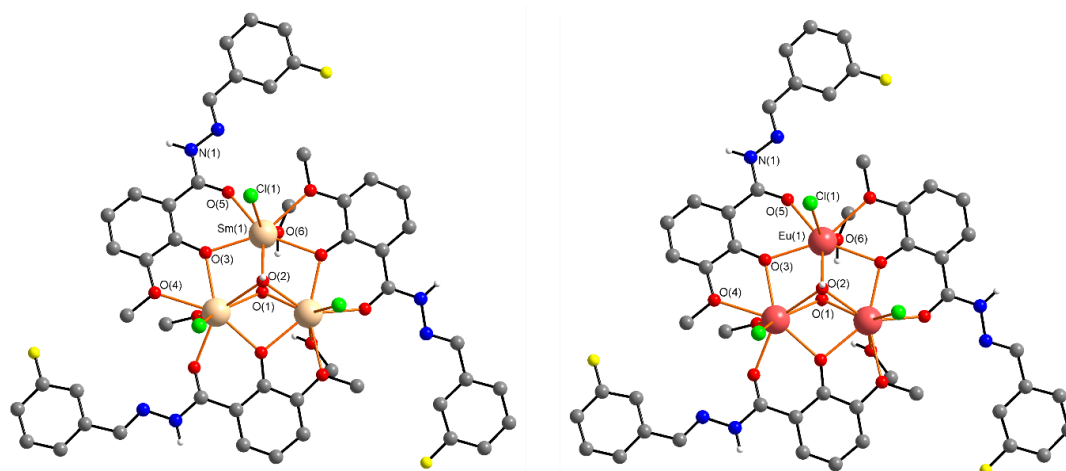


Figure 181. Molecular structure of (**Sm₃-70**) (left) and (**Eu₃-71**) (right).

In summary, it could be shown that changing the position of the fluoro substituent on the benzaldehyde has a significant impact on the crystal structure as well as the yield of the reaction. The fluorine atom on the remote phenyl of the ligand can be regarded as an innocent group in terms of intermolecular interactions since it is not likely to possess a significant σ -hole. Thus, it is unlikely to be involved in halogen bonds. It can be assumed that the position rather than the type of substituent is the reason for the changes in yields and crystal packing. The successful synthesis of the Eu^{III} - and Sm^{III} -

containing triangles, which incorporate larger lanthanide ions, shows that the influence of the lanthanide contraction on the structure of the triangles, which was observed in section 5.4.1, can be counteracted by careful ligand design resulting in all compounds crystallising in $R\bar{3}$.

5.4.2.2 Dy₃ Triangles with hydroxy substituted benzaldehydes

Exchanging the benzaldehyde used in the Schiff base ligand for a substituted version with potentially coordinating oxygen donor groups was investigated using *para*- and *meta*-hydroxy benzaldehyde. With these aldehydes two new Dy₃ triangles one (**Dy₃-77**) with the *p*-OH-benzaldehyde and the other (**Dy₃-78**) with the *m*-OH-benzaldehyde version of the Schiff base ligand were isolated. Single crystal XRD measurements revealed (**Dy₃-77**) to be different and (**Dy₃-78**) to be isomorphous with the already discussed Dy₃ with Schiff base ligands crystallising in the space group $R\bar{3}$ (section 5.4.1 and 5.4.2.1) and will thus not be described in detail again here. (**Dy₃-78**) has the molecular formula [Dy₃(Hmhbovh)₃(μ₃-OH)₂(MeOH)₃Cl₃]Cl·2MeOH.

Compound (**Dy₃-77**) [Dy₃(Hphbovh)₃(μ₃-OH)₂(MeOH)(H₂O)₂Cl₃]Cl·4MeOH·6H₂O crystallises in the trigonal space group $P\bar{3}c1$ with $Z = 4$. The molecular structure is shown in Figure 182. In line with the higher symmetry of the space group, the coordination environment and distribution of terminal ligands is the same as for the other trigonal Dy₃ compounds, *i.e.* one face of the triangle purely occupied by terminal Cl[−] ligands and the other side with two water and one MeOH ligand which are disordered across the three Dy^{III} ions. The crystal, in common with most triangles in this chapter, contains both enantiomers of the complex but oriented differently throughout the crystal structure compared to (**Dy₃-49**). The ligands here assume both the clockwise and anticlockwise sense of direction and alternate in stacks along the crystallographic *c* axis.

The crystal packing of (**Dy₃-77**) is shown in Figure 183. The view along the crystallographic *c* axis shows stacks which are similar to those for the structures crystallising in $R\bar{3}$.

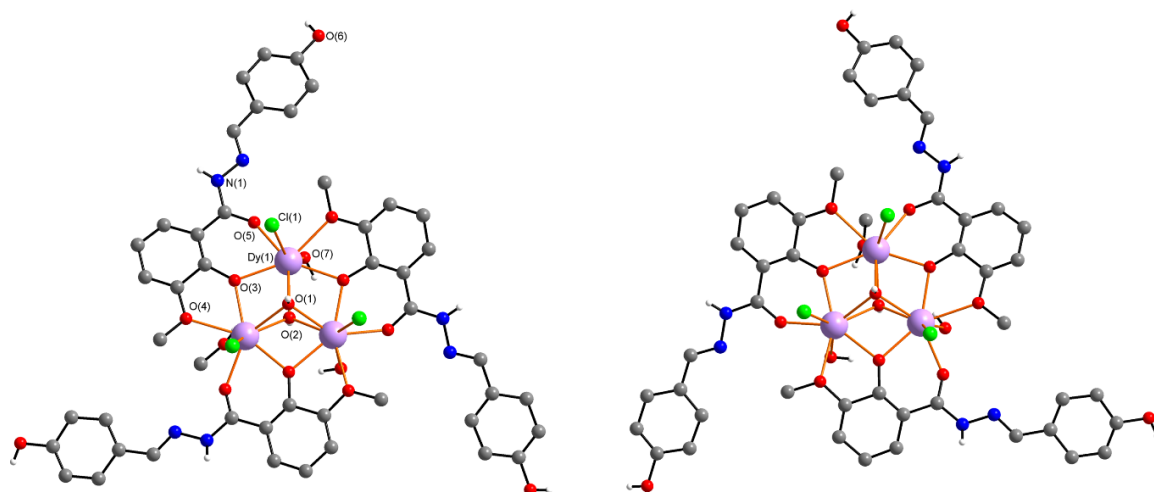


Figure 182. Molecular structure of (**Dy₃-77**) comparing the two enantiomers. Second hydrogen on the terminal ligands could not be refined due to the disordered MeOH ligands.

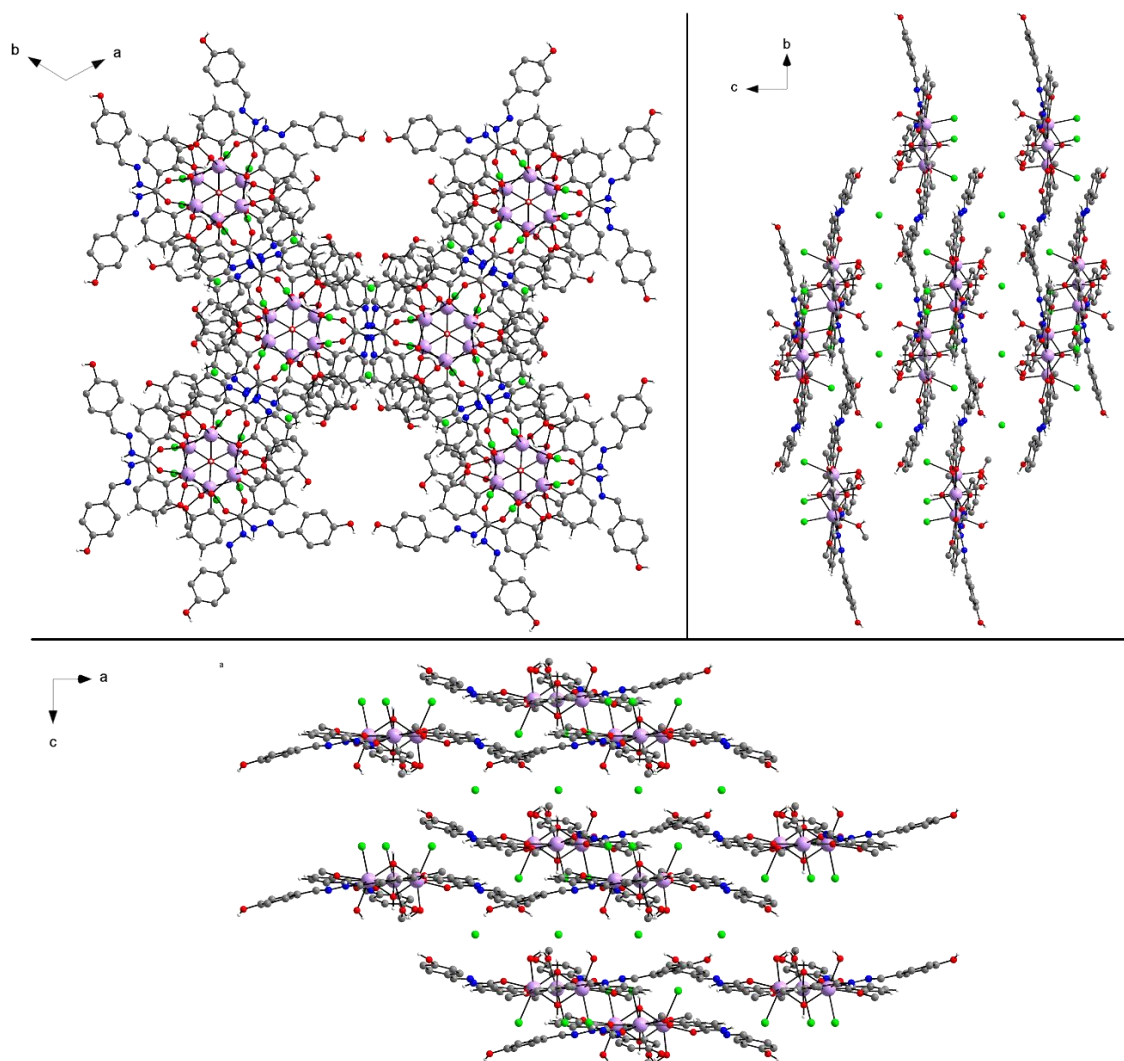


Figure 183. Packing along the crystallographic c (top left), a (top right) and b (bottom) axis for (**Dy₃-77**).

The pairs of enantiomers in neighbouring stacks are ordered in an alternating fashion, but the triangles in one stack always have the same orientation (Cl side always up or always down) whereas adjacent stacks have the opposite orientation. This means that one triangle in the stack differs from the next enantiomeric counterpart in terms of the Hphbovh⁻ ligands which assume a clockwise or anticlockwise orientation. Figure 184 gives a schematic illustration of how these enantiomeric effects can be understood.

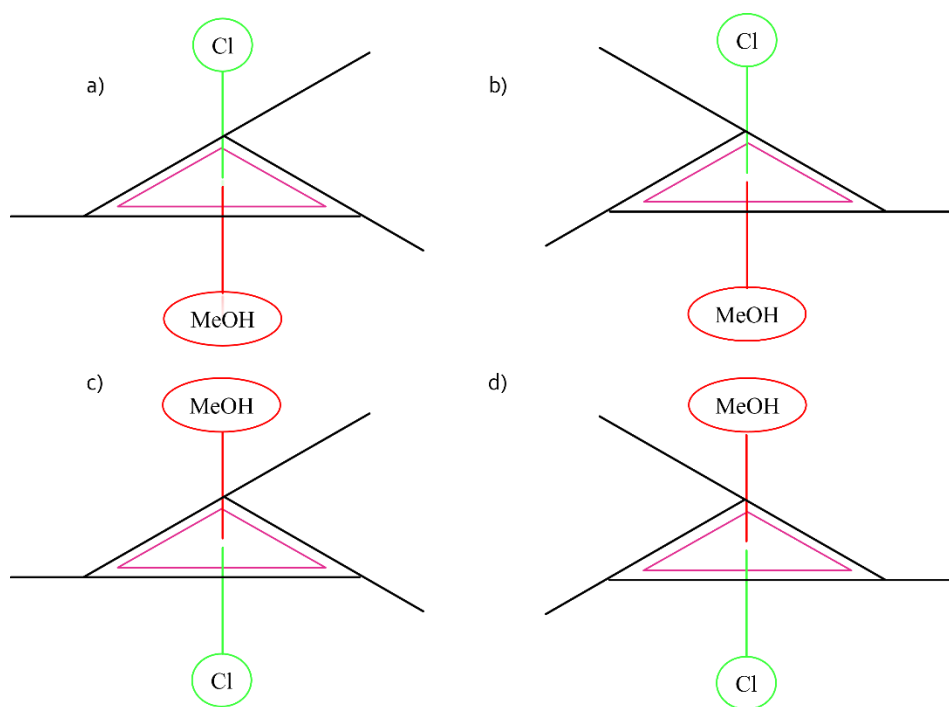


Figure 184. Scheme of (**Dy₃-77**) molecule in a), mirror image/enantiomer of it in b). b) turned 180° in the triangle plane in c) and a) turned 180° in triangle plane in d). Black lines represent Hphbovh⁻ ligand, purple triangle Dy₃ core and Cl/MeOH the three corresponding terminal ligands on that side.

This scheme allows us to describe and compare the stacking in the crystals of (**Dy₃-77**). Triangles of type a) and b) stack in an alternating fashion while for (**Dy₃-49**) and other triangles in the $R\bar{3}$ space group it is triangles of type a) and c) which alternate (see section 5.4.1).

The packing is dominated by intramolecular interactions giving rise to a 3D network. This network consists of 2D sheets, the structure of which is the same as shown for the other $R\bar{3}$ triangles. These are connected *via* the chloride counterions which accept hydrogen bonds from two of the hydroxy substituents (O(6)) on the ligand (see Figure 185). This is unusual since for the other $R\bar{3}$ triangles the Cl⁻ counterion is always on or near the threefold axes accepting hydrogen bonds from the μ_3 -OH. This difference in hydrogen bonding arises as a result of the extra OH groups. In contrast to the systems

with unsubstituted or fluoro-substituted ligands, this observation could be the reason why (**Dy₃-77**) crystallises in $P\bar{3}c1$.

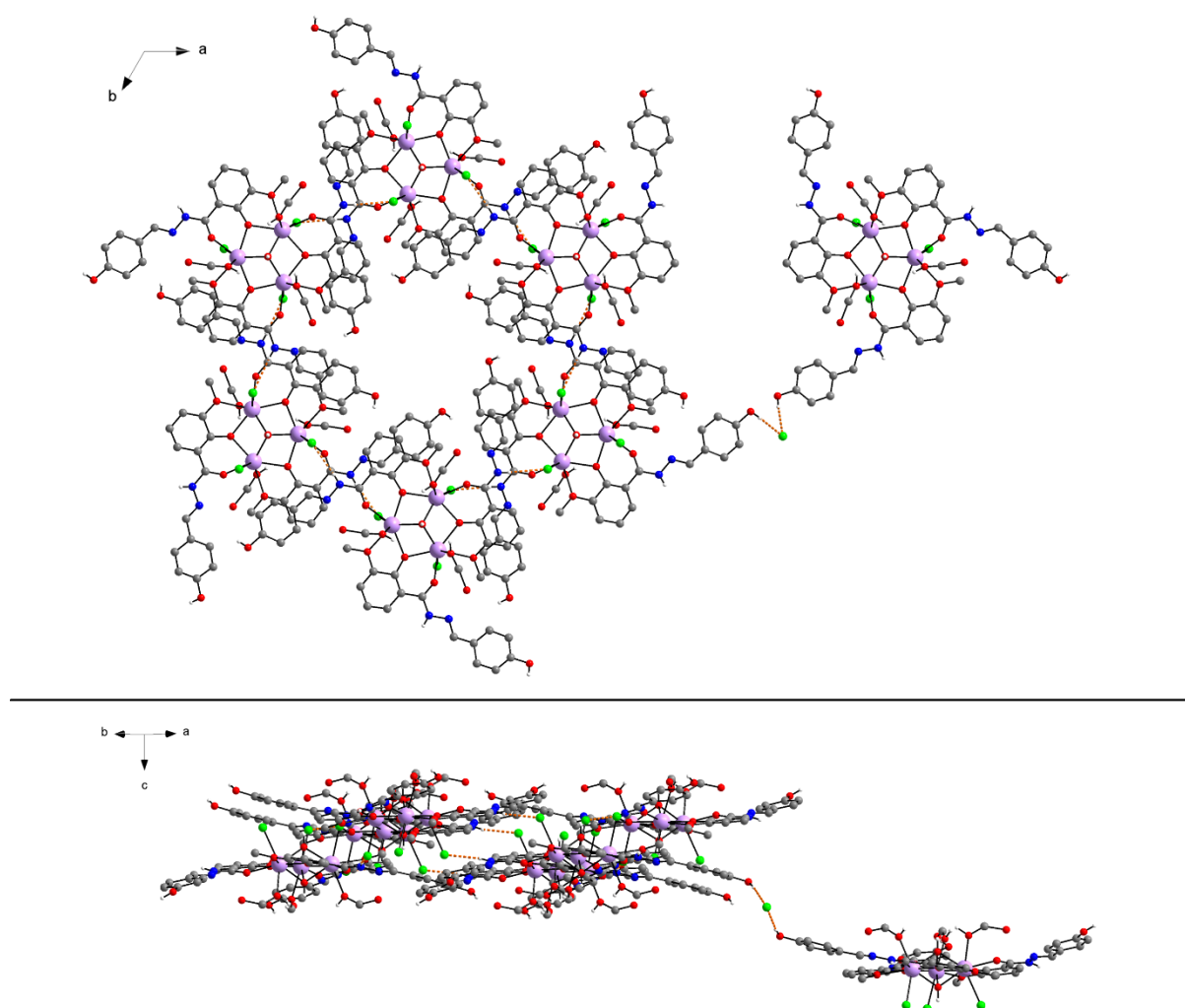


Figure 185. Intermolecular interactions in (**Dy₃-77**). View along crystallographic c axis (top) and sideview (bottom) showing the 2D network and H-bonds involving the Cl⁻ counterion which form the 3D network. Hydrogen bonds highlighted as orange dotted lines.

Varying the lanthanide ions for both compounds (**Dy₃-77**) and (**Dy₃-78**) in order gauge whether further lanthanides would be isostructural to both different series. The lanthanide ions were varied using the lanthanide chlorides from Sm^{III} to Lu^{III}. Only with Gd^{III} (**Gd₃-79**) and Tb^{III} (**Tb₃-80**) crystals were obtained with the H₂phbovh ligand (used in (**Dy₃-78**)) whereas using H₂mhbovh (used in (**Dy₃-77**)) only for Tb^{III} (**Tb₃-81**) and Ho^{III} (**Ho₃-82**) could crystals be obtained. All compounds were confirmed to be isostructural to their Dy^{III} analogues through PXRD measurements. Again, all samples had to be measured in capillary since the crystallinity is not maintained after exposure to moisture in the air (see Figure 186). The experimental and simulated powder

patterns for all compounds are in reasonable agreement with the peaks being slightly shifted compared to the simulation. Any exposure to air during sample preparation and the difference in temperature during PXRD and single crystal measurements can influence the results shown here and may be the cause for the discrepancies between experimental and simulated powder patterns. This is particularly relevant for the analogues of (**Dy₃-77**) since the compound loses crystallinity rapidly on exposure to air.

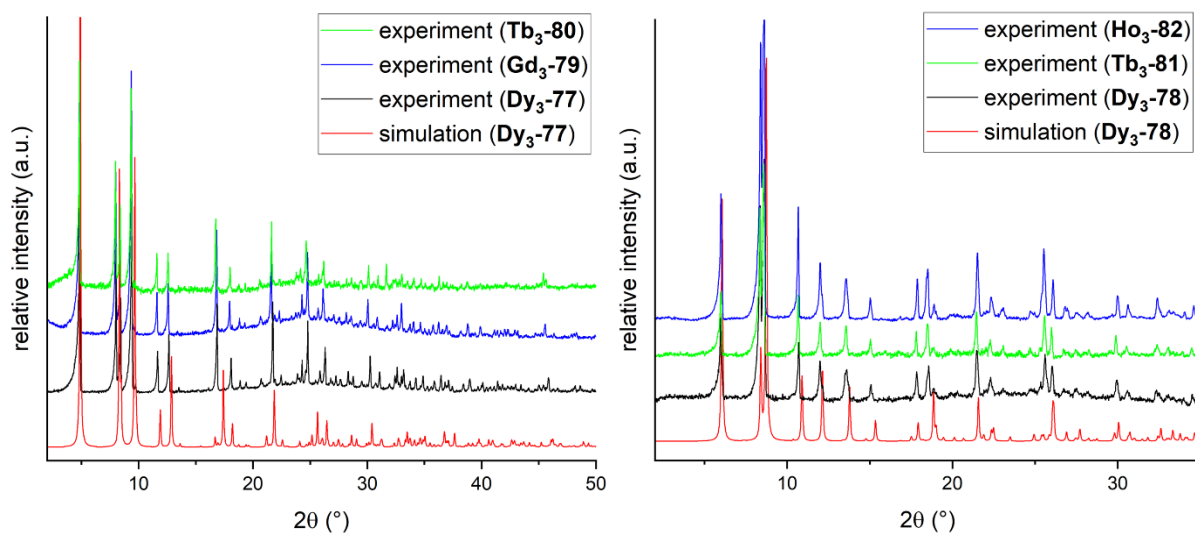


Figure 186. Experimental and simulated powder pattern of compounds (**Dy₃-77**), (**Gd₃-79**) and (**Tb₃-80**) (left) and (**Dy₃-78**), (**Tb₃-81**) and (**Ho₃-82**) (right). The small hump at ca 25° is an artifact from the capillary which appears due to too low sample volume.

Elemental analyses were performed on the Dy samples (**Dy₃-77**) and (**Dy₃-78**) to prove their consistency in terms of the purity of the compound batches. The calculated results could be fit to the experimentally determined values after taking into account additional lattice water as well as exchange of MeOH ligands for water. This behaviour is consistent with other Dy₃ triangles where the same procedure was adopted.^[37]

In conclusion both *meta*- and *para*-hydroxy substituted ligands yielded Dy₃ compounds with the targeted molecular structures. A single OH group in either position is not enough to change the structure of the resulting compound. Placing an oxygen at a site designed to be much more remote from the Dy₃ triangle led to a change in space group as a result of additional hydrogen bonds forming to the Cl⁻ counterion in the case of the *para* substitution. It was possible to keep the threefold symmetry and change the way the stacks are arranged. The formation of both enantiomers still poses significant

challenges which were discussed for (**Dy₃-49**). The biggest stumbling block is finding a way to remove the inversion centre in the space group.

5.4.2.3 Magnetic Characterisation

Magnetic measurements were performed on randomly oriented immobilised powder samples of (**Dy₃-59**) and (**Dy₃-67**) as well as (**Dy₃-77**) and (**Dy₃-78**) which use the H₂pfbovh, H₂mfbvh, H₂phbovh and H₂mhbvh ligands (see Figure 187) respectively. The characterisation includes DC, AC and magnetisation measurements which are compared to each other and (**Dy₃-49**) in the following.

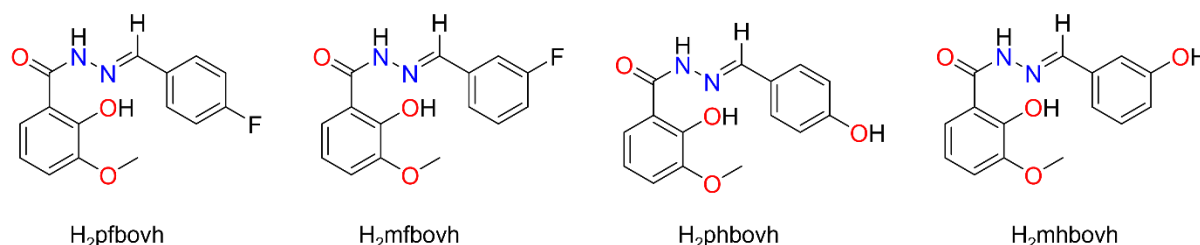


Figure 187. *In situ* synthesised ligands used in synthesis of (**Dy₃-59**), (**Dy₃-67**), (**Dy₃-77**) and (**Dy₃-78**) from left to right respectively.

DC susceptibility measurements were performed under an applied field of 0.1 T (see Figure 188). The RT $\chi_M T$ values are all between 41.1 cm³Kmol⁻¹ and 41.5 cm³Kmol⁻¹ which fits with the theoretical value of 42.51 cm³Kmol⁻¹ for three uncoupled Dy^{III} ions. The general trend of the curve is comparable to other previously described triangles and indicates the same combination of antiferromagnetic coupling and depopulation of m_J sub-levels. All curves overlap to a great extent which suggests a similar magnetic coupling. For better comparison and to prove the antiferromagnetic interactions the $1/\chi_M$ vs T plot was used for Curie-Weiss fits in the temperature range of 60 K to 300 K which gave the Curie constants C and Weiss constants θ listed in table 13. All values for θ are negative indicating antiferromagnetic interactions and are of similar magnitude with (**Dy₃-77**) having a slightly more negative Weiss constant.

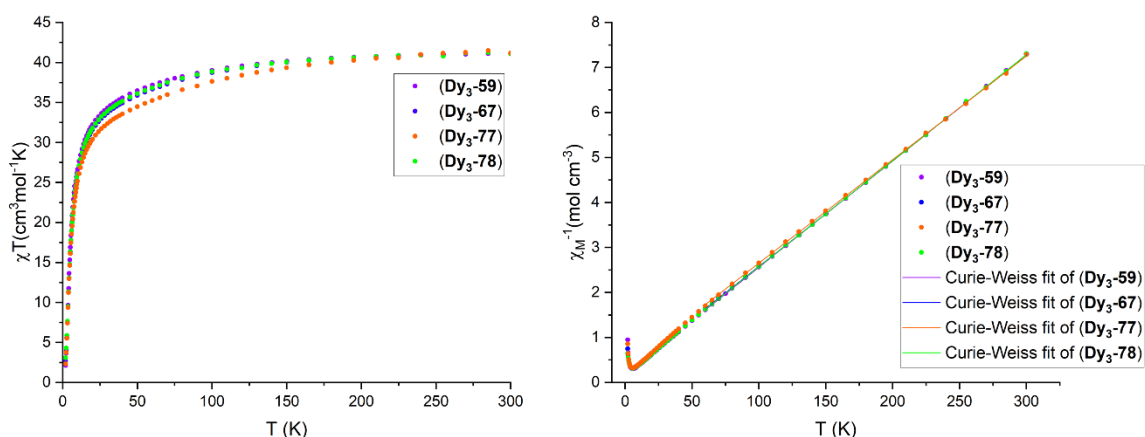


Figure 188. $\chi_M T$ vs T (left) and $1/\chi_M$ vs T (right) for (**Dy₃-59**), (**Dy₃-67**), (**Dy₃-77**) and (**Dy₃-78**) measured at 0.1 T.

Table 13. C and θ values for (**Dy₃-59**), (**Dy₃-67**), (**Dy₃-77**) and (**Dy₃-78**).

	(Dy₃-59)	(Dy₃-67)	(Dy₃-77)	(Dy₃-78)
θ in K	-8.21	-7.42	-12.63	-8.51
C in $\text{cm}^3\text{Kmol}^{-1}$	42.3	42.1	42.9	42.3

AC susceptibility measurements were performed under zero field between 2 K to 8 K (see Figure 189). The out-of-phase (χ_M'') signals display two distinct sets of maxima. To analyse these features, the out-of-phase data were simultaneously fitted with the in-phase susceptibility (χ_M') using a double generalised Debye model. The presence of these maxima confirms slow relaxation of magnetisation, indicative of single-molecule magnet (SMM) behaviour.

The first maximum in the χ_M'' plot shifts to higher frequencies and decreases in intensity with increasing temperature. In contrast, the second set of maxima increases in intensity as the temperature increases. For (**Dy₃-59**) and (**Dy₃-67**) the second maximum is only fully observable up to approximately 6 K for both compounds, beyond which the relaxation becomes too fast to be detectable under the current experimental setup. For (**Dy₃-77**) and (**Dy₃-78**) the maximum is within the measured frequency range up to 8 K. The temperature-dependent increase in intensity of this second set may be attributed to the involvement of thermally populated excited states in the relaxation process. These characteristics are seen for all measured compounds discussed here and match the behaviour found for (**Dy₃-49**).

This shows that substituting the phenyl group of the ligand does not change the overall dynamic relaxation properties qualitatively for this type of compound. Nevertheless, the first maximum is slightly shifted and varies in intensity for this group of compounds.

For the *meta*-substituted samples, the first maximum can be seen up to 3 K whereas for the *para*-substituted samples its visible until 2.6 K and with much lower intensity. After two months of storing the compound on the bench, a second measurement was performed on (**Dy₃-67**) and revealed the disappearance of the first set of maxima. PXRD of this sample confirmed that the structure still matches that from the original powder pattern suggesting that the compound did not decompose.

The intensity of the first maximum also appears to be lower for samples which were found to lose their crystallinity rapidly when exposed to air. Particularly for (**Dy₃-59**) (Figure 189 a) and (**Dy₃-77**) (Figure 189 c) this could also be observed when looking at the crystals under a microscope. Within seconds the initially clear crystals turn opaque indicating a loss of crystallinity. In compounds (**Dy₃-67**) (see Figure 189 b) and (**Dy₃-49**) where no initial loss of crystallinity was observed the first maximum is clearly present and with higher intensities. The elemental analysis for these compounds shows that they take up water from the atmosphere after being out of the mother liquor for more than a week. It should be mentioned here that all SQUID samples were prepared in the same way. Crystals were removed from the mother liquor, only lightly ground to generate a randomly oriented powder and subsequently immediately sealed in eicosane.

Given the use of this experimental procedure, it seems likely that the first set of maxima correspond to the “dry” form of the compound as seen for (**Dy₃-67**). For the other three compounds discussed here the varying intensity of the first maximum is an indication of their rate of uptake of water.

Whether this disappearance of a second set of relaxation processes is a result of the exchange of MeOH for water terminal ligands and/or the increased intermolecular hydrogen bonding opportunities through additional lattice water requires further investigations. For example, drying (**Dy₃-77**) under reduced pressure and therefore removing lattice water but not the coordinating terminal water ligands followed by the same set of AC measurements could give insights into the origin of the first maximum and its correlation to the water uptake. It would also be beneficial to combine this with a thermogravimetric analysis and further elemental analysis.

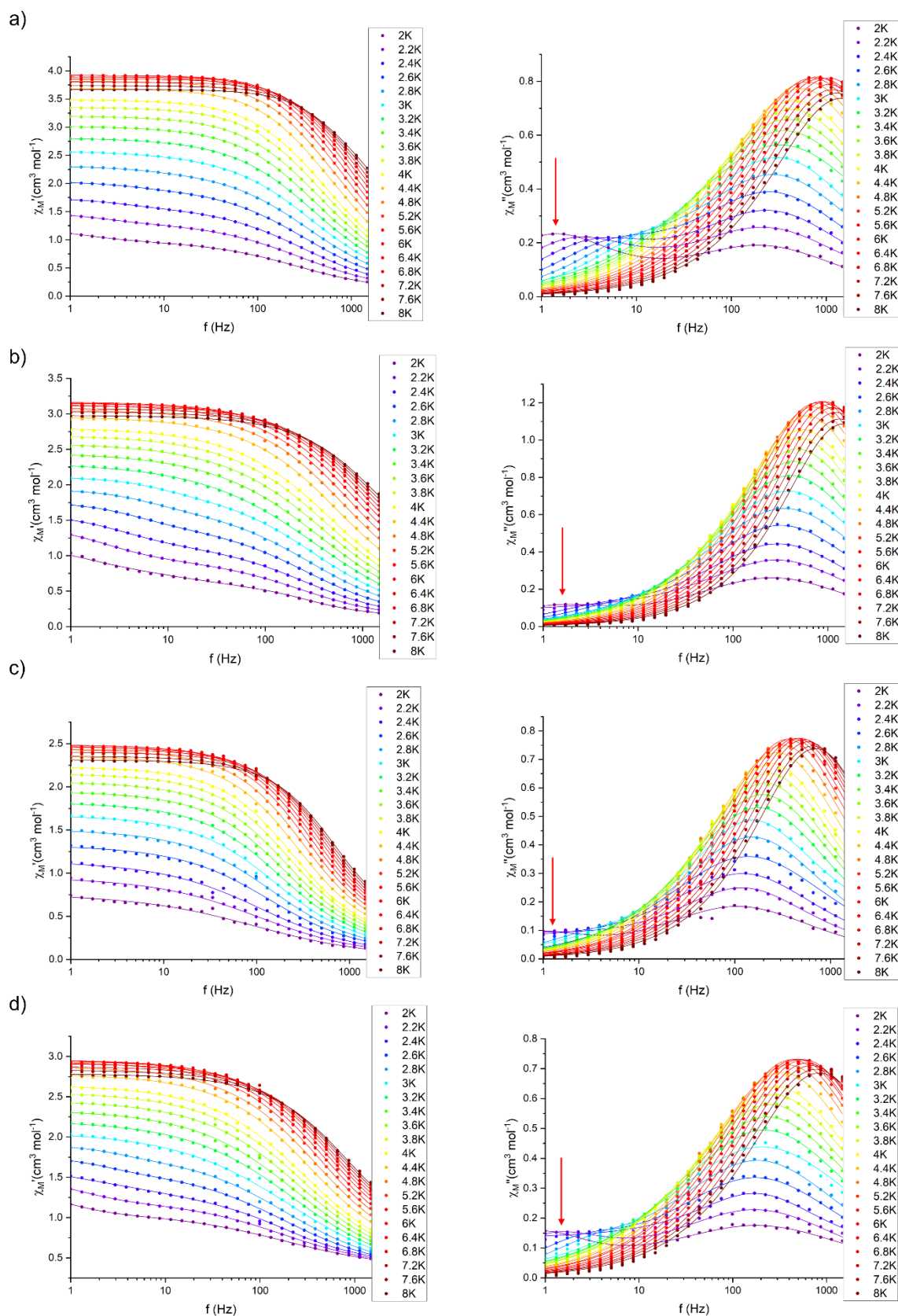


Figure 189. AC in-phase (left) and out-of-phase (right) data for **(Dy₃-59)** in a), **(Dy₃-67)** in b), **(Dy₃-77)** in c) and **(Dy₃-78)** in d). Red arrows highlighting first maximum.

Field-dependent DC magnetisation measurements were performed from 0 T to 7 T at temperatures between 2 K and 5 K (see Figure 190). The resulting M vs B plot reveals inflection points between 0.86 T for (**Dy₃-77**) to 0.93 T for (**Dy₃-78**) as shown by the derivative dM/dB (see inset of Figure 190). This suggests a level crossing between a potentially toroidal ground state and an excited state. However, as shown before the inflection point is no definitive proof for the existence of a toroidal ground state in these compounds but a hint towards magnetic behaviour similar to other toroidal Dy₃ triangle compounds. To prove toroidicity further measurements are necessary.

The level crossing and its relative position can be used to compare the relative stability of the ground state for these compounds. This shows that if there is a toroidal state it is more stable for (**Dy₃-78**) in the presence of an external magnetic field. At 2 T, the magnetisation begins to saturate, ultimately reaching 17.2 μ_B for (**Dy₃-59**), 14.7 μ_B for (**Dy₃-67**), 15.7 μ_B for (**Dy₃-77**) and 16.2 μ_B for (**Dy₃-78**) at 7 T. The linear increase beyond 2 T could result from contributions of low-lying excited states.

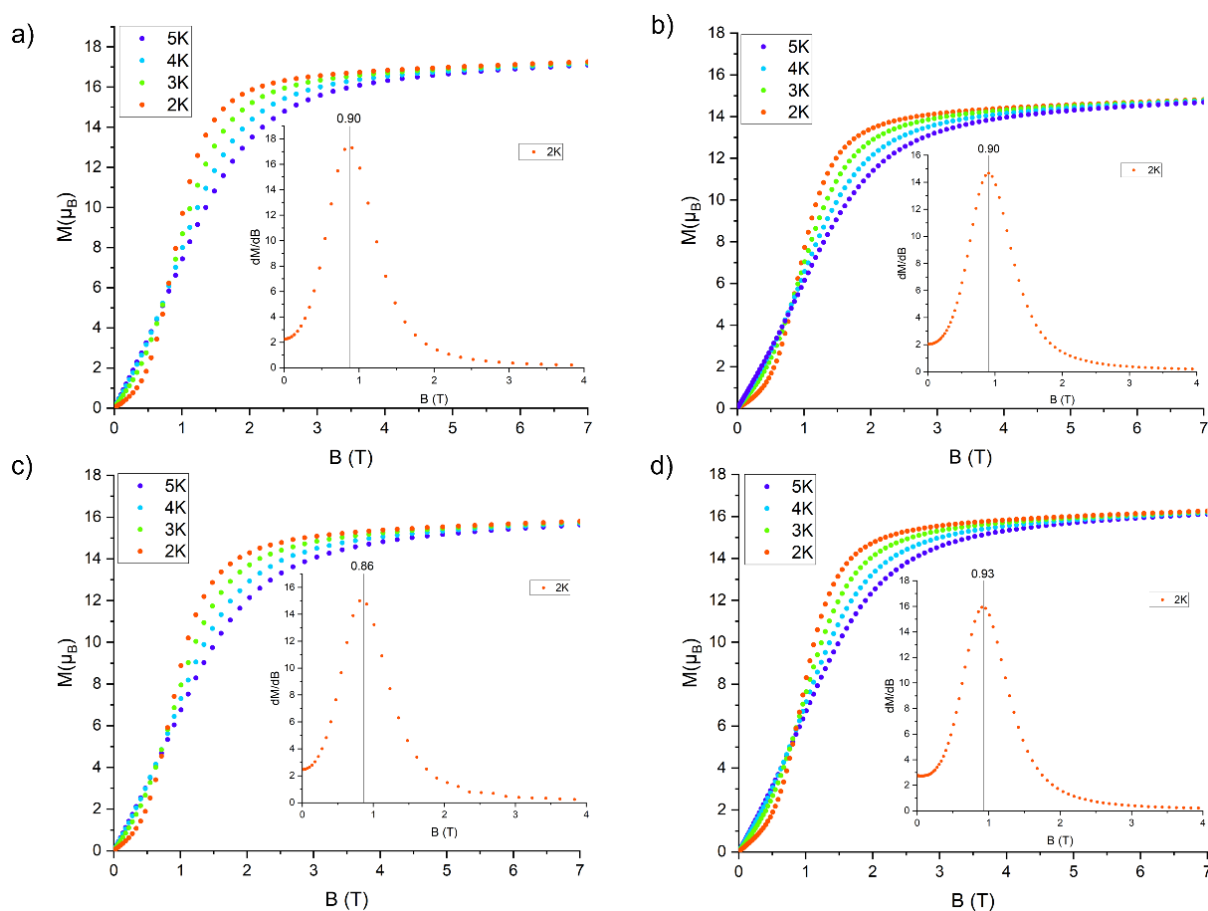


Figure 190. M vs B plots for (**Dy₃-59**) in a), (**Dy₃-67**) in b), (**Dy₃-77**) in c) and (**Dy₃-78**) in d). Insets show the first derivative dM/dB highlighting the position of the maximum.

Additionally, an analysis of the anisotropy axes using the MAGELLAN^[202] software was performed for (**Dy₃-59**) and (**Dy₃-77**) (see Figure 191). There was no need to analyse symmetric $R\bar{3}$ structures ((**Dy₃-67**) and (**Dy₃-78**)) using MAGELLAN^[202] since the behaviour can be expected to be the same as for (**Dy₃-49**) as a result of the identical coordination environment. For compound (**Dy₃-77**) the analysis reveals a similar in-plane arrangement of the anisotropy axes as seen for other toroidal Dy₃ compounds indicating that the exchange of MeOH ligands for water ligands does not significantly affect the orientation of anisotropy axes.

For (**Dy₃-59**) one of the axes is oriented perpendicular to triangle plane while the other two are in-plane. This seemingly unusual behaviour is similar to that found in the case of the triangles with halogenated *o*-van ligands (**Dy₃-21**), (**Dy₃-22**) and (**Dy₃-36**) described in section 5.2 above.

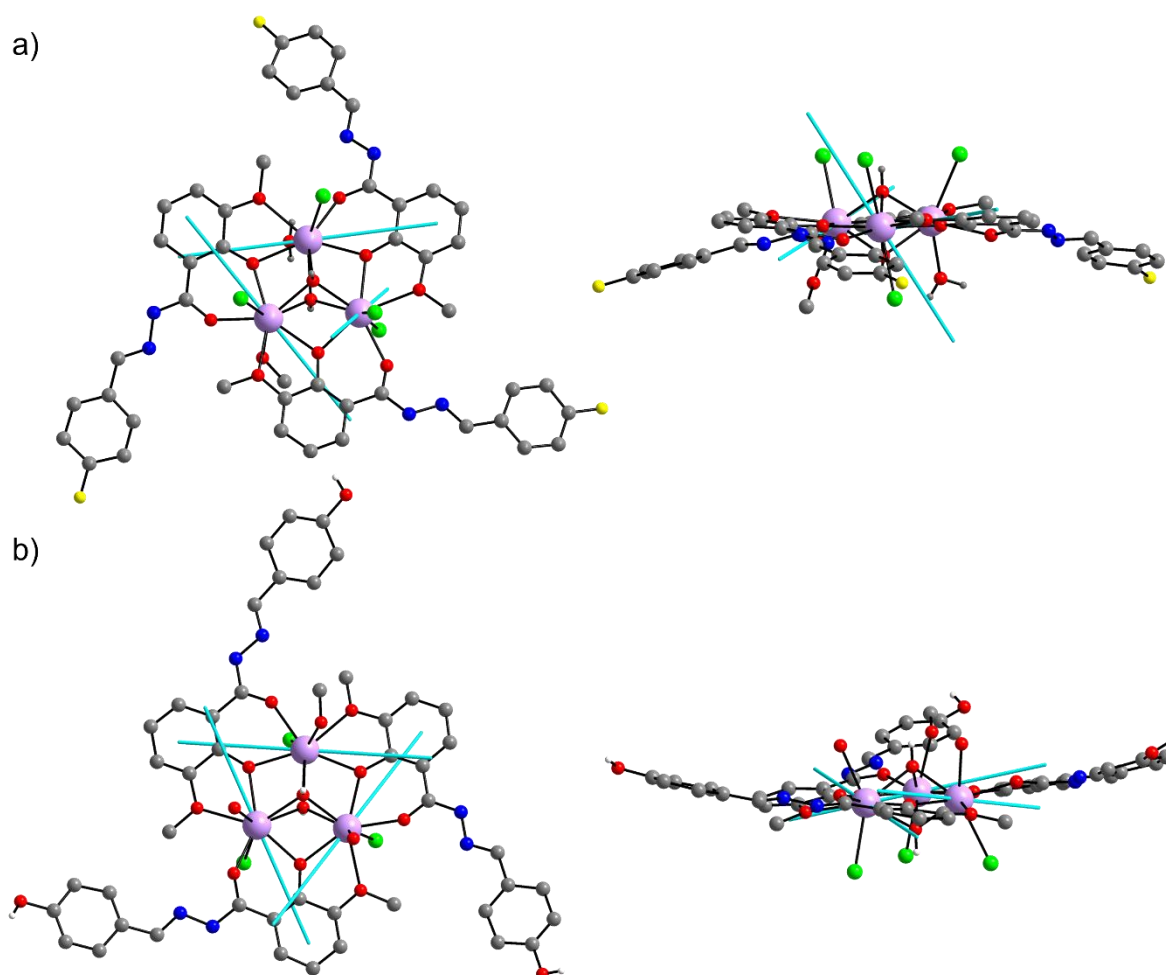


Figure 191. Anisotropy axes calculated with MAGELLAN^[202] in cyan with top and side view for (**Dy₃-59**) a) and (**Dy₃-77**) b).

To investigate the possibility of the lack of toroidicity further in (**Dy₃-59**) theory calculations similar to the ones described in section 5.2.4 are currently underway with the first results shown in Figure 192.

From the crystal data, a model cluster was chosen which contained all hydrogen bonding interactions of the core molecule. For this purpose, a terminal Cl⁻ ligand of a neighbouring molecule forming hydrogen bonds with a terminal water molecule was included. This results in a total charge of -1 for the model cluster. A geometry optimisation using the b-p functional and def2-TZVP basis was carried out in order to optimise the hydrogen positions. In order to perform a closed shell calculation Dy^{III} was replaced by Y^{III}. Subsequently, CASOCI (Complete Active Space Spin-Orbit Configuration Interaction)^[229] calculations (triple-zeta basis, DKH4) were performed individually for each of the centres using 9 electrons in 7 orbitals and including spin-orbit coupling.

In contrast to the MAGELLAN^[202] analysis, these calculations show that the third axis in (**Dy₃-59**) lies in the plane, indicating that the compound is likely toroidal. To determine which calculation more accurately represents the situation, further magnetic characterisation in the form of microSQUID measurements are necessary.

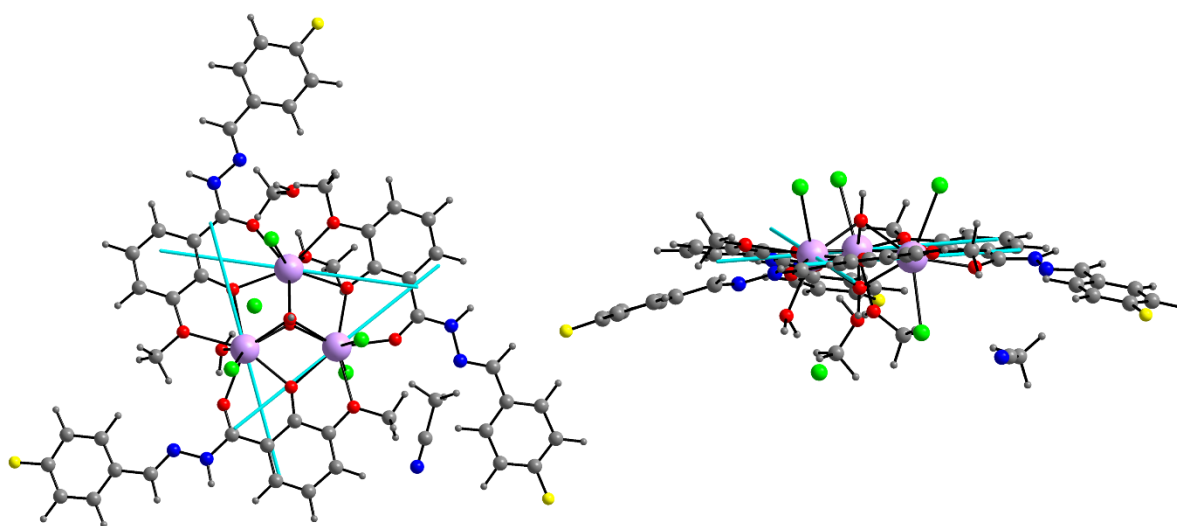


Figure 192. Magnetic main axis for each centre calculated from CASOCI for (**Dy₃-59**).

Furthermore, the *g* tensors for the first Kramers' doublet and the zero field splitting of the eight Kramers' doublets of the ⁶H_{15/2} state were calculated for each magnetic centre and the results are shown in Figure 193.

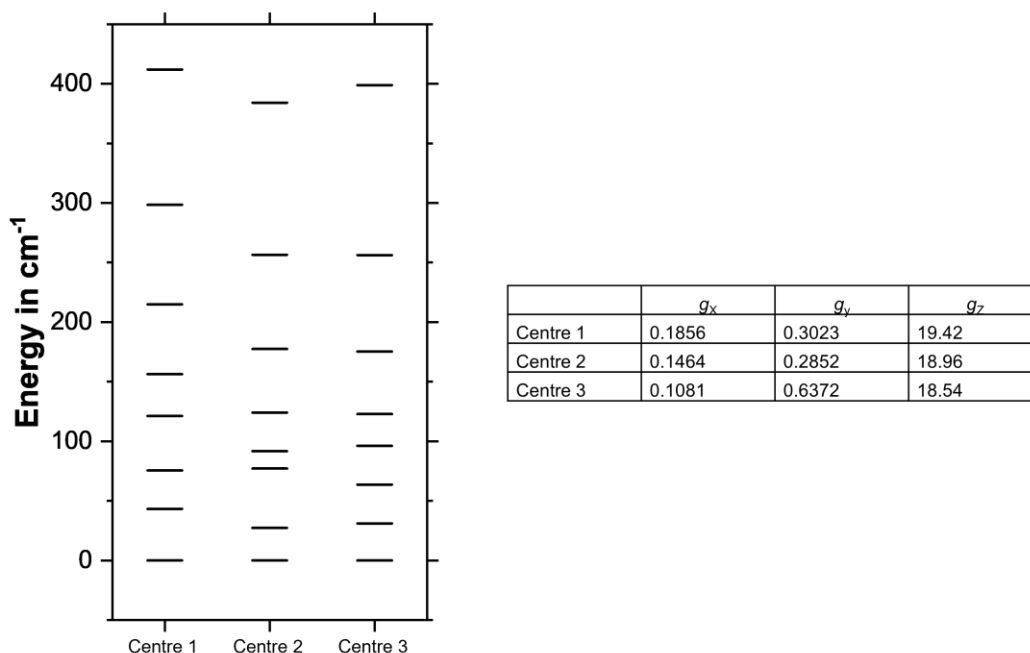


Figure 193. Zero field splitting of the three individual magnetic centres and g tensors in the ground state of (**Dy₃-59**). Centre 1, 2 and 3 correspond to Dy(1), Dy(2) and Dy(3) respectively.

5.4.2.4 Influencing the crystal packing – Ligand approach

The substitution of the ligand with the OH and F groups led to the crystallisation of the compounds in different symmetry space groups. Furthermore, this led to different numbers and distributions of the Cl⁻ terminal ligands which were shown to have the most significant influence on the orientation of the anisotropy axes. These results show that a substitution in *meta*-position is most likely to yield an $R\bar{3}$ structure. On the other hand *ortho*-substitution appears to either drastically decrease the yield of the compound or if potentially coordinating groups like OH are used to decorate the ligand, the obtained molecular structure is different (see section 5.4.2.6).

The occupation of the *meta*-position and the resulting tendency towards crystallising in highly symmetric $R\bar{3}$ structures was therefore further investigated. A range of different substitutions in the *para*-position was also tested given the observed potential for a greater variety of crystal space groups observed for such systems.

Compound (**Dy₃-83**) with the formula $[\text{Dy}_3(\text{Hmoxbovh})_3(\mu_3\text{-OH})_2(\text{MeOH})(\text{H}_2\text{O})\text{Cl}_4]\text{Cl}\cdot 4\text{MeOH}\cdot 4\text{MeCN}$ was synthesised *via* the Schiff base

approach using *m*-anisaldehyde (3-methoxybenzaldehyde) and *o*-vanillyl hydrazide. Given that a Schiff base ligand with a *meta*-substituted benzaldehyde subunit was used, (**Dy₃-83**) crystallises in $P\bar{1}$ with $Z = 2$ rather than the $R\bar{3}$ space group. The molecular structure is shown in Figure 194.

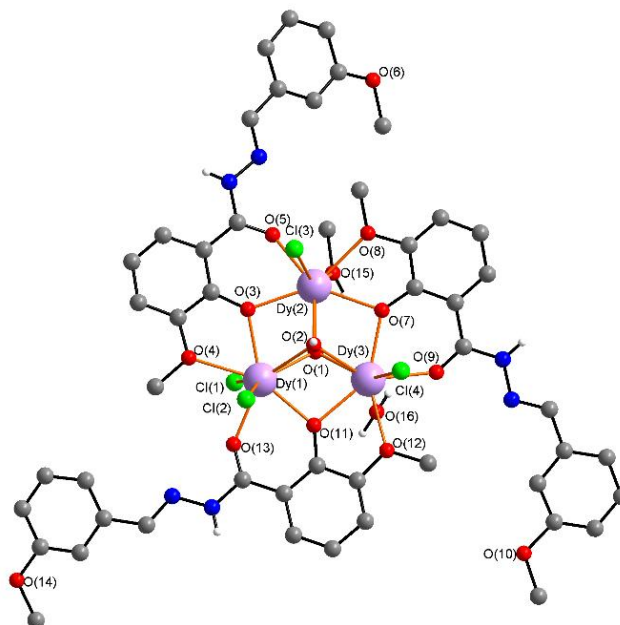


Figure 194. Molecular structure of (**Dy₃-83**).

The coordination environment of the Dy^{III} ions is the same as described for the other Dy₃ motifs in section 5.4 with the terminal ligands here being three Cl[−] on one side of the triangle and one MeOH, one H₂O and one Cl[−] coordinating on the other side. The packing is shown in Figure 195 along the three crystallographic axes and an additional view orthogonal to the triangle plane.

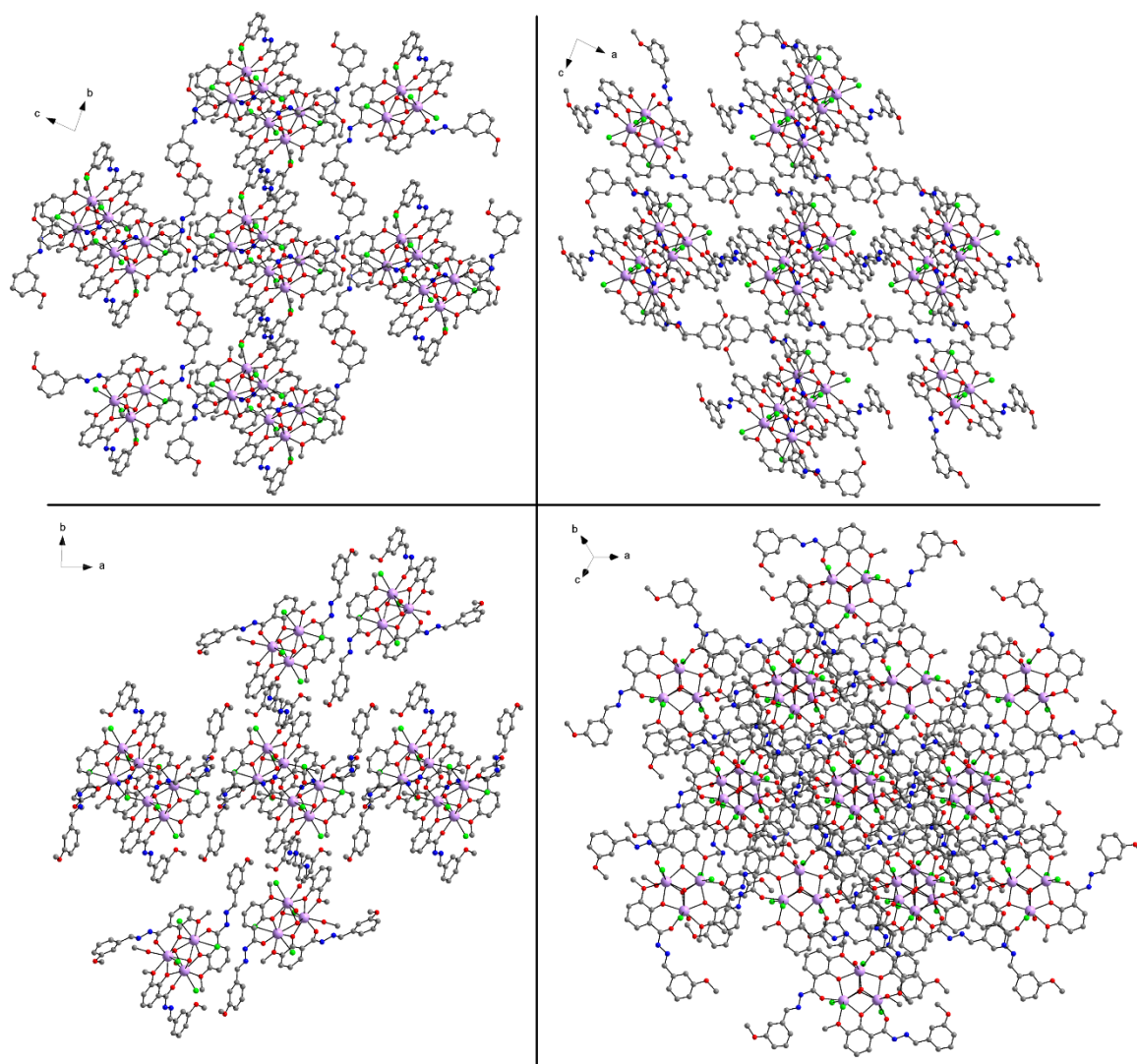


Figure 195. Packing of (**Dy₃-83**) along the crystallographic *a* (top left), *b* (top right) and *c* (bottom left) axis as well as in the [111] direction (bottom right).

The packing is influenced by two sets of hydrogen bonds which are both shown in Figure 196. The first set connects a 2D network throughout the lattice with hydrogen bonds between the NH hydrogen of the ligand and a terminal chloride of the neighbouring molecules. The second set connects one triangle with its inversion related counterpart through hydrogen bonds between the hydrogens on O(1), O(15) and O(16) and the single chloride terminal ligand on the other molecule. This interaction leads to the closest intermolecular Dy⋯Dy distance of 6.9923(5) Å and a distance between triangle planes in such stacks of 6.8300(3) Å.

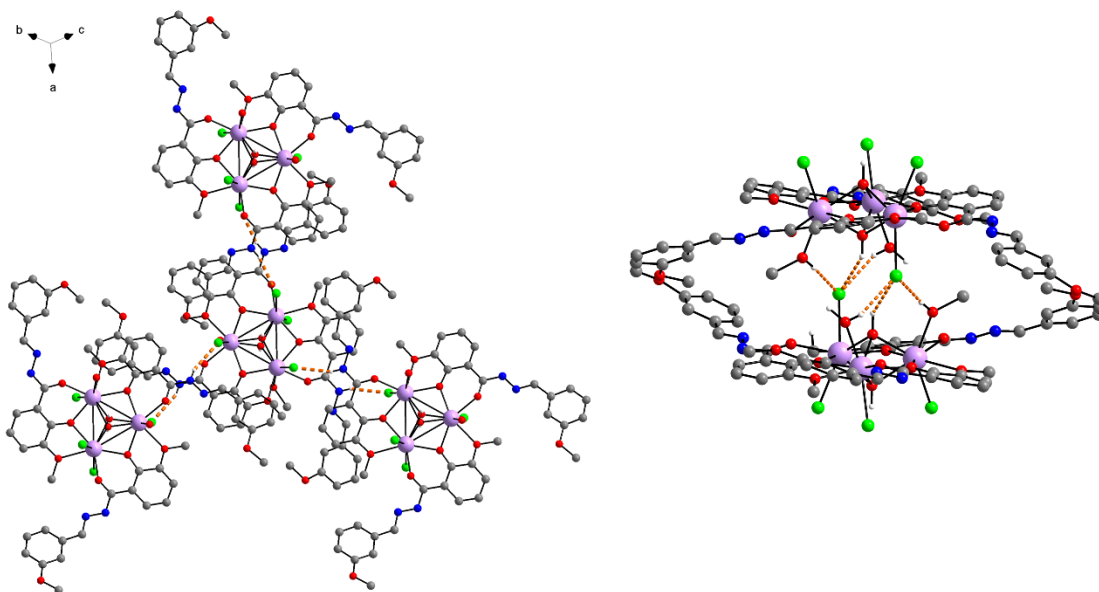


Figure 196. First set of hydrogen bonds resulting in a 2D network (left) and second set connecting two inversion related Dy_3 moieties (left).

To investigate further the influence of the substitution in the *para* position *p*-ethylbenzaldehyde was used in the Schiff base synthetic approach and led to the crystallisation of plate crystals of (**Y₃-84**) with $\text{H}_2\text{petbovh}$ ligands. The molecular structure is shown in Figure 197.

Single crystal measurements of the Dy^{III} version (**Dy₃-85**) showed the same cell parameters, thus the compounds are isostructural and only the structure of the Y-analogue is described. Compound (**Y₃-84**) crystallises in the orthorhombic space group Pbca with $Z = 8$ with the formula $[\text{Y}_3(\text{Hpetbovh})_3(\mu_3\text{-OH})_2(\text{H}_2\text{O})_5\text{Cl}]\text{Cl}_3 \cdot 5\text{MeCN} \cdot 5\text{MeOH} \cdot 3\text{H}_2\text{O}$. The terminal ligands consist of five water molecules and one Cl^- necessitating three Cl^- counterions in the lattice for charge balance. As seen for the archetypal Dy_3 , a low number of charged terminal ligands may lead to better toroidal properties, making the Dy^{III} -analogue (**Dy₃-85**) a promising candidate for the planned magnetic characterisation.

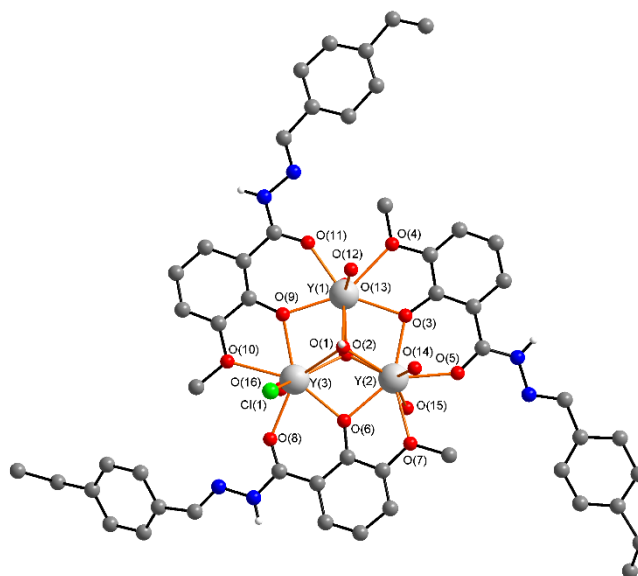


Figure 197. Molecular structure of (**Y₃-84**).

This compound is another example of how *para*-substitution of the benzaldehyde part of the Schiff base ligand can lead to space groups other than $R\bar{3}$ and $P\bar{1}$. In this case this is not a result of additional intermolecular interactions such as seen for (**Dy₃-77**) but from the location and hydrogen bonding possibilities of the counterions in the lattice.

Hydrogen bonds form between the NH hydrogen on the ligand and a terminal Cl^- ligand of a neighbouring molecule. For other Ln_3 species described in this thesis this resulted in a 2D network, but in the case of (**Y₃-84**) only one terminal chloride is present which restricts it to the formation of chains. These chains are interconnected through further hydrogen bonds between the remaining NH hydrogens and Cl^- counterions. In addition, these Cl^- counterions bond to hydrogens on the terminal water ligands of a molecule in a neighbouring chain (shown in light blue in Figure 198).

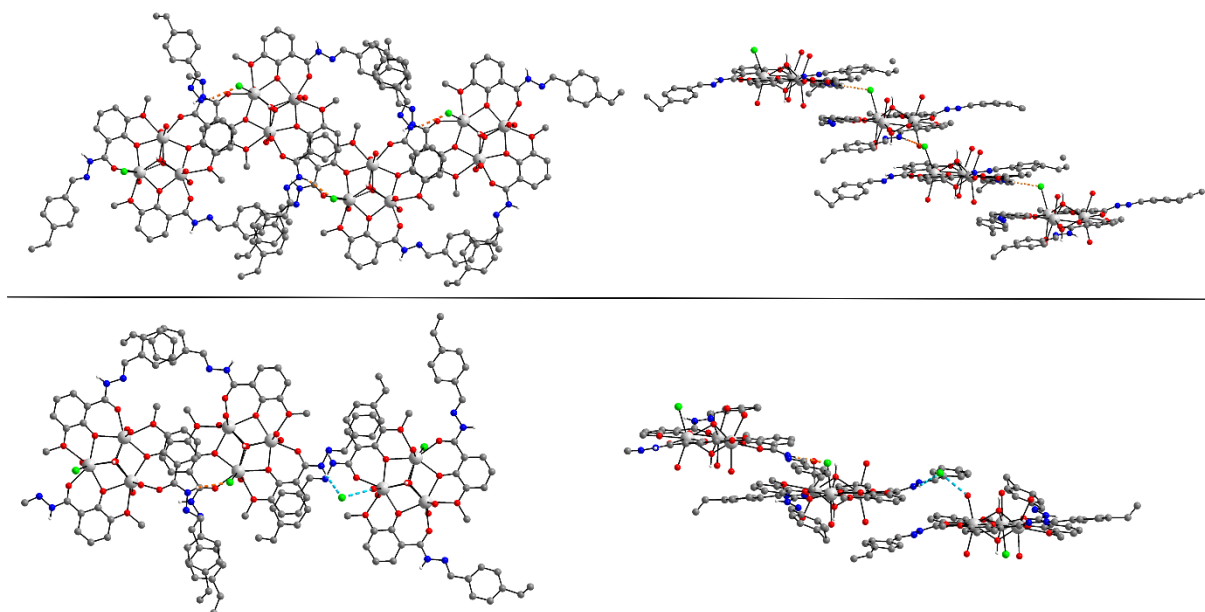


Figure 198. Hydrogen bonds in (**Y3-84**) forming chains throughout the lattice (orange dotted lines) (top left) with side view (top right) and interconnection between chains through hydrogen bonds which involve Cl⁻ counterions (light blue dotted lines) (bottom left) with side view (bottom right).

The packing is shown in Figure 199. Channels with a diameter of 11.8369(3) Å form along the crystallographic *a* axis. This layered structure can also be seen looking along both the *a* and the *c* axes. These open channels could be investigated in a future work in terms of possible gas storage capabilities.^[233]

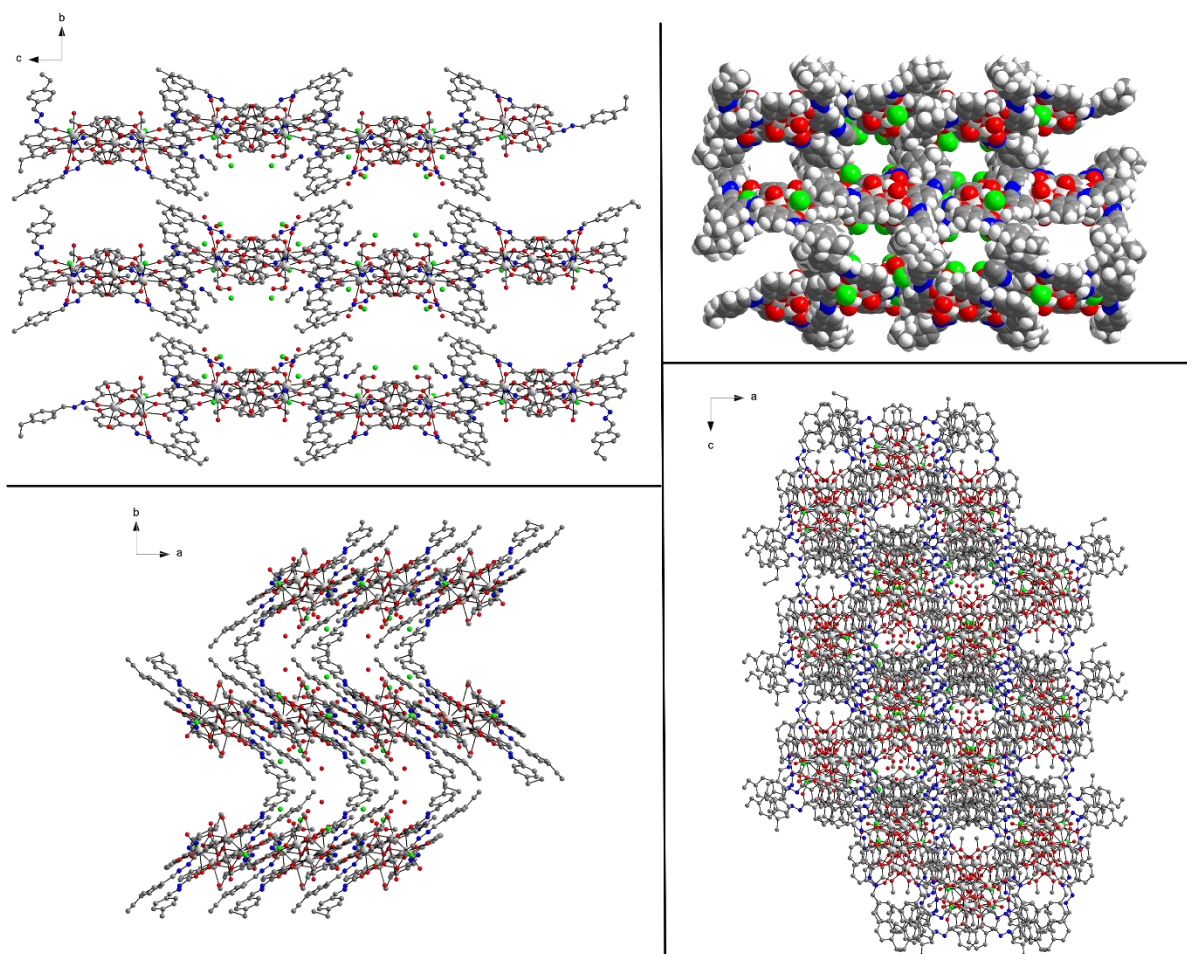


Figure 199. Packing of (**Y₃-84**) along the crystallographic a axis (top left) with a space filling model (top right) and along the crystallographic b (bottom right) and c (bottom left) axes.

Imposing chirality on the ligand

Since all triangles are chiral but crystallise as racemic mixtures of both enantiomers resulting in the inversion symmetry, it was tested whether additionally imposed chirality on the ligand could force the crystallisation of the compounds in acentric space groups. This was done by using the enantiopure aldehydes (*S*)-(-)-perillaldehyde for (**Dy₃-86**) or (1*R*)-(-)-Myrtenal for (**Dy₃-87**). The aldehydes which were used for the *in situ* Schiff base approach are shown in Figure 200.

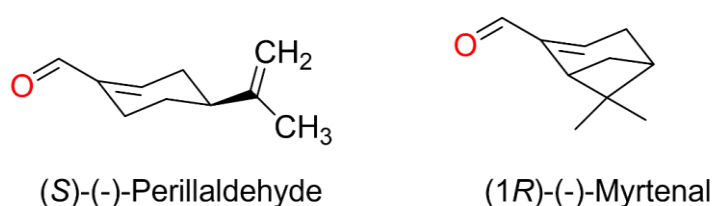


Figure 200. Enantiopure aldehydes used for chiral Schiff base ligands in (**Dy₃-86**) and (**Dy₃-87**).

Using (S)-(-)-Perillaldehyde and (1*R*)-(-)-Myrtenal compounds (**Dy₃-86**) and (**Dy₃-87**) with the respective formulae $[\text{Dy}_3(\text{S-Hperilovh})_3(\mu_3\text{-OH})_2(\text{H}_2\text{O})_4\text{Cl}_2]\text{Cl}_2 \cdot 4\text{MeOH} \cdot 3\text{H}_2\text{O}$ and $[\text{Dy}_3(\text{R-Hmyrovh})_3(\mu_3\text{-OH})_2(\text{H}_2\text{O})_4\text{Cl}_2]\text{Cl}_2 \cdot 4\text{MeOH} \cdot 3\text{H}_2\text{O}$ were isolated.

Compound (**Dy₃-86**) crystallises in a triclinic unit cell with $Z = 2$. Given that the (S)-(-)-perillyl groups on the ligands are enantiopure, and also highly unlikely to racemise during the synthesis and crystallisation, the space group should be the acentric $P1$. However, all the atoms in the cluster molecules apart from those of the perillyl groups conform almost exactly to $P\bar{1}$, with the two triangles essentially related by inversion symmetry. It appears that the perillyl groups occupy sites in the unit cell with very little steric hindrance, such that their chirality does not significantly affect the packing. This resulting pseudo-symmetry makes refinement in $P1$ impracticable due to severe correlation problems. However, refinement in $P\bar{1}$ was relatively straightforward, apart from the resulting apparent “disorder” of all the perillyl groups between both enantiomers. Compound (**Dy₃-87**), with (1*R*)-(-)-myrtenyl substituents, shows a similar pseudo-symmetry. There are four triangles in the unit cell, and refinement in $P1$ was impossible. However, solution and refinement of the structure in $P\bar{1}$, with two triangles now in the asymmetric unit, was again feasible for all of the cluster molecules except the (-)-myrtenyl groups, although the apparent disorder of the latter proved harder to model.

A similar effect had been noted for the butterfly cluster $[\text{Fe}_2\text{Dy}_2(\text{OH})_2(\text{Me-teaH})_2(\text{benz})_6]$, for which the cluster prepared from the enantiopure *R*- or *S*- ligands and crystallised in an almost identical triclinic unit cell to the racemic analogue. In this case the enantiopure compounds could be refined in $P1$ but could also be refined “satisfactorily” in $P\bar{1}$, with a similar apparent disorder of the ligand methyl group on the chiral centre between the two possible positions.^[18]

The molecular structure for (**Dy₃-86**) is shown in Figure 201. In this compound the terminal ligands are four water and two Cl^- ligands with two more Cl^- as counterions in the lattice.

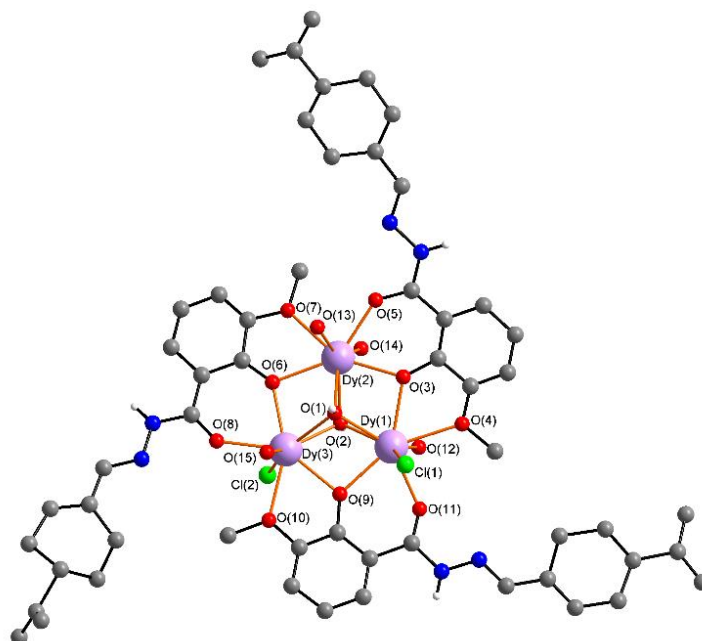


Figure 201. Molecular structure of (**Dy₃-86**).

Figure 202 shows the packing along the three crystallographic axes. The triangles are stacked in parallel without any relative rotation to one another along the *a* axis. Multiple stacks exist in the packing which are pseudo inverted with respect to one another. This may however serve as a proof-of-concept that the use of chiral ligands in such triangular compounds could yield structures in P1 with *Z* = 1 if chiral substituents with enough steric hindrance such that the packing is more significantly influenced are used.

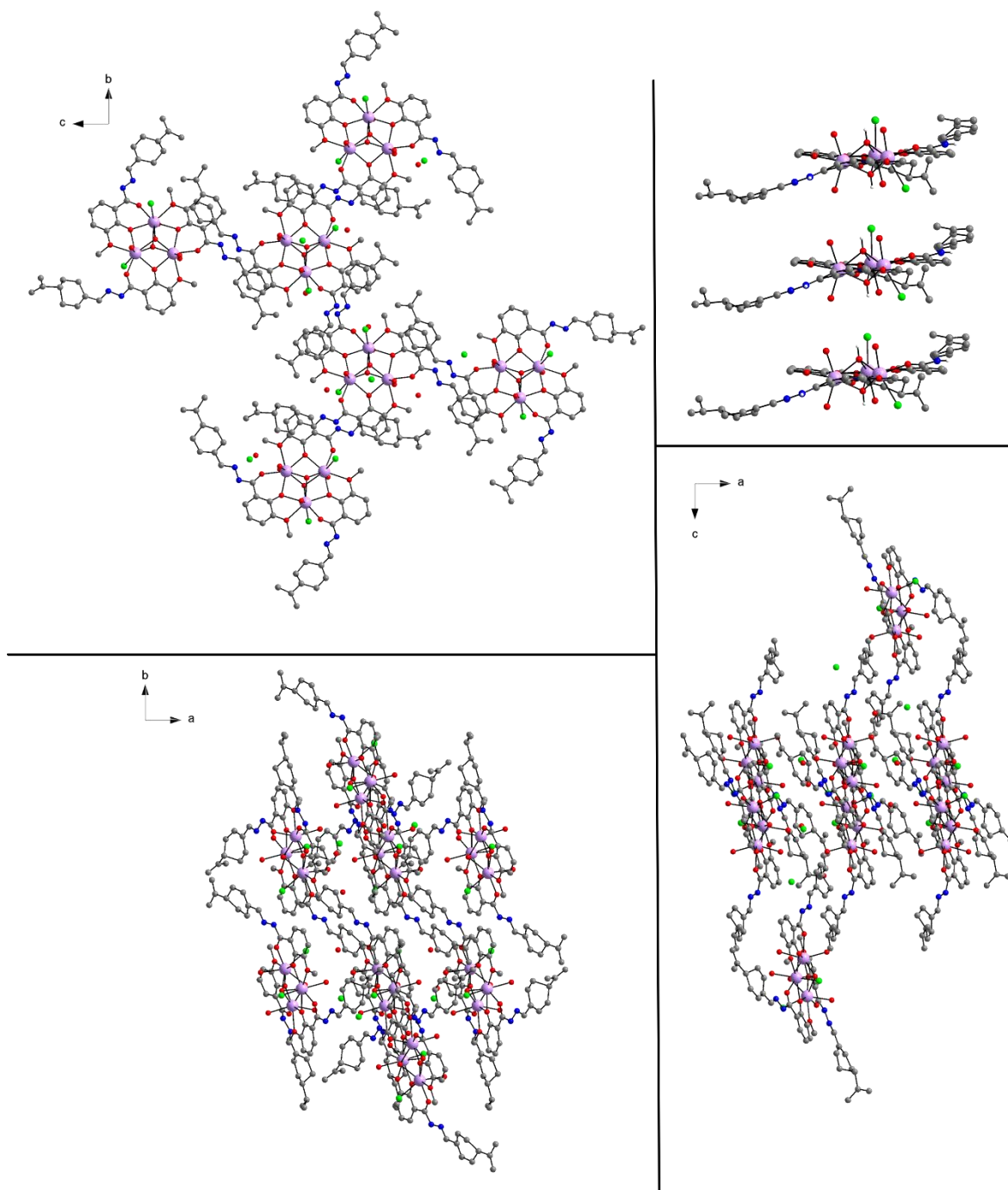


Figure 202. Packing of (**Dy₃-86**) along the crystallographic a (top left) b (bottom right) and c (bottom left) axes. Additional side view of one of the stacks forming along the a axis (top right).

Combining the Schiff base and 5-position halogen substitution approaches

The final ligand modification approach tested and described here involves the combination of concepts from the Schiff base approach with those of the halogen substituted triangles described in section 5.2.

It was possible to synthesise the *o*-vanillyl hydrazide with a Br atom in the 5-position. This compound was used for the *in situ* Schiff base approach with benzaldehyde yielding (**Dy3-88**) $[\text{Dy}_3(\text{HBrbovh})_3(\mu_3\text{-OH})_2(\text{MeOH})(\text{H}_2\text{O})_{1.5}\text{Cl}_{3.5}]\text{Cl}_{0.5}\cdot\text{MeOH}\cdot\text{MeCN}$. Compound (**Dy3-88**) crystallises in the triclinic space group $P\bar{1}$ with $Z = 2$. The molecular structure is shown in Figure 203.

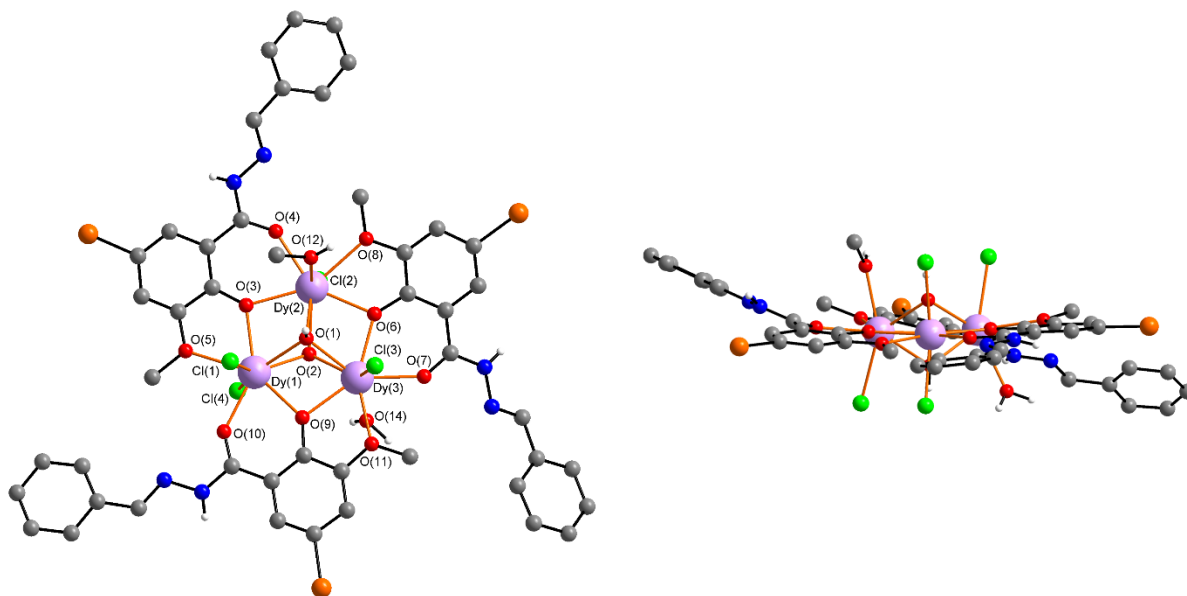


Figure 203. Molecular structure of (**Dy3-88**) (left) with side view (right).

The packing of (**Dy3-88**) is shown along the three crystallographic axes in Figure 204. This reveals stacks of triangles along the crystallographic *a* axis. The triangles are all parallel in the lattice but two different types of stacks exist in the structure which are turned 60° to each other and upside down.

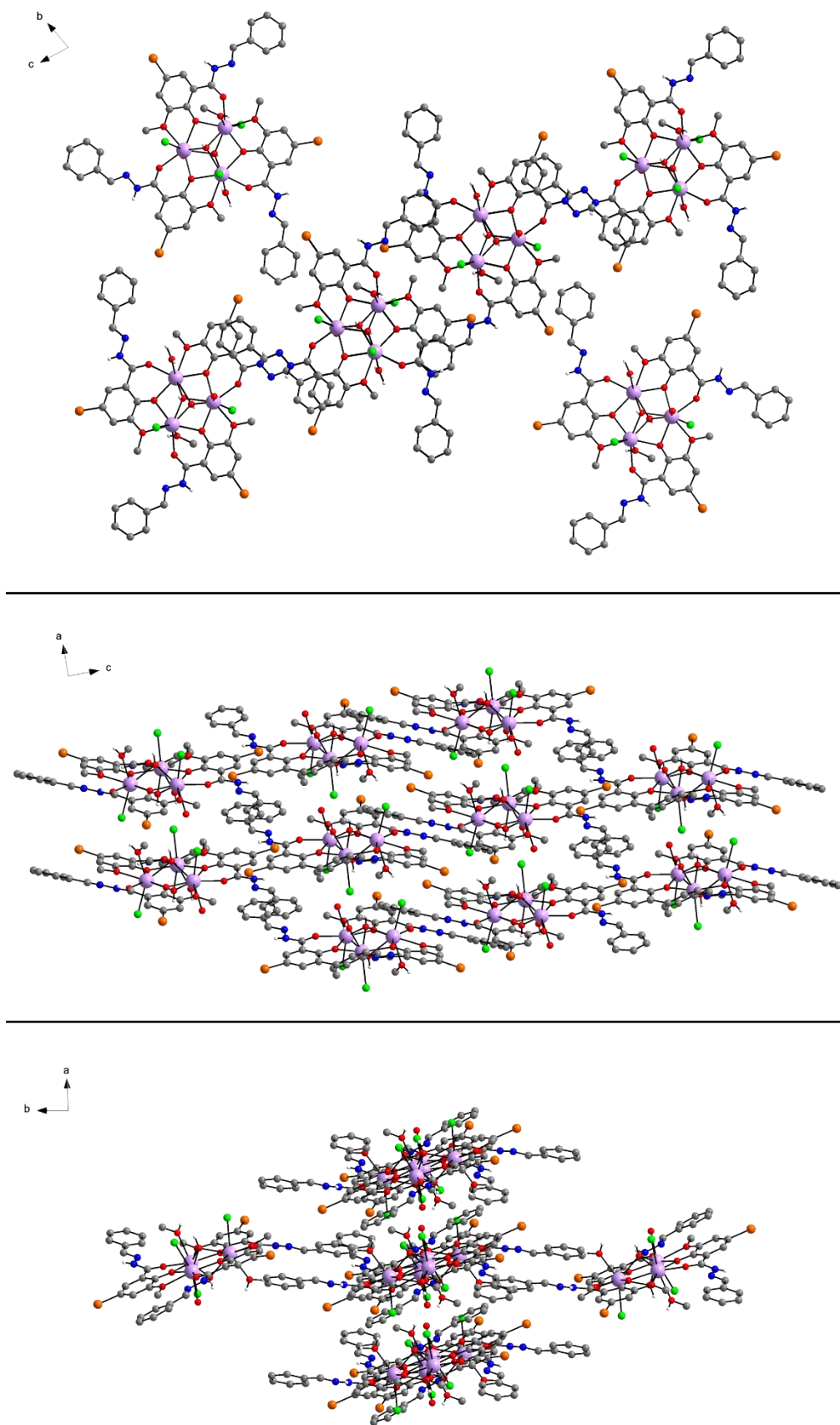


Figure 204. Packing of (**Dy₃-88**) along the crystallographic *a* (top) *b* (middle) and *c* (bottom) axes.

Dy₃ units within a stack are connected *via* hydrogen bonds between the hydrogens of terminal water ligands and Cl⁻ terminal ligands as well as between the hydrogen of the μ_3 -OH and terminal Cl⁻ ligands (see Figure 205). The closest Dy...Dy distance is 7.2837(5) Å. In contrast to the hydrogen bonding observed for most other Schiff base ligand-containing Dy₃ triangles in this work, the NH hydrogen of the ligand does not participate in hydrogen bonds between Dy₃ molecules. All NH hydrogens form hydrogen bonds to lattice solvent or the Cl⁻ counterion. The idea behind the introduction of the Br in the 5 position of the *o*-vanillin moiety was to promote the formation of halogen bonds or halogen interactions. The fact that this is not observed in this compound, as a result of no close contacts being observed between the Br and any of the nucleophilic atoms, suggests that this approach needs further optimisation.

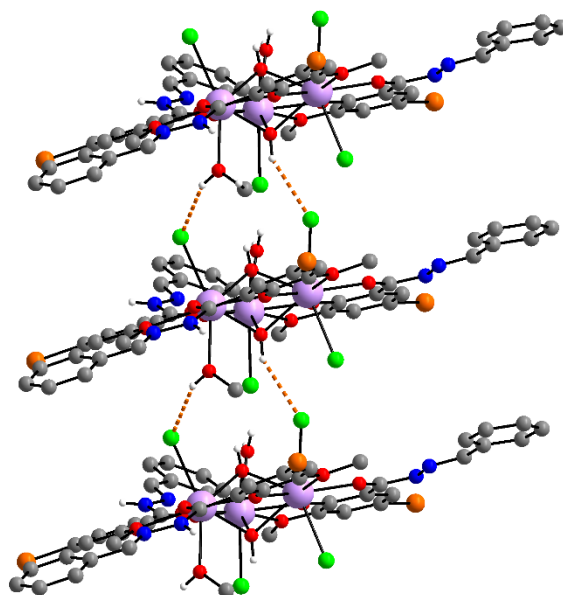


Figure 205. Hydrogen bonding in stacks along the crystallographic *a* axis in (**Dy₃-88**).

APXRD measurement on a powder sample of (**Dy₃-88**) was performed and the results are shown in Figure 206. Additionally, an elemental analysis was conducted which proved the sample to be phase pure.

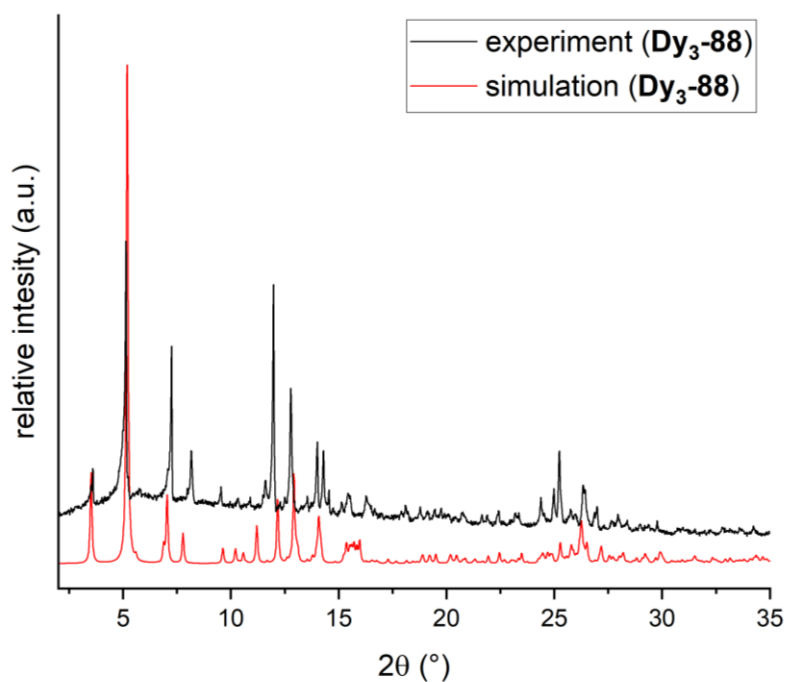


Figure 206. Experimental and simulated powder pattern of (**Dy₃-88**).

In conclusion for this section, the versatility of the Schiff base approach to provide ligand modifications to explore structural changes with implications for the magnetic behaviour by gauging the influence of the position and type of functionalisation of the aldehyde has been demonstrated. A proof-of-concept regarding how to control the outcome of the crystallisation in terms of the resulting space group was explored by imposing chirality on the ligand.

In an initial exploration for expanding these supramolecular design principles by introduction of halogen atoms in a targeted fashion to the Schiff base ligand opens an exciting avenue for further investigation of these fascinating systems.

5.4.2.5 Challenges in data evaluation and side products

It has been shown above that it is a big challenge to understand the role of water take up from the air in steering the properties of targeted compounds. In particular this can affect both the nature of the PXRD and the magnetic properties as judged from SQUID measurements. From the combination of SQUID measurements, PXRD and elemental analysis a connection between water intake and magnetic behaviour could be proposed. Here it was noted that very fast water uptake might be responsible for the diminishment of the low frequency peak in the AC measurement. Interestingly, for the

compounds that crystallised in $R\bar{3}$ it seems that some of these are less susceptible to moisture uptake from the air. Overall this indicates that the nature of the space group symmetry can have an impact on the subsequent physical properties such as the magnetic behaviour. Two examples where the uptake of atmospheric water was very rapid and single crystal XRD measurements thus not possible are discussed here in terms of their likely structures.

The two examples use Schiff base ligands with *p*-chloro-benzaldehyde (H₂pcbovh) and *p*-methyl-benzaldehyde (H₂pmbovh), respectively. The single crystal measurement is sufficient to indicate a Dy₃ core. PXRD measurements for these samples were performed and compared to the predicted powder patterns of other Dy₃ compounds that crystallise in $P\bar{1}$. This showed that all simulated and measured PXRD patterns of Dy₃ triangles with Schiff base ligands that crystallise in $P\bar{1}$ are rather similar. Since the compounds synthesised with H₂pmbovh and H₂pcbovh also had similar powder patterns this indicates that these should be essentially isomorphous to the other $P\bar{1}$ structures. The elemental analysis also fits with the theoretical composition of a Dy₃ compound with these ligands. Figure 207 shows the PXRD and IR of a $P\bar{1}$ structure (**Dy₃-59**) as well as its simulated powder pattern and the comparison to the PXRD for the H₂pmbovh and H₂pcbovh compounds.

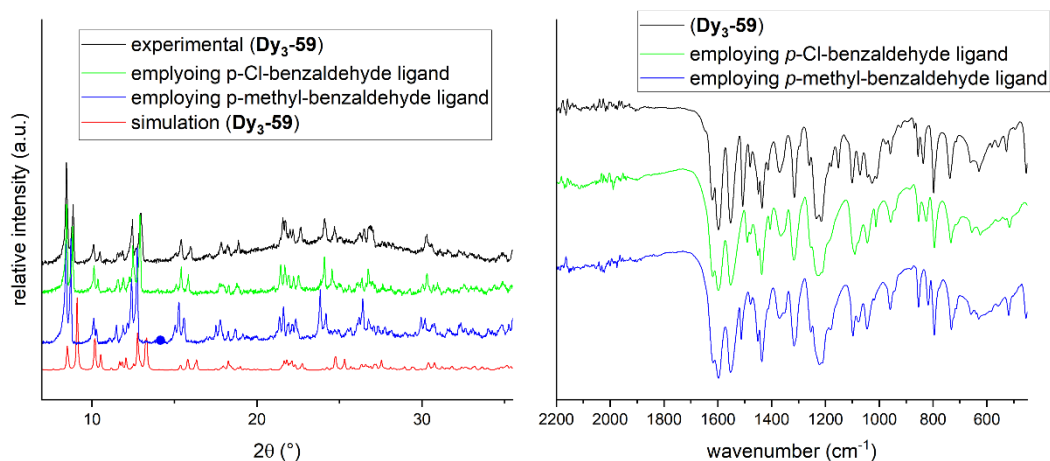


Figure 207. PXRD (left) and IR (right) comparing the products of the reaction between DyCl₃ and the Schiff base ligands which use H₂pmbovh and H₂pcbovh with (**Dy₃-59**).

5.4.2.6 Side products

In the previous sections it was shown that ligand design which preserves the *o*-vanillin moiety can yield Dy₃ compounds with toroidal magnetic properties. This is however not guaranteed particularly when aldehydes with additional coordination sites are used for the synthesis of the Schiff base ligand.

Here, three side products are presented which were synthesised using ligands that have the *o*-vanillin moiety but lead to compounds with neither the coordination geometry nor the nuclearity of the desired Dy₃ motif. The ligands used to target these compounds are shown in Figure 208. All the compounds which are presented here could only be characterised *via* SCXRD and MAGELLAN^[202] analyses in order to test whether these compounds could be magnetically interesting.

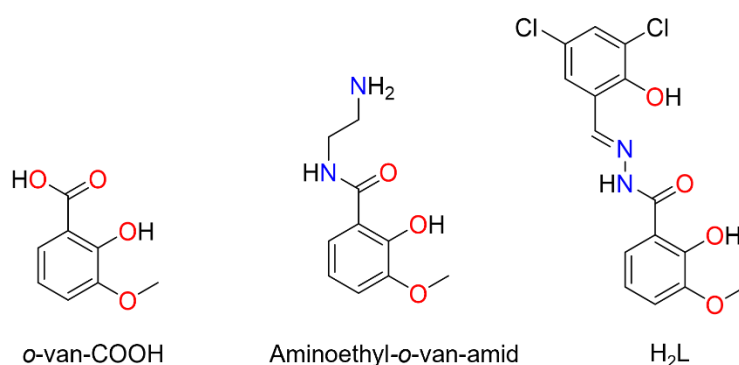


Figure 208. Ligands with *o*-van unit preserved that yielded non-Dy₃ triangle structures.

Using the 2-hydroxy-3-methoxybenzoic acid (*o*-van-COOH) led to (**Dy₁₂-89**) with the formula (Et₃NH)₂[Dy₁₂(van-CO₂)₁₂(Cl)₁₂(H₂O)₁₂]Cl₂·6H₂O·14MeCN. The molecular structure is shown in Figure 209. It demonstrates how an additional OH group probably in conjunction with the different reaction kinetics introduced by the carboxylic acid group can steer the coordination compound away from the Dy₃ motif in the synthesis. (**Dy₁₂-89**) crystallises in the trigonal space group $R\bar{3}$ with $Z = 6$. The metal core consists of six Dy^{III} ions in a cyclohexane-like arrangement with the van-CO₂ ligand bridging via the (μ_2 -O⁻) alkoxy oxygen to another Dy^{III} ion on each corner. The Et₃NH⁺ counterions could not be satisfactorily refined and were thus treated together with the lattice solvent molecules using SQUEEZE.^[234]

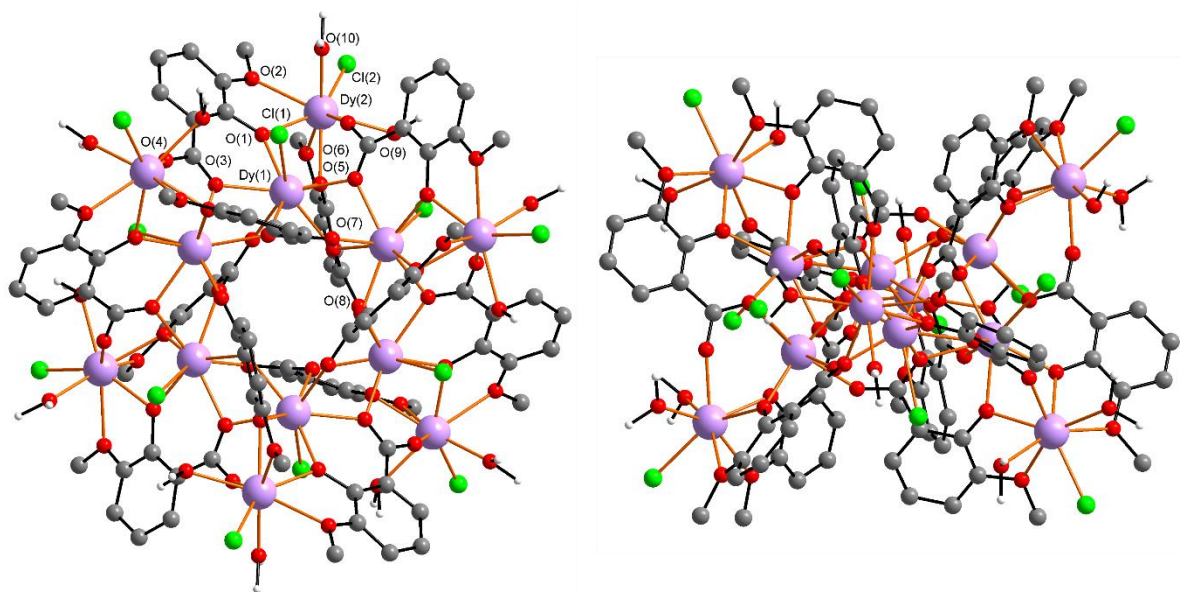


Figure 209. Molecular structure of (**Dy₁₂-89**) top (left) and side view (right).

The MAGELLAN^[202] analysis is shown in Figure 210. The axes of the Dy^{III} ions in the central cyclohexane-like motif are not ordered in a toroidal arrangement and are always parallel to Dy^{III} ions on the opposite side of the ring. The axes on the outer ions point towards the terminal chloride ligands.

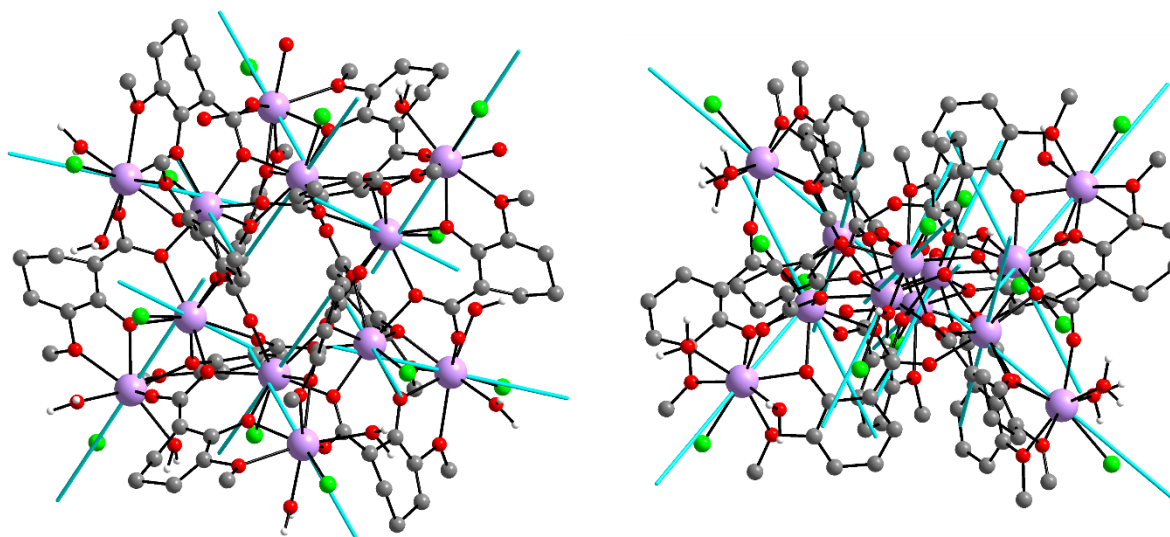


Figure 210. MAGELLAN^[202] analysis of (**Dy₁₂-89**).

A second side product of a triangle synthesis was obtained using N-(2-aminoethyl)-2-hydroxy-3-methoxybenzamide as the ligand (aminoethyl-*o*-van-amid). Here an aminoethyl amid was introduced on the *o*-vanillin instead of the aldehyde. The compound has a Dy₁₂ core and the formula [Dy₁₂(CO₃)₄(μ₃-OH)₄(μ₂-OH)₃(μ₂-OMe)₃(amoniomethyl-*o*-van-amid)₁₂]Cl₁₈·3H₂O·44MeCN (**Dy₁₂-90**) that crystallises in

the cubic space group $F432$ (see Figure 211). The ligand is neutral as a result of the alcohol group being deprotonated and the amine group being protonated. The core forms a truncated tetrahedron *i.e.* four Dy_3 triangles on the vertices of a tetrahedron. Four carbonates, most likely originating from the capture of aerial CO_2 , bridge between three Dy^{III} ions of the triangular faces. The absorption of atmospheric CO_2 is a common feature of lanthanide coordination clusters.^[235-237] The stability of carbonate-bridged lanthanide materials is expected given by their prevalence in lanthanide carbonate minerals.^[238-239]

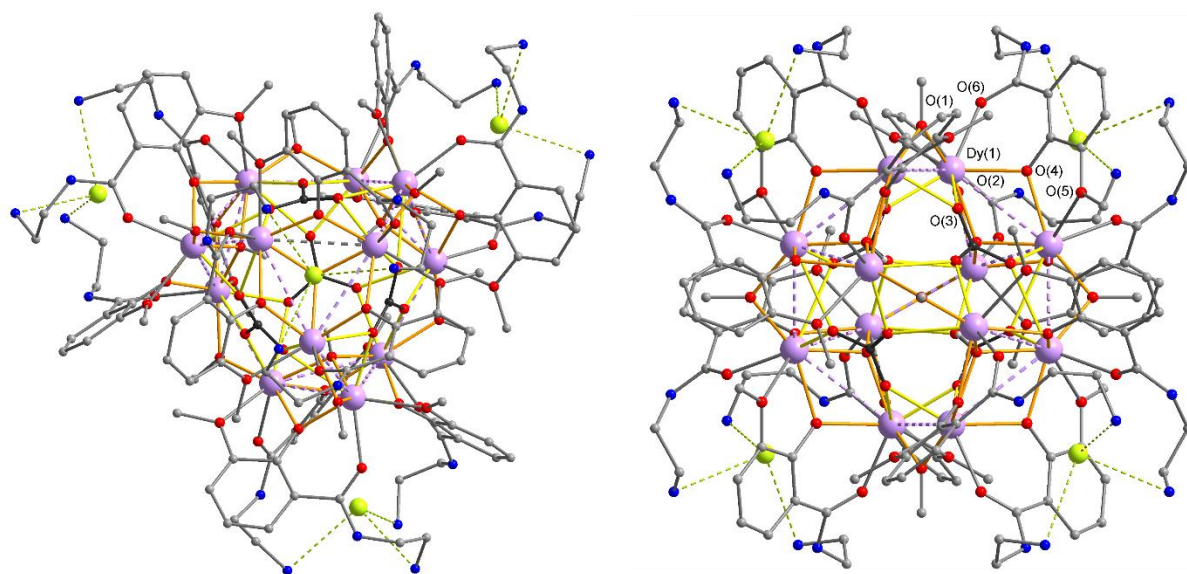


Figure 211. Molecular structure of (**Dy₁₂-90**).

Given that the metal core consists of four Dy_3 triangles on the vertices of a tetrahedron a MAGELLAN^[202] analysis was performed in order to investigate the possibility of toroidal arrangements of the anisotropy axes. As shown in Figure 212 the axes assume a vortex-like in-plane arrangement in each Dy_3 unit which indicates that each individual Dy_3 unit could be toroidal. This requires investigations on the magnetic properties in order to unravel how the interplay of four (potentially) toroidal triangles arranged in a tetrahedron may influence the magnetic behaviour.

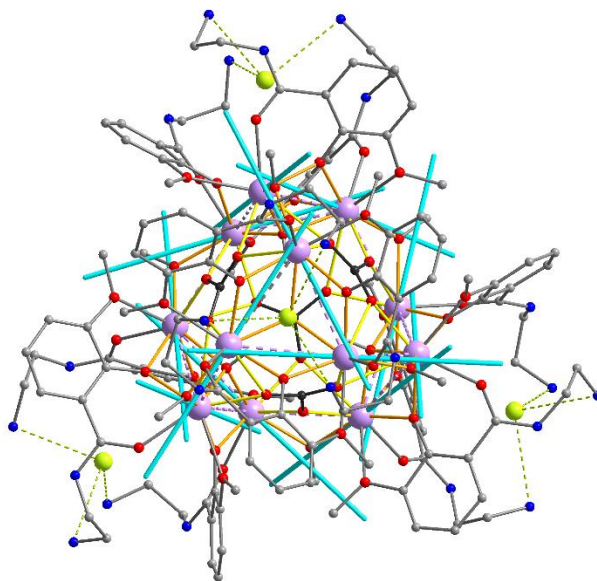


Figure 212. MAGELLAN^[202] axes in (**Dy₁₂-90**) shown as cyan lines.

A third side product was obtained from a synthesis using 3,5-dichloro-2-hydroxybenzaldehyde in an *in situ* Schiff base reaction. Although the desired ligand is formed it assumes a different mode in the Dy^{III} complex since the additional OH group coordinates to a Dy^{III}. Figure 213 shows the molecular structure of (**Dy₆-91**) which has the formula [Dy₆(OH)₂(HL)₆(H₂O)₁₀]Cl₅·4(H₂O)·10MeCN (H₂L= (3,5-dichloro-2-hydroxybenzylidene)-2-hydroxy-3-methoxybenzohydrazide, see Figure 208). It crystallises in the triclinic space group $P\bar{1}$ with $Z = 1$. Each Dy₃ unit has two of the main ligands coordinating via all four oxygens. The aldehyde and alkoxy oxygens assume μ_2 bridging modes. Two further main ligands bridge between the Dy₃ units by coordinating to one side with the methoxy and alkoxy oxygens of the vanillin part of the ligand while the aldehyde and other alkoxy oxygens coordinate to the other Dy₃ unit. The ligands forming the Dy₃ unit therefore have all oxygens oriented towards one side while the bridging ligands have two oxygens on each side which is achieved through rotation along the C(7)-C(8) bonds.

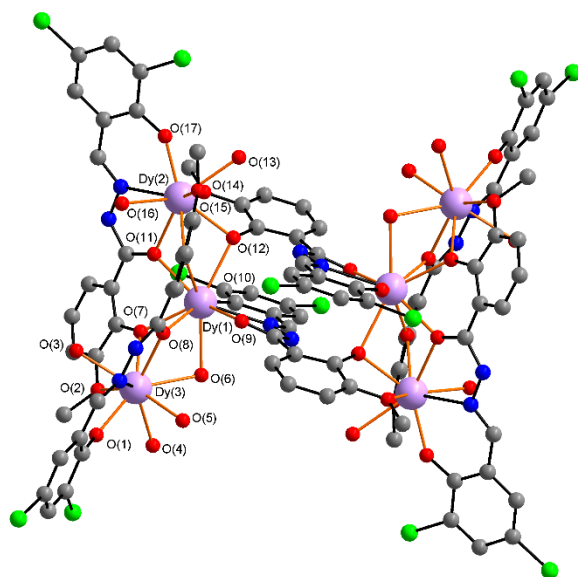


Figure 213. Molecular structure of (**Dy₆-91**).

A MAGELLAN^[202] analysis was performed for (**Dy₆-91**) (see Figure 214) which shows that the two outer Dy^{III} ions of both Dy₃ moieties have their axes tilted into the Dy₃ plane and oriented towards the middle Dy^{III}. For the middle Dy^{III} the axis is oriented orthogonal to the plane of the triangle. This suggests that no toroidal ground state will be found for this compound.

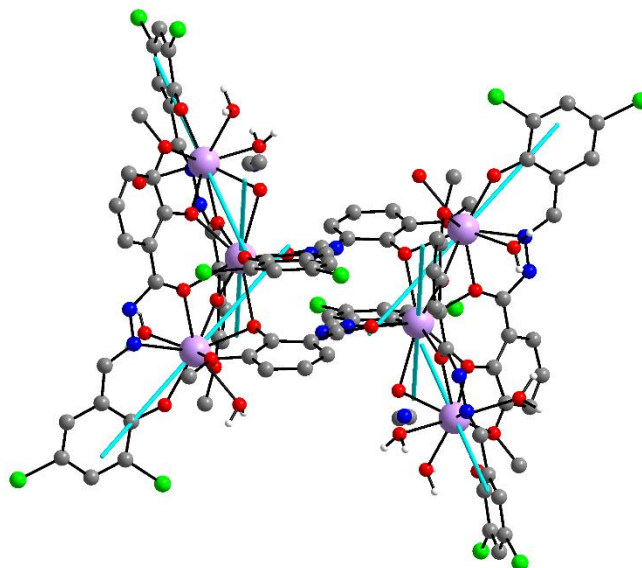


Figure 214. MAGELLAN^[202] axes for (**Dy₆-91**).

5.5 Dy₃ triangle systems conclusion and outlook

The strategies to obtain these possibly toroidal compounds can be categorised into the use of three different synthetic approaches:

1. The use of halogen substituted *o*-vanillin to introduce intermolecular halogen bonding.
2. Using an azo coupled ligand with the prospect of versatility through the remote position of the substituents.
3. Using infinitely variable Schiff base approach to modify the *o*-vanillin unit, thereby either enhancing interactions or deleting them, both of which should give valuable insights into targeting toroidal ground states.

The use of halogen substituted *o*-vanillin

Four Dy₃ triangles and 14 Ln variations with the halogen substituted *o*-vanillin ligands were synthesised and described in this section. Magnetic measurements were performed on the three Dy₃ compounds (**Dy₃-21**), (**Dy₃-22**) and (**Dy₃-36**). For all of these compounds, halogen-halogen interactions were successfully introduced and the influence on the packing and the toroidal ground state was investigated.

The microSQUID and SQUID magnetisation measurements indicate a level crossing and an almost non-magnetic ground state which suggest that the systems are toroidal. From theory calculations, which include CASOCI and a MAGELLAN^[202] analysis, the toroidal properties of the systems were evaluated. Furthermore, a comparison taking the archetypal Dy₃ as a benchmark reveals that the biggest differences are found in the nature of the dynamic magnetic properties as judged from the AC susceptibility data and also the shape of the hysteresis in the microSQUID data. For example the larger jump at zero field in the microSQUID data was related to less effective tunnelling to the toroidal state at the level crossing when sweeping to lower fields.

A toroidal character was also suggested from the quantum chemical calculations which revealed that the orientation of the anisotropy axes lie either in-plane or are canted out of the plane. Here it was established that both the position and distribution of the charged *i.e.* terminal Cl⁻ ligands as well as second sphere effects *i.e.* taking Cl⁻ ions from neighbouring molecules into account for the calculations, have a significant influence on the orientation of the anisotropy axes. From MAGELLAN^[202] it was also

found that the inclusion of Cl⁻ ions of neighbouring molecules can influence whether the spins on the triangle are in-plane or out-of-plane.

Given the large difference in the AC data amongst these three compounds in comparison to the archetypal Dy₃, it was hypothesised to result from the planned introduction of halogen-halogen bonds. These intermolecular interactions were investigated and visualised using an ELF approach whereby the stabilisation energies of the different interactions could be calculated.

Comparing the three compounds with Cl-, Br- and I-atoms on the ligand, respectively, it was found that the strength of the halogen bonds and the microSQUID data were similar for the Dy₃ compounds which use the Cl and Br substituted ligand. For the Dy₃ with the I-substituted ligand both the largest energies of halogen bonds and more significant differences in the microSQUID data were observed. This could be indicative of the influence of halogen bonds on the magnetic behaviour. Further investigations, which include the calculation of the Zeeman plots as well as some angle dependent microSQUID measurements, are necessary in order to establish the exact position of the anisotropy axes and thus evaluate the toroidal character.

Using halogen substituted azo-coupled ligands

Using an azo coupling reaction, it was possible to modify the *o*-vanillin unit creating the Cl/Br-pdavan ligands. This type of ligand has not yet been investigated in the context of coordination chemistry. Here it was used to synthesise two new Dy₃ triangles (**Dy₃-39**) and (**Dy₃-40**) as well as eight isostructural analogues with varied Ln^{III} ions for (**Dy₃-39**). Compound (**Dy₃-39**) which uses Cl-pdavan was magnetically characterised using DC, AC and magnetisation measurements as well as microSQUID measurements. Additionally, a MAGELLAN^[202] analysis was performed in order to establish the direction of the anisotropy axes.

Comparing the obtained data with other Dy₃ triangles in this work reveals a similar behaviour as seen for the halogen substituted triangles indicating comparable toroidal character of the ground state. The azo triangle system offers additional potential for comparative studies on the effect of different charged terminal ligands, since it employs terminal NO₃⁻ ligands in place of the previously used Cl⁻. It was concluded that further measurements on (**Dy₃-39**) are necessary in order to be able to establish

the orientation of the anisotropy axes and thus conclude on the toroidal character of the ground state.

The similarities between the halogen substituted Dy₃ systems and (**Dy₃-39**) may be related to the halogen on the Cl-pdavan ligand since its involved in the formation of halogen bonds. These form between the Cl and an oxygen atom from a nitrate acting as the electron density donor. Additionally, a large contribution from π - π stacking can be found between molecules leading to a closely packed layer structure. A significant increase in intermolecular interactions was found compared to the archetypal Dy₃ which might explain the changes in dynamic magnetic properties.

The ligand system itself presents a vast range of possible modifications for further investigation since it can be functionalised in positions which are remote from the *o*-vanillin coordination sites and therefore the metal core. This allows for modifications which can, in theory, be either additional coordination sites or sterically demanding groups, but neither interfere with the fundamental Dy₃ *o*-vanillin triangle motif.

Using a Schiff base approach

Lastly a Schiff base approach was used to synthesise Dy₃ triangles with imposed symmetry. A proof-of-concept for this was reported by Tang *et al.*^[166] for two Dy₃ triangles. In contrast to the other strategies designed to impose symmetry it appears to be feasible here through limiting the available intermolecular interactions rather than increasing them. This was successfully shown for the Dy₃ triangle synthesised using the Schiff base ligand resulting from *o*-vanillyl hydrazide and benzaldehyde (**Dy₃-49**). The compound crystallises in $R\bar{3}$ which significantly reduces the complexity of the system since all Dy^{III} ions are symmetry-related either by the threefold axis or the inversion centre.

The packing in parallel stacks along the crystallographic *c* axis also enables single crystal measurements along specific axes in respect to the triangle orientation. Initially a full magnetic characterisation was performed on powder samples of (**Dy₃-49**) including DC, AC and magnetisation measurements. The AC data were largely different from what was described for the azo coupled and halogen substituted triangles. However, the results are very similar to those obtained for the archetypal Dy₃.

Single crystal measurements using microSQUID and additionally cantilever torque magnetometry were performed with the potential advantages of the higher symmetry within the crystal in mind. To perform the torque measurements a single crystal was selected and indexed using SCXRD measurements to relate the laboratory reference frame XYZ to the crystallographic axes a , b and c which can be transformed to the orthogonal reference frame $ab'c^*$. By doing this, two rotations relative to the triangle plane were measured: One rotation along the crystallographic c axis which is perpendicular to the triangle plane and one rotation along an axis almost in the triangle plane were performed. The measured data were used to determine the angles of the anisotropy axes out of the plane (6°) and the deviation from the tangential direction (12°). This is proof for the in-plane vortex formation of spins and therefore the toroidal ground state. The full evaluation of the torque measurement needs additional calculations which are currently being done in collaboration with Prof. Dr. Alessandro Soncini.

Additionally, microSQUID measurements on single crystals were performed in collaboration with Appu Sunil and Dr. Sagar Paul from the group of Prof. Dr. Wolfgang Wernsdorfer. Because it was not possible to index the crystal beforehand, the direction of the measurement was related to the shape of the crystal and the position of the crystal was adjusted by hand. By doing this, measurements were performed along the easy axis of the system along one of the three anisotropy axes coplanar to the triangle, along an intermediate axis which is also in the plane of the triangle but perpendicular to one of the three anisotropy axis and along the crystallographic c axis which is orthogonal to the plane of the triangle. All three measurements showed hysteresis albeit with significant differences. The non-magnetic ground state at fields up to ca. 0.9 T (level crossing is dependent on the measurement angle) had a small magnetisation along the easy axis, an almost completely closed hysteresis and therefore very close to non-magnetic ground state along the in-plane intermediate axis or else showed a large open hysteresis along the c axis which also showed some artifacts which are related to misalignment of the crystal. Additionally, for the orientation along the easy axis the jump usually observed at zero field is not seen. The collected data along the three axes could be interpreted together with the calculated Zeeman diagrams. This resulted in evidence of pinning of spins and ordering of toroidal moments in the crystal which has been termed chirality selection. By applying

the magnetic field along one of the easy axes, one orientation (clockwise or anticlockwise) of toroidal arrangements is preferred when reducing the applied field. However, the inversion related counterpart in the crystal assumes the opposite orientation which then should lead to the toroidal moments cancelling and a net magnetisation in the *c* direction as is observed. This gives insights into the directionality one can impose on the toroidal arrangement using applied fields and thus the interpretation of the microSQUID data.

As a result of the higher symmetry the system is less complicated to describe. This in turn makes it easier to draw conclusion on the nature of toroidal states. Thus the results shown here also give reasons to revisit the data collected on the archetypal Dy₃ in order to explore whether the chirality selection effect is visible. Given that neither the improved microSQUID technique nor the current torque magnetometry setup were available at the time, this is an incentive to reexplore the archetypal system in even greater detail.

Eleven further Dy₃ triangles with the Schiff base type ligands were synthesised as well as a total of 28 Ln^{III} variations. The Schiff base ligands used were mainly based on substituted benzaldehyde derivatives. This allowed for a systematic investigation of the type of substituent and its position as well as their influence on the magnetic behaviour. For all the meta-substituted benzaldehydes there was a higher imposed symmetry through crystallisation in the space group $R\bar{3}$ was observed. As an exception one compound in this *meta* series crystallised in $P\bar{1}$. Interestingly the para substituted version mostly crystallises in $P\bar{1}$. However here there are also some exceptions which crystallise in space groups such as *Pbca* or $P\bar{3}c1$.

Furthermore, comparing the Dy₃ triangles with the *ortho*-, *meta*- and *para*-fluoro substitutions showed that the substitution on the ortho position significantly reduces the yield of the reaction crystallising however in the $R\bar{3}$ space group. Magnetic measurements on four types of Dy₃ triangles with the Schiff base ligands that were made using *p*-OH-, *m*-OH-, *p*-F- and *m*-F-benzaldehyde include DC, AC and magnetisation measurements on powder samples. The results of all measurements were similar with some small differences in the position of the inflection point in the magnetisation measurement. Comparing these results to the magnetic data on (Dy₃-

49) indicates that all of these compounds have similar magnetic properties and could be toroidal in nature.

However it is important to note that the lattice solvents can have an important effect on the dynamic magnetic behaviour as revealed from the AC data of (**Dy₃-59**), (**Dy₃-67**), (**Dy₃-77**) and (**Dy₃-78**) where the lattice solvent can exchange with moisture in the air leading to the demise of the first maximum in the AC signals. Compounds crystallising in $R\bar{3}$ are apparently less susceptible to this problem.

Since the crystallisation of all of these compounds always results in the presence of both enantiomers of the triangle complex, attempts were made to impose homochirality by using chiral aldehydes in the Schiff base reaction. First tests on this approach showed promising results since it was possible to synthesise the Dy₃ compound with the chiral unit attached to the ligand. The structure obtained from this was refined in $P\bar{1}$ due to the large disorder of the chiral groups although its true space group has to be $P1$. Future work on this system includes the change of the space group to, for example, $R3$ which would remove the other enantiomer and therefore should maximise the net toroidal moment. Current methods to do so involve the introduction of other chiral species during the crystallisation process of (**Dy₃-49**) which until now only yielded (**Dy₃-49**) still as a racemate crystallising in $R\bar{3}$. Another method which could force the crystallisation of only one enantiomer involves the use of chiral solvents.^[240] It might also be possible with favourable solubility conditions to use chiral columns for enantiomer separation.

The investigation of ligand modifications also made it able to gauge where the functionalisation can interfere with the formation of the Dy₃ motif. Three such compounds presented in this work were characterised using SCXRD measurements and MAGELLAN.^[202] These include a Dy₆ and two Dy₁₂ clusters. The structure of (**Dy₁₂-90**) is particularly interesting for future investigation given that MAGELLAN^[202] predicts all four Dy₃ moieties in the truncated tetrahedron to be individually toroidal.

Graphic overview of Dy₃ triangles in this thesis

To summarise, 17 new Dy₃ triangles were synthesised and structurally characterised. Figure 215 schematically illustrates the range of successfully implemented ligand modifications using *o*-vanillin as the structural basis plus ligand design for modifications.

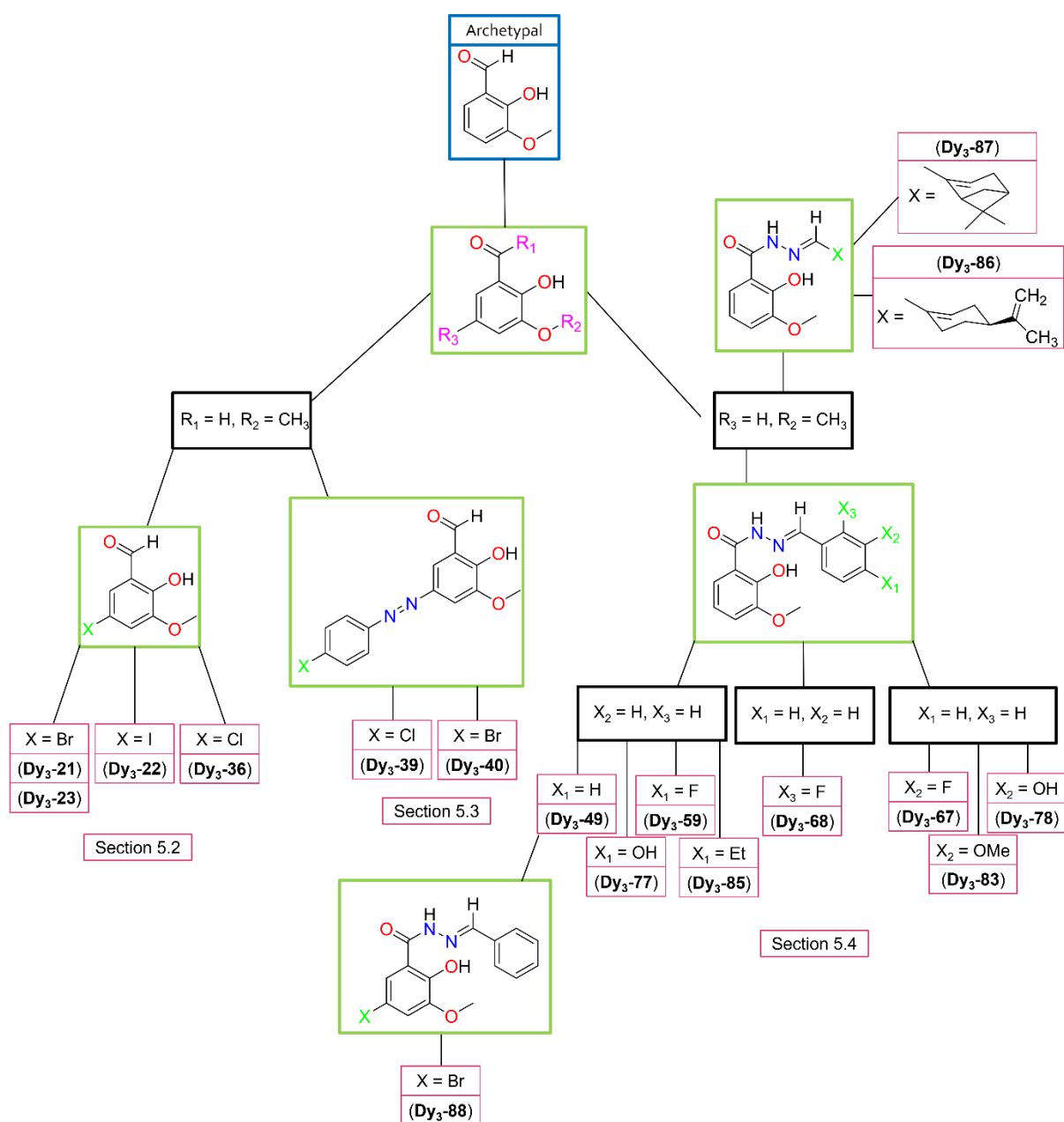


Figure 215. Diagram of *o*-vanillin base ligand modifications used to synthesise Dy₃ clusters in this work.

Table 14 gives an overview of changes in space group and the dominating types of intermolecular interactions in these triangles.

Table 14. Space groups and dominant intermolecular interactions of Dy₃ triangles.

ID	Space group	Interactions
(Dy ₃ -21)	R $\bar{3}$	Hal-bond
(Dy ₃ -22)	Cc	Hal-bond
(Dy ₃ -36)	P2 ₁ /c	Hal-bond

(Dy ₃ -23)	Pna21	H-bond
(Dy ₃ -39)	$P\bar{1}$	π - π /Hal-bond
(Dy ₃ -40)	$P\bar{1}$	π - π /Hal-bond
(Dy ₃ -49)	$R\bar{3}$	H-bond
(Dy ₃ -59)	$P\bar{1}$	H-bond
(Dy ₃ -67)	$R\bar{3}$	H-bond
(Dy ₃ -68)	$R\bar{3}$	H-bond
(Dy ₃ -77)	$P\bar{3}c1$	H-bond
(Dy ₃ -78)	$R\bar{3}$	H-bond
(Dy ₃ -83)	$P\bar{1}$	H-bond
(Dy ₃ -85)	Pbca	H-bond
(Dy ₃ -86)	P1	H-bond
(Dy ₃ -87)	P1	H-bond
(Dy ₃ -88)	$P\bar{1}$	H-bond

Nine of these compounds were magnetically characterised. Table 15 summarises the obtained switching fields from magnetisation measurements on powder samples as determined from the first derivatives of S-shaped M vs H magnetisation curves. The thus obtained value of the switching field for the compounds described here does not show any significant variation from an average of 0.9 T. This indicates that although ligand modifications and their effect on packing and intermolecular interactions can influence the properties of the toroidal ground state, the field dependence of the level crossing in a powder sample is largely unaffected.

Table 15. Switching fields of Dy₃ triangles.

ID	(Dy ₃ -21)	(Dy ₃ -22)	(Dy ₃ -36)	(Dy ₃ -39)	(Dy ₃ -49)	(Dy ₃ -59)	(Dy ₃ -67)	(Dy ₃ -77)	(Dy ₃ -78)
B_{sw} (T)	0.93	0.96	0.90	0.87	0.91	0.90	0.90	0.86	0.93

6. Linked triangles

6.1 Introduction

In section 3.6 it was described how linking Dy_3 moieties using intermediate transition metals can increase coupling and lead to ferrotoroidic order in the molecule. Examples for this were the $\text{Cu}^{\text{II}}/\text{Dy}^{\text{III}}$ 1D chiral polymers by Powell *et al.*^[136] where a Cu^{II} bis-valinate complex bridges between two of the archetypal Dy_3 units with *o*-van ligands or the Dy_3CrDy_3 by Murray *et al.*^[137] where a Cr^{III} bridges between the Dy_3 triangles. In the first case the coupling between toroidal moments is mediated by the Cu^{II} in the second it was found that the ferrotoroidic ground state is a result of intramolecular dipolar interactions between triangles.

The same concept of connecting Dy_3 triangles but without the use of transition metals is a subject of current research. A Dy_6 consisting of coupled Dy_3 moieties was published in 2012 by Tang *et al.*^[171] where an enhanced toroidal moment was observed. Strong coupling *via* the $(\mu_4\text{-O}^{2-})$ group stabilises similar orientations of the two toroidal moments. The microSQUID shows the non-magnetic ground state and a large hysteresis at higher fields (see Figure 216).

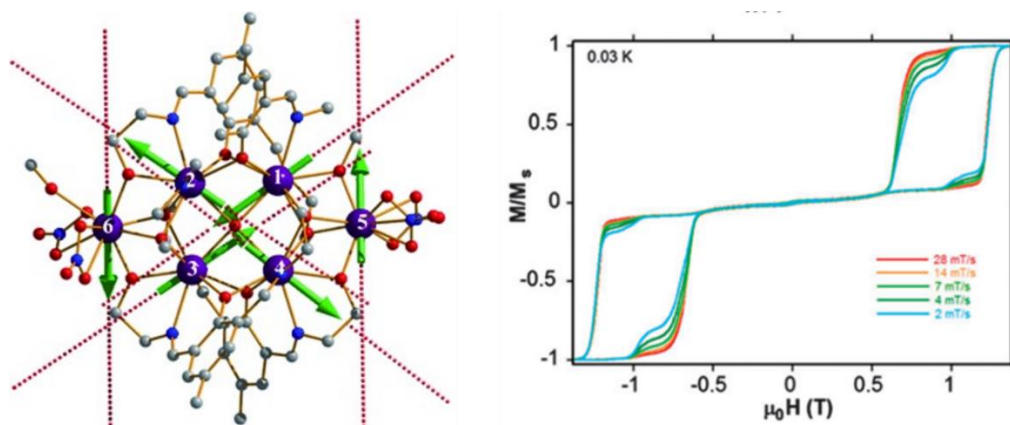


Figure 216. Linked Dy_3 triangles with anisotropy axes as green arrows (left) and microSQUID measurement at 0.03 K at different fields (right). Reprinted with permission from reference^[171] [John Wiley & Sons] copyright [2012].

The Dy_6 published by Powell *et al.* in 2010^[170] consists of two linked units of the archetypal Dy_3 . This was done through the addition of *o*-vanillinol to the reaction solution which replaces one of the *o*-vanillin units on both triangles. The alkoxy group assumes a $(\mu_2\text{-OR})$ bridging mode between the two triangles (see Figure 217).

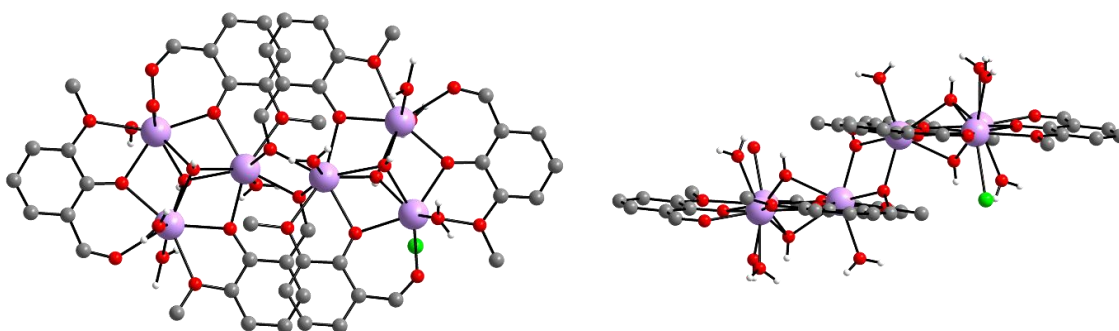


Figure 217. Dy₆ consisting of two archetypal Dy₃s with one *o*-vanillin exchanged for a *o*-vanillinol.^[170]

The compound was published to highlight the enhanced slow magnetic relaxation compared with the archetypal Dy₃. It was also shown that the anisotropy axes assume an in-plane orientation with some - compared to the Dy₃ - larger tilt of about 10° out of the plane.

This Dy₆ motif, in particular given the influence of structural modifications on its toroidal properties, was chosen to be investigated further here. The idea is that linking triangular units has thus been identified as a promising pathway to enhance toroidal moments this offers the prospect for identifying compounds with ferrotoroidic behaviour.

Since substituting the *o*-vanillin ligand with halogens has been shown to introduce halogen bonding as an intermolecular interaction which can impose desired symmetries. Additionally, halogen substitution enables the study of electron-withdrawing effects on toroidal properties. As mentioned above, it was previously shown that linking the triangles improved the SMM properties compared to the isolated Dy₃.^[170] A similar comparison to identify trends should be possible here since the isolated Dy₃ compounds with 5-I/Br/Cl-vanillin were also magnetically characterised in this work ((Dy₃-21), (Dy₃-22), (Dy₃-36) see section 5.2).

A second tuning handle in the structure of the Dy₆ motif is the bridging unit between Dy₃ units. The original Dy₆ with *o*-van ligands has two bridging alkoxy groups. In the course of my Master thesis^[219] synthetic work, it was discovered that other bridging species can form *in situ* when using differently substituted *o*-vanillin ligands. Employing only substituted *o*-vanillin and varying reaction conditions in an *in situ* synthesis yielded two bridging *o*-vanillin-derived species (NO₂-van' and NO₂-van''). A reduction of the aldehyde group for NO₂-van' and hydration of the aldehyde group for NO₂-van'' led to a Dy₆ with a comparable structure and a slight modification in the

bridging moieties (see Figure 218). In the Dy₆ compound with *o*-van ligands reported in the literature, Dy···Dy distances of 3.7262(4) Å were observed. The NO₂-substituted derivative with the formula [Dy₆(OH)₄(NO₂-van)₄(NO₂-van')₄(NO₂-van'')(Cl)₂(H₂O)₈]Cl₄·12MeOH has a nearly identical core geometry with the closest Dy···Dy distance between triangles of a single molecule being 3.745(2) Å.

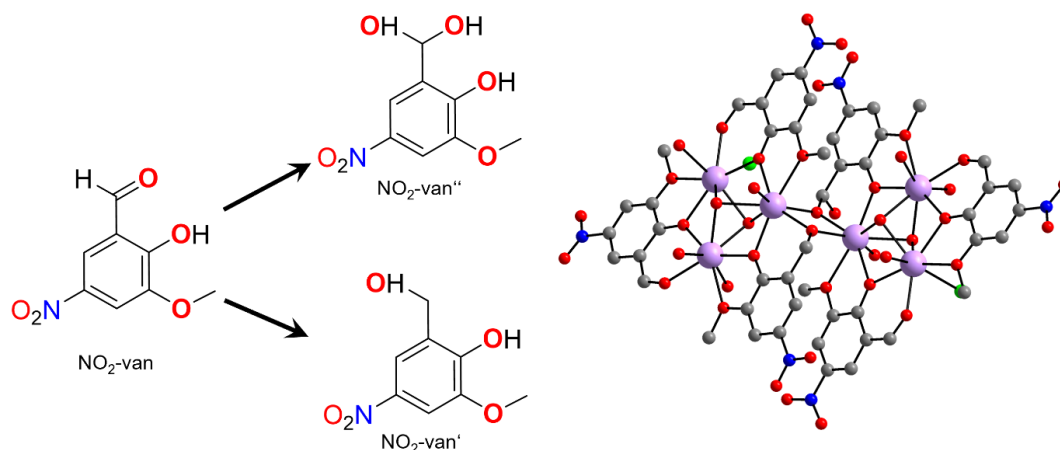


Figure 218. Formation of bridging ligand species from NO₂-van educt (left) and molecular structure of Dy₆ (right). Changes in bridging unit which could correlate with different Dy-O-Dy angles or Dy···Dy distances can have a significant influence on the coupling between magnetic centres and on the toroidicity of the system. It was thus chosen to further investigate the possibility of creating other bridging geometries *via in situ* generation of substituted *o*-vanillin derived species. The ability to control the distance between triangular units in a Dy₆ and thereby adjust the interactions between them could provide a powerful tool for studying and optimising magnetic and toroidal properties and is explored in this work.

6.2 Linking *via o*-vanillin type ligands

As first discovered in 2010 by Powell *et al.*^[170] a molecule consisting of two connected Dy₃ units can be synthesised using *o*-vanillin in combination with *o*-vanillinol where the aldehyde group of *o*-vanillin was reduced to an alcohol *in situ*. Initially this type of compound was accidentally discovered when the reaction that was supposed to produce the Tm^{III} version of the archetypal Dy₃ triangle with *o*-vanillin ligands yielded a Tm₆ structure with the alkoxide double bridge (from the *o*-vanillinol) between the triangular Dy₃ moieties. In order to steer the reaction to intentionally and reproducibly

obtain the Ln_6 compound, the *o*-vanillinol was separately added to the reaction mixture instead of relying on the *in situ* reduction of *o*-vanillin.

Here two modifications to this procedure are described. The first in which the *o*-vanillinol was added to a mixture of the lanthanide salt and *o*-vanillin which was substituted in the 5-position with halogens. The aim here was to introduce halogen interactions and observe their influence on the magnetic properties. The second approach used only the 5-substituted *o*-vanillin derivative in the reaction mixture and forms a different bridging *o*-vanillin derived species (*o*-vandiols) *in situ* allowing for different bridging geometries. This is in line with what was first observed during my Master thesis.^[219]

6.2.1 Adding *o*-vanillinol

The new Dy_6 compounds described here were made by modification of the synthesis of the halogen-substituted triangles described in section 5.2, replacing 1/3 of the ligand with *o*-vanillinol. Additionally, the solvent ratio of the MeCN/MeOH mixture had to be adjusted to obtain the product in a crystalline form suitable for single crystal measurements.

As part of this work, two new structures were found, both following the same motif of the Dy_6 compound published in 2010,^[170] but with the respective halogens on the *o*-vanillin units. It is important to note that while the *o*-vanillin was substituted the *o*-vanillinol was added in its unsubstituted form (see Figure 219).

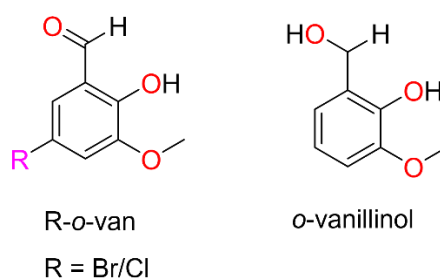


Figure 219. Halogen substituted *o*-vanillin and non-substituted *o*-vanillinol.

The two compounds use 5-chloro-substituted *o*-vanillin in the case of (**Dy₆-92**) and the Br-substituted ligand in the case of (**Dy₆-93**). (**Dy₆-92**) has the formula $[\text{Dy}_6(\mu_3\text{-OH})_4(\text{Cl-van})_4(\text{vanoxo})_2(\text{H}_2\text{O})_7\text{Cl}_3]\text{Cl}_3 \cdot \text{H}_2\text{O} \cdot 4\text{MeOH}$ and crystallises in the monoclinic

space group P21/n with $Z = 2$. Compound (**Dy₆-93**) with the formula $[\text{Dy}_6(\mu_3\text{-OH})_4(\text{Br-van})_4(\text{vanoxo})_2(\text{H}_2\text{O})_6\text{Cl}_4]\text{Cl}_2 \cdot 6\text{H}_2\text{O}$ is essentially isomorphous to (**Dy₆-92**). The molecular structures of both compounds are shown in Figure 220 and 221.

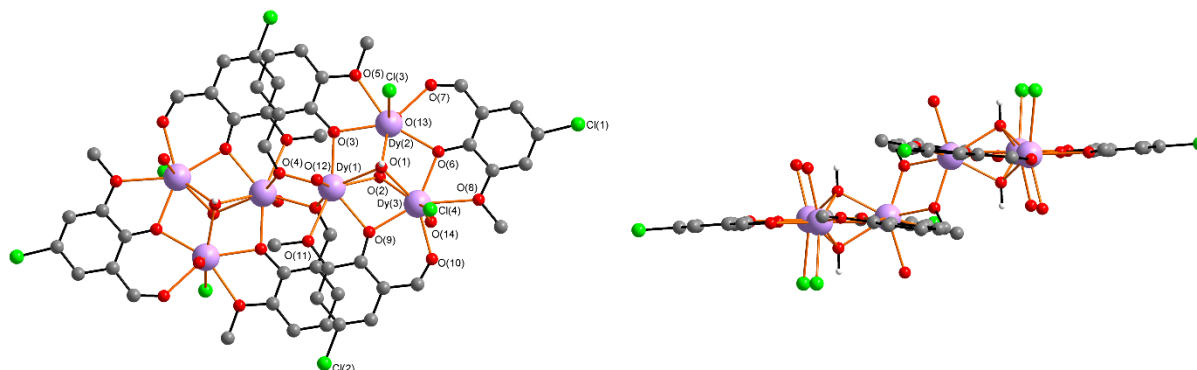


Figure 220. Molecular structure of (**Dy₆-92**) with sideview (right). Hydrogen atoms on the terminal water ligands were not refinable and disorder of Cl(4)/O(15) was omitted for clarity.

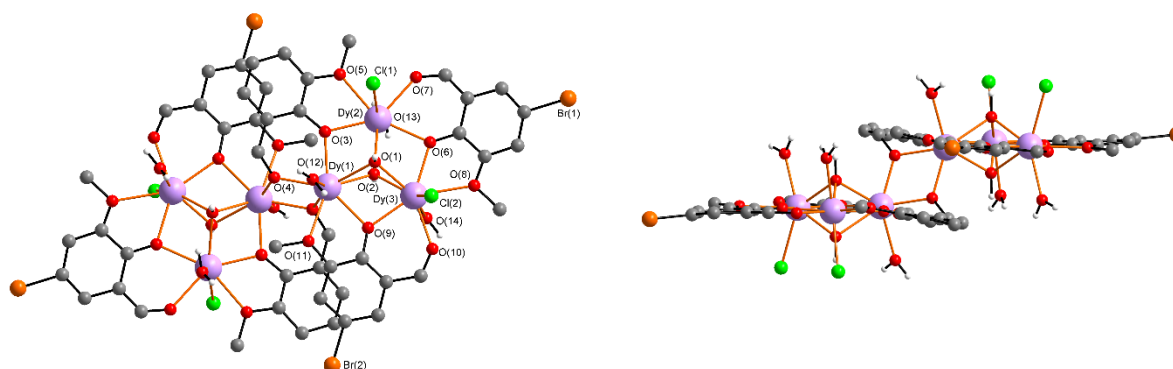


Figure 221. Molecular structure of (**Dy₆-93**) with side view (right).

The molecules consist of two Dy_3 units with the same overall coordination environment around the Dy^{III} ions as described above for the Dy_3 systems with the *o*-vanillin unit on each triangle exchanged for the *o*-vanoxo ligand which connects the two triangles *via* the μ_2 -alkoxide groups. The distribution of terminal chlorides is different compared to the original Dy_6 in which only one Cl^- occupies a terminal ligand position. In (**Dy₆-92**) three terminal Cl^- ligands coordinate leading to complex cation which in total is three times positively charged and accompanied by three lattice Cl^- counterions to provide charge balance. As for the Dy_6 from 2010 one of the chloride terminal ligands is 50/50 disordered with a water ligand. In the case of (**Dy₆-93**) the structure is ordered with four Cl^- terminal ligands two on each triangle and two lattice chloride counterions. The Dy_3 units in both compounds are co-parallel with the closest inter-triangle $\text{Dy} \cdots \text{Dy}$ distance being 3.7504(6) Å for (**Dy₆-92**) and 3.762(1) Å for (**Dy₆-93**). As a result of the

similarity amongst the three structures ((**Dy₆-92**), (**Dy₆-93**) and original Dy₆ with *o*-van ligands), in terms of the geometry of the Dy^{III} cores, the deciding difference which has an impact on the magnetic properties is the distribution of terminal chlorides.

The packing is described for (**Dy₆-92**) since the two compounds can be described as isomorphous. Along the crystallographic *b* axis the triangles are perfectly aligned in a stack (see Figure 222). The closest distance between Dy^{III} ions in a stack is 12.9641(7) Å and the closest distance between Dy^{III} ions of neighbouring stacks is 7.7991(7) Å meaning they are too far apart to expect significant interactions along either of these pathways.

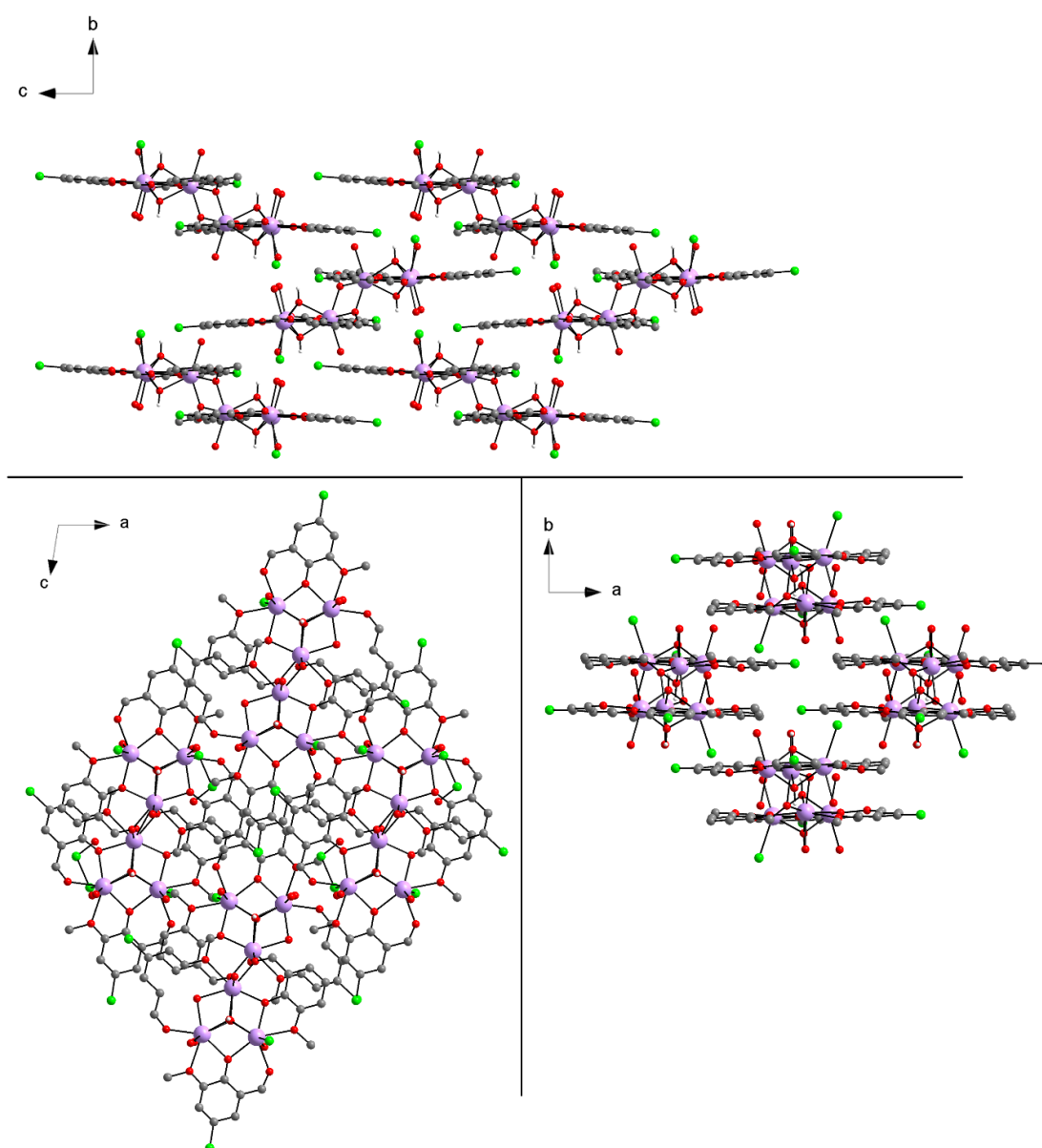


Figure 222. Packing for (**Dy₆-91**) along the crystallographic *a* axis (top), *b* axis (bottom left) and *c* axis (bottom right).

The packing is dominated by hydrogen bonds between a hydrogen atom on the terminal water ligand with O(14) and the Cl(4) terminal ligand (see Figure 223). These hydrogen bonds lead to the formation of sheets throughout the lattice. The Cl atoms on the 5-position of the *o*-vanillin based ligands are not involved in halogen bonding between molecules but show some halogen interactions with lattice chloride counterions (Cl(1) and a Cl⁻ counterion).

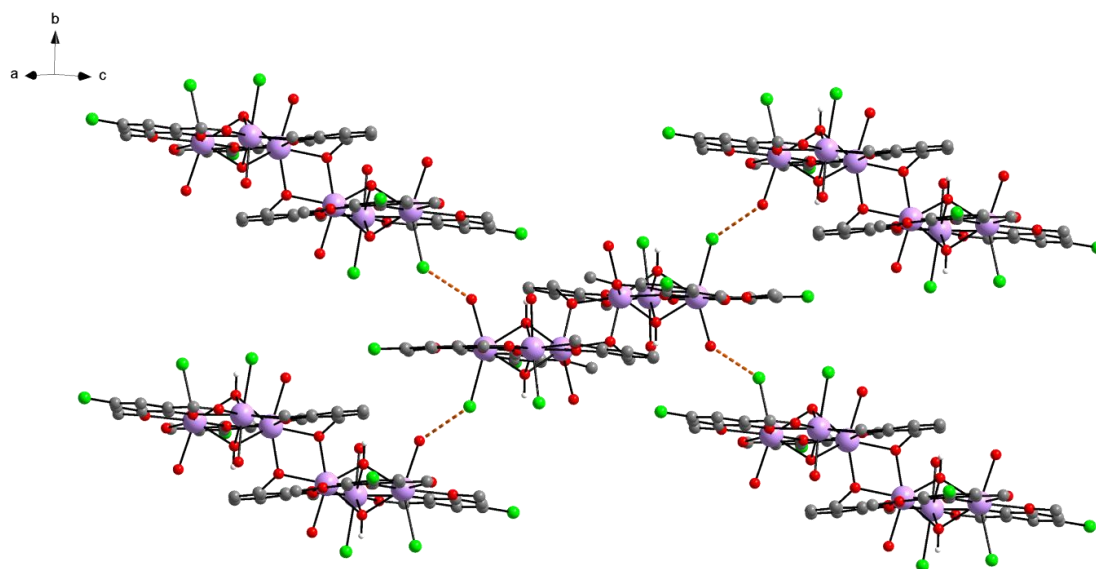


Figure 223. Hydrogen bonding interactions in (**Dy₆-92**).

The most sensitive tuning handle of the synthesis is the adjustment of the ratio between solvents mentioned above. With an excess of MeOH in the ratio the compound remains in solution whereas a higher amount of MeCN leading to dilution of MeOH results in the precipitation of the compound as an amorphous powder or crystallisation with impurities. For (**Dy₆-93**) it was possible to obtain a pure bulk sample as shown from PXRD measurements and elemental analysis (see Figure 224). The PXRD measurement is sufficient to show that the simulation and experimental powder patterns match and that there are no additional crystalline impurities also in line with the elemental analysis. The measurements performed on (**Dy₆-92**) suggested that this sample was not sufficiently pure to perform further magnetic characterisation. Therefore, magnetic characterisation was only performed on (**Dy₆-93**). The magnetic data recorded for (**Dy₆-93**) are shown and compared to another Dy₆ (**Dy₆-94**) compound in section 6.2.3 below.

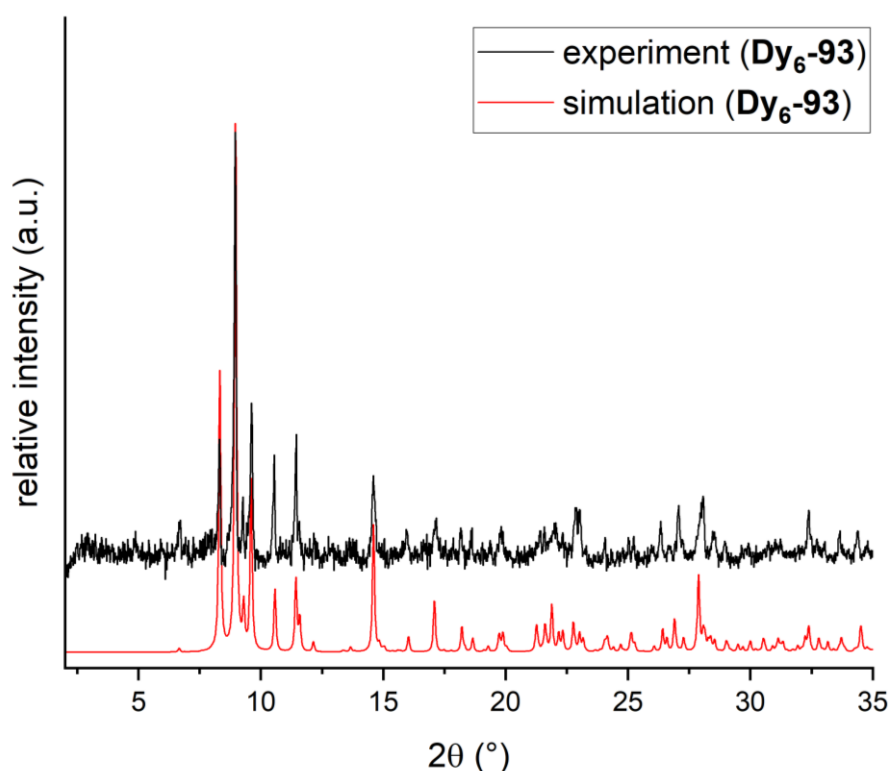


Figure 224. Simulated and experimental powder pattern for (**Dy₆-93**).

6.2.2 Using 5-CN-3-methoxy-2-hydroxybenzaldehyde

A previously described Dy₆ compound with NO₂-van ligands, which was synthesised during my Master thesis^[219] and followed the *in situ* approach formed two NO₂-van derived bridging species by reduction and hydration, respectively. Despite of changing the nature of the bridging unit, the Dy-O-Dy angles and Dy⋯Dy distance between linked triangles remained essentially unchanged. This was the inspiration for exploring the *in situ* formation of other bridging species which could have an influence on the core geometry and therefore the magnetic properties. Therefore, this idea was explored further within the context of this PhD thesis.

Originally the goal of using of 5-CN-3-methoxy-2-hydroxybenzaldehyde (CN-van) was to synthesise a Dy₃ triangle to investigate the effect of an electron-withdrawing substituent on its magnetic behaviour including the possibility of identifying a toroidal state. However, the targeted Dy₃ compound could not be isolated following the established synthetic procedure. Variation of the synthetic conditions, including solvothermal conditions did not result in the desired Dy₃ compound but rather a Dy₆.

In this case a bridging CN-*o*-van derived species formed *in situ* leading to the crystallisation of (**Dy₆-94**) with the formula [Dy₆(μ₃-OH)₄(CN-van)₄(CN-vandiolate)₂(H₂O)_{5.5}Cl_{4.5}][Cl_{1.5}·2.5H₂O·4MeOH] (see Figure 226). This transformation is not unlike what was observed for the Tm₆ published in 2010 which involved an *in situ* ligand adaptation.

Here the molecular structure forming the Dy₆ motif has bridging CN-vandiolate (3-formly-4,5-dihydroxybenzonitrile) ligands which have an additional (μ₂-O⁻) alkoxy group formed by decomposition of the methoxy group of the used CN-van ligand (see Figure 225).

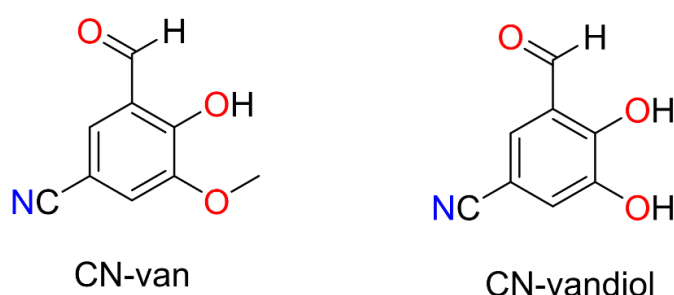


Figure 225. Structure of CN-van and CN-vandiol.

The terminal ligands consist of 4.5 Cl⁻ and 5.5 water ligands due to disorder between the water oxygen O(13) with an occupancy of 0.75 and Cl(1) with an occupancy of 0.25. Both hydroxy groups of the CN-vandiolate ligands are deprotonated and thus the ligand is two times negatively charged. There are 1.5 Cl⁻ counterions to balance the charge on the complex. Although this bridging unit between the triangles is now an alkoxy group derived from the methoxy group of CN-van, the bridging geometry remains largely unchanged compared to the vanillinol bridged Dy₆ clusters. The Dy···Dy distances of (**Dy₆-94**) and (**Dy₆-93**) are essentially identical at 3.7554(11) Å and 3.762(2) Å, respectively. The most notable difference lies in the Dy-O-Dy angle, which is 105.838(2)° for (**Dy₆-94**) and 111.249(3)° for (**Dy₆-93**). This difference arises from variations in the Dy···O bond lengths which are slightly longer in (**Dy₆-94**) at 2.337(7) Å and 2.371(7) Å than those in (**Dy₆-93**), at 2.278(2) Å and 2.280(9) Å. Compound (**Dy₆-94**) was selected for magnetic characterisation (see section 6.2.3) since these differences may influence the magnetic exchange interactions and thus lead to changes in the magnetic behaviour.

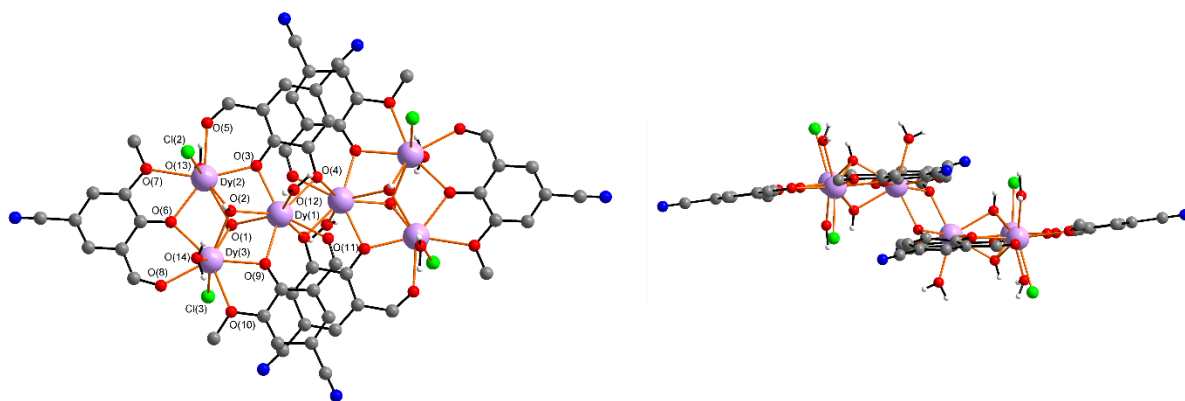


Figure 226. Molecular structure of (**Dy₆-94**) top (left) and side view (right). The disorder was omitted in favour of the water ligand with the higher occupancy (0.75).

Compound (**Dy₆-94**) crystallises in the triclinic space group $P\bar{1}$ with $Z = 1$. The packing is shown along the three crystallographic axes in Figure 227. The view along the c axis shows how the counterions occupy the empty space in between Dy₆ units.

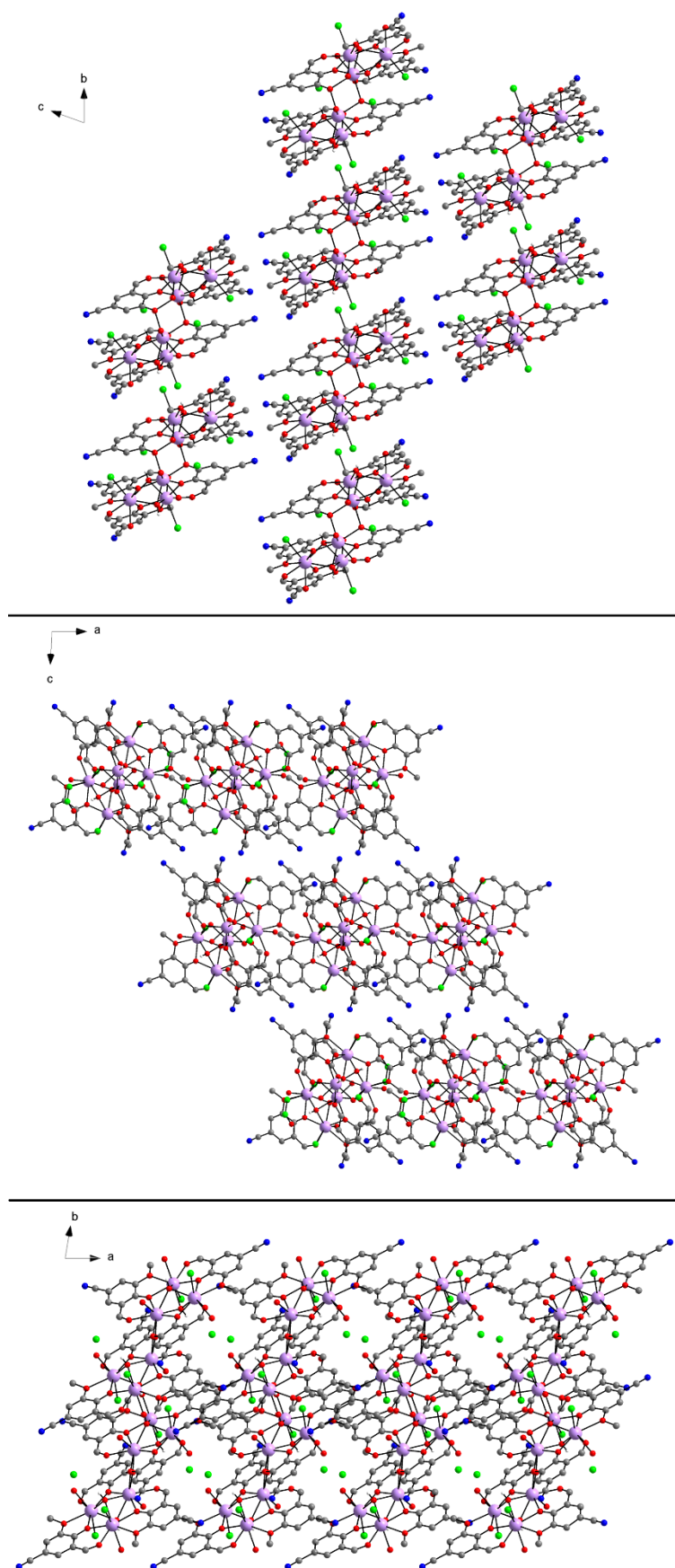


Figure 227. Crystal packing of (**Dy₆-94**) along the crystallographic *a* (top), *b* (middle) and *c* (bottom) axes.

The packing is directed by hydrogen bonds which lead to the formation of sheets in the **ab** plane (see Figure 228). In the *a* direction the hydrogens of terminal water ligands (O(14)) form hydrogen bonds to the nitrogen N(2) of the CN-van ligands of a neighbouring molecule. The interconnection in the *b* direction is given by hydrogen bonds between the terminal Cl⁻ ligands and the hydrogen on the (μ_2 -OH⁻) (O(2)) as well as the hydrogen on the terminal water ligands O(14) and O(12).

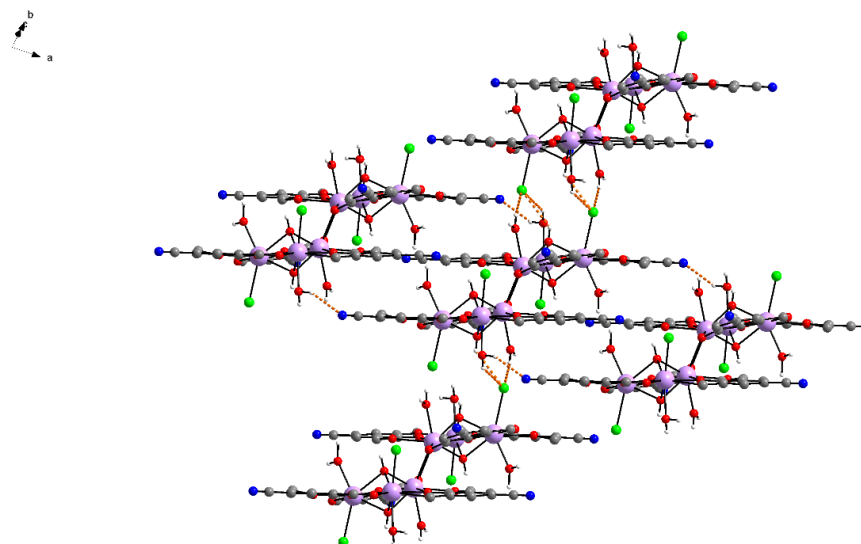


Figure 228. Hydrogen bonding network in (**Dy₆-94**). Hydrogen bonds are indicated by orange dotted lines.

PXRD measurements were performed on (**Dy₆-94**) (see Figure 229). The comparison of the experimental and simulated powder patterns as well as an elemental analysis on the bulk sample of (**Dy₆-94**) indicate that the sample is pure. Magnetic data on (**Dy₆-94**) is shown and compared to another Dy₆ in section 6.2.3.

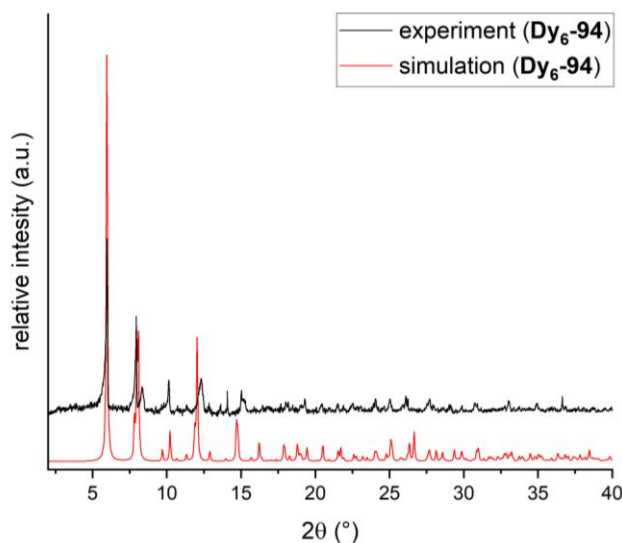


Figure 229. Simulated and experimental powder patterns of (**Dy₆-94**).

6.2.3 Magnetic characterisation of (Dy₆-93) and (Dy₆-94)

For compounds (Dy₆-92) and (Dy₆-94) magnetic data were collected on randomly oriented powder samples immobilised in eicosane. So far, no magnetic measurements using the microSQUID on single crystals could be performed since the aforementioned difficulties with the crystallisation process (see section 6.2.1/6.2.2) requires optimisation of the synthetic procedures leading to (Dy₆-93) and (Dy₆-94).

Temperature dependent DC measurements were performed on (Dy₆-93) and (Dy₆-94) (see Figure 230) with an applied field of 0.1 T. The theoretical $\chi_M T$ value for six non-interacting Dy^{III} ions is 85.02 cm³Kmol⁻¹ which is slightly higher than the experimentally observed values of 83.27 cm³Kmol⁻¹ for (Dy₆-93) and 82.46 cm³Kmol⁻¹ for (Dy₆-94). These slightly lower values are consistent with what was seen for other Dy triangle based compounds described in this thesis. On decreasing the temperature, the $\chi_M T$ value initially decreases gradually until approximately 11 K, below which the decrease becomes more rapid. This behaviour is probably a result of the combination of depopulation of excited m_J sub-levels and possible antiferromagnetic coupling between ions. To explore this further a Curie-Weiss analysis was performed in the temperature range 60 K to 300 K (see Figure 230). The fit gave a negative Weiss constant which corresponds to the x-intercept of the extrapolation of the linear fit with $\theta = -8.21$ K for (Dy₆-93) and $\theta = -6.37$ K for (Dy₆-94), and a Curie constant, $C = 85.47$ cm³Kmol⁻¹ for (Dy₆-93) and $C = 84.25$ cm³Kmol⁻¹ for (Dy₆-94). This is in line with the presence of antiferromagnetic interactions within these compounds.

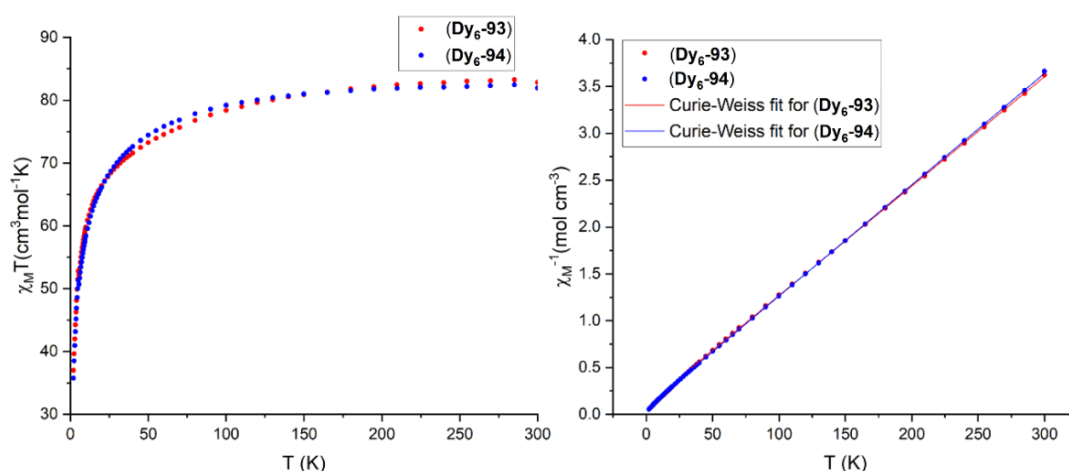


Figure 230. $\chi_M T$ vs T (left) and $1/\chi_M$ vs T with Curie-Weiss fit (right) for (Dy₆-93) and (Dy₆-94) measured at 0.1 T.

AC susceptibility measurements were performed at zero field and in the temperature range 2 K to 8 K for (**Dy₆-93**) (see Figure 231) and using the optimised applied field of 1750 Oe between 2 K and 6.4 K for (**Dy₆-94**) (see Figure 232). The optimised field is selected from measurements at different fields where the one with the largest AC signal was then chosen. The presence of an AC signal at zero field makes (**Dy₆-93**) a (zero field) SMM, whereas the absence of a zero field signal makes (**Dy₆-94**) a field induced SMM, indicative of a more accessible tunnelling pathway in this compound.

For (**Dy₆-93**) one broad peak with shoulders at high frequencies centred around *ca.* 1000 Hz. This becomes lower in intensity with higher temperatures. This maximum does not shift significantly to higher frequencies and the broadness of the peak makes the evaluation of any trends difficult to identify.

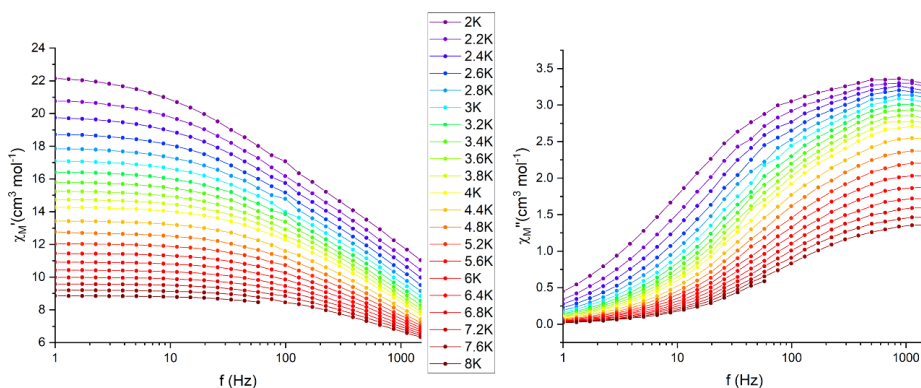


Figure 231. AC in-phase (left) and out-of-phase (right) data measured at zero field for (**Dy₆-93**). Lines are a guide to the eye.

Since compound (**Dy₆-94**) does not show any signals at zero field and it was therefore measured using the optimal field of 1750 Oe and shows one asymmetric set of maxima. This peak is observed at slightly lower frequencies than the one obtained for (**Dy₆-93**) but rapidly shifts to higher frequencies and out of the measurement window with increasing temperatures. No fitting to the Debye model was performed for either measurement since the low number of visible maxima and asymmetric shape of the curves make it impossible to fit with reliable and physically meaningful parameters.

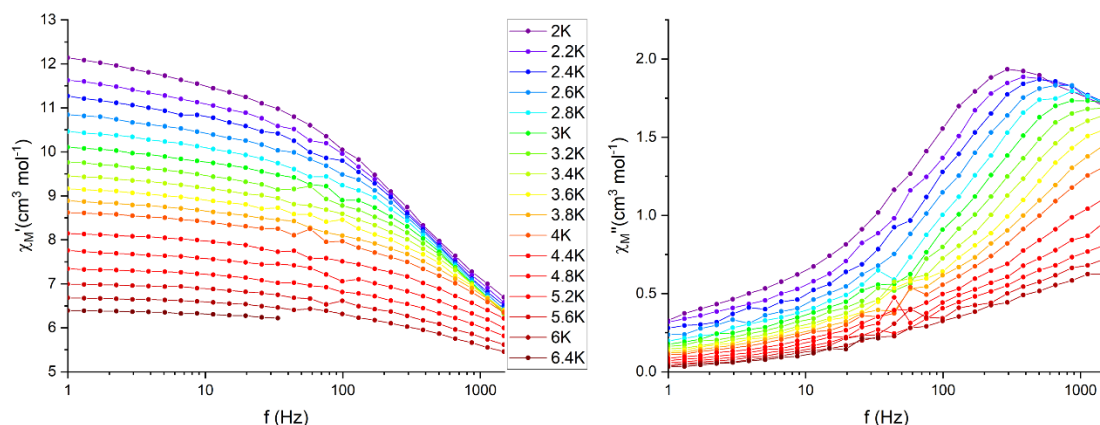


Figure 232. AC in-phase (left) and out-of-phase (right) data measured with an applied field of 1750 Oe for (**Dy₆-94**). Lines are a guide to the eye.

In addition, magnetisation measurements were performed from 0 T to 7 T at temperatures of 2 K to 5 K (see Figure 233). The magnetisation at low fields increases rapidly up to approximately 1.3 T at which point the slope decreases and the curve continues to increase essentially linearly reaching a value of 33.2 μ_B for (**Dy₆-93**) and 33.9 μ_B for (**Dy₆-94**) at 7 T. These values are slightly higher than the expected 30 μ_B for a Dy₆ compound which is probably a result of the population of low-lying excited states as indicated by the continuing slope at 7 T. The measurement of (**Dy₆-93**) shows some inconsistencies which probably results from problems in temperature stability.

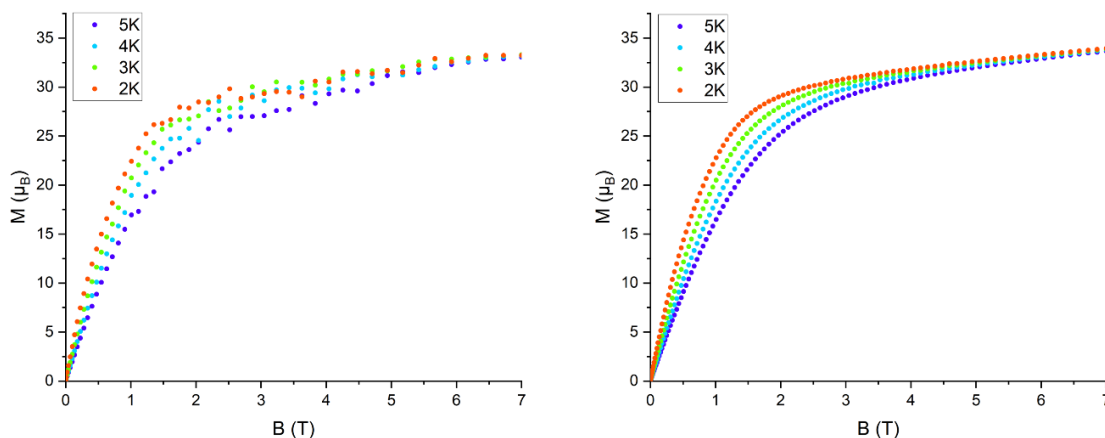


Figure 233. M vs B plot for (**Dy₆-93**) (left) and (**Dy₆-94**) (right).

From the magnetisation measurements it is not possible to discern any clear S-shape as observed for the other Dy₃ compounds or toroidal Dy₆ compounds in the literature. However, evaluation of the second derivative of the magnetisation curve of (**Dy₆-93**) leads to an x-intercept corresponding to an inflection point at ca. 0.0028 T. The first derivatives of the magnetisation curves of (**Dy₆-93**) and (**Dy₆-94**) suggest the

possibility that maxima could be seen at very low fields (see Figure 234). Further investigation is necessary to determine whether this is indicative of a level crossing from a possibly toroidal ground state or simply an artefact of the measurements. To clarify this, additional magnetic measurements at lower temperatures *i.e.* on a microSQUID would be informative.

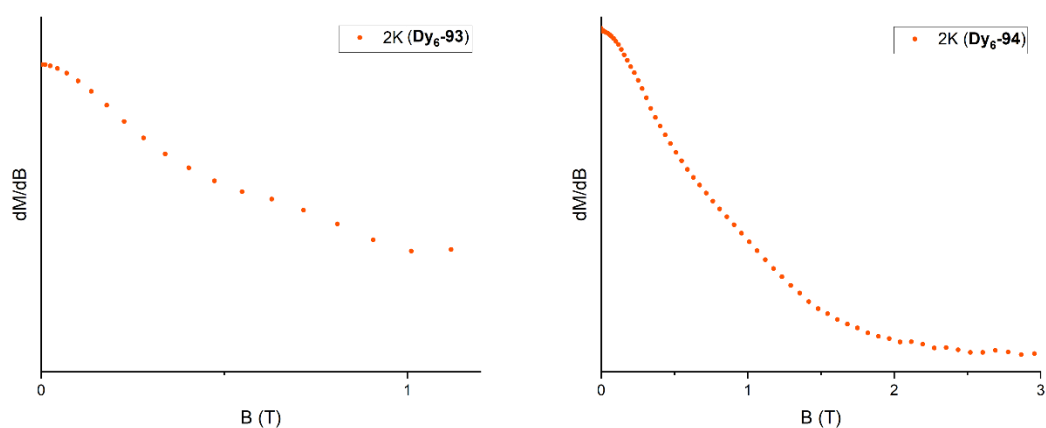


Figure 234. First derivative of magnetisation curve for **(Dy₆-93)** (left) and **(Dy₆-94)** (right).

MAGELLAN^[202] analyses were performed to investigate the possibility for toroidal arrangements of the anisotropy axes in compounds **(Dy₆-92)** **(Dy₆-93)** and **(Dy₆-94)** (see Figure 235). Compounds **(Dy₆-92)** and **(Dy₆-93)** show an in-plane toroidal arrangement of spins. The deviation from the tangential direction is larger for the Dy^{III} ions in the centre which are directly bridged to the other triangle unit. This is in line with what was observed for the Dy₆ with o-van/o-vanoxo ligands. For **(Dy₆-94)** the (75/25) disorder between O(13) of the terminal water ligand and Cl(1) on Dy(2) described above was omitted with one triangle assigned for the Cl⁻ and the other for the water ligand. This shows the effect of the two charged Cl⁻ terminal ligands which tilt the anisotropy axis of this Dy^{III} out of the triangle plane while the axes of ions with only one Cl⁻ stay in-plane.

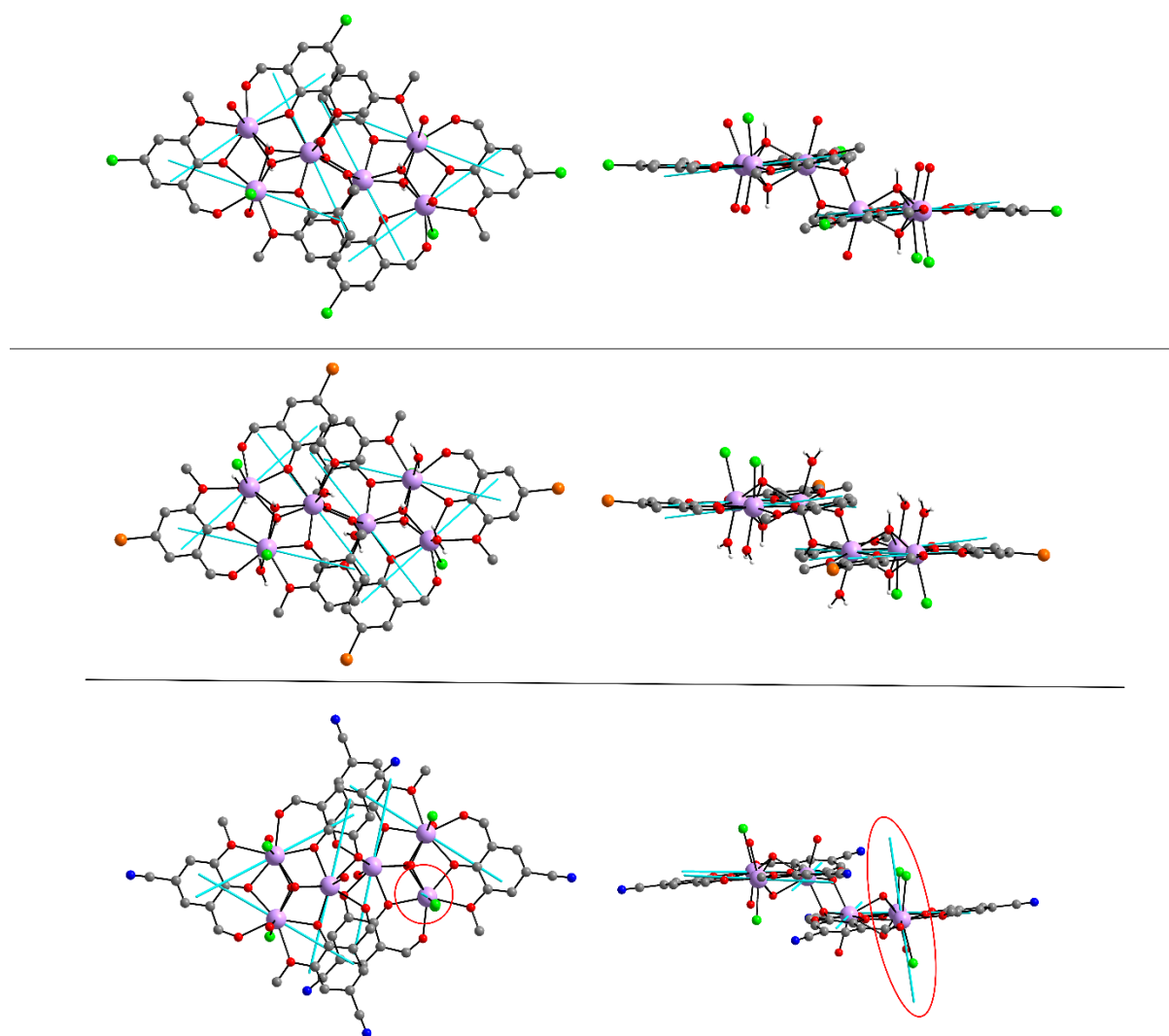


Figure 235. MAGELLAN^[202] analysis for (**Dy₆-92**) (top), (**Dy₆-93**) (middle) and (**Dy₆-94**) (bottom). Out-of-plane axis for (**Dy₆-94**) highlighted.

6.3 Linked triangle conclusion and outlook

Three new structures with the Dy₆ double triangle motif (**Dy₆-92**), (**Dy₆-93**) and (**Dy₆-94**) were synthesised and structurally characterised using single crystal XRD measurements. Compounds (**Dy₆-92**) and (**Dy₆-93**) serve as a proof-of-concept that it is possible to obtain Dy₆ structures with modified *o*-van type ligands and preserving the desired core geometry. It was attempted to introduce halogen-halogen interactions and study the effects of electronegative substituents on the magnetic behaviour by using Br and Cl substituted *o*-vanillin. Although no halogen-halogen interactions were

observed the effects of the terminal ligand distribution in the obtained compounds could be investigated.

Compound (**Dy₆-94**) uses an *in situ* formation of the CN-van derived bridging species to form the Dy₆ cluster. Thus, a new possible bridging motif was discovered using a diolate with the additional alcoholate in place of the methoxy group. This diolate type of bridging unit used in a targeted way to link two Dy₃ triangles to give the corresponding Dy₆ compounds. This should be used in future work to expand the range of accessible compounds with this bridging geometry and thereby establish magnetostructural correlations, given that the new bridging unit described here leads to the same Dy₆ core structure while subtly changing the Dy-O-Dy bond angles and distances.

Compounds (**Dy₆-93**) and (**Dy₆-94**) were subjected to standard SQUID magnetometry measurements and a MAGELLAN^[202] analysis was done for all three compounds to gauge the effects of the terminal ligand distribution on the formation of toroidal spin arrangements. Here it was possible to see the effect of additional Cl⁻ ligands which flip the anisotropy axis calculated from MAGELLAN^[202] out of the triangle plane when two Cl⁻ ligands are on the same Dy^{III}. Similar observations were made for the Dy₆ structures by Tang *et al.*^[172, 180] using terminal NO₃⁻ and SCN⁻ ligands and in the triangles described in section 5.2. The deviation of the orientation of the anisotropy axes from the tangential direction was observed for all three Dy₆ clusters, in line with the behaviour described for the Dy₆ with o-van/vanoxo ligands in the literature.^[170] The magnetisation measurements reveal a possible inflection point at very low fields which needs further investigation using microSQUID measurements.

The AC measurements show that (**Dy₆-93**) is a zero field SMM with maxima visible up to ca. 8 K but located close to the end of the measuring window at high frequencies. In contrast (**Dy₆-94**) does not show an AC signal in the measured frequency range of 1-1500 Hz at zero applied field. On applying the optimal DC field of 1750 Oe gave signals which could be evaluated in terms of SMM properties. Since no signal was observed at zero field, (**Dy₆-94**) can be categorised as a field induced SMM. The loss of SMM properties at zero field are likely to be linked to quantum tunnelling of the magnetisation.

In conclusion, the strategy of ligand modification led to changes in the magnetic and toroidal properties of the Dy₆ system. The loss of the characteristic inflection point in the bulk magnetisation measurements could be a temperature effect so that planned microSQUID measurements at sub-kelvin temperatures would be most informative. Furthermore, theory calculations are necessary to understand the reasons for the vanishing zero field SMM behaviour in (**Dy₆-94**) as well as to establish the possible toroidal character in the ground state.

7. General conclusion and outlook

In the motivation (Chapter 2) and the theoretical background (Chapter 3) the general ideas regarding the nature and possibilities of systems showing toroidal moments in addition, in some cases, to SMM behaviour are presented.

Simply put, a magnetic toroidal state is one in which a vortex-like arrangement of spins leads to a hidden state between a negative and positive coercive field limit. These states are often referred to as dark states given that any information contained within them can only be accessed at given applied magnetic fields which are called switching fields. This thesis deals with both SMM properties and toroidal states.

The first results chapter (Chapter 4) therefore introduces the nature of SMM properties arising in 3d-4f butterfly compounds as well as cyclic coordination clusters (CCCs) and how to steer the properties through a variety of tuning handles. These compounds have been known in this working group for a number of years and given that some very successful experiments were done using femtosecond pump-probe transient absorption spectroscopy on these CCCs, an exploration using this method was applied to selected Fe_2Dy_2 butterflies with ligand variations. In terms of the Fe-Ln based CCCs, the nuclearity was limited to a total of 20 metal centres where the Fe-Ln ratio could be varied according to reaction conditions.

Thus the previously described $\text{Fe}_{10}\text{Ln}_{10}$ system was taken as a starting point for further investigation in terms of the deviation of the ring compounds from circularity towards more elliptic rings based on the structural features for three $\text{Fe}_{10}\text{Dy}_{10}$ solvate compounds. The degree of ellipticity could be quantified in terms of a compression factor ε derived from the longest and shortest Ln-Ln distances across the interior cavity of the ring. These rings were investigated using femtosecond spectroscopy.

For the new rings presented here the second largest ellipticity in the series of $\text{Fe}_{10}\text{Ln}_{10}$ CCCs was observed for $[\text{Fe}_{10}\text{Dy}_{10}(\text{Et-tea})_{10}(\text{Et-teaH})_{10}(\text{NO}_3)_{10}] \cdot 18\text{MeCN}$ (**Fe₁₀Dy₁₀-9**). The $\text{Fe}_{10}\text{Dy}_{10}$ analogue was magnetically characterised and compared to other versions in the $\text{Fe}_{10}\text{Dy}_{10}$ family where a distinct negative influence of the ethyl residue of the triethanolamine ligand was found. An $\text{Fe}_{10}\text{Tb}_{10}$ compound was reproduced using an adapted synthetic procedure for the purpose of further magnetic characterisation

using microSQUID measurements. Here it was found that the Tb^{III} enhances the coercive field at 0.03 K from 0.054 T for Fe₁₀Dy₁₀ to 0.13 T for Fe₁₀Tb₁₀.

Keeping with the theme of 20 nuclearity Fe-Ln CCCs the next system to be explored was a structural adaptation of the Fe₁₀Ln₁₀ system where the ratio is now Fe₈Ln₁₂. The Fe₈Dy₁₂ contains Dy–Fe–Dy–Fe units very similar to those in the Fe₁₀Dy₁₀ but now linked *via* Dy ions leading to a different ring conformation which has a significant impact on the magnetic properties through reorientation of the anisotropy axes of the Dy^{III} ions. This previously unreproducible compound was successfully synthesised using an improved synthetic procedure which now ensures reproducibility. It was also possible to characterise the isostructural Ho^{III} analogue of this CCC.

Another series of 20 nuclearity CCCs of formula [Fe₁₆Tb₄(tea)₈(teaH)₁₂(μ-O₂CCH₃)₈](NO₃)₄·16H₂O·10MeCN^[35] was chosen in order to investigate the Tb^{III} analogue further which is of interest as a result of the S-shape of the magnetisation curve. The microSQUID data showed an inflection point which is related to the level crossing seen in the magnetisation data. This in conjunction with the collected data on the Fe₁₀Tb₁₀ shows that Tb^{III} based systems combined with 3d metal ions are worthy of further investigation.

In chapter 5 the idea of manipulating the Dy₃ triangle system which is the archetype of molecules showing toroidal moments in the ground state was explored. It was successfully shown how introducing halogens to generate halogen interactions in the lattice can have an impact on the crystal packing as well as the dynamic magnetic behaviour as shown from AC susceptibility measurements. Compared to the archetypal Dy₃ for which the molecules are only connected by hydrogen bonds the AC data changes when stronger intermolecular interactions such as halogen bonding are present. MicroSQUID measurements and theory calculations as well as MAGELLAN^[202] analyses were performed on three compounds with halogen bonds of different strengths showing the effect of terminal ligands as well as second sphere ions in terms of the relative positions of the anisotropy axes. An Electron Localisation Function (ELF) was used to visualise halogen interactions and CASOCI calculations and an Energy Decomposition Analysis (EDA) were performed in order to investigate contributions and strength of halogen bonding in three representative triangles [Dy₃(OH)₂(Br-van)₃(Cl)₃(MeOH)₃][Dy₃(OH)₂(Br-van)₃(Cl)₅(MeOH)]·4MeOH (**Dy₃-21**),

$[\text{Dy}_3(\text{OH})_2(\text{l-van})_3(\text{Cl})_3(\text{MeOH})_2(\text{H}_2\text{O})]\text{Cl}\cdot 3\text{MeOH}$ (**Dy₃-22**) and $[\text{Dy}_3(\text{OH})_2(\text{Cl-van})_3(\text{Cl})_3(\text{H}_2\text{O})_{0.5}(\text{MeOH})_{2.5}]\text{Cl}\cdot 2.5\text{MeOH}$ (**Dy₃-36**). This analysis was performed within the group of Prof. Dr. Karin Fink by Christian Pachtl.

The archetypal triangle was further adapted by introducing a substituted azo group through an azo coupling reaction in the 5-position of the *o*-vanillin ligand. For this type of reaction any aniline derivative can be used to modify the *o*-vanillin unit thus opening possibilities for a great range of ligand modifications. Here it was used to introduce *para*-halogen-substituted aniline groups with the idea of promoting halogen bonding. This approach was successful as shown for two novel compounds incorporating these ligands which have not been used in coordination chemistry prior to this study. The dynamic magnetic properties of the compound with the formula $[\text{Dy}_3(\mu_3\text{-OH})_2(p\text{-Cl-pdavan})_3(\text{NO}_3)_3(\text{H}_2\text{O})_3][\text{Dy}_3(\mu_3\text{-OH})_2(p\text{-Cl-pdavan})_3(\text{NO}_3)_4(\text{H}_2\text{O})_2](\text{NO}_3)_3\cdot 2(\text{H}_2\text{O})\cdot 19(\text{MeCN})$ (**Dy₃-39**) were again found to correlate with the degree of intermolecular interactions as a result of the interplay of π - π stacking and halogen bonding. MicroSQUID measurements and MAGELLAN^[202] analyses indicate an almost equivalent level of toroidicity in the ground state as seen for the halogen substituted triangles in section 5.2.

When a Schiff base approach was used to synthesise Dy₃ triangles with imposed symmetry, and in contrast to the other strategies so far designed to impose symmetry, it was found that limiting intermolecular interactions gave a positive way forward to enhancing toroidicity. For example, this was successfully shown for the Dy₃ triangle (**Dy₃-49**) synthesised using the Schiff base ligand H₂bovh. This compound crystallises in $R\bar{3}$ thereby significantly reducing the complexity of the system with a packing in parallel threefold-symmetric stacks along the crystallographic *c* axis.

Single crystal measurements using cantilever torque magnetometry along two rotations relative to the triangle plane were performed. The measured data were used to determine the angles of the anisotropy axes out of the triangle plane (6°) and the deviation from the tangential direction (12°). This is in agreement with a planar vortex arrangement of spins and therefore a toroidal ground state.

In addition, microSQUID measurements on single crystals were performed along the easy axis of the system along one of the three anisotropy axes coplanar to the triangle and along an intermediate axis which is also in the plane of the triangle but

perpendicular to one of the three anisotropy axis and along the crystallographic c axis which is orthogonal to the plane of the triangle. Measurements in all three directions showed hysteresis albeit with significant differences. The collected data along the three axes could be interpreted using the calculated Zeeman diagrams. This resulted in evidence of pinning of spins and ordering of toroidal moments in the crystal which has been termed chirality selection.

In a further Schiff base variation eleven further Dy₃ triangles were synthesised as well as a total of 28 Ln^{III} analogues. A systematic investigation of the type of substituent and its position as well as their influence on the magnetic behaviour was performed. This showed that structures with imposed symmetry crystallising in $R\bar{3}$ as well as structures in $P\bar{1}$, $P\bar{3}c1$ and $Pbca$ were accessible and the intermolecular interactions in the structures could be evaluated in terms of the nature of the interaction and the space group in which the compound crystallises.

Magnetic measurements were performed on four types of Dy₃ triangles with varying substituents and showed that the nature of the lattice solvents can have an important effect on the dynamic magnetic behaviour as revealed from the AC data of (**Dy₃-59**), (**Dy₃-67**), (**Dy₃-77**) and (**Dy₃-78**) where the lattice solvent can exchange with moisture in the air leading to the demise of the first maximum in the AC signals. Compounds crystallising in $R\bar{3}$ are apparently less susceptible to this problem.

Since the crystallisation of these compounds always results in the presence of both enantiomers of the triangle complex, attempts were made to induce homochirality by using chiral aldehydes in the Schiff base reaction. First tests on this approach showed promising results since it was possible to synthesise the Dy₃ compound with the chiral unit attached to the ligand. The compound obtained from this crystallises in a desired acentric space group, $P1$.

The investigation of ligand modifications also made it possible to gauge where the functionalisation can interfere with the formation of the Dy₃ motif. Three such compounds presented in this work were characterised using SCXRD measurements and MAGELLAN.^[202] These include a Dy₆ and two Dy₁₂ clusters. The structure of one of these compounds, (**Dy₁₂-90**), is particularly interesting for future investigation given that MAGELLAN^[202] predicts all four Dy₃ moieties in the truncated tetrahedron to be individually toroidal.

The last toroidal system explored was the Dy₆ double triangle system in which the triangles are linked *via* *o*-vanillin derived bridging species. It was possible to find a new bridging species by replacing the vanillinol with an *in situ* generated *p*-CN-vandiol. Three such compounds were isolated of which two were magnetically characterised. The changes in core geometry, as a result of the different bridging species, could be related to a demise in zero field SMM properties. A MAGELLAN^[202] analysis was performed indicating possible toroidal behaviour which needs further investigation on single crystals and lower temperature measurements.

In summary, the approach of balancing ligand modifications and intermolecular interactions, with a particular emphasis on ways to enhance toroidal moments, offers a highly promising avenue in terms of isolation, connection or manipulation of molecular-based toroidal moments.

8. Experimental

Synthetic conditions and chemicals

Chemicals were sourced commercially and used without further purification unless specifically mentioned. Lanthanide salts were prepared by reaction of the respective oxides and acids. All synthetic procedures were performed in air unless stated otherwise. All synthetic work was performed at the Institute of Nanotechnology (INT, KIT).

Used Instruments:

For ATR-IR spectroscopy a Nicolet iS 50 with ATR attachment was used. UV-Vis absorption spectroscopy was performed on a Agilent Cary 5000 UV-Vis spectrometer. Femtosecond spectroscopy was performed by Julia Weyandt working in the group of Prof. Dr. Andreas-Neil Unterreiner.

Powder X-ray diffraction (PXRD) was done on a STOE STADI-P with a Cu-K α source with a characteristic wavelength of 1.5405 Å.

Single crystal X-ray diffraction (SCXRD) was performed on a STADIVARI by STOE using Mo-K α radiation with a characteristic wavelength of 0.71073 Å, an IPDS II by STOE with Mo-K α radiation and on a STADIVARI by STOE with Ga-Jet X-ray source by Excillum using Ga-K α radiation with a wavelength of 1.3143 Å.

Crystal structures were solved and refined using Olex with ShelXL and ShelXT.^[241-243] Pictures of crystal structures were made using Diamond 4.0 and powder patterns were simulated with Mercury 3.8.^[244]

Elemental analyses were performed on an Elementar Vario MicroCube.

NMR spectroscopy was performed on a Bruker Avance III 500 MHz.

SQUID measurements were performed on a Quantum Design MPMS-XL-1 and Quantum Design MPMS-3 with the help of Dr. Sören Schlittenhardt from the group of Prof. Dr. Mario Ruben. SQUID measurements were also conducted on an MPMS-3 in collaboration with Jan Arneth from the working group of Prof. Dr. Rüdiger Klingeler from the University of Heidelberg.

MicroSQUID measurements were performed by Dr. Sagar Paul and Appu Sunil from the group of Prof. Dr. Wolfgang Wernsdorfer at the Institute of Physics KIT.

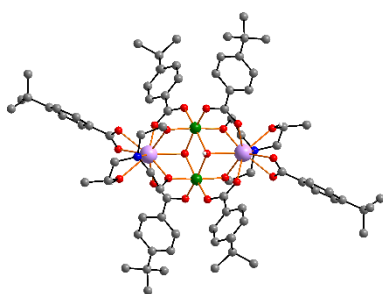
Cantilever torque magnetometry was performed at the University of Florence in collaboration with Prof. Dr. Mauro Perfetti and Leonardo Tacconi.

Quantum chemical calculations were done in collaboration with Christian Pachl in the working group of Prof. Dr. Karin Fink (KIT) and Prof. Dr. Alessandro Soncini from the University of Padova.

(Fe₂Dy₂-1) – [Fe₂Dy₂(μ₃-OH)₂(benzoic acid)₆(teaH)₂]·3MeCN

The title compound as well as the Fe₃ precursor complex were reproduced using a literature-known procedure.^[201] In a glass vial 300 mg teaH₃ (2 mmol) and 250 mg [Fe₃O(O₂CC₆H₄)₆(H₂O)₃](O₂CC₆H₄) (0.24 mmol) were dissolved in 20 ml MeCN. To this stirred precursor solution a solution of 116 mg Dy(NO₃)₃·6H₂O (0.25 mmol) dissolved in 30 ml MeCN and 3 ml MeOH were added. The mixture was stirred for 20 mins after which the resulting solution was filtered, transferred to another vial which was sealed and left undisturbed to allow for crystallisation of the product. After 3 days the product was isolated as yellow blocks in a yield of 69% (140 mg).

(Fe₂Dy₂-2) – [Fe₂Dy₂(μ₃-OH)₂(*p*-^tBu-benzoic acid)₆(Me-teaH)₂]·2(*p*-^tBu-benzoic acid)·4MeCN



The compound was reproduced using an improved synthetic procedure.^[201] In a glass vial 326 mg Me-teaH₃ (2 mmol) and 134 mg [Fe₃O(*p*-^tBu-O₂CC₆H₄)₆(H₂O)₃](*p*-^tBu-O₂CC₆H₄) (0.18 mmol) were dissolved in 30 ml MeCN and 3 ml MeOH. Under stirring a solution of 116 mg Dy(NO₃)₃·6H₂O (0.25 mmol) dissolved in 5 ml

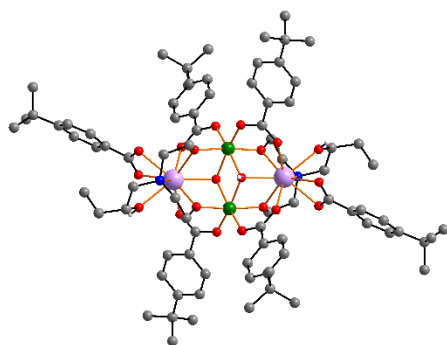
MeCN were added. The mixture was stirred for 60 mins after which it was filtered and the resulting clear yellow solution left undisturbed to allow for crystallisation of the product. After 2 weeks the product was isolated as pale-yellow plates in a yield of 76% (225 mg).

ATR-IR (4000-400 cm⁻¹): 3538(m); 3294(m); 2971(s); 2899(m); 2870(m); 1684(m); 1584(s); 1544(s); 1453(m); 1372(s); 1272(s); 1193(m); 1144(w); 1101(m); 1093(m);

1019(m); 969(w); 928(w); 903(m); 853(m); 791(s); 711(m); 579(m); 549(w); 472(m); 424(m).

Crystal Data for $C_{110}H_{150}Dy_2Fe_2N_6O_{24}$ ($M = 2377.05$ g/mol): monoclinic, space group $P2_1/c$ (no. 14), $a = 18.1908(3)$ Å, $b = 11.6823(2)$ Å, $c = 26.6786(5)$ Å, $\beta = 96.325(1)^\circ$, $V = 5634.97(17)$ Å³, $Z = 2$, $T = 180$ K, $\mu(1.3401270, 1.34 \text{ K}\alpha) = 8.555 \text{ mm}^{-1}$, $D_{calc} = 1.401 \text{ g/cm}^3$, 93748 reflections measured ($6.804^\circ \leq 2\theta \leq 125.024^\circ$), 13531 unique ($R_{int} = 0.0302$, $R_{sigma} = 0.0223$) which were used in all calculations. The final R_1 was 0.0357 ($I > 2\sigma(I)$) and wR_2 was 0.0931 (all data).

(Fe₂Dy₂-3) – [Fe₂Dy₂(μ₃-OH)₂(p-^tBu-benzoic acid)₆(Et-teaH)₂]·(p-^tBu-benzoic acid)·4MeCN



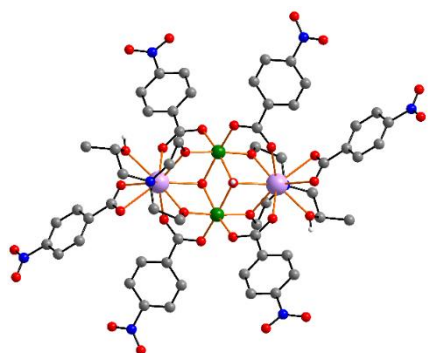
In a glass vial 175 mg Et-teaH₃ (1 mmol) and 67 mg [Fe₃O(p-^tbu-O₂CC₆H₄)₆(H₂O)₃](p-^tBu-O₂CC₆H₄) (0.09 mmol) which was synthesised beforehand using a well-known literature procedure^[201] were dissolved in 10 ml MeCN and 2 ml MeOH. Under stirring a solution of 58 mg Dy(NO₃)₃·6H₂O (0.125 mmol) dissolved in 5 ml MeCN were added.

The mixture was stirred for 60 mins after which it was filtered and the resulting clear yellow solution left undisturbed to allow for crystallisation of the product. After 2 weeks the product was isolated as colourless plates in a yield of 80% (120 mg).

ATR-IR (4000-400 cm⁻¹): 3542(m); 3303(m); 2963(s); 2904(m); 2875(m); 1676(m); 1591(s); 1539(s); 1462(m); 1377(s); 1267(s); 1189(m); 1148(w); 1104(m); 1086(m); 1016(m); 975(w); 920(w); 898(m); 861(m); 783(s); 706(m); 584(m); 544(w); 466(m); 429(m).

Crystal Data for $C_{112}H_{154}Dy_2Fe_2N_6O_{24}$ ($M = 2405.10$ g/mol): monoclinic, space group $P2_1/c$ (no. 14), $a = 18.2336(4)$ Å, $b = 11.7217(2)$ Å, $c = 26.6579(5)$ Å, $\beta = 96.351(2)^\circ$, $V = 5662.59(19)$ Å³, $Z = 2$, $T = 180$ K, $\mu(1.3401270, 1.34 \text{ K}\alpha) = 8.518 \text{ mm}^{-1}$, $D_{calc} = 1.411 \text{ g/cm}^3$, 60260 reflections measured ($6.802^\circ \leq 2\theta \leq 124.988^\circ$), 13559 unique ($R_{int} = 0.0353$, $R_{sigma} = 0.0367$) which were used in all calculations. The final R_1 was 0.0362 ($I > 2\sigma(I)$) and wR_2 was 0.0892 (all data).

(Fe₂Dy₂-4) – [Fe₂Dy₂(μ₃-OH)₂(p-NO₂-benzoic acid)₆(Me-teaH)₂]·6MeCN

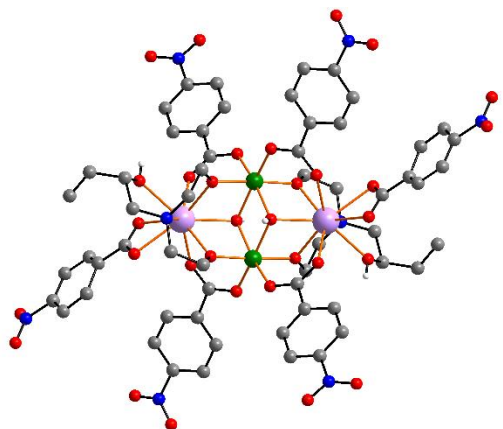


In a glass vial 326 mg Me-teaH₃ (2 mmol) and 270 mg [Fe₃O(p-NO₂-O₂CC₆H₄)₆(H₂O)₃](p-NO₂-O₂CC₆H₄) (0.21 mmol) which was synthesised beforehand using a well-known literature procedure^[201] were dissolved in 10 ml MeCN and 2 ml MeOH. Under stirring a solution of 116 mg Dy(NO₃)₃·6H₂O (0.25 mmol) dissolved in 5 ml MeCN were added. The mixture was stirred for 60 mins after which it was filtered and the resulting clear yellow solution left undisturbed to allow for crystallisation of the product. After 2 weeks the product was isolated as colourless plates in a yield of 47% (120 mg).

Elemental analysis (calculated, C₅₆H₇₂Dy₂Fe₂N₈O₄₀) C: 34.77 %, H: 3.75%, N: 5.79 %; (found) C: 35.05%, H: 3.29%, N: 5.53%. **ATR-IR (4000-400 cm⁻¹):** 3480(m); 2864(m); 1621(m); 1562(s); 1517(s); 1458(w); 1407(m); 1340(s); 1318(m); 1167(w); 1126(m); 1086(s); 1053(m); 1038(m); 1008(m); 912(w); 875(m); 820(m); 794(m); 721(s); 647(m); 591(w); 514(m); 466(m).

Crystal Data for C₆₈H₇₄Dy₂Fe₂N₁₄O₃₂ (*M* = 2036.11 g/mol): triclinic, space group *P* $\bar{1}$ (no. 2), *a* = 11.1655(2) Å, *b* = 13.6744(3) Å, *c* = 13.8949(3) Å, α = 99.397(2)°, β = 90.892(2)°, γ = 102.895(2)°, *V* = 2037.26(8) Å³, *Z* = 1, *T* = 180 K, μ (1.3401270, 1.34 K α) = 11.831 mm⁻¹, *D*_{calc} = 1.660 g/cm³, 28646 reflections measured (5.618° ≤ 2 θ ≤ 128.4°), 9911 unique (*R*_{int} = 0.0233, *R*_{sigma} = 0.0199) which were used in all calculations. The final *R*₁ was 0.0291 (*I* > 2 σ (*I*)) and *wR*₂ was 0.0790 (all data).

(Fe₂Dy₂-5) – [Fe₂Dy₂(μ₃-OH)₂(p-NO₂-benzoic acid)₆(Et-teaH)₂]·6MeCN



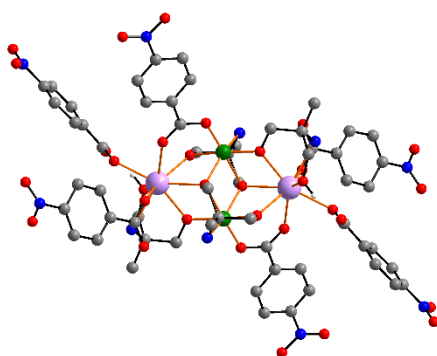
In a glass vial 350 mg Et-teaH₃ (2 mmol) and 270 mg [Fe₃O(p-NO₂-O₂CC₆H₄)₆(H₂O)₃](p-NO₂-O₂CC₆H₄) (0.21 mmol) which was synthesised beforehand using a well-known literature procedure^[201] were dissolved in 10 ml MeCN and 2 ml MeOH. Under stirring a solution of 116 mg Dy(NO₃)₃·6H₂O (0.25 mmol) dissolved in 5 ml MeCN were added. The mixture was stirred for 60 mins after which it was filtered and the resulting clear yellow

solution left undisturbed to allow for crystallisation of the product. After 2 weeks the product was isolated as colourless plates in a yield of 71% (184 mg).

ATR-IR (4000-400 cm^{-1}): 3657(m); 3542(w); 2860(w); 1621(m); 1587(s); 1558(s); 1517(s); 1491(w); 1466(m); 1388(s); 1340(s); 1314(s); 1222(w); 1126(w); 1086(s); 1012(m); 971(w); 920(w); 879(m); 831(m); 717(m); 691(m); 595(m); 514(w); 437(m); 400(m).

Crystal Data for $\text{C}_{70}\text{H}_{80}\text{Dy}_2\text{Fe}_2\text{N}_{14}\text{O}_{33}$ ($M = 2082.18$ g/mol): triclinic, space group $P\bar{1}$ (no. 2), $a = 11.1811(3)$ Å, $b = 13.9483(3)$ Å, $c = 14.0381(3)$ Å, $\alpha = 99.280(2)^\circ$, $\beta = 91.211(2)^\circ$, $\gamma = 103.695(2)^\circ$, $V = 2095.24(9)$ Å³, $Z = 1$, $T = 180$ K, $\mu(1.3401270, 1.34 \text{ K}\alpha) = 11.519 \text{ mm}^{-1}$, $D_{\text{calc}} = 1.650 \text{ g/cm}^3$, 30596 reflections measured ($7.094^\circ \leq 2\theta \leq 116.204^\circ$), 8704 unique ($R_{\text{int}} = 0.0357$, $R_{\text{sigma}} = 0.0429$) which were used in all calculations. The final R_1 was 0.0379 ($I > 2\sigma(I)$) and wR_2 was 0.1001 (all data).

(Fe₂Dy₂-6) – [Fe₂Dy₂(p-NO₂-benzoic acid)₆(ampd)₄]·8MeCN



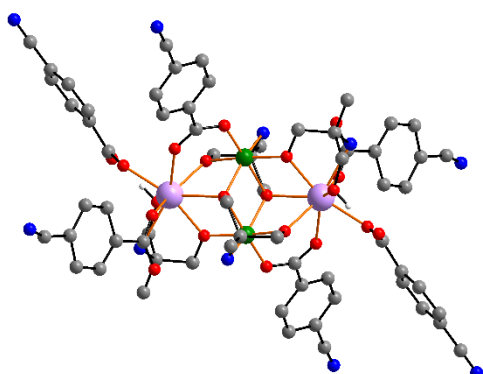
In a glass vial 210 mg 2-amino-2-methyl-1,3-propanediol (2 mmol) and 270 mg $[\text{Fe}_3\text{O}(\text{p-NO}_2\text{-O}_2\text{CC}_6\text{H}_4)_6(\text{H}_2\text{O})_3](\text{p-NO}_2\text{-O}_2\text{CC}_6\text{H}_4)$ (0.21 mmol) which was synthesised beforehand using a well-known literature procedure^[201] were dissolved in 10 ml MeCN and 2 ml MeOH. Under stirring a solution of 116 mg $\text{Dy}(\text{NO}_3)_3 \cdot 6\text{H}_2\text{O}$ (0.25 mmol)

dissolved in 5 ml MeCN were added. The mixture was stirred for 60 mins after which it was filtered and the resulting clear yellow solution left undisturbed to allow for crystallisation of the product. After 2 weeks the product was isolated as yellow plates in a yield of 65% (176 mg).

Elemental analysis (calculated, $\text{C}_{68}\text{H}_{62}\text{Dy}_2\text{Fe}_2\text{N}_{10}\text{O}_{37}$) C: 35.95%, H: 3.74%, N: 7.22%; (found) C: 36.08%, H: 3.23%, N: 6.78%. **ATR-IR (4000-400 cm^{-1}):** 3317(w); 3266(w); 3240(w); 3122(w); 3122(m); 2963(s); 2923(s); 2864(s); 1617(m); 1558(s); 1517(s); 1462(m); 1407(m); 1381(s); 1340(s); 1318(s); 1141(w); 1101(w); 1060(s); 1016(m); 1008(s); 971(w); 923(w); 875(m); 824(m); 794(m); 721(s); 625(m); 580(w); 521(s); 437(m).

Crystal Data for $C_{74}H_{86}Dy_2Fe_2N_{18}O_{32}$ ($M=2176.30$ g/mol): triclinic, space group $P\bar{1}$ (no. 2), $a = 9.8714(4)$ Å, $b = 14.8677(7)$ Å, $c = 17.7903(8)$ Å, $\alpha = 65.330(3)^\circ$, $\beta = 78.694(4)^\circ$, $\gamma = 85.857(4)^\circ$, $V = 2326.50(19)$ Å³, $Z = 1$, $T = 180$ K, $\mu(1.3401270, 1.34 \text{ K}\alpha) = 10.394 \text{ mm}^{-1}$, $D_{calc} = 1.553 \text{ g/cm}^3$, 22516 reflections measured ($7.946^\circ \leq 2\theta \leq 114.992^\circ$), 9517 unique ($R_{int} = 0.0613$, $R_{sigma} = 0.0549$) which were used in all calculations. The final R_1 was 0.0764 ($I > 2\sigma(I)$) and wR_2 was 0.2188 (all data).

(Fe₂Dy₂-7) – [Fe₂Dy₂(*p*-CN-benzoic acid)₆(ampd)₄]·2MeCN



In a glass vial 210 mg 2-amino-2-methyl-1,3-propanediol (2 mmol) and 270 mg [Fe₃O(*p*-CN-O₂CC₆H₄)₆(H₂O)₃](*p*-CN-O₂CC₆H₄) (0.23 mmol) which was synthesised beforehand using a well-known literature procedure^[201] were dissolved in 10 ml MeCN and 2 ml MeOH. Under stirring a solution of 116 mg Dy(NO₃)₃·6H₂O (0.25 mmol)

dissolved in 5 ml MeCN were added. The mixture was stirred for 30 mins after which the resulting solution was filtered, transferred to another vial which was sealed and left undisturbed to allow for crystallisation of the product. After 2 weeks the product was isolated as yellow plates in a yield of 80% (189 mg).

ATR-IR (4000-400 cm⁻¹): 3317(w); 3266(w); 3240(w); 3122(w); 3122(m); 2963(s); 2923(s); 2864(s); 2233(s); 1591(s); 1539(s); 1503(w); 1462(m); 1407(m); 1370(s); 1296(m); 1178(w); 1137(w); 1064(s); 1019(s); 1008(s); 923(w); 868(w); 842(w); 802(m); 780(s); 754(m); 691(m); 625(m); 595(w); 558(w); 544(s); 462(w); 414(m).

Crystal Data for $C_{72}H_{74}Dy_2Fe_2N_{14}O_{20}$ ($M=1892.15$ g/mol): monoclinic, space group $P2_1/c$ (no. 14), $a = 17.8696(3)$ Å, $b = 23.5447(4)$ Å, $c = 10.0219(2)$ Å, $\beta = 91.5030(10)^\circ$, $V = 4215.11(13)$ Å³, $Z = 2$, $T = 180$ K, $\mu(1.3401270, 1.34 \text{ K}\alpha) = 11.337 \text{ mm}^{-1}$, $D_{calc} = 1.491 \text{ g/cm}^3$, 73123 reflections measured ($5.402^\circ \leq 2\theta \leq 124.996^\circ$), 10151 unique ($R_{int} = 0.0397$, $R_{sigma} = 0.0226$) which were used in all calculations. The final R_1 was 0.0391 ($I > 2\sigma(I)$) and wR_2 was 0.1134 (all data).

(Fe₂Dy₂-8) – [Fe₂Dy₂(μ₃-OH)₂(*p*-CN-benzoic acid)₆(teaH)₂]·4H₂O

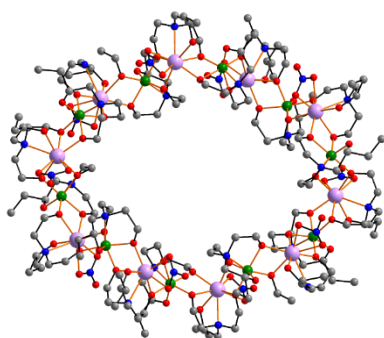
The compound as well as the used Fe₃ complex were reproduced using a literature-known procedure.^[201] In a glass vial 300 mg teaH₃ (2 mmol) and 250 mg [Fe₃O(*p*-CN-

$\text{O}_2\text{CC}_6\text{H}_4)_6(\text{H}_2\text{O})_3](p\text{-CN-O}_2\text{CC}_6\text{H}_4)$ (0.24 mmol) were dissolved in 20 ml MeCN. Under stirring a solution of 116 mg $\text{Dy}(\text{NO}_3)_3 \cdot 6\text{H}_2\text{O}$ (0.25 mmol) dissolved in 30 ml MeCN and 3 ml MeOH were added. The mixture was stirred for 20 mins after which the resulting solution was filtered, transferred to another vial which was sealed and left undisturbed to allow for crystallisation of the product. After 3 days the product was isolated as yellow blocks in a yield of 51.1% (113 mg).

Elemental analysis (calculated, $\text{C}_{64}\text{H}_{66}\text{Dy}_2\text{Fe}_2\text{N}_8\text{O}_{24}$) C: 43.48%, H: 3.76%, N: 6.34%; (found) C: 43.31%, H: 3.53%, N: 6.52%. **ATR-IR (4000 – 400 cm^{-1})**: 3525 (w), 3325 (w, b), 2861 (m), 2228 (s), 1600 (s), 1588 (s), 1542 (s), 1501 (w), 1459 (w), 1409 (s), 1370 (s), 1306 (m), 1293 (m), 1266 (w), 1196 (w), 1175 (w), 1163 (w), 1139 (w), 1088 (s), 1018 (m), 918 (m), 905 (m), 870 (m), 775 (s), 748 (m), 692 (m), 643 (w), 590 (m), 571 (m), 546 (m), 483 (w), 433 (w).

Crystal Data: $\text{C}_{64}\text{H}_{66}\text{Dy}_2\text{Fe}_2\text{N}_8\text{O}_{24}$ ($M = 1767.94$ g/mol): triclinic, space group $P\bar{1}$ (no. 2), $a = 10.4642(4)$ Å, $b = 12.3299(4)$ Å, $c = 14.6118(5)$ Å, $\alpha = 80.848(3)^\circ$, $\beta = 82.115(3)^\circ$, $\gamma = 71.184(3)^\circ$, $V = 1754.33(11)$ Å³, $Z = 1$, $T = 180.15$ K, $\mu(\text{GaK}\alpha) = 13.600$ mm⁻¹, $D_{\text{calc}} = 1.673$ g/cm³, 23689 reflections measured ($5.352^\circ \leq 2\theta \leq 124.99^\circ$), 8221 unique ($R_{\text{int}} = 0.0305$, $R_{\text{sigma}} = 0.0382$) which were used in all calculations. The final R_1 was 0.0306 ($I > 2\sigma(I)$) and wR_2 was 0.0748 (all data).

(Fe₁₀Dy₁₀-9) - [Fe₁₀Dy₁₀(Et-tea)₁₀(Et-teaH)₁₀(NO₃)₁₀]-18MeCN



In a glass vial 101 mg $\text{Fe}(\text{NO}_3)_3 \cdot 9\text{H}_2\text{O}$ (0.25 mmol) and 112 mg $\text{Dy}(\text{NO}_3)_3 \cdot 6\text{H}_2\text{O}$ (0.25 mmol) were dissolved in 5 ml MeOH. To this a second solution containing 133 mg of Et-teaH₃ (0.75 mmol) and 100 µl Et₃N (0.7 mmol) dissolved in 10 ml MeCN was added dropwise under stirring. After 10 minutes additional 80 µl of Et₃N (0.6 mmol) were added followed by further 10 minutes of

stirring. This resulted in a clear light brown solution which was sealed and left undisturbed. After 3 days the product was isolated as colourless block shaped crystals in a yield of 41% (based on Dy).

Elemental analysis (calculated, $\text{Fe}_{10}\text{Dy}_{10}\text{N}_{33}\text{O}_{90}\text{C}_{166}\text{H}_{339}$) C: 31.05%, H: 5.32%, N: 7.20%; (found) C: 31.05%, H: 5.08%, N: 7.40%. **ATR-IR (4000-400 cm^{-1})**: 2963(w); 2853(s); 2705(w); 1495(s); 1462(s); 1362(m); 1278(s); 1163(w); 1130(w); 1089(s);

1048(s); 1023(s); 979(m); 912(m); 890(s); 853(m); 816(m); 765(w); 739(m); 647(m); 617(m); 588(m); 558(m); 499(m); 459(m); 422(w).

Crystal Data for $C_{196}H_{384}Dy_{10}Fe_{10}N_{48}O_{90}$ ($M = 7036.99$ g/mol): triclinic, space group $P-1$ (no. 2), $a = 20.4737(10)$ Å, $b = 23.7752(10)$ Å, $c = 31.4562(14)$ Å, $\alpha = 84.633(4)^\circ$, $\beta = 83.868(4)^\circ$, $\gamma = 66.827(3)^\circ$, $V = 13973.7(11)$ Å³, $Z = 2$, $T = 180$ K, $\mu(1.3401270, 1.34 \text{ K}\alpha) = 17.023 \text{ mm}^{-1}$, $D_{calc} = 1.672 \text{ g/cm}^3$, 74720 reflections measured ($6.16^\circ \leq 2\theta \leq 71.356^\circ$), 18683 unique ($R_{int} = 0.0940$, $R_{sigma} = 0.0757$) which were used in all calculations. The final R_1 was 0.0870 ($I > 2\sigma(I)$) and wR_2 was 0.2618 (all data).

(Fe₁₀Y₁₀-10) - [Fe₁₀Y₁₀(Et-tea)₁₀(Et-teaH)₁₀(NO₃)₁₀]·18MeCN

(Fe₁₀Y₁₀-10) was synthesised using the same procedure as described above for the Dy version but using 112 mg Y(NO₃)₃·6H₂O (0.3 mmol) instead of Dy(NO₃)₃·6H₂O. After 1 day the product was isolated as colourless block shaped crystals in a yield of 30.4%.

ATR-IR (4000-400 cm⁻¹): 2955(w); 2847(s); 2713(w); 1498(s); 1467(s); 1355(m); 1284(s); 1156(w); 1124(w); 1083(s); 1044(s); 1030(s); 973(m); 921(m); 895(s); 846(m); 823(m); 758(w); 733(m); 654(m); 625(m); 594(m); 564(m); 494(m); 465(m); 422(w).

(Fe₁₀Tb₁₀-11) - [Fe₁₀Tb₁₀(Et-tea)₁₀(Et-teaH)₁₀(NO₃)₁₀]·18MeCN

(Fe₁₀Tb₁₀-11) was synthesised using the same procedure as described above for the Dy version but using 113 mg Tb(NO₃)₃·6H₂O (0.25 mmol) instead of Dy(NO₃)₃·6H₂O. After 1 day the product was isolated as colourless block shaped crystals in a yield of 37.4%.

ATR-IR (4000-400 cm⁻¹): 2958(w); 2848(s); 2710(w); 1488(s); 1456(s); 1368(m); 1274(s); 1168(w); 1137(w); 1095(s); 1041(s); 1017(s); 985(m); 919(m); 896(s); 849(m); 823(m); 773(w); 732(m); 656(m); 624(m); 595(m); 563(m); 506(m); 464(m); 422(w).

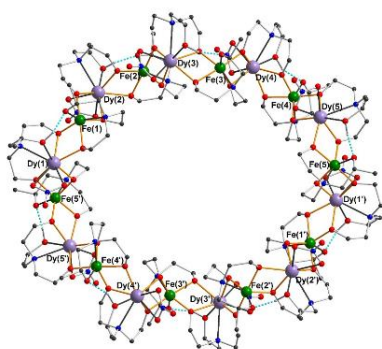
(Fe₁₀Ho₁₀-12) - [Fe₁₀Ho₁₀(Et-tea)₁₀(Et-teaH)₁₀(NO₃)₁₀]·18MeCN

(Fe₁₀Ho₁₀-12) was synthesised using the same procedure as described above for the Dy version but using 110 mg Ho(NO₃)₃·5H₂O (0.25 mmol) instead of Dy(NO₃)₃·6H₂O.

After 1 day the product was isolated as colourless block shaped crystals in a yield of 31.2%.

Elemental analysis (calculated, $\text{Fe}_{10}\text{Ho}_{10}\text{N}_{30}\text{O}_{105}\text{C}_{160}\text{H}_{360}$) C: 29.1%, H: 5.5%, N: 6.37%; (found) C: 29.04%, H: 5.08%, N: 6.33%. **ATR-IR (4000-400 cm^{-1})**: 2972(w); 2849(s); 2712(w); 1488(s); 1458(s); 1367(m); 1285(s); 1158(w); 1124(w); 1082(s); 1042(s); 1031(s); 972(m); 905(m); 897(s); 860(m); 823(m); 772(w); 731(m); 655(m); 624(m); 597(m); 565(m); 491(m); 453(m); 422(w).

(Fe₁₀Dy₁₀-13) - [Fe₁₀Dy₁₀(Me-tea)₁₀(Me-teaH)₁₀(NO₃)₁₀]-20MeCN



The literature-known^[201] compound was reproduced using an improved synthetic procedure. In a glass vial 101 mg $\text{Fe}(\text{NO}_3)_3 \cdot 9\text{H}_2\text{O}$ (0.25 mmol) and 112 mg $\text{Dy}(\text{NO}_3)_3 \cdot 6\text{H}_2\text{O}$ (0.25 mmol) were dissolved in 5 ml MeOH. To this a second solution consisting of 163 mg of Me-teaH_3 (1 mmol) and 100 μl Et_3N (0.7 mmol) dissolved in 10 ml MeCN was added dropwise under

stirring. After 10 minutes additional 80 μl of Et_3N (0.6 mmol) were added followed by further 10 minutes of stirring. This resulted in a clear light brown solution which was sealed and left undisturbed. After 2 weeks the product was isolated as colourless block shaped crystals in a yield of 77% (based on Dy).

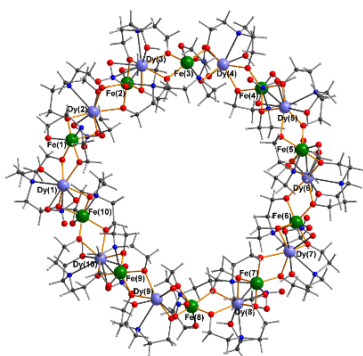
(Fe₁₀Tm₁₀-14) - [Fe₁₀Tm₁₀(Me-tea)₁₀(Me-teaH)₁₀(NO₃)₁₀]-9MeCN·11H₂O

(Fe₁₀Tm₁₀-14) was reproduced using an adapted literature procedure.^[201] A solution of 326 mg Me-teaH_3 (2.0 mmol), 202 mg $\text{Fe}(\text{NO}_3)_3 \cdot 9\text{H}_2\text{O}$ (0.5 mmol) and 224 mg $\text{Tm}(\text{NO}_3)_3 \cdot 6\text{H}_2\text{O}$ (0.5 mmol) in 25 ml/10 ml MeCN/MeOH was stirred for 10 minutes after which 0.3 ml Et_3N were added to the mixture, which was stirred for an additional 10 minutes and then filtered. The solution was left undisturbed to allow for crystallisation of the product. After 4 days it was isolated as colourless crystals.

(Fe₁₀Tb₁₀-15) - [Fe₁₀Tb₁₀(Me-tea)₁₀(Me-teaH)₁₀(NO₃)₁₀]-5H₂O

(Fe₁₀Tb₁₀-15) was reproduced using the same procedure as for (Fe₁₀Tm₁₀-14) but with $\text{Tb}(\text{NO}_3)_3 \cdot 6\text{H}_2\text{O}$ instead of the Tm salt. Additionally for crystallisation the mother liquor needed to be layered with an almost equal amount of Et_2O . Doing this resulted in colourless crystals after 5 days.

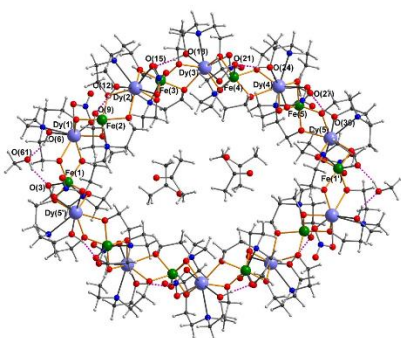
(Fe₁₀Dy₁₀-16) - [Fe₁₀Dy₁₀(tea)₁₀(teaH)₁₀(NO₃)₁₀]-13DMF



A solution of 109 mg teaH₃ (1 mmol) in 5 mL DMF was added to a stirred solution of 101 mg Fe(NO₃)₃·9H₂O (0.25 mmol) and 112 mg Dy(NO₃)₃·6H₂O (0.25 mmol) in 15 ml DMF. After five minutes, 0.28 ml Et₃N were added to the mixture, which was stirred for an additional 10 minutes and then filtered. After 1 week the product was isolated as colourless block shaped crystals in a yield of

44% (based on Fe).

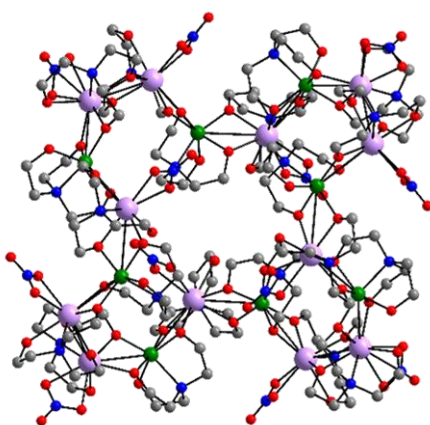
(Fe₁₀Dy₁₀-17) - [Fe₁₀Dy₁₀(tea)₁₀(teaH)₁₀(NO₃)₁₀]-8acetone·6MeOH



A solution of 109 mg teaH₃ (1 mmol) in 5 mL MeOH was added to a stirred solution of 101 mg Fe(NO₃)₃·9H₂O (0.25 mmol) and 112 mg Dy(NO₃)₃·6H₂O (0.25 mmol) in 15 ml MeOH. After five minutes, 0.28 ml Et₃N were added to the mixture, which was stirred for an additional 10 minutes and then filtered. The filtrate was layered with 30 ml of acetone and left undisturbed for

crystallisation. After 1 week the product was isolated as colourless block shaped crystals in a yield of 41% (based on Fe).

(Fe₈Dy₁₂-18) - [Fe₈Dy₁₂(tea)₈(teaH)₁₂(NO₃)₁₂]-8MeCN



In a glass vial 101 mg Fe(NO₃)₃·9H₂O (0.25 mmol) and 112 mg Dy(NO₃)₃·6H₂O (0.25 mmol) were dissolved in 5 ml MeOH. To this a second solution consisting of 109 mg of teaH₃ (1 mmol) and 100 µl Et₃N (0.7 mmol) dissolved in 10 ml MeCN was added dropwise under stirring. After 10 minutes additional 80 µl of Et₃N (0.6 mmol) were added followed by further 10 minutes of stirring. This

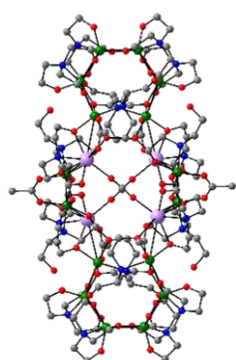
resulted in a clear light brown solution which was sealed and left undisturbed. After 2 weeks the product was isolated as colourless block shaped crystals in a yield of 47% (based on Dy).

Elemental analysis (calculated, $C_{142}H_{300}Dy_{12}Fe_8N_{40}O_{102}$) C: 25.50%, H: 4.34%, N: 8.75%; (found) C: 25.46%, H: 4.19%, N: 8.62%. **ATR-IR (4000-400 cm^{-1})**: 2963(w); 2849(s); 2705(w); 1628(w); 1458(s); 1366(m); 1289(s); 1163(w); 1060(s); 1023(s); 894(s); 814(m); 739(m); 621(m); 588(m); 551(m); 459(m).

(Fe₈Ho₁₂-19) - [Fe₈Ho₁₂(tea)₈(teaH)₁₂(NO₃)₁₂]·8MeCN

In a glass vial 101 mg Fe(NO₃)₃·9H₂O (0.25 mmol) and 110 mg Ho(NO₃)₃·6H₂O (0.25 mmol) were dissolved in 5 ml MeOH. To this a second solution consisting of 109 mg of teaH₃ (1 mmol) and 100 μ l Et₃N (0.7 mmol) dissolved in 10 ml MeCN was added dropwise under stirring. After 10 minutes additional 180 μ l of Et₃N (1.35 mmol) were added followed by further 10 minutes of stirring. This resulted in a clear light brown solution which was sealed and left undisturbed. After 2 weeks the product was isolated as colourless block shaped crystals in a very low yield. The compound was characterised by measurement of the unit cell *via* single crystal XRD. Further characterisation was not possible due to the low yield.

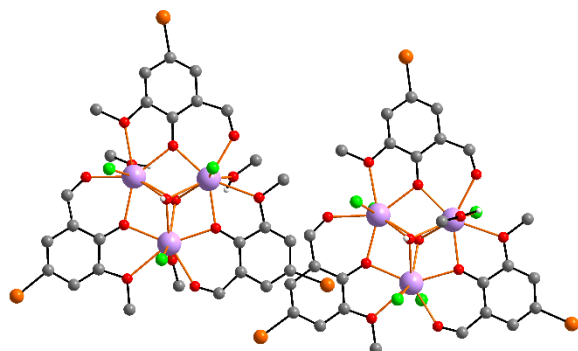
(Fe₁₆Tb₄-20) – [Fe₁₆Tb₄(tea)₈(teaH)₁₂(Oac)₈](NO₃)₄·16H₂O·nMeCN



The compound as well as the used Fe₃ complex were reproduced using an adapted literature-known procedure.^[35] In a glass vial 0.116 g Dy(NO₃)₃·6H₂O (0.25 mmol) were dissolved in 5 ml MeCN and added to a solution of 0.2 g [Fe₃O(O₂CCH₃)₆(H₂O)₃]Cl·6H₂O (0.272 mmol) and 0.3 g teaH₃ (2.00 mmol) in 25 ml MeCN. After stirring for 1 h at room temperature the solution was filtered and sealed with a plastic cap with small holes. Over a course of 2 months slow evaporation of the solvent led to crystallisation of the product in the form of large block shaped yellow crystals in a yield of 160 mg (55.4%).

The product was characterised by determination of the unit cell *via* single crystal XRD.

(Dy₃-21) - [Dy₃(μ₃-OH)₂(Br-van)₃(Cl)₃(MeOH)₃][Dy₃(μ₃-OH)₂(Br-van)₃(Cl)₅(MeOH)]·4MeOH



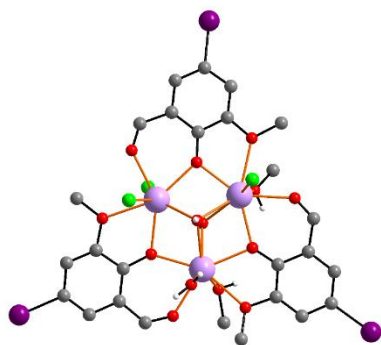
The compound was reproduced using an optimised version of the original synthetic procedure.^[219] In a glass vial 46 mg 5-

Bromo-2-hydroxy-3-methoxybenzaldehyde (0.2 mmol) and 75.4 mg DyCl₃·6H₂O (0.2 mmol) were dissolved in 5 ml of MeOH and 10 ml of

MeCN. Then 42 μl of Et₃N (0.3 mmol) were added dropwise under stirring. The mixture was stirred for 3h after which the solution was filtered and transferred into a glass vial suitable for solvothermal conditions. The vial was sealed and placed into an oven at 66°C. After 24 hours the product was isolated as red-brown block shaped crystals in a yield of 55.8 % (55 mg).

UV-VIS (MeOH): λ/nm = 200, 242, 281, 403.

(Dy₃-22) - [Dy₃(I-van)₃(μ₃-OH)₂(MeOH)₂(H₂O)Cl₃][Cl·3MeOH



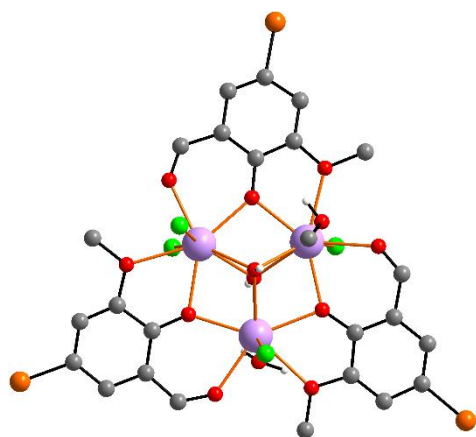
The compound was reproduced using an optimised version of the original synthetic procedure.^[219] In a glass

vial 56 mg 5-Iodo-2-hydroxy-3-methoxybenzaldehyde (0.2 mmol) and 113 mg DyCl₃·6H₂O (0.3 mmol) were dissolved in 5 ml of MeOH and 10 ml of MeCN. Then 42 μl of Et₃N (0.3 mmol) were added dropwise under stirring. The mixture was stirred for 3h after which the

vial was sealed with a cap with small holes and left undisturbed to allow for crystallisation of the product by slow evaporation of the solvent. After 5 days the product was isolated as yellow block shaped crystals in a yield of 63.9% (69 mg).

Elemental analysis (calculated, C₂₆H₃₆Cl₄Dy₃l₃O₁₇) C: 19.15%, H: 2.22%, N: 0.00%; (found) C: 19.01%, H: 2.02%, N: 0.00%. **ATR-IR (4000-400 cm⁻¹):** 3593(m); 3157(s); 3047(s); 2949 (m); 2846(m); 2795(m); 1638(s); 1539(s); 1451(s); 1421(s); 1403(s); 1348(m); 1300(s); 1238(s); 1209(s); 1114(m); 1077(m); 1004(m); 953(m); 890(m); 861(m); 770(s); 755(m); 700(m); 570(m); 462(m); 436(m). **UV-VIS (MeOH):** λ/nm = 205, 246, 283, 405.

(Dy₃-23) - [Dy₃(Br-van)₃(μ₃-OH)₂(MeOH)_{0.7}(H₂O)_{1.3}Cl₄]·3MeOH·0.3H₂O



In a glass vial 46 mg 5-Bromo-2-hydroxy-3-methoxybenzaldehyde (0.2 mmol) and 75.4 mg DyCl₃·6H₂O (0.2 mmol) were dissolved in 5 ml of MeOH. Then 42 μl of Et₃N (0.3 mmol) were added dropwise under stirring. The mixture was stirred for 3h after which the solution was filtered and transferred into one side of an H-tube and the other side filled with Et₂O to allow for slow ether

diffusion. After 24 hours the product was isolated as yellow plate shaped crystals in a yield of 60.0% (60 mg).

Crystal Data for C_{27.7}H₃₈Br₃Cl₄Dy₃O_{16.3} (*M* = 1500.81 g/mol): orthorhombic, space group Pna2₁ (no. 33), *a* = 22.0959(5) Å, *b* = 10.6536(3) Å, *c* = 18.1319(7) Å, *V* = 4268.3(2) Å³, *Z* = 4, *T* = 180 K, μ(Mo Kα) = 8.320 mm⁻¹, *D*_{calc} = 2.336 g/cm³, 47480 reflections measured (3.686° ≤ 2Θ ≤ 58.254°), 11461 unique (*R*_{int} = 0.0395, *R*_{sigma} = 0.0524) which were used in all calculations. The final *R*₁ was 0.0356 (*I* > 2σ(*I*)) and *wR*₂ was 0.0766 (all data).

(Y₃-24) - [Y₃(μ₃-OH)₂(Br-van)₃(Cl)₃(MeOH)₃][Y₃(μ₃-OH)₂(Br-van)₃(Cl)₅(MeOH)]·4MeOH

(Y₃-24) was synthesised using the same procedure as described above for (Dy₃-21) using 61 mg YCl₃·6H₂O (0.2 mmol) instead of DyCl₃·6H₂O. After 3 days the product was isolated as brown block shaped crystals in a yield of 36 % (29 mg).

ATR-IR (4000-400 cm⁻¹): 3177(s); 3051(s); 3004(m); 2945(m); 2838(w); 1639(s); 1602(s); 1547(s); 1458(s); 1429(s); 1403(s); 1348(s); 1296(s); 1233(s); 1207(s); 1078(m); 1008(m); 953(m); 875(m); 783(s); 754(m); 706(m); 558(m); 455(m); 426(m).

(Tb₃-25) - [Tb₃(μ₃-OH)₂(Br-van)₃(Cl)₃(MeOH)₃][Tb₃(μ₃-OH)₂(Br-van)₃(Cl)₅(MeOH)]·XMeOH/MeCN

(Tb₃-25) was synthesised using the same procedure as described above for (Dy₃-21) using 76 mg TbCl₃·6H₂O (0.2 mmol) instead of DyCl₃·6H₂O. After 1 day the product was isolated as brown block shaped crystals in a yield of 54.3 % (51 mg).

Elemental analysis (calculated, C₅₄H₈₃Br₆Cl₈Tb₆O₃₈N₁) C: 21.1%, H: 2.72%, N: 0.46%; (found) C: 20.64%, H: 2.28%, N: 0.67%. **ATR-IR (4000-400 cm⁻¹):** 3185(s); 3057(s); 3001(m); 2939(m); 2832(w); 1644(s); 1607(s); 1541(s); 1450(s); 1436(s); 1412(s); 1352(s); 1290(s); 1241(s); 1214(s); 1083(m); 1004(m); 961(m); 882(m); 792(s); 749(m); 699(m); 564(m); 462(m); 426(m).

(Ho₃-26) - **[Ho₃(μ₃-OH)₂(Br-van)₃(Cl)₃(MeOH)₃][Ho₃(μ₃-OH)₂(Br-van)₃(Cl)₅(MeOH)]·4MeOH**

(Ho₃-26) was synthesised using the same procedure as described above for (Dy₃-21) using 76 mg HoCl₃·6H₂O (0.2 mmol) instead of DyCl₃·6H₂O. After 24 hours the product was isolated as brown block shaped crystals in a yield of 51.8 % (44 mg).

ATR-IR (4000-400 cm⁻¹): 3182(s); 3055(s); 3007(m); 2940(m); 2829(w); 1632(s); 1599(s); 1549(s); 1464(s); 1432(s); 1412(s); 1343(s); 1290(s); 1228(s); 1215(s); 1083(m); 1000(m); 952(m); 874(m); 789(s); 759(m); 699(m); 565(m); 456(m); 423(m).

(Er₃-27) - **[Er₃(μ₃-OH)₂(Br-van)₃(Cl)₃(MeOH)₃][Er₃(μ₃-OH)₂(Br-van)₃(Cl)₅(MeOH)]·4MeOH**

(Er₃-27) was synthesised using the same procedure as described above for (Dy₃-21) 76 mg ErCl₃·6H₂O (0.2 mmol) instead of DyCl₃·6H₂O. After 1 day the product was isolated as brown block shaped crystals in a yield of 50.0 % (48 mg).

ATR-IR (4000-400 cm⁻¹): 3169(s); 3044(s); 3000(m); 2941(m); 2842(w); 1644(s); 1609(s); 1542(s); 1463(s); 1435(s); 1406(s); 1342(s); 1289(s); 1241(s); 1212(s); 1075(m); 1005(m); 947(m); 873(m); 779(s); 748(m); 701(m); 557(m); 451(m); 421(m).

(Tm₃-28) - **[Tm₃(μ₃-OH)₂(Br-van)₃(Cl)₃(MeOH)₃][Tm₃(μ₃-OH)₂(Br-van)₃(Cl)₅(MeOH)]·4MeOH**

(Tm₃-28) was synthesised using the same procedure as described above for (Dy₃-21) using 76 mg TmCl₃·6H₂O (0.2 mmol) instead of DyCl₃·6H₂O. After 1 day the product was isolated as brown block shaped crystals in a yield of 53.1 % (51 mg).

ATR-IR (4000-400 cm⁻¹): 3183(s); 3058(s); 3000(m); 2942(m); 2842(w); 1638(s); 1607(s); 1544(s); 1454(s); 1434(s); 1397(s); 1345(s); 1302(s); 1236(s); 1214(s); 1074(m); 1015(m); 961(m); 874(m); 782(s); 748(m); 702(m); 555(m); 450(m); 425(m).

(Y₃-29) - [Y₃(I-van)₃(μ₃-OH)₂(MeOH)₂(H₂O)Cl₃]Cl·XMeOH/MeCN

(Y₃-29) was synthesised using the same procedure as described above for (Dy₃-22) using 91 mg YCl₃·6H₂O (0.3 mmol) instead of DyCl₃·6H₂O. After 2 days the product was isolated as yellow block shaped crystals in a yield of 63.4% (60 mg).

Elemental analysis (calculated, C₂₈H_{37.5}Cl₄Y₃I₃O₁₆N_{0.5}) C: 23.57%, H: 2.65%, N: 0.49%; (found) C: 23.22%, H: 2.65%, N: 0.50%. **ATR-IR (4000-400 cm⁻¹):** 3616(m); 3284(s); 3047(s); 2941 (m); 2838(m); 2786(m); 1632(s); 1595(s); 1539(s); 1455(s); 1425(s); 1399(s); 1344(m); 1300(s); 1238(s); 1209(s); 1114(m); 1077(m); 1016(m); 949(m); 890(m); 861(m); 770(s); 755(m); 700(m); 570(m); 455(m); 433(m).

(Tb₃-30) - [Tb₃(I-van)₃(μ₃-OH)₂(MeOH)₂(H₂O)Cl₃]Cl·XMeOH/MeCN

(Tb₃-30) was synthesised using the same procedure as described above for (Dy₃-22) using 112 mg TbCl₃·6H₂O (0.3 mmol) instead of DyCl₃·6H₂O. After 3 days the product was isolated as yellow block shaped crystals in a yield of 36.1% (39 mg).

Elemental analysis (calculated, C₂₇H_{37.5}Cl₄Tb₃I₃O₁₇N_{0.5}) C: 19.77%, H: 2.3%, N: 0.43%; (found) C: 19.89%, H: 2.41%, N: 0.43%. **ATR-IR (4000-400 cm⁻¹):** 3590(m); 3284(s); 3047(s); 2941 (m); 2838(m); 2786(m); 1628(s); 1595(s); 1539(s); 1455(s); 1421(s); 1397(s); 1342(m); 1303(s); 1235(s); 1206(s); 1113(m); 1077(m); 1013(m); 944(m); 895(m); 861(m); 770(s); 753(m); 702(m); 574(m); 455(m); 433(m).

(Ho₃-31)- [Ho₃(I-van)₃(μ₃-OH)₂(MeOH)₂(H₂O)Cl₃]Cl·XMeOH/MeCN

(Ho₃-31) was synthesised using the same procedure as described above for (Dy₃-22) using 114 mg HoCl₃·6H₂O (0.3 mmol) instead of DyCl₃·6H₂O. After 2 days the product was isolated as yellow block shaped crystals in a yield of 55.4% (61 mg).

Elemental analysis (calculated, C₂₈H₄₃Cl₄Ho₃I₃O₁₉N) C: 19.60%, H: 2.5%, N: 0.81%; (found) C: 19.46%, H: 2.43%, N: 0.68%. **ATR-IR (4000-400 cm⁻¹):** 3586(m); 3280(s); 3050(s); 2945(m); 2832(m); 2781(m); 1622(s); 1592(s); 1535(s); 1459(s); 1416(s); 1405(s); 1334(m); 1308(s); 1240(s); 1214(s); 1118(m); 1082(m); 1009(m); 951(m); 895(m); 857(m); 776(s); 758(m); 696(m); 568(m); 449(m); 433(m).

(Er₃-32) - [Er₃(l-van)₃(μ₃-OH)₂(MeOH)₂(H₂O)Cl₃]Cl·XMeOH/MeCN

(Er₃-32) was synthesised using the same procedure as described above for (Dy₃-22) using 115 mg ErCl₃·6H₂O (0.3 mmol) instead of DyCl₃·6H₂O. After 1 day the product was isolated as yellow block shaped crystals in a yield of 47.3% (52 mg).

Elemental analysis (calculated, C₂₈H₄₃Cl₄Er₃l₃O₁₉N) C: 19.53%, H: 2.51%, N: 0.81%; (found) C: 19.29%, H: 2.53%, N: 0.77%. **ATR-IR (4000-400 cm⁻¹):** 3592(m); 2949(m); 2826(m); 2787(m); 1617(s); 1597(s); 1532(s); 1463(s); 1411(s); 1413(s); 1328(m); 1313(s); 1233(s); 1219(s); 1113(m); 1078(m); 1017(m); 946(m); 903(m); 864(m); 782(s); 753(m); 689(m); 573(m); 457(m); 433(m).

(Tm₃-33) - [Tm₃(l-van)₃(μ₃-OH)₂(MeOH)₂(H₂O)Cl₃]Cl·XMeOH/MeCN

(Tm₃-33) was synthesised using the same procedure as described above for (Dy₃-22) using 115 mg TmCl₃·6H₂O (0.3 mmol) instead of DyCl₃·6H₂O. After 1 day the product was isolated as yellow block shaped crystals in a yield of 50.6% (56 mg).

Elemental analysis (calculated, C₂₈H₄₃Cl₄Tm₃l₃O₁₉N) C: 19.47%, H: 2.51%, N: 0.81%; (found) C: 19.37%, H: 2.46%, N: 0.62%. **ATR-IR (4000-400 cm⁻¹):** 3591(m); 3286(s); 3045(s); 1628(s); 1597(s); 1533(s); 1463(s); 1423(s); 1412(s); 1343(m); 1300(s); 1247(s); 1219(s); 1111(m); 1074(m); 1013(m); 944(m); 903(m); 864(m); 781(s); 750(m); 692(m); 562(m); 440(m); 433(m).

(Yb₃-34) - [Yb₃(l-van)₃(μ₃-OH)₂(MeOH)₂(H₂O)Cl₃]Cl·XMeOH/MeCN

(Yb₃-34) was synthesised using the same procedure as described above for (Dy₃-22) using 116 mg YbCl₃·6H₂O (0.3 mmol) instead of DyCl₃·6H₂O. After 2 days the product was isolated as yellow block shaped crystals in a yield of 59.5% (66 mg).

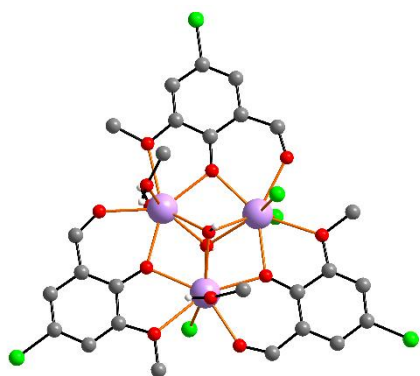
Elemental analysis (calculated, C₂₇H_{37.5}Cl₄Yb₃l₃O₁₇N_{0.5}) C: 19.27%, H: 2.24%, N: 0.41%; (found) C: 19.36%, H: 2.23%, N: 0.54%. **ATR-IR (4000-400 cm⁻¹):** 3610(m); 3279(s); 3043(s); 2933(m); 2844(m); 2781(m); 1637(s); 1601(s); 1533(s); 1463(s); 1417(s); 1404(s); 1348(m); 1292(s); 1231(s); 1216(s); 1119(m); 1083(m); 1020(m); 941(m); 897(m); 868(m); 763(s); 762(m); 696(m); 564(m); 450(m); 433(m).

(Lu₃-35) - [Lu₃(I-van)₃(μ₃-OH)₂(MeOH)₂(H₂O)Cl₃]Cl·XMeOH/MeCN

(Lu₃-35) was synthesised using the same procedure as described above for (Dy₃-22) using 117 mg LuCl₃·6H₂O (0.3 mmol) instead of DyCl₃·6H₂O. After 2 days the product was isolated as yellow block shaped crystals in a yield of 30.4% (34 mg).

Elemental analysis (calculated, C₂₇H_{37.5}Cl₄Lu₃l₃O₁₇N_{0.5}) C: 19.20%, H: 2.24%, N: 0.41%; (found) C: 19.31%, H: 2.11%, N: 0.36%. **ATR-IR (4000-400 cm⁻¹):** 3048(s); 2956(m); 2923(m); 2849(m); 1644(s); 1594(s); 1528(s); 1470(s); 1422(s); 1413(s); 1343(m); 1297(s); 1225(s); 1209(s); 1114(m); 1079(m); 1012(m); 949(m); 892(m); 862(m); 770(s); 769(m); 703(m); 557(m); 446(m); 433(m).

(Dy₃-36) - [Dy₃(Cl-van)₃(μ₃-OH)₂(MeOH)_{2.5}(H₂O)_{0.5}Cl₃]Cl·2.5MeOH



In a glass vial 55 mg 5-Chlor-2-hydroxy-3-methoxybenzaldehyde (0.3 mmol) and 169 mg DyCl₃·6H₂O (0.45 mmol) were dissolved in 5 ml of MeOH and 10 ml of MeCN. Then 63 μl of Et₃N (0.45 mmol) were added dropwise under stirring. The mixture was stirred for 3h after which the vial was sealed with a cap with small holes and left undisturbed to allow for crystallisation of the product by slow evaporation of the solvent. After 2 days the product was isolated as yellow block shaped crystals in a yield of 50.0 % (70 mg).

Elemental analysis (calculated, C₂₄H₃₂Cl₇Dy₃O₁₇) C: 21.70%, H: 2.428%, N: 0.00%; (found) C: 21.70%, H: 2.51%, N: 0.00%. **ATR-IR (4000-400 cm⁻¹):** 3172(s); 3055(s); 2951(m); 2846(m); 1638(s); 1550(s); 1451(s); 1429(s); 1403(s); 1348(m); 1300(s); 1238(s); 1209(s); 1077(m); 1004(m); 953(m); 890(m); 861(m); 799(s); 755(m); 726(m); 570(m); 462(m); 436(m). **UV-VIS (MeOH):** λ/nm = 243, 281, 402.

Crystal Data for C₂₉H₄₁Cl₇Dy₃O_{16.5} (*M* = 1389.27 g/mol): monoclinic, space group P2₁/c (no. 14), *a* = 11.4253(2) Å, *b* = 19.6099(5) Å, *c* = 20.2093(4) Å, β = 102.133(2)°, *V* = 4426.73(17) Å³, *Z* = 4, *T* = 180 K, μ(1.3401270, 1.34 Kα) = 28.890 mm⁻¹, *D*_{calc} = 2.085 g/cm³, 31866 reflections measured (5.524° ≤ 2θ ≤ 118.6°), 9697 unique (*R*_{int} = 0.0711, *R*_{sigma} = 0.0563) which were used in all calculations. The final *R*₁ was 0.0834 (*I* > 2σ(*I*)) and *wR*₂ was 0.2510 (all data).

(Ho₃-37) - [Ho₃(Cl-van)₃(μ₃-OH)₂(MeOH)_{2.5}(H₂O)_{0.5}Cl₃]Cl·2.5MeOH

(Ho₃-37) was synthesised using the same procedure as described above for (Dy₃-36) using 171 mg HoCl₃·6H₂O (0.45 mmol) instead of DyCl₃·6H₂O. After 1 day the product was isolated as yellow block shaped crystals in a yield of 51.8 % (72 mg).

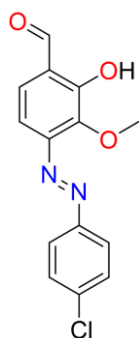
ATR-IR (4000-400 cm⁻¹): 3165(s); 3051(s); 2942(m); 2838(m); 1643(s); 1542(s); 1447(s); 1434(s); 1397(s); 1344(m); 1292(s); 1247(s); 1203(s); 1082(m); 1012(m); 962(m); 897(m); 854(m); 807(s); 749(m); 719(m); 564(m); 469(m); 436(m).

(Er₃-38) - [Er₃(Cl-van)₃(μ₃-OH)₂(MeOH)_{2.5}(H₂O)_{0.5}Cl₃]Cl·2.5MeOH

(Er₃-38) was synthesised using the same procedure as described above for (Dy₃-36) using 173 mg ErCl₃·6H₂O (0.45 mmol) instead of DyCl₃·6H₂O. After 4 days the product was isolated as yellow block shaped crystals in a yield of 40.9 % (59 mg).

ATR-IR (4000-400 cm⁻¹): 3166(s); 3051(s); 2944(m); 2850(m); 1644(s); 1548(s); 1444(s); 1433(s); 1411(s); 1353(m); 1295(s); 1242(s); 1201(s); 1083(m); 1011(w); 945(m); 882(m); 857(m); 791(s); 749(m); 733(m); 566(m); 454(m); 436(m).

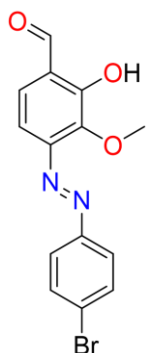
2-Hydroxy-3-methoxy-5-(4-chlorophenylazo)benzaldehyde



The compound was synthesised using a procedure adapted from the literature.^[230] To a 250 ml glass flask 1.275 g 4-chloroaniline (10 mmol), 50 ml of water and 2.5 ml of concentrated HCl were added and heated under stirring until fully dissolved. The resulting mixture was cooled in an ice bath while a solution of 1.22 g NaNO₂ (14 mmol) in water was added slowly. The solution was kept at 0°C and stirred for further 30 mins. After this 1.52 g (10 mmol) o-vanillin were dissolved in 20 ml water through addition of 0.4 g NaOH (10 mmol) and 4.24 g of Na₂CO₃ (10 mmol). The o-vanillin solution was added slowly to the now diazonium chloride containing first solution which is kept at 0°C. The mixture is stirred for a further 60 min period at 0°C after which it was allowed to warm up to room temperature. After filtration the orange solid was dissolved in hot MeOH and treated with 1.5 ml of concentrated HCl. The solvent was removed under reduced pressure and the resulting solid washed with water. The solid was then dried in the oven at 70°C. The product was obtained in the form of a light orange powder in a yield of 77% (2.2 g).

¹H-NMR (500 MHz, DMSO-d₆): δ/ppm = 10.36 (s, 1H, CH), 7.85 (m, 3H, CH_{Ar}), 7.63(m, 3H, CH_{Ar}), 3.93 (s, 3H, CH). **ATR-IR (4000-400 cm⁻¹):** 3069(s); 2978(w); 2905(w); 2839(w); 2652(w); 2447(w); 1784(w); 1663(s); 1605(s); 1590(s); 1484(s); 1425(s); 1399(s); 1260(s); 1183(m); 1150(s); 1125(m); 1092(m); 1070(m); 1008(m); 938(m); 894(m); 872(m); 828(m); 762(m); 726(m); 645(m); 623(m); 561(m); 495(w); 418(w).

2-Hydroxy-3-methoxy-5-(4-bromophenylazo)benzaldehyde

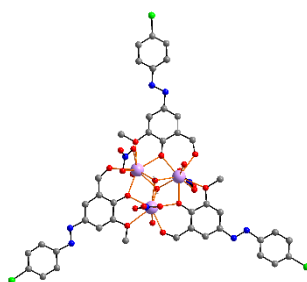


Uses the same procedure as described for 2-Hydroxy-3-methoxy-5-(4-chlorophenylazo)benzaldehyde above but using 1.72 g of 4-bromoaniline (10 mmol) instead of the 4-chloroaniline. The product was isolated as a brown orange powder in a yield of 2.3 g (70%).

¹H-NMR (500 MHz, DMSO-d₆): δ/ppm = 11.15 (s, 1H, OH), 10.39 (s, 1H, CH), 7.88 (d, 1H, CH_{Ar}), 7.81 (m, 4H, CH_{Ar}), 7.70 (d, 1H, CH_{Ar}), 3.97 (s, 3H, CH). **ATR-IR (4000-400 cm⁻¹):** 3069(s); 2978(w); 2905(w); 2839(w);

2652(w); 2447(w); 1784(w); 1663(s); 1605(s); 1590(s); 1484(s); 1425(s); 1399(s); 1260(s); 1183(m); 1150(s); 1125(m); 1092(m); 1070(m); 1008(m); 938(m); 894(m); 872(m); 828(m); 762(m); 726(m); 645(m); 623(m); 561(m); 495(w); 418(w).

(Dy₃-39) - [Dy₃(μ₃-OH)₂ (p-Cl-pdavan)₃(NO₃)₃(H₂O)₃]₃[Dy₃(μ₃-OH)₂ (p-Cl-pdavan)₃(NO₃)₄(H₂O)₂](NO₃)₃·2(H₂O)·19(MeCN)



In a glass vial 87 mg 2-Hydroxy-3-methoxy-5-(4-chlorophenylazo)benzaldehyde (0.3 mmol) and 137 mg Dy(NO₃)₃·6H₂O (0.3 mmol) were dissolved in 3 ml of MeOH and 12 ml of MeCN. Then 63 μl of Et₃N (0.45 mmol) were added dropwise under stirring. The mixture was stirred for 4 hours after which the mixture was filtered. The resulting clear

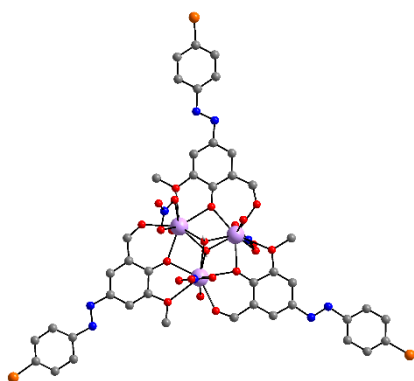
orange solution was transferred to a glass vial which was sealed with a cap with small holes and left undisturbed to allow for crystallisation of the product by slow evaporation of the solvent. After 2 days the product was isolated as orange block shaped crystals in a yield of 22.1% (40 mg).

Elemental analysis (calculated, Dy₃Cl₃C₄₂H₅₆O₃₅N₁₀) C: 27.19%, H: 3.04%, N: 7.55%; (found) C: 26.88%, H: 2.49%, N: 7.22%. **ATR-IR (4000-400 cm⁻¹):** 3406(s); 3000(m); 2897(m); 2641(w); 1638(s); 1612(s); 1546(m); 1480(m); 1447(s); 1407(s);

1378(w); 1304(s); 1246(m); 1202(w); 1154(w); 1121(m); 1085(m); 1037(m); 1000(m); 953(m); 879(s); 838(m); 810(m); 762(m); 744(m); 729(m); 707(w); 616(m); 576(w); 553(w); 502(m); 436(m); 414(m).

Crystal Data for $C_{206}H_{211}Cl_{12}Dy_{12}N_{59}O_{105}$ ($M=7568.73$ g/mol): triclinic, space group $P\bar{1}$ (no. 2), $a = 11.0794(4)$ Å, $b = 18.1426(5)$ Å, $c = 32.6032(8)$ Å, $\alpha = 85.047(2)^\circ$, $\beta = 83.972(2)^\circ$, $\gamma = 89.486(3)^\circ$, $V = 6493.0(3)$ Å³, $Z = 1$, $T = 180$ K, $\mu(\text{Mo K}\alpha) = 3.635$ mm⁻¹, $D_{\text{calc}} = 1.936$ g/cm³, 70430 reflections measured ($3.234^\circ \leq 2\theta \leq 52.744^\circ$), 26301 unique ($R_{\text{int}} = 0.0449$, $R_{\text{sigma}} = 0.0668$) which were used in all calculations. The final R_1 was 0.0516 ($I > 2\sigma(I)$) and wR_2 was 0.1490 (all data).

(Dy₃-40) - [Dy₃(μ₃-OH)₂ (p-Br-pdavan)₃(NO₃)₃(H₂O)₃](NO₃)₃·(H₂O)·3(MeCN)]



In a glass vial 100 mg 2-Hydroxy-3-methoxy-5-(4-Bromophenylazo)benzaldehyde (0.3 mmol) and 137 mg Dy(NO₃)₃·6H₂O (0.3 mmol) were dissolved in 5 ml of MeOH and 15 ml of MeCN. Then 63 μl of Et₃N (0.45 mmol) were added dropwise under stirring. The mixture was stirred for 4 hours after which the mixture was filtered. The resulting dark orange solution was

transferred to a glass vial which was sealed with a cap with small holes and left undisturbed to allow for crystallisation of the product by slow evaporation of the solvent. After 6 days the product was isolated as orange block shaped crystals in a yield of 25.0 % (49 mg).

PXRD experiments showed the product to be impure. Therefore, no further characterisation was performed.

Crystal Data for $C_{48}H_{49}Br_3Dy_3N_{13}O_{27}$ ($M=1967.23$ g/mol): triclinic, space group $P\bar{1}$ (no. 2), $a = 10.9121(6)$ Å, $b = 18.1497(6)$ Å, $c = 32.7416(11)$ Å, $\alpha = 94.436(3)^\circ$, $\beta = 94.134(4)^\circ$, $\gamma = 90.258(4)^\circ$, $V = 6447.9(5)$ Å³, $Z = 4$, $T = 180$ K, $\mu(1.3401270, 1.34 \text{ K}\alpha) = 19.768$ mm⁻¹, $D_{\text{calc}} = 2.026$ g/cm³, 69046 reflections measured ($6.102^\circ \leq 2\theta \leq 89.822^\circ$), 15494 unique ($R_{\text{int}} = 0.0942$, $R_{\text{sigma}} = 0.0811$) which were used in all calculations. The final R_1 was 0.0628 ($I > 2\sigma(I)$) and wR_2 was 0.1898 (all data).

(Y₃-41) - **[Y₃(*p*-Cl-pdavan)₃(NO₃)₃(H₂O)₃]₃[Y₃(*p*-Cl-pdavan)₃(NO₃)₄(H₂O)₂](NO₃)₃·2(H₂O)·19(MeCN)**

(Y₃-41) was synthesised using the same procedure as described above for (Dy₃-39) using 115 mg Y(NO₃)₃·6H₂O (0.3 mmol) instead of Dy(NO₃)₃·6H₂O. After 5 days the product was isolated as orange block shaped crystals in a yield of 19 % (31 mg).

ATR-IR (4000-400 cm⁻¹): 3409(s); 2997(m); 2899(m); 2643(w); 1635(s); 1610(s); 1544(m); 1478(m); 1448(s); 1409(s); 1375(w); 1302(s); 1249(m); 1201(w); 1152(w); 1119(m); 1083(m); 1035(m); 1002(m); 950(m); 882(s); 837(m); 811(m); 765(m); 743(m); 728(m); 709(w); 619(m); 578(w); 554(w); 501(m); 439(m); 412(m).

(Gd₃-42)- **[Gd₃(*p*-Cl-pdavan)₃(NO₃)₃(H₂O)₃]₃[Gd₃(*p*-Cl-pdavan)₃(NO₃)₄(H₂O)₂](NO₃)₃·2(H₂O)·19(MeCN)**

(Gd₃-42) was synthesised using the same procedure as described above for (Dy₃-39) using 135 mg Gd(NO₃)₃·6H₂O (0.3 mmol) instead of Dy(NO₃)₃·6H₂O. After 7 days the product was isolated as orange block shaped crystals in a yield of 17.9 % (33 mg).

ATR-IR (4000-400 cm⁻¹): 3404(s); 2998(m); 2900(m); 2639(w); 1639(s); 1614(s); 1548(m); 1482(m); 1446(s); 1405(s); 1376(w); 1306(s); 1245(m); 1204(w); 1153(w); 1117(m); 1087(m); 1039(m); 1003(m); 954(m); 877(s); 835(m); 813(m); 761(m); 741(m); 727(m); 705(w); 615(m); 579(w); 555(w); 503(m); 434(m); 415(m).

(Tb₃-43) - **[Tb₃(*p*-Cl-pdavan)₃(NO₃)₃(H₂O)₃]₃[Tb₃(*p*-Cl-pdavan)₃(NO₃)₄(H₂O)₂](NO₃)₃·2(H₂O)·19(MeCN)**

(Tb₃-43) was synthesised using the same procedure as described above for (Dy₃-39) using 136 mg Tb(NO₃)₃·6H₂O (0.3 mmol) instead of Dy(NO₃)₃·6H₂O. After 4 days the product was isolated as orange block shaped crystals in a yield of 30.5 % (56 mg).

ATR-IR (4000-400 cm⁻¹): 3407(s); 2996(m); 2898(m); 2638(w); 1640(s); 1611(s); 1549(m); 1483(m); 1444(s); 1408(s); 1379(w); 1305(s); 1247(m); 1203(w); 1155(w); 1118(m); 1084(m); 1036(m); 1001(m); 951(m); 878(s); 836(m); 809(m); 764(m); 742(m); 731(m); 708(w); 618(m); 575(w); 556(w); 504(m); 438(m); 416(m).

(Ho₃-44) - **[Ho₃(*p*-Cl-pdavan)₃(NO₃)₃(H₂O)₃]₃[Ho₃(*p*-Cl-pdavan)₃(NO₃)₄(H₂O)₂](NO₃)₃·2(H₂O)·19(MeCN)]**

(Ho₃-44) was synthesised using the same procedure as described above for (Dy₃-39) using 132 mg Ho(NO₃)₃·5H₂O (0.3 mmol) instead of Dy(NO₃)₃·6H₂O. After 8 days the product was isolated as orange block shaped crystals in a yield of 28.7 % (52 mg).

ATR-IR (4000-400 cm⁻¹): 3405(s); 2999(m); 2896(m); 2644(w); 1636(s); 1613(s); 1547(m); 1481(m); 1449(s); 1404(s); 1374(w); 1307(s); 1244(m); 1200(w); 1151(w); 1120(m); 1086(m); 1038(m); 999(m); 955(m); 881(s); 834(m); 808(m); 760(m); 740(m); 732(m); 704(w); 614(m); 574(w); 557(w); 506(m); 440(m); 411(m).

(Er₃-45) - **[Er₃(*p*-Cl-pdavan)₃(NO₃)₃(H₂O)₃]₃[Er₃(*p*-Cl-pdavan)₃(NO₃)₄(H₂O)₂](NO₃)₃·2(H₂O)·19(MeCN)]**

(Er₃-45) was synthesised using the same procedure as described above for Dy₃-(Dy₃-39) using 133 mg Er(NO₃)₃·5H₂O (0.3 mmol) instead of Dy(NO₃)₃·6H₂O. After 4 days the product was isolated as orange block shaped crystals in a yield of 27.2 % (50 mg).

ATR-IR (4000-400 cm⁻¹): 3410(s); 2995(m); 2894(m); 2640(w); 1641(s); 1615(s); 1543(m); 1485(m); 1445(s); 1403(s); 1378(w); 1301(s); 1243(m); 1206(w); 1150(w); 1116(m); 1081(m); 1033(m); 1005(m); 949(m); 876(s); 840(m); 807(m); 766(m); 739(m); 726(m); 711(w); 613(m); 576(w); 551(w); 508(m); 435(m); 417(m).

(Tm₃-46) - **[Tm₃(*p*-Cl-pdavan)₃(NO₃)₃(H₂O)₃]₃[Tm₃(*p*-Cl-pdavan)₃(NO₃)₄(H₂O)₂](NO₃)₃·2(H₂O)·19(MeCN)]**

(Tm₃-46) was synthesised using the same procedure as described above for (Dy₃-39) using 133 mg Tm(NO₃)₃·5H₂O (0.3 mmol) instead of Dy(NO₃)₃·6H₂O. After 4 days the product was isolated as orange block shaped crystals in a yield of 29.4 % (54 mg).

ATR-IR (4000-400 cm⁻¹): 3408(s); 3002(m); 2895(m); 2637(w); 1637(s); 1609(s); 1545(m); 1479(m); 1450(s); 1406(s); 1377(w); 1303(s); 1248(m); 1205(w); 1156(w); 1123(m); 1082(m); 1034(m); 1004(m); 952(m); 880(s); 839(m); 812(m); 763(m); 745(m); 730(m); 706(w); 617(m); 577(w); 552(w); 505(m); 437(m); 413(m).

(Yb₃-47) - **[Yb₃(*p*-Cl-pdavan)₃(NO₃)₃(H₂O)₃]₃[Yb₃(*p*-Cl-pdavan)₃(NO₃)₄(H₂O)₂](NO₃)₃·2(H₂O)·19(MeCN)**

(Yb₃-47) was synthesised using the same procedure as described above for (Dy₃-39) using 135 mg Yb(NO₃)₃·5H₂O (0.3 mmol) instead of Dy(NO₃)₃·6H₂O. After 5 days the product was isolated as orange block shaped crystals in a yield of 10.4 % (19 mg).

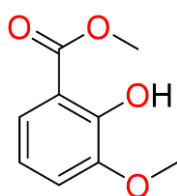
ATR-IR (4000-400 cm⁻¹): 3402(s); 3001(m); 2901(m); 2636(w); 1634(s); 1616(s); 1548(m); 1484(m); 1443(s); 1402(s); 1373(w); 1308(s); 1242(m); 1208(w); 1149(w); 1122(m); 1080(m); 1032(m); 1006(m); 956(m); 879(s); 836(m); 804(m); 761(m); 744(m); 725(m); 703(w); 616(m); 578(w); 550(w); 507(m); 441(m); 414(m).

(Lu₃-48) - **[Lu₃(*p*-Cl-pdavan)₃(NO₃)₃(H₂O)₃]₃[Lu₃(*p*-Cl-pdavan)₃(NO₃)₄(H₂O)₂](NO₃)₃·2(H₂O)·19(MeCN)**

(Lu₃-48) was synthesised using the same procedure as described above for (Dy₃-39) using 141 mg Lu(NO₃)₃·6H₂O (0.3 mmol) instead of Dy(NO₃)₃·6H₂O. After 4 days the product was isolated as orange block shaped crystals in a yield of 32.0 % (58 mg).

ATR-IR (4000-400 cm⁻¹): 3403(s); 3003(m); 2899(m); 2635(w); 1638(s); 1610(s); 1544(m); 1480(m); 1447(s); 1409(s); 1375(w); 1306(s); 1249(m); 1202(w); 1154(w); 1124(m); 1088(m); 1031(m); 1002(m); 950(m); 874(s); 838(m); 805(m); 759(m); 743(m); 728(m); 710(w); 620(m); 573(w); 554(w); 501(m); 436(m); 419(m).

Methyl-3-methoxysalicylat

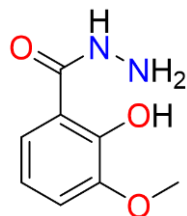


For the synthesis of methyl-3-methoxysalicylat a literature procedure was adapted.^[245-246] In a glass flask 9.75 g 2-hydroxy-3-methoxy benzoic acid (58 mmol) and 5.3 ml concentrated H₂SO₄ (98.8 mmol) were dissolved in 260 ml MeOH and refluxed for 24h. The brown precipitate was filtered, washed with water and dried resulting in a yield of 92% (9.61 g).

¹H-NMR (500 MHz, CD₃CN): δ/ppm = 10.81 (s, 1H, OH), 7.40 (m, 1H, CH_{Ar}), 7.14 (m, 1H, CH_{Ar}), 6.87 (m, 1H, CH_{Ar}), 3.92 (s, 3H, CH), 3.84 (s, 3H, CH). **ATR-IR (4000-400 cm⁻¹):** 3143(s); 3091(m); 2956(m); 2839(m); 1692(s); 1612(m); 1586(s); 1480(m); 1465(s); 1436(s); 1341(s); 1319(m); 1290(m); 1242(s); 1191(m); 1169(w); 1136(m);

1088(m); 1052(s); 982(m); 953(m); 894(w); 876(m); 832(s); 810(w); 777(m); 744(s); 718(m); 641(m); 597(m); 499(w); 451(m).

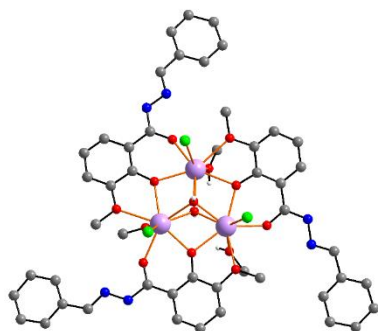
o-vanillyl hydrazide



A literature known procedure was adapted to synthesise *o*-vanillyl hydrazide.^[247] 1.5 g methyl-3-methoxy-salicylat (8.2 mmol) were added to a glass flask with 25 ml of absolute EtOH. Under stirring 3.9 ml hydrazine hydrate were added slowly. The solution was refluxed for 5h after which the flask was left to cool in the fridge overnight. The next day the crystalline precipitate was filtered and washed with Et₂O. The product was isolated in a yield of 75% (1.32 g) and was stored under nitrogen atmosphere.

¹H-NMR (500 MHz, DMSO-d₆): δ/ppm = 7.33 (m, 1H, CH_{Ar}), 6.90 (m, 1H, CH_{Ar}), 6.52 (m, 1H, CH_{Ar}), 5.47-4.35 (s, 2H, NH), 3.73 (s, 3H, CH). **ATR-IR (4000-400 cm⁻¹):** 3329(s); 3286(s); 3212(m); 3000(w); 2960(m); 2831(m); 1619(m); 1583(s); 1564(m); 1539(m); 1495(s); 1462(m); 1425(m); 1334(m); 1293(m); 1216(s); 1172(s); 1063(s); 975(m); 949(m); 901(m); 839(m); 795(s); 748(s); 696(s); 652(m); 597(s); 550(w); 502(w); 429(w).

(Dy₃-49) - [Dy₃(Hbovh)₃(μ₃-OH)₂(MeOH)₃Cl₃]Cl



A mixture of 370 mg *o*-vanillyl hydrazide (2 mmol) and 212 mg benzaldehyde (2 mmol) in 10 ml of MeOH and 10 ml of MeCN was refluxed for 1h resulting in a yellow solution. The solution was left to cool after adding 420 μl of Et₃N (3 mmol). Then 125 mg DyCl₃·6H₂O (0.33 mmol) were added to a glass vial and dissolved in 4 ml MeOH and 10 ml MeCN. Under stirring 2 ml of the before prepared ligand solution was added dropwise. The mixture was stirred for 20 min after which the solution was filtered and left undisturbed to allow for crystallisation of the product. After 3 days the product was isolated as colourless block shaped crystals in a yield of 27.6 % (30 mg).

Elemental analysis (calculated, C₄₅H₆₅N₆O₂₃Dy₃Cl₄) C: 32.03%, H: 3.88%, N: 4.98%; (found) C: 31.66%, H: 3.61%, N: 5.17%. **ATR-IR (4000-400 cm⁻¹):** 3221(s); 3071(s); 2953(m); 2846(m); 1616(s); 1594(s); 1552(s); 1493(w); 1477(w); 1448(m); 1436(s);

1365(m); 1312(s); 1233(s); 1212(s); 1098(m); 1065(m); 1042(m); 1023(w); 955(m); 853(m); 795(s); 732(m); 689(m); 665(w); 645(w); 611(w); 515(w); 464(m).

Crystal Data for $C_{50}H_{61}Cl_4Dy_3N_6O_{16}$ ($M = 1631.34$ g/mol): trigonal, space group $R\bar{3}$ (no. 148), $a = 20.8488(6)$ Å, $c = 24.1538(10)$ Å, $V = 9092.4(6)$ Å³, $Z = 6$, $T = 180$ K, $\mu(1.3401270, 1.34 \text{ K}\alpha) = 20.391 \text{ mm}^{-1}$, $D_{calc} = 1.788 \text{ g/cm}^3$, 40048 reflections measured ($7.378^\circ \leq 2\theta \leq 113.896^\circ$), 4120 unique ($R_{int} = 0.0999$, $R_{sigma} = 0.0461$) which were used in all calculations. The final R_1 was 0.0422 ($I > 2\sigma(I)$) and wR_2 was 0.1166 (all data).

(Y₃-50) - [Y₃(Hbovh)₃(μ_3 -OH)₂(MeOH/H₂O)₃Cl₃]Cl·XH₂O·XMeOH

(Y₃-50) was synthesised using the same procedure as for (Dy₃-49) with 100 mg YCl₃·6H₂O (0.33 mmol) instead of DyCl₃·6H₂O as the lanthanide salt. After 2 days the product was isolated as colourless block shaped crystals in a yield of 34.0 % (32 mg).

ATR-IR (4000-400 cm⁻¹): 3190(s); 3062(s); 2945(m); 2846(m); 1619(s); 1594(s); 1553(s); 1493(w); 1451(w); 1436(s); 1370(m); 1315(s); 1238(s); 1213(s); 1099(m); 1065(m); 1042(m); 952(m); 853(m); 792(s); 732(m); 689(m); 665(w); 645(w); 616(w); 513(w); 466(m).

(Sm₃-51) - [Sm₃(Hbovh)₃(μ_3 -OH)₂(MeOH)(H₂O)Cl₄]·4MeCN·2MeOH·4H₂O

(Sm₃-51) was synthesised using the same procedure as for (Dy₃-49) with 120 mg SmCl₃·6H₂O (0.33 mmol) instead of DyCl₃·6H₂O as the lanthanide salt. After 8 days the product was isolated as colourless block shaped crystals in a yield of 20.5 % (22 mg).

ATR-IR (4000-400 cm⁻¹): 3227(s); 3062(s); 2945(m); 2842(m); 1616(s); 1601(s); 1550(s); 1491(w); 1480(w); 1451(w); 1432(s); 1370(m); 1363(s); 1312(s); 1249(s); 1213(s); 1099(m); 1066(m); 1041(m); 951(m); 850(m); 792(s); 751(m); 729(m); 689(m); 665(w); 645(w); 601(w); 553(w); 513(w); 458(m).

(Eu₃-52) - [Eu₃(Hbovh)₃(μ_3 -OH)₂(MeOH)(H₂O)Cl₄]·4MeCN·2MeOH·4H₂O

(Eu₃-52) was synthesised using the same procedure as for (Dy₃-49) with 121 mg EuCl₃·6H₂O (0.33 mmol) instead of DyCl₃·6H₂O as the lanthanide salt. After 4 days the product was isolated as colourless block shaped crystals in a yield of 33.8 % (40 mg).

Elemental analysis (calculated, C₄₅H₅₉N₆O₂₀Eu₃Cl₄) C: 33.74%, H: 3.71%, N: 5.24%; (found) C: 33.47%, H: 3.40%, N: 5.56%. **ATR-IR (4000-400 cm⁻¹):** 3224(s); 3065(s); 2948(m); 2835(m); 1610(s); 1608(s); 1558(s); 1486(w); 1474(w); 1442(w); 1429(s); 1374(m); 1366(s); 1309(s); 1257(s); 1216(s); 1105(m); 1070(m); 1035(m); 954(m); 855(m); 786(s); 752(m); 735(m); 693(m); 671(w); 638(w); 593(w); 548(w); 508(w); 463(m).

Crystal Data for C_{56.5}H₇₆Cl₄Eu₃N₁₀O₁₈ (*M* = 1780.95 g/mol): triclinic, space group *P* $\bar{1}$ (no. 2), *a* = 14.9392(4) Å, *b* = 15.1394(4) Å, *c* = 16.2101(4) Å, α = 84.009(2)°, β = 84.376(2)°, γ = 87.911(2)°, *V* = 3627.40(16) Å³, *Z* = 2, *T* = 273.15 K, μ (MoK α) = 2.778 mm⁻¹, *D*_{calc} = 1.631 g/cm³, 46546 reflections measured (2.538° ≤ 2 θ ≤ 50.7°), 13042 unique (*R*_{int} = 0.0568, *R*_{sigma} = 0.0582) which were used in all calculations. The final *R*₁ was 0.0670 (*I* > 2 σ (*I*)) and *wR*₂ was 0.2083 (all data).

(Gd₃-53) - [Gd₃(Hbovh)₃(μ ₃-OH)₂(MeOH)(H₂O)Cl₄]·4MeCN·2MeOH·4H₂O

(Gd₃-53) was synthesised using the same procedure as for (Dy₃-49) with 123 mg GdCl₃·6H₂O (0.33 mmol) instead of DyCl₃·6H₂O as the lanthanide salt. After 7 days the product was isolated as colourless block shaped crystals in a yield of 21.5 % (23 mg).

Elemental analysis (calculated, C₄₅H₅₉N₆O₂₀Gd₃Cl₄) C: 33.41%, H: 3.68%, N: 5.20%; (found) C: 33.38%, H: 3.88%, N: 5.24%. **ATR-IR (4000-400 cm⁻¹):** 3231(s); 3055(s); 2950(m); 2839(m); 1620(s); 1603(s); 1547(s); 1488(w); 1477(w); 1445(w); 1428(s); 1372(m); 1356(s); 1306(s); 1244(s); 1217(s); 1101(m); 1061(m); 1046(m); 958(m); 852(m); 798(s); 755(m); 732(m); 694(m); 667(w); 639(w); 599(w); 558(w); 520(w); 452(m).

(Tb₃-54) - [Tb₃(Hbovh)₃(μ ₃-OH)₂(MeOH/H₂O)₃Cl₃]Cl·XH₂O·XMeOH

(Tb₃-54) was synthesised using the same procedure as for (Dy₃-49) with 123 mg TbCl₃·6H₂O (0.33 mmol) instead of DyCl₃·6H₂O as the lanthanide salt. After 3 days the product was isolated as colourless block shaped crystals in a yield of 28.7 % (31 mg).

ATR-IR (4000-400 cm⁻¹): 3213(s); 3067(s); 2961(m); 2842(m); 1609(s); 1600(s); 1558(s); 1484(w); 1480(w); 1444(m); 1428(s); 1373(m); 1305(s); 1242(s); 1218(s); 1094(m); 1062(m); 1048(m); 1032(w); 962(m); 847(m); 789(s); 735(m); 697(m); 667(w); 638(w); 610(w); 522(w); 462(m).

(Ho₃-55) - [Ho₃(Hbovh)₃(μ₃-OH)₂(MeOH/H₂O)₃Cl₃]Cl·XH₂O·XMeOH

(Ho₃-55) was synthesised using the same procedure as for (Dy₃-49) with 125 mg HoCl₃·6H₂O (0.33 mmol) instead of DyCl₃·6H₂O as the lanthanide salt. After 2 days the product was isolated as colourless block shaped crystals in a yield of 33.9 % (37 mg).

ATR-IR (4000-400 cm⁻¹): 3216(s); 3065(s); 2957(m); 2841(m); 1608(s); 1602(s); 1548(s); 1499(w); 1473(w); 1454(m); 1431(s); 1371(m); 1307(s); 1237(s); 1203(s); 1095(m); 1070(m); 1044(m); 1027(w); 952(m); 851(m); 792(s); 730(m); 692(m); 662(w); 649(w); 603(w); 518(w); 457(m).

(Er₃-56) - [Er₃(Hbovh)₃(μ₃-OH)₂(MeOH/H₂O)₃Cl₃]Cl·XH₂O·XMeOH

(Er₃-50) was synthesised using the same procedure as for (Dy₃-49) with 126 mg ErCl₃·6H₂O (0.33 mmol) instead of DyCl₃·6H₂O as the lanthanide salt. After 3 days the product was isolated as colourless block shaped crystals in a yield of 32.8 % (36 mg).

ATR-IR (4000-400 cm⁻¹): 3229(s); 3077(s); 2950(m); 2853(m); 1623(s); 1601(s); 1546(s); 1486(w); 1484(w); 1451(m); 1432(s); 1361(m); 1309(s); 1240(s); 1208(s); 1091(m); 1068(m); 1037(m); 1029(w); 953(m); 858(m); 800(s); 729(m); 683(m); 669(w); 640(w); 607(w); 516(w); 460(m).

(Tm₃-57) - [Tm₃(Hbovh)₃(μ₃-OH)₂(MeOH/H₂O)₃Cl₃]Cl·XH₂O·XMeOH

(Tm₃-57) was synthesised using the same procedure as for (Dy₃-49) with 126 mg TmCl₃·6H₂O (0.33 mmol) instead of DyCl₃·6H₂O as the lanthanide salt. After 2 days the product was isolated as colourless block shaped crystals in a yield of 26.4 % (29 mg).

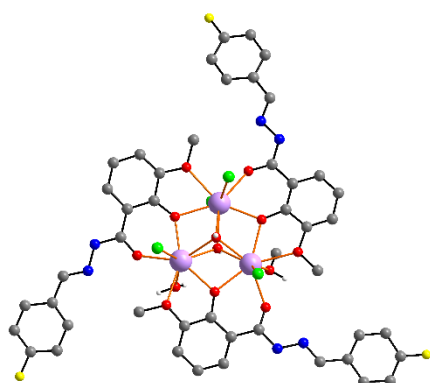
ATR-IR (4000-400 cm⁻¹): 3222(s); 3075(s); 2956(m); 2851(m); 1619(s); 1609(s); 1538(s); 1490(w); 1477(w); 1444(m); 1438(s); 1356(m); 1314(s); 1232(s); 1203(s); 1087(m); 1072(m); 1040(m); 1035(w); 960(m); 861(m); 794(s); 737(m); 688(m); 662(w); 648(w); 610(w); 518(w); 467(m).

(Yb₃-58) - [Yb₃(Hbovh)₃(μ₃-OH)₂(MeOH)₂(H₂O)Cl₃]Cl·H₂O·2MeOH

(Yb₃-58) was synthesised using the same procedure as for (Dy₃-49) with 126 mg YbCl₃·6H₂O (0.33 mmol) instead of DyCl₃·6H₂O as the lanthanide salt. After 3 days the product was isolated as colourless block shaped crystals in a very low yield.

Crystal Data for $C_{49}H_{61}Cl_4N_6O_{17}Yb_3$ ($M = 1666.95$ g/mol): trigonal, space group $R\bar{3}$ (no. 148), $a = 20.7055(19)$ Å, $c = 24.159(4)$ Å, $V = 8970(2)$ Å³, $Z = 6$, $T = 180$ K, $\mu(1.3401270, 1.34 \text{ K}\alpha) = 16.715 \text{ mm}^{-1}$, $D_{calc} = 1.852 \text{ g/cm}^3$, 16698 reflections measured ($9.154^\circ \leq 2\theta \leq 104.984^\circ$), 3439 unique ($R_{int} = 0.1566$, $R_{sigma} = 0.2069$) which were used in all calculations. The final R_1 was 0.0432 ($I > 2\sigma(I)$) and wR_2 was 0.0876 (all data).

(Dy₃-59) - [Dy₃(Hpfbovh)₃(μ_3 -OH)₂(MeOH)(H₂O)Cl₄]-4MeCN·4MeOH



(Dy₃-59) was synthesised using the same procedure as for (Dy₃-49) with 248 mg *p*-fluorobenzaldehyde (2 mmol) instead of benzaldehyde. After 4 days the product was isolated as colourless block shaped crystals in a yield of 24.9 % (31 mg). The product loses crystallinity fast upon exposure to water it the air.

Elemental analysis (calculated, $C_{46}H_{58}Cl_4Dy_3F_3N_6O_{20}$) C: 32.47%, H: 3.43%, N: 4.9%; (found) C: 32.24%, H: 3.19%, N: 5.09%. **ATR-IR (4000-400 cm⁻¹):** 3246(s); 3082(s); 2945(m); 2846(m); 2251(m); 1621(s); 1597(s); 1551(s); 1506(s); 1489(w); 1479(w); 1449(m); 1436(s); 1368(m); 1314(s); 1231(s); 1215(s); 1150(m); 1098(m); 1072(m); 1043(m); 1024(w); 959(m); 853(m); 838(m); 798(s); 739(m); 658(m); 628(w); 580(w); 558(w); 526(w); 454(m).

Crystal Data for $C_{58}H_{72}Cl_4Dy_3F_3N_{10}O_{17}$ ($M = 1867.55$ g/mol): triclinic, space group $P\bar{1}$ (no. 2), $a = 15.0717(5)$ Å, $b = 15.2548(5)$ Å, $c = 16.0103(5)$ Å, $\alpha = 83.666(2)^\circ$, $\beta = 83.403(3)^\circ$, $\gamma = 86.559(3)^\circ$, $V = 3630.1(2)$ Å³, $Z = 2$, $T = 180$ K, $\mu(\text{Ga-K}\alpha) = 17.137 \text{ mm}^{-1}$, $D_{calc} = 1.709 \text{ g/cm}^3$, 45949 reflections measured ($6.654^\circ \leq 2\theta \leq 114.988^\circ$), 14673 unique ($R_{int} = 0.0498$, $R_{sigma} = 0.0667$) which were used in all calculations. The final R_1 was 0.0379 ($I > 2\sigma(I)$) and wR_2 was 0.0899 (all data).

(Y₃-60) - [Y₃(Hpfbovh)₃(μ_3 -OH)₂(MeOH)(H₂O)Cl₄]-4MeCN·4MeOH

(Y₃-60) was synthesised using the same procedure as for (Dy₃-59) with 100 mg $YCl_3 \cdot 6H_2O$ (0.33 mmol) instead of $DyCl_3 \cdot 6H_2O$ as the lanthanide salt. After 3 days the product was isolated as colourless block shaped crystals in a yield of 35.8 % (39 mg).

ATR-IR (4000-400 cm⁻¹): 3661(m); 3193(m); 3075(s); 3043(m); 2951(m); 2847(m); 1624(s); 1597(s); 1559(s); 1510(s); 1490(w); 1456(m); 1417(s); 1370(m); 1351(w); 1316(s); 1297(s); 1257(w); 1240(s); 1211(s); 1154(m); 1096(m); 1074(m); 1048(m); 1014(w); 965(m); 939(m); 856(m); 835(m); 797(s); 731(m); 661(m); 634(w); 579(w); 560(w); 522(m); 457(m).

(Gd₃-61) - [Gd₃(Hpfbovh)₃(μ₃-OH)₂(MeOH)(H₂O)Cl₄]·4MeCN·4MeOH

(Gd₃-61) was synthesised using the same procedure as for (Dy₃-59) with 123 mg GdCl₃·6H₂O (0.33 mmol) instead of DyCl₃·6H₂O as the lanthanide salt. After 3 days the product was isolated as colourless block shaped crystals in a yield of 41.4 % (51 mg).

ATR-IR (4000-400 cm⁻¹): 3636(m); 3221(m); 3080(s); 3042(m); 2955(m); 2843(m); 1619(s); 1601(s); 1553(s); 1512(s); 1486(w); 1451(m); 1415(s); 1373(m); 1355(w); 1318(s); 1298(s); 1255(w); 1239(s); 1215(s); 1153(m); 1100(m); 1076(m); 1050(m); 1015(w); 961(m); 940(m); 855(m); 836(m); 801(s); 729(m); 658(m); 635(w); 578(w); 562(w); 525(m); 461(m).

(Tb₃-62) - [Tb₃(Hpfbovh)₃(μ₃-OH)₂(MeOH)(H₂O)Cl₄]·4MeCN·4MeOH

(Tb₃-62) was synthesised using the same procedure as for (Dy₃-59) with 123 mg TbCl₃·6H₂O (0.33 mmol) instead of DyCl₃·6H₂O as the lanthanide salt. After 2 days the product was isolated as colourless block shaped crystals in a yield of 33.9 % (42 mg).

ATR-IR (4000-400 cm⁻¹): 3659(m); 3196(m); 3077(s); 3045(m); 2949(m); 2842(m); 1621(s); 1595(s); 1558(s); 1506(s); 1491(w); 1455(m); 1418(s); 1374(m); 1354(w); 1319(s); 1296(s); 1252(w); 1235(s); 1216(s); 1151(m); 1101(m); 1075(m); 1051(m); 1016(w); 960(m); 942(m); 854(m); 832(m); 799(s); 733(m); 660(m); 631(w); 582(w); 561(w); 524(m); 456(m).

(Ho₃-63) - [Ho₃(Hpfbovh)₃(μ₃-OH)₂(MeOH)(H₂O)Cl₄]·4MeCN·4MeOH

(Ho₃-63) was synthesised using the same procedure as for (Dy₃-59) with 125 mg HoCl₃·6H₂O (0.33 mmol) instead of DyCl₃·6H₂O as the lanthanide salt. After 2 days the product was isolated as colourless block shaped crystals in a yield of 43.5 % (54 mg).

ATR-IR (4000-400 cm⁻¹): 3636(m); 3221(m); 3078(s); 3047(m); 2950(m); 2841(m); 1623(s); 1598(s); 1557(s); 1507(s); 1493(w); 1452(m); 1416(s); 1372(m); 1350(w); 1317(s); 1302(s); 1254(w); 1236(s); 1214(s); 1155(m); 1099(m); 1073(m); 1053(m); 1012(w); 963(m); 937(m); 857(m); 834(m); 796(s); 730(m); 663(m); 637(w); 583(w); 557(w); 521(m); 459(m).

(Er₃-64) - [Er₃(Hpfbovh)₃(μ₃-OH)₂(MeOH)(H₂O)Cl₄]·4MeCN·4MeOH

(Er₃-64) was synthesised using the same procedure as for (Dy₃-59) with 126 mg ErCl₃·6H₂O (0.33 mmol) instead of DyCl₃·6H₂O as the lanthanide salt. After 3 days the product was isolated as colourless block shaped crystals in a yield of 35.2 % (44 mg).

ATR-IR (4000-400 cm⁻¹): 3660(m); 3194(m); 3079(s); 3044(m); 2952(m); 2844(m); 1620(s); 1599(s); 1556(s); 1508(s); 1489(w); 1454(m); 1414(s); 1371(m); 1353(w); 1320(s); 1299(s); 1256(w); 1237(s); 1213(s); 1152(m); 1098(m); 1077(m); 1047(m); 1013(w); 962(m); 938(m); 853(m); 833(m); 798(s); 732(m); 659(m); 633(w); 580(w); 558(w); 523(m); 459(m).

(Tm₃-65) - [Tm₃(Hpfbovh)₃(μ₃-OH)₂(MeOH)(H₂O)Cl₄]·4MeCN·4MeOH

(Tm₃-65) was synthesised using the same procedure as for (Dy₃-59) with 126 mg TmCl₃·6H₂O (0.33 mmol) instead of DyCl₃·6H₂O as the lanthanide salt. After 4 days the product was isolated as colourless block shaped crystals in a yield of 46.8 % (59 mg).

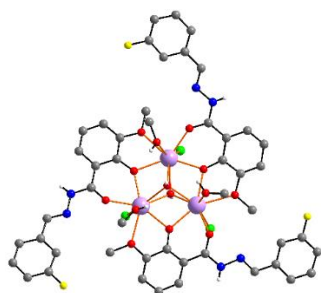
ATR-IR (4000-400 cm⁻¹): 3636(m); 3221(m); 3083(s); 3041(m); 2948(m); 2845(m); 1624(s); 1596(s); 1559(s); 1509(s); 1488(w); 1453(m); 1419(s); 1367(m); 1351(w); 1314(s); 1300(s); 1258(w); 1234(s); 1210(s); 1156(m); 1097(m); 1072(m); 1049(m); 1017(w); 964(m); 936(m); 851(m); 837(m); 800(s); 734(m); 657(m); 630(w); 579(w); 559(w); 526(m); 462(m).

(Yb₃-66) - [Yb₃(Hpfbovh)₃(μ₃-OH)₂(MeOH)(H₂O)Cl₄]·4MeCN·4MeOH

(Yb₃-66) was synthesised using the same procedure as for (Dy₃-59) with 126 mg YbCl₃·6H₂O (0.33 mmol) instead of DyCl₃·6H₂O as the lanthanide salt. After 4 days the product was isolated as colourless block shaped crystals in a yield of 41.7 % (53 mg).

ATR-IR (4000-400 cm⁻¹): 3665(m); 3190(m); 3082(s); 3046(m); 2953(m); 2843(m); 1618(s); 1595(s); 1553(s); 1513(s); 1492(w); 1450(m); 1413(s); 1375(m); 1354(w); 1321(s); 1295(s); 1253(w); 1238(s); 1215(s); 1154(m); 1095(m); 1071(m); 1046(m); 1011(w); 965(m); 941(m); 852(m); 836(m); 801(s); 729(m); 662(m); 635(w); 584(w); 556(w); 523(m); 458(m).

(Dy₃-67) - [Dy₃(Hmfbovh)₃(μ₃-OH)₂(MeOH)₃Cl₃]Cl·1.5MeCN·0.5MeOH

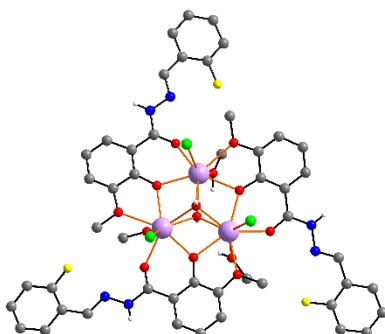


(Dy₃-67) was synthesised using the same procedure as for (Dy₃-49) with 248 mg *m*-fluorobenzaldehyde (2 mmol) instead of benzaldehyde. After 3 days the product was isolated as colourless block shaped crystals in a yield of 39.7 % (45 mg).

ATR-IR (4000-400 cm⁻¹): 3218(s); 3074(s); 2952(m); 2846(m); 1621(s); 1597(s); 1554(s); 1489(w); 1479(w); 1452(m); 1436(s); 1368(m); 1314(s); 1228(s); 1212(s); 1140(m); 1098(m); 1070(m); 1045(m); 1019(w); 975(m); 853(m); 795(s); 733(m); 682(m); 663(w); 642(w); 615(w); 556(w); 524(w); 464(m).

Crystal Data for C_{51.5}H_{56.5}Cl₄Dy₃F₃N_{7.5}O_{14.5} (*M* = 1698.84 g/mol): trigonal, space group R $\bar{3}$ (no. 148), *a* = 20.8912(7) Å, *c* = 23.7524(9) Å, *V* = 8977.7(7) Å³, *Z* = 6, *T* = 180 K, μ(1.3401270, 1.34 Kα) = 20.713 mm⁻¹, *D*_{calc} = 1.885 g/cm³, 45840 reflections measured (5.342° ≤ 2θ ≤ 118.538°), 4418 unique (*R*_{int} = 0.0765, *R*_{sigma} = 0.0373) which were used in all calculations. The final *R*₁ was 0.0328 (*I* > 2σ(*I*)) and *wR*₂ was 0.0810 (all data).

(Dy₃-68) - [Dy₃(Hofbovh)₃(μ₃-OH)₂(MeOH)₃Cl₃]Cl·2MeOH



(Dy₃-68) was synthesised using the same procedure as for (Dy₃-49) with 248 mg *o*-fluorobenzaldehyde (2 mmol) instead of benzaldehyde. After 7 days the product was isolated as colourless block shaped crystals in a very low yield.

Crystal Data for C₅₀H₅₈Cl₄Dy₃F₃N₆O₁₆ (*M* = 1685.32 g/mol): trigonal, space group R $\bar{3}$ (no. 148), *a* = 20.930(11) Å, *c* = 24.167(14) Å, *V* = 9168(11) Å³, *Z* = 6, *T* = 180 K, μ(1.3401270, 1.34 Kα) = 20.285 mm⁻¹, *D*_{calc} = 1.831 g/cm³, 48860 reflections measured (5.302° ≤ 2θ ≤ 113.93°), 4056 unique (*R*_{int} =

0.1102, $R_{\text{sigma}} = 0.0608$) which were used in all calculations. The final R_1 was 0.0367 ($I > 2\sigma(I)$) and wR_2 was 0.0913 (all data).

(Y₃-69) - [Y₃(Hmfbovh)₃(μ_3 -OH)₂(MeOH)₃Cl₃]Cl·1.5MeCN·0.5MeOH

(Y₃-69) was synthesised using the same procedure as for (Dy₃-67) with 100 mg YCl₃·6H₂O (0.33 mmol) instead of DyCl₃·6H₂O as the lanthanide salt. After 2 days the product was isolated as colourless block shaped crystals in a yield of 42.6 % (42 mg).

ATR-IR (4000-400 cm⁻¹): 3190(s); 3062(s); 2945(m); 2846(m); 1619(s); 1594(s); 1553(s); 1493(w); 1451(w); 1436(s); 1370(m); 1315(s); 1238(s); 1213(s); 1099(m); 1065(m); 1042(m); 952(m); 853(m); 792(s); 732(m); 689(m); 665(w); 645(w); 616(w); 513(w); 466(m).

(Sm₃-70) - [Sm₃(Hmfbovh)₃(μ_3 -OH)₂(MeOH)₃Cl₃]Cl·1.5MeCN·0.5MeOH

(Sm₃-70) was synthesised using the same procedure as for (Dy₃-67) with 120 mg SmCl₃·6H₂O (0.33 mmol) instead of DyCl₃·6H₂O as the lanthanide salt. After 7 days the product was isolated as colourless block shaped crystals in a yield of 29.7 % (33 mg).

ATR-IR (4000-400 cm⁻¹): 3207(s); 1615(s); 1594(s); 1545(s); 1479(w); 1449(w); 1434(s); 1360(m); 1308(s); 1253(s); 1219(s); 1134(m); 1097(m); 1064(m); 1038(m); 971(m); 849(m); 794(s); 732(m); 689(m); 660(w); 645(w); 601(w); 520(w); 453(s); 427(m).

Crystal Data for C₅₁H₆₂Cl₄F₃N₆O₁₇Sm₃ ($M = 1680.91$ g/mol): trigonal, space group R-3 (no. 148), $a = 21.0499(3)$ Å, $c = 23.7164(5)$ Å, $V = 9100.8(3)$ Å³, $Z = 6$, $T = 200$ K, $\mu(1.3401270, 1.34 \text{ K}\alpha) = 16.614 \text{ mm}^{-1}$, $D_{\text{calc}} = 1.840 \text{ g/cm}^3$, 52484 reflections measured ($7.308^\circ \leq 2\theta \leq 128.258^\circ$), 5091 unique ($R_{\text{int}} = 0.0854$, $R_{\text{sigma}} = 0.0291$) which were used in all calculations. The final R_1 was 0.0412 ($I > 2\sigma(I)$) and wR_2 was 0.1177 (all data).

(Eu₃-71) - [Eu₃(Hmfbovh)₃(μ_3 -OH)₂(MeOH)₃Cl₃]Cl·1.5MeCN·0.5MeOH

(Eu₃-71) was synthesised using the same procedure as for (Dy₃-67) with 121 mg EuCl₃·6H₂O (0.33 mmol) instead of DyCl₃·6H₂O as the lanthanide salt. After 7 days the product was isolated as colourless block shaped crystals in a yield of 40.5 % (45 mg).

ATR-IR (4000-400 cm⁻¹): 3202(s); 1619(s); 1594(s); 1549(s); 1478(w); 1451(w); 1433(s); 1362(m); 1310(s); 1228(s); 1139(w); 1094(m); 1065(m); 1042(m); 971(m); 853(m); 792(s); 737(m); 677(m); 665(w); 645(w); 603(w); 524(w); 454(s); 431(m).

Crystal Data for C₅₁H₆₂Cl₄Eu₃F₃N₆O₁₇ (*M* = 1685.74 g/mol): trigonal, space group R-3 (no. 148), *a* = 21.0354(4) Å, *c* = 23.7613(5) Å, *V* = 9105.5(4) Å³, *Z* = 6, *T* = 200 K, $\mu(1.3401270, 1.34 \text{ K}\alpha) = 17.504 \text{ mm}^{-1}$, *D*_{calc} = 1.845 g/cm³, 40376 reflections measured (5.318° ≤ 2θ ≤ 124.996°), 4904 unique (*R*_{int} = 0.0571, *R*_{sigma} = 0.0259) which were used in all calculations. The final *R*₁ was 0.0425 (*I* > 2σ(*I*)) and *wR*₂ was 0.1182 (all data).

(Tb₃-72) - [Tb₃(Hmfbovh)₃(μ₃-OH)₂(MeOH)₃Cl₃]Cl·1.5MeCN·0.5MeOH

(Tb₃-72) was synthesised using the same procedure as for (Dy₃-67) with 123 mg TbCl₃·6H₂O (0.33 mmol) instead of DyCl₃·6H₂O as the lanthanide salt. After 2 days the product was isolated as colourless block shaped crystals in a yield of 32.9 % (37 mg).

ATR-IR (4000-400 cm⁻¹): 3218(s); 3074(s); 2956(w); 2846(m); 1619(s); 1594(s); 1550(s); 1487(w); 1452(m); 1436(s); 1363(m); 1312(s); 1253(m); 1231(s); 1212(s); 1140(m); 1098(m); 1070(m); 1045(m); 1019(w); 975(m); 853(m); 795(s); 733(m); 682(m); 663(w); 642(w); 615(w); 556(w); 524(w); 464(m).

(Ho₃-73) - [Ho₃(Hmfbovh)₃(μ₃-OH)₂(MeOH)₃Cl₃]Cl·1.5MeCN·0.5MeOH

(Ho₃-73) was synthesised using the same procedure as for (Dy₃-67) with 125 mg HoCl₃·6H₂O (0.33 mmol) instead of DyCl₃·6H₂O as the lanthanide salt. After 1 day the product was isolated as colourless block shaped crystals in a yield of 36.6 % (41 mg).

ATR-IR (4000-400 cm⁻¹): 3221(s); 3071(s); 2955(w); 2848(m); 1623(s); 1592(s); 1554(s); 1488(w); 1451(m); 1432(s); 1366(m); 1314(s); 1255(m); 1233(s); 1214(s); 1144(m); 1100(m); 1071(m); 1047(m); 1023(w); 973(m); 851(m); 797(s); 735(m); 681(m); 665(w); 643(w); 617(w); 558(w); 526(w); 462(m).

(Er₃-74) - [Er₃(Hmfbovh)₃(μ₃-OH)₂(MeOH)₃Cl₃]Cl·1.5MeCN·0.5MeOH

(Er₃-74) was synthesised using the same procedure as for (Dy₃-67) with 126 mg ErCl₃·6H₂O (0.33 mmol) instead of DyCl₃·6H₂O as the lanthanide salt. After 2 days the product was isolated as colourless block shaped crystals in a yield of 38.9 % (44 mg).

ATR-IR (4000-400 cm^{-1}): 3215(s); 3078(s); 2958(w); 2844(m); 1617(s); 1593(s); 1547(s); 1485(w); 1450(m); 1434(s); 1361(m); 1315(s); 1252(m); 1234(s); 1211(s); 1143(m); 1101(m); 1072(m); 1048(m); 1021(w); 976(m); 854(m); 793(s); 731(m); 683(m); 666(w); 641(w); 616(w); 555(w); 521(w); 466(m).

(Tm₃-75) - [Tm₃(Hmfbovh)₃(μ_3 -OH)₂(MeOH)₃Cl₃]Cl·1.5MeCN·0.5MeOH

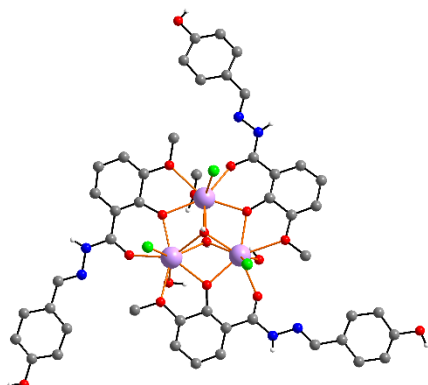
(Tm₃-75) was synthesised using the same procedure as for (Dy₃-67) with 126 mg TmCl₃·6H₂O (0.33 mmol) instead of DyCl₃·6H₂O as the lanthanide salt. After 3 days the product was isolated as colourless block shaped crystals in a yield of 28.9 % (33 mg).

ATR-IR (4000-400 cm^{-1}): 3220(s); 3072(s); 2959(w); 2850(m); 1615(s); 1597(s); 1549(s); 1483(w); 1453(m); 1433(s); 1367(m); 1310(s); 1251(m); 1232(s); 1215(s); 1142(m); 1096(m); 1074(m); 1049(m); 1020(w); 973(m); 855(m); 794(s); 730(m); 684(m); 664(w); 640(w); 614(w); 554(w); 522(w); 467(m).

(Yb₃-76) - [Yb₃(Hmfbovh)₃(μ_3 -OH)₂(MeOH)₃Cl₃]Cl·1.5MeCN·0.5MeOH

(Yb₃-76) was synthesised using the same procedure as for (Dy₃-67) with 126 mg YbCl₃·6H₂O (0.33 mmol) instead of DyCl₃·6H₂O as the lanthanide salt. After 6 days the product was isolated as colourless block shaped crystals in a very low yield. Single crystal XRD measurements were performed to obtain the unit cell which matches the cell of the Dy analogue making the two compounds isostructural.

(Dy₃-77) - [Dy₃(Hphbovh)₃(μ_3 -OH)₂(MeOH)(H₂O)₂Cl₃]Cl·4MeOH·6H₂O



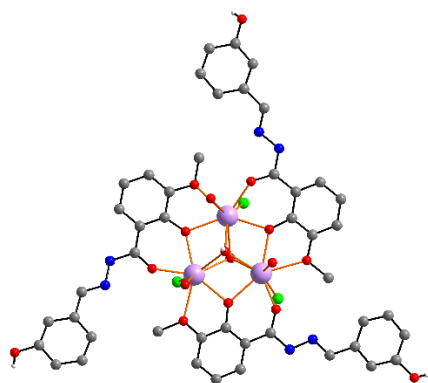
(Dy₃-77) was synthesised using the same procedure as for (Dy₃-49) with 244 mg *p*-hydroxybenzaldehyde (2 mmol) instead of benzaldehyde. After 1 day the product was isolated as colourless block shaped crystals in a yield of 37.2 % (45 mg). The product loses crystallinity fast upon exposure to water in the air.

Elemental analysis (calculated, C₄₅H₇₃N₆O₃₀Dy₃Cl₄) C: 29.90%, H: 4.07%, N: 4.65%; (found) C: 29.66%, H: 3.57%, N: 4.50%. **ATR-IR (4000-400 cm^{-1}):** 3198(s); 2850(m); 2689(m); 1590(s); 1553(s); 1531(s); 1452(m); 1436(s); 1367(m); 1315(s); 1231(s);

1165(m); 1099(m); 1077(m); 1045(m); 956(m); 854(w), 835(m); 795(s); 733(m); 660(w); 630(w); 528(w); 455(m).

Crystal Data for $C_{50}H_{77}Cl_4Dy_3N_6O_{27}$ ($M = 1823.47$ g/mol): trigonal, space group $P\bar{3}c1$ (no. 165), $a = 20.8020(4)$ Å, $c = 21.1059(7)$ Å, $V = 7909.4(4)$ Å³, $Z = 4$, $T = 180.15$ K, $\mu(\text{GaK}\alpha) = 15.735$ mm⁻¹, $D_{\text{calc}} = 1.531$ g/cm³, 112502 reflections measured ($4.268^\circ \leq 2\theta \leq 119.986^\circ$), 5944 unique ($R_{\text{int}} = 0.0941$, $R_{\text{sigma}} = 0.0372$) which were used in all calculations. The final R_1 was 0.0707 ($I > 2\sigma(I)$) and wR_2 was 0.2100 (all data).

(Dy₃-78) - [Dy₃(Hmhbovh)₃(μ_3 -OH)₂(MeOH)₃Cl₃]Cl·2MeOH



(Dy₃-78) was synthesised using the same procedure as for **(Dy₃-49)** with 244 mg *m*-hydroxybenzaldehyde (2 mmol) instead of benzaldehyde. After 5 days the product was isolated as colourless block shaped crystals in a yield of 30.2 % (33 mg). The product loses crystallinity fast upon exposure to water it the air.

Elemental analysis (calculated, $C_{45}H_{65}N_6O_{26}Cl_4Dy_3$) C: 31.14%, H: 3.77%, N: 4.84%; (found) C: 31.27% H: 3.393% N: 4.28%. **ATR-IR (4000-400 cm⁻¹):** 3642(w); 3196(s); 3074(s); 2952(m); 2846(m); 1621(s); 1597(s); 1554(s); 1495(w); 1452(m); 1436(s); 1377(w); 1355(w); 1314(s); 1228(s); 1212(s); 1098(m); 1070(m); 1045(m); 1019(w); 975(m); 898(m); 853(m); 795(s); 733(m); 682(m); 663(w); 642(w); 615(w); 556(w); 524(w); 464(m).

Crystal Data for $C_{47}H_{55}Cl_4Dy_3N_6O_{19}$ ($M = 1637.27$ g/mol): trigonal, space group $R\bar{3}$ (no. 148), $a = 21.024(3)$ Å, $c = 24.342(4)$ Å, $V = 9318(3)$ Å³, $Z = 6$, $T = 180$ K, $\mu(\text{GaK}\alpha) = 20.194$ mm⁻¹, $D_{\text{calc}} = 1.751$ g/cm³, 16449 reflections measured ($7.316^\circ \leq 2\theta \leq 79.894^\circ$), 1904 unique ($R_{\text{int}} = 0.1020$, $R_{\text{sigma}} = 0.0631$) which were used in all calculations. The final R_1 was 0.0620 ($I > 2\sigma(I)$) and wR_2 was 0.1702 (all data).

(Gd₃-79) - [Gd₃(Hphbovh)₃(μ_3 -OH)₂(MeOH)(H₂O)₂Cl₃]Cl·4MeOH·6H₂O

(Gd₃-79) was synthesised using the same procedure as for **(Dy₃-77)** with 123 mg GdCl₃·6H₂O (0.33 mmol) instead of DyCl₃·6H₂O as the lanthanide salt. After 8 days the product was isolated as colourless block shaped crystals in a yield of 27.2 % (33 mg).

ATR-IR (4000-400 cm⁻¹): 3198(s); 1612(m); 1590(s); 1553(s); 1513(s); 1480(w); 1440(s); 1370(m); 1312(s); 1275(w); 1231(s); 1187(w); 1161(m); 1099(m); 1070(m); 1041(m); 956(m); 854(w), 832(m); 792(s); 729(m); 660(w); 630(w); 528(w); 455(m).

(Tb₃-80) - [Tb₃(Hphbovh)₃(μ₃-OH)₂(MeOH)(H₂O)₂Cl₃]Cl·4MeOH·6H₂O

(Tb₃-80) was synthesised using the same procedure as for (Dy₃-77) with 123 mg TbCl₃·6H₂O (0.33 mmol) instead of DyCl₃·6H₂O as the lanthanide salt. After 6 days the product was isolated as colourless block shaped crystals in a yield of 33.9 % (41 mg).

ATR-IR (4000-400 cm⁻¹): 3195(s); 1613(m); 1592(s); 1551(s); 1510(s); 1482(w); 1438(s); 1371(m); 1310(s); 1277(w); 1229(s); 1185(w); 1159(m); 1101(m); 1068(m); 1043(m); 958(m); 852(w); 834(m); 794(s); 726(m); 662(w); 629(w); 526(w); 457(m).

(Tb₃-81) - [Tb₃(Hmhbovh)₃(μ₃-OH)₂(MeOH)₃Cl₃]Cl·2MeOH

(Tb₃-81) was synthesised using the same procedure as for (Dy₃-78) with 123 mg TbCl₃·6H₂O (0.33 mmol) instead of DyCl₃·6H₂O as the lanthanide salt. After 4 days the product was isolated as colourless block shaped crystals in a yield of 15.7 % (19 mg).

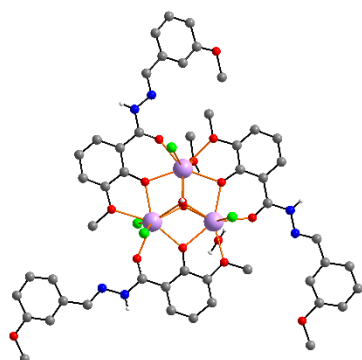
ATR-IR (4000-400 cm⁻¹): 3203(s); 1613(s); 1597(s); 1551(s); 1495(w); 1452(m); 1436(s); 1362(m); 1355(w); 1314(s); 1233(s); 1207(s); 1101(m); 1075(m); 1042(m); 953(m); 853(m); 795(s); 733(m); 654(w); 615(w); 459(m).

(Ho₃-82) - [Ho₃(Hmhbovh)₃(μ₃-OH)₂(MeOH)₃Cl₃]Cl·2MeOH

(Ho₃-82) was synthesised using the same procedure as for (Dy₃-78) with 125 mg HoCl₃·6H₂O (0.33 mmol) instead of DyCl₃·6H₂O as the lanthanide salt. After 4 days the product was isolated as colourless block shaped crystals in a yield of 20.1 % (22 mg).

ATR-IR (4000-400 cm⁻¹): 3203(s); 1617(s); 1597(s); 1551(s); 1495(w); 1452(m); 1436(s); 1362(w); 1355(w); 1314(s); 1233(s); 1207(s); 1101(m); 1075(m); 1042(m); 968(m); 853(m); 795(s); 733(m); 687(w); 459(m).

(Dy₃-83) - [Dy₃(Hmnoxbovh)₃(μ₃-OH)₂(MeOH)(H₂O)Cl₄]Cl·4MeOH·4MeCN

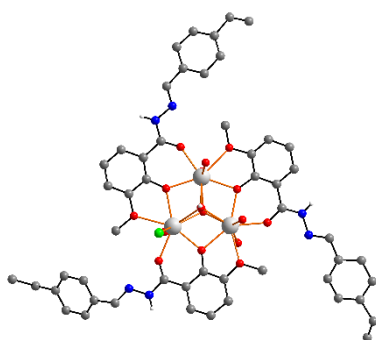


(Dy₃-83) was synthesised using the same procedure as for (Dy₃-49) with 272 mg *m*-anisaldehyde (2 mmol) instead of benzaldehyde. After 7 days the product was isolated as colourless block shaped crystals in a yield of 30.4 % (38 mg).

ATR-IR (4000-400 cm⁻¹): 3648(m); 3207(s); 1619(s); 1597(s); 1553(s); 1493(w); 1479(w); 1449(m); 1436(s); 1360(m); 1314(s); 1260(s); 1231(s); 1208(s); 1153(m); 1098(m); 1070(m); 1034(s); 968(w); 953(m); 853(m); 795(s); 731(m); 686(m); 663(w); 649(w); 612(w); 553(w); 464(m).

Crystal Data for C₆₁H₈₁Cl₄Dy₃N₁₀O₂₀ (*M* = 1903.65 g/mol): triclinic, space group *P* $\bar{1}$ (no. 2), *a* = 15.0259(6) Å, *b* = 15.3737(7) Å, *c* = 16.2504(8) Å, α = 82.703(4)°, β = 82.217(3)°, γ = 86.929(3)°, *V* = 3686.7(3) Å³, *Z* = 2, *T* = 200 K, μ (1.3401270, 1.34 K α) = 16.864 mm⁻¹, *D*_{calc} = 1.715 g/cm³, 66423 reflections measured (6.588° ≤ 2 θ ≤ 119.994°), 16331 unique (*R*_{int} = 0.0801, *R*_{sigma} = 0.0917) which were used in all calculations. The final *R*₁ was 0.0502 (*I* > 2 σ (*I*)) and *wR*₂ was 0.1336 (all data).

(Y₃-84) - [Y₃(Hpetbovh)₃(μ₃-OH)₂(H₂O)₅Cl]Cl₃·5MeCN·5MeOH·3H₂O



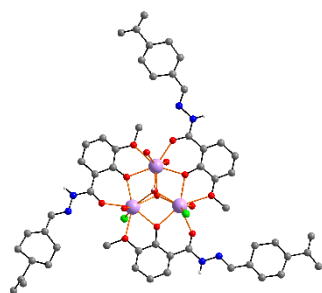
(Y₃-84) was synthesised using the same procedure as for (Dy₃-49) with 270 mg *p*-ethylbenzaldehyde (2 mmol) instead of benzaldehyde and YCl₃ instead of DyCl₃. After 5 days the product was isolated as colourless plate shaped crystals in a yield of 33% (36.5 mg).

Crystal Data for C₆₆H₁₀₄Cl₄N₁₁O₂₄Y₃ (*M* = 1844.13 g/mol): orthorhombic, space group *Pbca* (no. 61), *a* = 18.3608(7) Å, *b* = 29.355(2) Å, *c* = 31.9200(12) Å, *V* = 17204.4(16) Å³, *Z* = 8, *T* = 293(2) K, μ (GaK α) = 2.934 mm⁻¹, *D*_{calc} = 1.424 g/cm³, 62512 reflections measured (5.238° ≤ 2 θ ≤ 89.816°), 10360 unique (*R*_{int} = 0.1867, *R*_{sigma} = 0.1262) which were used in all calculations. The final *R*₁ was 0.1076 (*I* > 2 σ (*I*)) and *wR*₂ was 0.3217 (all data).

(Dy₃-85) - [Dy₃(Hpetbovh)₃(μ₃-OH)₂(H₂O)₅Cl]₃·5MeCN·5MeOH·3H₂O

(Dy₃-85) was synthesised using the same procedure as for (Y₃-86) DyCl₃ instead of YCl₃. The product was isolated as plate shaped crystals in a yield of 22.0% (26 mg). Due to bad crystal quality only the cell which matches the cell of (Y₃-86) was determined.

(Dy₃-86) - [Dy₃(S-Hperilovh)₃(μ₃-OH)₂(H₂O)₄Cl₂]₃·4MeOH·3H₂O



A mixture of 185 mg *o*-vanillyl hydrazide (1 mmol) and 150 mg (S)-(-)-Perillaldehyde (1 mmol) in 5 ml of MeOH and 5 ml of MeCN was refluxed for 1h resulting in a yellow solution. The solution was left to cool after adding 210 μl of Et₃N (1.5 mmol). Then 125 mg DyCl₃·6H₂O (0.33 mmol) was added to a glass vial and dissolved in 4 ml MeOH and 10 ml

MeCN. Under stirring 2 ml of the before prepared ligand solution was added dropwise. The mixture was stirred for 20 min after which the solution was filtered and left undisturbed to allow for crystallisation of the product. After 3 weeks the product was isolated as colourless block shaped crystals in a yield of 22.6 % (24.6 mg).

Crystal Data for C₅₈H₉₅Cl₄Dy₃N₆O₂₂ (*M* = 1857.69 g/mol): triclinic, space group *P* $\bar{1}$ (no. 2), *a* = 8.7462(6) Å, *b* = 21.4411(12) Å, *c* = 22.5342(14) Å, *α* = 115.254(4)°, *β* = 99.903(5)°, *γ* = 91.707(5)°, *V* = 3739.6(4) Å³, *Z* = 2, *T* = 293(2) K, *μ*(GaKα) = 16.614 mm⁻¹, *D*_{calc} = 1.650 g/cm³, 23157 reflections measured (7.71° ≤ 2*θ* ≤ 89.996°), 8978 unique (*R*_{int} = 0.1170, *R*_{sigma} = 0.2097) which were used in all calculations. The final *R*₁ was 0.0695 (*I* > 2σ(*I*)) and *wR*₂ was 0.1790 (all data).

(Dy₃-87) - [Dy₃(R-Hmyrovh)₃(μ₃-OH)₂(H₂O)₄Cl₂]₃·4MeOH·3H₂O

A mixture of 185 mg *o*-vanillyl hydrazide (1 mmol) and 150 mg (1*R*)-(-)-Myrtenal (1 mmol) in 5 ml of MeOH and 5 ml of MeCN was refluxed for 1h resulting in a yellow solution. The solution was left to cool after adding 210 μl of Et₃N (1.5 mmol). Then 125 mg DyCl₃·6H₂O (0.33 mmol) was added to a glass vial and dissolved in 4 ml MeOH and 10 ml MeCN. Under stirring 2 ml of the before prepared ligand solution was added dropwise. The mixture was stirred for 20 min after which the solution was filtered and left undisturbed to allow for crystallisation of the product. After 2 weeks the product was isolated as colourless block shaped crystals in a yield of 30.5 % (33 mg).

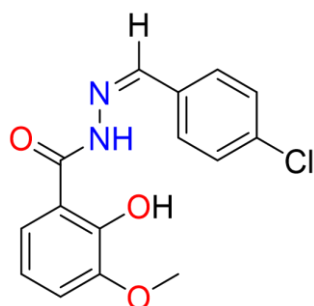
Crystal Data for $C_{49.75}H_{26}Cl_4Dy_3N_6O_{19.5}$ ($M = 1649.06$ g/mol): triclinic, space group $P\bar{1}$ (no. 2), $a = 20.3879(3)$ Å, $b = 20.4390(3)$ Å, $c = 22.3082(4)$ Å, $\alpha = 104.7710(10)^\circ$, $\beta = 99.3750(10)^\circ$, $\gamma = 119.9030(10)^\circ$, $V = 7310.9(2)$ Å³, $Z = 4$, $T = 293(2)$ K, $\mu(\text{MoK}\alpha) = 3.242$ mm⁻¹, $D_{\text{calc}} = 1.498$ g/cm³, 208914 reflections measured ($2.308^\circ \leq 2\theta \leq 52.046^\circ$), 28676 unique ($R_{\text{int}} = 0.1049$, $R_{\text{sigma}} = 0.0708$) which were used in all calculations. The final R_1 was 0.0767 ($I > 2\sigma(I)$) and wR_2 was 0.2512 (all data).

Dy₃-Hpmbovh

Dy₃-Hpmbovh was synthesised using the same procedure as for (**Dy₃-49**) with 240 mg *p*-methylbenzaldehyde (2 mmol) instead of benzaldehyde. After 2 days the product was isolated as colourless block shaped crystals not suitable for single crystal XRD thus no exact molecular formula could be determined. PXRD analysis suggests the compound to be isotypic to the other triangles crystallising in $P\bar{1}$.

Elemental analysis (calculated, $C_{48}H_{65}N_6O_{20}Dy_3Cl_4$) C: 34.41%, H: 3.91%, N: 5.01%; (found) C: 34.11%, H: 3.50%, N: 5.22%. **ATR-IR (4000-400 cm⁻¹)**: 3218(s); 3074(s); 2952(m); 2849(m); 1617(s); 1595(s); 1551(s); 1514(m); 1479(w); 1452(m); 1436(s); 1370(m); 1318(s); 1222(s); 1211(s); 1182(m); 1098(m); 1078(m); 1045(m); 1019(w); 960(m); 853(m); 794(s); 732(m); 658(w); 628(w); 556(w); 520(w); 455(m).

Para-Chlor-benzaldehyde-ortho-vanillyl hydrazine – H₂pcbovh



A mixture of 370 mg *o*-vanillyl hydrazine (2 mmol) and 280 mg *p*-Cl-benzaldehyde (2 mmol) in 10 ml of MeOH was refluxed for 1h resulting in a yellow solution. The solution was left to cool to allow the product to precipitate. The solid was filtered and dried yielding 300 mg (49%) of Hpcbovh in the form of a yellow powder.

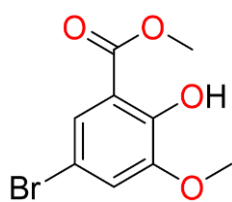
¹H-NMR (500 MHz, DMSO-*d*₆): δ /ppm = 8.72 (s, 1H, OH), 7.89 (m, 1H, CH_{Ar}), 7.66 (s, 1H, NH), 7.58 (m, 1H, CH_{Ar}), 7.47 (m, 1H, CH_{Ar}), 7.35 (m, 2H, CH_{Ar}), 7.06 (m, 1H, CH_{Ar}), 6.89 (m, 1H, CH), 6.77 (m, 1H, CH_{Ar}), 3.74 (s, 3H, CH₃). **ATR-IR (4000-400 cm⁻¹)**: 3308(s); 3179(s); 3047(m); 2945(m); 1638(s); 1627(s); 1601(s); 1586(s); 1531(s); 1480(s); 1454(s); 1403(m); 1370(m); 1348(m); 1312(s); 1246(s); 1172(s); 1150(m); 1088(s); 1055(s); 1011(m); 982(m); 956(m); 933(m); 861(s); 827(m); 792(m); 755(w); 718(m); 630(m); 601(m); 556(w); 499(s); 436(w).

Dy₃-Hpcbovh

To a solution of 125 mg DyCl₃·6H₂O (0.33 mmol) in 5 ml MeOH and 10 ml MeCN 60 mg Hpcbovh (0.2 mmol) were added. Under stirring 42 µl Et₃N were added dropwise resulting in a light-yellow solution. The mixture was stirred for 20 min after which the solution is filtered and left undisturbed to allow for crystallisation of the product. After 4 days the product was isolated as colourless block shaped crystals not suitable for single crystal XRD thus no exact molecular formula could be determined. PXRD analysis suggests the compound to be isotypic to the other triangles crystallising in P $\bar{1}$.

ATR-IR (4000-400 cm⁻¹): 3218(s); 3074(s); 2952(m); 2849(m); 1617(s); 1595(s); 1551(s); 1488(m); 1479(w); 1452(m); 1436(s); 1403(m); 1370(m); 1318(s); 1222(s); 1211(s); 1098(m); 1045(m); 1012(m); 960(m); 853(m); 794(s); 732(m); 658(w); 628(w); 556(w); 520(w); 429(m).

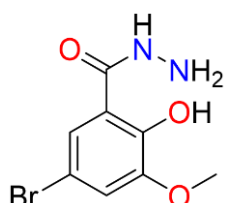
5-Br-Methyl-3-methoxysalicylate



In a glass flask 1 g 5-Br-2-hydroxy-3-methoxy benzoic acid (4 mmol) and 0.54 ml concentrated H₂SO₄ (10.6 mmol) were dissolved in 50 ml MeOH and refluxed for 24h. The brown precipitate was filtered, washed with water and dried resulting in a yield of 82% (0.86 g).

¹H-NMR (400 MHz, DMSO-d₆): δ/ppm = 7.47 (m, 1H, CH_{Ar}), 6.92 (m, 1H, CH_{Ar}), 3.73 (s, 3H, CH). **ATR-IR (4000-400 cm⁻¹):** 3091(m); 2993(m); 2945(m); 2842(m); 1674(s); 1612(m); 1575(s); 1476(m); 1465(s); 1436(s); 1392(w); 1348(s); 1286(m); 1253(s); 1224(m); 1198(w); 1164(m); 1055(s); 876(m); 861(s); 784(s); 726(m); 693(s); 634(m); 576(w); 499(m); 447(m).

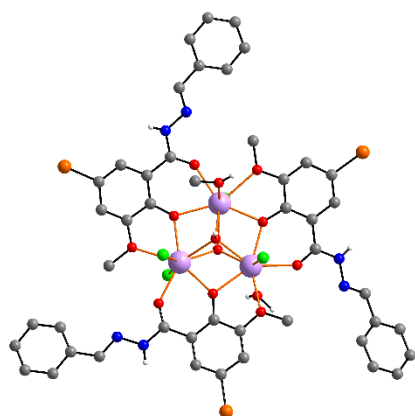
5-Br-o-vanillyl hydrazide



500 mg 5-Br-methyl-3-methoxy-salicylat (1.9 mmol) were added to a glass flask with 25 ml of absolute EtOH. Under stirring 3.9 ml hydrazine hydrate were added slowly. The solution was refluxed for 5h after which the flask was left to cool in the fridge overnight. The next day the crystalline precipitate was filtered and washed with Et₂O. The product was isolated in a yield of 53% (265 mg) and was stored under nitrogen atmosphere.

$^1\text{H-NMR}$ (400 MHz, DMSO-d_6): δ/ppm = 10.42 (s, 1H, OH), 7.42 (m, 1H, CH_{Ar}), 7.35 (m, 1H, CH_{Ar}), 3.88 (s, 3H, CH), 3.84 (s, 3H, CH). **ATR-IR (4000-400 cm^{-1}):** 3322(s); 3267(m); 3187(w); 3080(m); 3015(w); 2934(w); 2846(m); 1663(s); 1623(s); 1594(w); 1579(s); 1535(s); 1476(s); 1440(m); 1414(m); 1319(w); 1275(w); 1249(w); 1220(m); 1143(m); 1103(m); 1077(m); 993(s); 953(w); 923(m); 865(m); 839(s); 773(m); 693(m); 649(w); 594(w); 568(w); 528(w); 499(w); 445(m); 414(m).

(Dy₃-88) - [Dy₃(HbBrovh)₃(μ_3 -OH)₂(MeOH)(H₂O)_{1.5}Cl_{3.5}]Cl_{0.5}·1.5H₂O·2MeOH·MeCN



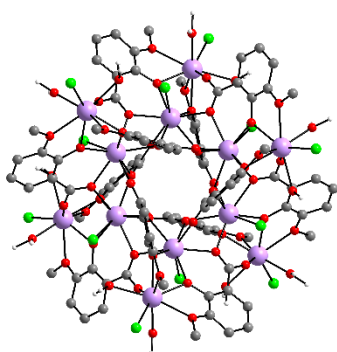
A mixture of 105 mg 5-Br-o-vanillyl hydrazine (0.4 mmol) and 42 mg benzaldehyde (0.4 mmol) in 2 ml of MeOH and 2 ml of MeCN was refluxed for 1h resulting in a grey solution. The solution was left to cool after adding 84 μl of Et_3N (0.6 mmol). Then 125 mg $\text{DyCl}_3 \cdot 6\text{H}_2\text{O}$ (0.33 mmol) were added to a glass vial and dissolved in 4 ml MeOH and 10 ml MeCN. Under stirring 2 ml of the before prepared

ligand solution was added dropwise. The mixture was stirred for 20 min after which the solution was filtered and left undisturbed to allow for crystallisation of the product. After 6 weeks the product was isolated as colourless needles in a yield of 32.0 % (39 mg).

Elemental analysis (calculated, $\text{Dy}_3\text{O}_{28}\text{H}_{78}\text{C}_{49}\text{N}_8\text{Br}_3\text{Cl}_4$) C: 28.08%, H: 3.75%, N: 5.34%; (found) C: 27.88%, H: 3.32%, N: 5.45%. **ATR-IR (4000-400 cm^{-1}):** 3196(s); 3059(s); 2951(m); 2857(m); 1616(s); 1591(s); 1548(s); 1490(w); 1447(s); 1418(s); 1367(m); 1346(w); 1310(s); 1248(s); 1223(s); 1086(m); 1068(m); 1046(m); 1025(m); 960(m); 869(m); 848(m); 815(m); 776(s); 758(m); 624(w); 559(w); 516(w); 462(m); 436(m).

Crystal Data for $\text{C}_{50}\text{H}_{48}\text{Br}_3\text{Cl}_4\text{Dy}_3\text{N}_6\text{O}_{16}$ ($M = 1857.97$ g/mol): triclinic, space group $P\bar{1}$ (no. 2), $a = 7.2837(2)$ Å, $b = 17.4822(5)$ Å, $c = 25.7173(7)$ Å, $\alpha = 77.244(2)^\circ$, $\beta = 88.116(2)^\circ$, $\gamma = 86.095(2)^\circ$, $V = 3185.94(16)$ Å³, $Z = 2$, $T = 180$ K, $\mu(1.3401270, 1.34 \text{ K}\alpha) = 20.874 \text{ mm}^{-1}$, $D_{\text{calc}} = 1.937 \text{ g/cm}^3$, 52277 reflections measured ($6.774^\circ \leq 2\theta \leq 116.206^\circ$), 13373 unique ($R_{\text{int}} = 0.0632$, $R_{\text{sigma}} = 0.0807$) which were used in all calculations. The final R_1 was 0.0373 ($I > 2\sigma(I)$) and wR_2 was 0.0801 (all data).

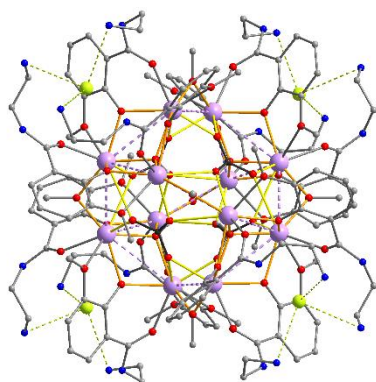
(Dy₁₂-89) - (Et₃NH)₂[Dy₁₂(van-CO₂)₁₂(Cl)₁₂(OH₂)₁₂]Cl₂·6H₂O·14MeCN



In a glass vial 108.4 mg of 2-hydroxy-3-methoxy-benzoic acid (0.6 mmol) and 169.6 mg DyCl₃·6H₂O (0.44 mmol) were dissolved in a mixture of 3 ml MeOH and 8 ml MeCN. After 5 minutes of stirring 63 μl of Et₃N (0.4 mmol) were added. After 6 hours of stirring at room temperature the mixture was filtered and left undisturbed to allow for crystallisation. The product was obtained after 2 weeks in a crystalline form suitable for single crystal measurements.

Crystal Data for C₁₃₆H₁₈₂Cl₁₄Dy₁₂O₆₆N₁₆ (*M* = 5543.27 g/mol): trigonal, space group R $\bar{3}$ (no. 148), *a* = 19.1830(2) Å, *c* = 84.7787(11) Å, *V* = 27017.8(7) Å³, *Z* = 6, *T* = 180.00 K, μ (GaK α) = 27.172 mm⁻¹, *D*_{calc} = 2.044 g/cm³, 46369 reflections measured (4.716° ≤ 2 θ ≤ 128.162°), 14020 unique (*R*_{int} = 0.0626, *R*_{sigma} = 0.0597) which were used in all calculations. The final *R*₁ was 0.1099 (*I* > 2 σ (*I*)) and *wR*₂ was 0.3352 (all data).

(Dy₁₂-90) - [Dy₁₂(CO₃)₄(μ₃-OH)₄(μ₂-OH)₃(μ₂-OMe)₃(amoniumethyl-o-van-amid)₁₂]Cl₁₈·3H₂O·44MeCN



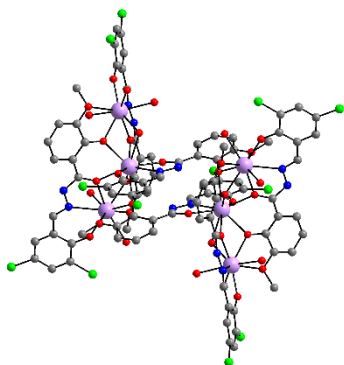
N-(2-aminoethyl)-2-hydroxy-3-methoxybenzamide was first synthesised using a literature procedure^[248] where 1g (5.5 mol) of 2-hydroxy-3-methoxy-benzoic acid was refluxed for 24 h in 10 ml MeOH together with 330 mg ethylenediamine (5.5 mmol). 42 mg of N-(2-aminoethyl)-2-hydroxy-3-methoxybenzamide (0.2 mmol) was then added to a glass vial together with 75 mg of DyCl₃·6H₂O (0.2 mmol) in a 5/10 mixture of MeOH and MeCN and

stirred for 5 minutes after which 42 μl of Et₃N was added. After further 3 h of stirring the vial was set aside and left undisturbed to allow for crystallisation of the product. After 2 weeks very small crystals of (Dy₁₂-90) were obtained that could be characterised using SCXRD measurements.

Crystal Data for C₂₁₅H₃₂₂Cl₁₈Dy₁₂N₆₈O₆₁ (*M* = 7423.49 g/mol): cubic, space group F432 (no. 209), *a* = 38.4638(4) Å, *V* = 56905.8(18) Å³, *Z* = 8, *T* = 180.15 K, μ (GaK α) = 17.566 mm⁻¹, *D*_{calc} = 1.733 g/cm³, 188403 reflections measured (5.654° ≤ 2 θ ≤

109.86°), 4559 unique ($R_{\text{int}} = 0.0903$, $R_{\text{sigma}} = 0.0242$) which were used in all calculations. The final R_1 was 0.0501 ($I > 2\sigma(I)$) and wR_2 was 0.1580 (all data).

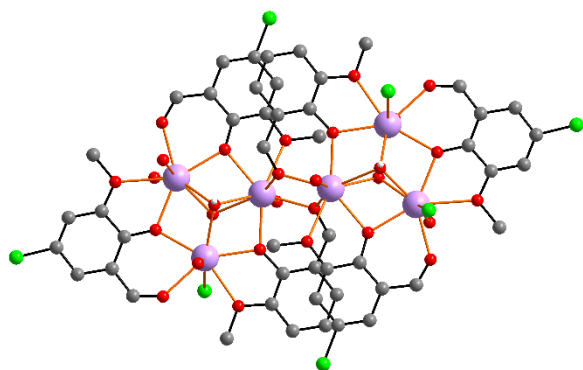
(Dy₆-91) - [Dy₆(OH)₂(Hmdohbovh)₆(H₂O)₁₀]Cl₅·4(H₂O)·10MeCN



(Dy₃-91) was synthesised using the same procedure as for (Dy₃-49) with 380 mg 3,5-dichloro-2-hydroxybenzaldehyde (2 mmol) instead of benzaldehyde. After 1 month the product was isolated as yellow block shaped crystals suitable for SCXRD.

Crystal Data for C₁₁₀H₁₂₂Cl₁₇Dy₆N₂₂O₄₀ ($M = 3969.94$ g/mol): triclinic, space group $P\bar{1}$ (no. 2), $a = 14.4425(7)$ Å, $b = 14.8676(7)$ Å, $c = 18.1977(8)$ Å, $\alpha = 72.450(3)^\circ$, $\beta = 71.319(3)^\circ$, $\gamma = 88.836(4)^\circ$, $V = 3516.7(3)$ Å³, $Z = 1$, $T = 180$ K, $\mu(1.3401270, 1.34 \text{ K}\alpha) = 18.730 \text{ mm}^{-1}$, $D_{\text{calc}} = 1.875 \text{ g/cm}^3$, 44918 reflections measured ($7.502^\circ \leq 2\theta \leq 121.154^\circ$), 15747 unique ($R_{\text{int}} = 0.0670$, $R_{\text{sigma}} = 0.0608$) which were used in all calculations. The final R_1 was 0.0719 ($I > 2\sigma(I)$) and wR_2 was 0.2193 (all data).

(Dy₆-92) - [Dy₆(μ_3 -OH)₄(Cl-van)₄(vanoxo)₂(H₂O)₇Cl₃]Cl₃·H₂O·4MeOH



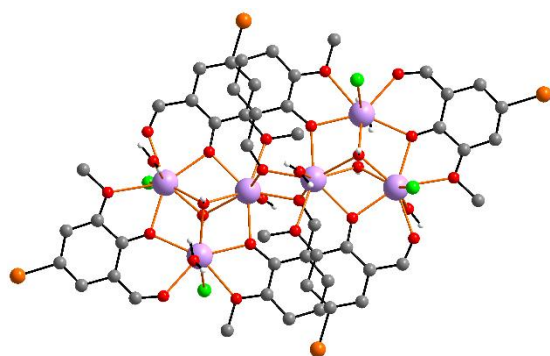
In a glass vial 49 mg 5-Chlor-2-hydroxy-3-methoxybenzaldehyde (0.26 mmol), 20 mg 2-(hydroxymethyl)-6-methoxyphenol (0.12 mmol) and 150 mg DyCl₃·6H₂O (0.4 mmol) were dissolved in 5 ml of MeOH and 15 ml of MeCN. Then 112 μ l of Et₃N (0.8 mmol) were added

dropwise under stirring. The mixture was stirred for 1h after which the vial was sealed with a cap with small holes and left undisturbed to allow for crystallisation of the product by slow evaporation of the solvent. After 1 week the product was isolated as yellow block shaped crystals in a yield of 52.0 % (86 mg).

PXRD experiments showed the product to be impure. Therefore, no further characterisation was performed.

Crystal Data for $C_{52}H_{62}Cl_{10}Dy_6O_{34}$ ($M = 2560.51$ g/mol): monoclinic, space group $P2_1/n$ (no. 14), $a = 15.8001(7)$ Å, $b = 12.9641(4)$ Å, $c = 19.2874(8)$ Å, $\beta = 99.199(3)^\circ$, $V = 3899.9(3)$ Å³, $Z = 2$, $T = 180$ K, $\mu(\text{Mo K}\alpha) = 6.099$ mm⁻¹, $D_{\text{calc}} = 2.180$ g/cm³, 21876 reflections measured ($3.63^\circ \leq 2\theta \leq 52.742^\circ$), 7907 unique ($R_{\text{int}} = 0.0403$, $R_{\text{sigma}} = 0.0521$) which were used in all calculations. The final R_1 was 0.0475 ($I > 2\sigma(I)$) and wR_2 was 0.1331 (all data).

(Dy₆-93) - [Dy₆(μ₃-OH)₄(Br-van)₄(vanoxo)₂(H₂O)₆Cl₄]Cl₂·6H₂O



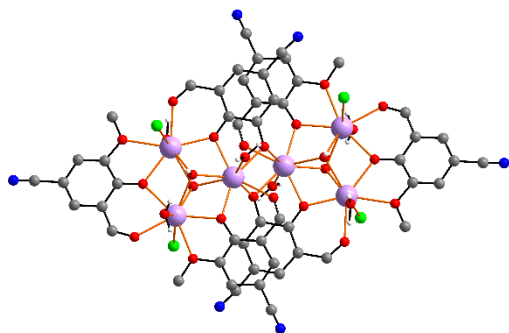
In a glass vial 30 mg 5-Brom-2-hydroxy-3-methoxybenzaldehyde (0.13 mmol), 10 mg 2-(hydroxymethyl)-6-methoxyphenol (0.06 mmol) and 75 mg DyCl₃·6H₂O (0.2 mmol) were dissolved in 5 ml of MeOH and 10 ml of MeCN. Then 56 μl of Et₃N (0.4 mmol) were added dropwise under

stirring. The mixture was stirred for 1 h after which the vial was sealed with a cap with small holes and left undisturbed to allow for crystallisation of the product by slow evaporation of the solvent. After 2 weeks the product was isolated as yellow block shaped crystals in a yield of 56.1 % (98 mg).

Elemental analysis (calculated, Dy₆Cl₆Br₄C₄₈H₉₄O₄₈) C: 19.56%, H: 3.21%, N: 0.00%; (found) C: 19.11%, H: 2.904%, N: 0.00%. **ATR-IR (4000-400 cm⁻¹):** 3280(s); 2956(m); 2889(m); 1635(s); 1547(s); 1477(m); 1458(s); 1433(s); 1403(s); 1351(w); 1303(s); 1285(m); 1263(w); 1233(s); 1207(s); 1064(m); 1038(m); 949(m); 923(m); 853(m); 780(s); 754(m); 732(m); 709(m); 621(w); 558(m); 503(w); 429(m).

Crystal Data for $C_{48}H_{68}Br_4Cl_6Dy_6O_{34}$ ($M = 2696.36$ g/mol): monoclinic, space group $P2_1/n$ (no. 14), $a = 15.7337(9)$ Å, $b = 12.7882(5)$ Å, $c = 19.3390(10)$ Å, $\beta = 100.597(4)^\circ$, $V = 3824.8(3)$ Å³, $Z = 2$, $T = 180$ K, $\mu(1.3401270, 1.34 \text{ K}\alpha) = 33.315$ mm⁻¹, $D_{\text{calc}} = 2.341$ g/cm³, 24513 reflections measured ($7.248^\circ \leq 2\theta \leq 107.814^\circ$), 6916 unique ($R_{\text{int}} = 0.0563$, $R_{\text{sigma}} = 0.0458$) which were used in all calculations. The final R_1 was 0.0856 ($I > 2\sigma(I)$) and wR_2 was 0.2706 (all data).

(Dy₆-94) - Dy₆(μ₃-OH)₄(CN-van)₄(CN-vandiolate)₂(H₂O)_{5.5}Cl_{4.5}]Cl_{1.5}·2.5H₂O·4MeOH



In a glass vial 53 mg 5-Cyano-2-hydroxy-3-methoxybenzaldehyde (0.3 mmol) and 117 mg DyCl₃·6H₂O (0.3 mmol) were dissolved in 4 ml of MeOH and 10 ml of MeCN. Then 63 μl of Et₃N (0.4 mmol) were added dropwise under stirring. The mixture was stirred for 3h after which it was filtered. The vial was left for 24 h at

55°C until the solvent was evaporated. Afterwards the orange solid was redissolved in 4 ml of MeOH under stirring. The resulting yellow solution was filtered and the vial sealed and left undisturbed to allow for crystallisation of the product. After 5 days the product was isolated as yellow block shaped crystals in a yield of 61.4 % (78 mg).

Elemental analysis (calculated, Dy₆Cl₆C₅₇H₇₁O₃₆N₇) C: 26.15%, H: 2.73%, N: 3.74%; (found) C: 25.98%, H: 2.97%, N: 3.47%. **ATR-IR (4000-400 cm⁻¹):** 3280(s); 2226(s); 1635(s); 1613(m); 1547(s); 1462(m); 1410(s); 1355(w); 1322(s); 1252(s); 1156(m); 1078(m); 968(w); 931(w); 883(w); 820(m); 765(w); 735(w); 617(w); 591(w).

Crystal Data for C₅₆H₆₆Cl₆Dy₆N₆O₃₄ (*M* = 2554.84 g/mol): triclinic, space group *P* $\bar{1}$ (no. 2), *a* = 11.2279(4) Å, *b* = 12.1449(5) Å, *c* = 15.7208(7) Å, *α* = 70.586(3)°, *β* = 89.851(3)°, *γ* = 81.035(3)°, *V* = 1994.34(15) Å³, *Z* = 1, *T* = 273.15 K, *μ*(MoKα) = 5.835 mm⁻¹, *D*_{calc} = 2.127 g/cm³, 21042 reflections measured (3.604° ≤ 2θ ≤ 50.7°), 7208 unique (*R*_{int} = 0.0399, *R*_{sigma} = 0.0564) which were used in all calculations. The final *R*₁ was 0.0570 (*I* > 2σ(*I*)) and *wR*₂ was 0.1540 (all data).

9. References

- [1] R. Sessoli, D. Gatteschi, A. Caneschi, M. A. Novak, *Nature* **1993**, 365, 141-143.
- [2] G. Christou, D. Gatteschi, D. N. Hendrickson, R. Sessoli, *MRS Bulletin* **2000**, 25, 66-71.
- [3] D. Gatteschi, R. Sessoli, J. Villain, *Molecular Nanomagnets, Vol. 1*, Oxford University Press, New York, **2006**.
- [4] J.-P. Launay, M. Verdaguer, *Electrons in Molecules, Vol. 1*, Oxford University Press, Oxford, **2014**.
- [5] I. G. Rau, S. Baumann, S. Rusponi, F. Donati, S. Stepanow, L. Gragnaniello, J. Dreiser, C. Piamonteze, F. Nolting, S. Gangopadhyay, O. R. Albertini, R. M. Macfarlane, C. P. Lutz, B. A. Jones, P. Gambardella, A. J. Heinrich, H. Brune, *Science* **2014**, 344, 988-992.
- [6] M. N. Leuenberger, D. Loss, *Nature* **2001**, 410, 789-793.
- [7] M. Affronte, F. Troiani, A. Ghirri, A. Candini, M. Evangelisti, V. Corradini, S. Carretta, P. Santini, G. Amoretti, F. Tuna, G. Timco, R. E. P. Winpenny, *J. Phys. D: Appl. Phys.* **2007**, 40, 2999-3004.
- [8] S. Bertaina, S. Gambarelli, T. Mitra, B. Tsukerblat, A. Müller, B. Barbara, *Nature* **2008**, 453, 203-206.
- [9] G. Aromi, D. Aguila, P. Gamez, F. Luis, O. Roubeau, *Chem. Soc. Rev.* **2012**, 41, 537-546.
- [10] R. Sessoli, *ACS Cent. Sci.* **2015**, 1, 473-474.
- [11] J. M. Zadrozny, J. Niklas, O. G. Poluektov, D. E. Freedman, *ACS Cent. Sci.* **2015**, 1, 488-492.
- [12] M. Shiddiq, D. Komijani, Y. Duan, A. Gaita-Arino, E. Coronado, S. Hill, *Nature* **2016**, 531, 348-351.
- [13] H. B. Heersche, Z. de Groot, J. A. Folk, H. S. van der Zant, C. Romeike, M. R. Wegewijs, L. Zobbi, D. Barreca, E. Tondello, A. Cornia, *Phys. Rev. Lett.* **2006**, 96, 206801.
- [14] L. E. Hueso, J. M. Pruneda, V. Ferrari, G. Burnell, J. P. Valdes-Herrera, B. D. Simons, P. B. Littlewood, E. Artacho, A. Fert, N. D. Mathur, *Nature* **2007**, 445, 410-413.

- [15] S. Sanvito, A. R. Rocha, *J. Comput. Theor. Nanosci.* **2006**, 3, 624-642.
- [16] M. Urdampilleta, S. Klyatskaya, J. P. Cleuziou, M. Ruben, W. Wernsdorfer, *Nat. Mater.* **2011**, 10, 502-506.
- [17] G. Abbas, M. Ibrahim, S. F. M. Schmidt, E. Moreno-Pineda, C. E. Anson, A. K. Powell, *Polyhedron* **2019**, 158, 255-261.
- [18] A. Baniodeh, D. Wagner, Y. Peng, H. Kaemmerer, N. Leblanc, S. Brase, J. V. Naubron, C. E. Anson, A. K. Powell, *Chem. Eur. J.* **2021**, 27, 15103-15109.
- [19] J. Bartolomé, G. Filoti, V. Kuncser, G. Schinteie, V. Mereacre, C. E. Anson, A. K. Powell, D. Prodius, C. Turta, *Phys. Rev. B* **2009**, 80, 014430.
- [20] S. K. Langley, D. P. Wielechowski, V. Vieru, N. F. Chilton, B. Moubaraki, B. F. Abrahams, L. F. Chibotaru, K. S. Murray, *Angew. Chem. Int. Ed.* **2013**, 52, 12014-12019.
- [21] M. Murugesu, A. Mishra, W. Wernsdorfer, K. A. Abboud, G. Christou, *Polyhedron* **2006**, 25, 613-625.
- [22] Y. Peng, H. Kaemmerer, A. K. Powell, *Chem. Eur. J.* **2021**, 27, 15043-15065.
- [23] Y. Peng, V. Mereacre, C. E. Anson, A. K. Powell, *ACS Omega* **2018**, 3, 6360-6368.
- [24] Y. Peng, A. K. Powell, *Coord. Chem. Rev.* **2021**, 426, 213490.
- [25] Y. Peng, M. K. Singh, V. Mereacre, C. E. Anson, G. Rajaraman, A. K. Powell, *Chem. Sci.* **2019**, 10, 5528-5538.
- [26] J. Braun, A. K. Powell, A. N. Unterreiner, *Chem. Eur. J.* **2024**, e202400977.
- [27] A. Baniodeh, C. E. Anson, A. K. Powell, *Chem. Sci.* **2013**, 4, 4354-4361.
- [28] A. Baniodeh, N. Magnani, S. Bräse, C. E. Anson, A. K. Powell, *Dalton Trans.* **2015**, 44, 6343-6347.
- [29] A. Baniodeh, N. Magnani, Y. Lan, G. Buth, C. E. Anson, J. Richter, M. Affronte, J. Schnack, A. K. Powell, *npj Quant. Mater.* **2018**, 3, 10.
- [30] P. King, T. C. Stamatatos, K. A. Abboud, G. Christou, *Angew. Chem. Int. Ed.* **2006**, 45, 7379-7383.
- [31] L. Munzfeld, S. Gillhuber, A. Hauser, S. Lebedkin, P. Hädinger, N. D. Knofel, C. Zovko, M. T. Gamer, F. Weigend, M. M. Kappes, P. W. Roesky, *Nature* **2023**, 620, 92-96.
- [32] G. A. Timco, S. Carretta, F. Troiani, F. Tuna, R. J. Pritchard, C. A. Muryn, E. J. McInnes, A. Ghirri, A. Candini, P. Santini, G. Amoretti, M. Affronte, R. E. Winpenny, *Nat. Nanotechnol.* **2009**, 4, 173-178.

- [33] F. Troiani, A. Ghirri, M. Affronte, S. Carretta, P. Santini, G. Amoretti, S. Piligkos, G. Timco, R. E. Winpenny, *Phys. Rev. Lett.* **2005**, *94*, 207208.
- [34] A. Baniodeh, Y. Liang, C. E. Anson, N. Magnani, A. K. Powell, A.-N. Unterreiner, S. Seyfferle, M. Slota, M. Dressel, L. Bogani, K. Goß, *Adv. Funct. Mater.* **2014**, *24*, 6280-6290.
- [35] A. Baniodeh, I. J. Hewitt, V. Mereacre, Y. Lan, G. Novitchi, C. E. Anson, A. K. Powell, *Dalton Trans.* **2011**, *40*, 4080-4086.
- [36] Y. Peng, J. Braun, M. Schulze, H. Kaemmerer, Y. F. Schneider, C. E. Anson, W. Wernsdorfer, A. K. Powell, *Dalton Trans.* **2024**, *53*, 894-897.
- [37] J. Tang, I. Hewitt, N. T. Madhu, G. Chastanet, W. Wernsdorfer, C. E. Anson, C. Benelli, R. Sessoli, A. K. Powell, *Angew. Chem. Int. Ed.* **2006**, *45*, 1729-1733.
- [38] L. F. Chibotaru, L. Ungur, A. Soncini, *Angew. Chem. Int. Ed.* **2008**, *120*, 4194-4197.
- [39] J. Luzon, K. Bernot, I. J. Hewitt, C. E. Anson, A. K. Powell, R. Sessoli, *Phys. Rev. Lett.* **2008**, *100*, 247205.
- [40] L. Ungur, W. Van den Heuvel, L. F. Chibotaru, *New J. Chem.* **2009**, *33*.
- [41] X. L. Li, J. Tang, *Dalton Trans* **2019**, *48*, 15358-15370.
- [42] L. Ungur, S. Y. Lin, J. Tang, L. F. Chibotaru, *Chem. Soc. Rev.* **2014**, *43*, 6894-6905.
- [43] K. R. Vignesh, G. Rajaraman, *ACS Omega* **2021**, *6*, 32349-32364.
- [44] E. A. Gurvitz, K. S. Ladutenko, P. A. Dergachev, A. B. Evlyukhin, A. E. Miroshnichenko, A. S. Shalin, *Laser Photonics Rev.* **2019**, *13*, 1800266.
- [45] V. Savinov, N. Papasimakis, D. P. Tsai, N. I. Zheludev, *Commun. Phys.* **2019**, *2*, 69.
- [46] C. S. Wood, S. C. Bennett, D. Cho, B. P. Masterson, J. L. Roberts, C. E. Tanner, C. E. Wieman, *Science* **1997**, *275*, 1759-1763.
- [47] Y. Yang, S. I. Bozhevolnyi, *Nanotechnology* **2019**, *30*, 204001.
- [48] E. Hecht, *Optik, Vol. 7*, Walter de Gruyter GmbH, Berlin/Boston, **2018**.
- [49] L. F. Wang, J. Z. Qiu, J. L. Liu, Y. C. Chen, J. H. Jia, J. Jover, E. Ruiz, M. L. Tong, *Chem. Commun.* **2015**, *51*, 15358-15361.
- [50] A. Jablonski, *Z. Phys.* **1935**, *94*, 38-46.
- [51] P. Atkins, J. de Paula, J. Keeler, *Atkin's Physical Chemistry*, Oxford University Press, Oxford, **2018**.
- [52] B. Weber, *Coordination Chemistry, Vol. 1*, Springer, Berlin, **2023**.

- [53] C. Janiak, H.-J. Meyer, D. Gudat, P. Kurz, *Moderne Anorganische Chemie*, Vol. 5, Walter de Gruyter GmbH, Berlin/Boston, **2018**.
- [54] J. Zhang, B. Zhu, L. Zhang, J. Yu, *Chem. Commun.* **2023**, 59, 688-699.
- [55] J.-M. Lehn, *Science* **1985**, 227, 849-856.
- [56] G. A. Jeffrey, *An Introduction to Hydrogen Bonding*, Oxford University Press, Oxford, **1997**.
- [57] L. Pauling, *The nature of the chemical bond and the structure of molecules and crystals: An Introduction to Modern Structural Chemistry*, Vol. 3, Cornell University Press, Ithaca, New York, **1960**.
- [58] C. A. Hunter, J. K. M. Sanders, *J. Am. Chem. Soc.* **1990**, 112, 5525-5534.
- [59] J. C. Ma, D. A. Dougherty, *Chem. Rev.* **1997**, 97, 1303-1324.
- [60] C. A. Hunter, K. R. Lawson, J. Perkins, C. J. Urch, *J. Chem. Soc., Perkin Trans. 2* **2001**, 651-669.
- [61] S. Grimme, *Angew. Chem. Int. Ed.* **2008**, 47, 3430-3434.
- [62] C. R. Martinez, B. L. Iverson, *Chem. Sci.* **2012**, 3, 2191-2201.
- [63] I. A. Rather, S. A. Wagay, R. Ali, *Coord. Chem. Rev.* **2020**, 415, 213327.
- [64] G. Cavallo, P. Metrangolo, R. Milani, T. Pilati, A. Priimagi, G. Resnati, G. Terraneo, *Chem. Rev.* **2016**, 116, 2478-2601.
- [65] P. Metrangolo, F. Meyer, T. Pilati, G. Resnati, G. Terraneo, *Angew. Chem. Int. Ed.* **2008**, 47, 6114-6127.
- [66] F. Biedermann, H. J. Schneider, *Chem. Rev.* **2016**, 116, 5216-5300.
- [67] J. D. Bernal, R. H. Fowler, *J. Chem. Phys.* **1933**, 1, 515-548.
- [68] T. M. Gasser, A. V. Thoeny, A. D. Fortes, T. Loerting, *Nat. Commun.* **2021**, 12, 1128.
- [69] F. London, *Z. Phys.* **1930**, 60, 491-527.
- [70] I. E. Dzyaloshinskii, E. M. Lifshitz, L. P. Pitaevskii, *Adv. Phys.* **1961**, 10, 165-209.
- [71] R. H. S. Winterton, *Contemp. Phys.* **1970**, 11, 559-574.
- [72] J. N. Israelachvili, *Contemp. Phys.* **1974**, 15, 159-177.
- [73] B. T. Wimberly, D. E. Brodersen, W. M. Clemons Jr, M.-W. R. J., A. P. Carter, V. C., T. Hartsch, V. Ramakrishnan, *Nature* **2000**, 407, 327-339.
- [74] F. Schlunzen, A. Tocilj, R. Zarivach, J. Harms, M. Gluehmann, D. Janell, A. Bashan, H. Bartles, I. Agmon, F. Franceschi, A. Yonath, *Cell* **2000**, 102, 615-623.

- [75] N. Ban, P. Nissen, J. Hansen, P. B. Moore, T. A. Steitz, *Science* **2000**, 289, 905-920.
- [76] J. Emsley, *Chem. Soc. Rev.* **1980**, 9, 91-124.
- [77] J. W. Larson, T. B. McMahon, *Inorg. Chem.* **1984**, 23, 2029-2033.
- [78] Y. Zhao, D. G. Truhlar, *J. Phys. Chem. A* **2005**, 109, 4209-4212.
- [79] O. Hassel, *Science* **1970**, 170, 497-502.
- [80] R. S. P. Mulliken, *J. Am. Chem. Soc.* **1950**, 72, 600-608.
- [81] D. Jovanovic, M. Poliyodath Mohanan, S. M. Huber, *Angew. Chem. Int. Ed.* **2024**, 63, e202404823.
- [82] G. R. Desiraju, P. S. Ho, L. Kloo, A. C. Legon, R. Marquardt, P. Metrangolo, P. Politzer, G. Resnati, K. Rissanen, *Pure Appl. Chem.* **2013**, 85, 1711-1713.
- [83] X. Yu, C. Houtman, R. H. Atalla, *Carbohydr. Res.* **1996**, 292, 129-141.
- [84] T. Clark, M. Hennemann, J. S. Murray, P. Politzer, *J. Mol. Model.* **2007**, 13, 291-296.
- [85] K. E. Riley, P. Hobza, *Phys. Chem. Chem. Phys.* **2013**, 15, 17742-17751.
- [86] A. Bondi, *J. Phys. Chem.* **1964**, 68, 441-451.
- [87] G. R. Desiraju, R. Parthasarathy, *J. Am. Chem. Soc.* **1989**, 111, 8725-8726.
- [88] S. Scheiner, *Cryst. Growth Des.* **2022**, 22, 2692-2702.
- [89] A. D. Becke, K. E. Edgecombe, *J. Chem. Phys.* **1990**, 92, 5397-5403.
- [90] E. Riedel, C. Janiak, *Anorganische Chemie, Vol. 9*, De Gruyter, Berlin, **2015**.
- [91] H. Luecken, *Magnetochemie, Vol. 1*, Teubner, Stuttgart - Leipzig, **1999**.
- [92] O. Kahn, *Molecular Magnetism, Vol. 1*, VCH Publishers, New York, Weinheim, Cambridge, **1993**.
- [93] P. Weiss, *J. Phys. Theor. Appl.* **1907**, 6, 661-690.
- [94] R. Wiesendanger, *Atomic- and Nanoscale Magnetism, Vol. 1*, Springer Nature Switzerland, Cham, **2018**.
- [95] W. H. Bragg, *Nature* **1915**, 95, 561.
- [96] S. Mugiraneza, A. M. Hallas, *Commun. Phys.* **2022**, 5, 95.
- [97] T. Lis, *Acta Crystallogr. A* **1980**, 36, 2042-2046.
- [98] D. Gatteschi, R. Sessoli, *Angew. Chem. Int. Ed.* **2003**, 42, 268-297.
- [99] A. M. Ako, I. J. Hewitt, V. Mereacre, R. Clerac, W. Wernsdorfer, C. E. Anson, A. K. Powell, *Angew. Chem. Int. Ed.* **2006**, 45, 4926-4929.
- [100] O. Waldmann, *Inorg. Chem.* **2007**, 46, 10035-10037.
- [101] J. D. Rinehart, J. R. Long, *Chem. Sci.* **2011**, 2, 2078-2085.

- [102] H. A. Kramers, *Proc. R. Acad. Sci.* **1930**, 33, 959-972.
- [103] D. Gatteschi, *Nat. Chem.* **2011**, 3, 830.
- [104] L. Ungur, L. F. Chibotaru, *Inorg. Chem.* **2016**, 55, 10043-10056.
- [105] N. Ishikawa, M. Sugita, T. Ishikawa, S.-Y. Koshihara, Y. Kaizu, *J. Am. Chem. Soc.* **2003**, 125, 8694-8695.
- [106] L. Ungur, L. F. Chibotaru, *Phys. Chem. Chem. Phys.* **2011**, 13, 20086-20090.
- [107] S. K. Singh, T. Gupta, G. Rajaraman, *Inorg. Chem.* **2014**, 53, 10835-10845.
- [108] J. J. Baldovi, S. Cardona-Serra, J. M. Clemente-Juan, E. Coronado, A. Gaita-Arino, A. Pali, *Inorg. Chem.* **2012**, 51, 12565-12574.
- [109] W. J. Xu, Q. C. Luo, Z. H. Li, Y. Q. Zhai, Y. Z. Zheng, *Adv. Sci.* **2024**, 11, e2308548.
- [110] S. D. Jiang, B. W. Wang, H. L. Sun, Z. M. Wang, S. Gao, *J. Am. Chem. Soc.* **2011**, 133, 4730-4733.
- [111] J. J. Le Roy, L. Ungur, I. Korobkov, L. F. Chibotaru, M. Murugesu, *J. Am. Chem. Soc.* **2014**, 136, 8003-8010.
- [112] J. D. Hilgar, M. G. Bernbeck, B. S. Flores, J. D. Rinehart, *Chem. Sci.* **2018**, 9, 7204-7209.
- [113] M. Briganti, E. Lucaccini, L. Chelazzi, S. Ciattini, L. Sorace, R. Sessoli, F. Totti, M. Perfetti, *J. Am. Chem. Soc.* **2021**, 143, 8108-8115.
- [114] S. T. Liddle, J. van Slageren, *Chem Soc Rev* **2015**, 44, 6655-6669.
- [115] C. E. Jackson, I. P. Moseley, R. Martinez, S. Sung, J. M. Zadrozny, *Chem. Soc. Rev.* **2021**, 50, 6684-6699.
- [116] A. Swain, T. Sharma, G. Rajaraman, *Chem. Commun.* **2023**, 59, 3206-3228.
- [117] M. Briganti, F. Santanni, L. Tesi, F. Totti, R. Sessoli, A. Lunghi, *J. Am. Chem. Soc.* **2021**, 143, 13633-13645.
- [118] L. Gu, R. Wu, *Phys. Rev. B* **2021**, 103, 014401.
- [119] L. Gu, R. Wu, *Phys. Rev. Lett.* **2020**, 125, 117203.
- [120] R. A. S. Ferreira, E. Mamontova, A. M. P. Botas, M. Shestakov, J. Vanacken, V. Moshchalkov, Y. Guari, L. F. Chibotaru, D. Luneau, P. S. André, J. Larionova, J. Long, L. D. Carlos, *Adv. Opt. Mater.* **2021**, 9, 2101495.
- [121] Y. Bi, C. Chen, Y. F. Zhao, Y. Q. Zhang, S. D. Jiang, B. W. Wang, J. B. Han, J. L. Sun, Z. Q. Bian, Z. M. Wang, S. Gao, *Chem. Sci.* **2016**, 7, 5020-5031.
- [122] K.-X. Yu, J. G. C. Kragsskow, Y.-S. Ding, Y.-Q. Zhai, D. Reta, N. F. Chilton, Y.-Z. Zheng, *Chem* **2020**, 6, 1777-1793.

- [123] V. S. Parmar, D. P. Mills, R. E. P. Winpenny, *Chem. Eur. J.* **2021**, *27*, 7625-7645.
- [124] J. D. Rinehart, M. Fang, W. J. Evans, J. R. Long, *Nat. Chem.* **2011**, *3*, 538-542.
- [125] S. Demir, I.-R. Jeon, J. R. Long, T. D. Harris, *Coord. Chem. Rev.* **2015**, 289-290, 149-176.
- [126] C. A. P. Goodwin, F. Ortu, D. Reta, N. F. Chilton, D. P. Mills, *Nature* **2017**, *548*, 439-442.
- [127] R. K. McClain, C. A. Gould, K. Chakarawet, S. J. Teat, T. J. Groshens, J. R. Long, B. G. Harvey, *Chem. Sci.* **2018**, *9*, 8492-8503.
- [128] A. Dey, J. Acharya, V. Chandrasekhar, *Chem. Asian J.* **2019**, *14*, 4433-4453.
- [129] T. Gupta, M. F. Beg, G. Rajaraman, *Inorg. Chem.* **2016**, *55*, 11201-11215.
- [130] A. M. Ako, V. Mereacre, R. Clerac, W. Wernsdorfer, I. J. Hewitt, C. E. Anson, A. K. Powell, *Chem. Commun.* **2009**, 544-546.
- [131] J. Braun, *The Influence of Intra- and Intermolecular Interactions on the Magnetic and Optical Properties of Lanthanide and Transition Metal Complexes*, Karlsruhe Institute of Technology (KIT), PhD Thesis (KIT) (Karlsruhe), **2023**.
- [132] S. Osa, T. Kido, N. Matsumoto, N. Re, A. Pochaba, J. Mrozinski, *J. Am. Chem. Soc.* **2004**, *126*, 420-421.
- [133] S. K. Langley, N. F. Chilton, L. Ungur, B. Moubaraki, L. F. Chibotaru, K. S. Murray, *Inorg. Chem.* **2012**, *51*, 11873-11881.
- [134] Y. Peng, V. Mereacre, C. E. Anson, A. K. Powell, *Dalton Trans.* **2017**, *46*, 5337-5343.
- [135] D. Schray, D. Westerbeck, J. Braun, Y. Lan, S. Gomez-Coca, W. Wernsdorfer, E. Ruiz, C. E. Anson, J. Schnack, A. K. Powell, *Inorg. Chem.* **2023**, *62*, 6642-6648.
- [136] G. Novitchi, G. Pilet, L. Ungur, V. V. Moshchalkov, W. Wernsdorfer, L. F. Chibotaru, D. Luneau, A. K. Powell, *Chem. Sci.* **2012**, *3*, 1169-1176.
- [137] K. R. Vignesh, A. Soncini, S. K. Langley, W. Wernsdorfer, K. S. Murray, G. Rajaraman, *Nat. Commun.* **2017**, *8*, 1023.
- [138] H. Kaemmerer, A. Baniodeh, Y. Peng, E. Moreno-Pineda, M. Schulze, C. E. Anson, W. Wernsdorfer, J. Schnack, A. K. Powell, *J. Am. Chem. Soc.* **2020**, *142*, 14838-14842.

- [139] K. L. Harriman, J. L. Brosmer, L. Ungur, P. L. Diaconescu, M. Murugesu, *J. Am. Chem. Soc.* **2017**, *139*, 1420-1423.
- [140] Y. C. Chen, J. L. Liu, L. Ungur, J. Liu, Q. W. Li, L. F. Wang, Z. P. Ni, L. F. Chibotaru, X. M. Chen, M. L. Tong, *J. Am. Chem. Soc.* **2016**, *138*, 2829-2837.
- [141] Y. S. Ding, N. F. Chilton, R. E. Winpenny, Y. Z. Zheng, *Angew. Chem. Int. Ed.* **2016**, *55*, 16071-16074.
- [142] A. B. Canaj, S. Dey, E. R. Marti, C. Wilson, G. Rajaraman, M. Murrie, *Angew. Chem. Int. Ed.* **2019**, *58*, 14146-14151.
- [143] F.-S. Guo, B. M. Day, Y. C. Chen, M.-L. Tong, A. Mansikkamäki, R. A. Layfield, *Science* **2018**, *362*, 1400-1403.
- [144] C. A. Gould, R. K. McClain, D. Reta, J. G. C. Kragoskow, D. A. Marchiori, E. Lachman, E.-S. Choi, J. G. Analytis, R. D. Britt, N. F. Chilton, B. G. Harvey, J. R. Long, *Science* **2022**, *375*, 198-202.
- [145] R. D. Cannon, U. A. Jayasooriya, W. R., S. K. arapKoske, J. A. Stride, O. F. Nielsen, R. P. White, G. J. Kearley, D. Summerfield, *J. Am. Chem. Soc.* **1994**, *116*, 11869-11874.
- [146] W. Cañón-Mancisidor, P. Hermosilla-Ibáñez, E. Spodine, V. Paredes-García, C. J. Gómez-García, G. M. Espallargas, D. Venegas-Yazigi, *Cryst. Growth Des.* **2021**, *21*, 6213-6222.
- [147] A. N. Georgopoulou, I. Margiolaki, V. Psycharis, A. K. Boudalis, *Inorg. Chem.* **2017**, *56*, 762-772.
- [148] B. Kintzel, M. Bohme, D. Plaul, H. Gorls, N. Yeché, F. Seewald, H. H. Klaus, A. A. Zvyagin, E. Kampert, T. Herrmannsdorfer, G. Pascua, C. Baines, H. Luetkens, W. Plass, *Inorg. Chem.* **2023**, *62*, 3420-3430.
- [149] F. E. Sowrey, C. Tilford, S. Wocadlo, C. E. Anson, A. K. Powell, S. M. Bennington, W. Montfrooij, U. A. Jayasooriya, R. D. Cannon, *Dalton Trans.* **2001**, 862-866.
- [150] J. Bartolome, E. Bartolome, F. Luis, E. Burzuri, A. Camon, G. Filoti, A. M. Ako, J. Braun, V. Mereacre, C. E. Anson, A. K. Powell, *Inorg. Chem.* **2024**, 24262-24273.
- [151] O. Kahn, *Chem. Phys. Lett.* **1997**, *265*, 109-114.
- [152] J. Schnack, *Dalton Trans.* **2010**, *39*, 4693-4707.

- [153] J. K. McCusker, J. B. Vincent, E. A. Schmitt, M. L. Mino, K. Shin, D. K. Coggin, P. M. Hagen, J. C. Huffman, G. Christou, D. N. Hendrickson, *J. Am. Chem. Soc.* **1991**, *113*, 3012-3021.
- [154] J. E. Greedan, *J. Mater. Chem.* **2001**, *11*, 37-53.
- [155] P. H. Guo, J. L. Liu, Z. M. Zhang, L. Ungur, L. F. Chibotaru, J. D. Leng, F. S. Guo, M. L. Tong, *Inorg. Chem.* **2012**, *51*, 1233-1235.
- [156] J. Wu, X. L. Li, M. Guo, L. Zhao, Y. Q. Zhang, J. Tang, *Chem. Commun.* **2018**, *54*, 1065-1068.
- [157] I. A. Zel'dovich, *J. Exptl. Theoret. Phys.* **1957**, *33*, 1531-1533.
- [158] K. Murray, *Single Molecule Toroids*, Springer Nature Switzerland AG, Australia, **2022**.
- [159] S. Hayami, M. Yatsushiro, Y. Yanagi, H. Kusunose, *Phys. Rev. B* **2018**, *98*, 165110.
- [160] A. S. Zimmermann, D. Meier, M. Fiebig, *Nat. Commun.* **2014**, *5*, 4796.
- [161] S. Gnewuch, E. E. Rodriguez, *J. Solid State Chem.* **2019**, *271*, 175-190.
- [162] K. M. Rabe, *Nature* **2007**, *449*, 674-675.
- [163] K. Hymas, A. Soncini, K. R. Vignesh, D. Chauhan, A. Swain, S. L. Benjamin, D. Borah, M. Shanmugam, W. Wernsdorfer, G. Rajaraman, S. K. Langley, K. S. Murray, *Npj Quant. Mater.* **2024**, *9*, 106.
- [164] Y.-X. Wang, W. Shi, H. Li, Y. Song, L. Fang, Y. Lan, A. K. Powell, W. Wernsdorfer, L. Ungur, L. F. Chibotaru, M. Shen, P. Cheng, *Chem. Sci.* **2012**, *3*, 3366-3370.
- [165] T. Ruppert, *The search for lanthanide containing Single Molecule Magnets with toroidal moments*, Karlsruher Institute of Technology (KIT), PhD Thesis (KIT) (Karlsruhe), **2021**.
- [166] S. Xue, X. H. Chen, L. Zhao, Y. N. Guo, J. Tang, *Inorg. Chem.* **2012**, *51*, 13264-13270.
- [167] G. Fernandez Garcia, D. Guettas, V. Montigaud, P. Larini, R. Sessoli, F. Totti, O. Cador, G. Pilet, B. Le Guennic, *Angew. Chem. Int. Ed.* **2018**, *57*, 17089-17093.
- [168] Q. Yang, L. Ungur, L. F. Chibotaru, J. Tang, *Chem. Commun.* **2022**, *58*, 1784-1787.
- [169] L. Ungur, S. K. Langley, T. N. Hooper, B. Moubaraki, E. K. Brechin, K. S. Murray, L. F. Chibotaru, *J. Am. Chem. Soc.* **2012**, *134*, 18554-18557.

- [170] I. J. Hewitt, J. Tang, N. T. Madhu, C. E. Anson, Y. Lan, J. Luzon, M. Etienne, R. Sessoli, A. K. Powell, *Angew. Chem. Int. Ed.* **2010**, *49*, 6352-6356.
- [171] S. Y. Lin, W. Wernsdorfer, L. Ungur, A. K. Powell, Y. N. Guo, J. Tang, L. Zhao, L. F. Chibotaru, H. J. Zhang, *Angew. Chem. Int. Ed.* **2012**, *51*, 12767-12771.
- [172] X. L. Li, J. Wu, J. Tang, B. Le Guennic, W. Shi, P. Cheng, *Chem. Commun.* **2016**, *52*, 9570-9573.
- [173] Q. Zhang, M. L. Baker, S. Li, M. P. Sarachik, J. J. Baldovi, A. Gaita-Arino, E. Coronado, D. I. Alexandropoulos, T. C. Stamatatos, *Nanoscale* **2019**, *11*, 15131-15138.
- [174] S. K. Langley, K. R. Vignesh, B. Moubaraki, G. Rajaraman, K. S. Murray, *Chem. Eur. J.* **2019**, *25*, 4156-4165.
- [175] S. K. Langley, K. R. Vignesh, T. Gupta, C. J. Gartshore, G. Rajaraman, C. M. Forsyth, K. S. Murray, *Dalton Trans.* **2019**, *48*, 15657-15667.
- [176] K. R. Vignesh, S. K. Langley, A. Swain, B. Moubaraki, M. Damjanovic, W. Wernsdorfer, G. Rajaraman, K. S. Murray, *Angew. Chem. Int. Ed.* **2018**, *57*, 779-784.
- [177] H. Wang, Z. Zhu, L. La Droitte, W. Liao, O. Cador, B. Le Guennic, J. Tang, *Chem. Sci.* **2023**, *14*, 7208-7214.
- [178] Q. Yang, L. Ungur, W. Wernsdorfer, J. Tang, *Inorg. Chem. Front.* **2022**, *9*, 784-791.
- [179] J. M. Ashtree, I. Borilović, K. R. Vignesh, A. Swain, S. H. Hamilton, Y. L. Whyatt, S. L. Benjamin, W. Phonsri, C. M. Forsyth, W. Wernsdorfer, A. Soncini, G. Rajaraman, S. K. Langley, K. S. Murray, *Eur. J. Inorg. Chem.* **2020**, *2021*, 435-444.
- [180] X. L. Li, H. Li, D. M. Chen, C. Wang, J. Wu, J. Tang, W. Shi, P. Cheng, *Dalton Trans.* **2015**, *44*, 20316-20320.
- [181] J. Goura, E. Colacio, J. M. Herrera, E. A. Sutura, I. Kuprov, Y. Lan, W. Wernsdorfer, V. Chandrasekhar, *Chem. Eur. J.* **2017**, *23*, 16621-16636.
- [182] W. J. Gee, J. G. MacLellan, C. M. Forsyth, B. Moubaraki, K. S. Murray, P. C. Andrews, P. C. Junk, *Inorg. Chem.* **2012**, *51*, 8661-8663.
- [183] A. Gharu, K. R. Vignesh, *Dalton Trans.* **2024**, *53*, 13394-13408.
- [184] B.-K. Ling, Y.-Q. Zhai, P.-B. Jin, H.-F. Ding, X.-F. Zhang, Y. Lv, Z. Fu, J. Deng, M. Schulze, W. Wernsdorfer, Y.-Z. Zheng, *Matter* **2022**, *5*, 3485-3498.

- [185] H.-L. Zhang, Y.-Q. Zhai, L. Qin, L. Ungur, H. Nojiri, Y.-Z. Zheng, *Matter* **2020**, 2, 1481-1493.
- [186] W. Wernsdorfer, K. Hasselbach, D. Mailly, B. Barbara, A. Benoit, L. Thomas, G. Suran, *J. Magn. Magn. Mater.* **1995**, 145, 33-39.
- [187] M. Perfetti, *Coord. Chem. Rev.* **2017**, 348, 171-186.
- [188] M. N. Akhtar, M. A. AlDamen, M. Fitta, M. Shahid, A. M. Kirillov, *Cryst. Growth Des.* **2022**, 22, 608-614.
- [189] H. Tian, L. Zhao, H. Lin, J. Tang, G. Li, *Chem. Eur. J.* **2013**, 19, 13235-13241.
- [190] Y.-L. Li, Z.-M. Huang, H.-L. Wang, Z.-H. Zhu, F.-P. Liang, H.-H. Zou, *CrystEngComm* **2023**, 25, 225-232.
- [191] K. R. Vignesh, S. K. Langley, K. S. Murray, G. Rajaraman, *Inorg. Chem.* **2017**, 56, 2518-2532.
- [192] A. S. Chesman, D. R. Turner, K. J. Berry, N. F. Chilton, B. Moubaraki, K. S. Murray, G. B. Deacon, S. R. Batten, *Dalton Trans.* **2012**, 41, 11402-11412.
- [193] E. C. Mazarakioti, L. Cunha-Silva, V. Bekiari, A. Escuer, T. C. Stamatatos, *RSC Adv.* **2015**, 5, 92534-92538.
- [194] A. V. Funes, M. Perfetti, M. Kern, N. Rußegger, L. Carrella, E. Rentschler, J. van Slageren, P. Alborés, *Eur. J. Inorg. Chem.* **2021**, 2021, 3191-3210.
- [195] E. Moreno Pineda, N. F. Chilton, F. Tuna, R. E. Winpenny, E. J. McInnes, *Inorg. Chem.* **2015**, 54, 5930-4591.
- [196] G.-P. Li, H.-Z. Tang, R.-C. Gao, Y.-Y. Wang, X. Sun, K. Zhang, *Cryst. Growth Des.* **2023**, 23, 1575-1580.
- [197] A. Baniodeh, V. Mereacre, N. Magnani, Y. Lan, J. A. Wolny, V. Schunemann, C. E. Anson, A. K. Powell, *Chem. Commun.* **2013**, 49, 9666-9668.
- [198] V. Mereacre, A. Baniodeh, C. E. Anson, A. K. Powell, *J. Am. Chem. Soc.* **2011**, 133, 15335-15337.
- [199] Y. Zheng, Y. Lan, C. E. Anson, A. K. Powell, *Inorg. Chem.* **2008**, 47, 10813-10815.
- [200] J. R. Machado, A. Baniodeh, A. K. Powell, B. Luy, S. Kramer, G. Guthausen, *ChemPhysChem* **2014**, 15, 3608-3613.
- [201] A. Baniodeh, *Cooperative effects in non-cyclic and cyclic FeIII/4f coordination clusters*, Karlsruher Institute of Technology (KIT), PhD Thesis (KIT) (Karlsruhe), **2013**.

- [202] N. F. Chilton, D. Collison, E. J. McInnes, R. E. Winpenny, A. Soncini, *Nat. Commun.* **2013**, 4, 2551.
- [203] B. N. Figgis, G. B. Robertson, *Nature* **1965**, 205, 694-695.
- [204] P. Albore, E. Rentschler, *Inorg. Chem.* **2008**, 47, 7960-7962.
- [205] A. N. Georgopoulou, Y. Sanakis, A. K. Boudalis, *Dalton Trans.* **2011**, 40, 6371-6374.
- [206] H. Kaemmerer, V. Mereacre, A. M. Ako, S. Mameri, C. E. Anson, R. Clérac, A. K. Powell, *Chem. Eur. J.* **2021**, 27, 15095-15101.
- [207] H. Kaemmerer, *Assisting Self-Assembly of 3d/4f Coordination Clusters*, Karlsruher Institute of Technology (KIT), PhD Thesis (KIT) (Karlsruhe), **2022**.
- [208] J. Weyandt, *Ultrafast Relaxation Dynamics of Fe-Ln Complexes*, Karlsruher Institute of Technology (KIT), Master Thesis (KIT) (KIT), **2024**.
- [209] A. Kebede, A. K. Singh, P. K. Rai, N. K. Giri, A. K. Rai, G. Watal, A. V. Gholap, *Lasers Med. Sci.* **2013**, 28, 579-587.
- [210] Y. P. He, Y. M. Miao, C. R. Li, S. Q. Wang, L. Cao, S. S. Xie, G. Z. Yang, B. S. Zou, C. Burda, *Phys. Rev. B* **2005**, 71, 125411
- [211] N. Varga, M. Smiesko, X. Jiang, R. P. Jakob, B. Wagner, T. Muhlethaler, P. Datwyler, P. Zihlmann, S. Rabbani, T. Maier, O. Schwardt, B. Ernst, *Angew. Chem. Int. Ed.* **2024**, 63, e202406024.
- [212] J. Leier, *Transiente Untersuchungen zu Ladungstransferprozessen photoangeregter Moleküle in Lösung im UV-Vis-NIR Bereich*, Karlsruhe Institute of Technology (KIT), PhD Thesis (KIT) (Karlsruhe), **2021**.
- [213] R. Berera, R. van Grondelle, J. T. Kennis, *Photosynth. Res.* **2009**, 101, 105-118.
- [214] N. C. Michenfelder, *Zeitaufgelöste Untersuchungen anorganischer Verbindungen in Lösung im UV-Vis-NIR-Bereich*, Logos Verlag Berlin GmbH, **2020**.
- [215] B. Valeur, M. N. Berberan-Santos, *Molecular fluorescence: principles and applications*, Wiley VCH, **2012**.
- [216] W. Rodriguez-Cordoba, L. Gutierrez-Arzaluz, F. Cortes-Guzman, J. Peon, *Chem. Commun.* **2021**, 57, 12218-12235.
- [217] S. Imatomi, T. Sato, T. Hamamatsu, R. Kitashima, N. Matsumoto, *Bull. Chem. Soc. Jpn.* **2007**, 80, 2375-2377.

- [218] S. Sold, B. C. Mummaneni, N. C. Michenfelder, Y. Peng, A. K. Powell, A. N. Unterreiner, G. Lefkidis, W. Hübner, *ChemistryOpen* **2022**, *11*, e202100153.
- [219] Y. F. Schneider, *Supramolecular Chemical Approach to Steering the Toroidal Properties of Dysprosium Triangles*, Karlsruher Institute of Technology (KIT), Master Thesis (KIT) (Karlsruhe), **2022**.
- [220] M. Gebrezgiabher, S. Schlittenhardt, C. Rajnak, J. Kuchar, A. Sergawie, J. Cernak, M. Ruben, M. Thomas, R. Boca, *RSC Adv.* **2022**, *12*, 21674-21680.
- [221] K. Binnemans, *Coord. Chem. Rev.* **2015**, *295*, 1-45.
- [222] J. Braun, D. Seufert, C. E. Anson, J. Tang, A. K. Powell, *Int. J. Mol. Sci.* **2023**, *25*, 264.
- [223] B. Li, S.-Q. Zang, L.-Y. Wang, T. C. W. Mak, *Coord. Chem. Rev.* **2016**, *308*, 1-21.
- [224] R. Busch, A. B. Carter, K. F. Konidaris, I. A. Kuhne, R. Gonzalez, C. E. Anson, A. Powell, *Chem. Eur. J.* **2020**, *26*, 11835-11840.
- [225] S. G. Balasubramani, G. P. Chen, S. Coriani, M. Diedenhofen, M. S. Frank, Y. J. Franzke, F. Furche, R. Grotjahn, M. E. Harding, C. Hattig, A. Hellweg, B. Helmich-Paris, C. Holzer, U. Huniar, M. Kaupp, A. Marefat Khah, S. Karbalaee Khani, T. Muller, F. Mack, B. D. Nguyen, S. M. Parker, E. Perlt, D. Rappoport, K. Reiter, S. Roy, M. Ruckert, G. Schmitz, M. Sierka, E. Tapavicza, D. P. Tew, C. van Wullen, V. K. Voora, F. Weigend, A. Wodynski, J. M. Yu, *J. Chem. Phys.* **2020**, *152*, 184107.
- [226] TURBOMOLE V7.5 2020, a development of University of Karlsruhe and Forschungszentrum Karlsruhe GmbH, 1989-2007, TURBOMOLE GmbH, since 2007; available from <https://www.turbomole.org>.
- [227] M. Bursch, E. Caldeweyher, A. Hansen, H. Neugebauer, S. Ehlert, S. Grimme, *Acc. Chem. Res.* **2019**, *52*, 258-266.
- [228] J. Zheng, X. Xu, D. G. Truhlar, *Theor. Chem. Acc.* **2010**, *128*, 295-305.
- [229] T. Bodenstein, K. Fink, A. Heimermann, C. van Wüllen, *Chem. Phys. Chem.* **2022**, *23*, e202100648.
- [230] H. Khanmohammadi, M. Erfantalab, *Spectrochim. Acta A* **2012**, *86*, 39-43.
- [231] R. Centore, M. Causà, S. Fusco, A. Carella, *Cryst. Growth Des.* **2013**, *13*, 3255-3260.
- [232] H. D. Flack, *Helv. Chim. Acta* **2003**, *86*, 905-921.

- [233] M. M. Deegan, M. R. Dworzak, A. J. Gosselin, K. J. Korman, E. D. Bloch, *Chem. Eur. J.* **2021**, *27*, 4531-4547.
- [234] A. L. Spek, *Acta Crystallogr. C* **2015**, *71*, 9-18.
- [235] L. Natrajan, J. Pecaut, M. Mazzanti, *Dalton Trans.* **2006**, 1002-1005.
- [236] B. Zhang, X. Zheng, H. Su, Y. Zhu, C. Du, M. Song, *Dalton Trans.* **2013**, *42*, 8571-8574.
- [237] S. K. Langley, B. Moubaraki, K. S. Murray, *Inorg. Chem.* **2012**, *51*, 3947-3949.
- [238] R. Janicki, P. Starynowicz, A. Mondry, *Eur. J. Inorg. Chem.* **2011**, *2011*, 3601-3616.
- [239] Y. Kanazawa, M. Kamitani, *J. Alloys Compd.* **2006**, *408-412*, 1339-1343.
- [240] S. Xue, P. Xing, J. Zhang, Y. Zeng, Y. Zhao, *Chem. Eur. J.* **2019**, *25*, 7426-7437.
- [241] G. M. Sheldrick, *Acta Crystallogr. A* **2008**, *64*, 112-122.
- [242] G. M. Sheldrick, *Acta Crystallogr. C* **2015**, *71*, 3-8.
- [243] O. V. Dolomanov, A. J. Blake, N. R. Champness, M. Schröder, *J. Appl. Cryst.* **2003**, *36*, 1283-1284.
- [244] C. F. Macrae, I. Sovago, S. J. Cottrell, P. T. A. Galek, P. McCabe, E. Pidcock, M. Platings, G. P. Shields, J. S. Stevens, M. Towler, P. A. Wood, *J. Appl. Crystallogr.* **2020**, *53*, 226-235.
- [245] J. W. Meringdal, A. Kilian, W. C. Li, M. J. B. Heinemann, M. Rausch, T. Schneider, D. Menche, *J. Org. Chem.* **2022**, *87*, 9375-9383.
- [246] E. Fischer, A. Speier, *Eur. J. Inorg. Chem.* **1895**, *28*, 3252-3258.
- [247] P. Q. Chan, Y. K. Lee, N. A. Rahman, *Asian J. Org. Chem.* **2018**, *7*, 707-710.
- [248] Y.-A. Liu, C.-Y. Wang, M. Zhang, X.-Q. Song, *Polyhedron* **2017**, *127*, 278-286.

10. Curriculum Vitae

Personal Details

Name: Yannik Schneider

Nationality: German

Education

09/2008 – 06/2016 Wilhelmi-Gymnasium, Sinsheim

Allgemeine Hochschulreife

10/2016 – 10/2017 Karlsruhe Institute of Technology

Bachelor program in Computer Science, KIT. Switched to the Bachelor of Chemistry after two semesters.

10/2017 – 10/2020 Karlsruhe Institute of Technology

Bachelor Chemie, Mark: 1.3

10/2020 – 10/2022 Karlsruhe Institute of Technology

Master Chemie, Mark: 1.1 (with distinction)

since 01/2023 PhD student under the supervision of Prof. Annie K. Powell, Karlsruhe Institute of Technology at the Institute of Nanotechnology (INT) using a Landesgraduiertenförderungsstipendium until 03/2025

Association with Project B4 of the CRC 1573 “4f for Future” (4f4f)

One-week stay at the University of Florence hosted by Prof. Dr. Mauro Perfetti 10/2023.

Supervision of IRES scholar Katie Vogt from Doane University, Nebraska (USA) for 2 months.

Extracurricular Activities

2021 – 2023 Personal tutoring in chemistry and math for students from 8-12th grade and in training to become a CTA (Chemisch Technische/r Assistant/in)

Conference Attendances

09/2022	Schau-Ins-Land Meeting in 2022 in Wildberg, oral contribution
09/2022	Koordinationschemietreffen (KCT) 2022 in Jena, poster presentation
10/2022	3MET Abschlusskonferenz in Heidelberg
03/2023	4f4f CRC Spring Seminar Days hosted at KIT, oral contribution.
09/2024	Schau-Ins-Land Meeting in 2024 in Michelbach, oral contribution
10/2024	Innovative Minds & Inclusive Science, Birthday Symposium dedicated to Prof. Dr. Annie K. Powell on the occasion of her 65 th Birthday, member of the organising committee

11. List of Publications

1. Y. Peng, J. Braun, M. Schulze, H. Kaemmerer, Y. F. Schneider, C. E. Anson, W. Wernsdorfer, A. K. Powell, Dalton Trans., „A nested spin structure and single molecule magnet behaviour in an Fe₈Dy₁₂ heterometallic cyclic coordination cluster”, **2024**, *53*, 894-897.
2. T. Ruppert, J. Mutschler, S. Schlittenhardt, Y. F. Schneider, M. Schulze, O. Fuhr, C. E. Anson, M. Ruben, W. Wernsdorfer, J. Braun, O. Waldmann, A. K. Powell, „Hard Magnetic Hysteresis in a Decorated Dy₃ Triangle“, **in preparation**.
3. J. Mutschler, T. Ruppert, Y. Peng, S. Schlittenhardt, Y. F. Schneider, J. Braun, C. E. Anson, J. Ollivier, Q. Berrod, J. Zanotti, M. Ruben, A. K. Powell, O. Waldmann, „Finding Lanthanide Magnetic Anisotropy Axes in 3d-4f Butterfly Single Molecule Magnets Using Inelastic Neutron Scattering”, **submitted**.
4. Y. F. Schneider, C. Pachi, A. Sunil, J. Braun, S. Paul, S. Schlittenhardt, T. Ruppert, C. E. Anson, M. Ruben, K. Flink, W. Wernsdorfer, A. K. Powell, „Using Halogens to Tune the Toroidicity in Dy₃ Triangles”, **in preparation**.
5. Y. F. Schneider, J. Braun, S. Paul, L. Tacconi, J. Arneth, C. E. Anson, M. Ruben, W. Wernsdorfer, A. Soncini, R. Klingeler M. Perfetti, A. K. Powell, „Observing chirality selection in a highly symmetric Dy₃ Single molecule Toric”, **in preparation**.
6. J. Braun, Y. Peng, T. Yadav, A. B. Carter, Y. F. Schneider, N. Leblanc, C. E. Anson, K. Fink, A. K. Powell, “How to stabilise a neutral radical ligand using complexation to 3d metal ions and supramolecular interactions”, **in preparation**.
7. F. K. Al-Zeidaneen, Y. F. Schneider, D. Westerbeck, S. Schlittenhardt, N. Suryadevara, R. F. Pflieger, T. Ruppert, O. Fuhr, G. Abbas, S. Malik, C. E. Anson, J. Braun, J. Schnack, A. K. Powell, “A cone shaped Fe₄Ln₄ complex in which an Fe₄ propeller steers the spin structure”, **in preparation**

12. Acknowledgments

First and foremost, I want to thank my supervisor Prof. Dr. Annie Powell for giving me the opportunity to do my PhD in her working group. Under her excellent supervision and guidance and on a topic which not only spikes my interests both regarding physical chemistry and synthetic work in the lab I was able to have the experience of autonomously working on a research topic but also had the opportunity to always ask for help, inspiration and in general assistance whenever I felt stuck.

I want to thank Dr. Christopher Anson for his help with the refinement of all my crystal structures which due to the quality of the crystals in a lot of cases was not easy. I am very grateful for all the support and advice he gave me. I gladly offered my assistance for his “Klausur” and the “Praktikum” since it was always great fun, even the boring bits.

I also want to thank Dr. Olaf Fuhr and Prof. Dr. Dieter Fenske for helping me measure single crystal data on all my structures. One especially big thank you to Dieter who really went the extra mile for some of my less well-behaved compounds to get a usable data set. Even if the sample was not suitable for SCXRD measurements I could always count on Dieter giving me some advice in what to try next to maybe improve the synthesis in terms of crystal quality of the product.

For being a good friend to share a lab, an office or a vacation with I want to thank Dr. Jonas Braun who had an immense influence on my academic journey and life in general. A big thanks for proofreading my thesis of course and for any motivation and help with any questions I had.

I also want to thank Prof. Dr. Mauro Perfetti and Leonardo Tacconi for their hospitality during my visit to Florence and their expertise for measuring my torque of my samples.

I want to thank the whole Powell group, present and past, especially Dr. Thomas Ruppert, Dr. Hagen Kämmerer, Dr. Rouven Pflieger and Daniel Seufert for making the group a welcoming and fun place to work in.

For their help with microSQUID measurements I want to thank Dr. Paul Sagar and Appu Sunil and for helping me with SQUID measurements I want to thank Dr. Sören Schlittenhardt.

I also want to thank Dr. habil. Benjamin Flavel and his group for their assistance and cooperation when lab space got scarce. The time in the lab together was really enjoyable and the good company made the work area we had appear a lot more spacious.

A big thank you to Gertraud Amschlinger for supporting me throughout everything bureaucracy related.

I also want to thank friends and family who have supported me during stressful times. I especially want to thank Svenja Graf for her support and proof reading of the thesis. It is always reassuring to know that there are people who I can rely on and who have my back.

13. Appendices

13.1 Table of Figures

1	Jablonski diagram with coloured arrows showing possible radiation induced processes.	8
2	Packing of ice XIX along the crystallographic c axis. Shading of hydrogen atoms corresponds to occupancy. Reprinted with permission from reference ^[68] [Springer Nature] copyright [2021].	10
3	Benzene as an example of an electron-rich aromatic system with electrostatic potential surfaces calculated using DFT and a scheme showing the electronegative and electropositive regions. Adapted from reference with permission from reference ^[62] [Royal Society of Chemistry] copyright [2012].	11
4	Off-centre parallel stacking and edge-to-face interactions as favoured and face-cantered stacking as disfavoured orientations between π - π stacked moieties. Adapted from reference with permission from reference ^[62] [Royal Society of Chemistry] copyright [2012].	12
5	Electrostatic potentials of $\text{CH}_3\text{F}_n\text{Br}$ (bottom) and CF_3X with $\text{X} = \text{F}, \text{Br}, \text{Cl}, \text{I}$ (top) and their influence on the strength of associated halogen bonds. Adapted with permission from reference ^[84] [Springer] copyright [2007] and from reference ^[85] [Royal Society of Chemistry] copyright [2013].	13
6	Geometries in Type I halogen-halogen interactions and Type II halogen-halogen bonds.	14
7	Orbital overlap in strict Type II geometry (left) and the two contributions from weaker overlap in the Type I geometry (middle and right) in FBr. Purple and green indicate opposite signs of the wavefunction. Adapted with permission from reference ^[42] [American Chemical Society] copyright [2022]	14
8	ELF along two planes through a water molecule.	15
9	Paramagnetic (left) and diamagnetic (right) material in a magnetic field. Field lines as black arrows. Adapted from reference ^[44] .	15
10	Temperature dependence of χ for diamagnetic and paramagnetic materials. Adapted from reference ^[44] .	16
11	Types of collective magnetism and the orientation of spins associated with them.	17
12	χ against T (top left), χT against T (top right), and $1/\chi$ against T (Curie-Weiss plot) (bottom) for para-, ferro-, ferri-, and antiferromagnetic materials. Adapted from reference ^[44] .	18
13	Magnetic hysteresis in blue with new curve in red. M_R is the magnetic remanence, M_S the saturation magnetisation, H_C the coercive field and H_S the saturation field. ^[44]	19
14	Double well potential and population of states for the example of a 3d ion-containing SMM in zero field (a), with an applied field (b) and after the external field is switched off (c). Adapted with permission from reference ^[63] [John Wiley & Sons] copyright 2003].	20

15	4 f electron densities approximation for Ln^{III} ions. Adapted with permission from reference ^[66] [Royal Society of Chemistry] copyright [2011].	21
16	Illustrations of the low- and high-energy arrangements of 4f-orbital electron density in relation to the crystal field environment for a 4f ion with oblate (left) and prolate (right) electron density distributions. Adapted with permission from reference ^[66] [Royal Society of Chemistry] copyright [2011].	22
17	Illustration of direct process (left) and Raman process (right). Adapted with permission from reference ^[79] [Royal Society of Chemistry] copyright [2021].	23
18	Relaxation time τ against temperature, showing τ_{switch} and T_B^{100} . Adapted with permission from reference ^[87] [Elsevier] copyright [2020].	24
19	Influence of different effects on the splitting of electronic states in lanthanide ions and their respective energies. Adapted from reference ^[123] .	25
20	Molecular structure of dysprosocenium-type high temperature SMMs. ^[107-108]	26
21	Ferromagnetic arrangement of Ising spins in a triangular metal core (left). Spin frustration in different geometries for antiferromagnetic coupling (right). Adapted with permission from reference ^[114] [Royal Society of Chemistry] copyright [2000]	27
22	Toroidal clockwise (C) and anticlockwise (A) arrangement of spins in a triangular and a square core.	28
23	Formation of a toroidal moment T (green arrow) as a consequence of a poloidal electric current J (blue arrows) which induces a toroidal magnetic field B (left) or resulting from head to tail arrangement of spins S (red arrows) in a vortex in-plane formation around a centre with the radius r (right). Adapted from reference ^[158] .	28
24	Combination of toroidal dipole and electric dipole forming an anapole. Adapted with permission from reference ^[123] [Springer] copyright [2019].	29
25	The four primary ferroic orders and their symmetry regarding space-inversion or time-reversal. Reprinted with permission from reference ^[125] [Science Direct] copyright [2019].	31
26	Molecular structure of the original toroidal Dy_3 with tangential in-plane arrangements of anisotropy axes (red arrows). Reprinted with permission from reference ^[128] [John Wiley & Sons] copyright [2008].	31
27	Planar Dy_4 with anisotropy axes as green arrows in a), reprinted with permission from reference ^[145] [American Chemical Society] copyright [2012], cubane Dy_4 with anisotropy axes in core below in b), reprinted with permission from reference ^[165] [John Wiley & Sons] copyright [2018], and tetrahedral Dy_4 with anisotropy axes as green arrows in c), reprinted with permission from reference ^[166] [Royal Society of Chemistry] copyright [2022].	33
28	Dy_3+Dy_3 with SCN^- ligands (left) with one anisotropy axis out of plane and in-plane arrangement of spins for Dy_3+Dy_3 with water ligands (right). Adapted with permission from reference ^[180] [Royal Society of Chemistry] copyright [2015] (left) and from reference ^[172] [Royal Society of Chemistry] copyright [2016] (right).	33
29	Molecular structure and orientation of anisotropy axes with microSQUID for Zn_3Dy_3 in a), adapted with permission from reference ^[168] [American Chemical	34

	Society] copyright [2016], and for Dy ₃ Cr ₃ in b), adapted with permission from reference ^[171] [Elsevier B.V.] copyright [2022].	
30	Dy ₆ by Murray <i>et al.</i> in a) by Powell <i>et al.</i> in b). Adapted with permission from reference ^[154] [American Chemical Society] copyright 2012 in a) and adapted with permission from reference ^[26] [Royal Society of Chemistry] copyright [2015] in b).	35
31	Toroidal Tb ₃ in a), Ho ₃ in b) and Tb ₄ in c). Adapted with permission from reference ^[160] [Royal Society of Chemistry] copyright [2019] a) and b). Adapted with permission from reference ^[163] [Royal Society of Chemistry] copyright [2022] in c).	35
32	Structure and orientation of anisotropy axes with microSQUID for CrDy ₆ (top), adapted with permission from reference ^[135] [Springer] copyright [2017], CuDy ₃ polymer (middle), adapted with permission from reference ^[134] [Royal Society of Chemistry] copyright [2012], and Fe ₁₈ Dy ₆ (bottom), adapted with permission from reference ^[136] [American Chemical Society] copyright [2020].	36
33	Molecular structures and anisotropy axes of Ln ions in top-down view of Tb ₆ Cu ₆ (left) and Fe ₈ Dy ₈ (right). Adapted with permission from reference ^[146] [Royal Society of Chemistry] copyright [2018] left and with permission from reference ^[172] [Elsevier Inc.] copyright [2020] right.	36
34	MicroSQUID in-plane and perpendicular to the triangle plane a) reprinted with permission from reference ^[35] [John Wiley & Sons] copyright [2006], magnetisation with inset of low field range b), Zeeman diagrams for an applied field in and out of the plane of the triangle in c) and d) for the Dy ₃ with α -vanillin ligands by Powell <i>et al.</i> , reprinted with permission from reference ^[38] [Royal Society of Chemistry] copyright [2009].	38
35	Scheme showing the body and wingtip positions of a butterfly type structure in a), core of a Type I in b) and core of a Type II butterfly in c). Reprinted with permission from reference ^[22] [John Wiley & Sons] copyright [2021].	39
36	Possible modifications on the Fe ₂ Ln ₂ testbed system on the example of [Fe ₂ Dy ₂ (μ_3 -OH) ₂ (teaH) ₂ (O ₂ CPh) ₄ (NO ₃) ₂]-6MeCN. Adapted from reference with permission ^[20] [John Wiley & Sons] copyright [2021].	40
37	Synthesis and molecular structures of the Fe ₂ Ho ₂ by Christou <i>et al.</i> and the Fe ^{III} triangle precursor. ^[19]	41
38	Molecular structures of Cr ₂ Dy ₂ butterflies with benzoate as co-ligand and dea ²⁻ in a), Et-dea ²⁻ in b), ⁿ Bu-dea ²⁻ in c), teaH ²⁻ in d) as ligand. Reprinted with permission from reference ^[22] [Elsevier Inc.] copyright [2021].	42
39	Molecular structure of Fe ₁₀ Dy ₁₀ with Me-tea ³⁻ and Me-teaH ²⁻ ligands with a top- (left) and sideview (right). ^[185]	43
40	Molecular structure of Fe ₈ Dy ₁₂ (left) and building blocks making up the Fe ₈ Dy ₁₂ (top right) and Fe ₁₀ Dy ₁₀ (bottom right) with differences marked as pale Fe ^{III} or Dy ^{III} ions. Reproduced from reference ^[34] .	44
41	Three sets of anisotropy axes from the MAGELLAN ^[202] analysis of Fe ₈ Dy ₁₂ marked in different colours. Reprinted from reference ^[34] .	45
42	Molecular structure of Fe ₁₆ Dy ₄ with view from the top and side of the molecule. ^[33]	45

43	Molecular structure of an Fe ₃ precursor. Adapted with permission from reference ^[20] [John Wiley & Sons] copyright [2021].	46
44	Diethanolamine based ligand and benzoic acid which can be varied by substitution at the highlighted positions.	47
45	Molecular structure of ethanolamine type ligands used for Fe ₂ Dy ₂ butterflies.	49
46	Molecular structures of (Fe₂Dy₂-2) (left) and (Fe₂Dy₂-3) (right).	51
47	Experimental and simulated powder patterns (left) and IR spectra (right) for compounds (Fe₂Dy₂-2) and (Fe₂Dy₂-3).	51
48	Scheme showing the packing of the core structures of (Fe₂Dy₂-2) and (Fe₂Dy₂-3) along the crystallographic a (left), b (middle) and c (right) axes.	52
49	Intermolecular interactions in (Fe₂Dy₂-2) showing hydrogen bonds as dotted orange lines.	53
50	Molecular structures of (Fe₂Dy₂-4) (left) and (Fe₂Dy₂-5) (right).	53
51	Experimental and simulated powder patterns (left) and IR spectra (right) for compounds (Fe₂Dy₂-4) and (Fe₂Dy₂-5).	54
52	Packing represented by the arrangement of the core structures along the crystallographic a (left), b (middle) and c (right) axis for (Fe₂Dy₂-4) and (Fe₂Dy₂-5).	54
53	Intermolecular interactions for (Fe₂Dy₂-4) and (Fe₂Dy₂-5) on the example of (Fe₂Dy₂-4). Classical and non-classical hydrogen bonds indicated by orange dotted lines.	55
54	Molecular structures of (Fe₂Dy₂-6) (left) and (Fe₂Dy₂-7) (right).	56
55	Simulated and experimental powder pattern (left) and IR spectra (right) of (Fe₂Dy₂-6) and (Fe₂Dy₂-7).	57
56	Packing of (Fe₂Dy₂-6) along the crystallographic a (top), b (middle) and c (bottom) axis. Hydrogen bonding in the ac plane indicated as orange dotted lines (middle).	58
57	Packing of (Fe₂Dy₂-7) along the crystallographic a (top), b (middle) and c (bottom) axis with hydrogen bonds shown as orange dotted lines. Hydrogen bonds in picture showing the view along the b axis omitted for clarity.	59
58	Scheme showing the experimental set-up for the femtosecond transient absorption spectroscopy measurements performed on the Fe-Ln complexes.	63
59	Possible transitions stimulated by the probing pulls (dotted arrows) after excitation of the sample (orange arrow). ^[195]	64
60	UV-Vis spectra for (Fe₂Dy₂-1) before and after the transient absorption spectroscopy measurements.	64
61	Transient absorption spectra for (Fe₂Dy₂-1) in DMF for delay times from 200 fs to 5 ps.	65
62	Single transient absorption spectrum for (Fe₂Dy₂-1) with fit.	65
63	Single transient of the measured Fe ₂ Dy ₂ samples in DMF. 1 mm quartz glass cuvette, 330 nm/0.5-0.75 μJ pump pulse, 550-560 nm probe pulse.	66
64	Ring structure of Fe ₁₀ Ln ₁₀ (left) with repeating unit (top right) and "standing wave" structure alternating above and below the mean plane of the metal ions (bottom right). ^[34]	69
65	Distances d ₁ and d ₂ used for calculation of compression factor ε on the example of Fe ₁₀ Dy ₁₀ using teaH ₃ ligands.	70

66	Differences in ellipticity of the three different solvates of Fe ₁₀ Dy ₁₀ with teaH ₃ ligands crystallised from DMF (left), MeCN (middle) and MeOH/acetone (right). Ellipticity quantified with compression factor.	70
67	Molecular structure of (Fe₁₀Dy₁₀-9) (left) with sideview (bottom right). Hydrogen atoms were omitted for clarity.	72
68	Arrangement of the molecular units making up the unit cell with a Z of two.	73
69	The two molecules of (Fe₁₀Dy₁₀-9) in the unit cell with mean planes through the metal atoms of each ring shown in blue.	73
70	Distances used to calculate the compression factor for both triangles in the unit cell of (Fe₁₀Dy₁₀-9).	74
71	Packing of (Fe₁₀Dy₁₀-9) along the crystallographic a (top), b (middle) and c (bottom) axis.	75
72	Experimental and simulated powder pattern for (Fe₁₀Dy₁₀-9).	76
73	Experimental powder diffractograms for compounds (Fe₁₀Dy₁₀-9) to (Fe₁₀Ho₁₀-12).	77
74	Molecular structure of (Fe₁₀Tb₁₀-15) (right), sideview (left).	77
75	$\chi_M T$ vs T plot for (Fe₁₀Dy₁₀-9) measured at 0.1 T with an inset showing the low temperature range.	78
76	Curie-Weiss plot of (Fe₁₀Dy₁₀-9) and Curie-Weiss fit (red line).	79
77	χ_M' against f (left) and χ_M'' against f (right) for (Fe₁₀Dy₁₀-9), lines are a guide to the eyes.	79
78	M vs B plot for (Fe₁₀Dy₁₀-9) with an inset of the reduced magnetisation plot.	80
79	MicroSQUID data for (Fe₁₀Tb₁₀-15) at a sweep rate of 16 mT/s at different temperatures (left) and at 30 mK with varying sweep rates (right).	81
80	MicroSQUID data for Fe ₁₀ Dy ₁₀ at a sweep rate of 16 mT/s at different temperatures (left) and at 30 mK with varying sweep rates (right). ^[185]	81
81	UV-Vis spectra before and after transient absorption experiment for compound (Fe₁₀Dy₁₀-13) in water.	82
82	UV-Vis spectra of compounds (Fe₁₀Dy₁₀-13) – (Fe₁₀Dy₁₀-17) in aqueous solution.	83
83	Transient absorption spectrum for (Fe₁₀Dy₁₀-13).	83
84	Single transient absorption spectrum at 549.87 nm for (Fe₁₀Tb₁₀-15) with fit.	84
85	Single transient absorption spectra for compounds (Fe₁₀Dy₁₀-13), (Fe₁₀Tm₁₀-14) and (Fe₁₀Tb₁₀-15). 321 nm/ 0.6 μ J pump pulse, probed at 553.11 nm for (Fe₁₀Dy₁₀-13), 330 nm/ 0.74 μ J pump pulse, probed at 552.02 nm for (Fe₁₀Tm₁₀-14), 321 nm/ 0.44 μ J pump pulse, probed at 549.87 nm for (Fe₁₀Tb₁₀-15). Measured in H ₂ O solution in a 1 mm quartz glass cuvette.	85
86	Single transient absorption spectra for compounds (Fe₁₀Dy₁₀-16) and (Fe₁₀Dy₁₀-17). 321 nm/ 0.5 μ J pump pulse, probed at 554.21 nm for (Fe₁₀Dy₁₀-16), 321 nm/ 0.5 μ J pump pulse, probed at 548.8 nm for (Fe₁₀Dy₁₀-17). Measured in H ₂ O solution in a 1 mm quartz glass cuvette.	86
87	Molecular structure of (Fe₈Dy₁₂-18). Reprinted with permission from reference ^[36] [Royal Society of Chemistry] copyright 2024.	88
88	Simulated and experimental powder pattern for (Fe₈Dy₁₂-18).	89
89	UV-Vis spectra from 200 to 800 nm of compounds (Fe₈Dy₁₂-18) and (Fe₁₀Dy₁₀-16) measured in aqueous solution.	90

90	Simulated powder pattern for (Fe₈Dy₁₂-18) and experimental powder pattern for (Fe₈Ho₁₂-19).	91
91	Molecular structure of (Fe₁₆Tb₄-20) (left) with magnetisation data (right). Adapted with permission from reference ^[33] [Royal Society of Chemistry] copyright [2011].	92
92	Crystals of compound (Fe₁₆Tb₄-20) with approximate dimensions.	92
93	MicroSQUID measurement, temperature dependence at 16 mT/s (top left) with first derivative (top left), sweep rate dependence (bottom left) and temperature dependence zoomed in (bottom right).	93
94	Molecular structure of the o-van ligand (left) and the archetypal Dy ₃ compound (right). ^[35]	97
95	Different ligand modifications and the Dy ₃ structure that can be obtained by using them. Dy ₃ structures with Schiff base ligands by Tang <i>et al.</i> in a) ^[166] and b). Dy ₃ by Thomas Ruppert in c) ^[165] and from my Master thesis in d). ^[219]	98
96	Molecular structure of o-vanillin with the modifiable positions highlighted.	99
97	Structure of one formula unit of (Dy₃-21) consisting of two triangle moieties (left and middle) where the disorder was omitted for clarity. Asymmetric unit of (Dy₃-21) with the disorder indicated by paler coloured atoms and hydrogen bond as orange dotted line. ^[203]	101
98	Molecular structure of (Dy₃-22). ^[203]	101
99	Halogen bonding in (Dy₃-21) (a) and in (Dy₃-22) (b) with the important angles and distances highlighted (only one example of the halogen bonds is shown here for each molecule). ^[203]	102
100	Packing of (Dy₃-21) along the crystallographic a (top left), b (right) and c (bottom left) axes.	103
101	Packing of (Dy₃-22) along the crystallographic a (top left), b (top right) and c (bottom left) axes. Additional view of the packing along the crystallographic a-b vector showing the strong presence of halogen bonds throughout the crystal lattice. Halogen bonds indicated by orange dotted lines.	104
102	Molecular structure of (Dy₃-23).	105
103	Experimental powder patterns for compounds (Y₃-24) to (Tm₃-28) compared to simulated pattern for (Dy₃-21).	106
104	Experimental and simulated powder pattern for (Dy₃-22) with experimental powder patterns of compounds (Y₃-29) to (Lu₃-35).	107
105	Molecular structure of (Dy₃-36), Cl ⁻ counterion was omitted.	108
106	Halogen bonding in (Dy₃-36).	108
107	Packing for (Dy₃-36) along the crystallographic a (top left), b (bottom left) and c (right) axis.	109
108	Simulated and experimental powder pattern for (Dy₃-36) as well as experimental powder patterns for compounds (Ho₃-37) and (Er₃-38).	110
109	$\chi_M T$ vs T (left) and $1/\chi_M$ vs T with Curie-Weiss fit (right) for (Dy₃-21), (Dy₃-22) and (Dy₃-36) measured at 0.1 T.	111
110	AC in-phase (left) and out-of-phase (right) data for (Dy₃-36) in a), (Dy₃-21) in b) and (Dy₃-22) in c).	112

111	M vs B plots for (Dy₃-36) (top), (Dy₃-21) (middle) and (Dy₃-22) in (bottom) with insets of the first derivative of the magnetisation at 2K with the maxima highlighted.	114
112	MicroSQUID measurements at varying temperatures at a sweep rate of 8 mT/s (left) and first derivative (right) for (Dy₃-36) in a), (Dy₃-21) in b) and (Dy₃-22) in c).	116
113	MAGELLAN ^[202] analysis of (Dy₃-36) in a), (Dy₃-22) in b) and (Dy₃-21) in c).	117
114	Sweep rate dependent microSQUID measurements at 30 mK for (Dy₃-36) in a), (Dy₃-21) in b) and (Dy₃-22) in c).	118
115	Electron localization function mapped on a molecule of (Dy₃-36) (Cl) a), (Dy₃-21) (Br) b) and (Dy₃-22) (I) c) with their halogen bonding counterparts highlighted by yellow circles. The red areas suggest localized electrons, whereas white is delocalised (free electron gas) and blue an electron localisation probability of zero. The images shown above were modified from the original calculated results for better visual representation focusing on the electron density around the halogen bonds.	120
116	Model for halogen bond calculations. The position of the Na is fixed.	121
117	Energy decomposition analysis for (Dy₃-36), (Dy₃-21) and (Dy₃-22). Negative energies correspond to attractive contributions and positive energies refer to repulsion, demonstrating the fine balance between attractive and repulsive forces in the Br-analogue.	122
118	MAGELLAN ^[202] (cyan) and CASOCl (green) results for (Dy₃-21) of an isolated triangle (left) and with Cl ⁻ ions in proximity taken into account (right). Some molecular components discoloured.	123
119	Zero field splitting and g tensors for the ground state of (Dy₃-21) with the extra Cl ⁻ ligand from neighbouring molecules considered and without (bare).	124
120	Reaction conditions and molecular components for the synthesis of the azo-coupled ligands <i>p</i> -Cl-pdavan using <i>para</i> -Cl-anillin and <i>p</i> -Br-pdavan using <i>para</i> -Br-anillin.	125
121	a) ¹ H-NMR of <i>p</i> -Cl-pdavan with H atoms labelled in the molecular structure; b) ¹ H-NMR spectrum of <i>p</i> -Cl-pdavan when too much base is added during the synthesis, shifting into three distinct multiplets highlighted.	126
122	Molecular structure of (Dy₃-39) (left) and (Dy₃-40) (right). Hydrogen atoms were omitted for clarity.	128
123	The other two inversion related triangles in (Dy₃-39) with unidentate nitrate ligand/water ligand disorder through inversion centre (cyan dot). The disorder was omitted for clarity.	128
124	Packing along crystallographic a (top), b (middle) and c (bottom) axis for (Dy₃-39).	130
125	Packing of (Dy₃-39) showing the layer structure.	131
126	Packing diagram of (Dy₃-39) highlighting the benzyl rings involved in the intermolecular π - π stacking.	131
127	Second set of π - π interactions in (Dy₃-39) highlighting the involved benzyl rings.	132
128	Halogen-nitrate interactions in (Dy₃-39).	132
129	Simulated and experimental powder pattern for (Dy₃-39).	133
130	Simulated and experimental powder pattern for (Dy₃-40).	134

131	Experimental powder patterns for compounds (Y₃-41), (Gd₃-42), (Tb₃-43), (Ho₃-44), (Er₃-45), (Tm₃-46), (Yb₃-47) and (Lu₃-48) compared to the simulation of (Dy₃-39).	134
132	IR spectra of compounds (Dy₃-39) to (Lu₃-48).	135
133	$\chi_M T$ vs T for (Dy₃-39) measured at 0.1 T.	136
134	Curie-Weiss plot and fit of (Dy₃-39).	136
135	χ_M' against f (left) and χ_M'' against f (right) for (Dy₃-39).	137
136	M vs B plot for (Dy₃-39) with an inset of the derivative dM/dB for the 2 K curve.	138
137	The two independent triangles of (Dy₃-39) with the anisotropy axes from MAGELLAN ^[202] as cyan lines.	139
138	Temperature dependent microSQUID measurements of (Dy₃-39) (top left) and derivative (bottom left), sweep rate dependent measurements (top right) with zoomed in excerpt (bottom right).	139
139	General reaction conditions and molecular components for the synthesis of the Schiff base ligands used in this section. R-CHO here refers to a benzaldehyde derivative.	140
140	Molecular structure of (Dy₃-49) and picture of crystals under a microscope.	142
141	Packing of (Dy₃-49) along the crystallographic a (left) and c (right) axes.	143
142	Connection of Dy ₃ moieties through hydrogen bonds between Cl and H-N (left), excerpt of two triangles these interactions highlighted (top right), hydrogen bonds between three 1/3 occupancy chloride counterions and the terminal MeOH ligands (bottom right).	144
143	Dy ₃ triangles in (Dy₃-49) indicated by blue, red, yellow and green polyhedra. Yellow and red as well as blue and green are the same enantiomer. Layers formed by blue and red, as well as green and yellow triangles (left) with the top down view showing how stacks result from overlaying the planes.	145
144	View along the crystallographic c axis showing only the planes made up of red and blue (left) and green and yellow (right) triangles.	145
145	Simulated and experimental powder pattern for (Dy₃-49).	146
146	Molecular structure of (Eu₃-52).	146
147	Molecular structure of (Yb₃-58). The disorder described above is removed for clarity.	147
148	Experimental powder pattern for compounds (Y₃-50), (Tb₃-54), (Ho₃-55), (Er₃-56) and (Tm₃-57) compared to the simulation of (Dy₃-49) and experimental pattern of (Sm₃-51), (Eu₃-52) and (Gd₃-53) compared to the simulation for (Eu₃-52) on the left and right respectively.	148
149	IR spectra of compounds (Dy₃-49) to (Tm₃-57).	149
150	MAGELLAN ^[202] analysis of (Dy₃-49) with anisotropy axes shown in cyan top (left) and side view (right).	150
151	$\chi_M T$ vs T for (Dy₃-49) measured at 0.1 T and 1 T.	150
152	χ_M^{-1} vs T plot with Curie-Weiss fit for (Dy₃-49).	151
153	χ_M' against f (left) and χ_M'' against f (right) for (Dy₃-49).	152
154	χ_M' against f (left) and χ_M'' against f (right) for (Dy₃-49) with an applied field of 0.81 T (top) and 1.75 T (bottom). For 1.75 T the lines are a guide to the eye, for 0.81 T a standard Debye model fit was used.	153

155	M vs B plot for (Dy₃-49) measured using a sweep rate of 40 Oe/s. The inset shows the derivative dM/dB for the 1.8 K curve highlighting the presence of a level crossing below 1 T.	154
156	MicroSQUID measurements on (Dy₃-49) at different temperatures with a sweep rate of 16 mT/s (top left), at different sweep rates with a temperature of 30 mK (top right), derivative field map (bottom left), angle dependent measurements (bottom right).	156
157	MicroSQUID measurements of (Dy₃-49) at different temperatures with a sweep rate of 16 mT/s with the field aligned with the plane of a triangle perpendicular to one anisotropy axis (left) and parallel to one of the axes (middle), in-plane and out of plane of the triangles microSQUID measurement for Dy ₃ with o-vanillin ligands (right), adapted with permission from reference ^[35] [John Wiley & Sons] copyright [2006].	157
158	MicroSQUID measurements of (Dy₃-49) at 30 mK with a sweep rate of 100 mT/s with the field aligned with the plane of a triangle and parallel to an anisotropy axis (top left), in the plane of the triangle and perpendicular to an anisotropy axis (top right) and perpendicular to the plane of the triangle (bottom left). Excerpt of angle dependent microSQUID measurements showing the angle dependence of the hysteresis width (bottom right) the blue curve (0°) corresponds to the measurement shown in the top left.	158
159	Schematic explanation of chirality selection with the two triangle orientations in the crystal of (Dy₃-49). B _{sw} is the switching field A and C are anticlockwise and clockwise, and FM is a ferromagnetic state. Red arrows indicate spins flipping through the change in applied field.	159
160	Scheme representing the two in-plane orientations of the magnetic fields intercepting the in-plane projection of the easy axes in the triangle (direction 1) and intermediate axis (direction 2) (top left), angle α and alignment of the Y lab axis with crystallographic c axis (top right), third axis perpendicular to the triangle plane (bottom). For all axes shown here (direction 1, 2 and perpendicular to the triangle plane) a Zeeman diagram is shown in Figure 161.	162
161	Zeeman levels for a field B parallel to the in-plane projection of one anisotropy axis (easy axis) of Dy ₃ in a), for B perpendicular to the in-plane projection of one easy axis of Dy ₃ (intermediate axis) in b), for B aligned with the crystallographic c-axis, and thus perpendicular to the Dy ₃ plane in c). Related microSQUID is shown in Figure 158 top left for a), top right for b) and bottom left for c).	163
162	Rotational axis (red dot, oriented into the paper plane) and direction of B field with θ being the angle the sample was rotated from the origin (aligned with B).	165
163	Scheme showing the orientation of the crystal lattice planes in relation to the B field (left). Picture of the chosen and indexed crystal on the cantilever under a microscope (right).	166
164	Magnetic torque measurement for (Dy₃-49) at 2 K and magnetic field between 1 T (red dots) and 9 T (blue dots). The first 0 for the torque is indicated by a blue line at 45°.	167

165	Magnetic torque measured for (Dy₃-49) at 5 K and 4 T to 6 T (left) and at 10 K with fields between 5 T to 7 T (right).	167
166	Crystal (triangular face indicating the lattice plane perpendicular to the c* axis) orientation in relation to the B field. Green and red stripe are visual aids for the experimental alignment of the crystal.	168
167	Magnetic torque measurement of (Dy₃-49) at 2 K and fields between 1 T and 9 T (left), representation of in-plane experimental axis (right). First zero at ca. 15° indicating a hard axis highlighted (blue line).	169
168	Magnetic torque measurements for (Dy₃-49) rotating in the ab plane with fields of 6 T to 9 T for the 5 K measurement (left) and 7 T to 9 T for the 10 K measurement (right).	169
169	High field modelling fit of magnetic torque measurements of (Dy₃-49) for both measured rotations (in a plane nearly containing the c axis (left) and rotation in ab' plane (right)).	170
170	Anisotropy axis (yellow arrows) for (Dy₃-49) obtained from magnetic torque measurements. Top-down view on Dy ₃ core along c* axis (left) and side view in the ab' plane (right).	171
171	Top (left) and side view (right) of the molecular structure of (Dy₃-59).	172
172	Packing along crystallographic a (top left), b (top right) and c (bottom left) axis as well as an additional view for (Dy₃-59).	173
173	Hydrogen bonds in plane (left), with solvent molecules (top right) and along chain (bottom right) for (Dy₃-59).	174
174	Simulated and experimental powder pattern for (Dy₃-59).	175
175	IR measurements immediately, 1 min and 5 minutes after taking the crystals of (Dy₃-59) out of the mother liquor.	176
176	Experimental powder pattern of compounds (Y₃-60) to (Yb₃-66) with simulation of (Dy₃-59) (top). IR spectra of compounds (Dy₃-59) to (Yb₃-66) (bottom).	177
177	Molecular structure of (Dy₃-67) (left) and (Dy₃-68) (right).	178
178	Disorder of solvent molecules (MeOH/MeCN) in (Dy₃-67).	178
179	Intermolecular interactions between solvent molecules and counterions forming pairs of two molecules of (Dy₃-67) in the stacks in the crystal structure.	179
180	Experimental powder pattern of compounds (Y₃-69), (Dy₃-67), (Tb₃-72) to (Tm₃-75) with simulation for (Dy₃-67) (left) and IR spectra (right).	180
181	Molecular structure of (Sm₃-70) (left) and (Eu₃-71) (right).	180
182	Molecular structure of (Dy₃-77) comparing the two enantiomers. Second hydrogen on the terminal ligands could not be refined due to the disordered MeOH ligands.	182
183	Packing along the crystallographic c (top left), a (top right) and b (bottom) axis for (Dy₃-77).	182
184	Scheme of (Dy₃-77) molecule in a), mirror image/enantiomer of it in b). b) turned 180° in the triangle plane in c) and a) turned 180° in triangle plane in d). Black lines represent Hphbovh ⁻ ligand, purple triangle Dy ₃ core and Cl/MeOH the three corresponding terminal ligands on that side.	183
185	Intermolecular interactions in (Dy₃-77). View along crystallographic c axis (top) and sideview (bottom) showing the 2D network and H-bonds involving	184

	the Cl ⁻ counterion which form the 3D network. Hydrogen bonds highlighted as orange dotted lines.	
186	Experimental and simulated powder pattern of compounds (Dy₃-77), (Gd₃-79) and (Tb₃-80) (left) and (Dy₃-78), (Tb₃-81) and (Ho₃-82) (right). The small hump at <i>ca</i> 25° is an artifact from the capillary which appears due to too low sample volume.	185
187	<i>In situ</i> produced ligands used in synthesis of (Dy₃-59), (Dy₃-67), (Dy₃-77) and (Dy₃-78) from left to right respectively.	186
188	$\chi_M T$ vs T (left) and $1/\chi_M$ vs T (right) for (Dy₃-59), (Dy₃-67), (Dy₃-77) and (Dy₃-78) measured at 0.1 T.	187
189	AC in-phase (left) and out-of-phase (right) data for (Dy₃-59) in a), (Dy₃-67) in b), (Dy₃-77) in c) and (Dy₃-78) in d). Red arrows highlighting first maximum.	189
190	M vs B plots for (Dy₃-59) in a), (Dy₃-67) in b), (Dy₃-77) in c) and (Dy₃-78) in d). Insets show the first derivative dM/dB highlighting the position of the maximum.	190
191	Anisotropy axes calculated with MAGELLAN ^[202] in cyan with top and side view for (Dy₃-59) a) and (Dy₃-77) b).	191
192	Magnetic main axis for each centre calculated from CASOCI for (Dy₃-59).	192
193	Zero field splitting of the three individual magnetic centres and <i>g</i> tensors in the ground state of (Dy₃-59). Centre 1, 2 and 3 correspond to Dy(1), Dy(2) and Dy(3) respectively.	193
194	Molecular structure of (Dy₃-83).	194
195	Packing of (Dy₃-83) along the crystallographic a (top left), b (top right) and c (bottom left) axis as well as in the [111] direction (bottom right).	195
196	First set of hydrogen bonds resulting in a 2D network (left) and second set connecting two inversion related Dy ₃ moieties (left).	196
197	Molecular structure of (Y₃-84).	197
198	Hydrogen bonds in (Y₃-84) forming chains throughout the lattice (orange dotted lines) (top left) with side view (top right) and interconnection between chains through hydrogen bonds which involve Cl ⁻ counterions (light blue dotted lines) (bottom) with side view (bottom right).	198
199	Packing of (Y₃-84) along the crystallographic a axis (top left) with a space filling model (top right) and along the crystallographic b (bottom right) and c (bottom left) axes.	199
200	Enantiopure aldehydes used for chiral Schiff base ligands in (Dy₃-86) and (Dy₃-87).	199
201	Molecular structure of (Dy₃-86).	201
202	Packing of (Dy₃-86) along the crystallographic a (top left) b (bottom right) and c (bottom left) axes. Additional side view of one of the stacks forming along the a axis (top right).	202
203	Molecular structure of (Dy₃-88) (left) with side view (right).	203
204	Packing of (Dy₃-88) along the crystallographic a (top) b (middle) and c (bottom) axes.	204
205	Hydrogen bonding in stacks along the crystallographic a axis in (Dy₃-88).	205
206	Experimental and simulated powder pattern of (Dy₃-88).	206

207	PXRD (left) and IR (right) comparing the products of the reaction between DyCl ₃ and the Schiff base ligands which use H ₂ pmbvh and H ₂ pcbv with (Dy₃-59).	207
208	Ligands with o-van unit preserved that yielded non-Dy ₃ triangle structures.	208
209	Molecular structure of (Dy₁₂-89) top (left) and side view (right).	209
210	MAGELLAN ^[202] analysis of (Dy₁₂-89).	209
211	Molecular structure of (Dy₁₂-90).	210
212	MAGELLAN ^[202] axes in (Dy₁₂-90) shown as cyan lines.	211
213	Molecular structure of (Dy₆-91).	212
214	MAGELLAN ^[202] axes for (Dy₆-91).	212
215	Diagram of o-vanillin base ligand modifications used to synthesise Dy ₃ clusters in this work.	219
216	Linked Dy ₃ triangles with anisotropy axes as green arrows (left) and microSQUID measurement at 0.03 K at different fields (right). Reprinted with permission from reference ^[156] [John Wiley & Sons] copyright [2012].	221
217	Dy ₆ consisting of two archetypal Dy ₃ s with one o-vanillin exchanged for a o-vanillinol.	222
218	Formation of bridging ligand species from NO ₂ -van educt (left) and molecular structure of Dy ₆ (right).	223
219	Halogen substituted o-vanillin and non-substituted o-vanillinol.	224
220	Molecular structure of (Dy₆-92) with sideview (right). Hydrogen atoms on the terminal water ligands were not refinable and disorder of Cl(4)/O(15) was omitted for clarity.	225
221	Molecular structure of (Dy₆-93) with side view (right).	225
222	Packing for (Dy₆-91) along the crystallographic a axis (top), b axis (bottom left) and c axis (bottom right).	226
223	Hydrogen bonding interactions in (Dy₆-92).	227
224	Simulated and experimental powder pattern for (Dy₆-93).	228
225	Structure of CN-van and CN-vandiol.	229
226	Molecular structure of (Dy₆-94) top (left) and side view (right). The disorder was omitted in favour of the water ligand with the higher occupancy (0.75).	230
227	Crystal packing of (Dy₆-94) along the crystallographic a (top), b (middle) and c (bottom) axes.	231
228	Hydrogen bonding network in (Dy₆-94). Hydrogen bonds are indicated by orange dotted lines.	232
229	Simulated and experimental powder patterns of (Dy₆-94).	232
230	$\chi_M T$ vs T (left) and $1/\chi_M$ vs T with Curie-Weiss fit (right) for (Dy₆-93) and (Dy₆-94) measured at 0.1 T.	233
231	AC in-phase (left) and out-of-phase (right) data measured at zero field for (Dy₆-93). Lines are a guide to the eye.	234
232	AC in-phase (left) and out-of-phase (right) data measured with an applied field of 1750 Oe for (Dy₆-94). Lines are a guide to the eye.	235
233	M vs B plot for (Dy₆-93) (left) and (Dy₆-94) (right).	235
234	First derivative of magnetisation curve for (Dy₆-93) (left) and (Dy₆-94) (right).	236
235	MAGELLAN ^[202] analysis for (Dy₆-92) (top), (Dy₆-93) (middle) and (Dy₆-94) (bottom). Out-of-plane axis for (Dy₆-94) highlighted.	237

13.2 Table of Tables

1	Multipoles and their respective symmetry towards parity (space inversion) and time reversal with (-) indicating odd (change of sign) and (+) even symmetry (no change of sign). ^[122]	29
2	Ligand combinations in compounds (Fe₂Dy₂-1)-(Fe₂Dy₂-7).	50
3	Intra- and Intermolecular hydrogen bonding in (Fe₂Dy₂-6) with donor, acceptor and H atoms as well as corresponding angles and distances.	58
4	Acceptor, Donor and H atoms involved in hydrogen bonding as well as the respective distances and angles of the formed H-bonds for (Fe₂Dy₂-7).	60
5	Relevant distances and angles for compounds (Fe₂Dy₂-1) to (Fe₂Dy₂-7).	60
6	Fitting parameters, ΔmOD , excitation wavelength and energy as well as probing wavelength for all measured Fe ₂ Dy ₂ samples.	67
7	Fitting parameters, ΔmOD , excitation wavelength/energy and probing wavelength for compounds (Fe₁₀Dy₁₀-13), (Fe₁₀Tm₁₀-14) and (Fe₁₀Tb₁₀-15).	86
8	Fitting parameters, ΔmOD , excitation wavelength/energy and probing wavelengths for compounds (Fe₁₀Dy₁₀-16) and (Fe₁₀Dy₁₀-17).	87
9	C and θ values from the Curie-Weiss fit for compounds (Dy₃-21), (Dy₃-22) and (Dy₃-36).	111
10	Angles and distances of halogen bonds in (Dy₃-36), (Dy₃-21) and (Dy₃-22) with the respective calculated energies.	121
11	<i>g</i> tensors and energy levels for the eight lowest Kramers' doublets in (Dy₃-49).	161
12	Euler angles extracted from evaluation of high field modelling for the magnetic torque measurements of (Dy₃-49).	170
13	C and θ values for (Dy₃-59), (Dy₃-67), (Dy₃-77) and (Dy₃-78).	187
14	Space groups and dominant intermolecular interactions of Dy ₃ triangles.	219
15	Switching fields of Dy ₃ triangles.	220

13.3 Crystallographic Tables

Compound	(Fe ₂ Dy ₂ -2)	(Fe ₂ Dy ₂ -3)
Empirical formula	C ₁₁₀ H ₁₅₀ Dy ₂ Fe ₂ N ₆ O ₂₄	C ₁₁₂ H ₁₅₄ Dy ₂ Fe ₂ N ₆ O ₂₄
Formula weight	2377.05	2405.10
Temperature/K	180	180
Crystal system	monoclinic	monoclinic
Space group	P2 ₁ /c	P2 ₁ /c
a/Å	18.1908(3)	18.2336(4)
b/Å	11.6823(2)	11.7217(2)
c/Å	26.6786(5)	26.6579(5)
α/°	90	90
β/°	96.325(1)	96.351(2)
γ/°	90	90
Volume/Å ³	5634.97(17)	5662.59(19)
Z	2	2
ρ _{calc} /cm ³	1.401	1.411
μ/mm ⁻¹	8.555	8.518
F(000)	2456.0	2488.0
Crystal size/mm ³	0.15 × 0.09 × 0.03	0.12 × 0.06 × 0.03
Radiation	1.3401270, 1.34 Kα (λ = 1.34143)	1.3401270, 1.34 Kα (λ = 1.34143)
2θ range for data collection/°	6.804 to 125.024	6.802 to 124.988
Index ranges	-22 ≤ h ≤ 24, -15 ≤ k ≤ 5, -35 ≤ l ≤ 34	-24 ≤ h ≤ 23, -15 ≤ k ≤ 4, -35 ≤ l ≤ 34
Reflections collected	93748	60260
Independent reflections	13531 [R _{int} = 0.0302, R _{sigma} = 0.0223]	13559 [R _{int} = 0.0353, R _{sigma} = 0.0367]
Data/restraints/parameters	13531/18/657	13559/18/711
Goodness-of-fit on F ²	1.028	1.025
Final R indexes [I ≥ 2σ (I)]	R ₁ = 0.0357, wR ₂ = 0.0888	R ₁ = 0.0362, wR ₂ = 0.0829
Final R indexes [all data]	R ₁ = 0.0453, wR ₂ = 0.0931	R ₁ = 0.0550, wR ₂ = 0.0892
Largest diff. peak/hole / e Å ⁻³	1.09/-0.68	0.52/-0.53

Compound	(Fe ₂ Dy ₂ -4)	(Fe ₂ Dy ₂ -5)
Empirical formula	C ₆₈ H ₇₄ Dy ₂ Fe ₂ N ₁₄ O ₃₂	C ₇₀ H ₈₀ Dy ₂ Fe ₂ N ₁₄ O ₃₃
Formula weight	2036.11	2082.18
Temperature/K	180	180
Crystal system	triclinic	triclinic
Space group	P-1	P-1
a/Å	11.1655(2)	11.1811(3)
b/Å	13.6744(3)	13.9483(3)
c/Å	13.8949(3)	14.0381(3)
α/°	99.397(2)	99.280(2)
β/°	90.892(2)	91.211(2)
γ/°	102.895(2)	103.695(2)
Volume/Å ³	2037.26(8)	2095.24(9)
Z	1	1
ρ _{calc} /g/cm ³	1.660	1.650
μ/mm ⁻¹	11.831	11.519
F(000)	1020.0	1046.0
Crystal size/mm ³	0.18 × 0.15 × 0.12	0.1 × 0.06 × 0.02
Radiation	1.3401270, 1.34 Kα (λ = 1.34143)	1.3401270, 1.34 Kα (λ = 1.34143)
2θ range for data collection/°	5.618 to 128.4	7.094 to 116.204
Index ranges	-10 ≤ h ≤ 14, -18 ≤ k ≤ 18, -18 ≤ l ≤ 14	-6 ≤ h ≤ 14, -17 ≤ k ≤ 17, -17 ≤ l ≤ 16
Reflections collected	28646	30596
Independent reflections	9911 [R _{int} = 0.0233, R _{sigma} = 0.0199]	8704 [R _{int} = 0.0357, R _{sigma} = 0.0429]
Data/restraints/parameters	9911/2/543	8704/11/581
Goodness-of-fit on F ²	1.035	1.051
Final R indexes [I ≥ 2σ (I)]	R ₁ = 0.0291, wR ₂ = 0.0777	R ₁ = 0.0379, wR ₂ = 0.0963
Final R indexes [all data]	R ₁ = 0.0311, wR ₂ = 0.0790	R ₁ = 0.0477, wR ₂ = 0.1001
Largest diff. peak/hole / e Å ⁻³	0.99/-1.04	0.68/-1.17

Compound	(Fe ₂ Dy ₂ -6)	(Fe ₂ Dy ₂ -7)
Empirical formula	C ₇₄ H ₈₆ Dy ₂ Fe ₂ N ₁₈ O ₃₂	C ₇₂ H ₇₄ Dy ₂ Fe ₂ N ₁₄ O ₂₀
Formula weight	2176.30	1892.15
Temperature/K	180	180
Crystal system	triclinic	monoclinic
Space group	P-1	P2 ₁ /c
a/Å	9.8714(4)	17.8696(3)
b/Å	14.8677(7)	23.5447(4)
c/Å	17.7903(8)	10.0219(2)
α/°	65.330(3)	90
β/°	78.694(4)	91.5030(10)
γ/°	85.857(4)	90
Volume/Å ³	2326.50(19)	4215.11(13)
Z	1	2
ρ _{calc} /g/cm ³	1.553	1.491
μ/mm ⁻¹	10.394	11.337
F(000)	1096.0	1896.0
Crystal size/mm ³	0.15 × 0.08 × 0.04	0.12 × 0.08 × 0.03
Radiation	1.3401270, 1.34 Kα (λ = 1.34143)	1.3401270, 1.34 Kα (λ = 1.34143)
2θ range for data collection/°	7.946 to 114.992	5.402 to 124.996
Index ranges	-12 ≤ h ≤ 6, -18 ≤ k ≤ 18, -22 ≤ l ≤ 21	-23 ≤ h ≤ 23, -30 ≤ k ≤ 31, -6 ≤ l ≤ 13
Reflections collected	22516	73123
Independent reflections	9517 [R _{int} = 0.0613, R _{sigma} = 0.0549]	10151 [R _{int} = 0.0397, R _{sigma} = 0.0226]
Data/restraints/parameters	9517/7/514	10151/28/471
Goodness-of-fit on F ²	1.014	1.037
Final R indexes [I ≥ 2σ (I)]	R ₁ = 0.0764, wR ₂ = 0.2015	R ₁ = 0.0391, wR ₂ = 0.1074
Final R indexes [all data]	R ₁ = 0.0924, wR ₂ = 0.2188	R ₁ = 0.0475, wR ₂ = 0.1134
Largest diff. peak/hole / e Å ⁻³	2.62/-1.69	1.52/-0.67

Compound	(Fe ₁₀ Dy ₁₀ -9)	(Dy ₃ -23)
Empirical formula	C ₁₉₆ H ₃₈₄ Dy ₁₀ Fe ₁₀ N ₄₈ O ₉₀	C _{27.7} H ₃₈ Br ₃ Cl ₄ Dy ₃ O _{16.3}
Formula weight	7036.99	1500.81
Temperature/K	180	180
Crystal system	triclinic	orthorhombic
Space group	P-1	Pna2 ₁
a/Å	20.4737(10)	22.0959(5)
b/Å	23.7752(10)	10.6536(3)
c/Å	31.4562(14)	18.1319(7)
α/°	84.633(4)	90
β/°	83.868(4)	90
γ/°	66.827(3)	90
Volume/Å ³	13973.7(11)	4268.3(2)
Z	2	4
ρ _{calc} /g/cm ³	1.672	2.336
μ/mm ⁻¹	17.023	8.320
F(000)	7072.0	2822.0
Crystal size/mm ³	0.1 × 0.053 × 0.03	0.21 × 0.157 × 0.08
Radiation	1.3401270, 1.34 Kα (λ = 1.34143)	Mo Kα (λ = 0.71073)
2θ range for data collection/°	6.16 to 71.356	3.686 to 58.254
Index ranges	-17 ≤ h ≤ 17, -20 ≤ k ≤ 20, -20 ≤ l ≤ 27	-17 ≤ h ≤ 30, -14 ≤ k ≤ 13, -24 ≤ l ≤ 24
Reflections collected	74720	47480
Independent reflections	18683 [R _{int} = 0.0940, R _{sigma} = 0.0757]	11461 [R _{int} = 0.0395, R _{sigma} = 0.0524]
Data/restraints/parameters	18683/32/1309	11461/17/516
Goodness-of-fit on F ²	1.030	0.979
Final R indexes [I ≥ 2σ (I)]	R ₁ = 0.0870, wR ₂ = 0.2289	R ₁ = 0.0356, wR ₂ = 0.0722
Final R indexes [all data]	R ₁ = 0.1338, wR ₂ = 0.2618	R ₁ = 0.0567, wR ₂ = 0.0766
Largest diff. peak/hole / e Å ⁻³	1.51/-0.71	2.36/-1.89

Compound	(Dy ₃ -36)	(Dy ₃ -39)
Empirical formula	C ₂₉ H ₄₁ Cl ₇ Dy ₃ O _{16.5}	C ₂₀₆ H ₂₁₁ Cl ₁₂ Dy ₁₂ N ₅₉ O ₁₀₅
Formula weight	1389.27	7568.73
Temperature/K	180	180
Crystal system	monoclinic	triclinic
Space group	P2 ₁ /c	P-1
a/Å	11.4253(2)	11.0794(4)
b/Å	19.6099(5)	18.1426(5)
c/Å	20.2093(4)	32.6032(8)
α/°	90	85.047(2)
β/°	102.133(2)	83.972(2)
γ/°	90	89.486(3)
Volume/Å ³	4426.73(17)	6493.0(3)
Z	4	1
ρ _{calc} /g/cm ³	2.085	1.936
μ/mm ⁻¹	28.890	3.635
F(000)	2656.0	3696.0
Crystal size/mm ³	0.18 × 0.16 × 0.14	0.08 × 0.07 × 0.06
Radiation	1.3401270, 1.34 Kα (λ = 1.34143)	Mo Kα (λ = 0.71073)
2θ range for data collection/°	5.524 to 118.6	3.234 to 52.744
Index ranges	-11 ≤ h ≤ 14, -25 ≤ k ≤ 24, -25 ≤ l ≤ 15	-13 ≤ h ≤ 13, -22 ≤ k ≤ 22, -40 ≤ l ≤ 31
Reflections collected	31866	70430
Independent reflections	9697 [R _{int} = 0.0711, R _{sigma} = 0.0563]	26301 [R _{int} = 0.0449, R _{sigma} = 0.0668]
Data/restraints/parameters	9697/17/550	26301/7/1558
Goodness-of-fit on F ²	1.094	1.022
Final R indexes [I ≥ 2σ (I)]	R ₁ = 0.0834, wR ₂ = 0.2362	R ₁ = 0.0516, wR ₂ = 0.1290
Final R indexes [all data]	R ₁ = 0.1001, wR ₂ = 0.2510	R ₁ = 0.0994, wR ₂ = 0.1490
Largest diff. peak/hole / e Å ⁻³	4.32/-3.64	2.88/-1.53

Compound	(Dy ₃ -40)	(Dy ₃ -49)
Empirical formula	C ₄₈ H ₄₉ Br ₃ Dy ₃ N ₁₃ O ₂₇	C ₅₀ H ₆₁ Cl ₄ Dy ₃ N ₆ O ₁₆
Formula weight	1967.23	1631.34
Temperature/K	180	180
Crystal system	triclinic	trigonal
Space group	P-1	R-3
a/Å	10.9121(6)	20.8488(6)
b/Å	18.1497(6)	20.8488(6)
c/Å	32.7416(11)	24.1538(10)
α/°	94.436(3)	90
β/°	94.134(4)	90
γ/°	90.258(4)	120
Volume/Å ³	6447.9(5)	9092.4(6)
Z	4	6
ρ _{calc} /g/cm ³	2.026	1.788
μ/mm ⁻¹	19.768	20.391
F(000)	3788.0	4782.0
Crystal size/mm ³	0.12 × 0.11 × 0.1	0.06 × 0.05 × 0.04
Radiation	1.3401270, 1.34 Kα (λ = 1.34143)	1.3401270, 1.34 Kα (λ = 1.34143)
2θ range for data collection/°	6.102 to 89.822	7.378 to 113.896
Index ranges	-11 ≤ h ≤ 11, -19 ≤ k ≤ 18, -25 ≤ l ≤ 34	-25 ≤ h ≤ 26, -26 ≤ k ≤ 19, -27 ≤ l ≤ 30
Reflections collected	69046	40048
Independent reflections	15494 [R _{int} = 0.0942, R _{sigma} = 0.0811]	4120 [R _{int} = 0.0999, R _{sigma} = 0.0461]
Data/restraints/parameters	15494/52/1543	4120/8/242
Goodness-of-fit on F ²	0.941	0.948
Final R indexes [I ≥ 2σ (I)]	R ₁ = 0.0628, wR ₂ = 0.1635	R ₁ = 0.0422, wR ₂ = 0.1073
Final R indexes [all data]	R ₁ = 0.1203, wR ₂ = 0.1898	R ₁ = 0.0707, wR ₂ = 0.1166
Largest diff. peak/hole / e Å ⁻³	2.02/-1.00	1.34/-0.68

Compound	(Eu ₃ -52)	(Yb ₃ -58)
Empirical formula	C _{56.5} H ₇₆ Cl ₄ Eu ₃ N ₁₀ O ₁₈	C ₄₉ H ₆₁ Cl ₄ N ₆ O ₁₇ Yb ₃
Formula weight	1780.95	1666.95
Temperature/K	273.15	180
Crystal system	triclinic	trigonal
Space group	P-1	R-3
a/Å	14.9392(4)	20.7055(19)
b/Å	15.1394(4)	20.7055(19)
c/Å	16.2101(4)	24.159(4)
α/°	84.009(2)	90
β/°	84.376(2)	90
γ/°	87.911(2)	120
Volume/Å ³	3627.40(16)	8970(2)
Z	2	6
ρ _{calc} /g/cm ³	1.631	1.852
μ/mm ⁻¹	2.778	16.715
F(000)	1772.0	4866.0
Crystal size/mm ³	0.16 × 0.14 × 0.12	? × ? × ?
Radiation	MoKα (λ = 0.71073)	1.3401270, 1.34 Kα (λ = 1.34143)
2θ range for data collection/°	2.538 to 50.7	9.154 to 104.984
Index ranges	-17 ≤ h ≤ 12, -18 ≤ k ≤ 18, -19 ≤ l ≤ 16	-24 ≤ h ≤ 16, -16 ≤ k ≤ 24, -25 ≤ l ≤ 28
Reflections collected	46546	16698
Independent reflections	13042 [R _{int} = 0.0568, R _{sigma} = 0.0582]	3439 [R _{int} = 0.1566, R _{sigma} = 0.2069]
Data/restraints/parameters	13042/9/677	3439/7/241
Goodness-of-fit on F ²	0.975	0.752
Final R indexes [I ≥ 2σ (I)]	R ₁ = 0.0670, wR ₂ = 0.1904	R ₁ = 0.0432, wR ₂ = 0.0735
Final R indexes [all data]	R ₁ = 0.1008, wR ₂ = 0.2083	R ₁ = 0.1500, wR ₂ = 0.0876
Largest diff. peak/hole / e Å ⁻³	2.14/-0.76	0.81/-0.62

Compound	(Dy ₃ -59)	(Dy ₃ -67)
Empirical formula	C ₅₈ H ₇₂ Cl ₄ Dy ₃ F ₃ N ₁₀ O ₁₇	C _{51.5} H _{56.5} Cl ₄ Dy ₃ F ₃ N _{7.5} O _{14.5}
Formula weight	1867.55	1698.84
Temperature/K	180	180
Crystal system	triclinic	trigonal
Space group	P-1	R-3
a/Å	15.0717(5)	20.8912(7)
b/Å	15.2548(5)	20.8912(7)
c/Å	16.0103(5)	23.7524(9)
α/°	83.666(2)	90
β/°	83.403(3)	90
γ/°	86.559(3)	120
Volume/Å ³	3630.1(2)	8977.7(7)
Z	2	6
ρ _{calc} /g/cm ³	1.709	1.885
μ/mm ⁻¹	17.137	20.713
F(000)	1838.0	4962.0
Crystal size/mm ³	0.05 × 0.043 × 0.04	0.13 × 0.11 × 0.08
Radiation	Ga-Kα (λ = 1.34143)	1.3401270, 1.34 Kα (λ = 1.34143)
2θ range for data collection/°	6.654 to 114.988	5.342 to 118.538
Index ranges	-18 ≤ h ≤ 17, -13 ≤ k ≤ 19, -20 ≤ l ≤ 19	-26 ≤ h ≤ 26, -26 ≤ k ≤ 25, -15 ≤ l ≤ 30
Reflections collected	45949	45840
Independent reflections	14673 [R _{int} = 0.0498, R _{sigma} = 0.0667]	4418 [R _{int} = 0.0765, R _{sigma} = 0.0373]
Data/restraints/parameters	14673/41/764	4418/15/290
Goodness-of-fit on F ²	0.913	0.983
Final R indexes [I ≥ 2σ (I)]	R ₁ = 0.0379, wR ₂ = 0.0827	R ₁ = 0.0328, wR ₂ = 0.0769
Final R indexes [all data]	R ₁ = 0.0702, wR ₂ = 0.0899	R ₁ = 0.0488, wR ₂ = 0.0810
Largest diff. peak/hole / e Å ⁻³	1.08/-0.70	0.84/-0.95

Compound	(Dy ₃ -68)	(Sm ₃ -70)
Empirical formula	C ₅₀ H ₅₈ Cl ₄ Dy ₃ F ₃ N ₆ O ₁₆	C ₅₁ H ₆₂ Cl ₄ F ₃ N ₆ O ₁₇ Sm ₃
Formula weight	1685.32	1680.91
Temperature/K	180	200
Crystal system	trigonal	trigonal
Space group	R-3	R-3
a/Å	20.930(11)	21.0499(3)
b/Å	20.930(11)	21.0499(3)
c/Å	24.167(14)	23.7164(5)
α/°	90	90
β/°	90	90
γ/°	120	120
Volume/Å ³	9168(11)	9100.8(3)
Z	6	6
ρ _{calc} /g/cm ³	1.831	1.840
μ/mm ⁻¹	20.285	16.614
F(000)	4926.0	4962.0
Crystal size/mm ³	0.04 × 0.037 × 0.03	0.15 × 0.117 × 0.1
Radiation	1.3401270, 1.34 Kα (λ = 1.34143)	1.3401270, 1.34 Kα (λ = 1.34143)
2θ range for data collection/°	5.302 to 113.93	7.308 to 128.258
Index ranges	-26 ≤ h ≤ 26, -26 ≤ k ≤ 22, -21 ≤ l ≤ 30	-27 ≤ h ≤ 9, -23 ≤ k ≤ 28, -31 ≤ l ≤ 31
Reflections collected	48860	52484
Independent reflections	4056 [R _{int} = 0.1102, R _{sigma} = 0.0608]	5091 [R _{int} = 0.0854, R _{sigma} = 0.0291]
Data/restraints/parameters	4056/3/245	5091/3/247
Goodness-of-fit on F ²	0.895	1.088
Final R indexes [I ≥ 2σ (I)]	R ₁ = 0.0367, wR ₂ = 0.0843	R ₁ = 0.0412, wR ₂ = 0.1159
Final R indexes [all data]	R ₁ = 0.0637, wR ₂ = 0.0913	R ₁ = 0.0438, wR ₂ = 0.1177
Largest diff. peak/hole / e Å ⁻³	0.90/-0.81	1.06/-1.16

Compound	(Eu ₃ -71)	(Dy ₃ -77)
Empirical formula	C ₅₁ H ₆₂ Cl ₄ Eu ₃ F ₃ N ₆ O ₁₇	C ₅₀ H ₇₇ Cl ₄ Dy ₃ N ₆ O ₂₇
Formula weight	1685.74	1823.47
Temperature/K	200	180.15
Crystal system	trigonal	trigonal
Space group	R-3	P-3c1
a/Å	21.0354(4)	20.8020(4)
b/Å	21.0354(4)	20.8020(4)
c/Å	23.7613(5)	21.1059(7)
α/°	90	90
β/°	90	90
γ/°	120	120
Volume/Å ³	9105.5(4)	7909.4(4)
Z	6	4
ρ _{calc} /g/cm ³	1.845	1.531
μ/mm ⁻¹	17.504	15.735
F(000)	4980.0	3604.0
Crystal size/mm ³	0.1 × 0.087 × 0.08	? × ? × ?
Radiation	1.3401270, 1.34 Kα (λ = 1.34143)	GaKα (λ = 1.34143)
2θ range for data collection/°	5.318 to 124.996	4.268 to 119.986
Index ranges	-24 ≤ h ≤ 27, -27 ≤ k ≤ 23, -31 ≤ l ≤ 23	-13 ≤ h ≤ 26, -26 ≤ k ≤ 18, -27 ≤ l ≤ 27
Reflections collected	40376	112502
Independent reflections	4904 [R _{int} = 0.0571, R _{sigma} = 0.0259]	5944 [R _{int} = 0.0941, R _{sigma} = 0.0372]
Data/restraints/parameters	4904/4/245	5944/22/256
Goodness-of-fit on F ²	1.106	1.110
Final R indexes [I ≥ 2σ (I)]	R ₁ = 0.0425, wR ₂ = 0.1155	R ₁ = 0.0707, wR ₂ = 0.1985
Final R indexes [all data]	R ₁ = 0.0475, wR ₂ = 0.1182	R ₁ = 0.1003, wR ₂ = 0.2100
Largest diff. peak/hole / e Å ⁻³	Largest diff. peak/hole / e Å ⁻³	1.88/-0.94

Compound	(Dy ₃ -78)	(Dy ₃ -83)
Empirical formula	C ₄₇ H ₅₅ Cl ₄ Dy ₃ N ₆ O ₁₉	C ₆₁ H ₈₁ Cl ₄ Dy ₃ N ₁₀ O ₂₀
Formula weight	1637.27	1903.65
Temperature/K	180	200
Crystal system	trigonal	triclinic
Space group	R-3	P-1
a/Å	21.024(3)	15.0259(6)
b/Å	21.024(3)	15.3737(7)
c/Å	24.342(4)	16.2504(8)
α/°	90	82.703(4)
β/°	90	82.217(3)
γ/°	120	86.929(3)
Volume/Å ³	9318(3)	3686.7(3)
Z	6	2
ρ _{calc} /g/cm ³	1.751	1.715
μ/mm ⁻¹	20.194	16.864
F(000)	4782.0	1886.0
Crystal size/mm ³	? × ? × ?	0.1 × 0.093 × 0.08
Radiation	GaKα (λ = 1.34143)	1.3401270, 1.34 Kα (λ = 1.34143)
2θ range for data collection/°	7.316 to 79.894	6.588 to 119.994
Index ranges	-20 ≤ h ≤ 20, -17 ≤ k ≤ 20, -22 ≤ l ≤ 23	-13 ≤ h ≤ 19, -19 ≤ k ≤ 19, -20 ≤ l ≤ 18
Reflections collected	16449	66423
Independent reflections	1904 [R _{int} = 0.1020, R _{sigma} = 0.0631]	16331 [R _{int} = 0.0801, R _{sigma} = 0.0917]
Data/restraints/parameters	1904/0/208	16331/128/712
Goodness-of-fit on F ²	0.899	0.917
Final R indexes [I ≥ 2σ (I)]	R ₁ = 0.0620, wR ₂ = 0.1570	R ₁ = 0.0502, wR ₂ = 0.1190
Final R indexes [all data]	R ₁ = 0.1075, wR ₂ = 0.1702	R ₁ = 0.1012, wR ₂ = 0.1336
Largest diff. peak/hole / e Å ⁻³	1.67/-0.46	1.55/-1.57

Compound	(Y ₃ -84)	(Dy ₃ -86)
Empirical formula	C ₆₆ H ₁₀₄ Cl ₄ N ₁₁ O ₂₄ Y ₃	C ₅₈ H ₉₅ Cl ₄ Dy ₃ N ₆ O ₂₂
Formula weight	1844.13	1857.69
Temperature/K	293(2)	293(2)
Crystal system	orthorhombic	triclinic
Space group	Pbca	P-1
a/Å	18.3608(7)	8.7462(6)
b/Å	29.355(2)	21.4411(12)
c/Å	31.9200(12)	22.5342(14)
α/°	90	115.254(4)
β/°	90	99.903(5)
γ/°	90	91.707(5)
Volume/Å ³	17204.4(16)	3739.6(4)
Z	8	2
ρ _{calc} /g/cm ³	1.424	1.650
μ/mm ⁻¹	2.934	16.614
F(000)	7632.0	1854.0
Crystal size/mm ³	? × ? × ?	? × ? × ?
Radiation	GaKα (λ = 1.34143)	GaKα (λ = 1.34143)
2θ range for data collection/°	5.238 to 89.816	7.71 to 89.996
Index ranges	-19 ≤ h ≤ 9, -30 ≤ k ≤ 30, -26 ≤ l ≤ 33	-9 ≤ h ≤ 7, -18 ≤ k ≤ 22, -23 ≤ l ≤ 23
Reflections collected	62512	23157
Independent reflections	10360 [R _{int} = 0.1867, R _{sigma} = 0.1262]	8978 [R _{int} = 0.1170, R _{sigma} = 0.2097]
Data/restraints/parameters	10360/87/763	8978/97/734
Goodness-of-fit on F ²	1.054	0.873
Final R indexes [I ≥ 2σ (I)]	R ₁ = 0.1076, wR ₂ = 0.2896	R ₁ = 0.0695, wR ₂ = 0.1481
Final R indexes [all data]	R ₁ = 0.1693, wR ₂ = 0.3217	R ₁ = 0.1720, wR ₂ = 0.1790
Largest diff. peak/hole / e Å ⁻³	1.71/-0.65	1.34/-0.86

Compound	(Dy ₃ -87)	(Dy ₃ -88)
Empirical formula	C _{49.75} H ₂₆ Cl ₄ Dy ₃ N ₆ O _{19.5}	C ₅₀ H ₄₈ Br ₃ Cl ₄ Dy ₃ N ₆ O ₁₆
Formula weight	1649.06	1857.97
Temperature/K	293(2)	180
Crystal system	triclinic	triclinic
Space group	P-1	P-1
a/Å	20.3879(3)	7.2837(2)
b/Å	20.4390(3)	17.4822(5)
c/Å	22.3082(4)	25.7173(7)
α/°	104.7710(10)	77.244(2)
β/°	99.3750(10)	88.116(2)
γ/°	119.9030(10)	86.095(2)
Volume/Å ³	7310.9(2)	3185.94(16)
Z	4	2
ρ _{calc} /g/cm ³	1.498	1.937
μ/mm ⁻¹	3.242	20.874
F(000)	3154.0	1778.0
Crystal size/mm ³	? × ? × ?	0.08 × 0.04 × 0.02
Radiation	MoKα (λ = 0.71073)	1.3401270, 1.34 Kα (λ = 1.34143)
2θ range for data collection/°	2.308 to 52.046	6.774 to 116.206
Index ranges	-25 ≤ h ≤ 24, -25 ≤ k ≤ 25, -19 ≤ l ≤ 27	-5 ≤ h ≤ 9, -21 ≤ k ≤ 22, -31 ≤ l ≤ 32
Reflections collected	208914	52277
Independent reflections	28676 [R _{int} = 0.1049, R _{sigma} = 0.0708]	13373 [R _{int} = 0.0632, R _{sigma} = 0.0807]
Data/restraints/parameters	28676/95/1351	13373/19/752
Goodness-of-fit on F ²	1.036	0.873
Final R indexes [I ≥ 2σ (I)]	R ₁ = 0.0767, wR ₂ = 0.2311	R ₁ = 0.0373, wR ₂ = 0.0747
Final R indexes [all data]	R ₁ = 0.1197, wR ₂ = 0.2512	R ₁ = 0.0699, wR ₂ = 0.0801
Largest diff. peak/hole / e Å ⁻³	2.22/-1.20	0.86/-0.93

Compound	(Dy ₁₂ -89)	(Dy ₁₂ -90)
Empirical formula	C ₁₃₆ H ₁₈₂ Cl ₁₄ Dy ₁₂ O ₆₆ N ₁₆	C ₂₁₅ H ₃₂₂ Cl ₁₈ Dy ₁₂ N ₆₈ O ₆₁
Formula weight	5543.27	7423.49
Temperature/K	180.00	180.15
Crystal system	trigonal	cubic
Space group	R-3	F432
a/Å	19.1830(2)	38.4638(4)
b/Å	19.1830(2)	38.4638(4)
c/Å	84.7787(11)	38.4638(4)
α/°	90	90
β/°	90	90
γ/°	120	90
Volume/Å ³	27017.8(7)	56905.8(18)
Z	6	8
ρ _{calc} /g/cm ³	2.044	1.733
μ/mm ⁻¹	27.172	17.566
F(000)	16008.0	29392.0
Crystal size/mm ³	? × ? × ?	0.04 × 0.037 × 0.03
Radiation	GaKα (λ = 1.34143)	GaKα (λ = 1.34143)
2θ range for data collection/°	4.716 to 128.162	5.654 to 109.86
Index ranges	-25 ≤ h ≤ 25, -25 ≤ k ≤ 25, -108 ≤ l ≤ 110	-46 ≤ h ≤ 46, -46 ≤ k ≤ 46, -46 ≤ l ≤ 17
Reflections collected	46369	188403
Independent reflections	14020 [R _{int} = 0.0626, R _{sigma} = 0.0597]	4559 [R _{int} = 0.0903, R _{sigma} = 0.0242]
Data/restraints/parameters	14020/0/575	4559/4/191
Goodness-of-fit on F ²	1.202	1.051
Final R indexes [I ≥ 2σ (I)]	R ₁ = 0.1099, wR ₂ = 0.3110	R ₁ = 0.0501, wR ₂ = 0.1450
Final R indexes [all data]	R ₁ = 0.1364, wR ₂ = 0.3352	R ₁ = 0.0639, wR ₂ = 0.1580
Largest diff. peak/hole / e Å ⁻³	7.35/-2.33	1.58/-0.96

Compound	(Dy ₆ -91)	(Dy ₆ -92)
Empirical formula	C ₁₁₀ H ₁₂₂ Cl ₁₇ Dy ₆ N ₂₂ O ₄₀	C ₅₂ H ₆₂ Cl ₁₀ Dy ₆ O ₃₄
Formula weight	3969.94	2560.51
Temperature/K	180	180
Crystal system	triclinic	monoclinic
Space group	P-1	P2 ₁ /n
a/Å	14.4425(7)	15.8001(7)
b/Å	14.8676(7)	12.9641(4)
c/Å	18.1977(8)	19.2874(8)
α/°	72.450(3)	90
β/°	71.319(3)	99.199(3)
γ/°	88.836(4)	90
Volume/Å ³	3516.7(3)	3899.9(3)
Z	1	2
ρ _{calc} /g/cm ³	1.875	2.180
μ/mm ⁻¹	18.730	6.099
F(000)	1941.0	2424.0
Crystal size/mm ³	0.22 × 0.18 × 0.14	0.12 × 0.1 × 0.08
Radiation	1.3401270, 1.34 Kα (λ = 1.34143)	Mo Kα (λ = 0.71073)
2θ range for data collection/°	7.502 to 121.154	3.63 to 52.742
Index ranges	-18 ≤ h ≤ 14, -19 ≤ k ≤ 18, -23 ≤ l ≤ 13	-17 ≤ h ≤ 19, -15 ≤ k ≤ 16, -24 ≤ l ≤ 19
Reflections collected	44918	21876
Independent reflections	15747 [R _{int} = 0.0670, R _{sigma} = 0.0608]	7907 [R _{int} = 0.0403, R _{sigma} = 0.0521]
Data/restraints/parameters	15747/22/786	7907/2/445
Goodness-of-fit on F ²	1.030	0.973
Final R indexes [I ≥ 2σ (I)]	R ₁ = 0.0719, wR ₂ = 0.1991	R ₁ = 0.0475, wR ₂ = 0.1216
Final R indexes [all data]	R ₁ = 0.0940, wR ₂ = 0.2193	R ₁ = 0.0773, wR ₂ = 0.1331
Largest diff. peak/hole / e Å ⁻³	2.60/-1.81	1.58/-1.23

Compound	(Dy ₆ -93)	(Dy ₆ -94)
Empirical formula	C ₄₈ H ₆₈ Br ₄ Cl ₆ Dy ₆ O ₃₄	C ₅₆ H ₆₆ Cl ₆ Dy ₆ N ₆ O ₃₄
Formula weight	2696.36	2554.84
Temperature/K	180	273.15
Crystal system	monoclinic	triclinic
Space group	P2 ₁ /n	P-1
a/Å	15.7337(9)	11.2279(4)
b/Å	12.7882(5)	12.1449(5)
c/Å	19.3390(10)	15.7208(7)
α/°	90	70.586(3)
β/°	100.597(4)	89.851(3)
γ/°	90	81.035(3)
Volume/Å ³	3824.8(3)	1994.34(15)
Z	2	1
ρ _{calc} /g/cm ³	2.341	2.127
μ/mm ⁻¹	33.315	5.835
F(000)	2532.0	1214.0
Crystal size/mm ³	0.12 × 0.1 × 0.08	0.03 × 0.03 × 0.02
Radiation	1.3401270, 1.34 Kα (λ = 1.34143)	MoKα (λ = 0.71073)
2θ range for data collection/°	7.248 to 107.814	3.604 to 50.7
Index ranges	-18 ≤ h ≤ 15, -9 ≤ k ≤ 15, -21 ≤ l ≤ 23	-7 ≤ h ≤ 13, -14 ≤ k ≤ 14, -18 ≤ l ≤ 18
Reflections collected	24513	21042
Independent reflections	6916 [R _{int} = 0.0563, R _{sigma} = 0.0458]	7208 [R _{int} = 0.0399, R _{sigma} = 0.0564]
Data/restraints/parameters	6916/15/444	7208/27/480
Goodness-of-fit on F ²	1.004	1.025
Final R indexes [I ≥ 2σ (I)]	R ₁ = 0.0856, wR ₂ = 0.2311	R ₁ = 0.0570, wR ₂ = 0.1410
Final R indexes [all data]	R ₁ = 0.1249, wR ₂ = 0.2706	R ₁ = 0.0924, wR ₂ = 0.1540
Largest diff. peak/hole / e Å ⁻³	2.88/-0.91	2.79/-1.41